Proceedings of the Indian Academy of Sciences
(Earth and Planetary Sciences)

Volume 94, 1985

CONTENTS

Tracing quartz through the environment *D Lal and J R Arnold* 1

Comparison of electron density models with incoherent scatter radar observations at the equator *B T Vikram Kumar and P B Rao* 7

Hydrography and circulation off the Antarctica in the Indian Ocean region *G S Sharma and Basil Mathew* 13

Quasi-biennial oscillation in geomagnetic disturbance field *G K Rangarajan* 29

Vertical component MAGSAT anomalies and Indian tectonic boundaries *J G Negi, P K Agrawal and N K Thakur* 35

The Mannapra syenite, Central Kerala, India: Geochemistry, petrogenesis and bearing on anorogenic magmatism *M Santosh and K G Thara* 43

Petrology of thermally metamorphosed pelitic rocks in the Champawat Area, Kumaun Himalaya *Brijraj K Das* 57

Analysis of gravity gradients over a thin infinite sheet *G D J Sivakumar Sinha and H V Ram Babu* 71

Detection of large scale electron density irregularities during IPS observations at 103 MHz *S K Alurkar, H O Vats, R V Bhonsle and A K Sharma* 77

Basal flow rate of Changme-Khangpu glacier, Sikkim Himalaya based on ^{32}Si and ^{210}Pb chronology *V N Nijampurkar* 83

An analytical technique for rapid determination of surface rock density *G Ramadass, S M Varaprasada Rao and M S Vijaya Raghava* 91

Preliminary studies on the geochemistry of the Cauvery river basin *V Subramanian, L Van t'Dack and R Van Grieken* 99

Anomaly map of Z component of the Indian sub-continent from magnetic satellite data *M G Arur, P S Bains and Jeevan Lal* 111

Summer cooling of the Arabian Sea—a review *J S Sastry and V Ramesh Babu* 117

Monthly-mean wind stress along the coast of the north Indian Ocean *Satish R Shetye, S Satheesh Chandra Shenoi, M K Antony and V Krishna Kumar* 129

Global temperature changes: relative importance of greenhouse constituents of the atmosphere as calculated with a 1-d radiative-convective model *M Lal and K C S Rao* 139

Interaction of monsoon with northern hemisphere mid-latitude circulation *S T Awade, M Y Totagi and S M Bawiskar* 147

Short range prediction with a multi-level primitive equation model *S S Singh* 159

Correction of the paper "A study of meteorite falls" *Frans E Wickman and Carl D Palmer* 185

Interannual and long-term variability of the summer monsoon and its possible link with northern hemispheric surface air temperature *R K Verma, K Subramaniam and S S Dugam* 187

Relationship between all-India summer monsoon rainfall and southern oscillation/eastern equatorial pacific sea surface temperature *D A Mooley, B Parthasarathy and N A Sontakke* 199

Global features of upper-tropospheric zonal wind and thermal fields during anomalous monsoon situations *L S Hingane, S D Patil and K Rupa Kumar* 211

The sensitivity of the northern hemisphere summer mean meridional circulation to changes in the large scale eddy forcing *B N Goswami* 219

Remote sensing of atmospheric water vapour from Bhaskara II SAMIR data and its comparison with NOAA-7 water vapour data *P N Pathak, B S Gohil and A Sarkar* 237

A study on the sensitivity of the radar scattering coefficient to oceanic winds *Abhijit Sarkar and Raj Kumar* 249

HF doppler observations on the occurrence of equatorial spread-F *B T Vikram Kumar, P Velayudhan Nair and P B Rao* 261

Transient electromagnetic response due to a pair of horizontal conducting sheets in a loop field *R Nagendra, I B Ramaprasada Rao and Satyanarayan Kabra* 269

Emission spectrographic estimation of gold *K C Joseph* 279

Oxygen and hydrogen isotopic ratios in groundwaters and river waters from India *S K Bhattacharya, S K Gupta and R V Krishnamurthy* 283

Geochemistry of bauxites of Belgaum (Karnataka) and Yeracaud (Tamil Nadu) areas *J N Pattan and S M Appangoudar* 297

The Purimetla gabbros, Prakasam District, Andhra Pradesh, India *J Ratnakar and C Leelanandam* 305

Framboidal pyrite from Mussoorie phosphorite and its geological implication *S C Tripathi* 315

A study of the monsoonal beach processes around Alleppey, Kerala *N P Kurian, T S Shahul Hameed and M Baba* 323

Subject Index 333

Author Index 338

Tracing quartz through the environment

D LAL* and J R ARNOLD**

*Scripps Institute of Oceanography, La Jolla, CA 92093, USA

Also Physical Research Laboratory, Ahmedabad 380 009, India

**Calif. Space Institute, A-021, University of California, San Diego, La Jolla, CA 92093, USA

MS received 24 December 1984

Abstract. Quartz, SiO_2, a pure mineral with tight crystal structure, is widespread in rocks and soil. Cosmic rays produce ^{10}Be ($t_{1/2} = 1{\cdot}5 \times 10^6$ yr) and ^{26}Al ($t_{1/2} = 7{\cdot}05 \times 10^5$ yr) in quartz exposed at or near the earth's surface. The use of accelerator mass spectrometry permits measurement of these nuclides in samples exposed at sea level for typical periods. *In situ* production makes interpretation relatively straightforward. Potential applications include age determination, measurement of erosion and deposition rates, and use as a tracer for continental weathering processes.

Keywords. Quartz; cosmic ray produced isotopes; erosion; accelerator mass spectroscopy.

The development of accelerator mass spectrometry (AMS) has allowed measurement of ^{10}Be in natural materials (Brown 1984). The ^{10}Be atoms investigated so far are those mainly produced in the atmosphere and admixed into these materials. Monaghan *et al* (1983) and Pavich *et al* (1984) have shown the value of this technique for soil deposition studies, but the processes involved are complex. *In situ* production (Jha and Lal 1981; Yiou *et al* 1984), offers an attractive alternative for such studies. We discuss here the *in situ* production in quartz, which seems to offer several advantages.

Quartz, the common form of SiO_2, is an ideal target material for production of two longlived isotopes, ^{10}Be and ^{26}Al. Impurities, including Al, are usually present at or below a few hundred ppm. The intact crystal is impermeable to water and ions. It is abundant and easy to isolate. The two isotopes, ^{10}Be and ^{26}Al, are produced at rates of the order of 10 atoms/gram year at sea level, permitting a measurement in about 10 grams of quartz exposed for 10^4 years.

The production rates of ^{10}Be and ^{26}Al in diverse target materials can be estimated fairly accurately (Jha and Lal 1981; Lal and Peters 1967). For a more comprehensive recent treatment, see Lal *et al* (1985).

The nucleonic isotope production dominates in any material exposed at altitudes above sea level. The energy spectrum of nucleons at any given latitude remains invariant in the atmosphere at depths exceeding 200 g cm^{-2}, the so-called nuclear cascade equilibrium region. The depth variation of production within a rock exposed in the equilibrium region will closely follow the absorption mean free path, observed in the atmosphere. Its value varies from 150 to 170 g cm^{-2}, decreasing with increasing latitude, reaching a constant value for 50°–90° latitudes. The estimated production rates of ^{10}Be and ^{26}Al in quartz are given in table 1 for the equilibrium region at high latitudes. For lower geomagnetic latitudes, production rates in table 1 can be scaled using the latitude–altitude variation given by Lal and Peters (1967) in figure 4 for ^{10}Be and other isotopes.

Table 1. *In situ* cosmic ray production rates of ^{10}Be and ^{26}Al in quartz, at geomagnetic latitudes 50°–90°

		Atoms/g $SiO_2 \cdot$yr			
Altitude (km)	Atmospheric pressure, p (g cm^{-2})	Nucleon spallation ^{10}Be	Nucleon spallation ^{26}Al	Negative mu-meson capture* ^{26}Al	^{10}Be/^{26}Al ratio at production
0 (Sea level)	1030	6·5	21	6·5	0·236
1	925	15	48	10·0	0·258
3	730	63	210	22·0	0·271
5	550	2×10^2	670	46·0	0·279

*Negative mu-meson capture in SiO_2 does not lead to production of ^{10}Be. At depths exceeding 1000 g cm^{-2} below sea level ^{10}Be production due to nuclear interactions of fast mu-mesons becomes dominant (Jha and Lal 1981; Lal and Peters 1967). The production rate of ^{26}Al due to negative mu-meson capture is based on procedures discussed earlier (Jha and Lal 1981; Winsberg 1956; Hampel *et al* 1975), that for nuclear spallation is based on published cross sections (Tobailem 1981) for formation of ^{26}Al from proton bombardment of ^{28}Si and the nucleon energy spectrum in the atmosphere (Lal and Peters 1967).

The slow mu-meson component attenuates with a larger absorption mean free path, $\Lambda = 245$ g cm^{-2}. Capture of negative mu-mesons produces ^{26}Al ($\mu^- + {}^{28}\mathrm{Si} \rightarrow 2\mathrm{n} + {}^{26}\mathrm{Al}$). ^{10}Be is not produced by negative mu-meson capture in oxygen, but fast mu-meson coulombic interactions can produce ^{10}Be from oxygen. At depths exceeding 1000 g cm^{-2} below sea-level, production of ^{10}Be and ^{26}Al from fast meson interactions in SiO_2 becomes dominant (Jha and Lal 1981). Nucleonic production becomes unimportant at these depths. We have considered only cosmogenic production since radiogenic alphas and neutrons do not contribute to production of ^{10}Be or ^{26}Al in quartz.

For atmospheric depths, (200–1030) g cm^{-2}, isotope production rates due to capture of negative mesons can be estimated from values in table 1 using an absorption mean free path of 245 g cm^{-2}. At depths below sea level, the same exponent continues up to 600 g cm^{-2}, the absorption mean free path becomes larger at greater depths, but fast mu-meson interactions dominate.

Calculations in table 1 are based on the procedures developed earlier (Lal and Peters 1967). The energy spectrum of nucleons in the troposphere is known fairly well. Primary uncertainty arises in particular due to non-availability of the neutron excitation function for formation of ^{10}Be from oxygen; most of the ^{10}Be production in the troposphere is expected to occur due to neutron interactions. However, based on disintegrations in Si is calculated to be 0·5 %.

Our calculations differ widely from those published earlier by Yokoyama *et al* (1977), for both ^{10}Be and ^{26}Al. Comparing our values with those for granite (SiO_2 = 73 %), we find that their production rates are lower and higher by factors of about 3 and 2 for ^{10}Be and ^{26}Al respectively. They estimate a value of 0·048 for the ^{10}Be/^{26}Al ratio at production (due to nucleons), which has to be compared with our value of 0·31.

Comparing our production estimates with the values available in literature, we note that Yiou *et al* (1984) found the lowest ^{10}Be/^{26}Al ratio in Libyan desert glass, 0·37. Two other glasses studied, Australites and Darwin glass, had values of $> 4{\cdot}0$ and 1·37 respectively. Our estimated ratio at production corresponds to a minimum value of 0·24 for the ^{10}Be/^{26}Al ratio, which is not inconsistent with the value observed for Libyan glass. Our calculated ratio at production is also close to that expected from observed values in meteorites.

The calculated isotope ratio ^{10}Be/^{26}Al at production in SiO_2 is given in table 1; the calculation is uncertain by 30 % or more. Still the ratio is expected to remain constant at production within rather narrow limits, ± 10 %, for a variety of exposure conditions, as long as the sum of atmospheric depth and the depth within the rock does not exceed 1300 $\mathrm{g\,cm^{-2}}$. This postulate can of course be verified experimentally. Davis and Schaeffer (1955) measured ^{36}Cl in a rock sample bearing glacial scour marks, and hence not appreciably eroded since post-glacial exposure. Such samples are suitable for testing the variation with depth of ^{26}Al and ^{10}Be production.

Because the production ratio is or can be known, one important application is as a dating method. The applicable half-life, for an exposure in fixed geometry, is calculated from $\lambda = \lambda_{\mathrm{Al}} - \lambda_{\mathrm{Be}}$. This corresponds to a half-life of $1{\cdot}3 \times 10^6$ years. The expected error is defined by the predictability of the ratio at the end of bombardment, and the measurement error. A precision of 3×10^5 years or better seems attainable.

One can consider a variety of models for *in situ* exposure of quartz grains, involving cosmic ray exposure prior to their being dislodged from the host rock, and subsequent irradiation during transport through the fluvial systems or by wind and burial. Trajectories will be complex, but two elements are important, and common to most models: (i) rock weathering and release of quartz grains; (ii) burial of quartz grains by sedimentation.

Rock weathering leads to an *in situ* production dependent on altitude and erosion rate. The expected concentration of an isotope i in a rock at atmospheric pressure $p(\mathrm{g\,cm^{-2}})$, in a sample at depth x (cm) from surface, $N_i(p, x)$ is given by:

$$N_i(p, x) = P_i(1030) \exp\left[(1030 - p - \rho x)/\Lambda\right] \cdot \frac{1}{\lambda + \rho\varepsilon/\Lambda}, \tag{1}$$

where P_i (1030) is the isotope production rate in the surface of a rock exposed at sea level and ρ is the density of the rock. Equation (1) assumes a steady state erosion rate of $\varepsilon\ \mathrm{cm\,yr^{-1}}$. The characteristic time of irradiation in an eroding rock is $\Lambda/(\Lambda\lambda + \rho\varepsilon)$. Model calculations for a range of erosion rates are given in table 2.

The other case of irradiation is that of a grain buried by material sedimenting on it. Any initial amount $N_i(0)$, in the grain will then decay exponentially. The total amount including the *in situ* production in a grain buried to a depth x by a constantly

Table 2. Expected ^{10}Be and ^{26}Al concentrations in a rock exposed at sea level, eroding at a steady rate.

Erosion rate (cm yr^{-1})	^{10}Be concentration (atoms/g)	Effective time or irradiation for ^{10}Be (yrs)	Ratio ^{10}Be/^{26}Al
10^{-5}	$9{\cdot}7 \times 10^{6}$	$1{\cdot}5 \times 10^{6}$	0·46
10^{-4}	$2{\cdot}3 \times 10^{6}$	$3{\cdot}6 \times 10^{5}$	0·31
10^{-3}	$2{\cdot}7 \times 10^{5}$	$4{\cdot}2 \times 10^{4}$	0·26
10^{-2}	$2{\cdot}8 \times 10^{4}$	$4{\cdot}3 \times 10^{3}$	0·26
10^{-1}	$2{\cdot}8 \times 10^{3}$	$4{\cdot}3 \times 10^{2}$	0·26

accumulating sediment $N_i(p, x)$, is given by:

$$N_i(p, x) = N_i(0) \exp(-\lambda x/s) + \frac{P_i(1030) \exp[(1030 - p)/\Lambda]}{\rho s/\Lambda - \lambda} \cdot \times [\exp(-\lambda x/s) - \exp(-\rho x/\lambda)], \tag{2}$$

where the rate of sedimentation is s cm · yr^{-1}.

We will now consider some direct applications of studies of ^{10}Be and ^{26}Al activities in quartz. A clear cut case is the deposition of aeolian quartz in deep sea or lake sediments. In this case there is essentially no production within the sediment and the age of the sediment is then given by $1{\cdot}9 \times 10^{6} \ln(R_0/R_m)$, where R_0 is the ^{10}Be/^{26}Al ratio at production and R_m that measured. From tables 1 and 2, it can be seen that the initial ratio is expected to be close to 0·26 for grains released in the weathering process. Continental erosion rates range upward from about 10^{-4} cm yr^{-1} to much higher values.

Except for the very slowest erosion and deposition rates (10^{-4} cm/yr^{-1} or less), and for loose sand deposits which may have quite complex histories, a complete erosion-deposition cycle will be completed in a time short compared to the effective half-life. Thus the ratio after deposition should be predictable. Studies of ^{10}Be/^{26}Al ratios in quartz in sediments promise to yield ages of the sediments, *i.e.* the time since the episodes of exposure at or near the surface.

In the unusual case where either erosion or deposition is very slow and steady, the ratio will shift as the duration of bombardment becomes comparable to the half-life. Table 2 illustrates this. For desert or beach sands, many episodes of erosion, transport, and deposition may take place; the ratio will have some value between that for production in the original rock (altered by decay) and that for the present day. Because the original production was (usually) at a higher altitude, this episode may weigh more heavily.

Individual source regions for sediments can be expected to have distinctive ^{10}Be and ^{26}Al content, depending on altitude and exposure history. These may serve as markers, assisting in the understanding of ocean and lake sediments, and the climatic regimes in which they formed. Identification and dating both should be possible in favourable cases.

The depositional history of any soil sequence or sedimentary rock can be studied in great detail by measuring ^{10}Be and ^{26}Al in quartz grains as a function of depth. A monotonic change will indicate a continuous sequence. Interruptions can be easily seen. (Supplementary information can be obtained from the study of chemically adsorbed ^{10}Be on soil grains. Note that essentially no ^{26}Al is expected from this source.)

Exposure dating of strata or horizons on a million year time scale using quartz, may have a wide range of applications, since the half-life falls between ^{14}C and the longlived radioactive clocks. While the difficulties can only be understood by experimental study, the broad distribution of quartz and the expected constancy of the production ratio suggest that the method has great promise. Early man sites represent one intriguing possibility (Curtis 1981). If a present surface horizon to be dated can be traced to a present depth of 5–10 meters, quartz samples may be suitable for dating the most important period of original surface exposure.

On other planetary bodies, where alteration processes are less active, a wider range of minerals can be used. This has already been demonstrated in lunar samples (Nishiizumi *et al* 1979).

Acknowledgements

We thank Gustaf Arrhenius, Louis Brown, Albert Engel, Miriam Kastner, S. Krishnaswami, Roy Middleton, Douglas Macdougall, Kanihiko Nishiizumi and E. L. Winterer for valuable discussions on the problem.

References

Brown L 1984 *Annu. Rev. Earth Planet. Sci.* **12** 39

Brown L, Sacks I S, Tera F, Klein J and Middleton R 1981 *Earth Planet. Sci. Lett.* **55** 370

Curtis G H 1981 *Phil. Trans. R. Soc. London* **B292** 7

Davis R and Schaeffer O A 1955 *Ann. N. Y. Acad. Sci.* **62** 105

Hampel W, Takagi J, Sakamoto K and Tanaka S 1975 *J. Geophys. Res.* **80** 3757

Jha R and Lal D 1981 *Proc. Second Symp. on Natural Radiation Environment* (eds) K G Vohra, K C Pillai, U C Mishra and S Sadasivan (New Delhi: Wiley Eastern Press) p. 629

Lal D 1984 in Abstracts Workshop on Cosmogenic Nuclides, Los Alamos National Laboratory, (Lunar and Planetary Science Institute, Houston TX)

Lal D, Nishiizumi K and Arnold J R 1985 (in preparation)

Lal D and Peters B 1967 in *Handbuch der Physik*, *XLVI*/2 (Berlin: Springer Verlag) p. 551

Monaghan M C, Krishnaswami S and Thomas J H 1983 *Earth Planet. Sci. Lett.* **65** 51

Nishiizumi K, Imamura M, Kohl C P, Murrell M T, Arnold J R and Russ, G P III 1979 *Earth Planet. Sci. Lett.* **44** 409

Pavich M J, Brown L, Klein J and Middleton R 1984 *Earth Planet. Sci. Lett.* **68** 198

Tobailem J 1981 Note CEA-N-1466 (5) Commissanat a' l' Energie Atomique, Centre D' Etudes Nucleaires de Saclay, 91191, Gif Sur Yvette, France

Winsberg L 1956 *Geochim. Cosmochim. Acta* **9** 183

Yiou F, Raisbeck G M, Klein J and Middleton R 1984 *J. Non-Cryst. Solids* **67** 503

Yokoyama Y, Reyss J L and Guichard F 1977 *Earth Planet. Sci. Lett.* **36** 44

Proc. Indian Acad. Sci. (Earth Planet. Sci.), Vol. 94, No. 1, March 1985, pp. 7–11.
© Printed in India.

Comparison of electron density models with incoherent scatter radar observations at the equator

B T VIKRAM KUMAR and P B RAO

Department of Physics, University of Kerala, Kariavattom, Trivandrum 695 581, India

MS received 18 May 1984; revised 11 September 1984

Abstract. This paper points out certain discrepancies when the incoherent scatter radar observations at Jicamarca and the electron density models, (the Bent and IRI) were compared. In all cases the bottomside semi-thickness of the observed profile was significantly greater than that of both Bent and IRI models. The decay constants associated with the topside ionosphere for the observed profiles were generally greater than that of the two models, the difference being more pronounced in the IRI model. The results call for a revision of the models so that they accurately represent the electron density distribution at the equator.

Keywords. Electron density model; incoherent scatter radar; equator; Bent; International Reference Ionosphere.

1. Introduction

Ionospheric models are essential not only for the study of various geophysical problems connected with the upper atmosphere but also for applications like high frequency propagation predictions and evaluation of trans-ionospheric effects on radar and satellite communications. A number of models including the International Reference Ionosphere (IRI) have been developed for many of the above applications (e.g. Nisbet 1971; Ramakrishnan and Rawer 1972; Bent *et al* 1975; Somayajulu and Ghosh 1979). Some of these provide electron density profiles for any geographic location, local time, season and solar activity. It is important that these models are tested for accuracy by comparing them with observational profiles before they are put to use. This, however, has not been done in a systematic manner for the equatorial latitudes.

In this paper, electron density profiles based on several years' incoherent scatter radar data from Jicamarca (11·95°S, 76·87°W) were compared with the two widely used models, the Bent and IRI models. The comparison highlights the significant differences between the observational profiles and the empirical models and indicates the need for effecting appropriate corrections.

2. Description of the models and the observed profiles

Bent model (Bent *et al* 1975) is an empirical model derived by using a large number of bottomside and topside soundings as well as satellite-based electron density probe data. The profile is constructed on the basis of the best fit analytical expressions. For this purpose, the entire altitude range below 1000 km is divided into five segments. The region below the F_2- peak is represented by a biparabola. The region between the F_2- peak and the starting point of the topside exponential portion is represented by a parabola. The semithickness parameters of the biparabola and parabola are given functions of F_0F_2 and the local time. The topside exponential portion is fitted wi three segments of differing decay constants which represent the inverse of t corresponding plasma scale heights. The decay constants are given as functions of F_0 and solar flux index. Hence, by feeding in F_0F_2, $h_{\max}$ and the various constants, t electron density profile can be obtained.

Following the widespread use of atmospheric models like CIRA, a similar effort in t direction of ionospheric modelling was considered worthwhile and the result is t development of an International Reference Ionosphere (Ramakrishnan and Raw 1972; Rawer 1975). In the IRI model, the general shape of the profile is characterized by topside exponential portion, a parabolic F_2-peak region, and another parabol supplement to represent the F_1-region. Based on reasonable amount of data, a detail computer program was developed for which the inputs were the geographic c ordinates, sunspot number, month of the year and the time of the day. For the specified conditions various layer parameters were internally calculated and based these the profile was derived.

The observational profiles were based on the incoherent scatter radar observations Jicamarca. A total of 207 electron density profiles were collected, stretched over almo a full solar cycle. The profiles were classified into low and high levels of solar activi taking the $F_{10\cdot 7}$ cm solar flux of 100 units as the dividing limit. They are further divid into three seasons like summer, winter and equinox. The averaged profiles are obtain for each of the groups for different time periods of the day.

3. Comparison between the observation and model profiles

The observational profiles are compared with the Bent and IRI models for the noo time for which the data representation is relatively better than at other times. T corresponding Bent and IRI models for the equator were computed on the basis of t formulations mentioned in §2. The Bent model requiring F_0F_2 and $h_{\max}$ as inp parameters is normalized naturally at the F_2-peak with the observational profile. T IRI model, however computes the layer parameters internally and it is found that th differ quite significantly from that of the observational profile. In order to facilitate easy comparison with the other two, the IRI model is also normalized at the F_2-pea Such a modification is also relevant (Rawer 1984). The two models along with t observational profile are shown for different seasons and solar activities in figures 1 a 2. Due to non-availability of data, the comparison could not be done for the summer high solar activity. The figures show that the observational and model profiles dif significantly. The discrepancies noted among the profiles can be understood by maki an approximate fit of the observational and IRI profiles with the Bent model. Using t analytical expressions of Bent model, the decay constants and the thickness paramet are calculated for the corresponding observational and IRI profiles. The Be parameters extracted for the three profiles given in table 1 show that in all cases, t bottomside semi-thickness of the observational profile is greater than that of both Be and IRI models. The Bent model assumes equal semi-thickness values for bo bottomside and topside portions, for $F_0F_2 < 10$ MHz which is the case for t observational profiles. But the observational profile shows consistently lower values the topside portion. The IRI model does not show any consistency in this matter. It c

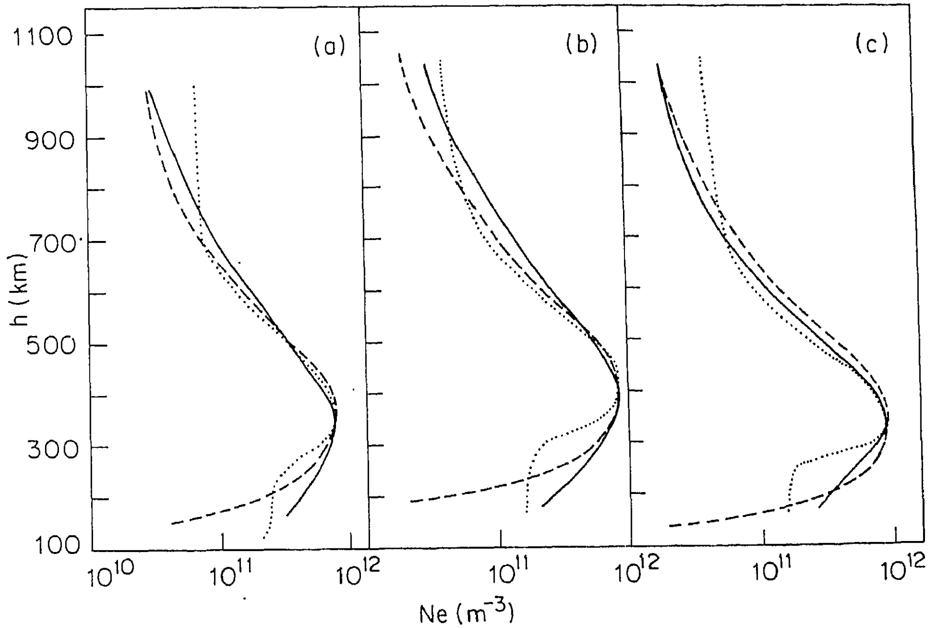

Figure 1. Noon-time profiles of electron density —— observational profile, --- Bent model, ... IRI model for (**a**) winter (**b**) equinox (**c**) summer during low solar activity.

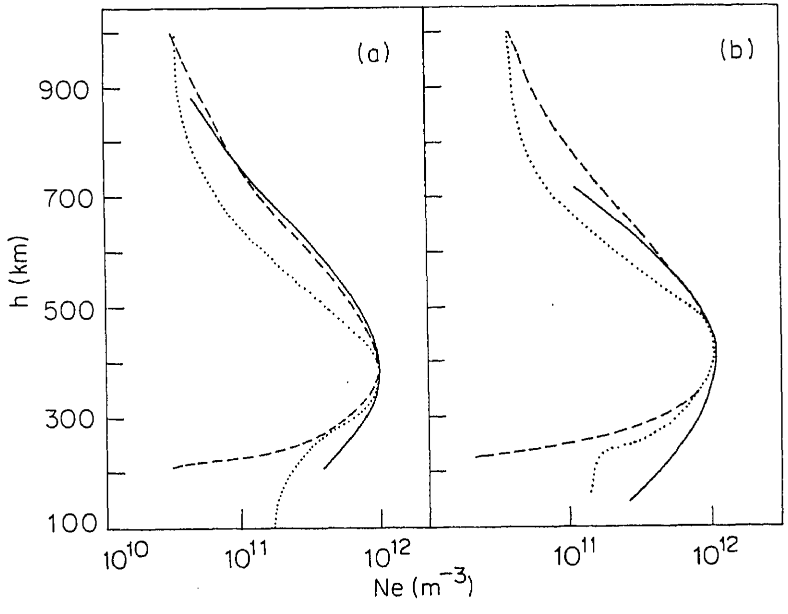

Figure 2. Same as in figure 1 but for (**a**) winter and (**b**) equinox during high solar activity.

Table 1. Bent parameters for observational profile (O), Bent model (B) and IRI model (I).

Group		Bottomside semi-thickness (km)	Topside semi-thickness (km)	Decay constants of exponential segments in units of 10^{-8}/M		
				K_1	K_2	K_3
Low-winter	O	263	124	6·79	6·08	3·78
	B	233	233	9·45	5·55	2·70
	I	188	118	8·85	7·73	1·36
Low-equinox	O	258	232	7·43	7·14	3·01
	B	227	227	9·50	5·65	2·70
	I	138	177	10·71	4·78	1·22
Low-summer	O	268	138	10·29	7·36	3·01
	B	215	215	9·60	5·80	2·75
	I	113	123	11·21	4·27	1·10
High-winter	O	296	213	7·04	7·11	..
	B	209	209	8·00	6·60	3·65
	I	239	144	9·80	4·32	1·51
High-equinox	O	325	207	10·24	..	..
	B	203	203	8·0	6·85	3.75
	I	232	134	10.20	4.64	0.90

be seen that for low solar activity, the Bent model is in better agreement with the observational profile than the IRI model as indicated by the bottomside semi-thickness parameters. For high solar activity, however both models seem to differ quite significantly from the observational profile. It is clear that significant modifications are needed in the Bent and IRI model semi-thickness parameters in order that they match the observational profiles around F_2-peak and below.

If we consider the topside, the decay constants of the first exponential segment for the three profiles are comparable indicating good agreement for the region. The second and third decay constants for the observational profile are generally greater than those for the Bent and IRI models, although the differences noted for the Bent model are considerably smaller as compared to IRI model. The IRI model takes very small values for the third decay constant, which resulted in the pronounced disagreement with the other two models. The small decay constants imply large scale heights which would result normally from the assumption of a lower height level for the heavy-to-light ion transition. It may be that the IRI model is somewhat biased to the mid- and high-latitude regions where the transition levels are known to be comparatively lower than that at equator. It, therefore, seems essential to correct the IRI model for the discrepancy noted above, so that it may fall in agreement with the observational profile.

On the whole it appears that for equatorial latitudes, Bent model agrees better with the observational profiles than the IRI model, presumably because the Bent model is based on a large amount of data from top and bottomside sounders as well as satellite-based electron density probe data with a good latitudinal coverage. On the other hand, IRI model is based on the incoherent scatter radar data, and of the different incoherent scatter radars in the world; only that at Jicamarca is in the equatorial region. It is therefore possible that the IRI model is somewhat biased to the mid- and high-latitude regions.

The discrepancies noted in the comparison appear to call for a revision in the models, especially IRI, before adopting them to equatorial latitudes. The Bent parameters presented in table 1 clearly suggest the nature of modifications to be effected so that they accurately represent the electron density distribution at the equator.

Acknowledgements

The authors would like to thank Dr C A Reddy and Dr V V Somayajulu for encouragement and to Dr A P Mitra for providing a computer print-out of the IRI models. Thanks are also due to Dr C V Devasia for assistance. One of the authors (BTVK) would like to thank CSIR for a research fellowship.

References

Bent R B, Llewellyn S K, Nestercuk G and Schmid P E 1975 in *Effect of the ionosphere on space systems and communications* (eds) John M Goodman, Naval Research Laboratory, (Washington D C: Naval Res. Lab.) p. 13

Nisbet H 1971 *Radio Sci.* **6** 437

Ramakrishnan S and Rawer K 1972 *Space Res.* **12** 1253

Rawer K 1975 *Space Res.* **15** 295

Rawer K 1984 *J. Atmos. Terr. Phys.* **46** 91

Somayajulu Y V and Ghosh A B 1979 *Indian J. Radio Space Phys.* **8** 47

Hydrography and circulation off the Antarctica in the Indian Ocean region

G S SHARMA AND BASIL MATHEW*

School of Marine Sciences, University of Cochin, Cochin 682016, India

*Present address: Naval Physical and Oceanographic Laboratory, Cochin 682004, India

MS received 23 May 1984; revised 9 November 1984

Abstract. The hydrography and circulation pattern off Antarctica in the Indian Ocean region are studied using vertical sections of temperature, salinity and oxyty approximately along 20°E, 77°E and 90°E, and the dynamic topography of the sea surface with reference to 1000 db. Based on the oceanographic characteristics, the whole region under study can be divided into three zones, the extreme ends being characterised by the frontal structure. The dicothermal layer is conspicuous during summer south of 50°S. The surface flow around Antarctica is mainly zonal. The East Wind Drift, found as a narrow westward flow near Antarctica, is observed at a lower latitude in the eastern Indian Ocean where the land extends northword. Contrary to expectation there is evidence of a westward flowing surface current at about 35°S between 45°E and 65°E.

Keywords. Hydrography; circulation pattern; Antarctica; Indian Ocean; meridional section.

1. Introduction

The poles and the neighbouring oceanic regions act as the sinks of the heat budget of the oceans and atmosphere. The oceanic and atmospheric circulations, to a large extent, depend on the conditions in these regions. Hence, it is imperative to know the conditions of the polar regions to understand the oceanic and atmospheric circulations.

Of the two poles, the south pole plays a major role as it is connected with the three major oceans of the world while the north pole has no connection with the Indian Ocean. Due to this land-locked nature on its northern boundary, the oceanic circulation in the North Indian Ocean and the atmospheric circulation over the intertropical Indian Ocean deviate very much from those of the other two major oceans. Further, 45% of the coastline of Antarctica is bounded by floating glacial ice sheets known as ice shelves. Thus, an understanding of their effect on the surrounding ocean seems to be necessary for establishing mass and heat balances for the waters around Antarctica.

In view of the significance of the Antarctic region in controlling the oceanic and atmospheric circulation, concentrated efforts have been made to study this region during the last decade. Most of these efforts are concerned with the oceanography off Antarctica in the regions of the Pacific and Atlantic.

Our basic understanding about the physical oceanography of the southern oceans came mainly from the German south polar expedition 1901–1902 (Meinardus 1923), R.R.S. Discovery II Cruise (Deacon 1933, 1937; Mackintosh 1946), Norwegian Antarctica Expedition 1927–1928 (Mosby 1934) and B.A.N.Z. Antarctica Research Expedition 1921–1931 (Sverdrup 1940). Further knowledge was gained through subsequent studies (Gordon 1967, 1971a, b, 1972, 1975, 1978, 1981; Gordon and Tche 1972; Gordon *et al* 1977a, b, 1978; Houtman 1964; Heath *et al* 1978; Georgi 1978, 1 1981; Emery 1977; Ivanov 1961; Jacobs and Georgi 1977; Joyce *et al* 1978, 1 McGinnes 1974; Molinelli 1981; Nowlin *et al* 1977; Sciremammano 1979; Sievers Emery 1978; Whitworth 1980). All these investigations, with the exception of a were confined to the regions in the Atlantic and Pacific, and very little is known ab the hydrography off Antarctica in the Indian Ocean region. An attempt was there made to study the hydrography of the region and the circulation pattern using oceanographic data already available.

2. Materials and methods

The oceanographic data for the present study came from 283 stations covered various vessels. The details are given in table 1 and the station positions are show figure 1. Stations encircled are used for vertical sections.

The *in situ* temperature at times instead of decreasing increases with de particularly in the deeper layers displaying an apparent instability due to pres effect. To avoid ambiguity the potential temperature is computed using the nomog prepared by Montgomery and Pollak from Helland-Hansen's formula (Hella Hansen 1930).

Three meridional sections of potential temperature, salinity and oxyty are prese in figures 2a, b, c to 4a, b, c approximately along 20°E, 77°E and 90° respectivel study the hydrography off Antarctica in Indian Ocean. The vertical gradients of hydrographic properties in the upper layers are very strong while they are weak in deeper layers. Therefore the depth scale is exaggerated in the upper 400 m compare that below.

Table 1. List of stations used for the present study (figure 1)

Name of the Vessel	Symbol used	No. of stations	Period
OB	⊙	20	4 March 1956 to 28 May 1956
OB	⊙	105	14 Jan. 1957 to 19 April 1957
Umitaka Maru	+	16	12 Dec. 1956 to 6 March 1957
Africana	□	19	3 July 1961 to 15 July 1961
Africana	□	13	2 June 1962 to 11 July 1962
Africana	□	7	7 April 1963 to 13 April 1963
Argo	×	5	2 Nov. 1962 to 16 Dec. 1962
Fuji	●	8	19 Dec. 1965 to 21 Feb. 1966
Fuji	●	10	25 Dec. 1973 to 24 Feb. 1974
Fuji	●	3	24 Dec. 1974 to 25 Feb. 1975
Akademic Shirshov	▽	24	21 Nov. 1970 to 6 Dec. 1970
Akademic Shirshov	▽	9	3 July 1970 to 9 July 1970
Fusakaze	▲	8	24 Dec. 1971 to 6 April 1972
Eltanin	◬	7	28 Feb. 1971 to 15 March 1971
Eltanin	◬	6	24 July 1971 to 3 Aug. 1971
Eltanin	◬	13	18 Sept. 1971 to 7 Oct. 1971
Eltanin	◬	10	27 June 1972 to 6 July 1971

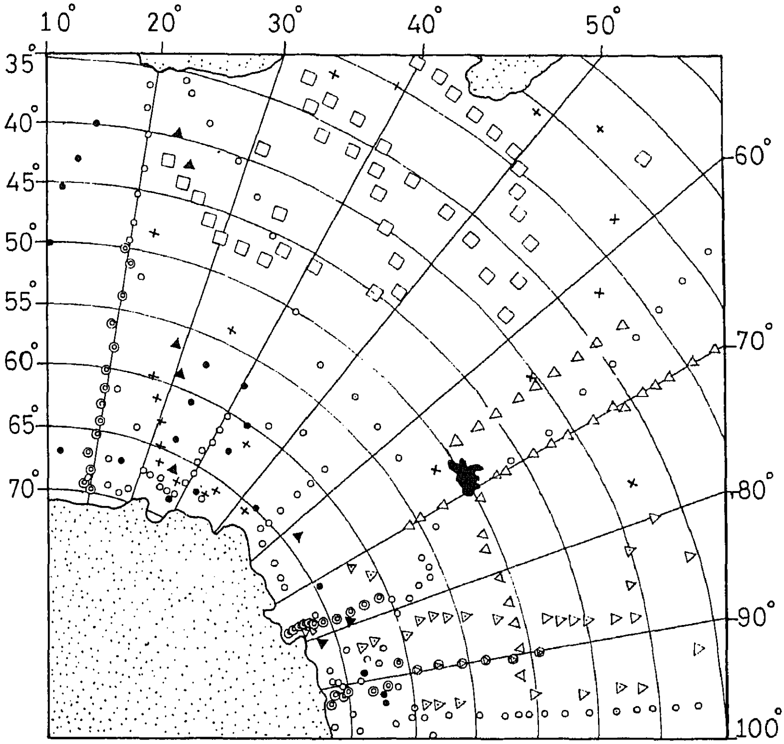

Figure 1. Station positions as in table 1.

To study the circulation at the surface and subsurface at the depths of 100 and 200 m, dynamic topographic charts with reference to 1000 db surface have been worked out. On examination, the circulation pattern at all these levels is similar except that the horizontal gradients of dynamic height are weak at subsurface depths. Therefore, only the surface circulation through dynamic height is presented in figure 5.

Deacon (1982) critically discussed the nomenclature used for different zones in the southern oceans and it is obvious that there is diversity in the nomenclature. The intention of this paper is not to go into those details but to adopt our own nomenclature.

3. Distribution of hydrographic properties

3.1 *Meridional section along* 20°*E*

The distribution of temperature is conspicuously divided into three zones in this section. The southernmost and northernmost regions are marked by meridional temperature gradients. The central zone is conspicuous in its vertical temperature gradients in the upper 200 m. The southernmost region, south of 68 °S is termed the Polar Front Zone while the region north of 54° is the Sub-Antarctic Convergence Zone

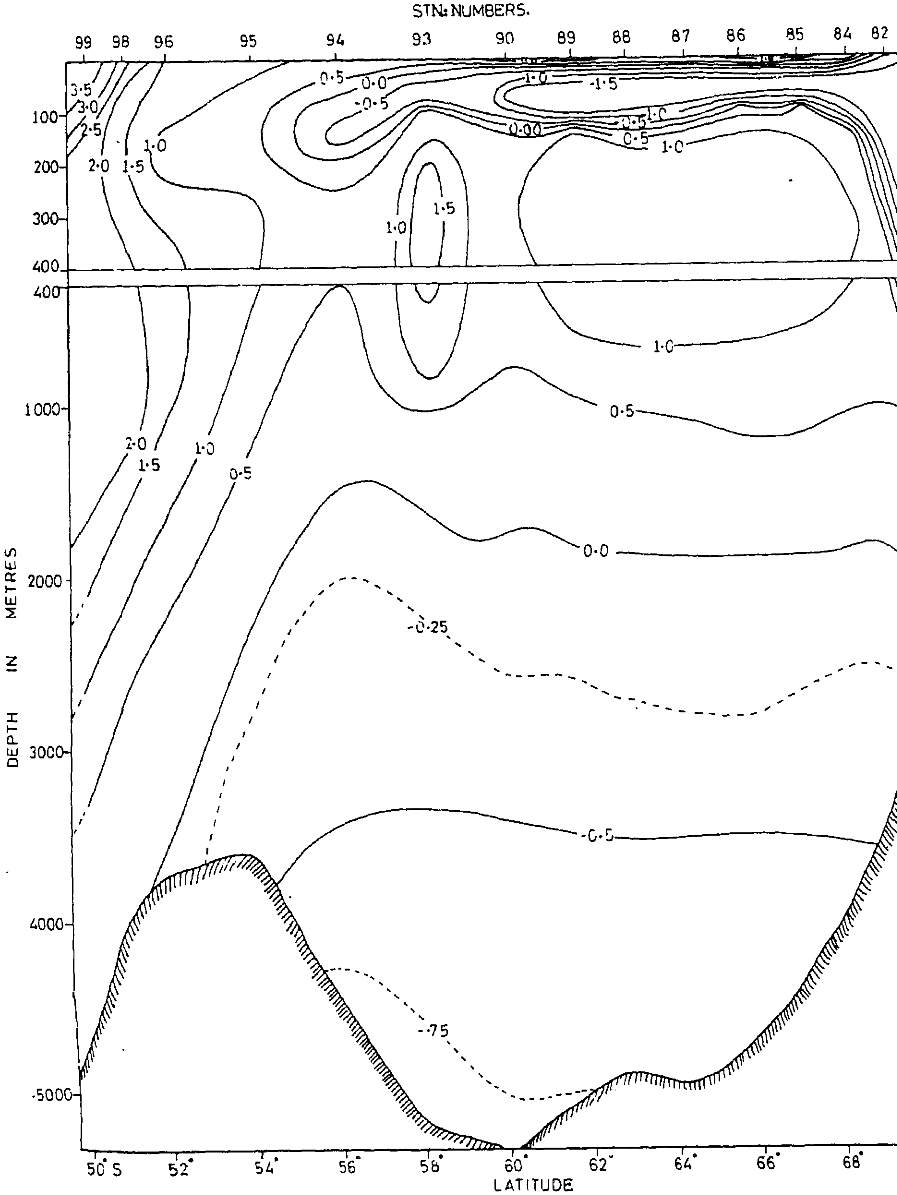

Figure 2(a). Vertical section of potential temperature (°C) approximately along 20°

(Polar Front according to Deacon 1982), characterised by frontal structure. Whil surface temperature between 52°S and 68°S ranges from 0·64 to 1·49°C only, temperature difference in both the frontal zones over a horizontal distance of abou latitude is more than 2°C.

The strong meridional gradient in the temperature in the Polar Front Zone app to be the consequence of the boundary between the East and West Wind drifts. Wi

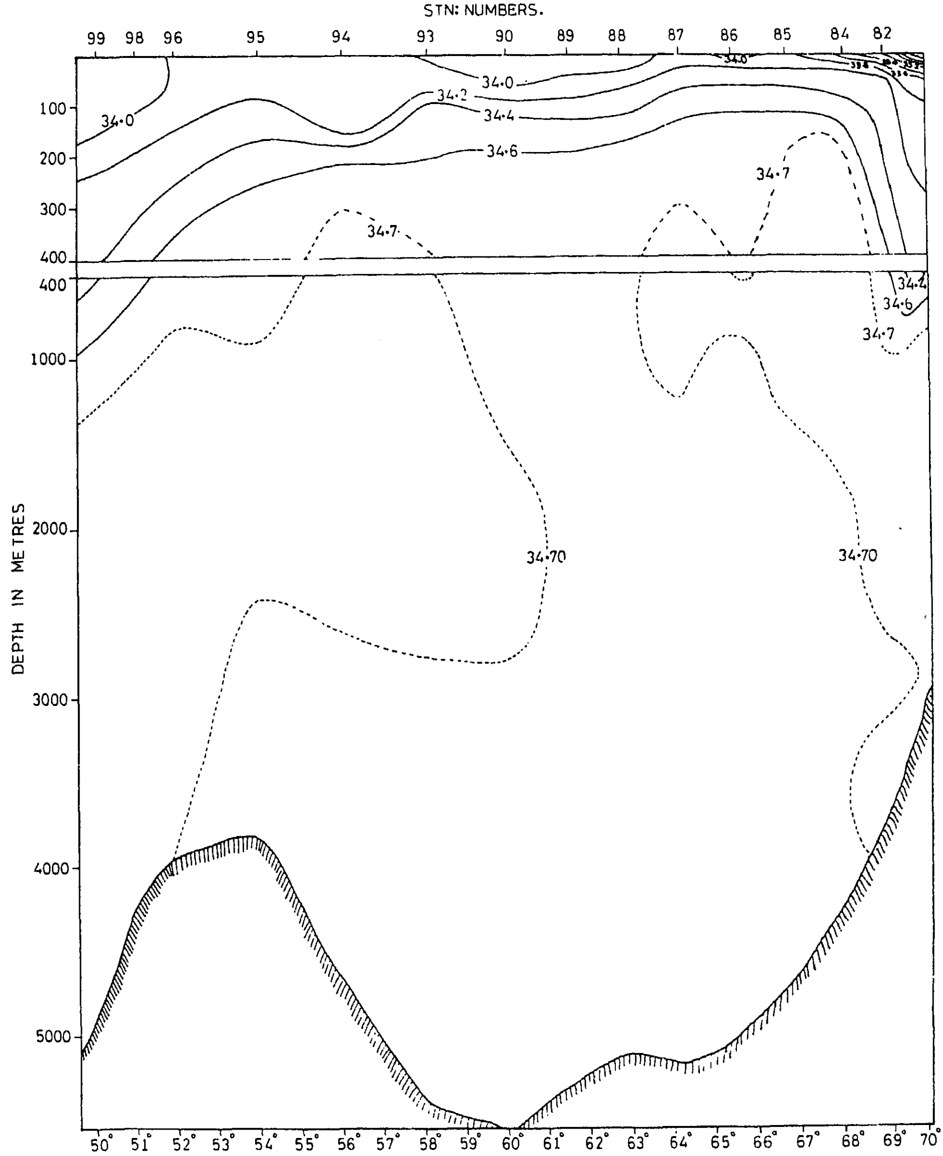

Figure 2(b). Vertical section of salinity ($^0/_{00}$) approximately along 20°E.

the Polar Front Zone the orientation of isotherms, isohalines and isolines of oxyty is almost similar and they indicate the gliding of the subsurface water to deeper layers accompanied by the sliding of the Antarctic Water at the surface. In the central region the temperature decreases with depth attaining the lowest and then increases. From south to north within this zone, the subsurface temperature minimum deepens, decreases in magnitude and finally terminate at about 54°S.

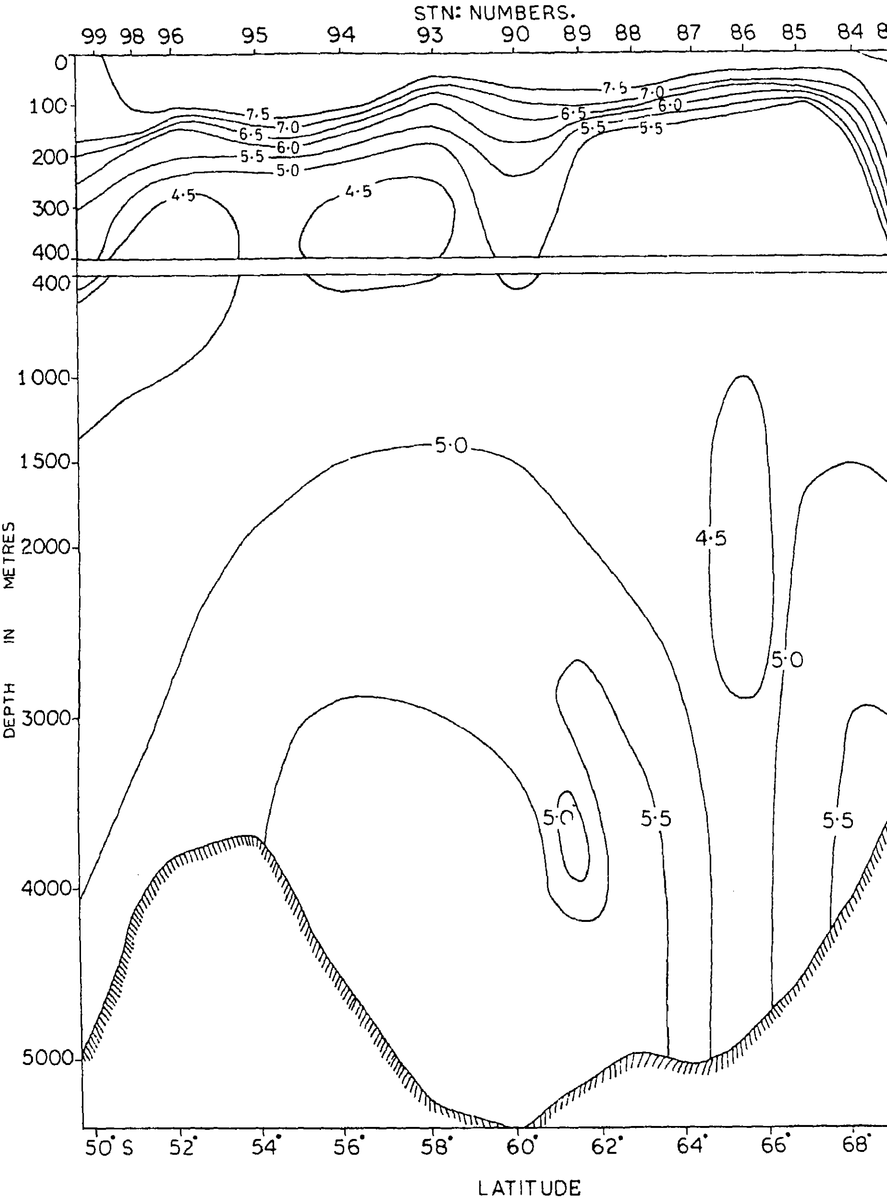

Figure 2(c). Vertical section of oxyty (ml/l) approximately along 20°E.

but the effect of the temperature is overcompensated by the increase in salini

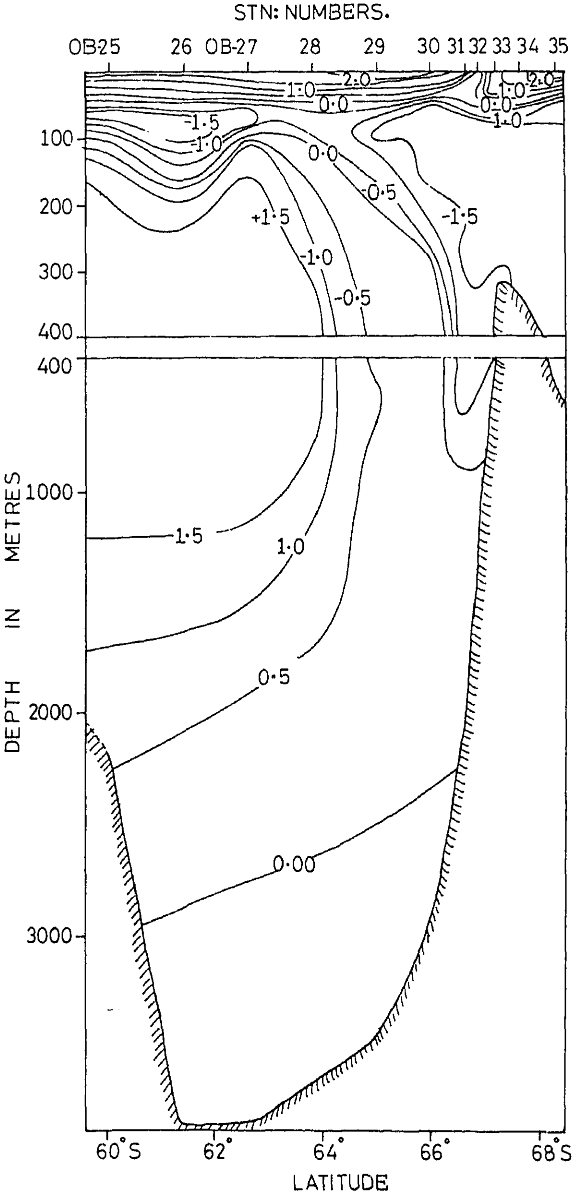

Figure 3(a). Vertical section of potential temperature (°C) approximately along 77°E.

3.2 *Meridional section along 77°E*

This section runs across 60°S to 68°19′S. The surface water between 60° and 65°S is almost isothermal south of which the temperature decreases meridionally upto 67°S and then increases. The highest temperature of 2·68°C recorded at the surface at the southernmost point may perhaps be due to continuous summer heating. The

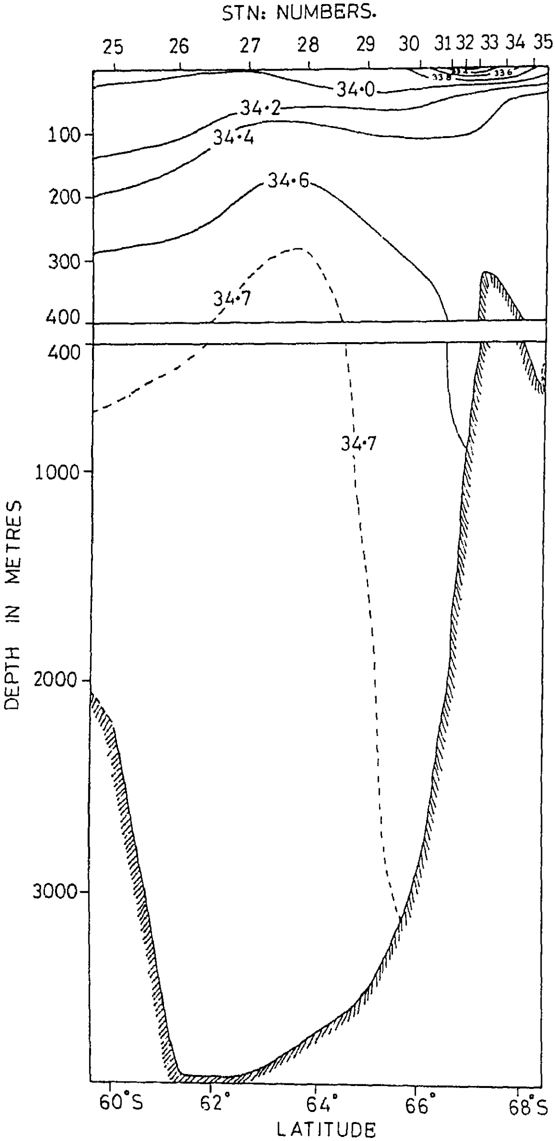

Figure 3(b). Vertical section of salinity (‰) approximately along 77°E.

temperature minimum layer in the southern region of the section extends from ab 50 m to more than 300 m. The lowest temperature recorded is in a basin in the slop Antarctica. The coldest water is associated with relatively higher salinity and hig oxyty. This water seems to have been trapped in the basin during the previous winte

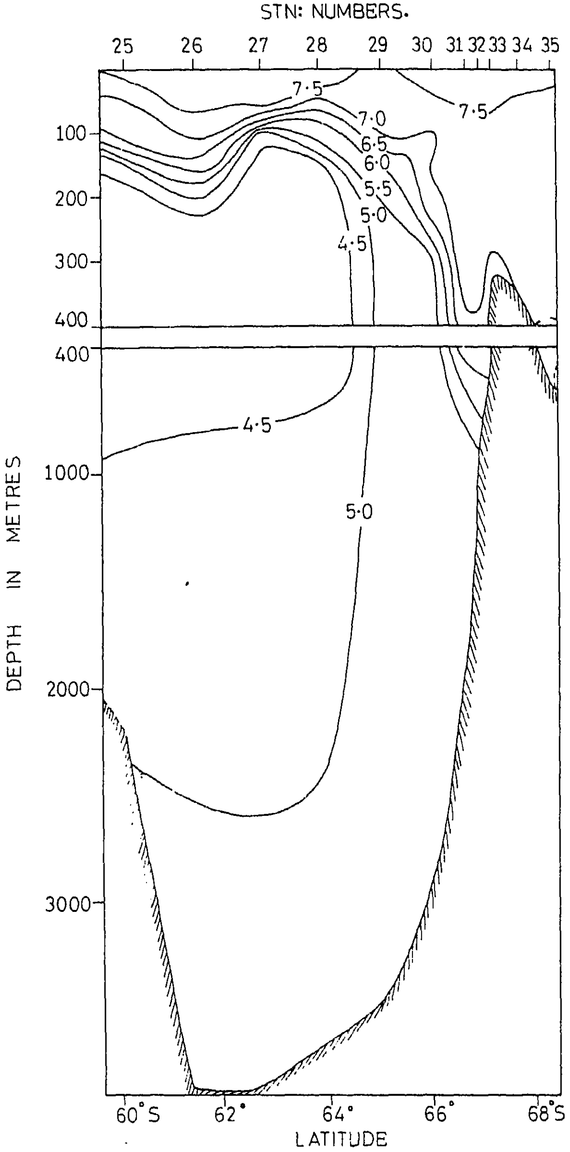

Figure 3(c). Vertical section of oxyty (ml/l) approximately along 77°E.

trapped approximately within the depth range of 200 to 1000 m. The deep waters are almost homogenous in character.

3.3 *Meridional section along 90°E*

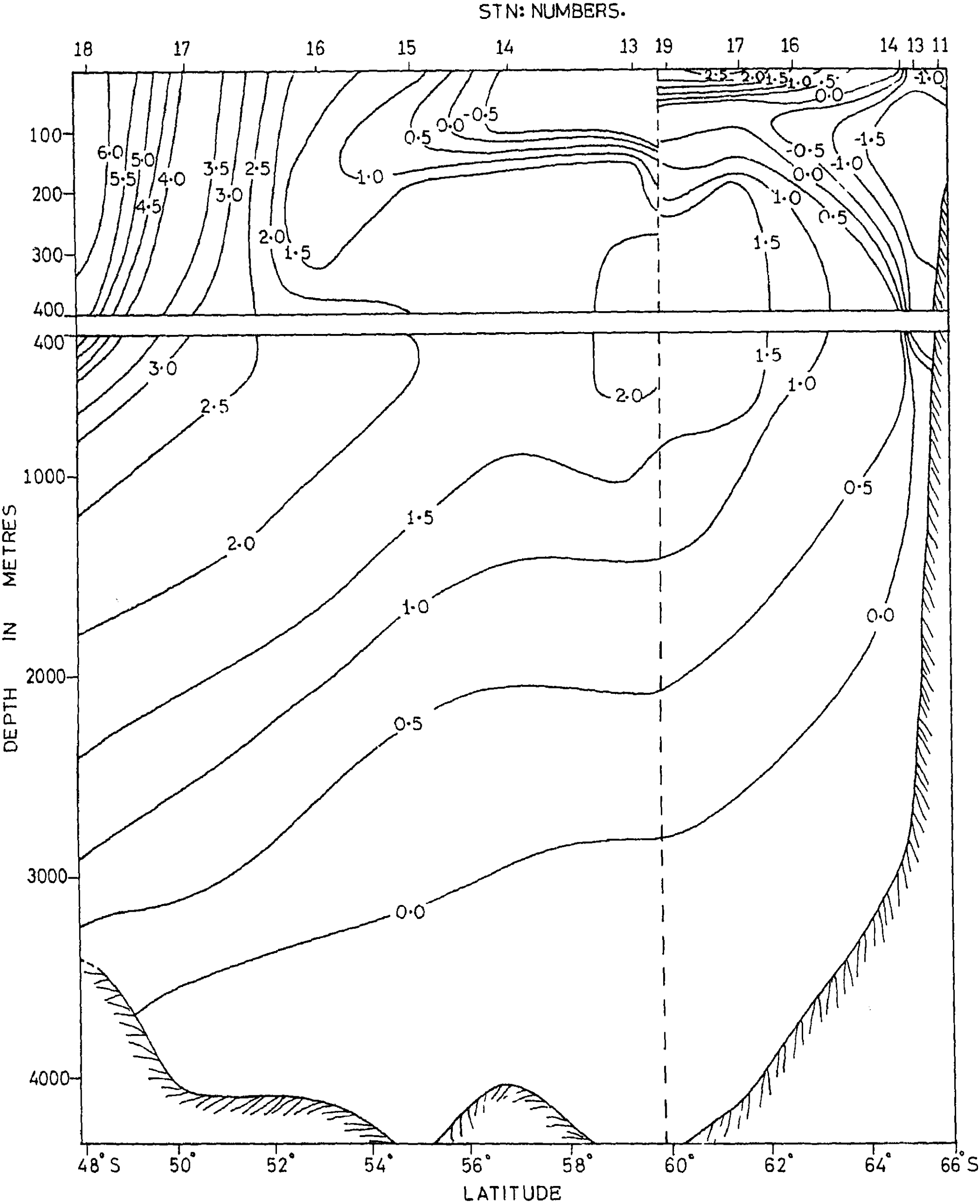

Figure 4(a). Vertical section of potential temperature (°C) approximately along 90°E.

summer. From this section it is evident that the temperature minimum in subsurface depths does not occur in winter but it is a phenomenon associated only with summer. The surface temperature continuously decreases southward and the lowest temperatures might have been recorded near the continental shelf due to lack of radiation for about 6 months. It can also be inferred from this section that during winter, the

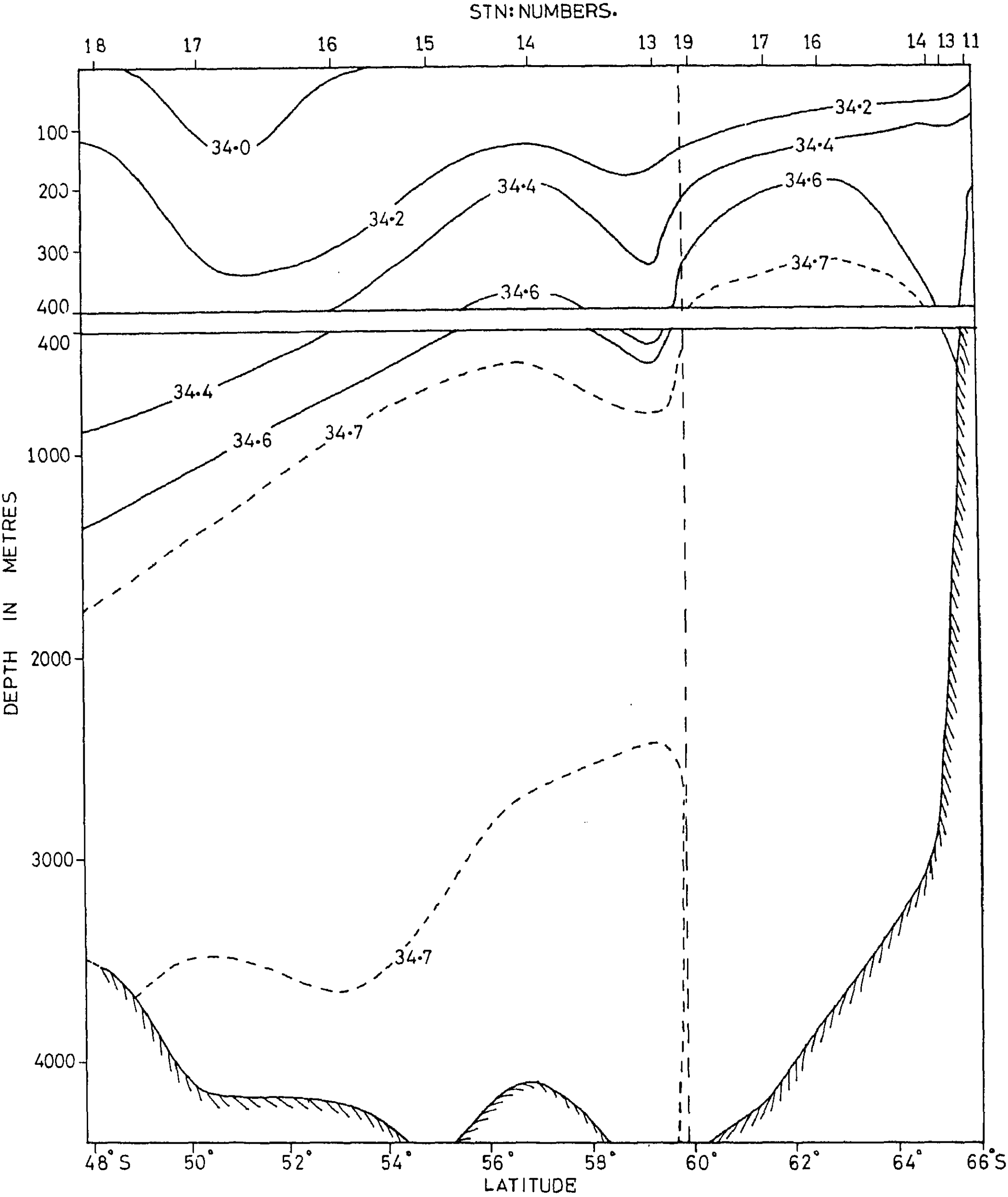

Figure 4(b). Vertical section of salinity (‰) approximately along 90°E.

Subantarctic Convergence Zone shifts southward and the meridional gradients also strengthen. The thickness of the warmer water in the subsurface depths is much higher in winter compared to that in summer. Within the Polar Front Zone a subsurface maximum in oxygen and a minimum in salinity are seen to extend from the surface layer downward to the north. Surprisingly, the vertical salinity gradient is the least in this

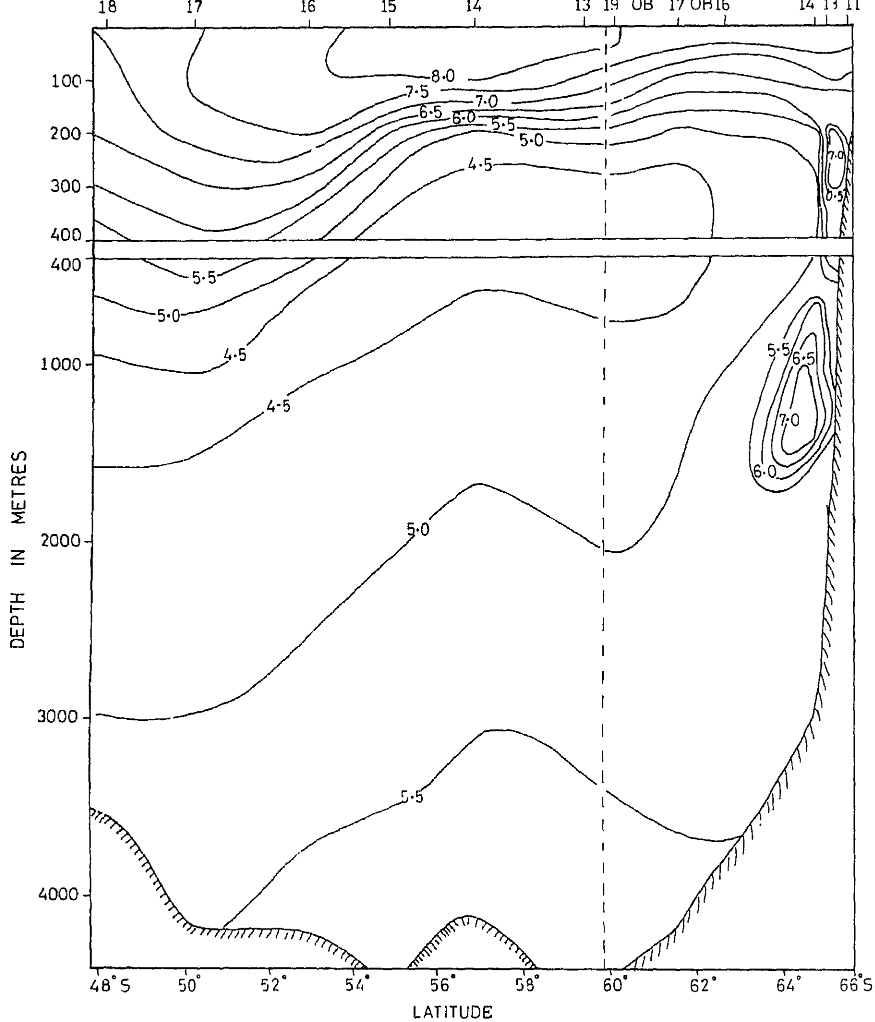

Figure 4(c). Vertical section of oxyty (ml/l) approximately along 90°E.

section, probably, because of winter convection. During winter the oxygen minimum layer becomes thinner and deeper northward.

4. Circulation

Near the Antarctic continent the East Wind Drift is present, north of which the Circumpolar Current is noticed. The Circumpolar Current has northwest to southeast orientation between 50°S at 10°E and 65°S at 70°E. The northward continuation of the Circumpolar Current in the Indian Ocean region merges with the West Wind Drift.

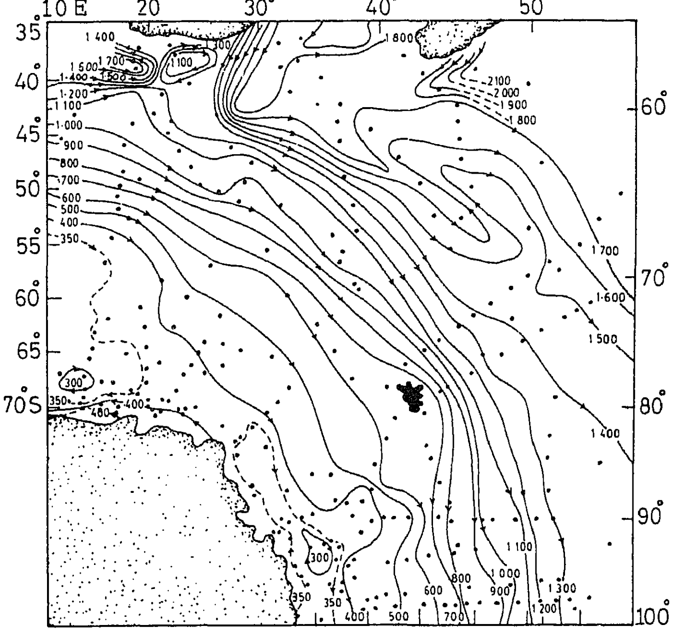

Figure 5. Dynamic topography of the sea surface with reference to 1000 db.

Within the West Wind Drift system a westerly flow between 45°E and 65°E, at about 35°S is noticed.

5. Discussion

According to the vertical sections presented, the whole region under study can be divided into three zones, the extreme ends being characterized by frontal structure. The southern one is designated as the Polar Front Zone while the northern one is termed as the Sub-Antarctic Convergence Zone.

Polar Front Zone is formed near Antarctica due to intense cooling near the continent during winter. This Front is confined only to subsurface depths. Due to freezing of surface water near the continent, the salinity increases resulting in an increase of density. The denser water near the continental shelf flows to the deepermost layers and this is the Antarctic Bottom Water characterized by lower temperature, higher salinity and higher oxyty compared to the water above, which is called the Antarctic Deep Water. The coldest water which is relatively fresh spreads in the subsurface layers towards the lower latitudes. With summer heating the surface waters are warmed and they spread upto the Sub-Antarctic Zone. Such a situation gives rise to low-saline and highly oxygenated subsurface waters with temperature having extreme values below −1 °C and characterized by strong meridional gradients not only at the surface but extending to deeper layers. The surface water in the southern side of the convergence zone being colder, sinks to the deeper layers as a consequence of which the meridional gradients are strong. This water being fresh from the surface is characterized by lower salinity, and higher oxyty and is known as the Antarctic Intermediate Water. McCartney (1977) propsed that Antarctic Intermediate Water forms north of the Sub-Antarctic Zone primarily in the southeast Pacific Ocean where the coldest water and fresher variety of Sub-Antarctic Mode Water is transformed into Antarctic Intermediate Water. He suggested a mechanism whereby late winter heat loss to the atmosphere results in deep convection and formation of relatively homogeneous water mass, the sub-Antarctic Mode Water. Molinelli (1981) concludes that the Antarctic Intermediate Water is the composite of waters formed by late winter convection. The thermal structure in this region shows a peculiar nature of the cold water sandwiched between the warm layers above and below. This layer is called dicothermal layer (Pickard and Emery 1982) which is conspicuous only during summer (figure 4a) extending upto even 50°S in the western region due to relatively high salinity water of Antarctic origin whereas it is confined to south of 60°S in the eastern region.

The surface waters between the Polar Front Zone and the Sub-Antarctic Convergence are marked by least meridional gradients, because either surplus radiation in summer or deficit radiation in winter is used only for melting of ice or freezing of water respectively, but not to change the temperature. Nevertheless, the Sub-Antarctic Convergence Zone shifts meridionally to higher latitudes in winter and lower latitudes in summer.

The surface flow around Antarctica is mainly zonal as in the Atlantic and Pacific regions. The East Wind Drift appears as a very narrow current close to Antarctica. The boundary between the East and West Wind drifts is at a lower latitude in the eastern side of the Indian Ocean where the land extends northward compared to the western Indian Ocean. Contrary to expectations a westward flow is observed near 35°S between 45°E and 65°E. A similar flow is also noticed around the same latitude in I.I.O.E. Atlas (Wyrtki 1971). As the data in the atlas is averaged over 5-degree-latitude-longitude quadrangle, it is not certain whether this flow is a permanent feature or not and a more detailed study is required for a clear understanding of this interesting phenomenon.

6. Conclusions

In the regions of dicothermal layer the velocity of sound decreases with depth and then increases. In the regions of such sound velocity structure the sound channel extends to very long distances. Further the dicothermal layer is formed in the depth range of 50 to 100 m. The Antarctic region can be used for long distance transmission at shallow depths and this channel can even be found extended round the globe between 50°S and 60°S.

In the region between the Polar Front Zone and the Sub-Antarctic Convergence Zone the meridional variation of temperature is minimum which results in the least atmospheric pressure gradients. The winds in this region are therefore expected to be relatively very weak unlike in the two frontal zones on either side of this region where strong blizzards prevail throughout the year creating operational hazards. Hence, the region between 55°S and 60°S can be used for operations and installation of energy extraction units.

The present knowledge of the hydrography and circulation off Antarctica, particularly in the Indian Ocean region is based on the meagre oceanographic data available. For a detailed study it may be necessary to carry out oceanographic survey at closure intervals and also systematically along the longitudes and latitudes so that the zonal as well as the meridional flow pattern can be worked out with more precision, particularly in the region of Sub-Antarctic Convergence Zone.

References

Deacon G E R 1933 *Discovery Rep.* 7 171

Deacon G E R 1937 *Discovery Rep.* **15** 1

Deacon G E R 1982 *Deep Sea Res.* **29** 1

Emery W J 1977 *J. Phys. Oceanogr.* 7 811

Georgi D T 1978 *J. Geophys. Res.* **83** 4579

Georgi D T 1979 *J. Phys. Oceanogr.* **9** 456

Georgi D T 1981 *J. Geophys. Res.* **86** 6566

Gordon A L 1967 Am. Geophys. Soc. Antarctica Map Folio Series: Folio 6 14 *Plates*

Gordon A L 1971a *Research in the Antarctica Washington D.C. Am. Ass. Adv. Sci.* 609

Gordon A L 1971b *Antarctic Oceanology I Am. Geophys. Un.* **15** 205

Gordon A L 1972 *Antarctic Oceanology II Am. Geophys. Un.* **19** 71

Gordon A L 1975 *Deep Sea Res.* **22** 355

Gordon A L 1978 *J. Phys. Oceanogr.* **8** 600

Gordon A L 1981 *Deep Sea Res.* **28** 1239

Gordon A L and Tchernia P 1972 *Antarctic Oceanology II Am. Geophys. Un.* **19** 59

Gordon A L, Georgi D T and Taylor H W 1977a *J. Phys. Oceanogr.* **7** 309

Gordon A L, Georgi D T and Taylor 1977b Antarctic oceanographic zonation In *Polar Oceans* 45

Gordon A L, Molinelli E and Baker T 1978 *J. Geophys. Res.* **87** 3023

Heath R A, Bryden and Hayers S P 1978 *Antarctica J. United States* **13** 76

Helland-Hansen B 1930 *Rep. Sans N. Atl. Deep Sea Exped.* **1** 317

Houtman Th J 1964 *N.Z. Geol. Geophys.* **7** 245

Ivanov Yu A 1961 *Okeanologicheskiya Issledovaniya* **3** 30

Jacobs S S and Georgi D T 1977 In, *A voyage of Discovery*; *Deep Sea Res. Suppl.* **24** 43

Joyce T M, Zenck W and Toole J M 1978 *J. Geophys. Res.* **83** 6093

Joyce T M, Patterson S L and Millard R C 1981 *Deep Sea Res.* **28** 1265

Mackintosh N A 1946 *Discovery Rep.* **23** 177

McCartney M S 1977 *Deep Sea Res.* **24** (Suppl) 103

McGinnes R F 1974 *Science* **186** 736

Meinardus W 1923 *Deut Sudpolar Exped.* III Meteorol. **1**

Molinelli E 1981 *J. Mar. Res.* **39** 267

Mosby H 1934 *Scientific results of the Norwegian Antarctic expedition* 1927–1928 **2** 1

Nowlin W D (Jr), Whitworth T and Pillsbury R D 1977 *J. Phys. Oceanogr.* **7** 788

Pickard G L and Emery W J 1982 *Descriptive physical oceanography* 4th Ed., (New York: Pergamon Press) pp. 249

Sievers H A and Emery W J 1978 *J. Geophys. Res.* **83** 3010

Sciremammano F (Jr) 1979 *J. Phys. Oceanogr.* **9** 221

Sverdrup H U 1940 *Antarctic Research Expedition* 1921–1931, *Oceanogr.* III **3** 88

Whitworth T 1980 *Deep Sea Res.* **27** 497

Wyrtki K 1971 Oceanographic Atlas of the International Indian Ocean Expedition, National Science Foundations, Washington D.C. pp. 531

Proc. Indian Acad. Sci. (Earth Planet. Sci.), Vol. 94, No. 1, March 1985, pp. 29–34.
© Printed in India.

Quasi-biennial oscillation in geomagnetic disturbance field

G K RANGARAJAN
Indian Institute of Geomagnetism, Colaba, Bombay 400 005, India

MS received 18 July 1984; revised 15 October 1984

Abstract. Using the techniques of second derivatives, digital filtering and power spectral analysis, the fine structure of the quasi-biennial oscillation (QBO) in the equatorial geomagnetic field in the Indian zone is studied. The salient results are: (i) in the quiet day field, QBO is weak and the signal strength has no local time dependence; (ii) in the disturbance field the signal is strongest in the afternoon and evening hours and (iii) larger magnitudes are manifested closer to the dip equator. The difference in dawn and dusk amplitudes of the signal and the absence of significant strength close to noon in the electrojet region rules out EUV flux as the responsible agent.

Keywords. Quasi-biennial oscillation; geomagnetic field; second derivatives; digital filtering; power spectral analysis.

1. Introduction

Attempts to identify a biennial cycle in meteorological, geophysical and solar parameters through several statistical approaches have been undertaken for quite some time now. While the existence of a clear 26-month cycle has been well-established in stratospheric zonal wind oscillations and temperature, total zone, tropopause height etc (Angell and Korshover 1964) similar attempts on geomagnetic time series have met only with partial success. Stacey and Westcott (1962) found that while the QBO was noticeable at Alibag (19°N) and (Apia 14°S) it was very weak in Huancayo (12°S), located close to the dip equator. They also suggested that while the oscillations of quiet-day H values were periodic, it may be randomly excited. Yacob and Bhargava (1968) showed, from spectral analysis of long-series of Alibag H data confined to quiet days, that the existence of 26-month variation in Sq (H) range is a reality and suggested its source as the Sun, as similar spectral peak was observed in Zurich relative sunspot number R_z. Two-year periodicity in R_z was earlier shown to be marginally significant by Shapiro and Ward (1962). Raja Rao and Joseph (1971) utilized the technique of band-pass filter to isolate the QBO at several low latitude stations and suggested that the amplitude varied as a function of latitude. It should be reemphasized that for all these attempts quiet-time components of the geomagnetic field were utilized.

Recently Sugiura (1976) and Sugiura and Poros (1977) provided clear evidence for the existence of QBO in geomagnetic disturbance field and showed its close correlation with R_z and 10·7 cm solar radio flux. Sugiura (1976) preferred the time domain analysis of the data because the frequency of the QBO changes with time and the spectra provide only the average characteristic. Even in time domain the signal is weakened by other natural and artificial irregular oscillations. The second order time derivatives derived from annual mean values of H were found to show the QBO remarkably well if the quality of the observations was very good. The annual mean eliminates the high-frequency components and the second derivative acts as an effective trend-eliminating filter. Sugiura and Poros (1977) mention that the second derivative of a parabola fitted to the data is equivalent to the simple three-point difference scheme for the second derivative. They also utilized the technique of digital filtering of mean monthly values of the H field at several stations to show clearly the existence of QBO in the disturbance field, its time variation and the correlation between stations separated in latitude and longitude, with R_z and with D_{st}.

In this paper, we proceed to analyse the geomagnetic field at Alibag (Geog. Lat. 18° 38′N, Dip 24° N) and at Trivandrum (Lat. 8° 29′ N, Dip 1°S) close to the dip equator using both the techniques suggested by Sugiura. In addition, we confine the analysis to data for one hour at a time to see the nature of the local time change in the signal. Such an approach was first initiated by Bhargava (1972) in his analysis of the annual and semiannual modulation of the geomagnetic field. The motivation for this is the anticipation that if QBO is related to solar features and manifests strongly in the disturbance field then a forenoon/evening asymmetry in the strength of the signal should exist as the ring current responsible for low latitude field reduction is known to be inflated in the evening sector. Such an asymmetry was shown for the strength of the 27-day recurrence signal by Bhargava and Rangarajan (1975), and by Rangarajan and Bhattacharyya (1983).

2. Data analysis and discussion

2.1 *QBO in horizontal intensity through second-derivatives*

Mean monthly H values at Trivandrum derived from restricting the data to only international disturbed (ID) days were combined to derive the mean annual values for each hour. This string, for each hour, was then subjected to the method of three-point difference scheme for second derivatives. According to Sugiura (1976) high frequency components are eliminated when annual means are utilized and second-order differentiation effectively eliminates variation with period in excess of 6 years. In figure 1 we show the time variation of the second derivative for some selected hours to demonstrate the variability of the signal. The main feature is the clear existence of QBO and the dependence of its strength on local time. Data for 20 hr (75° EMT) has the most consistent signals. Sugiura and Poros (1977) caution that "the use of annual means is not recommended except for a crude survey of the presence or absence of the QBO without detailed information on the wave". We have, indeed, shown the presence of the signal.

2.2 *QBO in H at Trivandrum and Alibag through digital filters*

Here, we utilized monthly mean hourly values of H derived from data of international disturbed (ID) days and international quiet (IQ) days. For Alibag, the data extended for the period 1925 to 1980, and that for Trivandrum from 1958 to 1980.

A 51-weight band pass filter was designed following Behannon and Ness (1966). The peak response was between 25 and 22·7 month as the preliminary analysis of the data indicated periodicities in this range rather than at 26 months, usually identified as the QBO.

Results of application of this filter on long series of Alibag H (disturbance) data corresponding to 16 hr (75° EMT) is shown in figure 2. This hour would have the largest signal to noise ratio for the QBO, as seen from power spectral analysis.

It becomes at once apparent that the signal strength is highly variable so that spectral analysis of such strings of data may not reveal all the facets. Close to the year of solar minimum (1934, 1944, 1954, 1964 . . .) the signal nearly vanishes, the exception being that of 1975. However, several other geophysical and solar wind features were known to be different for the solar cycle 20 (1964–76) as compared to previous cycles (Gosling *et al* 1977). Next, we considered the filtered data for the years 1960–76 for both the stations Trivandrum and Alibag restricting the data to IQ and ID days respectively. The data for some hours when the signals were strongest are shown in figure 3. It is clear that

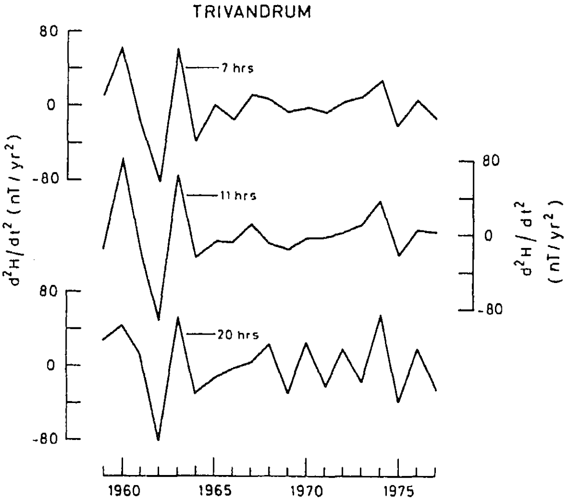

Figure 1. Time variations in second derivative of the annual mean horizontal intensity (derived from data on disturbed days only) for selected hours (75° EMT) at Trivandrum.

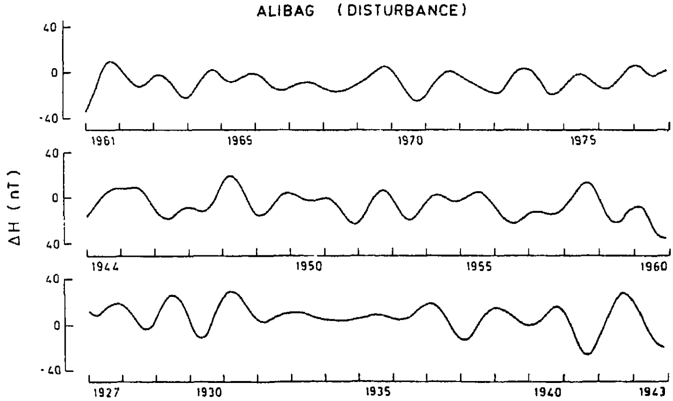

Figure 2. Band-pass filtered H (disturbed days) data derived from observations at 16 hr (75° EMT) at Alibag between 1927 and 1977.

the QBO manifests more clearly in the disturbance field in relation to quiet-time fields and at Trivandrum the stationarity of the QBO seems better preserved, when compared with Alibag. The coherence of the fluctuation between the two stations is striking. For some years, as between 1960 and 1964, even the quiet day field exhibits the QBO signal.

2.3 *QBO through spectral analysis*

With the advent of fast fourier transform (FFT) routines, computation of reliable power spectra giving information on both amplitude and phase has become quite easy. Using a version of FFT (Rangarajan and Bhargava 1974) power spectra were computed for the band-pass filtered time series, restricting the data again to one hour at a time and to IQ and ID days. The local time variation in power spectral density (proportional to the square of the amplitude of QBO) for Trivandrum (quiet and disturbed) and Alibag (disturbed) are shown in figure 4. From a comparison of the power densities for the two

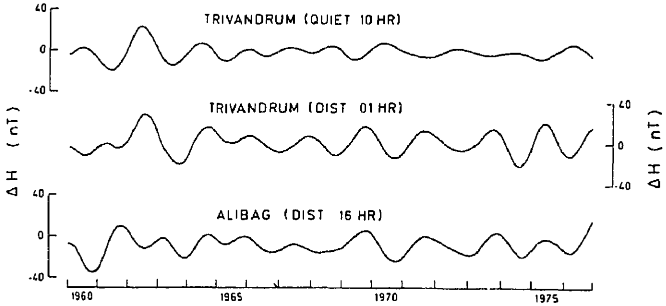

Figure 3. Band-pass filtered H data from Trivandrum and Alibag between 1960 and 1976.

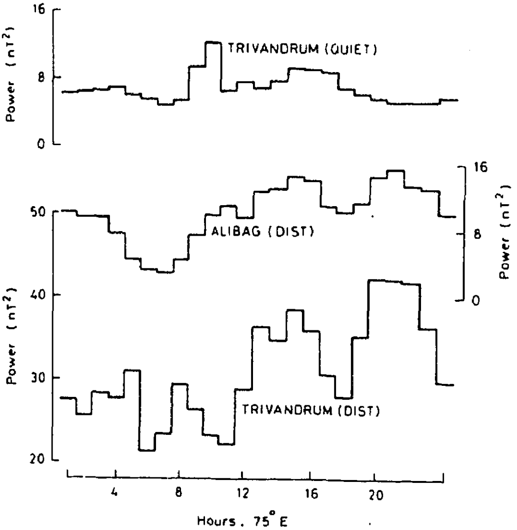

conditions of the geomagnetic field at Trivandrum it becomes clear that during quiet times (i) power densities are smaller by a factor of 4 and (ii) there is a relatively small but significant dependence on local time. When the power densities at Alibag are compared with those of Trivandrum (disturbed field) it is seen that the QBO strength is consistently larger at Trivandrum. However the fine structure of the local time variation is quite comparable at both places with a morning minimum and two maxima in the afternoon and late evening. The afternoon maxima are consistent with the anticipation of the contribution due to asymmetric ring current, as suggested earlier in the introduction. The complex pattern of the power density variations however is not very clearly understood. Between the electrojet and non-electrojet stations, there appears a large difference (nearly a factor of 3 or 4) in the average level of the power spectral density. This difference may be caused by the enhanced level of continuum in the power spectra. The continuum is generally attributed to geomagnetic storm modulation of the field (Eckhardt *et al* 1963). Towards the dip equator, day-time disturbance field gets enhanced and consequently all periodic oscillations also have larger amplitudes and can be associated with enhanced continuum. There have been several attempts to establish the elusive link that combines solar, geomagnetic and climate changes with variable degree of success (Pittock 1978). The late-evening (20–21 hr 75° E time) peak suggests that for any further analysis that aims at relating solar geomagnetic and climatic changes for QBO, the largest signals can be obtained by confining the data to this hour. The fact that there is a clear dawn/dusk asymmetry in the strength of the QBO signal and the weakness of the same close to noon clearly indicates that the responsible mechanism is not related to electromagnetic waves from the sun, consistent with Sugiura (1976) who asserts that QBO in geomagnetic field is not due to modulation of EUV flux. He suggests that the QBO in geomagnetic field, whose strength is a function of magnetic activity is due to secular variation on the sun, possibly through the interplanetary magnetic field (IMF) orientation.

3. Conclusion

The long series of H data from Alibag demonstrates the non-stationarity of the QBO signal at low latitudes. Closer to the dip equator it is seen that the QBO manifests more clearly in the disturbance field and the strength of the signal has a pronounced dusk/dawn asymmetry. This asymmetry coupled with the absence of any significant signal close to local noon even at Trivandrum suggests that EUV flux from the sun cannot be the agent responsible for the QBO in the geomagnetic field variations.

Acknowledgement

The author is thankful to Prof. R G Rastogi for scrutiny of the manuscript and to the referees for suggesting improvements to the paper.

References

Bhargava B N 1972 *Planet. Space Sci.* **20** 423
Bhargava B N and Rangarajan G K 1975 *J. Geomag. Geoelec.* **27** 257
Eckhardt D, Larner K and Madden T 1963 *J. Geophys. Res.* **68** 6279
Gosling J T, Asbridge J R and Bame S J 1977 *J. Geophys. Res.* **82** 3311
Pittock A B 1978 *Rev. Geophys. Space Phys.* **16** 400
Raja Rao K S and Joseph K T 1971 *J. Atmos. Terr. Phys.* **33** 797
Rangarajan G K and Bhargava B N 1974 *Proc. Indian Acad. Sci.* **A80** 249
Rangarajan G K and Bhattacharyya A 1983 *Proc. Indian Acad. Sci.* (*Earth Planet. Sci.*) **92** 5
Shapiro R and Ward F 1962 *J. Atmos. Sci.* **19** 506
Stacey F D and Westcott P 1962 *Nature* (*London*) **198** 730
Sugiura M 1976 *Geophys. Res. Lett.* 3 643
Sugiura M and Poros D J 1977 *J. Geophys. Res.* **82** 5621
Yacob A and Bhargava B N 1968 *J. Atmos. Terr. Phys.* **30** 1907

Vertical component MAGSAT anomalies and Indian tectonic boundaries

J G NEGI, P K AGRAWAL and N K THAKUR
National Geophysical Research Institute, Hyderabad 500 007, India

MS received 18 February 1984; revised 15 October 1984

Abstract. MAGSAT vertical component (Z-component) of crustal anomalies are correlated for the first time with major geological and tectonic boundaries/features of the Indian subcontinent. A prominent 'low' is consistently observed on all the profiles centred between 19° and 23° latitudes over the broad Peninsular 'high'. The other conspicuous 'low' indicated from the present work is confined to the region above Sarda depression (29° N to 31° N) in the foothills of Himalayas. Interesting magnetic signatures are identified over the Narmada-Son rift and Godavari graben.

Keywords. MAGSAT anomalies; tectonic boundaries; correlation studies.

1. Motivation

The investigations through POGO satellite data revealed the presence of prominent crustal magnetic anomalies even at the satellite heights. The distribution of the crustal magnetic anomalies at satellite level is expected to be controlled by the juxtaposition of he large size geological and tectonic features in addition to magnetic and thermal properties of different deep-rooted structures. The presence of anomalous signatures at satellite heights would necessitate a novel approach for the estimation of parameters of he deep-seated causative sources. These global and regional anomalies of long spatial wavelengths have been correlated to subsurface lithological features by Regan *et al* (1975) and Langel *et al* (1980).

More precise and accurate data of MAGSAT have confirmed the results of POGO and in few areas resolved new shorter wavelength anomalies (Langel *et al* 1982; Frey 1982). However, Sailor *et al* (1982) concluded from the spectral characteristics of the MAGSAT data that anomalies of wavelength of the order of 700 km can be resolved well, and around 250 km wavelength with some uncertainty.

The present mapping of world-wide POGO and MAGSAT data has identified a magnetic low' over Himalayas and 'high' over the Peninsular India. The Indian subcontinent is comprised of several tectonic provinces of different nature and origin, and it is in this view interesting to (i) study the finer structure of these anomalies, and (ii) define constraints for understanding of the deep-rooted causes of these features.

2. Data selection and profile description

It has been customary to prepare the total intensity map from the satellite data. However, presentation of such data is likely to pose the following problems for the Indian region:

(i) The amplitude of observed total field anomalies are generally too small to be significant for correlating mainly with crustal features of short wavelengths ($\approx$ 300 km). On the other hand, MAGSAT vertical intensity data seems to resolve the anomalies better as is evident from the figure 1.

(ii) The intercomparison of the magnetic anomalies due to crustal sources distributed over different regions bring in complications due to: (a) assumption of induced magnetisation, (b) induction processes at high and low geomagnetic latitudes, and (c) their distribution over different geomagnetic latitudinal zones.

For better comparison, it is thus natural to reduce the total intensity data to pole. However, such transformation from the low latitude data may not be worthwhile owing to the dominance of the horizontal component of the field, and

(iii) The transient geomagnetic variations for night hours are mainly due to magnetospheric currents, whose configuration is such that they produce uniform but significant horizontal field variations and almost negligible vertical transient field variations at the surface of the earth at low geomagnetic latitudes (Schmucker 1970).

Under the above considerations we have preferred to present the vertical component profiles over the Indian region (figure 2). The latitudinal extent of all the selected

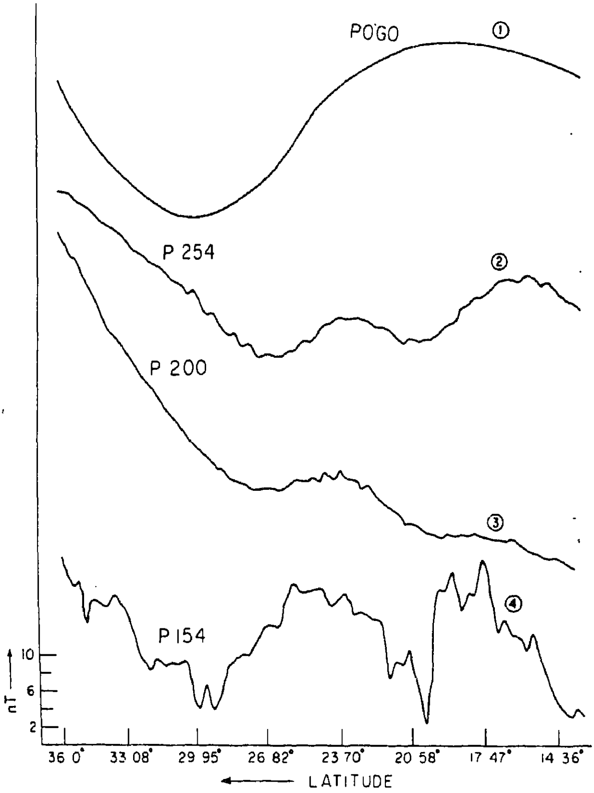

Figure 1. Magnetic responses at satellite level: 1. POGO—Total intensity (scalar) 2 and 3

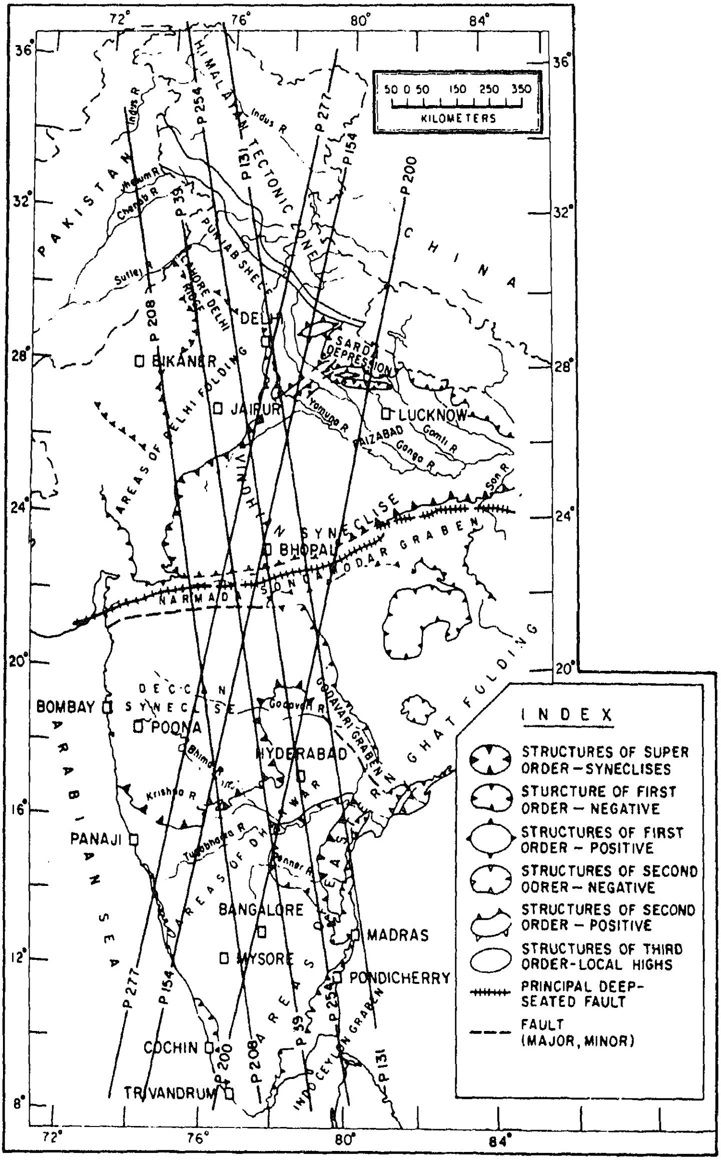

Figure 2. MAGSAT passes over major geological and tectonic features of the Indian subcontinent.

rofiles is from 36° N to 9° N with different longitudinal trajectories. The profiles cut cross the major geological and tectonic boundaries of India. The data obtained from AGSAT investigator-B tapes was sampled at 36 km spacing. The range of altitude for

Table 1. Altitude range of the spacecraft for the selected MAGSAT Passes

Pass No.		254	131	208	39	200	277	154
Altitude range (km)	Max	368	406	379	444	411	439	397
	Min	398	448	412	489	450	482	437
Mean altitude (km)		388	427	395	466	433	460	417

the ionosphere and magnetosphere, and (b) fields due to crustal origin. The former can be minimised by selecting data for magnetically quiet period. In the present case, the selected profiles are generally for night hours and the K_p index ranges from 0 to 20. The geomagnetic variations as observed at Hyderabad Observatory for the chosen profiles produce insignificant time-varying fields.

Under the above considerations, we are left with data which might be expected to contain magnetic response from the subsurface features. However, such data is superimposed on different noises which are (a) long wavelength fields (due to magnetospheric ring currents), (b) instrumental noise (high frequency oscillations of the order of 1 nT; Mayhew *et al* 1980), and (c) fields due to local external currents.

Due to the presence of these, extraction of meaningful signatures and their interpretation in terms of causative sources really becomes difficult. It may, however, be mentioned here that the present investigations are mainly confined to detect the magnetic responses which are superimposed over broad linear trends. Correction for these trends are not applied as it may not necessarily very much improve the response we are looking for. One way of overcoming the problem due to other noise levels is to look for consistent pattern of magnetic signatures over the known geological and tectonic features in different satellite passes. The repeatability of responses in various passes coincident with geological and tectonic boundaries indicates that the response from a particular geological configuration is indeed real.

3. Correlation studies

The crustal anomalies at satellite level are expected to be controlled by (i) lateral variations in the physical, chemical and thermal properties of various subsurface rock formations forming different types of tectonic and geological boundaries, and (ii) the variations in thickness of the uniformly magnetised crustal layers. The assemblage of these factors produce magnetic signatures of different shapes and amplitudes at the observing site. In view of this, an attempt to investigate meaningful signatures of the complex geological and tectonic boundaries of the Indian subcontinent through the MAGSAT data may be illuminating.

4. Long wavelength anomalies

In most of the profiles (figure 3) we confirm the broad 'low' over Himalayas and 'high' over Peninsular India as obtained by Regan *et al* (1975), Langel *et al* (1982) and Frey

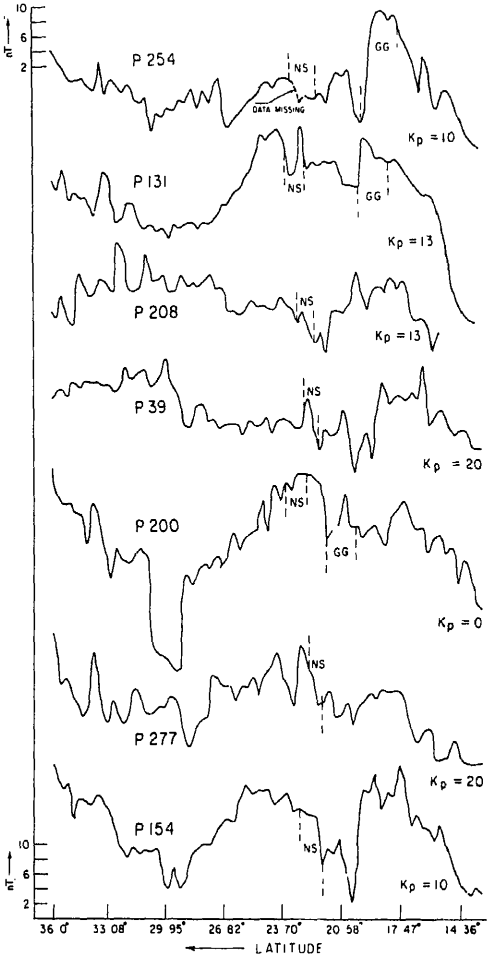

Figure 3. MAGSAT vertical intensity response along different passes. NS and GG represent respectively the Narmada-Son lineament and Godavari graben.

982) from total intensity data. The additional striking feature brought out here on ost of the profiles is a 'low' centred between 19° and 23° latitudes over the broad eninsular 'high'. Interestingly, the present area encompasses the major rift zones of eninsular India which is also evident from the gravity anomaly pattern of the region. he features could be attributed either to lateral changes in magnetic intensity of the bsurface geological formations or to changes in thickness of uniformly magnetised bsurface layers or both. The deep seismic sounding results of Kaila *et al* (1981) ggest downwarping of the crust in this area. The nature of long wavelength anomalies ver Peninsular India indicates that the sources are deep-rooted possibly extending own to lithosphere.

The other prominent 'low' as indicated by the present work is confined to the region –E of Ganga basin and above the Sarda depression under the foothills of Himalayas 9° N to 31° N). The gravity map of India (Qureshy 1970) shows sharp gradient over this region. Geomagnetic depth sounding results (Arora *et al* 1982) indicated a prominent conductive structure which coincides with the seismically active Delhi-Haridwar ridge (Kaila and Narain 1976). The presence of magnetic signatures in most of the passes over this region is indicative of deep-rooted structure in the foot-hills of Himalayas. The correlation of the above mentioned geophysical results assumes importance in understanding the proper geodynamical significance of the area. Superimposed on these are relatively smaller wavelength anomalies which are described here.

5.1 *Narmada-Son structure*

The Narmada-Son lineament traverses west to east and almost bisects the Indian subcontinent. This is a tectonic feature of Precambrian origin and is characterised by two faults *viz* Narmada-Son and Tapti faults. The faults give rise to rift valleys delimiting the Satpura horst. The faults are reported to be reaching quite deep extending even upto upper mantle (Ray 1967).

The magnetic signatures in most of the profiles over Narmada-Son are characterised by an initial rise and then a sharp fall (North-south direction) indicative of a fault-like structure. The presence of this signature at satellite height confirms the deep-rooted cause of the structure as suggested by Ray (1967).

5.2 *Godavari graben anomaly?*

Godavari graben also had its origin in Precambrian times and possibly connected to eastern ghat orogeny. Cratonic and sedimentary basin studies by Naqvi *et al* (1974) and Sastri *et al* (1981) indicate respectively that the graben extends 800 km in length and its width varies from 50 to 100 km or even more. The Godavari graben extends upto Narmada-Son lineament which probably indicates that the structure is wider near the vicinity of the rift junction (figure 2). The present MAGSAT passes cut across the graben where the width is substantially large.

Over the Godavari graben (between 20° and 22° latitudes) a rise in amplitude is observed. It is quite intriguing, however, to observe such an anomaly in different passes (P 131, 200, 254) at the satellite level. Similar nature of anomaly in all the three profiles suggests that the response from the structure is real. This magnetic signature might possibly indicate differences in broad subsurface configuration at deeper level and needs detailed study with finer grid data in the light of existing geophysical information.

6. Conclusions

In the present work the hitherto untried vertical component MAGSAT profile data brings out magnetic anomalies which coincide with the major geological and tectonic boundaries of the Indian subcontinent. A new finding from the present data is a conspicuous magnetic 'low' over the broad Peninsular 'high' suggesting a deep basin-like structure. Besides, magnetic 'low' above the Ganga basin, a 'low' over Narmada-Son rift and a 'high' over the northern part of Godavari graben are the significant

The anomalous response of Godavari graben is quite intriguing and needs further ailed study. The quantitative interpretation of satellite data needs to be done with at caution in view of the varying altitudes and geomagnetic inclinations.

knowledgements

e investigation has been carried out, with the aid of MAGSAT data made available by SA, to Survey of India. The authors are grateful to NASA, Surveyor General and Col. r.) Arur of Survey of India, Dehradun for providing us the copy of the tapes of the GSAT data. Thanks are also due to Dr M N Qureshy of the Department of Science d Technology, New Delhi (India) for coordinating various aspects of MAGSAT earch programmes in India. The authors are also thankful to Messrs P. V. Swamy, K. Ganesh, J. P. Sastry and Sł. m Vaidya for assistance.

ferences

ra B R, Lilley F E M, Slone M N, Singh B P, Srivastava B J, and Prasad S N 1982 *Geophys. J.R. Astr. Soc.* **69** 459
y H 1982 *Geophys. Res. Lett.* **9** 299
la K L, Murthy P R K, Rao V K and Kharetchko G E 1981 *Tectonophysics* **73** 365
la K L and Narain H 1976 *Proc. Himalayan Geol. Sem. Section* 2 pp. 1–30
gel R A, Coles R and Mayhew M A 1980 *Can. J. Earth Sci.* **17** 876
gel R A, Phillips J D and Horner R J 1982 *Geophys. Res. Lett.* **9** 269
yhew M A, Johnson B D and Langel R A 1980 *Earth Planet. Sci. Lett.* **51** 189
qvi S M, Rao V D and Narain H 1974 *Precambrian Res.* **1** 345
eshy M N 1970 *Proc. II Symp. Upper Mant. Proj. Hyd.* 1–24
S 1967 *Sci. Cult.* **33** 252
an R D, Cain J C and Davis W M 1975 *J. Geophys. Res.* **80** 794
lor R V, Lazarowics A R and Bramer R F 1982 *Geophys. Res. Lett.* **9** 289
tri V V, Venkatachala B S and Narain V 1981 *Int. Symp on continental margin* (Amsterdam: Elsevier)
mucker U 1970 *Bull. Scripps. Inst. Oceanogr.* **13** 1

The Mannapra syenite, Central Kerala, India: Geochemistry, petrogenesis and bearing on anorogenic magmatism

M SANTOSH and K G THARA

Centre for Earth Science Studies, P.B. 2235, Sasthamangalam, Trivandrum 695010, India.

MS received 27 January 1984; revised 15 September 1984

Abstract. Occurrence of a syenite body near Mannapra, Trichur district, Kerala, is reported. The syenite, emplaced within charnockitic country rocks along the Idamalayar fault-lineament, is exposed over an area of 8 km^2. The rock, classified as quartz alkali feldspar syenite based on Q-A-P proportions, has alkali feldspar as the dominant mineral constituent which shows variation in perthitic texture from crypto- to micro- and patch-perthites. Both ortho- and clino-pyroxenes are present, with the former showing blebs of plagioclase suggesting Al-unmixing. Clinopyroxene shows subsolidus reequilibration with greenish pleochroic grain margins and local conversion to alkali amphibole. The petrochemical characters indicate that the syenite crystallized from a partial melt which equilibrated from K-rich, Rb-depleted source in the upper mantle, in response to crustal distension and mantle degassing prior to the rifting of the continent. Reaction between early formed minerals and the late peralkaline liquid towards the residual phase resulted in subsolidus reequilibration textures. The syenite is envisaged to be yet another example of the manifestation of anorogenic magmatism in this part of the Indian shield.

Keywords. Syenite; mineralogy; geochemistry; petrogenesis; subsolidus reequilibration; anorogenic magmatism.

1. Introduction

Occurrences of a number of alkali plutons have been recently noted in the Kerala region, showing spatial relationship with regional fault-lineaments (*e.g.* Nair *et al* 1983; Santosh and Nair 1985). As the region occupies a significant portion of the south-western part of the Indian shield and the western continental margin of India, studies on the petrochemistry and tectonics of these intrusives have been taken up to understand their role in the geologic and tectonic evolution of the region. Available geochronologic data suggest a Late Precambrian-Early Paleozoic taphrogenic magmatism with imprints of related metallogeny to which phase the alkaline intrusives and pegmatites of the region are correlated (Santosh and Nair 1983; Santosh 1984a).

The close relationship between alkaline magmatism and rift-tectonics is well known (Bailey 1974; Murthy and Venkataraman 1964). As the plutons, ranging from alkali granites to alkali syenites and carbonatites (Nair *et al* 1984a, b) are spatially related to fault-lineaments which have probable mantle extension, it is presumed that the magmatism which is anorogenic in nature, is a precursor to the rift-tectonics of the continental margin (Santosh and Nair 1985). The occurrence of a syenite pluton near Mannapra, Trichur district, Kerala, is reported here. Based on its geochemical characters, an attempt has been made to evaluate its petrogenetic aspects.

2. Geological setting

The major part of the lithology of the Trichur district comprises charnockite group of rocks made up of hypersthene and/or diopside bearing granulites and hornblende

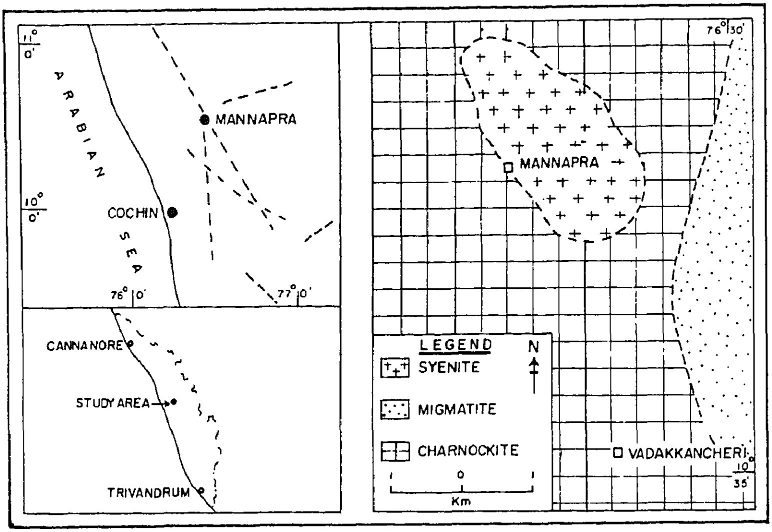

Figure 1. Generalised geological map of the Mannapra area. The inset shows location of the syenite along the NW-SE trending Idamalayar fault-lineament.

granulites (Mahadevan 1964; Rao 1978). The charnockites show development of a foliation which has a general NNW-SSE to N-S trend with steep dips towards west. In the Mannapra locality, the charnockite is medium to coarse-grained variety with a feeble NW-SE foliation trend. Towards east of the locality, the charnockites show contact with migmatitic gneisses containing hornblende and biotite.

The syenite is exposed as a NW-SE elongated body around 8 km^2 within the charnockites near the charnockite-migmatite contact. It occurs along the NW-SE trending Idamalayar lineament (figure 1). This lineament is an active fault along which a suite of gabbroic dykes of Tertiary age and the alkaline pluton of Sholayar are emplaced (Tilak 1980; Nair *et al* 1984b; Santosh and Sankar 1984). The syenite shows rather sharp contacts with the charnockitic rocks. From the quartz-hypersthene-feldspar assemblage of the charnockite, there is an abrupt change to interlocking pyroxene-feldspar assemblage of the syenite as discernible in few localities. The syenite is medium-to-coarse grained at its exposed peripheries and tends to be coarse grained towards the centre.

3. Mineralogy

In thin sections, the syenite shows a general hypidiomorphic granular texture. However, the alkali feldspar tends to form megacrysts in some cases. The mineralogical assemblage comprises alkali feldspar, orthopyroxene, clinopyroxene and amphibole with minor plagioclase, biotite and opaques. Accessories include apatite, zircon, sphene, epidote, chlorite and calcite. Point counting with an electrical integrator shows average model contents of 4·2% quartz, 72·1% alkali feldspar, 5·5% plagioclase, 7·2% pyroxenes, 3·3% amphibole, 2·4% biotite and 2·2% opaques with accessories

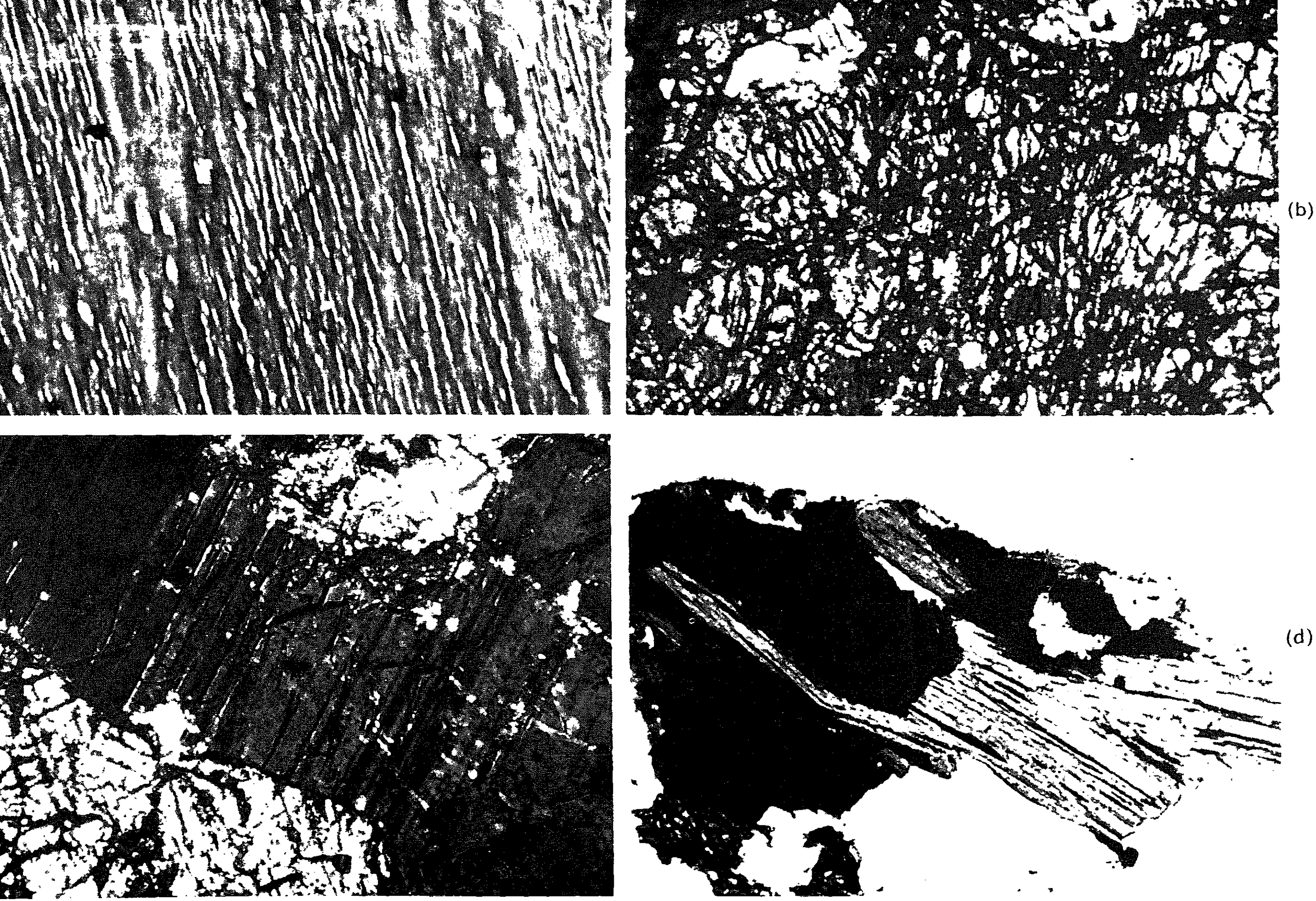
(b)
(d)

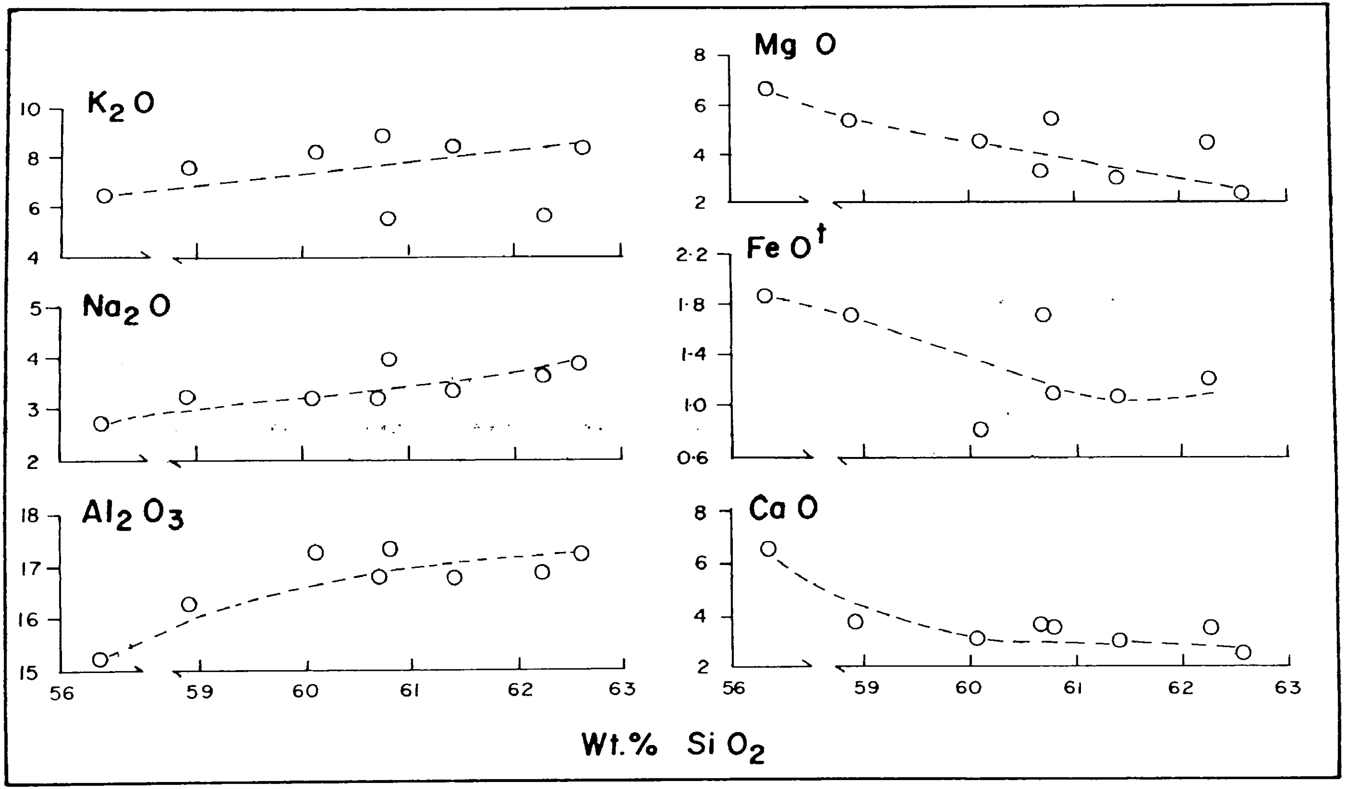

Figure 3. Major element variations in the Mannapra syenite

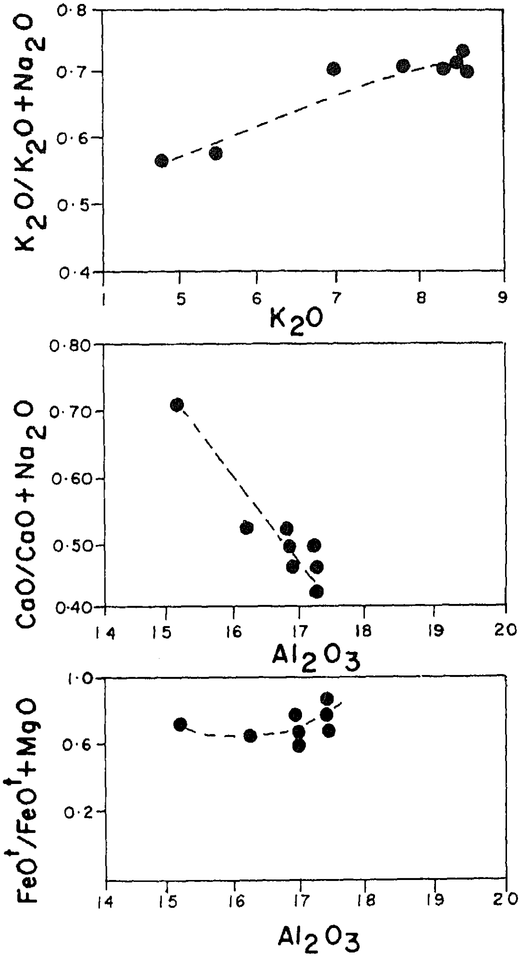

Figure 4. $K_2O/K_2O + Na_2O$ *vs* K_2O, $CaO/CaO + Na_2O$ *vs* Al_2O_3 and $FeO'/FeO' + MgO$ *vs* Al_2O_3 diagrams.

nstituting the rest 3·1 %. The recalculated Q-A-P proportions (5·13 : 88·14 : 6·73) rrespond to that of quartz alkali feldspar syenite, following Streckeisen's (1976) heme.

Alkali feldspar, which forms the dominant mineral constituent, occurs as subhedral anhedral grains exhibiting varied perthitic textures. The exsolved Na-phase in the st K-feldspar that generally lacks microcline cross-hatching is found as braids to arser blebs and patches. The perthitic textures could be classified as varying from fine yptoperthite to coarse braid microperthite and patch perthite (figure 2a). Plagioclase relatively rare and occurs as subhedral laths showing lamellar twinning with tinction angles corresponding to a range in composition of $Ab_{90}An_{10}$ to $Ab_{80}An_{20}$. agioclase is generally seen as minor discrete grains but also occurs as inclusions in kali feldspar.

Pyroxene constitute the major mafic silicate in the syenite and occur as large bhedral crystals. In the absence of data on mineral chemistry, estimation of their

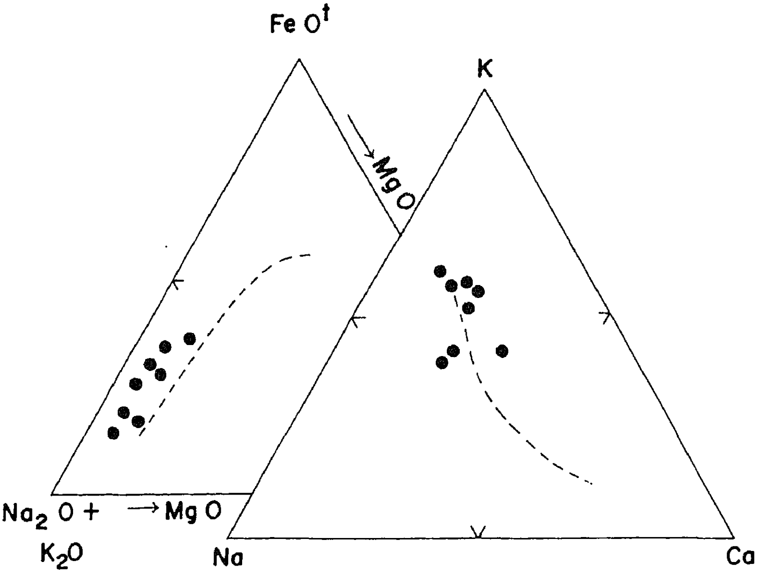

Figure 5. A-F-M and K-Na-Ca variations in the syenite. The broken line represents calc-alkaline trend (after Barker and Arth 1976).

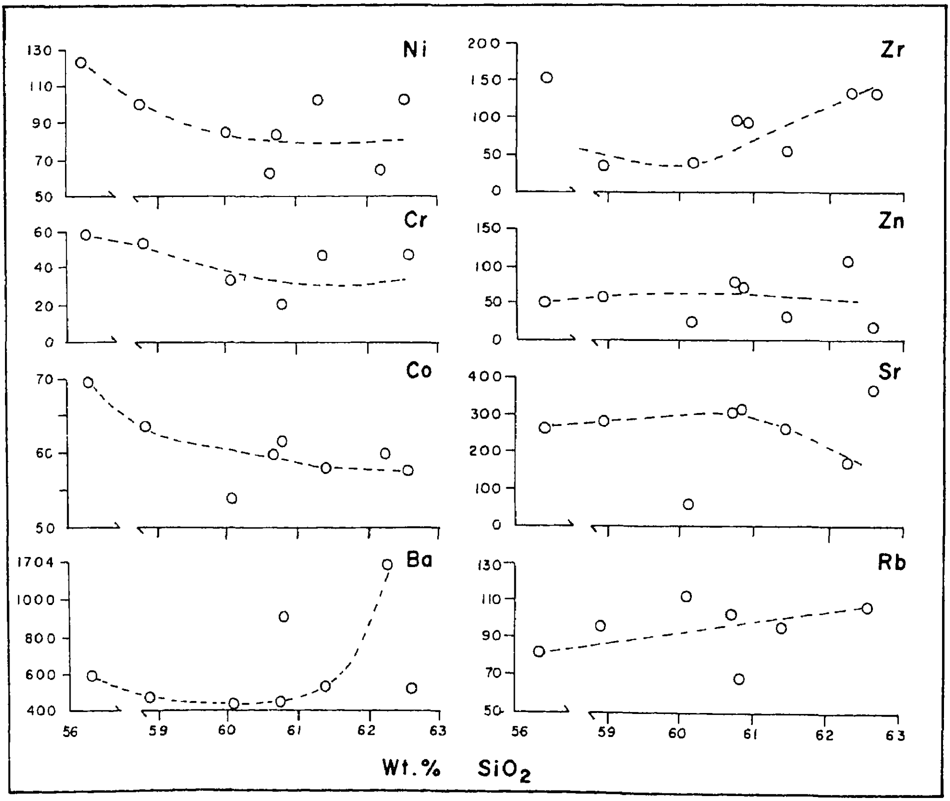

ecise composition is difficult. But some inferences could be drawn based on their tical characters. Both ortho- and clino-pyroxenes are present in the syenite, with the ter being more dominant. The orthopyroxene shows moderate pleochroism with an sorption as X = pale pink, Y = yellowish green and Z = greenish pink. Basal tions of the orthopyroxene show symmetrical extinction and (001) sections show aight extinction. Elongated patches of plagioclase are observed within the ortho- roxene laths (figures 2b, c). This texture closely resembles that described by Emslie 975) and suggests Al-unmixing from the pyroxene solid solution as a result of vering of pressure. Clinopyroxene is pale brownish and non-pleochroic with $Z \wedge c$ 40–44°. In many cases, the grain margins show feeble to moderate pleochroism with = greenish brown, Y = greenish yellow and Z = green with a slight increase in the $\wedge c$ value. The pyroxenes are rarely fresh and unaltered. A moderate degree of bsolidus alterations is common, characterised by the development of greenish aphiboles. Some grains show partial breakdown to an assemblage of magnetite- otite turquoise chlorite-amphibole.

In addition to the occurrence as a subsolidus reaction product, amphibole is also ınd as discrete laths exhibiting strong pleochroism as X = greenish yellow, Y yellowish green and Z = deep green with $Z \wedge c = 13°$, indicative of an alkaline mposition.

Biotite is found as two textural varieties. It generally occurs as thin laths fringing ıgnetite grains (figure 2d). Biotite is also found as an interstitial phase along with aphibole and quartz. In both cases, it shows moderate pleochroism from brownish llow to reddish brown. Euhedral crystals of zircon and apatite are generally found as clusions within pyroxenes. Calcite is apparently primary as it is not found as an eration product along with other ferromagnesium minerals, but frequently occurs as interstitial phase between the grain boundaries of alkali feldspars, comparable with nilar occurrences in other alkaline rocks of the region (Nair and Santosh 1984a). ie opaques are mainly represented by magnetite and subordinate ilmenite. Minor rite and chalcopyrite are also found.

Geochemistry

ght representative samples of the Mannapra syenite were analysed for major and ected trace elements. The samples for analyses were collected from working quarries ound Mannapra area. Major elements were analysed by wet chemical methods and ıce elements by atomic absorption spectrophotometer (Perkin-Elmer 4000). The ecision and accuracy were checked by performing duplicate analyses. The analytical ta summarised in table 1, shows comparison with average values of the Sholayar enite (SH), an alkali feldspar syenite in central Kerala (Nair *et al* 1984b) and with ose averaged for alkali syenite (AS) by Nockolds (1954). All the analyses show quartz- rmative character with significant amount of normative diopside implying alkaline ture (table 2).

The SiO_2 content shows a moderate variation from 58·94 to 62·62 with a mean at ·45, comparable with AS (61·86) and SH (64·14). Al_2O_3 values are fairly consistent th a mean at 16·76. The variations in the levels of Fe_2O_3 (1·53–5·21), FeO (1·02–2·79), ıO (2·46–6·94) and MgO (0·80–1·76) are significant and show mean values (2·81, 1·88, 36 and 1·34 respectively) which are comparable with those of SH and AS, except in the

Table 1. Major and trace element analyses of Mannapra syenite compared with those of similar syenites

	MP-1	MP-2	MP-3	MP-4	MP-5	MP-6	MP-8	MP-10	Mean (MP)	Mean (AS)	Mean (SH)
Major elements, wt. %											
SiO_2	61·39	60·69	60·83	62·26	62·62	56·72	60·14	58·94	60·45	61·86	64·14
Al_2O_3	16·82	16·82	17·33	16·82	17·33	15·29	17·33	16·31	16·76	16·91	16·82
TiO_2	0·32	0·10	0·39	0·52	0·23	0·14	0·16	0·44	0·29	0·58	0·49
Fe_2O_3	2·22	1·53	3·46	1·93	1·58	5·21	3·54	3·18	2·81	2·32	2·62
FeO	1·02	1·78	2·28	2·79	1·10	2·14	1·38	2·53	1·88	2·63	0·82
MnO	0·04	0·07	0·05	0·06	0·03	0·12	0·03	0·06	0·06	0·11	0·02
MgO	1·12	1·76	1·12	1·28	0·96	1·92	0·80	1·76	1·34	0·96	0·64
CaO	3·14	3·81	3·81	3·58	2·46	6·94	3·36	3·81	3·86	2·54	2·64
Na_2O	3·37	3·24	4·04	3·65	3·39	2·84	3·20	3·21	3·37	5·46	2·59
K_2O	8·34	8·53	5·46	4·82	8·50	6·90	8·44	7·75	7·34	5·91	7·87
P_2O_5	0·16	0·18	0·15	0·21	0·12	0·23	0·34	0·41	0·23	0·19	0·05
Moisture	0·21	0·39	0·26	0·12	0·14	0·24	0·27	0·17	0·23	—	0·23
L.O.I.	0·28	0·34	0·33	0·63	0·27	0·63	0·39	0·43	0·41	—	0·33
K_2O/Na_2O	2·47	3·14	1·35	1·32	2·50	2·43	2·64	2·41	2·28	—	3·04
Fe_2O_3/FeO	2·18	0·86	1·52	0·69	1·44	2·43	2·57	1·26	1·62	—	3·20
$Mg/Mg+Fe^t$	0·22	0·30	0·14	0·18	0·23	0·18	0·12	0·20	0·20	—	—
Agpaitic index	0·87	0·87	0·73	0·67	0·85	0·80	0·83	0·84	0·81	—	—
Trace elements, ppm.											
Ba	844	440	918	1704	530	608	416	494	744	—	445·2
Bi	94	90	78	112	60	70	58	66	78·5	—	—
Co	64	60	62	56	58	70	54	64	61	—	—
Cr	48	—	22	24	48	60	54	56	44·5	—	25·2
Cu	—	40	22	6	6	36	6	8	12·5	—	43·6
Ni	98	60	82	50	100	124	84	102	87·5	—	32·0
Pb	50	38	10	16	38	40	54	38	35·5	—	20·6
Rb	98	106	70	54	110	84	116	98	92	—	170
Sr	272	320	328	196	382	278	70	292	267	—	8·8
V	—	40	60	60	—	60	—	40	52	—	—
Zn	40	88	78	124	26	56	30	60	62·75	—	29·8
Zr	60	100	100	140	140	160	40	40	97·5	—	108·2
K/Ba	82·3	160·93	49·37	23·48	133·13	94·21	168·41	130·23	105·22	—	—
Ba/Sr	3·10	1·38	2·80	8·69	1·39	2·19	5·94	1·69	3·4	—	57·2
K/Rb	706·43	668·00	647·47	740·94	641·45	681·87	603·97	656·46	668·3	—	408
Rb/Sr	0·36	0·33	0·21	0·28	0·29	0·30	1·66	0·34	0·47	—	—

Mean (MP)—Mean of Mannapra syenite analyses; Mean (AS) Average of alkali syenite from Nockolds (1954); Mean (SH) Average ightly higher levels of CaO. In the absence of Ca-rich plagioclase, this component ust reflect the compositional variation of the pyroxenes. The unusually higher Fe_2O_3 ıd CaO contents in one sample (MP-6) is reflected in the high modal contents of rromagnesium minerals. Na_2O (av. 3·37) and K_2O (av. 7·34) are comparable with ıose of SH (av. 2·59 and 7·87 respectively) but differ from AS in having higher K_2O and $_2O/Na_2O$ ratios (av. 2·28). Higher K_2O content is, however, noted to be a general ature of all alkaline plutons of the Kerala region (Nair and Santosh 1984a). $Na_2O +$ $_2O$ (av. 10·71) is less than Al_2O_3 (av. 16·76) and in most cases is less than 1/6 SiO_2, assifying the syenite and plumasitic (Polanski 1949). With respect to total alkalies, ıere is a pronounced deficiency in alumina, expressed in the occurrence of up to ·89 % normative diopside (table 2). Agpaitic indices calculated for the syenite show an erage of 0·81, being close to unity. Fe_2O_3/FeO levels (av. 1·62) are slightly lower than ıose of SH (av. 3·20). $Mg/Mg+Fe^t$ ratios show a variation from 0·30 to 0·12, ınsistent with a moderate degree of fractionation.

Major element variations are shown in figure 3, where they are plotted against SiO_2. ll the elements show overall smooth trends of variations consistent with the empirical ws governing magmatic crystallization. Al_2O_3, K_2O and Na_2O show increasing ends with increasing SiO_2. The sympathetic behaviour of these oxides is in cordance with the petrographic observation of alkali feldspar being the major quidus phase towards the late stages of crystallization. MgO, FeO^t and CaO show ıarp decrease with increasing silica saturation, consistent with early crystallization of rromagnesium minerals. The inter-element variations are shown in figure 4, where $_2O/K_2O+Na_2O$ *vs* K_2O plots show smooth increase supporting the evidence of kali feldspar fractionation. The $CaO/CaO+Na_2O$ *vs* Al_2O_3 plots show a sharp ecline. Since plagioclase occurs only as a minor constituent, this variation records the ıange in pyroxene and amphibole compositions towards more sodic end members, hich in turn is a reflection of the increasing peralkalinity of the liquid. Mitchell and latt (1978) and Stephenson and Upton (1982) suggest that peralkalinity has a direct ontrol over Na-enrichment whereas silica saturation is rather unimportant. In this gard, the bulk rock analyses need not show peralkalinity (av. mol % Na_2O $K_2O/Al_2O_3 = 0{\cdot}81$ in the present case) as exemplified by a majority of rock suites of ıe Gardar Province of Greenland. FeO^t/FeO^t+MgO *vs* Al_2O_3 plots do not show uch variation, testifying to the above view that alkalies played the determining role, as emplified in the A-F-M and K-Na-Ca diagrams (figure 5), where the plots of the enite closely follow an alkali enrichment trend relative to the F-M join, with a specific crease in K and Na relative to Ca.

Among trace elements, the mean levels of Co (61 ppm), Cr (44·5 ppm), Ni (87·5 ppm) ıd Zn (62·8 ppm) are higher than those of Sholayar syenite (30·4, 25·2, 32 and ·8 ppm respectively). This correlates well with their entry in ferromagnesium inerals, the modal content of which is almost double (18·2 %) than that of Sholayar v. 9·7 %). Ba (av. 744 ppm), Sr (av. 267 ppm) and Zr (av. 97·5 ppm) show higher levels here as Rb (av. 92 ppm) is rather low. The range is as follows: Ba 416–1704 ppm, Sr –382 ppm, Rb 54–116 ppm and Zr 40–160 ppm.

The K/Rb ratio is high (668·3) compared to SH (av. 408) and that reported for

Table 2. Normative composition of Mannapra syenite

		MP-1	MP-2	MP-3	MP-4	MP-5	MP-6	MP-8	MP-10	Mean
Q		3·9	0·66	7·86	12·36	4·92	2·04	2·88	2·34	4·62
or		49·48	50·60	32·25	28·36	50·04	40·59	50·04	45·59	43·37
ab		28·30	27·25	34·06	30·92	28·82	24·10	27·25	27·25	28·49
an		6·12	6·12	13·07	15·01	6·95	8·62	7·78	7·23	8·86
di	wo	3·25	4·64	2·09	0·81	1·86	10·09	3·02	3·83	3·70
	en	2·80	3·00	1·50	0·40	1·50	4·80	2·00	2·70	2·34
	fs	—	1·32	0·40	0·40	0·13	—	—	0·79	0·61
hy	en	—	0·66	1·72	3·70	1·19	—	—	2·24	1·90
	fs	—	1·40	0·20	2·20	0·10	—	—	0·40	0·86
mt		2·32	2·32	5·10	1·86	2·32	6·96	3·94	4·64	3·68
he		0·64	—	—	—	—	0·48	2·72	—	1·28
il		0·61	0·15	0·76	1·06	0·46	0·30	0·30	0·91	0·57
ap		0·67	0·67	0·34	0·34	0·34	0·67	0·67	1·01	0·59
	Ab	33·73	32·45	42·91	41·62	33·56	32·88	32·03	34·03	35·40
	An	7·29	7·28	16·46	20·21	8·10	11·76	9·15	9·03	11·16
	Or	58·98	60·27	40·63	38·17	58·34	55·36	58·82	56·94	53·44

bearing phases. This increase in Ba with silica saturation supports the deduction that alkali feldspar constitutes the dominant fractionating phase in the syenite. Sr shows a slight increase initially, to be followed by a decrease with higher SiO_2 levels, marking early precipitation of Ca-bearing minerals, mainly apatite and pyroxene. Cr, Ni and Rb show scatter. However, K/K + Na *vs* Rb shows a positive correlation. Interelement correlations show that Ba and Sr contents of the syenite maintain a reciprocal relationship whereas Sr *vs* Rb and Sr *vs* Ca plots yield overall positive correlations. Zr concentrates towards the residual phase.

5. Discussion

The absence of highly coarse mesoperthites in contrast to the Sholayar syenite and of microcline cross-hatching in the host K-feldspar imply higher equilibration temperatures for the Mannapra syenite. The variation in the perthitic texture from fine cryptoperthite to coarser braid and patch perthites is indicative of increasing degree of fractionation aided by slow cooling rate and presence of fluids (Parsons 1978; Santosh and Nair 1985). Build-up of a fluid phase towards later stages of crystallization is best exemplified by the texture of ferromagnesium minerals. Clinopyroxenes exhibit pronounced subsolidus reaction resulting in the development of greenish pleochroic grain margins reflecting interaction between the early crystallized pyroxene and late peralkaline fluid (Mitchell and Platt 1978; Stephenson and Upton 1982). Biotite fringes around magnetite are consistent with the reaction:

$KAlSi_3O_8$ (sanidine) + Fe_3O_4 (magnetite) + H_2O = $KFe_3AlSi_3O_{10}(OH)_{22}$ (biotite) + 1/2 O_2 (Parsons 1980).

The magnetite-biotite-chlorite-amphibole assemblage also indicates subsolidus reactions (Mitchell and Platt 1982).

The presence of plagioclase laths in orthopyroxene is significant. Such textures are ported by Philpotts (1966) and Emslie (1975), largely from pyroxenes in anorthositic cks. Experimental data on synthetic systems and natural rock compositions monstrate that pyroxenes with high Al_2O_3 contents are stable at high pressures and nperatures (Green and Ringwood 1967). It is recognised that aluminous pyroxenes in balkaline and some alkaline rocks have crystallized at moderate to high pressures. ıe presence of exsolved Al in the form of a silica saturated phase (plagioclase) denotes at the original pyroxene did not crystallize from silica-deficient magmas. The roxene contained the plagioclase components in solid solution. Decompression of an itially homogeneous orthopyroxene solid solution resulted in the exsolution of a $aAlSi_2O_6$-rich component (Kushiro 1969). The probability of the plagioclase laths ing inclusions is not favoured since, as deduced from petrochemical features, roxene crystallized much earlier than plagioclase and hence the latter will not be ikilitically included in the former under normal crystallization-fractionation ocesses.

Petrogenesis

ısed on the available petrochemical data, some inferences could be drawn regarding e petrogenesis of the syenite. Four main aspects have to be considered: (i) mposition of source material, (ii) mode of melting including depth, (iii) the extent of elting and (iv) the changes in magma prior to solidification.

To start with, we assume that the source is lower crust or upper mantle. This sumption is based on the general geochemical characters of the syenite including high ınsition element levels and K/Rb ratios. This assumption is substantiated by servations made on similar alkalic plutons of Kerala region (Nair and Santosh 84a, b; Santosh and Nair 1985) as well as from the adjacent terrains (Bose *et al* 82). Moreover, the syenite is emplaced along an active fault-lineament which has obable extension to mantle-depths (Nair *et al* 1984b) like other fault-lineaments of e region (Santosh and Sankar 1984).

In order to produce melting in the mantle, a geotherm is required to intersect the propriate melting curve. The general processes of heating within the earth, dioactivity, thermal radiation and thermal conduction would be too diffuse to cause at focussing (Bailey 1977). In the absence of sufficient evidences to invoke a 'mantle ume' theory, other methods of raising the temperature could be considered, namely, ctional heating or heating of the overlying rocks by a body of rising magma. The most obable mechanism of melting in stable plate interiors is mantle upwarping, oducing rapid decompression melting, resulting in anorogenic magmatism. Bailey 974, 1977) showed that crustal distension can cause large-scale mantle degassing ıding to the addition of volatiles to the overlying rocks causing localised melting. At gher temperatures, gas fluxing can cause heat focussing which function as a doubly icacious mechanism of melting. The intrinsic association of CO_2 with metamorphic lewton *et al* 1980; Harris *et al* 1982; Santosh 1984b) and magmatic (Nair *et al* 1984a; ntosh 1984a) regimes of the region is significant. We presume that the NW-SE and

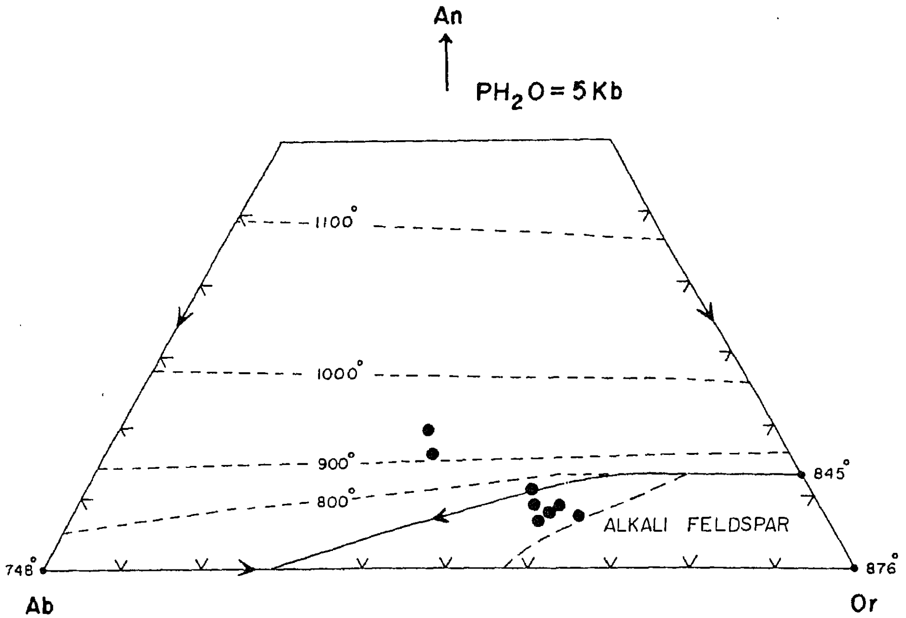

Figure 7. Part of Ab-An-Or ternary diagram with isotherms (after Yoder *et al* 1957) showing the plots of the Mannapra syenite.

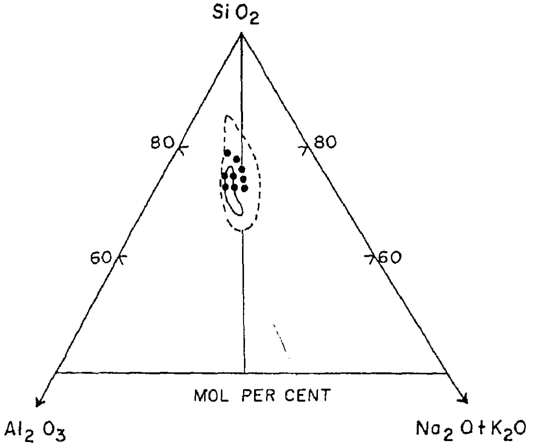

Figure 8. SiO_2-Al_2O_3-$Na_2O + K_2O$ (mol %) plots of the Mannapra syenite. The broken line represents the field of syenites of the Nile Province (after Harris 1982) and the continuous line represents the field of Sholayar syenite (after Nair *et al* 1984b).

Paleozoic taphrogenic magmatism (Santosh and Nair 1983, 1985) serves as a keynote to the pre-rift tectonics of the Indian continental margin, as the genetic link between alkaline magmatism and rift-tectonics is well known (Bailey 1974; Murthy and Venkataraman 1964). Anorogenic magmatism of similar age has been reported from other shield areas also (Greenberg 1981; Harris 1982).

The data presented here are insufficient to make precise estimates of the nature of source rock. However, some general deductions could be made. Melting of mica-rich ıntle will generate potash-rich magmas whereas more sodic magmas result when ıphibole-rich mantle is melted (Lloyd and Bailey 1975). Higher K and K/Rb levels licate a K-rich, but Rb-depleted source. Low Mg/Mg + Fe^t levels and higher Sr-ntent together with the absence of associated mafic differentiates eliminate rivation by differentiation from a basic magma and suggest partial melting. perimental studies show that as a consequence of the incongruent melting of thopyroxene, silica-saturated alkaline magmas can be generated from olivine-rich rent rocks (Reay and Harris 1964). The investigations of Yoder and Tilley (1962) and Hara (1968) indicate that at higher pressures, the mineral stabilities change, resulting the change of position of the thermal divide in the fosterite-silica-nepheline-diopside stem, leading to the formation of alkaline magmas directly by fusion and indirectly by ctionation from hypersthene-normative liquids.

Subsequent change in the magma is marked by the development of peralkalinity. ochemical characters suggest that alkali feldspar was the dominant fractionating ase. Fractionation of feldspar ultimately leads to the development of a peralkaline iduum in any suite, especially when there is a deficiency of alumina with respect to total alkalies (Bailey and Macdonald 1969). Feldspar being the major liquidus ase, the Ab-An-Or system has been chosen to evaluate the present data. Plots in the stem (figure 7) mainly fall in the alkali feldspar solid solution field and within the unds of 800°C isotherm, with a general trend towards the Or-apex. Log Sr *vs* log Rb ots (Condie 1973) indicate that the pressures were largely of the order of 8 Kb. In system relevant to peralkaline rocks, namely, the SiO_2-Al_2O_3-$Na_2O + K_2O$, the ots of syenite fall within the field of similar syenites belonging to phase 2 magmatism the Nile Province (Harris 1982) and close to the field of the Sholayar syenite (figure Interestingly, the plots define a fractionation trend away from the SiO_2-apex wards the region of alkalies, similar to the trend of the syenites of the Illimaussaq mplex in Greenland (Macdonald 1974), consistent with the view of development of a e-stage peralkaline character, supplemented by the occurrence of up to 14·39% rmative diopside. This peralkaline liquid brought about such textures as the arsening of perthites and the subsolidus reactions of pyroxenes.

knowledgements

ıe study forms part of the CESS project (R.A.D.-4), "Acid magmatism and related etallogeny in Kerala". The authors thank the Director, Centre for Earth Science ıdies, for research facilities, and Dr N G K Nair, CESS for constant encouragement.

ferences

ley D K 1974 In *The alkaline rocks* (ed.) H Sorensen (New York: John Wiley) p. 148
ley D K 1977 Igneous rocks and the degassing of earth; Tomkeieff mem. Lecture, Univ. Newcastle. 41 p.
ley D K and Macdonald R 1969 *Am. J. Sci.* **267** 242
ker F and Arth J G 1976 *Geology* **4** 596
se M K, Ghosh-Roy A K and Czygan W 1982 *Lithos* **15** 77

Greenberg J K 1981 *Geol. Soc. Am. Bull.* **92** 749
Harris N B W 1982 *Tectonophysics* **83** 243
Harris N B W, Holt R W and Drury S A 1982 *J. Geol.* **90** 509
Kushiro I 1969 *Min. Soc. Am. Spec. Pub.* **2** 179
Lloyd F E and Bailey D K 1975 *Phys. Chem. Earth* **9** 389
Macdonald R 1974 in *The alkaline rocks* (ed.) H Sorensen (New York: John Wiley) p. 442
Mahadevan T M 1964 *Proc. Int. Geol. Cong.* **22** Sess III 88
Mitchell R H and Platt R G 1978 *J. Petrol.* **19** 627
Mitchell R H and Platt R G 1982 *J. Petrol.* **23** 186
Murthy M V N and Venkataraman P K 1964 *The Upper Mantle Symp.* New Delhi p. 127
Nair N G K and Santosh M 1983 *Proc. Indian Acad. Sci. (Earth Planet. Sci.)* **92** 129
Nair N G K and Santosh M 1984a *J. Geol. Soc. India* **25** 35
Nair N G K and Santosh M 1984b *Neues Jb. Miner. Abh.* (in press)
Nair N G K, Santosh M and Thampi P K 1983 *Neues Jb. Miner. Abh.* **148** 223
Nair N G K, Santosh M and Thampi P K 1984a *Proc. Indian Acad. Sci. (Earth Planet. Sci.)* **93** 149
Nair N G K, Santosh M and Thampi P K 1984b *Indian J. Earth Sci.* **11** 148
Newton R C, Smith J V and Windley B 1980 *Nature (London)* **288** 45
Nockolds S R 1954 *Bull. Geol. Soc. Am.* **69** 1007
O'Hara M J 1968 *Earth Sci. Rev.* **4** 69
Parsons I 1978 *Mineral. Mag.* **42** 1
Parsons I 1980 *Trans. R. Soc. Edinburgh* **71** 1
Philpotts A R 1966 *J. Petrol.* **7** 1
Polanski A 1949 *Bull. Soc. Amis Sci. Lett. Poznam. Serie* **10** 119
Rao P S 1978 *Geol. Surv. India Misc. Pub.* **34** 61
Reay A and Harris P G 1964 *Bull. Volcan.* **27** 115
Santosh M 1984a *Neus Jb. Miner. Mh.* **6** 241
Santosh M 1984b *Neus Jb. Miner. Mh.* **8** 337
Santosh M and Nair N G K 1983 *Proc. Indian Acad. Sci. (Earth Planet. Sci.)* **92** 297
Santosh M and Nair N G K 1985 *J. Geol. Soc. India* (in press)
Santosh M and Sankar G 1984 *J. Geol. Soc. India* (under pub.)
Stephenson D and Upton B G J 1982 *Mineral. Mag.* **46** 283
Streckeisen A L 1976 *Earth Sci. Rev.* **12** 1
Tilak N B G 1980 *Geol. Surv. India Spec. Publ.* **5** 77
Yoder H S, Stewart D B and Smith J R 1957 *Carnegie Inst. Washington Paper* **1277** 206
Yoder H S and Tilley C E 1962 *J. Petrol.* **3** 342

oc. Indian Acad. Sci. (Earth Planet. Sci.), Vol. 94, No. 1, March 1985, pp. 57–70.
Printed in India.

etrology of thermally metamorphosed pelitic rocks in the hampawat Area, Kumaun Himalaya

BRIJRAJ K DAS
Centre of Advanced Study in Geology, Punjab University, Chandigarh 160014, India

MS received 27 May 1983; revised 5 September 1984

Abstract. In the Champawat area, Kumaun Himalaya, greenschist facies regionally metamorphosed rocks *viz* chlorite-phyllite and schist have been subjected to thermal metamorphism due to emplacement of batholithic granite/granodiorite body. As a consequence, biotite, garnet, andalusite, fibrolite, sillimanite and perthite minerals have formed in the contact rocks. The conspicuous absence of cordierite and staurolite reported from such aureole rocks is due to higher FeO/MgO ratio of the bulk rock composition in the former while the absence of staurolite is due to low Al_2O_3/FeO + MgO ratio in the schists. AFM diagram demonstrates that in muscovite-bearing schist, the bulk composition of chlorite- and cordierite-bearing rocks are restricted to low FeO/MgO side and thus the restricted occurrence of former and the absence of latter in the contact rocks of the area. This is further evident from the common occurrence of almandine-rich garnet in the rocks.

Keywords. Pelitic; hornfels; Champawat; Hornblende-hornfels facies; grano-diorite; batholith.

Introduction

e batholithic-sized granodioritic body out-cropping in Champawat area has tracted the attention of many geologists (*e.g.* Kharkwal 1951; Valdiya 1962; Sharma d Awasthi 1980). All of them considered it to be magmatic in origin, but none corded the evidence of contact metamorphism in this region. During the present vestigation the development of typical pelitic hornfels (Das and Singh 1981) curring in the granodiorite body, though sporadically has been recorded. Curiously, visible thermal aureole around the main batholith is observed, which may be either ncealed or eroded as the aureole tend to be confined to roof portions of the country ck. Moreover, the hornfelses typically consist of biotite, garnet and andalusite semblage but the cordierite is absent and staurolite is rare in these rocks. This shows parture from the common assemblages reported from similar areas elsewhere. In this per an attempt has been made to discuss the petrology and the paragenesis of mineral semblages of the hornfels of the area and to estimate the PT condition of etamorphism.

Geological setting

e Champawat area consist predominantly of igneous and low-grade metamorphic is remarkably sharp, being overlain abruptly by phyllites and quartzites of Gumalikhet Formation, along a dislocation having a northwardly dip, while the southern contact is gradational and flanked by augen gneiss, feldspathic schist associated with biotite schist, garnet-mica schist and micaceous quartzite of Gorakhnath Formation (figure 1).

The spotted hornfels is exposed towards the southern contact of batholith about 6 km south of Champawat and extends further in strike direction about 2 km from Banlekh to Dhaun on Tanakpur road. The pelitic and semi-pelitic rocks recrystallized to spotted hornfels of the type described by Compton (1960). Besides the hornfels, xenolith of fine-grained dark grey, biotite-rich country rocks of the size from a fraction of a centimetre to those measurable in metres are common, which according to Valdiya (1980) may represent roof pendents.

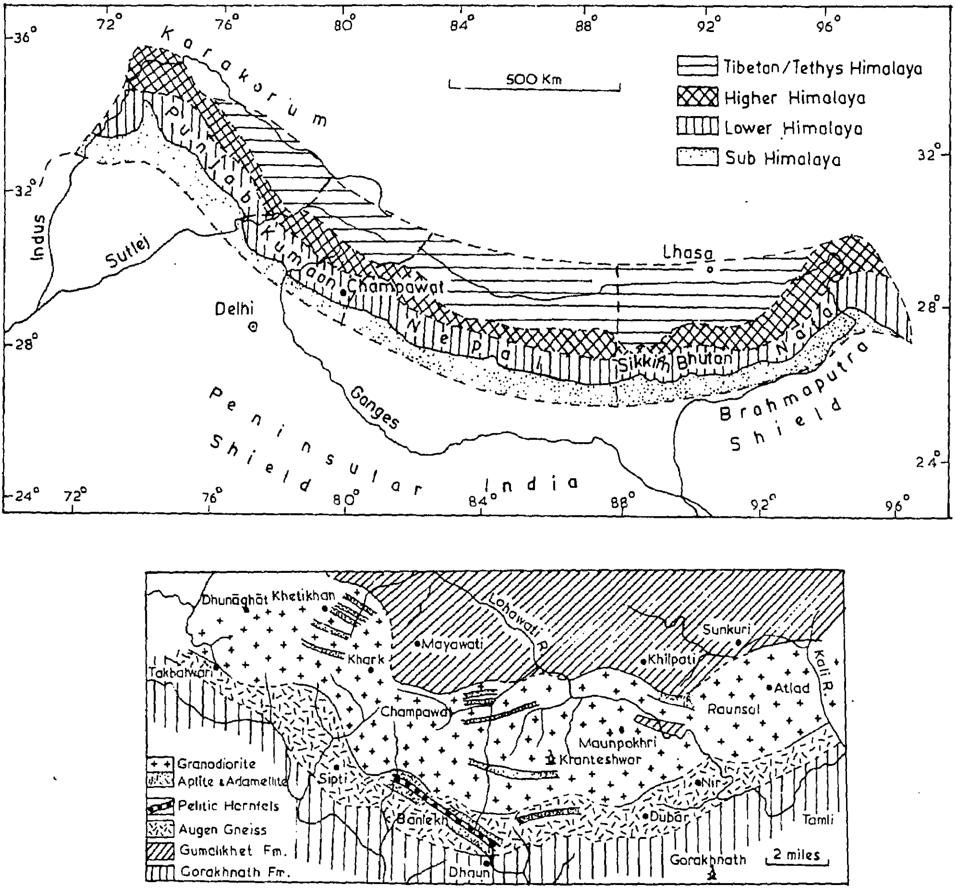

Figure 1. Geological sketch map of the Champawat area (lower) showing expanse of granodiorite and the outcrops of hornfelses exposed near Banlekh and Dhaun. The bands of the late magmatic adamellite and aplitic granite is also shown (modified after Valdiya 1980). The map above shows the location of Champawat in Kumaun Himalaya (after Gansser 1964).

3. Petrographic characters

The pelitic hornfelses are fine-to medium-grained, light to dark greyish coloured spotted rocks. The semi-pelitic variety is very hard and compact. The spots are 0·5–1 mm in elongation, oval or rounded in shape and irregularly scattered or segregated in some parts of the rock. The spots are mostly of poikiloblastic chlorite and/or segregation of phyllosilicates. In thin section it exhibits hornfelsic texture defined by decussate arrangement of scaly or short poikiloblastic biotite and less commonly white mica. The reddish brown sieved biotite is sub-parallel to S_1 foliation or irregularly disposed in the matrix of the rock (figure 2a). In some thin sections the S_1 foliation marked by sericite and scaly chlorite is microfolded or crenulated together with the poikiloblastic chlorite, which represents the aureole chlorite developed during thermal metamorphism (figure 2b). Such chloritic mass represents the spots over which scaly biotite, less commonly muscovite, often sieved and highly spongy garnet often with polygonal outline, are grown (figure 2c).

Besides the fine mica and chlorite of phyllite, small sieved flakes of muscovite and ggregates of scaly muscovite overprinting the groundmass are aureole muscovite. iotite also occurs in thin layers or in streaky form some times replacing chlorite, and is ighly sieved with quartz and opaques and encloses poikiloblastic andalusite figure 2d). The textural relation suggests that the crystallization of andalusite is related o chlorite and white mica. The associated biotite may be a product phase.

Large, pinkish, poikiloblastic and highly sieved, with quartz and opaques and keletal garnet overprint the groundmass, and shows replacive relation with the streaky iotite, which also occurs as relict in the former (figure 2c). The garnet of mica schist is eformed showing syntectonic rotational trails (si) while the aureole garnet does not ow such a feature. The textural relation of garnet in the latter shows its crystallization ring a static thermal phase post dating the deformation.

Staurolite is rare and embedded in a mesh of randomly oriented muscovite film and aces of relicts of biotite and grains of opaques are scattered in the mesh of muscovite gure 2e). It is associated with the aggregate or bundle of needle sillimanite without y evidence of resorption or replacement (figure 2f). The mode of occurrence licates that the staurolite and white mica formed by rehydration reaction of dalusite and biotite.

Andalusite is a common aureole mineral of the pelitic hornfels and occurs in kiloblastic, spongy and skeletal form (figures 3a, b). It is often sieved with coarse rtz grains of the size forming the groundmass (figure 2d). Inclusion of opaques and ociation with biotite streaks are common (figures 3a, b) and the latter partly or pletely surrounds it. In a few thin sections andalusite is altered to shimmer and the ct of former occurs in the latter (figures 3c, d). In those rocks which occur near the tact, the sillimanite needles protrude the andalusite crystals and partly replace it re 3e) indicating partial resorption. Andalusite is faintly pinkish and pleochroic pinkish shade is deeper at certain spots of the same crystal).

llimanite occurs in three different forms such as fine needles fringing the hyroblastic minerals or included in them; as robust needles or prismatic crystals rring in a few thin sections of the rocks from the vicinity of magmatic body, in h biotite is intensely fibrolitized and as coarse prismatic

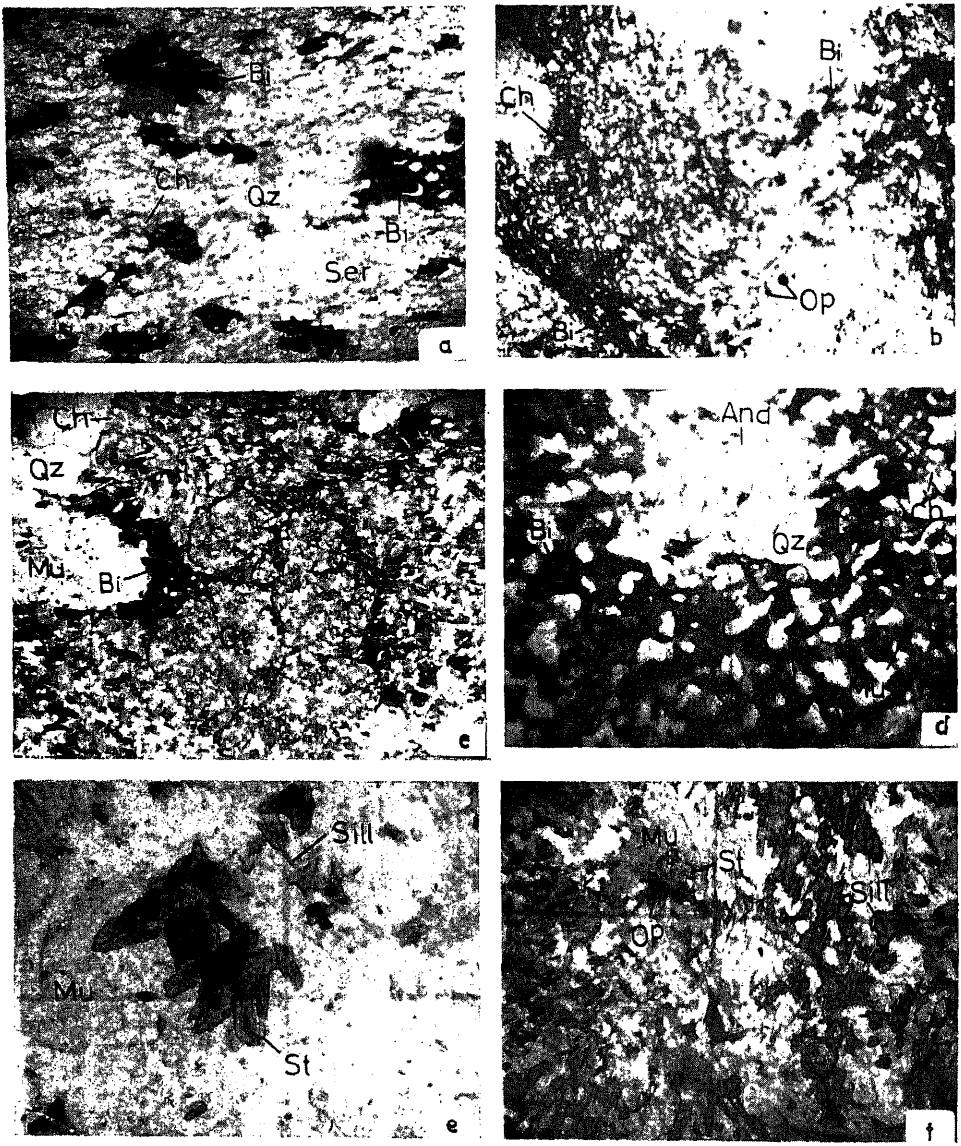

Figures 2a–f. a. Low-grade phyllite showing foliation (S_1) defined by the specks of sericite (Ser) and chlorite (Ch). Note the subsequent development of highly sievèd aureole biotite (Bi) porphyroblast imprinting the groundmass. **b.** Highly sieved and patchy chlorite (Ch) showing deformation and is folded along with the foliation (S_1). Note the fine grains of opaques (Op) and streaky biotite (Bi) associated with it. **c.** Highly spongy garnets (Gt) with polygonal outline grown over the chlorite (Ch), biotite (Bi) and sericite (Ser) matrix. Note the segregation of small laths of muscovite (Mu) containing inclusions of opaques (Op) and replacing biotite (Bi). **d.** Poikiloblastic andalusite (And) overprinting the ground mass of quartz (Qz), chlorite (Ch) and muscovite (Mu). It is almost completely surrounded by the streaky highly sieved biotite (Bi). Notice the hornfelsic texture and decussate structure. **e.** Prismatic crystals of zoned staurolite (St) intergrown with late muscovite film (Mu). The core is darker in colour than the periphery. Note the needle sillimanite (Sill) also

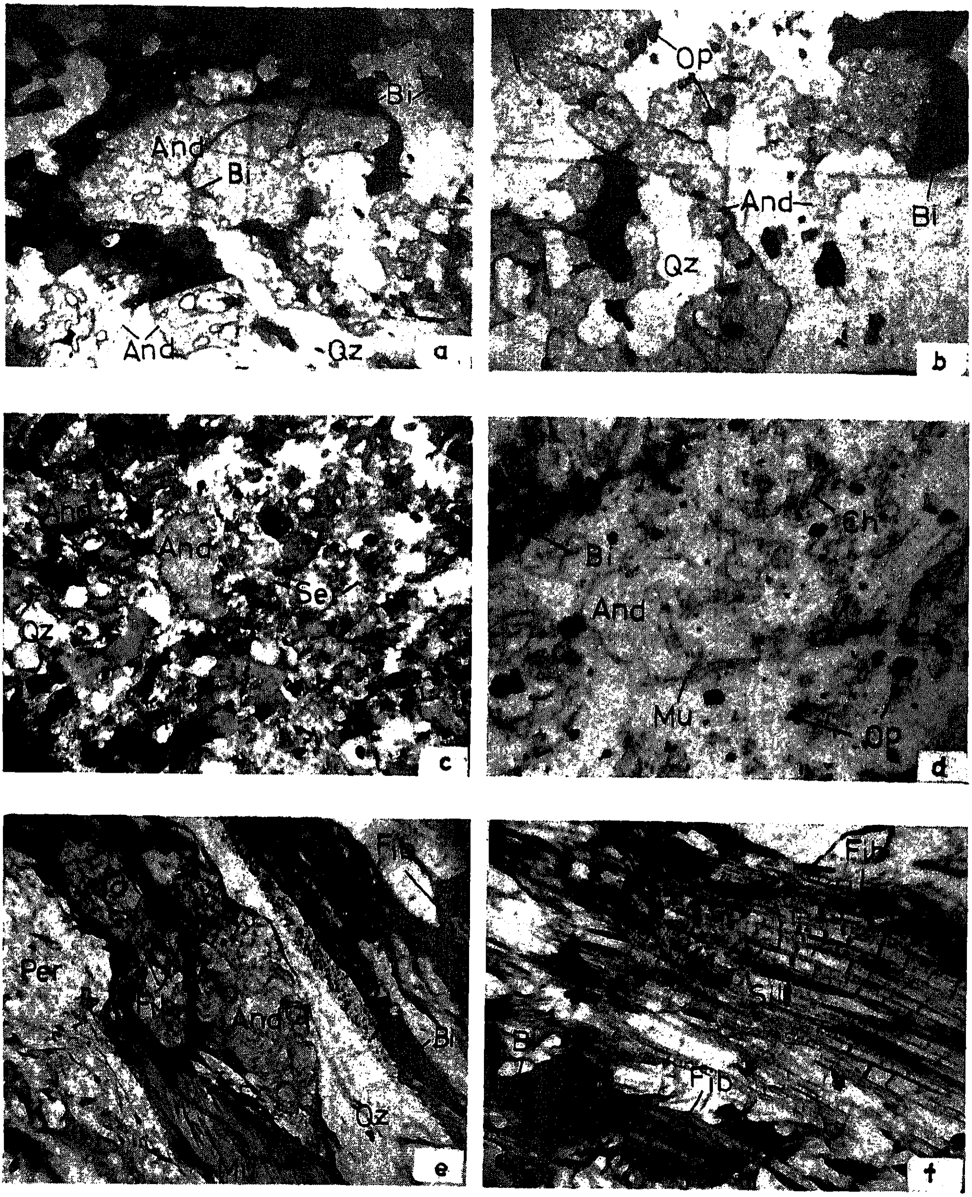

Figures 3a–f. a. Idioblastic crystals of andalusite (And) which are often sieved with quartz (Qz) and closely associated with biotite (Bi) the latter also occurs along the cracks of andalusite. The crystals are over printing the groundmass. **b.** Skeletal andalusite (And) grown over the groundmass and at places replacing streaky biotite (Bi) and contains inclusion of opaques (Op). **c.** Andalusite (And) is altered to shimmer of sericite (Ser) in which relict of former

muscovite indicating its later crystallization. Sillimanite pseudomorph after andalusite has been observed and a similar character has been noticed by Chinner (1961) and Green (1963) in Scottish Highlands and Northern New Hampshire respectively.

Among the feldspars perthitic microcline and/or microcline are common though plagioclase also occurs in most of the rocks and is often sieved with quartz and opaques. The former contains fine almost parallel lamellae of plagioclases which are in some cases bent and deformed. The extinction angle varies from 9°–24° or even more indicating albite or oligoclase composition of plagioclase.

Quartz is ubiquitous in all the rocks and shows strong undulatory extinction suggesting subsequent impress of strong deformation. Among the accessories apatite, tourmaline, opaques, epidote, zircon, etc. are common.

4. Paragenesis of the mineral assemblages

The petrographic characters described above suggest that the changes are partly related to dehydration and rehydration reactions, besides rapid heating by the magmatic intrusion. This is consistent with the view of other petrologists, *viz* Green (1963), Naggar and Atherton (1970) and others. The petrographic study has revealed the following mineral assemblages in the rocks:

4.1 *Pelitic and semi-pelitic*

(i) Chl-Ser-Mus-Op
(ii) Chl-Ser-Ep-Pl-Qtz-Op
(iii) Bio-Chl-Gt-Pl-Ep-Qtz
(iv) Bio-Mus-Gt-St-Pl-Ep-Qtz
(v) Bio-Gt-Fib-Pl-Qtz
(vi) Bio-Mus-Chl-Fib-Pl-Per-Qtz
(vii) Bio-Mus-St-Gt-Sill-Pl-Qtz
(viii) And-Bio-Chl-Mus-Gt-Fib-Pl-Qtz
(ix) And-Bio-Mus-Fib-Per-(± Pl, Mic)
(x) And-Bio-Mus-Gt-(± Pl, Chl)
(xi) And-Bio-Mus-Fib-Pl-Per-Qtz
(xii) And-Chl-Mus-Bio-Sill-Pl-Per-(± Op)

In addition to these apatite, opaques, tourmaline, sphene, zircon etc. occur as accessory constituents.

4.2 *Quartzo-feldspathic*

(xiii) Mus-Bio-Pl-Mic-Qtz
(xiv) Bio-Pl-Mic-Ep-Sp-Qtz
(xv) Bio-Mus-Pl-Mic-Zo-Clzo-Qtz-(± Per)

The chemical analyses of the phyllites and the hornfelses given in table 1 show no basic variation in their chemical composition. In the latter relatively higher silica and related to alkali-metasomatism in the contact rocks, also pointed out by Compton)60) in the Santa Rosa area.

The mineral assemblages of the rocks of the area are depicted in AKF diagram and 'M projection (figures 4, 5). The mineral points represent the ideal composition. In : AKF diagram (figure 4) the phyllite plots on the muscovite-chlorite join and the iscovite-biotite schist close to the ideal muscovite-biotite tie-line while the hornfelses)t in muscovite-biotite-almandine three phase field below the muscovite-almandine n demonstrating that the bulk composition of the rocks is in general not highly minous. On the other hand feldspathic schist/gneiss plot in the K-feldspar-biotite-iscovite field.

lorite solid solution join whereas the biotite-bearing phyllite/schist lie in the chlorite-)tite two phase field close to the chlorite solid solution tie-line (sample no. 6). The emical composition of the hornfelses 1 plot in the alumino-silicate (A-apex)-biotite-orite triangle and the sample nos. 3, 7 and 9 which are either devoid of or very poor in lorite plot on or close to the A-apex-biotite join (figure 5B). Many hornfelses (table 1) ntain greater number of phases than is expected to occur at equilibrium according to : phase rule *viz* Chl-Bio-And-Sill-Gt-Mus, Bio-Mus-Gt-St-Sill, And-Chl-Bio-Mus-l and are thus incompatible with the topology of the AFM projection (figure 5B). any such reports are available in literature showing that the pelitic rocks contain an ra phase in the Al_2O_3-K_2O-FeO-MgO tetrahedron. Various possibilities have been cussed by Hietanen (1961), Woodland (1963), Green (1963) and others to explain the esence of an extra-phase in such assemblages. Green (1963) postulated that in thermal reole due to rapid heating of the rocks mineral reactions proceed towards the mation of much less hydrous phases *viz* staurolite, cordierite and aluminum silicate m muscovite and chlorite and if all the H_2O could not escape readily enough, these ctions would be incomplete and an extra phase may thus occur because of the crease in variance of the system. Besides this garnet may occur as an extra phase either e to its refractory nature, zoning, Mn/Ca content or overstepping of reaction may d to metastable coexistence of a phase or the assemblage may represent equilibrium.

Many petrologists have shown that almandine in the low-pressure metamorphism ntains considerable amount of Mn or Ca, hence stabilizing it outside the stability ld of the equilibrium assemblages (Miyashiro 1953; Chinner 1962; Okrusch 1971; Lal d Ackermand 1981 and others). The Mn-content in the garnet of the area ranges from 8–2·81 showing a tendency to increase from periphery to core. This implies that the lier garnet of the low grade regionally metamorphosed rock is probably somewhat gher in Mn-content than the later peripheral garnet. Moreover as the garnet is rich in nandine-content it may be occurring as an extra phase due to its refractory nature or ning. The textural relation suggests that the garnet may have formed from chlorite d muscovite by the following reactions:

$$\mathrm{Chl} + \mathrm{Mus} + \mathrm{Qtz} \rightleftharpoons \mathrm{Gt} + \mathrm{Bio} + H_2O, \quad \text{(Hollister 1969)} \qquad (1)$$

$$\mathrm{Chl} + \mathrm{Mus} \rightleftharpoons \mathrm{Bio} + \mathrm{Gt} + H_2O. \quad \text{(Naggar and Atherton 1970)} \qquad (2)$$

e formation of garnet from biotite, as suggested by Okrusch (1971) is not evident in : area.

Table 1. Chemical compositions of the metapelites and the hornfelses of Champawat area.

Ref. No. Sample No.	1 CP-21	2 CP-11	3 CP-14	4 CP-18	5 CP-19	6 CP-20	7 CP-15	8 CP-16	9 CP-15(a)	10 CP-12
SiO_2	67·89	73·30	64·39	65·59	67·78	65·29	64·69	67·09	64·69	69·75
TiO_2	0·54	0·53	0·62	0·51	0·54	0·50	0·79	0·71	0·62	0·39
Al_2O_3	17·15	12·64	18·27	14·90	15·51	16·20	17·18	15·86	15·89	15·53
Fe_2O_3	2·99	0·55	0·87	2·00	2·52	2·77	1·07	2·85	1·69	0·30
FeO	2·58	2·68	4·55	1·72	1·59	2·31	4·80	3·42	5·22	2·19
MnO	0·05	0·06	0·09	0·09	0·09	0·11	0·12	0·20	0·12	0·04
MgO	1·59	1·70	1·82	2·11	1·84	2·30	2·28	2·41	2·23	1·17
CaO	0·63	1·09	0·83	3·34	2·21	2·43	0·86	0·96	1·02	1·79
Na_2O	2·30	1·60	2·00	1·55	1·55	1·50	3·20	2·60	1·30	2·95
K_2O	3·40	3·00	4·10	2·90	2·70	2·70	3·30	2·90	4.10	4.60
H_2O^+	2.50	3·00	2·00	2·90	2·30	2·50	2·10	1·50	2·20	1·90
P_2O_5	0·07	0·16	0·12	1·67	0·87	1·31	0·21	0·24	0·24	0·21
Total	101·69	100·31	99·66	99·26	99·50	99·92	100·60	100·74	99·32	100·82
FeO/MgO ratio	0·92	0·88	1·40	0·46	0·49	0·56	1·19	0·79	1·31	1·03

Analyst **B K** Das

	Mode									
Quartz	+	+	+	+	+	+	+	+	+	+
Plagioclase	+	+	+	+	+	+	+	+	+	+
K-feldspar	–	–	+	–	–	+	+	+	–	+
Muscovite	+	+	+	+	+	–	+	+	–	+
Sericite	+	–	–	+	–	+	–	–	–	–
Chlorite	+	+	(greymica)	–	+	+	+	+	–	–
Biotite	–	+	+	+	+	+	+	+	+	–
Garnet	–	–	–	+	–	–	+	–	+	–
Andalusite	–	–	+	–	–	–	–	+	–	–
Staurolite	–	–	–	–	–	–	+	–	–	–
Sillimanite	–	–	+	+	+	+	+	+	–	–
Fibrolite	–	–	(fibrolite)	(fibrolite)	–	–	–	(fibrolite)	–	–
Kyanite (needles)	–	–	–	–	–	–	+	–	–	–
Ores	+	+	+	+	+	+	+	+	+	+
Apatite	+	–	–	+	+	+	–	+	+	–
Tourmaline	+	+	–	+	+	+	+	+	+	+
Epidote	+	–	+	+	+	+	+	–	–	–
Zircon	+	–	+	–	–	–	–	–	–	–

+ Present, – Absent.

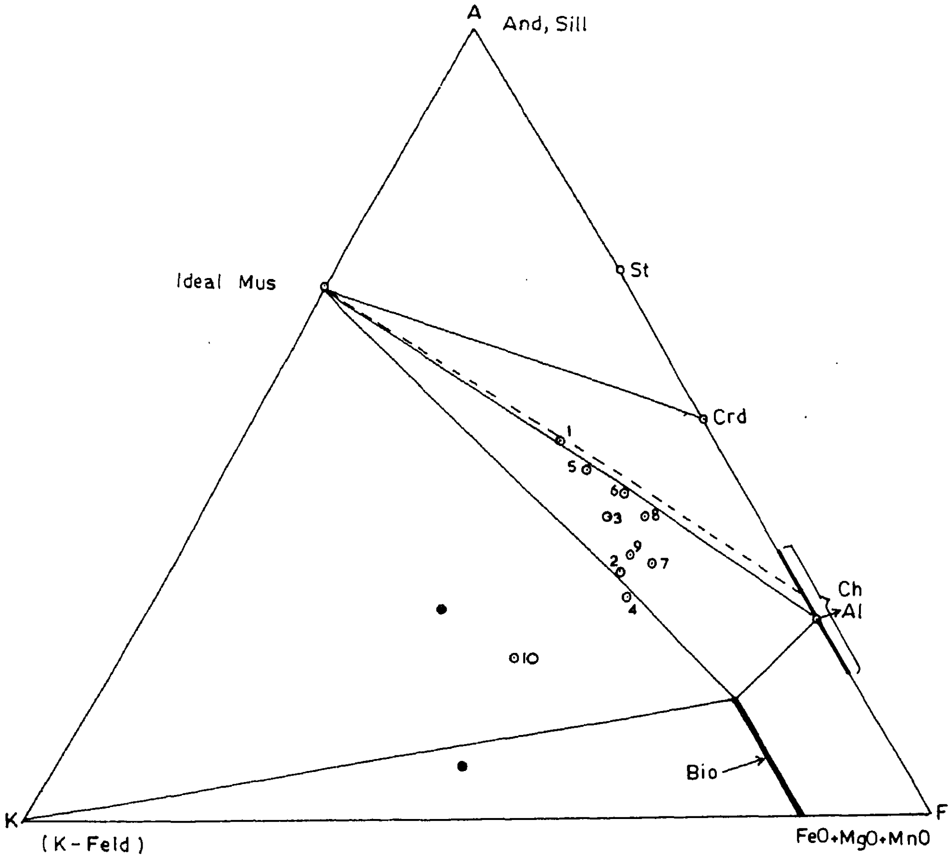

Figure 4. AKF diagram showing the plots of chemical composition of Champawat pelitic rocks (open circles). The mineral points represent the ideal composition. The plots of hornfelses lie in the three phase field Mus-Bio-Alm and that of phyllite plot on the Mus-Chl-join. The solid circles schematically depict the mineral assemblages.

Staurolite is not formed as a common phase except its scarce development in a mesh of white mica and the latter contains traces of relict biotite and opaques indicating that it has formed by the following rehydration reaction:

$$31\mathrm{And} + 4\mathrm{Bio} + 3\mathrm{H_2O} \rightleftharpoons 6\mathrm{st} + 4\mathrm{Mus} + 7\mathrm{Qtz}. \tag{3}$$

The general absence of staurolite in the hornfels of Champawat may be due to lower $Al_2O_3/FeO + MgO$ ratio which is evident from the AKF and AFM diagrams (figures 4, 5b). In the former the bulk analyses plot below the muscovite-almandine join while the points which lie above this join generally contain staurolite. In the latter the rock composition plots are restricted to three phase And-Bio-Chl field.

Andalusite is a common phase occurring in most of the hornfelses. It is commonly reported from the outer most zone of a thermal aureole indicating relatively low temperature and probably more hydrous conditions which is followed by the appearance of cordierite and cordierite-sillimanite and/or K-feldspar in the inner

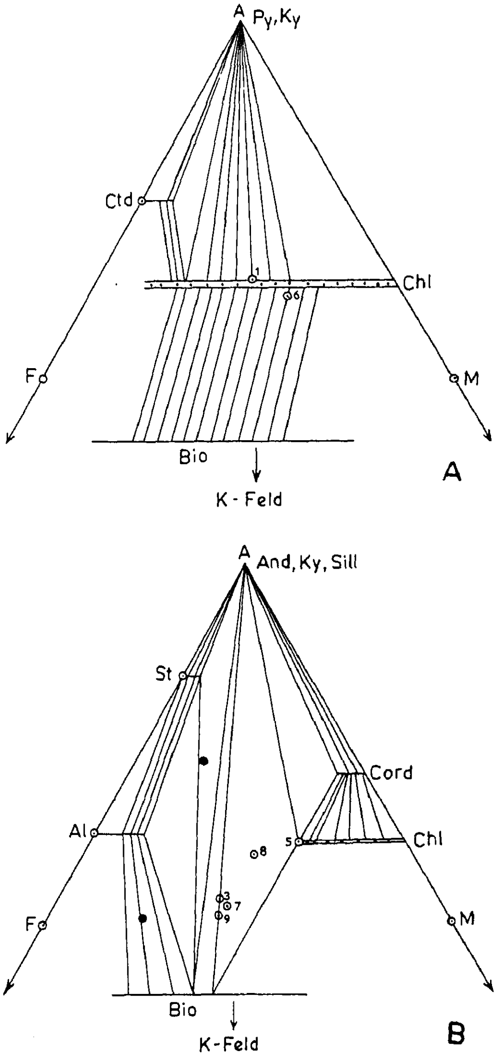

Figure 5. The Thompson's AFM projection, ($A = (Al_2O_3 + Fe_2O_3) - (3K_2O + Na_2O + CaO)$, $F = FeO + MnO$, and $M = MgO$, in mol %) showing the mineral assemblages of the pelitic hornfelses of the Champawat area (open circles). The solid circles represent the mineral assemblages schematically.

temperature and low stress for its formation. This is consistent with the earlier view of Streckeisen (1938) who stated that staurolite-free andalusite assemblages form at lower pressure or at a higher partial pressure of water. The first appearance of andalusite with quartz in the upper greenschist or albite-epidote hornfels facies (Turner 1968) is shown at about 400°C from reaction of pyrophyllite (Kerrick 1968). The mineral assemblage and the chemistry of rocks (low-alumina) do not indicate its formation from pyrophyllite. On the other hand the textural relation suggests its formation from:

$$\mathrm{Chl} + \mathrm{Mus} + \mathrm{Qtz} \rightleftharpoons \mathrm{And} + \mathrm{Bio} + H_2O, \tag{4}$$

$$\text{White mica} + \mathrm{Chl} \rightleftharpoons \mathrm{And} + \mathrm{Bio} + \mathrm{Qtz} + H_2O. \tag{5}$$

This is consistent with the view of Seki (1954) who stated that in the north-eastern Japan, andalusite is stable in the chlorite zone.

The absence of cordierite in the pelitic hornfelses of Champawat area is rather intriguing. It is a common mineral in the aureole rocks of the other areas of the world. According to Best and Weiss (1964) the absence of cordierite in muscovitic and some perthitic assemblages at Isabella may be on account of insufficient magnesian rocks whose bulk compositions would not fall in the cordierite stability field, or that cordierite was not a stable phase at the prevailing set of external variables, or both. As the bulk analyses of Isabella hornfels are not given, a comparison in this respect is not possible. However, the common occurrence of chlorite-andalusite-muscovite-bearing assemblage probably indicates that the composition field of the cordierite-bearing rocks is restricted towards lower FeO/MgO side in the AFM projection (figure 5B), and as this ratio is high in the pelitic rocks of the area, cordierite is absent. The diagram also demonstrates that because of stable andalusite-biotite join, composition field of chlorite lies towards lower FeO/MgO side of the projection. Therefore compositional constraint seems to be the main cause for its absence in the area. A similar situation has been noticed for the absence of cordierite in muscovite-bearing pelitic schist of Khetri copper belt of Rajasthan by Lal and Shukla (1975).

The fibrolite and sillimanite are also problematic in these rocks. The evidence of polymorphic transformation of andalusite to sillimanite is not very common and only in one specimen, from the contact of magmatic body sillimanite needles and prisms penetrate in adjacent andalusite and show replacive relation indicating resorption (figure 2f). The fibrolite and sillimanite are mostly formed independently from biotite and less commonly from muscovite and their association with biotite as observed texturally may be due to epitaxial growth of sillimanite in Champawat (Chinner 1961). The typical occurrence of sillimanite in the area may be due to higher temperature conditions in proximity of magmatic body (Holdaway 1971). As the formation of fibrolite from andalusite requires large amount of overstepping which is not evident in the area and also not possible as the temperature gradient is not high, such transformation is not common. Moreover, in fine needles of sillimanite surrounding quartz, perthite, plagioclase and even andalusite, etc there is late sillimanite as described by Tozer (1955), Pitcher and Berger (1972) and others and in all probability related to metasomatic activity in the area.

5. Metamorphic facies and physical conditions of metamorphism

The regionally metamorphosed rocks of the area represent greenschist facies conditions of metamorphism (Turner 1968) but the contact metamorphic assemblages cause ambiguity because of very scarce epidote, absence of staurolite and cordierite and common occurrence of garnet and sillimanite. However, the presence of biotite, muscovite, chlorite, andalusite, fibrolite, plagioclase and perthite in the assemblages of

1968). The greenschist facies rocks were subsequently superimposed by thermal metamorphism due to emplacement of magmatic body which caused rapid heating during which spongy garnet crystallized from the assemblage muscovite and chlorite rendering 'available' composition more aluminous (Atherton and Brotherton 1972). The rapid heating and low prevailing pressure gave rise to the formation of andalusite in the rocks. The textural evidence indicates that the new aureole minerals mainly grew directly from the ground-mass of quartz-muscovite-chlorite and/or biotite. The aluminium silicates did not form from one another whilst they grew from a series of dehydration reactions involving the layered minerals. The sillimanite and fibrolite usually formed independently of andalusite except in few cases.

Andalusite is a characteristic porphyroblastic mineral of pelitic hornfels of Champawat area which according to Turner (1968) may be used as a pressure index, limiting the probable pressure field of the hornblende-hornfels facies to less than about 3 kb. Hirschberg and Winkler (1968) have shown on the basis of experimental data that almandine can form at 500°C at 4 kb and 600°C at 5 kb and that the pressure values may be lower by 2 kb if appreciable amount of spessartine component is present in garnet which is consistent with the opinion of other petrologists *e.g.* Miyashiro (1953). As mentioned earlier the Mn-content of garnet is not high in the hornfelses of the area, therefore a pressure condition of about 3 kb may be estimated. The coexistence of chlorite + quartz, chlorite + quartz + muscovite, chlorite + andalusite + quartz etc and the absence of cordierite suggests temperature of 550°C at 5 kb P_{H_2O} and 500°C at 2 kb P_{H_2O} as demonstrated experimentally by Fawcett and Yoder (1966). But some samples from the immediate contact of magmatic body contain well-crystallized sillimanite and/or fibrolite nucleating on mica, may indicate a higher temperature condition (Holdaway 1971). However, a stable coexistence of muscovite and quartz suggests that the breakdown temperature of these phases has not reached. Therefore the upper limit of temperature of about 600°C may be estimated for these rocks. It may therefore be concluded that a temperature of about 500 ± 50°C approaching 600° at pressure of about 2–3 kb may have reached during thermal metamorphism of Champawat area.

The general absence of thermal aureole around the main batholith may be due to erosion since the thermal aureole tend to be confined to roof portions of the country rock.

Acknowledgements

The author is grateful to Prof. R C Misra for his suggestions. He also wishes to place on record his thanks to the University Grants Commission, New Delhi, for financial assistance.

References

Atherton M P and Brotherton M S 1972 *J. Geol.* 203
Best M G and Weiss L F 1964 *Am. Miner.* **49** 1240
Chinner G A 1961 *J. Petrol.* **2** 312
Chinner G A 1962 *J. Petrol.* **3** 316
Compton R R 1960 *Bull. Geol. Soc. Am.* **71** 1383
Das B K and Singh C 1981 *Bull. Indian Geol. Assoc.* **14** 83

Fawcett J J and Yoder H S 1966 *Am. Miner.* **51** 353
Gansser A 1964 Geology of the Himalayas (London: Wiley-Interscience)
Green J C 1963 *Am. Miner.* **48** 991
Hietanen A 1961 *Finlande Comm. Geol. Bull.* **33** 73
Hirschberg A and Winkler H G F 1968 *Contrib. Miner. Petrol.* **18** 17
Holdaway M J 1971 *Am. J. Sci.* **271** 97
Hollister L S 1969 *Geol. Soc. Am. Bull.* **80** 2465
Kerrick D M 1968 *Am. J. Sci.* **266** 204
Kharkwal A D 1951 *Q. J. Geol. Min. Soc. India* **23** 135
Lal R K and Shukla R S 1975 *N. Jb. Miner. Abh.* **124** 294
Lal R K and Ackermand D 1981 *N. Jb. Miner. Abh.* **141** 161
Misra R C and Sharma R P 1967 *J. Geol. Soc. India* **3** 110
Miyashiro A 1953 *Geochim. et Cosmochim Acta* **4** 179
Naggar M H and Atherton M P 1970 *J. Petrol.* **11** 549
Okrusch M 1971 *Contrib. Miner. Petrol.* **32** 1
Pitcher W S and Berger A R 1972 *The geology of Donegal: A study of granite emplacement and unroofing* (New York: Wiley-Interscience)
Pitcher W S and Read H H 1960 *Q. J. Geol. Soc. London* **116** 1
Seki Y 1954 *Saitama Univ. Sci. Rep. Ser. B.Z.* 309
Sharma R P and Awasthi D D 1980 *Indian Miner.* **21** 21
Streckeisen A 1938 *Schweizer Min. Petrol. Mitt.* **8** 87
Tozer C F 1955 *Geol. Mag.* **92** 310
Turner F J 1968 *Metamorphic petrology* (New York: McGraw Hill)
Valdiya K S 1962 *Indian Miner.* **3** 6
Valdiya K S 1980 Wadia Inst. Him. Geol., Dehradun
Woodland B G 1963 *Am. J. Sci.* **261** 354

Analysis of gravity gradients over a thin infinite sheet

G D J SIVAKUMAR SINHA and H V RAM BABU

National Geophysical Research Institute, Hyderabad 500007, India

MS received 9 September 1983; revised 22 January 1985

Abstract. Expressions are derived for the horizontal and vertical gradients of the gravity anomaly over a thin dipping sheet of infinite depth extent. The resultant of these two gradients, known as the complex gradient, is also derived and properties of the amplitude and phase responses of the complex gradient are studied. It is shown that the amplitude plot is a symmetric curve whose shape is independent of the dip (θ) of the sheet whereas the phase plot is an antisymmetric curve with an offset value equal to $\theta - \pi/2$. The depth to top of the sheet is obtained from the amplitude plot. The method is applied on a field example and the results are in good agreement with the results obtained by earlier workers.

Keywords. Gravity interpretation; thin sheet; complex gradient.

1. Introduction

In recent years, gravity gradients are being precisely measured and it was reported that the gradients have higher resolving power than the gravity itself (Hammer 1979). Recently, the term complex gradient was introduced (Atchuta Rao *et al* 1981, 1983; Atchuta Rao and Ram Babu 1981) which is defined as the resultant of both the horizontal and vertical gradients of gravity or magnetic anomaly. The present paper describes a method to evaluate the parameters of a thin sheet of infinite depth extent by analysing the amplitude and phase plots of the complex gradient of its gravity anomaly.

2. Theory

Let there be a thin sheet (figure 1) of infinite depth extent whose upper edge is buried at a depth h. If θ is the dip and σ is the density contrast of the sheet to its surroundings, the expression for the horizontal and the vertical gradients of the gravity anomaly over the thin sheet may be derived from the expression for the gravity anomaly over a thin sheet of finite depth extent as follows.

The expression ($\Delta g(x)$) for the gravity anomaly over a thin sheet of finite depth extent is given by Rao and Murthy (1978) as follows:

$$\Delta g(x) = 2G\sigma t\left[\tfrac{1}{2}\sin\theta \ln\frac{(x-a)^2+H^2}{x^2+h^2} + \cos\theta\left(\tan^{-1}\frac{x}{h} - \tan^{-1}\frac{x-a}{H}\right)\right], \tag{1}$$

in which G is the universal gravitational constant, σ is the density contrast, t is the thickness of the sheet, θ is the dip of the sheet, h is the depth to the upper edge of the sheet, H is the depth to the lower edge of the sheet, and $a = (H-h)/\tan\theta$.

The horizontal $(\Delta g_x(x))$ and the vertical $(\Delta g_z(x))$ gradients of the gravity anomaly over a thin sheet of finite depth extent may be written from equation (1) as follows:

$$\Delta g_x(x) = M\left[\frac{h\cos\theta - x\sin\theta}{x^2+h^2} + \frac{(x-a)\sin\theta - H\cos\theta}{(x-a)^2+H^2}\right], \tag{2}$$

and

$$\Delta g_z(x) = M\left[\frac{H\sin\theta + (x-a)\cos\theta}{(x-a)^2+H^2} - \frac{x\cos\theta + h\sin\theta}{x^2+h^2}\right], \tag{3}$$

where $M = 2G\sigma t$. When the sheet extends to infinity in the down dip direction, *i.e.*, $H \to \infty$, equations (2) and (3) may be re-written as follows:

$$\Delta g_x(x) = M\frac{h\cos\theta - x\sin\theta}{x^2+h^2}, \tag{4}$$

and

$$\Delta g_z(x) = -M\frac{x\cos\theta + h\sin\theta}{x^2+h^2}. \tag{5}$$

Equations (4) and (5) are the expressions for the horizontal and the vertical gradients, respectively, of the gravity anomaly over a thin sheet of infinite depth extent. The horizontal and vertical gradients of the gravity anomaly over an assumed sheet with $h = 10$ m; $\theta = 60°$ and $P = 100$ c.g.s. units is shown in figure 1.

The complex gradient $\overline{\Delta g_c}$ of Δg is defined by Atchuta Rao *et al* (1981) as follows:

$$\overline{\Delta g_c}(x) = \Delta g_z(x) + j\Delta g_x(x). \tag{6}$$

The amplitude $A(x)$ and phase $\phi(x)$ of $\overline{\Delta g_c}(x)$ are given by

$$A(x) = [\Delta g_x^2(x) + \Delta g_z^2(x)]^{1/2}, \tag{7}$$

and

$$\Phi(x) = \tan^{-1}[\Delta g_x(x)/\Delta g_z(x)]. \tag{8}$$

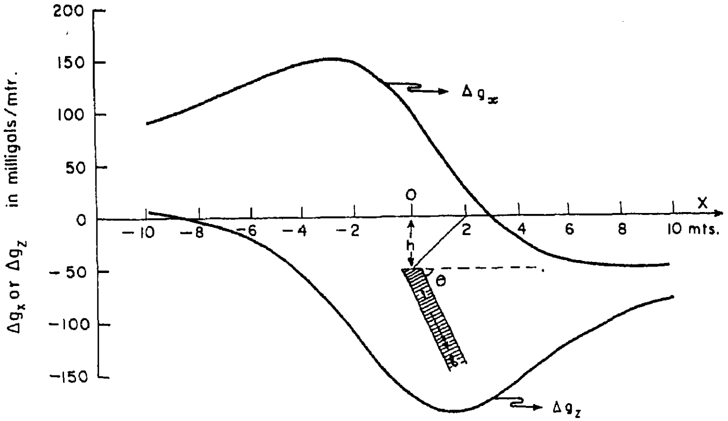

From equations (3) through (6) we write the complex gradient for the gravity anomaly due to the thin infinite sheet as

$$\overline{\Delta g_c}(x) = \frac{-M}{x^2+h^2}[(x\cos\theta + h\sin\theta) - j(h\cos\theta - x\sin\theta)]. \tag{9}$$

From equations (4), (5), (7) and (8), the amplitude $A(x)$ and phase, $\Phi(x)$ of $\overline{\Delta g_c}(x)$ may be written as follows:

$$A(x) = M/(x^2+h^2)^{1/2}, \tag{10}$$

and

$$\Phi(x) = \tan^{-1}\left[\frac{x\sin\theta - h\cos\theta}{x\cos\theta + h\sin\theta}\right]. \tag{11}$$

The theoretical amplitude $A(x)$ and phase $\Phi(x)$ of the complex gradient of the gravity anomaly over an infinite sheet with $h = 10$ mtrs, $\theta = 60°$ and $P = 100$ c.g.s. units is shown in figure 2.

2.1 *Analysis of $A(x)$ and $\Phi(x)$*

It may be noted from (10) that the amplitude function $A(x)$ is even and hence a plot of $A(x)$ versus x will be a symmetric curve with respect to the origin, $x = 0$. $A(x)$ attains its maximum value directly over the origin. The maximum value of $A(x)$ is given by the following equation.

$$A(x)|_{x=0} = M/h = A_{\max}. \tag{12}$$

At $x = \pm h = X_1$, the amplitude is as follows:

$$A(x)|_{x=\pm h} = \frac{M}{h\sqrt{2}} = 0{\cdot}7072\, A_{\max}. \tag{13}$$

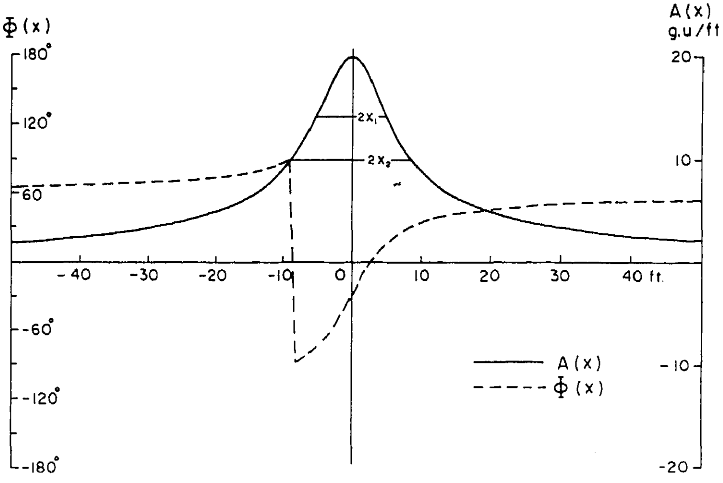

Figure 2. Amplitude $[A(x)]$ and phase $[\Phi(x)]$ plots of complex gradient of the gravity anomaly over a thin sheet.

It is also easy to derive from (10) that $A(x)$ falls off to half its maximum value when $x = \pm h\sqrt{3} = X_2$;

i.e. $$A(x)|_{x=\pm h\sqrt{3}} = \frac{M}{2} = 0{\cdot}5\,A_{\max}. \qquad (1$$

The following properties of the phase function $\Phi(x)$ may be derived from (11).

$$\Phi(x)|_{x=0} = \theta - \pi/2 = \Phi_0. \qquad (1$$

and $$\Phi(x) + \Phi(-x) = 2\theta. \qquad (1$$

Using the above properties of $A(x)$ and $\Phi(x)$ the parameters of the sheet may evaluated in the following way.

3. Practical approach

Let there be a gravity anomaly (Δg) assumed to be due to a sheet-like structure extendi to a great depth. The horizontal gradient Δg_x of $\Delta g(x)$ may be calculated using t following formula:

$$\Delta g_x(x) = [\Delta g(x+\Delta x) - \Delta g(x-\Delta x)]/(2\Delta x),$$

where Δx is the interval of observations.

If the vertical gradient measurements are not available, they may be comput using the Hilbert transform as the vertical gradient of the gravity anomaly over a tw dimensional structure is the Hilbert transform of the horizontal gradient (Stanley a Green 1976). The amplitude and phase functions of the complex gradient are comput using (7) and (8) and are plotted on linear scales. The amplitude plot will be a symmet curve whose maximum occurs directly over the origin. On the amplitude plot, t distances X_1 and X_2 corresponding to 70% and 50% maximum amplitude of $A(x)$ a read and using the properties given by (13) and (14) the depth (h) to the top may found. The value of the phase function directly over the origin is given by (15) fro which the dip (θ) of the sheet may be calculated. The amplitude factor M may evaluated using the property given by (12) from which the thickness (t) of the sheet m be evaluated by assuming the density contrast.

4. Field example

The gravity anomaly across the Moburn ore body (Noranda, Quebec) analysed Grant and West (1965, figure 10-10), using the Ribbon Model is shown in figure 3. T horizontal and vertical gradients of this anomaly are computed which are also show figure 3. The amplitude and phase plots (figure 4) of the complex gradient are found a analysed to yield the parameters given in table 1. The thickness of the sheet is evalua using a density contrast of 1·9 g/cm^3. The depth to top of the ore body obtained by R (1966) using the method of continuation is also tabulated for comparison.

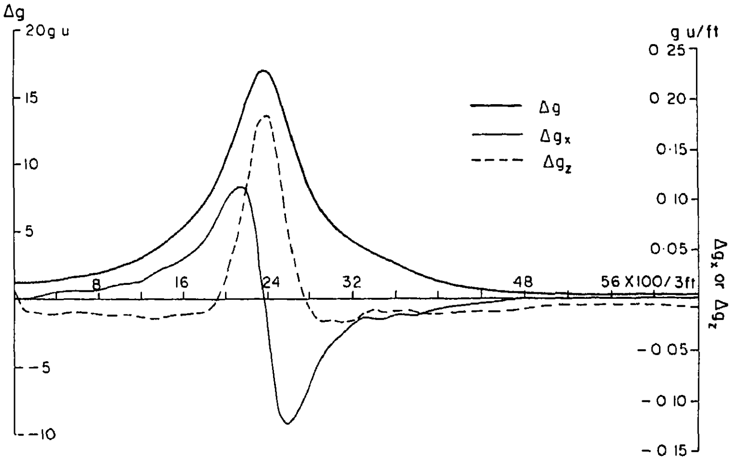

Figure 3. Gravity anomaly (Δg) over Moburn ore body and its horizontal (Δg_x) and vertical (Δg_z) gradients.

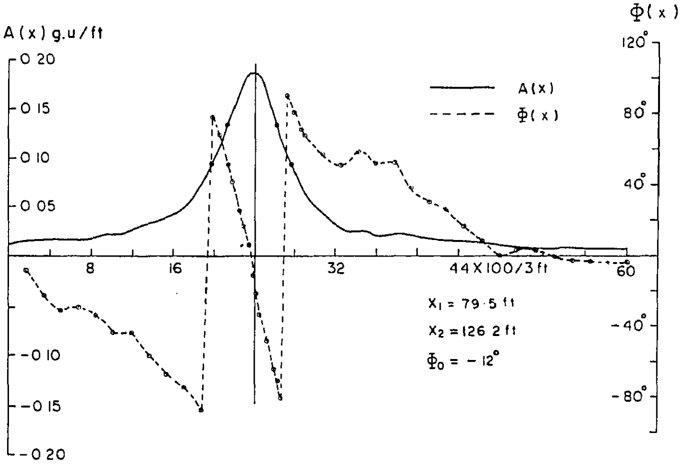

Figure 4. Amplitude $A(x)$ and phase $\Phi(x)$ plots of the complex gradient of the gravity anomaly shown in figure 3.

Table 1. Comparison of results obtained by using the present method with those obtained by other methods.

Parameter	Present method	Grant and West (1965)	Roy (1966)	Drilling
Depth to top	80 ft	56 ft	100 ft	100 ft
Thickness	79 ft	116 ft	—	—
Dip (θ)	79°N	83°N	—	—

Acknowledgements

The authors thank Dr D Atchuta Rao for encouragement.

References

Atchuta Rao and Ram Babu H V 1981 *Geoviews* **9** 41
Atchuta Rao D, Rambabu H V and Sanker Narayan P V 1981 *Geophysics* **46** 1572
Atchuta Rao D, Sivakumar Sinha G D J and Ram Babu H V 1983 Journal of Association of Exploration Geophysicists 4 25
Grant F S and West G F 1965 *Interpretation theory in applied geophysics* (New York: McGraw Hill)
Hammer S 1979 *Geophysics* **44** 99
Rao B S R and Murthy I V R 1978 *Gravity and magnetic methods of prospecting* (New Delhi: Arnold Heinemann)
Roy A 1966 *Geoexploration* **4** 65
Stanley J M and Green R 1976 *Geophysics* **41** 1370

STATEMENT ABOUT OWNERSHIP AND OTHER PARTICULARS ABOUT PROCEEDINGS OF THE INDIAN ACADEMY OF SCIENCES

(Earth and Planetary Sciences)

1. Place of Publication	..	Bangalore
2. Periodicity of Publication	..	Minimum of three issues a year
3. Printer's Name	..	C N R Rao Indian Academy of Sciences Bangalore 560 080
4. and 5. Publisher and Editor	..	C N R Rao
6. Nationality	..	Indian
7. Address	..	Indian Academy of Sciences P B No. 8005 Bangalore 560 080
8. Name and Address of the Owner	..	Indian Academy of Sciences Bangalore 560 080

I, **C N R Rao**, hereby declare that the particulars given above are true to the best of my knowledge.

C N R Rao
Signature of Publisher

Dated 1st March 1985

Detection of large scale electron density irregularities during IPS observations at 103 MHz

S K ALURKAR, H O VATS, R V BHONSLE and A K SHARMA

Physical Research Laboratory, Ahmedabad 380009, India

MS received 25 July 1984; revised 22 October 1984

Abstract. Angular displacements in the positions of the quasar 3C 298 were observed during its interplanetary scintillation (IPS) observations made using a correlation interferometer at 103 MHz at Thaltej near Ahmedabad. These changes in the apparent positions of the source could be seen as variations in the declination of 3C 298. Two possibilities which might cause such effects are considered; refraction of the radio waves either in the earth's ionosphere or in the interplanetary medium (IPM) by large scale plasma density inhomogeneities. Order of magnitude calculations for both are presented. Further studies using two-site observations are suggested to decide between the two mechanisms.

Keywords. Compact radio source; correlation interferometer; interplanetary scintillation; ionospheric refraction; gravity waves.

1. Introduction

It is well known that the apparent positions of radio sources as well as artificial satellites undergo quasi-periodic variations. These have been attributed to refraction of radio waves by inhomogeneities of electron density in the ionosphere. This effect has been reported mainly in the case of strong extended radio sources, such as Cassiopea and Cygnus A (Okoye and Hewish 1968), and solar noise storm (Bougeret 1981).

In this paper, we report observations made using a sensitive correlation interferometer with receiver fringes having high resolution in declination. This enables accurate determination of shift in the declination of a radio source. The radio source under observation, 3C 298, is a compact (0·4 arc sec) scintillating source.

2. Observations

Observations of angular displacements of the position of the compact radio source 3C 298 have been made while recording its IPS using a correlation interferometer at a frequency of 103 MHz (Alurkar *et al* 1982) at Thaltej (72° 36′E, 23° 02′N) Ahmedabad. The interferometer operation is effected by multiplying the response of the southern half of the antenna aperture with its northern half, the separation between their phase centers being 93 m, corresponding to 32 wavelengths. The resulting antenna response in declination, together with the SIN and COS fringes of the correlation type receiver, are displayed in figure 1. The half power beam width (HPBW) of this declination aerial response is 1·87°. The HPBW in right ascension near zenith is 7·5°. This interferometer has an advantage that the source stays on the same SIN and/or COS fringes at a fixed position during its transit.

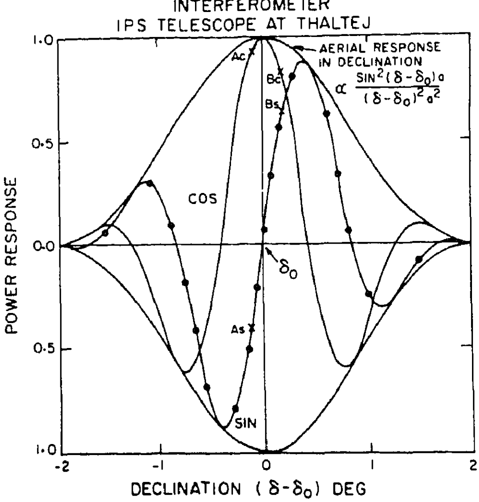

Figure 1. Receiver fringes of correlation interferometer of IPS telescope at Thaltej. A_c, A_s and B_c, B_s are two assumed positions of 3C 298 on cos and sin fringes.

Regular observations of 3C 298 were made over the solar elongation range of about 20°–80° at Thaltej. There were 70 observations in this solar elongation range, of which 35 were in the elongation range of 20° to 33°. These latter observations can be grouped into five types and one each of these types is shown in figure 2. Beyond 33° all the records are as in figure 2(a). The record (a) on 13–10–83 indicates strong d.c. as well as scintillating flux on the cos channel, while very small flux increase is seen on the sin channel. Note that this increase is on the same side as that on the cos channel. The corresponding positions of 3C 298 on the cos and sin fringes in figure 1 can be thought of as near the peak of the cos fringe and near the zero-crossing of the sin fringe respectively. The recordings (b) and (c) on 15–10–83 and 20–10–83 indicate good enhancements on the sin channel also, with the latter showing reversed deflection. The record in (c) will result if the source positions were at A_c and A_s on the cos and sin fringes in figure 1 and the record (b) will result if they were at B_c and B_s.

The events in figure 2(d, e) on 14–11–83 and 21–11–83 correspond to solar elongations of 28° and 33°. The wavy pattern of the sin channel between 1118 and 1136 hrs is a result of the change in declination of 3C 298 from a position such as at B_s to very near zero-crossing and back to B_s within about 18 min time. A comparable time interval is taken by the event on 21–11–83.

3. Data analysis and results

In order to estimate the change in declination of the source from the variations in the mean flux level in the sin channel, we plotted the magnitude ratios A_c/A_s and B_c/B_s as functions of declination. The observed ratios of average peak fluctuations of the cos and sin records in the presence of the events in figure 2(d, e) as well as during normal events were determined. For (d) this was done by extrapolating the peak flux on the sin

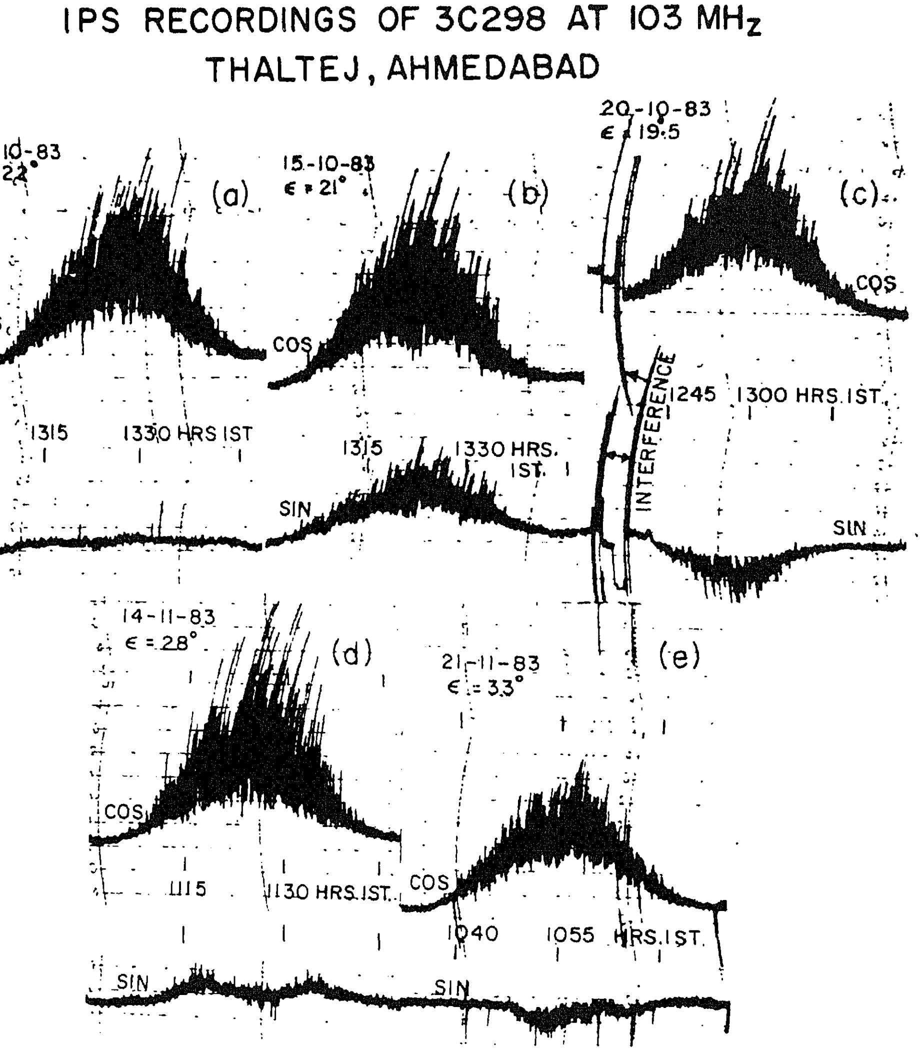

Figure 2. Typical IPS records of 3C 298 showing (**a**) normal record and (**b**)–(**e**) records with the effect of large scale electron density inhomogeneities in the ionosphere or IPM.

rd between 1118 and 1136 hrs. The declinations corresponding to these ratios were ained from the graph of A_c/A_s and B_c/B_s versus declination. The difference between e two values gave the maximum change in the declination of 3C 298. For the event 14–11–83 this amounted to about 5 arc minutes in the declination plane.

Discussion

s effect may be caused due to refraction (a) by either a large scale ionospheric gularity or a gravity wave propagating in the *F*-region of the ionosphere or (b) by a large scale plasma density irregularity in the interplanetary medium. In the following we shall discuss both these possibilities.

(a) In the case of gravity waves, these would be of medium scale according to the classification of Georges (1968). The irregularity or gravity wave should be at the point of intersection of the line of sight (source-observer line) with the ionosphere. If we assume the ionospheric drift to be 100 m/sec, (Sardesai *et al* 1983), the scale size L of the irregularity or the wavelength of the gravity wave, corresponding to the time interval of 18 min between 1118 and 1136 hrs in figure 2d, works out to about 100 km. These agree well with periods (12–40 min) and horizontal wavelength (50–300 km) of medium scale gravity waves (Bougeret 1981).

At the latitude region in question ionospheric irregularities are not field-aligned, so the angular displacement in the direction of the drift would be the same as observed in the declination plane i.e. 5′ arc $\sim 1{\cdot}5 \times 10^{-3}$ rad. The r.m.s. phase deviation $\phi_0 = L\theta_r \cdot f/c$ in this case would be ~ 50 rad. The phase deviation is related to integrated mean square deviation of ionization density $\int \overline{(\Delta N)^2}\, dz$ (Booker 1981) as

$$\phi_0 = 4r_e^2 \cdot \sec\chi,\ \lambda^2 \cdot L \int \overline{(\Delta N)^2}\, dz,$$

where r_e = classical electron radius, χ = zenith angle of the source, and λ = wavelength of operation.

From this, $\int \overline{(\Delta N)^2}\, dz$ turns out to be $7{\cdot}5 \times 10^{25}$ m^{-5}. If we assume the thickness of the irregularity, or of the region in which gravity waves exist, to be equal to the thickness of the F-region (~ 300 kms), we get the r.m.s. deviation of electron density $\sim 1{\cdot}6 \times 10^{10}$ el/m^3. This is around 3% of the average ambient density which is $5{\cdot}8 \times 10^{11}$ el/m^3 (Chandra *et al* 1979). Inference of such irregularities or waves that could cause density perturbations, have been reported through other ionospheric measurements and calculations (Titheridge 1972; Yeh and Liu 1974; Jain 1977; Vats and Deshpande 1980; Bougeret 1981; Vats *et al* 1981). Thus our calculations in the case of a large scale inhomogeneity of electron density in the ionosphere provide a reasonable magnitude.

(b) Alternatively, the same effect can be explained by a large scale plasma density irregularity in the interplanetary medium. In this case, the angular displacement of the source would be caused by a density irregularity being convected in the solar wind across the line of sight. Then assuming a solar wind velocity $V = 400$ kms/sec and referring to the same figure 2d, the scale size L of the irregularity works out to be $\sim 5 \times 10^5$ kms. Now assuming an axial ratio of 1 : 10 for such a large scale field-aligned irregularity (Sawant *et al* 1976), the observed apparent change in the declination of the source could be caused by an irregularity, aligned with the proper Archimedes spiral traced out by the interplanetary magnetic field. The model of such an irregularity is shown in figure 3. Such large scale plasma density irregularities in the solar wind were theoretically predicted by Shishov (1973) and were observed by Cole and Slee (1980). These observations were explained as due to large scale plasma density irregularities in the IPM by Hewish (1980).

It is important to note that the change in the apparent position of 3C 298 is observed in the solar elongation range of 20° to 33° only and not seen even once out of 35 observations beyond 33°. This may happen if it were caused by a large scale plasma density irregularity in the IPM 'although effects of solar radio transients for low solar elongation observations cannot be ruled out. There is also a possibility that the

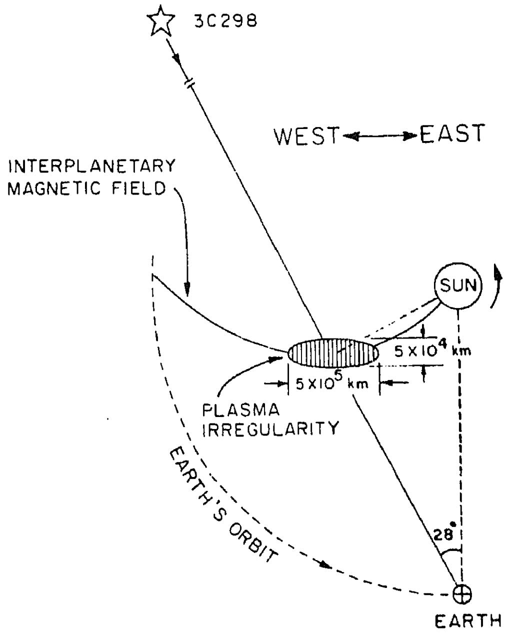

Figure 3. Model of large scale plasma density irregularity in the interplanetary medium for the event on 14–11–1983.

ionosphere was more disturbed on those days when the radio source was at lower solar elongations than for the days of higher elongations. However, from the statistics described above, it seems more likely that the large scale irregularities in the interplanetary medium might have been the cause of the observed refraction. It needs to be verified by making simultaneous observations of a scintillating radio source using two telescopes 200 km or more apart. A large scale density inhomogeneity in the IPM should then produce changes in the apparent position of the source in both the records.

Acknowledgements

We thank Prof. B J Rickett, University of California, San Diego, and Prof. Jack Klobuchar, AFGL, Bedford, USA, for useful discussions. We also thank our colleagues for assistance. Financial support for this work came from the Departments of Science and Technology and Space, Government of India.

References

Alurkar S K, Bhonsle R V, Sharma R, Bobra A D, Sohanlal, Nirman N S, Venat P and Sethia G 1982 *J. Inst. Electron. Telecommun. Eng.* **28** 577
Booker H G 1981 *J. Atmos. Terr. Phys.* **43** 1215
Bougeret J L 1981 *Astron. Astrophys.* **96** 259
Chandra H, Janve A V, Sethia G and Rastogi R G 1979 *Indian J. Radio Space Phys.* **8** 1

Georges T M 1968 *J. Atmos. Terr. Phys.* **30** 735
Hewish A 1980 *Nature* **285** 95
Jain R K 1977 *Indian J. Radio Space Phys.* **6** 223
Okoye S E and Hewish A 1968 *J. Atmos. Terr. Phys.* **30** 163
Sardesai D V, Rai R K, Vyas G D and Chandra H 1983 *Indian J. Radio Space Phys.* **12** 18
Sawant H S, Bhonsle R V and Alurkar S K 1976 *Solar Phys.* **50** 481
Shishov Y I 1973 *Astron. Zh.* **50** 941
Titheridge J E 1972 *Planet. Space Sci.* **19** 1593
Vats H O, Booker H G and Majidi Ahi G J 1981 *J. Atmos. Terr. Phys.* **43** 1235
Vats H O and Deshpande M R 1980 *Proc. Indian Acad. Sci.* (*Earth Planet. Sci.*) **89** 137
Yeh K C and Liu C H 1974 *Rev. Geophys. Space Phys.* **12** 193

asal flow rate of Changme-Khangpu glacier, Sikkim Himalaya based 1 ^{32}Si and ^{210}Pb chronology

V N NIJAMPURKAR
Physical Research Laboratory, Ahmedabad 380 009, India

MS received 5 January 1985; revised 22 March 1985

Abstract. Using environmental radioisotopes silicon-32 and lead-210, the radiometric ages of ice at the surface and at 5 m depth at the snout of the Changme-Khangpu (CK) glacier have been calculated to be 100 and > 650 years respectively. Based on i) these age estimates, ii) a net uniform accumulation rate of 0·7 m/yr of ice in the accumulation zone; and iii) applying a simple ice flow model assuming melting of ice of 1 cm/yr at the base of the glacier, it is demonstrated that the average basal flow rate of the CK glacier is much smaller (at least by a factor of three) than that of 40 m/yr estimated for the surface ice. This observation is in good agreement with the earlier work on basal flow rates and indicates that the deeper ice near the bed rock travels much slower than the surface ice.

Keywords. Himalaya; basal flow; environmental radioisotopes.

Introduction

ıe Himalayas form one of the most important temperate glacier systems on the earth. ıe annual mass budget of these glaciers controls to a large extent the dynamics of ice .d plays a vital role in meltwater contributions to north Indian rivers. Direct easurement of glacier flow rates and accumulation and ablation rates of some selected imalayan glaciers have been made in the past using conventional methods of onitoring the stakes installed at shallow depths in different parts of the glacier over a riod of a few months (Geological Survey of India 1984; Raina *et al* 1977).

It is known since three decades, both from mathematical models and from a number bore-hole experiments (Paterson 1981) that the motion of ice in a glacier slowly creases with increasing depths and reduces to minimal level near the bed rock. Basal w rate, which contributes significantly to the understanding of average flow rate of e glacier, depends on many factors like nature and slope of the bed, thickness of the acier, impurities and suspended material trapped within the ice. Estimation of ice ovement by conventional methods at depths is usually cumbersome and gives formation only about short term flow rates. The modern radioisotopic techniques, wever, provide a unique approach to investigate flow rates over a period of a few nturies (Bhandari *et al* 1982; Nijampurkar *et al* 1982, 1984). An attempt is made in is paper to estimate the past average basal flow rate of the Changme-Khangpu glacier ing natural radioisotopes like cosmogenic silicon-32 (half-life = 105 years; utschera *et al* 1980) and radiogenic lead-210.

Changme-Khangpu glacier, a small valley glacier in the Sikkim Valley of the eastern imalayas, is located in the Tista river basin at 27°58′ N, 88°42′ E and is situated at titudes ranging from 4850–5800 m above sea level. The glacier is 5·8 km long with a rface area of about 4·6 km^2. The average thickness of the glacier ice is about 70 m which thins down to about 5 m at the terminus of the glacier. The surface of the glacier is very dirty and covered with a thick supraglacial morainic debris in its entire ablation area. The glacier has shown a negative mass balance of 2×10^3 m^3/yr since 1978 and a receding trend for the past few years. There is strong geological evidence that this glacier has gone through at least four cycles of advance and recession in the past. The geological and geomorphological details are discussed elsewhere in detail (Nijampurkar *et al* 1984).

Results of analysis of the basal ice flow rate of the CK glacier are reported here and are compared with the surface flow rates determined by Bhandari *et al* (1982) and Nijampurkar *et al* (1984). The findings are discussed in terms of glacier movement.

2. Sample collection and analytical techniques

Three deep ice samples (CK-2, CK-5 and CK-7), at the snout of the CK glacier, close to the bed-rock at 5 and 12 m depth (tables 1, 2) along with eight other samples of different types (fresh snow, surface ice and meltwater emerging out from the terminus of the glacier) were collected during two glacier expeditions to the CK glacier in 1978 and 1981 (tables 1, 2 and figure 2). These samples were processed for ^{32}Si and ^{210}Pb activities using analytical procedures described by Nijampurkar *et al* (1982). In short, ^{32}Si and ^{210}Pb activities were extracted from a few tons and a few litres of meltwaters respectively, using Fe(OH)$_3$ as a scavenger. The respective radioactive daughters ^{32}P and ^{210}Bi (of ^{32}Si and ^{210}Pb respectively) were radiochemically separated, purified and counted as $Mg_2P_2O_7$ and $BiPO_4$ for several half-lives, using low background (0·8 cph) GM detectors with a NaI(Tl) active anticoincidence shield (Bhandari 1969). A typical decay curve of ^{32}P in fresh snow sample is shown in figure 1.

Table 1. Experimental data on measurements of ^{32}Si in snow and ice samples of CK glacier, Sikkim

Sample code	Nature/date of collection	Altitude (m)	Water collected (L)	Net ^{32}P (cph)	^{32}Si (dpm/ ton)	^{32}Si* apparent age (yrs)
CK-1-81	Fresh snow 30.7.81 to 6.8.81	5200	800	10·5	0·88 ± 0·09	0
CK-2-81	Snout ice (at 5 m depth) 7.8.81 to 10.8.81	4850	1035	<0·1	<0·01	>650
CK-36-78	Snout melt water	4850	1640	9·0	†0·5 ± 0.05	51
CK-38-78	Surface snout ice (0–30 cm) 28.8.78 to 7.9.78	4850	2380	3·7	†0·34 ± 0·03	109

*Half-life of ^{32}Si taken for calculation is 105 years; †Average value of repeat milkings. The corrected ^{32}Si activity for freshwater contribution, using the two component models (Nijampurkar *et al* 1982) has been taken for calculation of age.

Table 2. Experimental data on measurements of ^{210}Pb in snow and ice samples of CK glacier, Sikkim

Sample code	Nature	Date of collection	Altitude (m)	Volume processed (L)	Total ^{210}Bi activity (cpm)	^{210}Pb Activity dpm/L	^{210}Pb Age (yr)
CK-3-81	Fresh snow	6.8.1981	5200	33	37·95	8·50 ± 0·90	0
CK-4-81	Snout ice (0–30 cm)	9.8.1981	4850	10	0·38	0·33 ± 0·02	100
CK-5-81	Snout ice at 5 m depth	9.8.81	4850	50	0·63	0·08 ± 0·01	150
CK-6-81	Surface ice (0–30 cm)	10.8.81	4900	14	0·72	0·58 ± 0·06	85
CK-7-81	Deep ice at 12 m depth	10.8.81	4900	9·5	0·12	0·088 ± 0·03	145
[†]CK-39-78	Snout ice (0–30 cm)	3.9.78	4850	60	2·85	0·21 ± 0·02	115
CK-37-78	Snout water	5.9.78	4850	100	33·85	1·3 ± 0·10	60

[†] From Nijampurkar *et al* 1984.

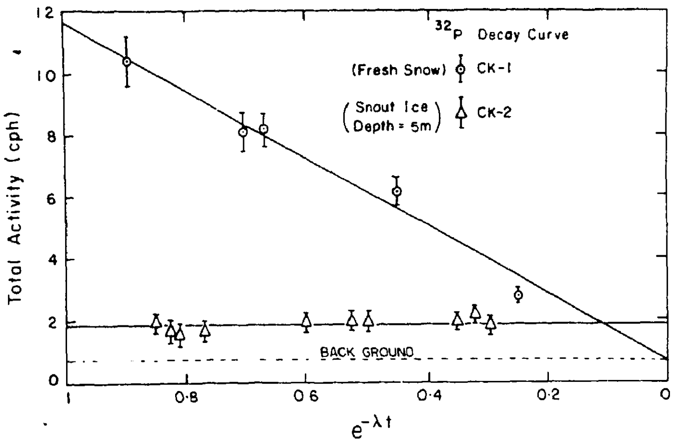

Figure 1. Observed decay plot of ^{32}P activity (cph) for the samples fresh snow (CK-1-81) and the snout ice at 5 m depth (CK-2-81). The dashed line represents the background.

3. Results

3.1 *Dating of surface and deep ice samples by radioisotopes*

The intercomparison of the past flow rates with contemporary flow rates can best be done by dating the surface and deep ice samples of the glacier using radioisotopes such as ^{32}Si, ^{210}Pb. Additionally, bomb-produced ^{137}Cs in an ice core can be used as a time marker to date deep ice samples and estimate past accumulation rates of ice. Dating of snow, firn and glacier ice by radioisotopes requires proper knowledge of their half-life values and average fallout values in the precipitation. Based on various considerations, discussed in detail by Nijampurkar *et al* (1982), the apparent ages of the surface and deep ice samples have been calculated using appropriate half-lives for cosmogenic ^{32}Si (105 yr) and radiogenic ^{210}Pb (22·3 yr). Mean weighted fallout values in precipitation of 0·7 dpm/ton for ^{32}Si and 8 dpm/L for ^{210}Pb are adopted in the present work for calculation of age (Nijampurkar *et al* 1982). The ^{32}Si and ^{210}Pb activities in one year's fallout of fresh snow samples (CK-1, CK-3) were found to be $0{\cdot}88 \pm 0{\cdot}09$ dpm/ton and 8·5 dpm/L respectively which are a little higher than the values adopted for age calculations and those reported in the literature (Bhandari *et al* 1982; Clausen *et al* 1967; Nijampurkar *et al* 1982, 1984). The ages of these samples are, therefore, assumed to be zero for calculation of ice flow rates.

Results from table 1 clearly show that the ^{32}Si activity in the surface ice sample of snout (CK-38) has decayed by 50% and that of snout ice at 5 m depth (CK-2) by over 95 % (figure 2). The age of the deep snout ice, estimated to be > 650 years using ^{32}Si (table 1) is thus older than that of the surface ice sample by at least 550 years.

The ^{210}Pb ages of surface samples CK-6 (150 m away from the snout in the ablation zone) (figure 2) and CK-4 (snout ice) are estimated to be 85 ± 10 and 100 ± 10 respectively which are in good agreement with that of the snout ice (CK-38, about 100 ± 10 years), obtained earlier through ^{32}Si measurements. A very low activity of

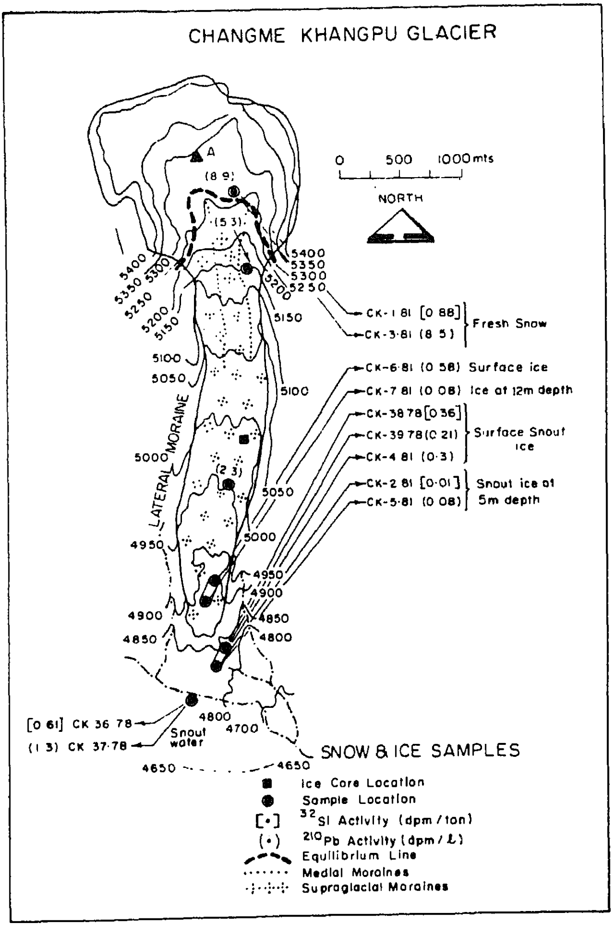

Figure 2. Distribution of ^{32}Si activity (dpm/ton) and ^{210}Pb activity (dpm/L) in snow, surface and deep ice on CK glacier. The ^{210}Pb activities (5·3) and (2·3) of surface ice shown in the map (not discussed in text) and melt water (1·3) emerging from terminus (i.e. snout water) are given for comparison with those of fresh snow and snout ice.

) and therefore the ages of the deep ice samples CK-5 (150 years) and CK-7 (145 s) obtained by ^{210}Pb method can be taken as a lower limit of the age estimates le 2).

he meltwater collected near the snout at the glacier is much younger (55 ± 5 years CK-36 and CK-37) than the surface snout ice (tables 1, 2 and figure 2). Its age estimate been given only for comparison with that of the ice samples, and to show that the age residence time of meltwater in the glacier is much smaller than that of deep ice nout.

Discussion

general pattern of flow of surface and deep ice in a glacier has been studied earlier

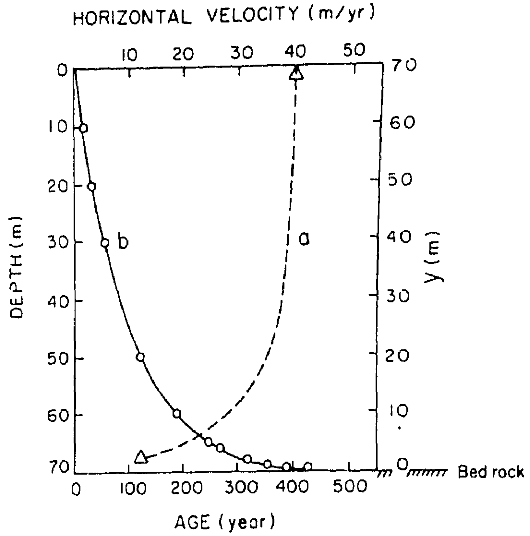

Figure 3. Variation of horizontal velocity and ice flow model ages with depth; a) Probable horizontal velocity profile in CK glacier based on past average surface and basal ice flow rates assuming vertical velocity gradient of Paterson (1981); b) Age of ice in the accumulation zone of CK glacier as a function of the distance y from the bottom (bed-rock) calculated using the modified formula for the ice flow model ages [see text (1)].

Hutter 1982; Lliboutry 1976; Paterson 1981; Paterson and Waddington 1984). These studies indicate that the deepest ice at the terminus of the glacier ice is fed by the deeper ice from the accumulation and ablation zones and would, therefore, be the oldest. For calculation of basal flow rates one requires estimates of the ice ages of the deeper ice in accumulation zone. In view of practical difficulties that arise in getting deeper ice samples from accumulation zones of temperate Himalayan glaciers and the limitations of the isotopes ^{32}Si and ^{210}Pb to date the ice samples layer by layer, indirect methods based on (i) bomb-produced ^{137}Cs as a time marker and (ii) ice flow models, are employed to obtain the ages of the deeper ice.

Using the depth profile of bomb-produced ^{137}Cs in an ice core from the accumulation zone, a net accumulation rate of ice of 0·7 m/yr has been calculated for the high altitude region over the CK glacier (Shukla *et al* 1983). Assuming a uniform deposition rate of snow over a period of past few decades, the radiometric age of the ice at 70 m depth near the bed rock has been estimated, as a first approximation (as lower limit), to be 100 years.

Considering the thinning of ice with depth (Paterson and Waddington 1984) and applying a simple ice flow model, assuming a constant vertical strain rate and melting rate of 1 cm of ice per year at the base of the glacier (which corresponds to an average geothermal heat flux and a deformational heat production caused by a sliding velocity of 10 m/yr), the ages of the deeper ice in the accumulation zone are calculated using Nye's formula (1963), modified by Hammer *et al* (1978).

umulation rate of ice (m/yr), y is the distance (m) from the bed rock, λ_0 is the annual ation (cm/yr) from the bottom at $y = 0$ and $\Delta H = (H\lambda_0)/(\lambda H - \lambda_0)$.

'he ages of the deeper 10 m ice lying over the bed rock (from $y = 0$–10 m) lie in the ge of 200–430 years (figure 3b). Based on these age estimates and that of the deep ice nout, the average basal flow rate of the glacier ice has been found to be much smaller 13 m/yr) than that of the average surface flow rate of about 40 m/yr calculated for past century (Nijampurkar *et al* 1984). Figure 3b also shows the most probable ocity profile with depth drawn on the basis of only two points (assuming horizontal ocity gradient of Paterson 1981), obtained by radiometric and flow model age mates for the surface and deep ice samples. This clearly indicates that sliding velocity his glacier is not more than 30% of the surface velocity, and that the travelling time leeper ice from accumulation zone to the terminus of the glacier is at least 3 times ger than that for the surface ice.

knowledgement

ank Professors David J Demaster, M Kuhn and N Bhandari for their critical nments and suggestions. My thanks also to Shri V M K Puri, Shri Sanjay Sharma, S Chatterjee and other members of the CK glacier expedition. I also thank Kameswara Rao for his technical assistance.

erences

ndari N 1969 *Nucl. Instrum. Methods* **67** 251
ndari N, Nijampurkar V N and Vohra C P 1982 in *Variations of the Global Water Budget, Proc. Symp. Oxford* (eds.) A Street Perrot, M Beran and R Ratcliffe (Oxford: D Reidel) 207
sen H B, Buchmann B and Ambach W 1967 *IUGG Conf. Snow and Ice Commission, Bern*
sen H B 1973 *J. Glaciol.* **12** 411
Geological Survey of India 1984 Classified reports on i) Interdepartmental expeditions to CK Glacier, Sikkim, 1978, 1979; ii) Multidisciplinary expeditions to Nehnar glacier, Kashmir, 1977–80
nmer C U, Clausen H B, Dansgaard W, Gundestrup N, Johnsen S J and Reeh R 1978 *J. Glaciol.* **20** 3
er K 1982 *Am. Sci.* **70** 26
schera W, Henning W, Paul M, Smither R K, Stephensen E J, Yntema J L, Alburger D E, Cumming J B nd Harbottle G 1980 *Phys. Rev. Lett.* **45** 592
outry L A 1976 *J. Glaciol.* **16** 151
mpurkar V N, Bhandari N, Krishnan V and Vohra C P 1982 *J. Glaciol.* **28** 91
mpurkar V N, Bhandari N, Borole D V and Bhattacharya U 1984 *J. Glaciol.* **51** (In press)
J F 1963 *J. Glaciol.* **4** 785
rson W S B 1981 *The physics of glaciers* 2nd ed. (Oxford: Pergamon Press) p. 380
rson W S B and Waddington E D 1984 *Rev. Geophys. Space Phys.* **22** 123
a V K, Kaul M K and Surinder Singh 1977 *J. Glaciol.* **18** 415
kla P N, Bhandari N, Nijampurkar V N, Puri V M K and Sharma S 1983 *Proc. Ind. Acad. Sci. (Earth Planet. Sci.)* **92** 255

ndian Acad. Sci. (Earth Planet. Sci.), Vol. 94, No. 2, July 1985, pp. 91–97.
inted in India.

nalytical technique for rapid determination of surface rock density

G RAMADASS, S M VARAPRASADA RAO and M S VIJAYA RAGHAVA

Centre of Exploration Geophysics, Osmania University, Hyderabad 500007, India.

MS received 28 February 1984; revised 15 October 1984

Abstract. Computation of the coefficient of correlation between the Bouguer reduced gravity and the ground relief apparently helps minimize the subjectivity inherent in the Nettleton's method of surface rock density determination. The ideal density is the one that results in zero correlation between them. The iterative procedure in sweeping the calculations through the range of densities chosen can be avoided by taking advantage of the linear relationship between this coefficient and the density. Linear interpolation is therefore suggested to arrive at the ideal density. The suggested procedure consequently consists of correlation coefficient computations for the two-density extremum values within which the density of the surface rock formations is expected to lie. The computer program for this method is also presented. The procedure involved and the efficacy of the method are illustrated with some practical analyses.

Keywords. Surface rock density; correlation coefficient; Bouguer reduced gravity; ground relief; linear interpolation.

ntroduction

ice rock density determinations from field gravity measurements make use of the on between the gravity variation and the ground relief. Operating on this onship Nettleton (1939) first provided a basis for working out the correct surface density from graphical constructions. Seigert (1942) and Parasnis (1952) proposed tical techniques to process gravity data free from any structural effects to obtain urface density by the least squares procedure. Rao and Murthy (1973) examined ossibility for extending the Parasnis method in the presence of linear regional ground. Nettleton's method however is more widely in use although the choice of ight density that renders the Bouguer anomaly least related to topographic ges remains purely subjective. Rao *et al* (1980) provided a statistical basis to nize this difficulty by seeking an optimum value of the coefficient of correlation een the Bouguer reduced gravity and elevation. Here, the iterative procedure ent in the approach is shown to be amenable to simplification by an interpolation ss for more rapid evaluation of surface formation density.

3asis of the method

eton's method of surface rock density determination is known to consist tially of Bouguer reduction of the observed gravity values. Combined elevation ction is computed under this method for assumed values of density to obtain the ced Bouguer anomaly along the entire traverse of measurements. The Bouguer aly is compared with the ground relief. The density, obtained from a range of surface formation density. Details of the basis behind the approach are presented by Rao *et al* (1980) who also proposed the computation of the coefficient of correlation to minimize the subjectivity of Nettleton's method.

Attempts by the authors to arrive at the minimum coefficient of correlation by repeat calculations for varied densities indicate that the correlation coefficient is linearly and inversely related to density as expected. In so far as densities higher than the correct value tend to produce a mirror image of the relief in the Bouguer anomaly, the correlation coefficient also seems to undergo reversal in its sign with densities larger than characteristic values of the near surface rock formations. The crossover point obviously indicates the ideal density with absolutely no relation to the ground relief to the corresponding Bouguer anomaly. However, errors of measurements in both the gravity and elevation obviate this possibility in practical situations. Consequently, the correlation coefficient obtains non-zero minimum values for practical data, the densities corresponding to which may be considered as the reliable range relevant to the field situation.

The choice of the minimum non-zero value of the correlation coefficient is difficult for the obvious reason that the number of iterations could be extremely large. Besides, the errors of gravity measurements prescribe the limit below which the value of correlation coefficient loses significance. It is therefore suggested that the density at the crossover point be corrected by the following factor assuming that the elevation measurements are of negligible error (Berëzkin 1967):

$$\Delta\sigma = \pm \Delta g_{\mathrm{error}} / 0{\cdot}04185\ \overline{\Delta h}\ \mathrm{g/cc} \qquad (1)$$

where, $\Delta g_{\mathrm{error}}$ in milligals is the gravity measurements error and $\overline{\Delta h}$ is the average elevation in meters with respect to the chosen datum. The error in elevation measurements by repeat observations is of the order of ±0·5 m in the present case.

The true density may thus be computed to an accuracy dependent on the accuracy of the gravity survey itself. Evidently, data on large average elevation over the datum are better suited for practical evaluations.

3. Interpolation

Since a linear relationship is expected between density and the corresponding value of the coefficient of correlation between the reduced gravity and the surface relief, by a suitable method of interpolation, the coordinates $(\sigma, 0)$ of the point K shown in figure 1 may be found out from known values of any two points A and Q on the line AKQ. Thus, following James and Scarborough (1966), we get, γ_1 and γ_2 minimum and maximum

$$\sigma = \sigma_1 + (\sigma_2 - \sigma_1)|\gamma_1| \Big/ (|\gamma_1| + |\gamma_2|) \qquad (2)$$

where σ = density in g/cc considered; γ_1 and γ_2 are corresponding coefficients of correlation. By substituting the numerical values of σ_1, γ_1, σ_2 and γ_2, the density corresponding to the ideal situation of zero correlation can be evaluated. The density correction is computed using (1) to prescribe the limits within which the actual density of surfacial formation lies.

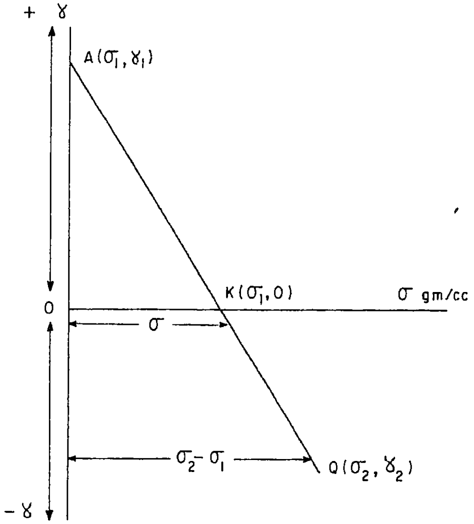

Figure 1. Fixing the coordinates of an intermediate point by interpolation.

4. Calculation procedure

Practical density evaluations by the present method require computation of the correlation coefficients corresponding to any two assumed density extremum values to the combined correction factor. The Fortran program developed for this method is listed in the appendix. It is only necessary to prescribe the minimum and maximum possible densities within which the actual density is expected to occur in practical cases. The tedious course of considering the correlation coefficients by incremental changes from the assumed density therefore becomes unnecessary.

4.1 *Test analysis*—1

Gravity and ground relief data of a couple of traverse runs over the Kamthi sandstones of the Lower Gondwana formations in a part of the Godavary valley, India, have been used to compute the density of these sandstones by the present approach. The basic data of these two traverses roughly 500 m apart are as shown in figures 2a, b. As may be noticed, the total elevation change in these two traverses is not considerable, but careful gravity measurements, provide an accuracy to enable the density determination to be reliable.

Coefficients of correlation computed following Cramer (1946) for varied densities with an increment of 0·01 g/cc from the initial values of 2·0 g/cc and plotted against the corresponding densities are shown in figures 3(a) and 3(b) for the data of figures 2(a) and 2(b) respectively. Linear relationship between these two parameters within experimental errors in evidenced in these figures. The densities corresponding to zero correlation between the reduced gravity and the elevation are seen to be 2·40 g/cc and 2·43 g/cc for the data of these traverses. Although the graphs in figure 3 are constructed

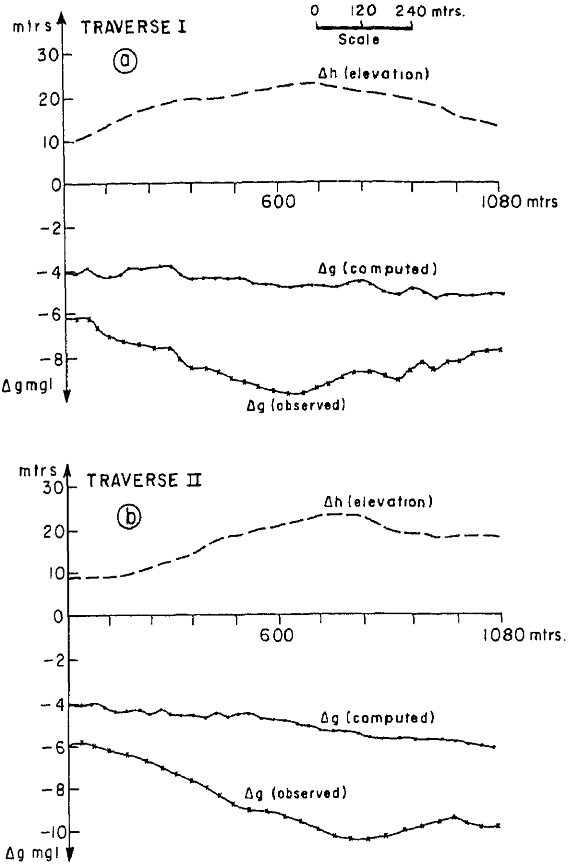

Figure 2. Gravity and elevation plots.

to illustrate the nature of the relationship between density and correlation coefficient, iterative and hence tedious calculations are not practically warranted. The ideal density corresponding to the zero correlation coefficient value may be directly computed by the interpolation technique using (2). The minimum and maximum density values prescribed for the two cases and the final densities computed by (1) and (2) are summarised in table 1.

4.2 *Test analysis*—2

The present technique is used to estimate the surface density of sedimentary rocks consisting of phyllitic shales and limestones in parts of Varikunta-Zangamrajupalle belt in eastern Cuddapah basin. An average density of 2·65 g/cc was obtained for these

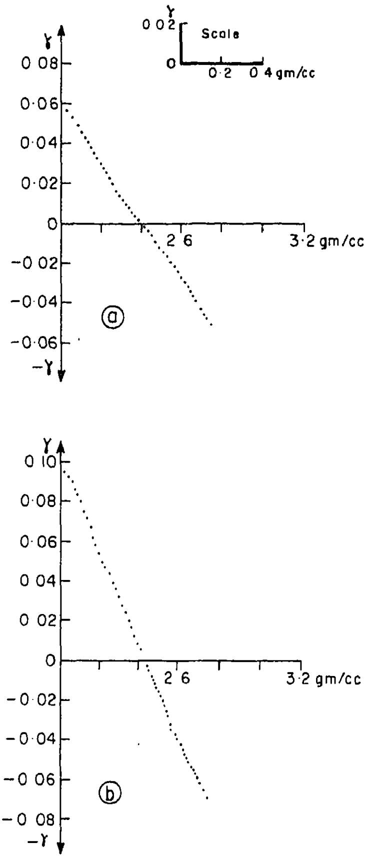

Figure 3. Relationship between correlation coefficient and density.

Table 1.

averse .	Density minimum σ_1 (g/cc)	Correlation coefficient γ_1	Density maximum σ_2 (g/cc)	Correlation coefficient γ_2	Density at the cross over point with correction factor σ (g/cc)
	2·0	0·062	2·74	−0·052	2·40 ± 0·08
	2·0	0·099	2·74	−0·070	2·43 ± 0·11

ones (Cuddappah super group) from the bore holes in the vicinity of these ses have been measured in the laboratory. Measurements on the dry samples red yield values of 2·33 ± 0·01 g/cc and 2·63 g/cc for the Kamthi and phyllitic

Table 2.

Method	Kamthi formations (Lower Gondwana)		Phyllitic shales and limestones (Cuddappah super group)
	Traverse-I Density g/cc	Traverse-II Density g/cc	Density g/cc
Nettleton's	2·35	2·36	2·59
Seigert's	3·24	3·30	2·52
Parasnis's	3·62	4·54	2·54
Present work	2·32	2·32	2·65

All the known methods were utilised on these field data and the results obtained by earlier methods as well as here are compared in table 2.

5. Conclusion

With the data of measured gravity and elevation and by prescribing the lowest and highest density values, surface rock density is reliably computed by the present technique. Use of any modern calculator or the given computer program (appendix) is recommended. Practical limits to the computed ideal density are prescribed by the accuracy of gravity measurements. Also it is evident that gravity data of traverses with large elevation changes are to be preferred.

Acknowledgements

The authors are grateful to Dr N L Mohan for guidance.

Appendix

```
C    PROGRAM FOR DENSITY DETERMINATION
C    GOBS OBSERVED GRAVITY IN MGALS
C    HELV ELEVATION IN METERS
C    ASDEN ASSUMED DENSITIES
C    GCAL CALCULATED GRAVITY WITH ASSUMED DENSITY
C    R COEFFICIENT OF CORRELATION
C    TDEN TRUE DENSITY
C    GCTR CALCULATED GRAVITY FOR TRUE DENSITY
     COMMON GOBS(500), HELV(500), DG(500), DH(500), GCL(500), DCG(500)
   1 DCH(500), GCLR(500), DGR(500), DNGR(500), GCTR(500)
     DIMENSION R(5), ASDEN(5)
     NSD = 2
     DO 100 MAN = 1, NSD
     READ(3, 200) NS
 200 FORMAT(I3)
```

```
300   FORMAT(12F6.2)
400   FORMAT(16F5.2)
      SGHS = 0·0
      SHSS = 0·0
      M = NS - 1
      DO 600 L = 1, 2
      A = L
      ASDEN(L) = 1·5*A
      DO 700 N = 1, NS
      GCAL(N) = GOBS(N) + (0·3086 - 0·04185 *ASDEN(L))* HELV(N)
700   CONTINUE
      SUMG = 0·0
      SUMH = 0·0
      SUMGS = 0·0
      SUMHS = 0·0
      SUMGH = 0·0
      DO 800 J = 1, M
      DCG(J) = GCAL(J + 1) - GCAL(J)
      DCH(J) = HELV(J + 1) - HELV(J)
      SUMG = SUMG + DCH(J)
      SUMH = SUMH + DCH(J)
      SUMGS = SUMGS + DCG(J)*DCG(J)
      SUMHS = SUMHS + DCH(J)*DCH(J)
      SUMGH = SUMGH + DCG(J)*DCH(J)
800   CONTINUE
      AM = M
      S1 = SUMHS/AM - (SUMH/AM**2)
      S2 = SUMGS/AM - (SUMH/(AM*AM))
      S1 = ABS(S1)
      S2 = ABS(S2)
      SGH = SQRT(S1)
      SGG = SQRT(S2)
      CNSTP = (SUMGH/AM) - (SUMG*SUMH/(AM*AM))
      R(L) = CNSTP/(SGG*SGH)
600   CONTINUE
      RN = (ASDEN(2) - ASDEN(1))*ABS(R(1))
      DR = ABS(R(1)) + ABS(R(2))
      TDEN = ASDEN(1) + (RN/DR)
      WRITE(4,900)TDEN
900   FORMAT(E20·8)
100   CONTINUE
      STOP
      END
```

ences

in V M *Consideration of ground relief and the surfacial layer in gravity detailed surveys* (Moscow: dra)

r H 1946 *Mathematical methods of statistics* (Princeton: University Press)

B and Scarborough 1966 *Numerical mathematical analysis* (New Delhi: Oxford & IBH Pub. Co.)

on L L 1939 *Geophysics* **4** 176

is D S 1952 *Mon. Not. R. Astron. Soc.* **6** 252

A J F 1942 *Geophysics* **7** 29

M V, Bhimasankaram V L S and Soloview G A 1980 *J. Assoc. Explor. Geophys.* **1** 43

B and Murty B V S 1973 *Pure Appl. Geophys.* **110** 1927

Indian Acad. Sci. (Earth Planet. Sci.), Vol. 94, No. 2, July 1985, pp. 99–110.
inted in India.

liminary studies on the geochemistry of the Cauvery river basin

V SUBRAMANIAN, L VAN t' DACK* and R VAN GRIEKEN*
School of Environmental Sciences, Jawaharlal Nehru University, New Delhi 110067, India
*Chemistry Department, U.I.A., B-2610, Wilrijik, Belgium

MS received 31 October 1983; revised 27 August 1984

Abstract. Samples of water and sediments were collected over a three year period from the entire region of Cauvery river basin excluding the estuary. On the basis of our observations, we have calculated the average composition of the Cauvery river at several locations from the catchment to the river mouth, the downstream profile of sediment load, annual erosion rates, solute and sediment fluxes and have predicted on long term changes. The sediment chemistry was determined by x-ray fluorescence (XRF) technique, and calculated mean compositions of the Cauvery and its tributary bed and the suspended sediment were compared to those of world average river sediments. Downstream profiles of some of the elements appear to be controlled by size and mineralogical characteristics besides local factors specific to the location of the samples. Interelemental relationships indicated good correlation among the transition elements indicating their co-genetic behaviour within the drainage basin.

Keywords. Geochemistry; Cauvery river basin; sediment load; annual erosion rates; x-ray fluorescence; co-genetic behaviour.

ntroduction

hemical cycling of elements is receiving wide attention due to the need for rstanding the pathways of pollutants through our present environment. River esses form a major link in the geochemical cycle. Several attempts have recently made to understand river transport of materials. The most important of these are ibbs (1977), Martin and Meybeck (1979) and by Milliman and Meade (1983). al estimates on fluxes given by Garrells *et al* (1975), Martin and Meybeck (1979) Nriagu (1979) are largely based on studies of a few low-sediment rivers such as the zon and Yukon and some large North American rivers. Asian rivers contribute than 70% of the global sediment input to world oceans (Milliman and Meade ; thus any understanding of the geochemical behaviour of elements in our onment would require the study of large Asian rivers. With this objective in mind, uthors have been studying the large rivers of the Indian sub-continent. The present t is based on preliminary studies on the geochemistry of the entire Cauvery river .

he Cauvery river basin

cauvery river is the eighth largest river (in terms of discharge) in the Indian ontinent. It has a drainage area of about 90,000 km^2 covering a distance of 800 km, Coorg in the Western Ghats to the river mouth at the Bay of Bengal. Hemavati, ni, Bhavani and Amaravati are the major tributaries. Some of the important

Table 1. Some hydrological characteristics of the Cauvery river basin

River site	Annual run off[a] (million m^3/yr)	Drainage area[a] (km^2)	Mean discharge[b] (m^3/sec)	TDS[c] (ppm)	TSM[c] ppm
Hemavathi	2520	5200	80	95–221	1–30
Krishnaraja sagar	6200	—	197	110–167	7–45
Kabini	2600	6700	83	105–246	5–8
Mettur dam	14380	—	457	83–238	1–5
Bhavani	3090	7144	98	115–337	10–50
Amaravati	1080	5200	34	128–617	20–35
Upper Anicut	18970	—	602	138–321	15–50
Lower Anicut	20950	87900	665	125–274	1–30

[a]Annual run-off and drainage area (from Rao 1975); [b]calculated from annual run-off: [c]range of values; TDS—total dissolved solids.

While the upper reaches of the river basin drain predominently the Precambrian shield rocks, the downstream regions lie on the Tertiary sedimentary rocks and Plio-Pleistocene sediments. The upper reaches cover an elevated (topographic high) plateau and the river drops its height sharply by more than 200 metres into the plains after the Sivasamudram falls. Boreholes near the river mouth indicates cretaceous and probably upper Gondwana sediments, below 3000 m (Wadia 1975).

The Cauvery is one of the most intensively utilised river basins in India. Since most of the water is withdrawn for irrigation at several stations along its course, several distributaries form a net work of broad (about 100 km) and shallow delta at the river mouth.

3. Methodology

Samples of river water, suspended and bed sediments were collected at 16 locations along the river as well as the tributaries. The locations were chosen so to represent all the regions of the river basin, major urban areas, dams etc. Between 1979 and 1982, samples were collected 4 times (October 15–31, 1979; December 1–25, 1980; May 17–June 5, 1981; August 2–31, 1982) to broadly cover seasonal variations (summer, monsoon, post-monsoon and winter). Figure 1 shows the flow pattern and sample locations in the river basin. While measurement of suspended sediments and water chemical analysis were carried out on all samples in each batch collected, suspended sediment mineralogy, bed sediment size studies and chemistry of bed and suspended sediments were carried out on limited samples only.

Standard analytical procedures (atomic absorption spectrophotometer-cations; calorimetry-anions and silica; pH-ion analyser for pH, Cl^- and F^-) were adopted for water chemistry and sediment filtration. Suspended sediments were filtered with a Millipore filter (0·45 micron). Grain size analysis of bed sediments was done by the sieving technique and the chemistry of bed and suspended sediments was done by x-ray fluorescence technique (details reported in Van Grieken *et al* 1980). For cation analysis,

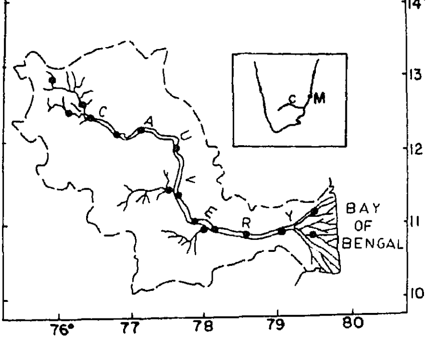

Figure 1. Drainage basin map of Cauvery river basin with sampling locations.

: sediment analysis by XRF, IAEA standard soil-5 was also run, table 2 gives observed l recommended values for the standard.

Discharge data for the Cauvery river at important locations were obtained from oublished reports of the Irrigation and Water Resources sections of the Karnataka l Tamil Nadu Governments.

Results and discussion

Chemical and suspended load

nong the 16 sampling locations, eight are on either side of the junctions of the butaries with the Cauvery. The average chemical composition of various tributaries l of the Cauvery river at important locations in the Cauvery and her tributaries are nmarized in table 3. The average values were calculated from the data obtained in

Table 2. Analysis ($\mu g g^{-1}$) of IAEA soil 5 standard by XRF

ment	Average value*	Standard deviation per	Standard deviation on	Recommended value
ɡ	16,000	1,800	780	15,000
	73,100	1,800	800	81,900 ± 2,800
	247,000	5,000	2,000	330,000
	15,400	300	140	18,600 ± 1,500
	22,100	900	410	22,000
	195	15	7	151
	28	6	2	28 ± 3
ı	908	47	21	852 ± 37
	43,600	2,200	980	44,500 ± 1,900
	30	—	—	15 ± 1
	10	1	0	13
	88	5	2	77 ± 5
	379	19	9	368 ± 8

*Average of six measurements.

Table 3. Average[a] chemical composition of Cauvery river water.

Location	pH	Conductivity (ms/cm)	HCO_3^{-1}	SO_4^{-2}	Cl^{-1}	$H_4SiO_4^0$	Na^+	K^+	Ca^{+2}	Mg^{+2}	TDS
			ppm								
Krishnaraja sagar	8·1	0·23	50	8	11	7	23	2	7	12	120
Sivasamudram falls	8·6	0·22	38	34	11	7	25	1	18	14	130
Mettur dam	8·3	0·27	52	44	17	6	36	2	19	11	160
Grand Anicut	8·1	0·30	50	51	13	7	38	2	13	12	170
Thanjavur	8·4	0·32	51	29	9	9	39	2	16	16	180
Hemavati	8·3	0·26	32	8	8	9	25	2	19	12	120
Kabini	7·6	0·21	50	29	13	6	23	1	11	18	150
Bhavani	8·4	0·41	55	60	15	9	43	4	16	20	220
Amaravati	8·5	0·85	102	87	65	16	16	7	20	25	300

[a] Discharge weighted

ur seasons. The upstream regions of the Cauvery as well as its tributaries in this gion have TDS (total dissolved solids) values less than the corresponding downstream lues. The two distinct regions of the basins have geological as well as geographical fferences. Marginal increase of TDS downstream may be due to two reasons: (a) highly eatherable tertiary sediments; (b) very dense population and hence increasing impact use of water on water quality. The bulk of the TDS values is made up of alkalinity and me of the tributaries, such as Amaravati, carry a large SO_4^{-2} load as well. Most of the O_4^{-2} is likely to be of secondary source, as was reported for the Ganges river water by anda (1972).

Figure 2 shows an example of the downstream profile in the Cauvery river basin. onductivity is used here to illustrate changes in the dissolved constituents. Similar wnstream changes in the profile of suspended sediments are also shown. Unlike ajor Indian rivers such as Ganges (Subramanian 1979), there are several dams and servoirs along the course of the Cauvery. The suspended sediments settle in these gions; as a result, TSM (total suspended matter) profile is generally negative wnstream. There is an abrupt change in the basin bed topography from high plateau flat plain at Sivasamudram falls and the resultant force of water causes resuspension bed sediments. The TSM profile shows a small increase in this region. In addition, the spended waste materials brought by tributary Amaravati adds upto the TSM load after e tributary junction.

The mean composition of the tributaries reflect the sub-basin geology, and in the maravati region the varying levels of local human influences on water quality. Though

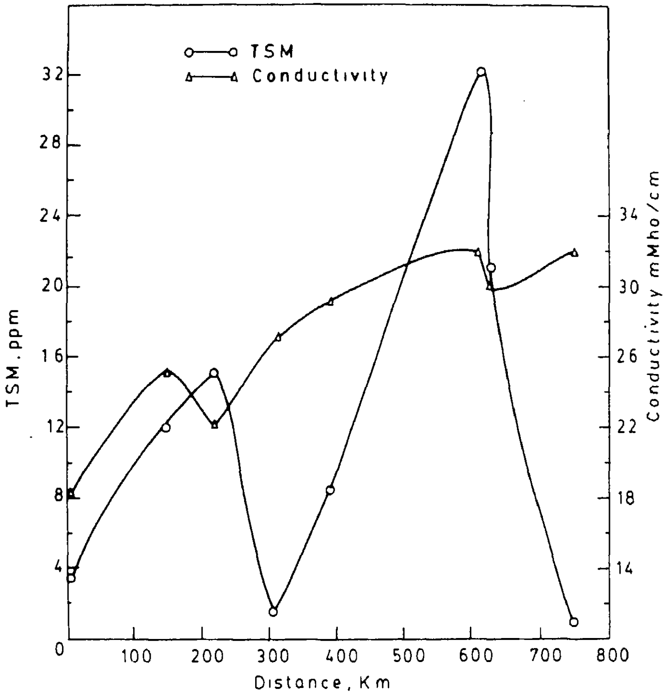

Figure 2. Downstream profile for conductivity and total suspended matter (TSM) in the Cauvery river basin.

no corrections have been made for atmospheric recycling, the chemical load and composition of the Cauvery at its mouth is close to that of Indian average (Subramanian 1979) which is slightly higher than the world average of Livingstone (1963).

4.2 *Erosion rates*

Based on mean TDS, TSM values from this work (table 1) and the annual run off at several locations (Rao 1975), fluxes, erosion rates and other denudation parameters have been calculated. These data are presented in table 4. For comparison, the average values for the Indian subcontinent from Subramanian (1978), and the average for the continents are shown. The only significant contribution of the Cauvery basin to the subcontinent wide process is in terms of total chemical load and the chemical erosion rates (CER) (1·6% the chemical load and 25% the CER of the Indian average). Total fluxes and erosion rates for the Indian subcontinent are of course very high, relative to the global averages, due to the extreme levels of sediment loads in the Ganges-Brahmaputra system (Milliman and Meade 1983; Subramanian 1979).

Within the Cauvery basin, various fluxes and rates indicate no uniformity, primarily due to different sub-basin geology, elevation and various degrees of human impact on water chemistry. Since the chemical fluxes and rates are based on observed TDS values, corrections for atmospheric recycling and substraction of urban and agricultural drain-off contribution will yield the component of TDS truly derived by chemical weathering. At present sufficient data are not available to effect these corrections. Hence table 4 values perhaps show the upper limit. In similar studies on Chinese rivers, Hui Ming Hui *et al* (1982) also observed high TDS values without correction for precipitation chemistry and pollution components. On the other hand, Stallard and Edmond (1982) improved on Gibbs (1977) data for the Amazon after extensive monitoring of precipitation chemistry over the Amazon basin. Thus, our fluxes and rates though averaged over a 3 year period may not truely reflect natural geochemical processes in the Cauvery river basin.

4.3 *Bed sediment*

Size analysis of bed sediments indicate that fractions greater than 1000 μm are the important size population, in the river basin. Dominance of quartz is consistent with the coarseness of the bed sediments. Sand fraction is generally dominent except near the river mouth where silt becomes significant. Clays fractions which dominate the particulates (Subramanian 1980) were generally absent in the bed sediments. Within the sand fraction, distribution of individual size population varies longitudinally but not systematically. Figure 3 shows the general trend in the downstream profile of mean size (graphic mean) and organic matter content. The maxima and minima in the plot generally correspond to either a reservoir region or tributary. The upstream region (above Sivasamudram falls) has sediments (dominant population above 1000 μm) which are coarser relative to the downstream region (river mouth area). Godavari and Krishna sediment have size population in the silt-clay range (Naidu 1966; Subramanian

Table 4. Erosion rates in the Cauvery river basin.

River site	Chemical load	Sediment load 10^6 kg/yr	Total load	CER 10^4 kg km^2/yr	SER	TER	Decrease in mm/ 1000 yr	Time to MSL (million years)
Hemavati	330	50	335	6·4	0·1	6·5	25	60
Krishnaraja sagar[a]	760	75	835	—	—	—	—	
Kabini	380	15	395	5·7	0·2	5·9	22	46
Mettur dam[a]	2600	43	2643	—	—	—	—	
Bhavani	670	37	707	9·4	0·5	9·9	37	20
Amaravati	250	33	283	4·8	0·7	5·5	21	13
Lower Anicut	3500	42	3542	4·0	0·1	4·1	15	61
India average[b]	$2·2 \times 10^5$	$1·2 \times 10^6$	$1·4 \times 10^6$	8·6	46·8	55·4	210	5
World average	390×10^{10}	1830×10^{10}	2220×10^{10}	2·3	10·8	13·1		

[a] Reservoir/dam region; CER, SER, TER-chemical, sediment and total erosion rates respectively; MSL—mean sea level; [b] From Subramanian (1978).

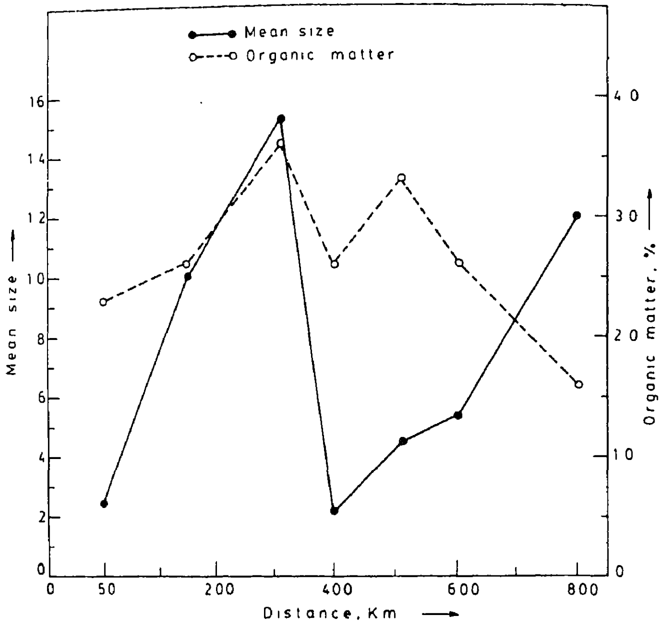

Figure 3. Downstream profile in mean grain size (graphic mean expressed in Phi units) ($\phi = -\log_2 D_{mm}$ where D_{mm} is diameter in mm) and organic matter content in the bed sediments.

generally coarse (sand) bed sediments (Singh 1974). Physical weathering is not very efficient in the Cauvery river basin (chemical/physical ratio is about 40, see table 3). In addition, several dams in the river arrest the process of abrasion so that the sediment grains remain in similar size classes released during the initial weathering process.

4.4 *Sediment chemistry*

Table 5 summarises the chemical composition of bed sediments from the Cauvery basin. There are no earlier published reports on the chemistry of Cauvery river sediments. However, for other river basins in India, partial sediment chemistry have been reported; Borole *et al* (1982) for Narmada and Tapti, Sarin *et al* (1979) for river mouth sediments of Krishna, Godavari and Ganga, Handa (1972) for Ganga at Allahabad; and Subramanian *et al* (1985) for the sub-continent as a whole. The Cauvery bed sediments have 50% more Si than the world average sediments (Si = 28·5%, Cauvery mean Si = 41·9%) of Martin and Meybeck (1979) because of the dominance of quartz in the bed load. As a result, other elements are depleted in the Cauvery bed sediments relative to the world average. Individual tributaries show wide variation in their chemistry. All of them differ from the main Cauvery itself. The tributaries drain a wide variety of geological terrain; for example, the Bhavani drains unconsolidated sediments and the hill slopes of the intensively cultivated Nilgiris and shows higher

Table 5. Chemical composition of bed sediments in the Cauvery river basin

	H	*K*	*B*	*A*	*C*
t *N*	6	6	6	6	31
	9600	8100	13000	10000	8100
	52100	35400	53000	61600	37600
	353000	344000	319000	336000	410000
	18300	5350	7700	17400	8610
	8740	7920	14600	15300	6290
	1080	6880	4500	2010	2750
	35	95	145	75	74
	98	180	130	49	54
	204	360	535	184	212
	7090	17800	32600	11800	12600
	10	19	22	16	15
	28	31	35	12	12
	4	9	12	3	3
	9	17	44	14	13
	74	22	28	50	29
	239	245	317	624	231
	20	6	12	19	7

values in μg/gm; *N* = number of samples; *H* = Hemavati; *K* = Kabini; *B* = Bhavani; *A* aravati; *C* = Cauvery basin as a whole

Table 6. Heavy metals concentration in the suspended sediments of the Cauvery river basin

	H	*K*	*B*	*A*	*C*[a]
nt *N*	6	6	6	6	31
	51400	9300	6000	5100	3200
	3400	800	400	300	300
	5600	670	210	200	150
	46000	24500	4600	1900	1300
	91100	21000	10200	86000	62000
	1100	280	200	150	100
	3500	500	230	150	150
	400	420	100	100	60
	4500	4200	2900	450	500
	450	400	200	80	40

bbreviations as in table 5; All values in μg/gm

nriched in Fe, Mn and other transition elements relative to the bed sediments. Fe ent of Cauvery particulates (6·2% average of 31 samples) compare with the Fe s reported for Krishna (Fe = 6·9%) and Godavari (Fe = 7·23%) sediments by *et al* (1982). Similarly, results for other transition elements, such as Cr, Mn, Co, Cu and Mn for Cauvery particulates agree with those of Godavari and Krishna. The value for heavy metals in the Cauvery particulates exceed those of world average artin and Meybeck (1979). Several authors (Borole *et al* 1982; Gibbs 1977; Martin 1971; Turekian and Scott 1967) have observed varying levels of enrichments of tributaries of the Cauvery have their own distinct particulate chemistry. For example, tributary Hemavati has its catchment covering parts of the Kudremukh iron-formation and the iron contents of particulates is very high (9·11 % mean of six samples); on the other hand, Amaravati drains an area of dense population, intensive cultivation and a large number of electroplating and leather industries. Hence in this case the high Fe-levels (8·6 %, mean of six samples) do not reflect the true natural geochemical background.

Figures 4a and b show the longitudinal profile of Fe as well as the Fe/Al ratio in the bed and suspended sediments. In both cases, Fe levels (figure 4a) in the upstream region (before Sivasamudram falls) differ from those in the downstream region. On the other hand, variation in the Fe/Al ratio downstream (figure 4b) was found to be erratic for particulates and systematic for bed sediments. Because of contribution from the upstream tributory Hemavati, both the Fe content and the Fe/Al ratio in the particulate are initially high. Due to deposition (as a result of reservoir/dam regions) of suspended

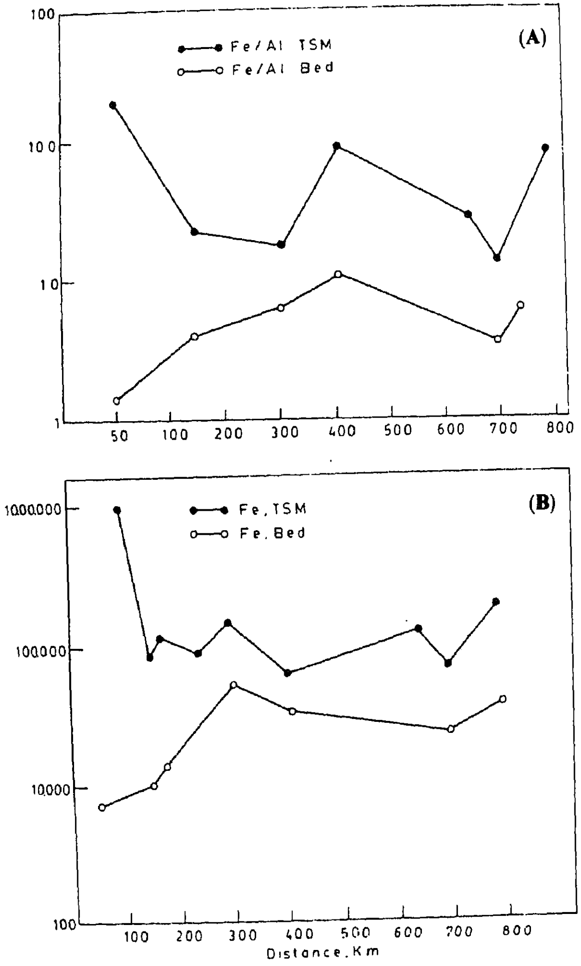

Figure 4. Downstream profile in the Fe content (**A**) of suspended sediments and bed sediments, and (**B**) the respective Fe/Al ratios. Fe values are in ppm.

Table 7. Correlation matrix for elemental analysis of bed sediments.

Elements	Al	Mg	Si	K	Ca	V	Cr	Mn	Fe	Co	Ni	Cu	Zn
Al	1												
Mg	0·30	1											
Si	−0·51	−0·73	1										
K	−0·09	−0·19	0·45	1									
Ca	0·20	0·92	−0·80	−0·23	1								
V	0·22	0·76	−0·73	−0·19	0·83	1							
Cr	0·26	0·52	−0·41	0·02	0·36	0·53	1						
Mn	0·19	0·88	−0·78	−0·24	0·87	0·92	0·57	1					
Fe	0·35	0·84	−0·79	−0·28	0·81	0·92	0·66	0·96	1				
Co	0·24	0·89	−0·81	−0·32	0·89	0·84	0·63	0·93	0·93	1			
Ni	0·38	0·70	−0·57	−0·22	0·51	0·53	0·91	0·63	0·71	0·73	1		
Cu	0·29	0·80	−0·77	−0·29	0·79	0·81	0·72	0·84	0·87	0·88	0·79	1	
Zn	0·15	0·50	−0·57	−0·34	0·48	0·56	0·50	0·61	0·65	0·64	0·61	0·70	1

sediments, Fe as well as Fe/Al ratio in bed sediments increase downstream. Forstner and Whittman (1981) have compiled several case studies where levels of Fe and other transition element varied longitudinally in diverse aquatic environments.

Interelemental correlation was attempted for some of the transition elements. Table 7 shows the correlation matrix for bed sediments. All the elements showed good correlation with each other. In similar analysis of data for the particulates, the correlation was found to be 0·90 or above for all the element pairs.

5. Summary

The water chemistry of Cauvery river is similar to that of average river water from the Indian subcontinent. Individual sub-basins as well as regions of urban population show variations compared to the main river. Chemical weathering in the Cauvery basin is very significant and compared to other river basins, solute erosion rates are high. The bed sediments are dominated by sand size fractions and quartz.

The chemistry of bed sediments differ from the world average river sediments due to the dominance of high silica minerals (quartz) in the bed load. On the other hand, the very fine particulates show enrichment of heavy metals relative to the world average. Transition elements correlate very well with each other in suspended as well as bed sediments.

References

Borole D V, Sarin M M and Somayajulu B L K 1982 *Indian J. Mar. Sci.* **11** 51

Forstner U and Whittman G T W 1981 *Metal pollution in the aquatic environment* (Berlin: Springer-Verlag)

Garrells R M, Mackenzie F T and Hunt C 1975 *Chemical cycles and the global environment* (California: William Kaufmann)

Gibbs R J 1977 *Bull. Geol. Soc. Am.* **88** 829

Handa B K 1972 *Indian Geohydrol.* **8** 71

Hai Ming Hui, Stallard R F and Edmond J 1982 *Nature (London)* **298** 550

Livingstone D 1963 *Chemical composition of river water, V.S.G.S. paper* D440

Martin J M and Meybeck M 1979 *Mar. Chem.* **7** 1

Martin J M, Kulbick K and Degroot G 1973 *Hydrochemistry* (New York: Clarke & Co.,) vol. 2, pp. 463–483

Milliman J D and Meade R 1983 *J. Geol.* **9** 21

Naidu A S 1966 in *Deltas in their geological framework* (ed.) M L Shirley (Houston: Geological society) pp. 125–137

Nriagu J O 1979 *Nature (London)* **279** 409

Rao K L 1975 *India's water wealth* (Delhi: Oxford University Press)

Sarin M M, Borole D V and Krishnaswamy S 1979 *Proc. Indian Acad. Sci.* (Earth Planet. Sci.) **A88** 131

Singh I B 1974 *Sediment. Geol.* **12** 53

Stallard R F and Edmond J 1982 *J. Geophys. Res.* **86** 9844

Subramanian V 1978 *Proc. Indian Acad. Sci.* (Earth Planet. Sci.) **A77** 77

Subramanian V 1979 *J. Hydrol.* **27** 33

Subramanian V 1980 *Mar. Geol.* **36** M1

Subramanian V 1982 *Int. Assoc. Hydrol. Sci.* **137** 238

Subramanian V, Van t'dack L and Van Grieken R 1985 *Chem. Geol.* **48** 271–279

Turekian K and Scott M 1967 *Environ. Sci. Technol.* **1** 940

Van Grieken R, Van t'dack L and Costra Dantas C 1980 *Anal. Chim. Acta.* **52** 1859

Wadia D N 1975 *Geology of India* (Delhi: McGraw Hill)

Anomaly map of *Z* component of the Indian sub-continent from magnetic satellite data

M G ARUR, P S BAINS and JEEVAN LAL

Survey of India Geodepic and Research Branch, Dehra Dun 248 001, India

MS received 30 November 1983; revised 19 February 1985

Abstract. An anomaly map of the *Z* component has been produced for the region of the Indian sub-continent for the first time by the Survey of India using MAGSAT data. Data of thousands of kilometres of satellite tracks of varying altitude have been reduced to a common elevation of 400 km by removing the external field and linear trend. The entire data was plotted on a map of 1:6 M and mean values of 2° × 2° blocks then accepted for contouring. A prominent magnetic low is reflected over the Himalayas and a prominent high over the Indian peninsula. The dividing line of positive and negative anomalies between the Himalayas and Deccan Traps falls along the Narmada lineament.

Keywords. Anomaly map; *Z* component; MAGSAT data; magnetic low; magnetic high; Narmada lineament.

1. Introduction

In recent years, it has been realised that crustal magnetic anomalies exist which are of longer wavelengths than those found by exploration geophysicists and that these longer wavelength (> 150 km) anomalies are indicative of geologic and tectonic features in the deep crust (Pakiser and Zietz 1965; Zietz *et al* 1966; Shuey *et al* 1973; Hall 1974; Krutikhovskaya and Pashkevich 1977). Regan *et al* (1975) and Langel *et al* (1980) demonstrated that long wavelength lithospheric anomalies could be mapped successfully from satellites. Such a map showed a global distribution of anomalies of about 500–3000 km scale size which were never before mapped and whose very existence, in most cases, was discovered for the first time. Although such maps are distorted by variation in altitude over the data set and by contamination from magnetospheric field, Regan *et al* (1975) were able to demonstrate that the probable source of the anomalies is indeed the lithosphere. The map which was derived from data from the Polar Orbiting Geophysical Observatories (POGO), 2, 4 and 6 satellites showed a magnetic 'low' over the Himalayas and a 'high' over peninsular India.

In the present investigation, an anomaly map for the *Z* component has been prepared based on MAGSAT data reduced for a common elevation of 400 km.

2. Limitations of satellite data

One of the principal limitations of anomaly mapping with satellite data is that only large features are resolvable. Langel and Thorning (1982) indicate that the resolution of the POGO data is in the 250–500 km range. MAGSAT was designed to increase this resolution to 150–300 km by acquiring data at lower altitudes. The altitude range for the POGO spacecraft is 400–1510 km; that of MAGSAT is 200–550 km. The MAGSAT data were acquired between November 1979 and June 1980.

POGO satellites data provided a data set of earth's total intensity while MAGSAT collected data on vector components also.

3. Method of deriving the anomaly map

To derive the anomaly map, the earth's main field and the fields due to external currents have been accounted for by the procedure developed by Regan *et al* (1975), Mayhew (1979), and Langel *et al* (1980). The investigations have been carried out, with the aid of MAGSAT data on quiet days made available by NASA on three data tapes covering the Indian region. The data tapes were decoded and the anomaly information was derived by subtracting the model values of the Z component from that of observed Z values at the varying satellite altitudes. From this data set the field due to magnetospheric currents was removed. For each satellite pass the values of e (magnetic field due to external currents) and i (magnetic field due to induced internal currents) have been accepted as given in NASA Technical Memorandum 82160. The data set thus obtained was reduced to a common elevation of 400 km by the method described by Henderson and Cordell (1971). The linear trend from each pass was also removed during this reduction. The residuals so obtained would represent crustal anomalies. In this procedure, the data reduced from geographically coincident passes matched well. The map is made from all the passes with varying Kp index from 0 to 33. The average value of all the points falling in each 2° × 2° block was calculated. The individual values which differed by more than thrice the standard deviation of the mean from the initial block average were neglected. Langel *et al* (1982) also used a similar method and eliminated all points within each block which differ by more than twice standard deviation from the initial block average. New averages were computed and these mean values were contoured to derive the map at a contour interval of 5 nT (nanotesla) on a scale of 1 : 16 M. In the final map, the average number of points per block is 9 and total number of data points is 2198 from which 648 have been neglected. No adjustments have been made for the varying geomagnetic inclinations.

4. The anomaly map

Figure 1 shows the resulting MAGSAT crustal anomaly map of the Z component of the Indian sub-continent bounded by the area 8°N to 36°N latitude and 64°E to 100°E longitude at contour intervals of 5 nT and on a scale 1 : 16 M. Amplitudes vary from $+20$ to -27 nT. A prominent zero level in the north coincides more or less with the

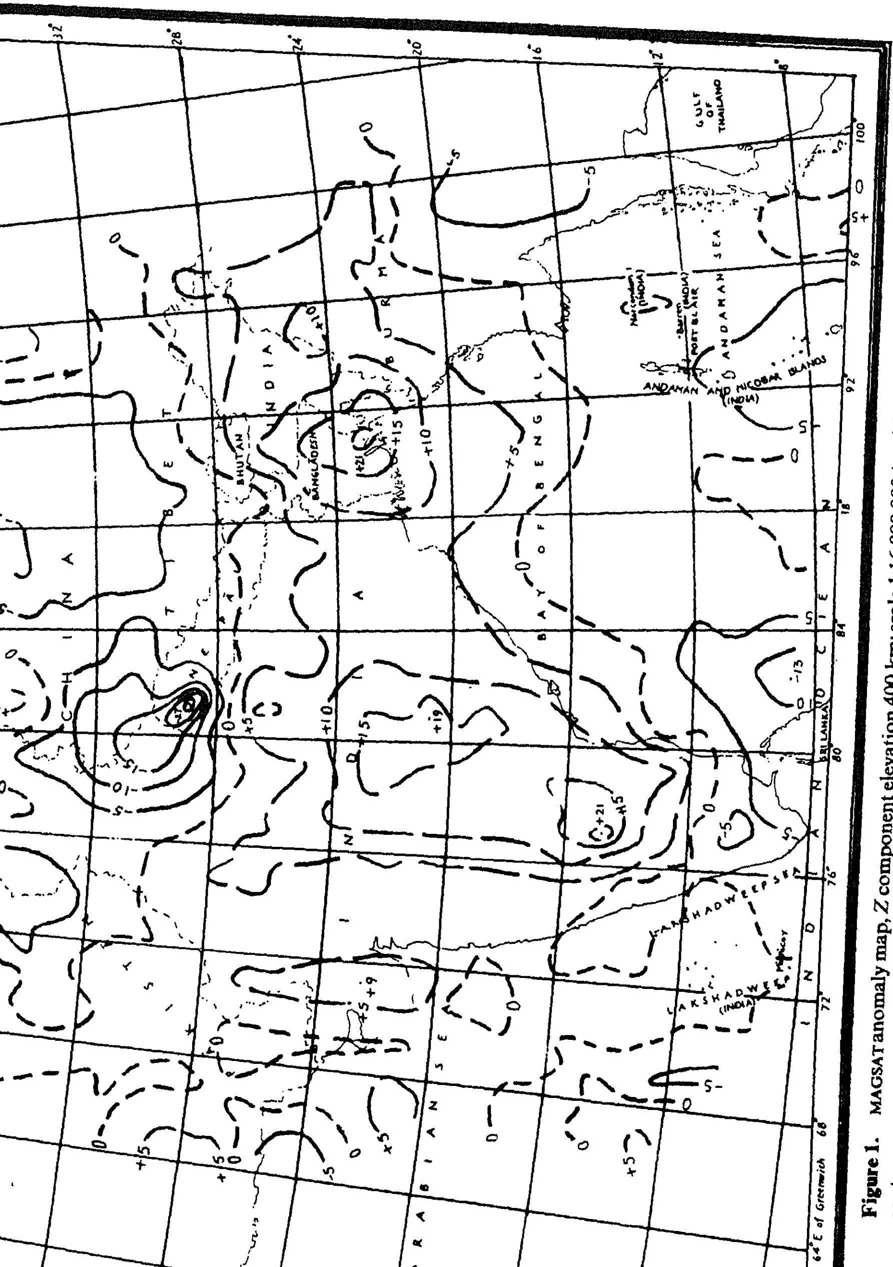

Figure 1. MAGSAT anomaly map, Z component elevation 400 km; scale 1:16,000,000 (positive contours ——+5——; negative contours – – –5– – –).

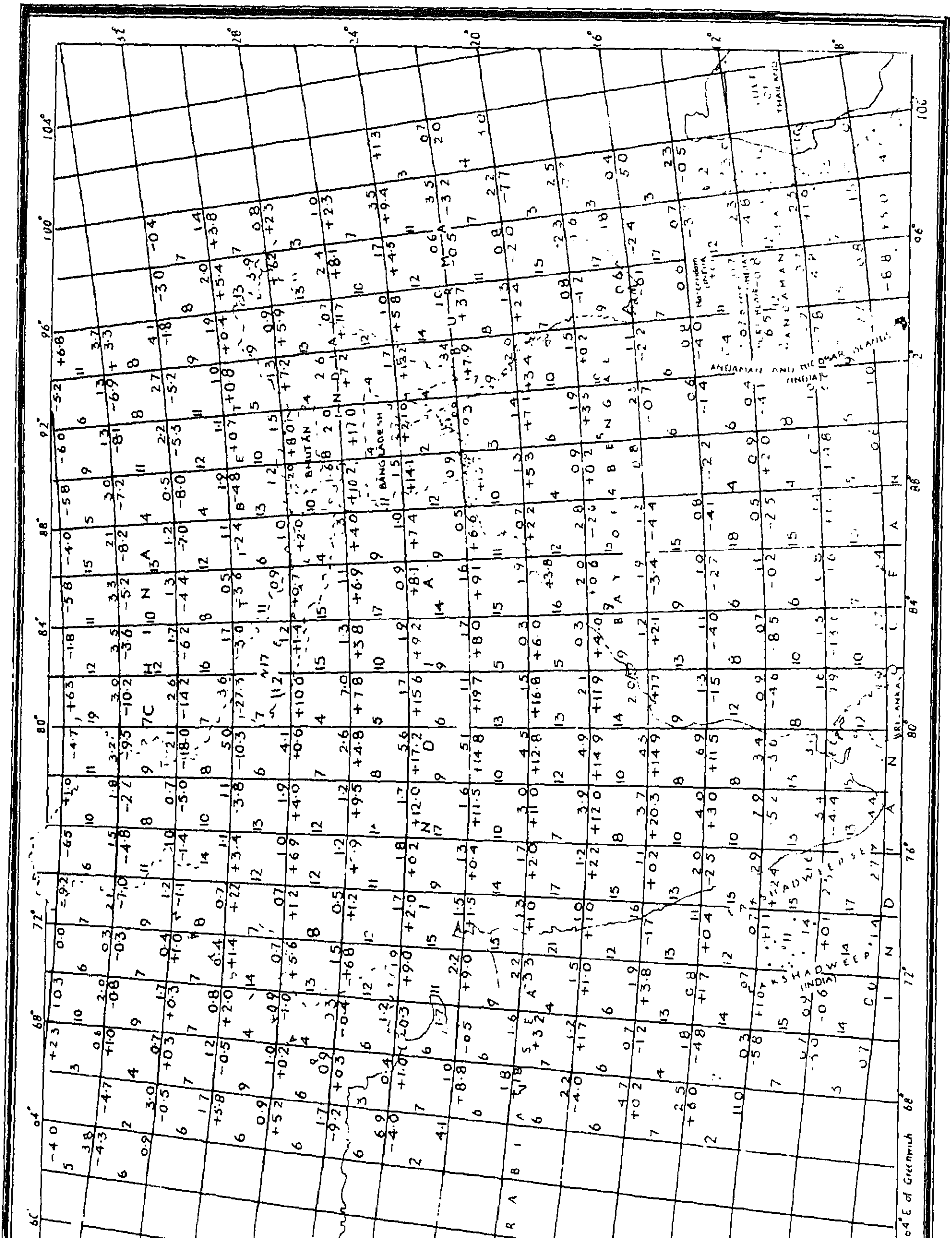

MAGSAT data, *Z* component anomalies at altitude 400 km, chart showing mean values (top right of each block), number of data points (mid-
standard deviation (lower right) in 2° × 2°blocks. (scale 1:16,000,000).

5. Conclusions

A Z vector anomaly map of the Indian sub-continent has been prepared for the first time at an altitude of 400 km. The anomalies vary from $+20$ to -27 nT. Positive anomalies prevail over the Deccan Traps and Bangladesh and negative anomalies are predominent over the Himalayas and in the Indian Ocean. It is interesting to note that Z anomalies obtained from *ground data* over the lower Himalayan region are generally positive, but both positive and negative over peninsular India.

If we compare our Z anomaly map with the MAGSAT Scalar Anomaly map prepared by NASA, we notice that the NASA map also shows negative anomalies over western Nepal and positive anomalies over peninsular India and Bangladesh.

Acknowledgements

The authors are thankful to Dr B N P Agarwal of the Indian School of Mines for valuable guidance in developing the computer programme for the reduction of satellite data. The authors are grateful for the data, literature and computer programs received from NASA. The close support of the Surveyor General of India, Principal Investigator of the Project, Indian Space Research Organisation, the Indian Institute of Geomagnetism, Dr M N Qureshy of the Department of Science and Technology and the Oil and Natural Gas Commission for this research work is thankfully acknowledged.

References

Hall D H 1974 *J. Geophys.* **40** 403
Henderson R G and Cordell L 1971 *Geophys.* **36** 856
Krutikhovskaya Z A and Pashkevich I K 1977 *Can. J. Earth Sci.* **14** 2718
Langel R A, Coles R and Mayhew M A 1980 *Can. J. Earth Sci.* **17** 876
Langel R A and Thorning L 1982 In *Nares strait and the drift of Greenland: a conflict in plate tectonics* (eds) P R Dawes and J W Kerr (Meddr. Greenland, Geosci)
Langel R A, Phillips J D and Horner R J 1982 *Geophys. Res. Lett.* **9** 269
Mayhew M A 1979 *J. Geophys.* **45** 119
Naqvi S M, Divakara Rao and Hari Narain 1978 *Tectonophysics* **6** 323
Pakiser L C and Zietz I 1965 *Rev. Geophys.* **3** 505
Regan R D, Cain J C and Davis W M 1975 *J. Geophys. Res.* **80** 794
Shuey R T, Schellinger D R, Johnson E H and Alley L G 1973 *Geology* **1** 107
Zietz I, King E R, Geddes W and Lidiak E G 1966 *Geol. Soc. Am. Bull.* **77** 1427

Proc. Indian Acad. Sci. (Earth Planet. Sci.), Vol. 94, No. 2, July 1985, pp. 117–128.
© Printed in India.

Summer cooling of the Arabian Sea—a review

J S SASTRY and V RAMESH BABU

National Institute of Oceanography, Dona Paula, Goa 403 004, India

MS received 24 November 1983; revised 31 January 1985

Abstract. The summer cooling of the Arabian Sea has been reviewed in relation to the dynamic and thermodynamic processes. The differences in the quantum of cooling in the coastal regions have been attributed to the variations in the strength of coastal upwelling along the respective coasts. In the central portions of the Arabian Sea, the thickness of the surface layer and the thermal structure appear to be predominantly governed by the turbulent mixing of cold waters entrained into the surface layer in association with the deepening of current shear zone. The surface heat losses during the passage of a cyclone over the east central Arabian Sea account for only 40 % of the total heat change in the surface layer while the rest is lost into the interior. Also presented are climatological mean patterns of the forcing parameters and their variations during certain years.

Keywords. Summer cooling; Arabian Sea; turbulent mixing; surface heat losses; climatological mean patterns.

1. Introduction

The summer cooling of the Arabian Sea is an anomalous feature in tropical oceans. While water bodies similarly situated geographically show an increase in the sea surface temperature (SST) with the advance of the northern summer, the Arabian Sea surface temperature is known to lower. As the sea surface temperature forms one of the bottom boundary conditions for the development of numerical predictive models of the atmosphere, meteorologists and physical oceanographers are interested in understanding the causative factors for this anomalous behaviour. The available information suggests that the quantum of lowering of SST differs from region to region. Off the coast of Somalia, the SST decrease on occasions has been found to be as high as 10°C between May and July while off the west coast of India, it is between 2 to 3°C. There is a substantial lowering of SST off the Arabian coast. In the northern regions, the sea warms up with increase in SST towards the Gulfs of Oman and Persia. In this paper, some of the dynamic and thermodynamic processes are discussed to explain the Arabian Sea cooling and also presented is the variability of the forcing parameters.

2. Climatological patterns of cooling

Figures 1a, b and c show the May minus June, May minus July and May minus August sea surface temperatures respectively to exhibit the quantum of cooling over the Arabian Sea based on the mean SST data (Koninklijk Nederlands Meteorologisch Instituut's Atlas 1952). By June (figure 1a) the cooling is predominant off the Somalia coast and off the southwest coast of India. The presence of an area of zonal minimum cooling between 68° and 72°E indicates that the spreading of cold waters off Somalia is confined to the western Arabian Sea in the month of June. In the northern regions the SST increases progressively northward with a maximum increase of 3°C in the Persian Gulf. Figure 1b shows an intensification of these features in July. Off the Somalia and the Arabian coasts the decrease in SST is more than 4°C while off the southwest coast of India, it is higher than 2°C separated again by a zonal minimum cooling centred around 70°E. The zone of increase in SST has shifted northward and by this time, the highest increase is about 4·5°C in the Persian Gulf. The May minus August temperature distribution (figure 1c) shows that the maximum cooling exceeding 5°C occurs off the Arabian Coast while the other features are almost similar to those in figure 1b. These suggest that the cooling off the coasts of Somalia, Arabia and southwest India has to be treated separately and spreading of cold waters is limited to the respective regions.

3. Circulation and resultant surface layer

3.1 *Mean pattern*

Figure 2a shows the mean surface currents in the Indian Ocean during August according to Deutsches Hydrographisches Institut's Atlas (1960). During the southwest monsoon period, one can visualise a great clockwise circulation in the northwestern region of the Indian Ocean. The mean circulation presented has been derived on the basis of the data collected over several years from ship's logs. As per this circulation

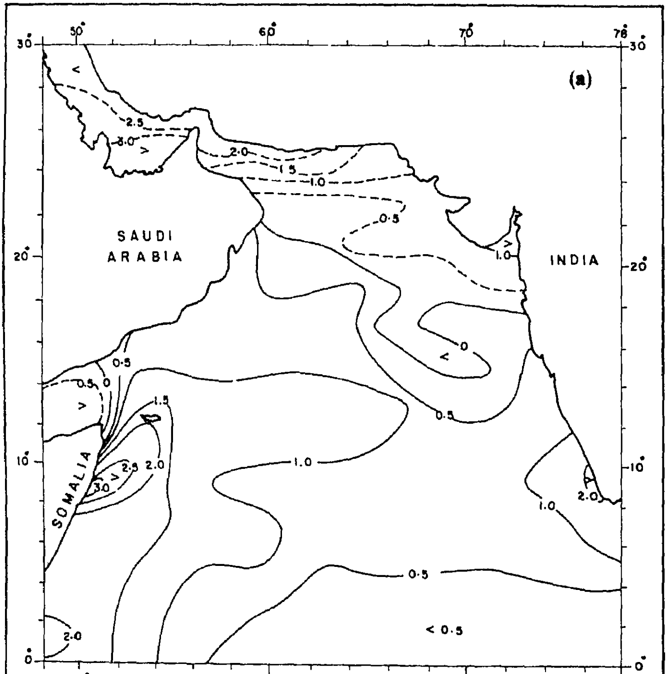

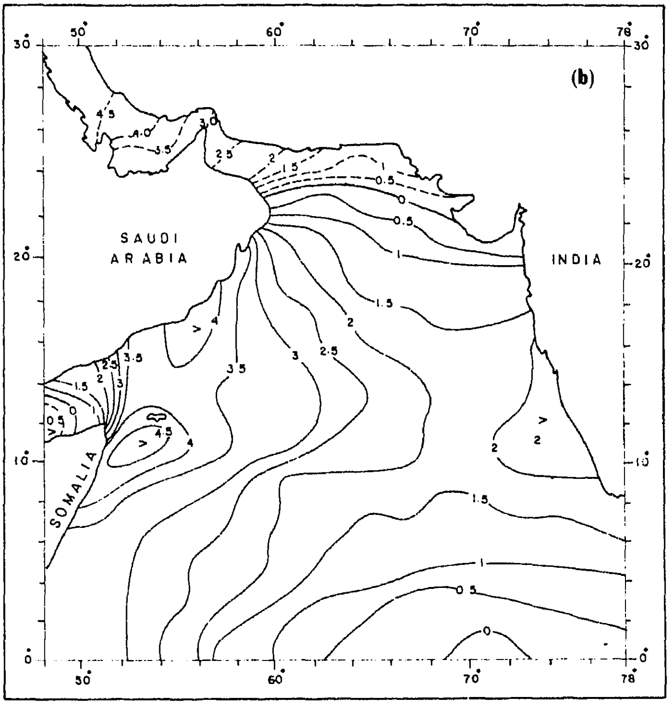

May — July

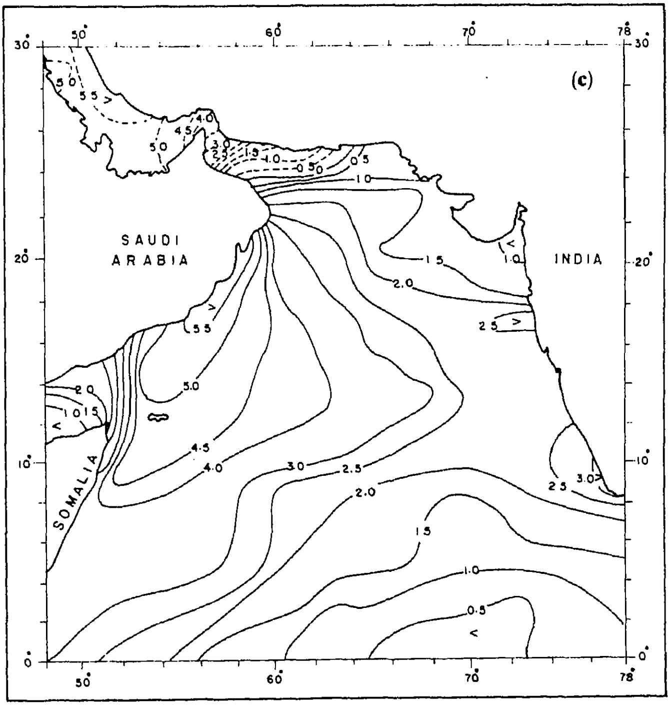

May — August

Figure 1. (**a**) May minus June SST (°C), (**b**) May minus July SST (°C), and (**c**) May minus August SST (°C) in the Arabian Sea.

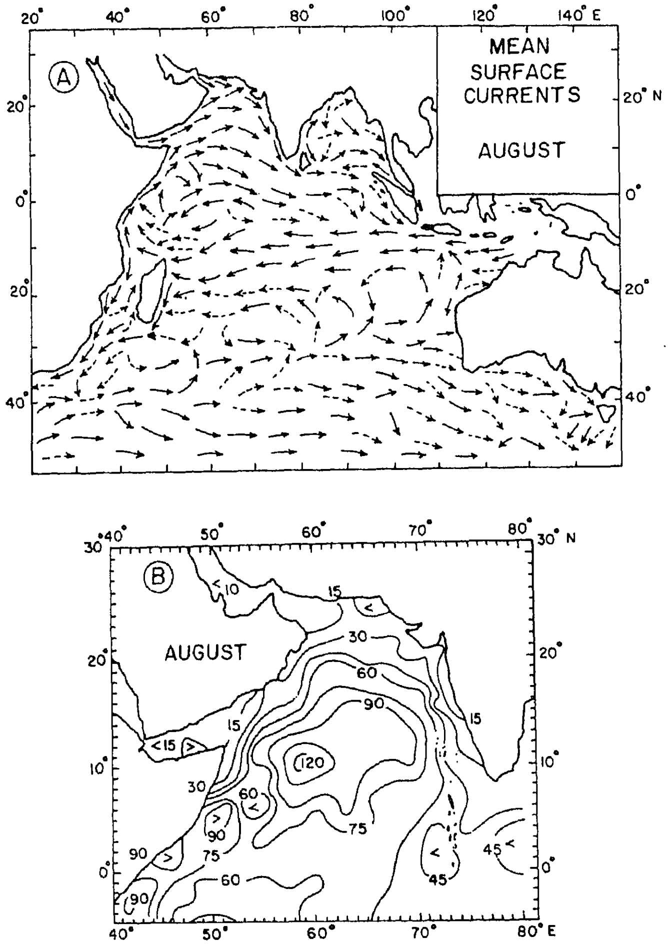

Figure 2. (**a**) August mean surface currents in the Indian Ocean (after Deutsches Hydrographisches Institut Atlas 1960), and (**b**) August mean depth (m) of the thermocline in the northwestern Indian Ocean (after Robinson *et al* 1979).

pattern, one would expect coastal upwelling all along coastal boundaries and hence cooling off Somalia, Arabia and West Coast of India. By June, the Somali current sets in and the process of upwelling is initiated. By July, upwelling intensifies and the coldest temperatures occur here. This fits into the scheme of things according to which the differential quanta of cooling in different regions over the Arabian Sea are noticed. The figure further suggests that convergence takes place in the central portion of the northwestern Indian Ocean associated with this type of circulation resulting in the increase of the thickness of the surface layer. This is quite evident from figure 2b which

3.2 *IIOE studies*

The International Indian Ocean Expedition (IIOE) revealed for the first time the complex flow pattern in the Arabian Sea (Bruce 1968; Düing 1970; Sastry and D'souza 1971). The flow patterns consist of a series of clockwise and anti-clockwise gyres in the zonal belt south of 15°N in contrast to the climatic features presented in figure 2a. Associated with this type of circulation, one would expect convergences in the clockwise cells and divergences in the anticlockwise cells which govern the thickness of the surface layer. The surface layer deepens in the clockwise cells while in the anticlockwise cells, it shallows up. Figure 3 presents the geostrophic current relative to 1000 db along 10°N in the Arabian Sea during the summer monsoon of 1963 (Bruce 1981) which shows alternate bands of north–south flows penetrating deeper upto about 500 m in the western Arabian Sea. The top of thermocline along the same section shows a wavy pattern with troughs and crests coinciding with the clockwise and anticlockwise gyres. The strength of these cells decreases eastward and the thermocline shows a general upward slope towards the Indian coast. The downward slope of the thermocline to the west off the west coast of India and the very shallow surface layer off Somalia which are seen in the mean patterns could also be seen in figure 3. Associated with these flows, intense upwelling takes place off Somalia and the spreading of cold waters is seen in the western Arabian Sea only (Sastry and D'souza 1972). The 25°C isothermal surface is found cutting the sea surface in the western regions and towards east, this surface is found at depths varying upto 120 m. Recently, Bruce (1981) utilising the XBT data along the tanker route off the African coast has also indicated the possibility of restricted spreading of cold waters under the influence of a large quasi-permanent anti-cyclonic eddy found off the Somalia coast.

4. Wind stress patterns

The mean pattern of the wind stress curl for the month of July is shown in figure 4a (Bruce 1981) while figure 4b shows the wind stress curl for a typical active monsoon day

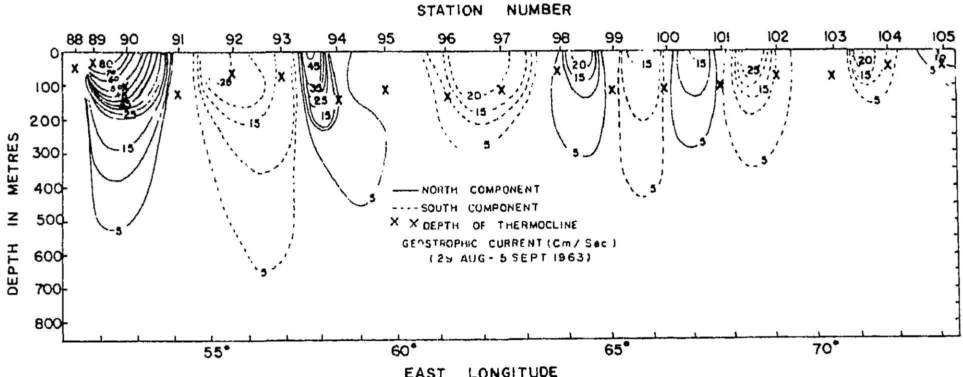

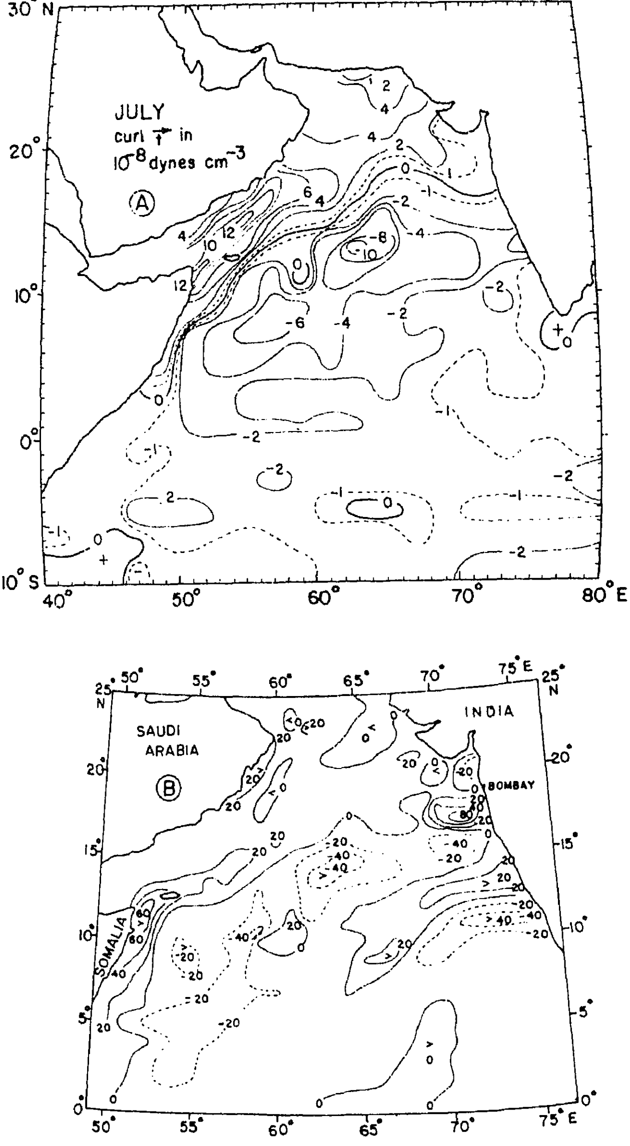

Figure 4. Surface wind stress curl (10^{-8} dynes cm $^{-3}$) over the Arabian Sea. (**a**) Mean pattern in July (after Bruce 1981), (**b**) Typical active monsoon day (2nd July, 1963) (after Sastry and Ramesh Babu 1979).

(Sastry and Ramesh Babu 1979). These figures show that the wind stress curl is predominantly negative south of a line joining Somalia coast and Bombay. To the north of this line, it is predominantly positive. These figures suggest that the wind stress curl could be an order of magnitude more in strong monsoon conditions.

One of the major features of atmospheric circulation at the time of the onset of monsoon is the development of vortices over the southeastern Arabian Sea. These may intensify and move either north or northwest. Associated with these circulations, a positive wind stress curl would prevail within their active area. As the cyclone intensifies, the wind field over the Arabian Sea not only strengthens but gives rise to a negative wind stress curl in the south-western Arabian Sea (Krishnamurti *et al* 1981). Thereafter, with the advance of the cyclone and continuation of the active monsoon, the wind stress curl distribution will be as shown in figure 4b. Figure 5 shows the variation of wind stress curl in the area bounded by 10·5–14·5°N lat. and 64–68°E long. of the east central Arabian Sea during 1977 monsoon season (Ramesh Babu and Sastry 1984). The positive wind stress curl during 8–11 June, 1977 is due to a cyclone passing through the study area. Subsequently the region has come under the influence of the negative wind stress curl.

Associated with this type of wind stress curl distribution convergences and divergences would develop with consequent vertical velocities which are estimated to be of the order of 10^{-3} cm/sec in the Ekman layer (Cox 1970; Sastry and Ramesh Babu 1979). As the wind stress is the main forcing function and as its interannual variability and the variability within the same season are considerable, the near surface circulation patterns could change considerably.

5. Cooling processes in the eastern Arabian Sea

The negative wind stress curl gives rise to the development of a strong southerly current off the west coast of India with a consequent upsloping of thermocline towards the Indian coast. This results in an apparent upwelling close to the Indian coast and sinking farther off-shore. Figure 6 shows the evolution of the thermal structure during 1977 monsoon season at 12·5°N and 68°E (Ramesh Babu and Sastry 1984). The thickness of surface layer, which is around 40 m before the onset of the monsoon, increases to about 100 m by mid July. The depth-temperature profile on June 10 shows a slight decrease in SST as well as a slight rising of the thermocline. As mentioned earlier, this region has come under the influence of positive wind stress curl around that time associated with the cyclone. The slight rise in the thermocline could be interpreted as due to upwelling associated with the cyclonic motion. The lowering of SST by 0·6°C could be partly due to surface heat losses. Further deepening of surface layer and further cooling seem to be associated with the dynamic processes at the thermocline such as the entrainment of cold sub-surface waters by vertical current sheer instability. Figures 7a and b show the SST, spot currents and the thickness of surface layer around the same area prior to and after the onset of monsoon respectively. The most important features to note in figure 7 are: (1) deepening of surface circulation whereby the current shear zone is shifted from about 50 m to more than 100 m, (2) a slight decrease in the surface layer thickness on 10 June, (3) a gradual increase in the thickness of surface layer as well as a decrease in surface temperature thereafter. With the shift of the current shear zone to deeper levels, the cold subsurface waters are entrained into the surface layer and further mixing reduces the SST and also increases the thickness of surface layer.

During Monex '79 experiment, the evolution of depth-temperature profiles in the east central Arabian Sea from 24 May–1 July, 1979 has been studied (Murty *et al* 1983; Ramesh Babu and Sastry 1984). Their studies indicate a drop in SST by about 1·2°C immediately after the cyclone has passed over the area on 18 June. As noted earlier, the thermocline slightly rises upward. By July, the SST falls by 2·5°C from the maximum temperature occurring on 9th June. Initially before the onset of monsoon, the surface

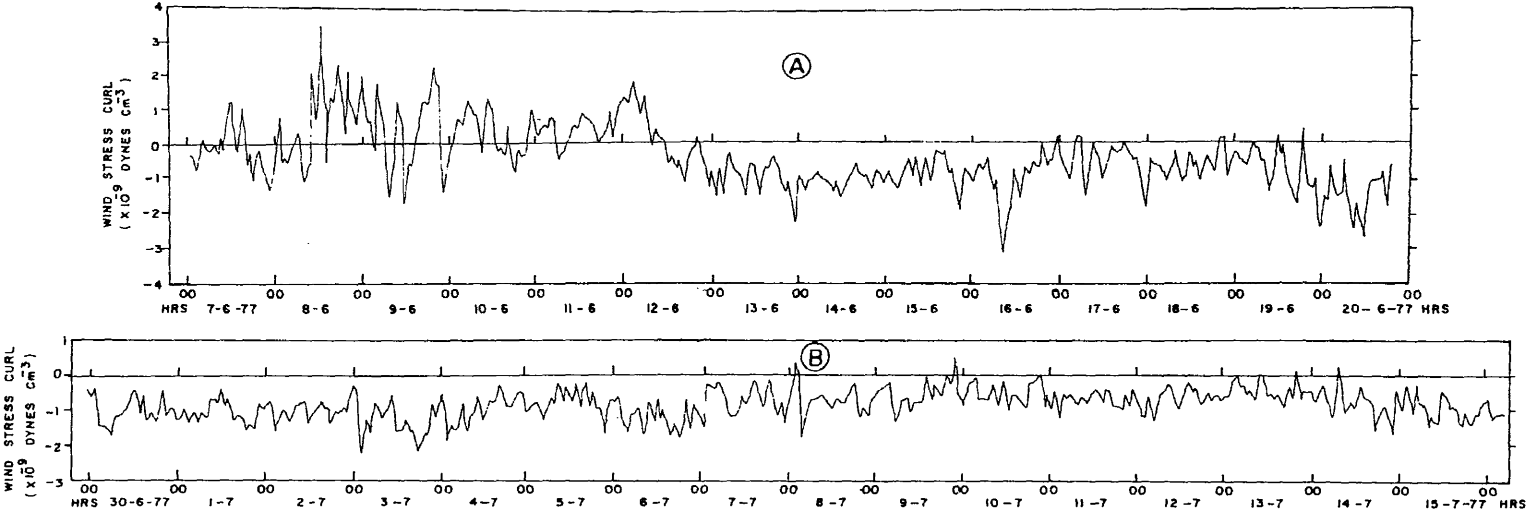

Figure 5. Wind stress curl in the area bounded by 10·5 to 14·5°N lat. and 64 to 68°E long. of the east central Arabian Sea during 7–20 June, 1977 (**a**) and 30 June–15 July 1977 (**b**) (after Ramesh Babu and Sastry 1984).

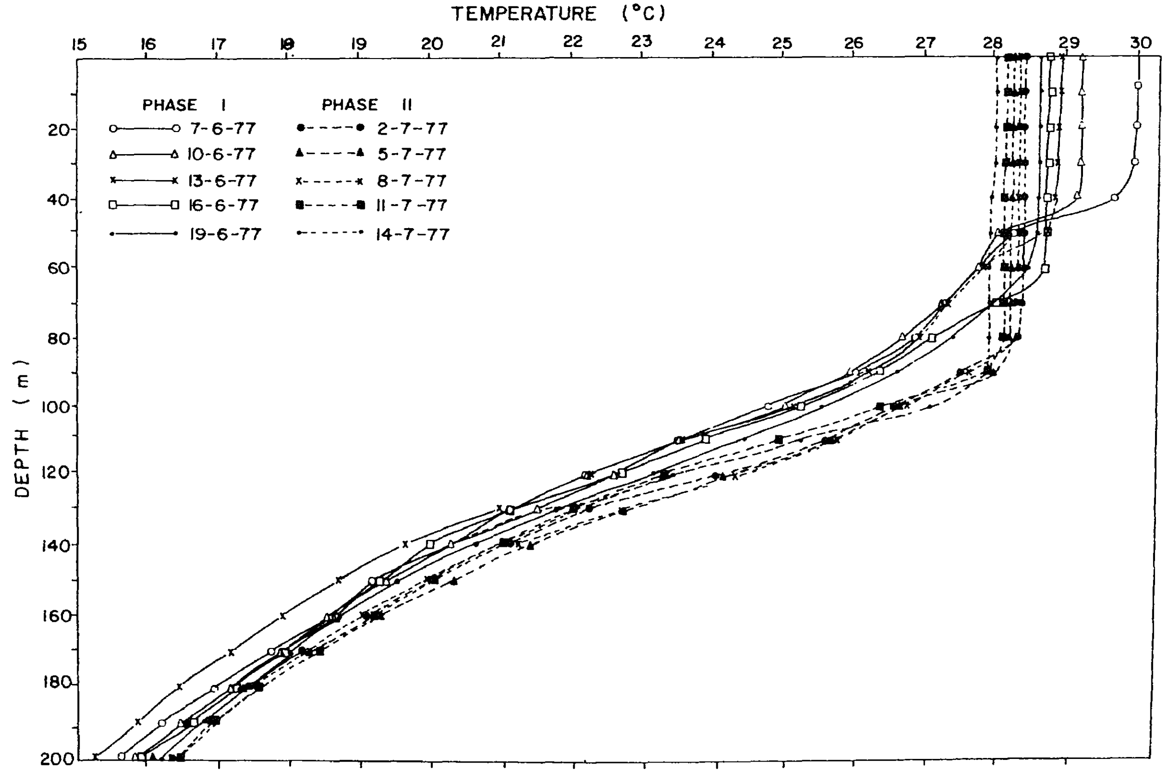

Figure 6. Evolution of thermal structure in the east central Arabian Sea (at 12·5°N & 68°E) in relation to the summer monsoon, 1977 (after Ramesh Babu and Sastry 1984).

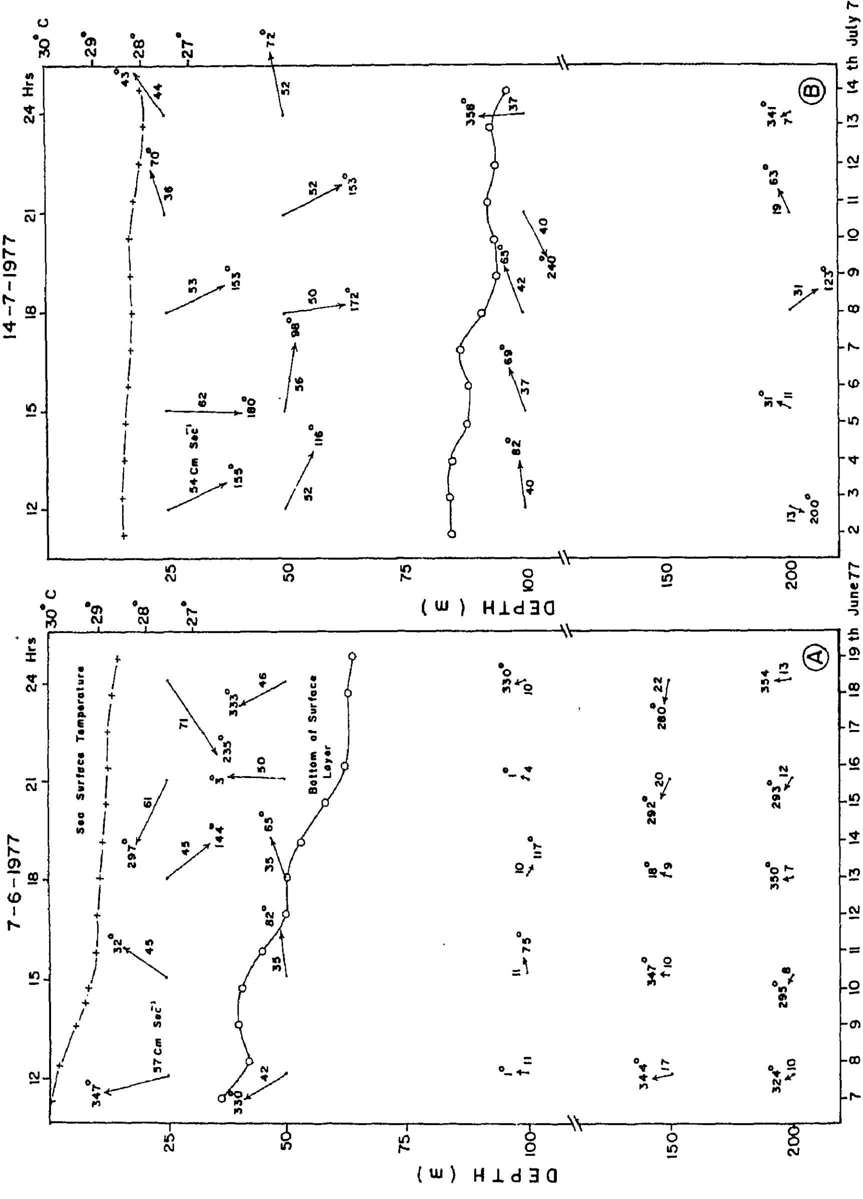

Spot current vectors at 25, 50, 100, 150 & 200 m depths on 7.6.1977 prior to the onset of monsoon at 12·5°N and 68°E (upper abscissa scale). Daily variation of id depth of bottom of surface layer (O—O—O) during 7 to 19 June, 1977 (lower abscissa scale). (**b**) Spot current vectors at 25, 50, 100 & 200 m depths on the onset of monsoon at 12·5°N and 64°E (upper abscissa scale). Daily variation of SST (+ + +) and depth of bottom of surface (O—O—O) during 2 to 14 July, scissa scale). The numbers at arrows in both (**a**) and (**b**) represent the magnitude (cm/sec) and direction (degrees true north) of the spot currents (after Ramesh

Table 1. Estimation of heat energy lost during 15–17 June, 1979

Total energy lost in the surface layer (40 m thickness)	$Q_T = 4370$ Cal.
Energy lost by evaporation	$Q_e = 1420$ Cal.
Energy lost by sensible heat	$Q_s = 270$ Cal.
Energy lost by effective back radiation	$Q_b = 129$ Cal.
Total energy lost across the sea surface $(Q_e + Q_s + Q_b)$	$Q_A = 1819$ Cal.
Energy lost from surface layer due to interior oceanic processes (predominant downward flux)	$Q_T - Q_A = 2551$ Cal.

(After Murty *et al* 1983)

s not well defined. After the cyclone has passed over the area and after the on has stabilised, a well defined surface layer forms. Near the coast, the surface ; 50 m thick and the thickness of surface layer is 70 m at about 150 km farther 'his is the result of the development of the slope of the thermocline associated ie southerly flow.

rate of evaporation over the east central Arabian Sea during 8–15 June 1979 has ed to 0·5 cm day^{-1} till the area came under the influence of the cyclone and later a ncrease in the rate of evaporation exceeding 1 cm day^{-1} is seen (Murty *et al* The total heat losses due to evaporation, back radiation and sensible heat r during 15–17 June, 1979 have been computed. A balance was sought between al surface heat losses and the change in the heat storage in the surface layer. The heat losses accounted for only about 40 % of the total heat loss in the surface 'he balance is the amount of heat lost to the interior of the ocean due to mixing the thermocline (table 1).

nclusion

trainment of cold waters into the surface layer and the subsequent turbulent play a dominant role in decreasing the SST in the east central Arabian Sea. In the ı Arabian Sea upwelling and spreading of cold upwelled waters off Somalia and are the major processes for lowering the SST.

Persian Gulf water, which is warmer and saltier due to high evaporation, ıtes into the Arabian Sea at depths of 200–300 m where its heat is given to the ıment. Similarly the Red Sea water penetrates at depths of 600–800 m. Their ıtion to the overall heat budget of the Arabian Sea needs to be studied. A survey ıe Arabian Sea with four or five research aircrafts equipped with dropsondes, ıe expendable bathythermographs and velocity profiling systems together with a earch ships occupying fixed positions would be extremely useful.

References

Bruce J G 1968 *Deep-Sea Res.* 5 665

Bruce J G 1981 Variations in the thermal structure and wind field occurring in the western Indian Ocean during monsoons, Naval Oceanographic Office Tech. Rep. No. 272, Dept. of Navy, NSTL Station, St. Louis

Cox M D 1970 *Deep-Sea Res.* **17** 47

Deutsches Hydrographisches Institut 1960 Monatskarten für den Indischen Ozean Publ. No. 2422, Hamburg

Düing W 1970 *The monsoon regime of the currents in the Indian Ocean* (Honolulu: East-West Centre Press)

Koninklijk Nederlands Meteorologisch Instituut 1952 Indische Ocean oceanografische en meteorologische gegevens, 2nd Ed., Publ. No. 135, De Bilt.

Krishnamurti T N, Ardanuy P, Ramanathan Y and Pasch R 1981 *Mon. Weather Rev.* **109** 344

Murty V S N, Rao D P and Sastry J S 1983 *Mahasagar—Bull. natn. Inst. Oceanogr. India.*, **16** 67

Ramesh Babu V and Sastry J S 1984 *Mausam* **35** 17

Robinson M K, Bauer R A and Schroeder E H 1979 Atlas of North Atlantic-Indian Ocean monthly mean temperatures and mean salinities of the surface layer, Naval Oceanographic Office Rep. Pub. 18, Dept. of Navy, Washington.

Sastry J S and D'souza R S 1971 *Indian J. Meteorol. Geophys.* **22** 23

Sastry J S and D'souza R S 1972 *Indian J. Mar. Sci.* **1** 17

Sastry J S and Ramesh Babu V 1979 *Mahasagar—Bull. natn. Inst. Oceanogr. India* **12** 201

Proc. Indian Acad. Sci. (Earth Planet. Sci.), Vol. 94, No. 2, July 1985, pp. 129–137.
© Printed in India.

Monthly-mean wind stress along the coast of the north Indian Ocean

SATISH R SHETYE, S SATHEESH CHANDRA SHENOI, M K ANTONY and V KRISHNA KUMAR

National Institute of Oceanography, Dona Paula, Goa 403 004, India

MS received 17 April 1985

Abstract. Monthly-mean wind stress and its longshore and offshore components have been computed using the bulk aerodynamic method for each of a string of 36 two-degree-latitude by two-degree-longitude squares along the coast of the north Indian Ocean. The data source for the computation is the sixty-year mean resultant winds of Hastenrath and Lamb. The main features exhibited by the components, taking the longshore components as positive (negative) when the Ekman transport is away from (towards) the coast, are: (1) Along the coasts of Somalia and Arabia, the magnitude of the wind stress is among the highest in the north Indian Ocean, and its direction is generally parallel to the coastline. This results in a longshore component which is large (as high as 2·5 dyne/cm^2) and positive during the southwest monsoon, and weaker (less than 0·6 dyne/cm^2) and negative during the northeast monsoon. (2) Though weak (less than 0·2 dyne/cm^2) during the northeast monsoon, the monthly-mean longshore component along the west coast of India remains positive throughout the year. The magnitude of the offshore component during the southwest monsoon is much larger than that of the longshore component. (3) The behaviour of the wind stress components along the east coast of India is similar to that along the Somalia-Arabia coast, but the magnitudes are much smaller.

Keywords. North Indian Ocean; coastal circulation; wind stress; upwelling; Ekman transport.

1. Introduction

Oceanographic studies in the coastal regions of the world have identified the stress exerted on the ocean surface by the local winds as one of the main forcing functions influencing the coastal processes. The importance of these winds in controlling the coastal dynamics was first brought out by the studies of Ekman (1905), Thorade (1909), and their contemporaries during the early part of this century. The present ideas on local wind-driven coastal currents have been summarized in Csanady (1982) among other references.

The north Indian Ocean is one of the very few oceanic regimes which come under the influence of the monsoons, and hence experiences a wind field which is very energetic at times and which possesses a well marked annual cycle. What controls the coastal processes in this ocean? An essential component of the answer to this many faceted question is the knowledge of the stress exerted by the winds in the vicinity of the coastline. With this consideration in mind, we have computed the montly-mean wind base and the method followed for computing the wind stress. The main features stress field and its longshore and offshore components are presented in §3.

2. Data source and method of computation

Hasternrath and Lamb (1978) give sixty-year (1911–1970) monthly mean clima circulation over the Indian Ocean. Charts 14–25 in their atlas give the resultant w a 1°-latitude by 1°-longitude grid. These form the basic data for our computatio determine the pattern of the coastal wind stress field we chose a string of 36 sq each 2°-latitude by 2°-longitude, along the coast of the north Indian Ocean. W refer to each of these squares as a TDS, meaning a two-degree-square. Wind stre been computed for each TDS for each month of the year.

To understand the influence of wind stress on coastal processes, it is conveni express the stress in terms of the longshore and the offshore component. For com these, the orientation of the coastline needs to be defined. As the scale of resoluti determining the wind stress has been chosen to be (2° × 2°), it may suffice to dete the mean orientation of the coastline for each TDS. There is, however, some ambig defining the orientation of a coastline. It could be defined as a line where the depth approaches zero, or as the line of the continental shelf break. The influence bottom topography on shelf circulation is not known in detail sufficient to between either of these two possibilities. Along the coast of India the shelf break approximately at the 200 m isobath. On moving offshore from this isobath the increases rapidly from 200 m to more than 2000 m. In the present discussion w the 200 m isobath as the indicator of the "coastline". Fortunately, the subjectivity choice of the coastline orientation is not a source of serious discrepancy; at least, a large fraction of the coastline. This is because the 200 m isobath runs more parallel to the zero-meter isobath along most of the coast. A notable exception region immediately to the south of Sourashtra. The configuration of the 36 TDS ha chosen such that, firstly, the 200 m isobath in the north Indian Ocean is adeq covered, and secondly, wind stress computed for each TDS is representative for a upto an offshore distance of an internal radius of deformation from the 200 m is To compute the longshore and the offshore component the 200 m isobath was ide by a straight line for each TDS. The 36 TDS and the idealised 200 m isobath are sho figure 1.

The stress field has been computed by using the well known bulk aerodyn formula

$$\tau = \rho_a C_D V^2.$$

τ is the magnitude of the wind stress (Newton/m^2), ρ_a is the density of (1·175 kg/m^3) and C_D is the dimensionless drag coefficient. The direction of th stress was taken to be the same as the direction of the monthly-mean resultant w a TDS. There has been extensive discussion on the choice of a value for C_D (s example, Bunker 1976). Suggested values range between a low of $0{\cdot}7 \times 10^{-3}$ f wind speeds and a high approaching 4×10^{-3} for high winds. Here we use a co value of $1{\cdot}3 \times 10^{-3}$ because it has been found appropriate in earlier investigati coastal regions (see, for example, Prell and Streeter (1982)). Figure 2 summari annual cycle of the computed stress field.

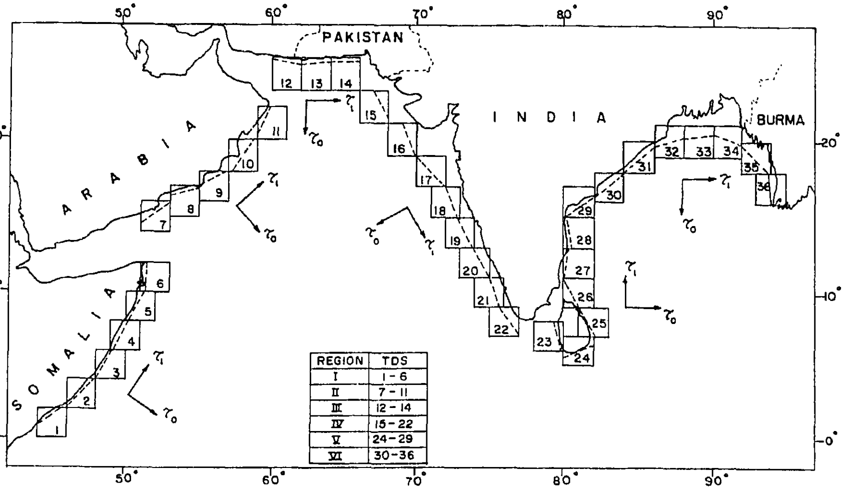

REGION	TDS
I	1 - 6
II	7 - 11
III	12 - 14
IV	15 - 22
V	24 - 29
VI	30 - 36

Figure 1. The region of interest. The dashed line shows the idealized geometry of the 200 m isobath. Each of the numbered squares is two-degree-latitude by two-degree-longitude. The grouping of the two-degree-squares, for plotting the longshore and the offshore component in figures 3 and 4, is as follows: the two-degree-squares 1–6, 7–11, 12–14, 15–22, 24–29, and 30–36 form regions I, II, III, IV, V and VI respectively. Approximate orientation of (τ_l, τ_o) frame for each region is also shown.

To compute the longshore (τ_l) and the offshore (τ_o) component, the stress vector for each TDS was decomposed along the tangent and the normal to the straight line idealizing the 200 m isobath for that TDS. The (τ_l, τ_o) reference frame was chosen such that for a positive longshore component the Ekman transport would be away from the coast. Once the direction of positive longshore component is defined, the cross-shore positive direction is fixed at right angle in the clockwise direction. To summarize the annual cycle of τ_l and of τ_o we divided the 36 TDS into regions I to V. Each region covers

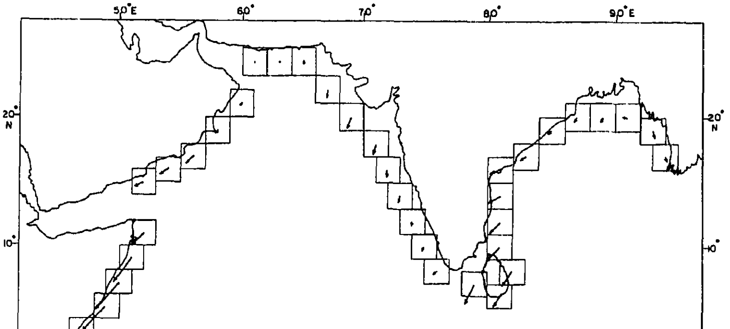

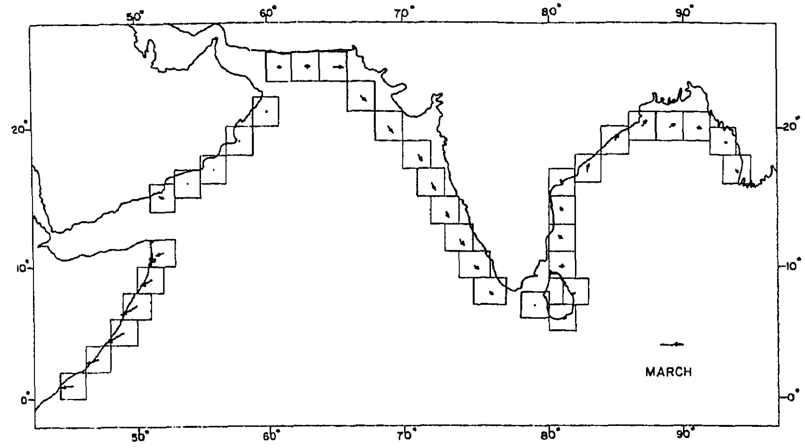
50°
60°
70°
80°
90°
20°
10°
0°
MARCH

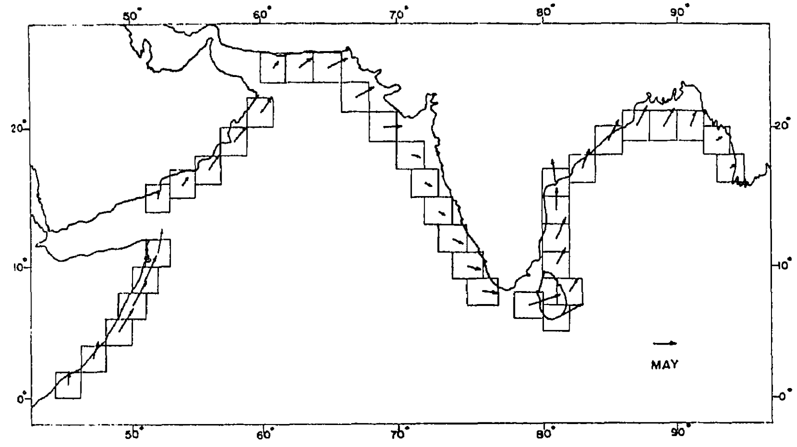
50°
60°
70°
80°
90°
20°
10°
0°
MAY

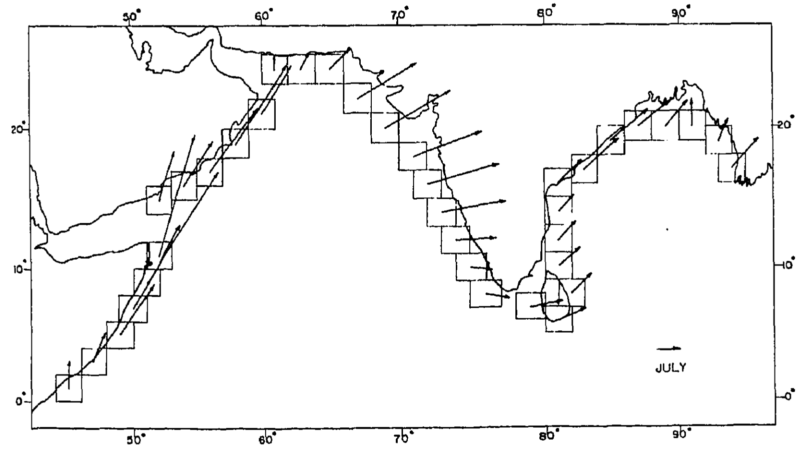
50°
60°
70°
80°
90°
20°
10°
0°
JULY

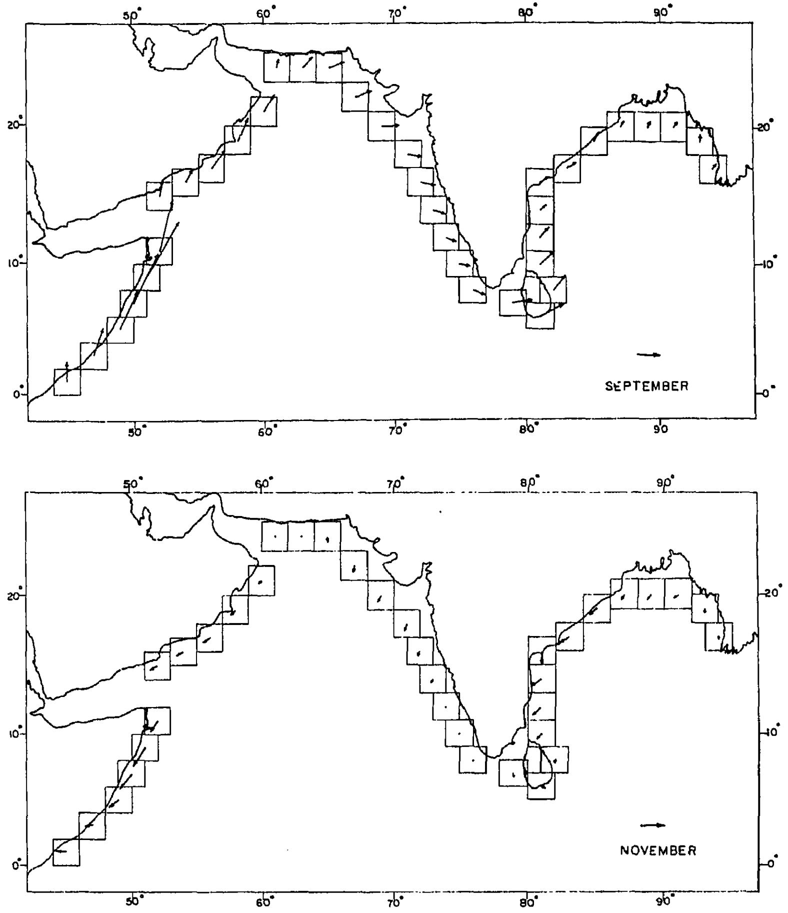

Figure 2. Monthly-mean wind stress for each two-degree square. The month is shown in the lower right hand corner. The magnitude of the arrow shown just above the month is 0·5 dyne/cm^2. The arrow for a two-degree-square has been drawn such that its origin is at the center of the square; the arrowhead points in the direction of the stress. Whenever the magnitude of the stress is equal to or less than 0·05 dyne/cm^2, only a dot has been shown at the center of the square.

an approximately straight portion of the coastline. The TDS belonging to each region are defined in figure 1. The annual cycle of τ_l and that of τ_o is summarized in figures 3 and 4 respectively.

3. Results and discussion

The winds over the north Indian Ocean are dominated by the monsoon circulation. During November through February the winds blow predominantly from the northeast; during May through September they blow from the southwest. Though these two are the mean directions for the two seasons for the monsoon area as a whole,

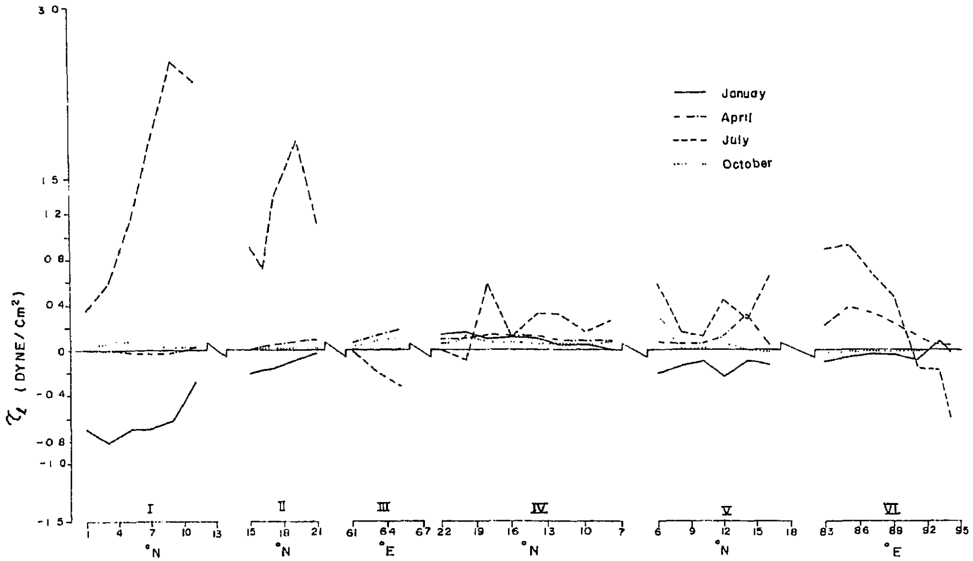

Figure 3. Spatial variation of the longshore component (τ_l) during January, April, July and October. The Roman numbers (I to VI) refer to regions defined in figure 1, which also shows the orientation of the (τ_l, τ_o) frame for each region.

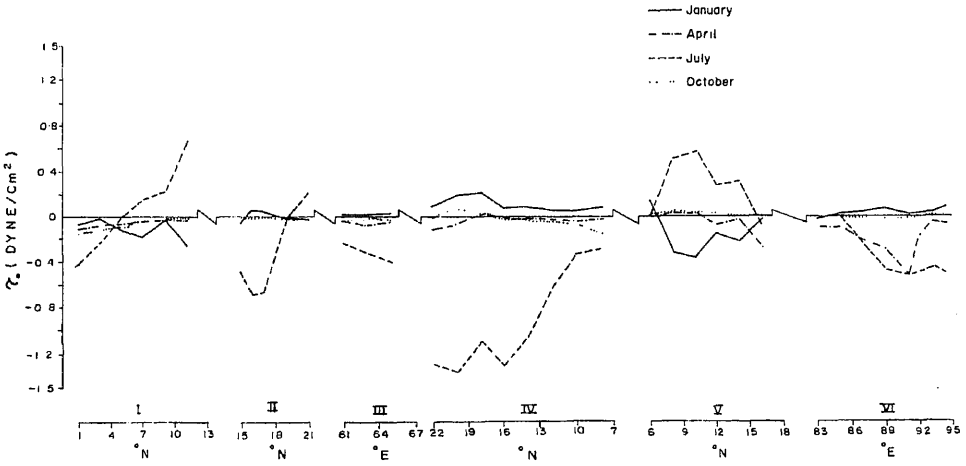

Figure 4. Spatial variation of the offshore component (τ_o) during January, April, July and October. See caption to figure 3 for other details.

significant variations in the orientation of the winds from these directions are seen from location to location. For example, over the southwest coast of India the winds during the southwest monsoon are more or less westerly. It is the combination of the local wind stress direction, and the orientation of the coastline, that determines the nature of variation of (τ_l, τ_o) along the coastline.

Winds off Somalia and Arabia are among the largest in the region of interest, and stay more or less parallel to the coastline throughout the year. As a result, the magnitude of

τ_l stays quite large in comparison to τ_o. τ_l is positive and reaches a peak (2·5 dyne/cm^2) at around 9 N in the month of July. Very high upwelling rates have been reported in this area during this month (see, Duing and Leetmaa 1980). During the northeast monsoon the longshore component off this coast is negative. However, its peak magnitude is almost one-fourth of the peak longshore component during the southwest monsoon.

The west coast of India poses a contrast to the Somalia-Arabia region. The longshore component along the west coast remains positive throughout the year. It reaches a peak (0·5 dyne/cm^2) around July; between November and February this component is quite weak (< 0·1 dyne/cm^2). Another interesting feature of this coast is that the magnitude of the offshore component is generally much larger than the longshore component. Along the east coast of India the longshore component reverses sign; it is positive during the southwest monsoon season and negative during northeast season. The temporal variability of the stress is similar to that along the Somalia and the Arabia coastline. However, the magnitude of the stress along the east coast of India is much smaller than that in the western Arabian sea.

The offshore Ekman transport due to local winds is given by

$$M_E = \tau_l / f,$$

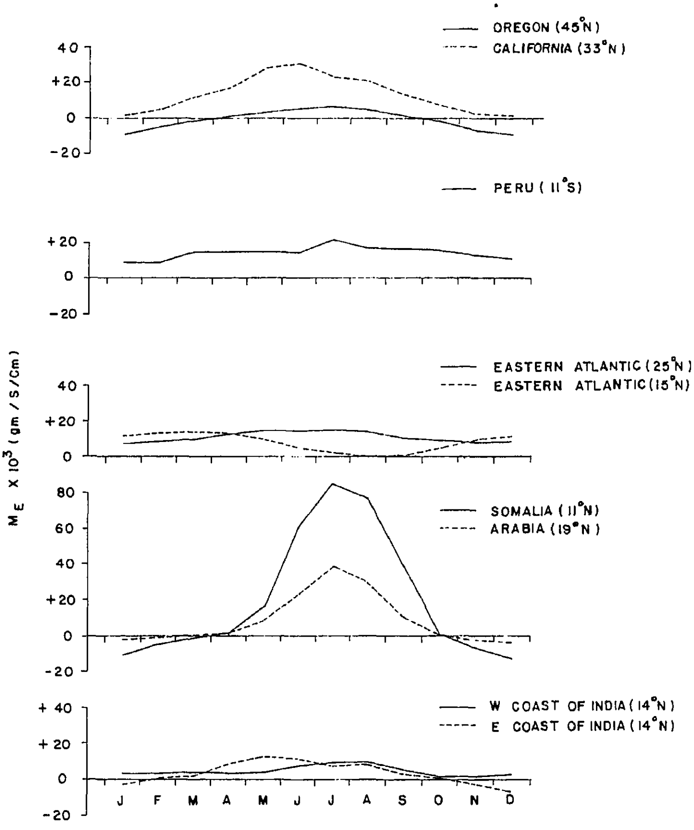

Figure 5. A comparison of the annual march of the offshore Ekman transport (M_E gm/s/cm)

where f is the Coriolis parameter. M_E is an indicator of the potential for upwelling in the coastal areas where the local winds form the dominant forcing function for the coastal processes (see Wooster and Reid 1963). It is of interest to compare the variation of M_E at a few locations in the north Indian Ocean with M_E at some of the better known upwelling centres of the world. This has been done in figure 5. The data for the coastal regions of California (33 N) and Oregon (45 N) are taken from Bakun (1973). Wyrtki and Meyers (1975) estimate of wind stress in the Pacific was used for computing the longshore component off Peru (10–12 S). The data for the eastern N. Atlantic are based on Wooster *et al* (1976). TDS 6 (10–12 N) and 10 (18–20 N) were used to represent the coast of Somalia and Arabia respectively. TDS 19 (13–15 N, west coast of India) and 28 (13–15 N, east coast of India) represent the west and the east coast of India. The drag coefficient C_D was put equal to $1{\cdot}3 \times 10^{-3}$ in all computations. As seen from figure 5, the monthly-mean wind stress in the coastal regions of California, Peru, eastern north Atlantic and the west coast of India is conducive to upwelling throughout the year. This is in contrast to the conditions off Oregon, Arabia, Somalia and the east coast of India, where the longshore component changes sign. At these locations, the winds are favourable to upwelling only between April and October. The amplitude of the annual cycle of the longshore component is larger off Oregon than that off the east coast of India. Coasts of California, Somalia and Arabia are conspicuous for the large longshore wind stress they experience.

To use M_E as an indicator of the potential for upwelling it must first be established that the local winds provide the dominant forcing for the coastal processes. There has been little discussion so far on the question of the dominant forcing functions for the circulation along the coast of the north Indian Ocean. A notable exception is the coast of Somalia (see for example, Lighthill 1969 and Anderson and Rowland 1976). In a forthcoming study we shall examine the extent to which the monthly-mean coastal circulation in the north Indian Ocean can be attributed to the wind stress field described in the present paper.

Acknowledgements

During the course of this study one of the authors (S. R. S) was supported by a N.I.O. Research Associateship. Director, N.I.O. made the necessary facilities available during the preparation of the study. This paper has benefitted from the comments of Drs. J S Sastry and C S Murty. Ravindranath Uchil drafted the figures.

References

Anderson D L T and Rowland P B 1976 *J. Mar. Res.* **34** 395

Bakun A 1973 NOAA Technical report NMFS SSRF-671, U.S. Department of commerce.

Bunker A F 1976 *Mon. Weather Rev.* **104** 1122

Csanady G T 1982 *Circulation in the coastal ocean.* (Dordrecht; D. Reidel)

Duing W and Leetmaa A 1980 *J. Phys. Oceanogr.* **10** 307

Ekman V 1905 *Ark. f. Mat. Antr. Och. Fysik. k. Sv. Vet. Ak., Stockholm*, 2

Hastenrath S and Lamb P J 1978 *Climatic atlas of the Indian Ocean, Part I: Surface Climate and Atmospheric Circulation.* (Madison; University of Winconsin Press.)

Lighthill M J 1969 *Philos. Trans. R. Soc. Lond.* **A265** 45

Prell W L and Streeter H F 1982 *J. Mar. Res.* **40** 143

Shetye S, Shenoi S S C, Antony M K and Kumar V K 1984 Technical Report, National Institute of Oceanography, Goa.

Thorade H 1909 *Aun. d. Hydrogr. U. Mar. Meteor.* 37 17

Wooster W S and Reid J L 1963 *The Sea* (ed) M N Hill (New York: Interscience) Vol 2 p. 253

Wooster W S, Bakun A and McLain D 1976 *J. Mar. Res.* **34** 131

Wyrtki K and Meyers G 1975 Technical Report, Hawaii Institute of Geophysics.

Global temperature changes: relative importance of greenhouse constituents of the atmosphere as calculated with a 1-d radiative–convective model

M LAL and K C S RAO

Centre for Atmospheric Sciences, Indian Institute of Technology, Hauz Khas, New Delhi 110016, India

MS received 11 April 1984; revised 9 November 1984

Abstract. Most modelling endeavours concerning the CO_2-climate problem address only the question of the climatic response to increasing atmospheric carbon dioxide, while the amounts of other atmospheric gases remain fixed. But associated changes, either climatologically or anthropogenically induced, of minor atmospheric constituents can also be of significance in producing a substantial global warming. We have analysed the climatic response to changes in a number of atmospheric trace gases as they may enhance or counteract CO_2-induced warming if their abundance should change. A comparison of the increase in equilibrium global-mean surface temperature due to plausible changes in the concentration of several trace gases in the atmosphere based on our calculations with a one-dimensional radiative–convective model is presented in this paper. Our results indicate that roughly 35 % of global surface warming could be due to changes in trace gases other than CO_2 and water vapour. The possible climatic consequences of the ongoing anthropogenic changes in the minor constituents of the atmosphere are also discussed.

Keywords. Global temperature changes; atmospheric carbon dioxide; trace gases; 1-d radiative–convective model; anthropogenic changes.

1. Introduction

One of the basic processes for determining the influence of radiation factors on climate is the greenhouse effect of the atmosphere. It is well recognised that the thermal structure of the earth's atmosphere is affected by the presence of water vapour and carbon dioxide. The main radiative effect of atmospheric carbon dioxide is through absorption of upward infrared radiation and re-radiation at the local temperature; this blanketing leads to an increase in surface temperature, the so-called greenhouse effect. The atmosphere also contains a large number of minor trace gases which can have a significant effect on the atmosphere's thermal structure because they have strong absorption bands within the 7–14 μm atmospheric window. The concentrations of atmospheric trace gases such as nitrous oxide, methane, ammonia and freons etc., have undergone substantial changes during the last few decades under the influence of anthropogenic effects e.g., intensive use of organic fertilizers, fuel burning etc. As such, the prevailing hypothesis that the origin of current and possibly future climatic changes can be attributed exclusively to variations in carbon dioxide content of the atmosphere is a simplification of reality.

To gain some perspective on the greenhouse effect of a selected list of minor trace gases together with that of atmospheric carbon dioxide and water vapour, we have calculated the changes in radiative heating of the earth-troposphere system and surface with a few modifications: (i) the model's boundary layer thickness is changed to 100 m from its original value of 40 m to account for vertical mixing and surface exchange processes more effectively; (ii) our model has a moist adiabatic lapse rate in the convective region rather than a fixed lapse rate. As shown elsewhere (Lal and Ramanathan 1984), this causes the equilibrium surface temperature to be less sensitive to radiative perturbations and both surface and tropospheric warmings due to the greenhouse effect are better resolved; (iii) the radiative treatment of various minor gases have also been included in the model. Although the model excludes horizontal transports and a number of other mechanisms, it serves as a convenient tool for comparing the relative importance of different radiative perturbations and provides a first order estimate of the assumed perturbation on globally-averaged thermal structure.

Our primary objective in this study is to compare the relative contribution to global surface warmings of several atmospheric trace constituents in a coherant manner and elucidate their role in climatic changes.

2. The Model

The model used here in its simplest form is a variant of the fixed relative-humidity, one-dimensional radiative–convective model of Ramanathan (1981). It represents the global and annual mean thermal structure of the atmosphere at equilibrium. For an assumed initial atmospheric composition, global mean surface albedo and initial global mean vertical distributions of temperature and clouds, the solar and thermal flux divergences averaged over clear and cloudy fractions are computed at 16 unequally-spaced altitudes covering the lowest 54 kms of atmosphere. The model has a boundary layer whose thickness is taken to be 100 m and all of the boundary layer variables are defined at the layer mid-point. The ocean has two layers and the uppermost oceanic mixed layer (50 m) exchanges energy with the atmosphere through the diffusion process. It is assumed that at the lower boundary of the ocean (500 m) no heat flux exists. The model atmosphere has four diabatic heating processes, viz., solar radiation, longwave radiation, vertical eddy heat flux and latent heat flux, of which the vertical eddy heat flux vanishes, in general, above the first model layer. The troposphere is coupled to the surface through exchange of latent, sensible and radiative heat fluxes between the surface and the boundary layer. As explained in Ramanathan (1981), the model explicitly computes the boundary layer relative humidity (RH_s) and the latent heat release within the atmosphere such that the H_2O balance equations are satisfied. The tropospheric relative humidity (RH_z) is computed using the relative humidity distribution function of Manabe and Wetherald (1967):

$$(RH_z) = RH_s[(p/p_s) - 0.02]$$

where p and p_s are the atmospheric and surface pressures respectively. The typical vertical distribution of relative humidity given by this linear function is in good agreement with the hemispheric mean of relative humidity obtained by Telegadas and London (1954), Murgatroyd (1960) and Mastenbrook (1963). The model employs the moist adiabatic adjustment scheme wherein the critical lapse rate within each model layer is assumed to be the moist adiabatic lapse rate appropriate for the layer pressure and temperature. The effect of clouds is incorporated by adopting the equivalent single cloud model of Cess (1974). This equivalent single cloud represents a global average over many cloud layers. Adopting the three-layer cloud model of Manabe and Strickler (1964), and performing the averaging procedure suggested by Cess (1974), the three-level clouds are replaced by a single cloud with cloud top altitude of 6·25 km and a fractional cloud cover of 0·45.

The radiation model is similar to that described in Ramanathan and Dickinson (1979) with the following modifications: (i) inclusion of radiative effect of trace gases considered in the study, and (*ii*) use of pressure as a vertical coordinate so as to conserve mass automatically. The model includes radiative transfer processes such as pressure and doppler broadening, H_2O continuum, hot and minor isotopic bands of CO_2 and overlap of H_2O continuum and rotation bands with CO_2 and O_3 bands. The model computes radiational cooling/heating due to H_2O, CO_2, O_3 and other optically active gases. The atmospheric distributions of carbon dioxide, ozone and other minor gases prescribed in the model are given in table 1. The trace constituents N_2O, CH_4, NH_3, CF_2Cl_2 and CH_3Cl are assumed to be uniformly mixed with their respective abundances from ground to an altitude of 10 km, while the constituents C_2H_4 and SO_2 are assumed to be uniformly mixed from ground to an altitude of only 2 km. Above these altitudes, the relative abundance of each of these trace gases decreases exponentially to a further 2 km height. These concentrations have been compiled from a variety of sources including observations and photo-chemical model results.

3. Experiments on greenhouse effect of anthropogenic gases

In our one-dimensional radiative–convective model, the atmosphere is allowed to attain radiative–convective equilibrium thermal structure for an initially prescribed global atmospheric composition. We first obtain a vertical steady-state temperature profile for the atmosphere containing the trace constituents with their present-day concentrations as listed in table 1. Next, the concentration of one of the trace constituents is varied at a time from its present value to a two-fold increase and a new

Table 1. Concentrations of various atmospheric trace constituents prescribed in the model

Constituent		Approximate present-day concentration	
CO_2	abundance	330	ppm V
N_2O	abundance	0·28	ppm V
CH_4	abundance	1·60	ppm V
NH_3	abundance	6×10^{-3}	ppm V
CF_2Cl_2	abundance	1×10^{-4}	ppm V
CH_3Cl	abundance	5×10^{-4}	ppm V
SO_2	abundance	2×10^{-3}	ppm V
C_2H_4	abundance	2×10^{-4}	ppm V
O_3	column amount	3·43	mm STP
NO_2	column amount	2×10^{-3}	mm STP
HNO_3	column amount	$4{\cdot}87 \times 10^{-3}$	mm STP

vertical temperature profile is computed. We thus obtain the model computed changes in atmospheric thermal structure for perturbations in each of the atmospheric constituents.

Table 2 summarizes the surface temperature change due to doubling of the concentrations of each of the twelve atmospheric trace gases considered in the present study. Here, the doubling of the water vapour content is considered above 10 km. Below this the H_2O content is determined by the condition of fixed relative humidity. Our estimates of global surface warming for a two-fold increase in the trace gases suggest that the minor atmospheric constituents may have a significant effect on the earth's climate. The surface warming due to doubling of CO_2 in the atmosphere is about 39% of the surface warming due to the combined effect of CO_2 and other trace gases considered here. The surface warming due to doubling of water vapour concentration in the upper atmosphere is comparable to that due to the combined effect of other trace gases examined in this study excluding only the effects of CO_2 and O_3. The doubling of atmospheric ozone warms the earth's surface by 0·67°K which is about 15% of the total surface warming due to all trace constituents. The doubling of N_2O concentration in the atmosphere leads to an increase in the mean temperature of the earth's surface by 0·5°K, while the doubling of methane and ammonia concentrations brings about further temperature increases by 0·24 and 0·11°K respectively. The doubled concentration of freons (CF_2Cl_2) results in a further additive greenhouse effect of about 0·02°K.

Our calculations show further that the largest warming due to increase in atmospheric trace constituents occurs in the upper troposphere and not at the earth's surface. The moist adiabatic lapse rate formulation in our model produces CO_2-induced warming of about 1·8°K at the surface and over 3°K in the upper troposphere. The temperature response to other constituents also increases with height at roughly the same rate as that of CO_2 upto an altitude of about 8 km with a decreasing trend further upwards.

The above calculations are based on the assumption that the concentration of major

Table 2. Greenhouse effect due to doubling of various minor atmospheric constituents

Constituent	Surface warming, T_s (°K)
CO_2	1·78
H_2O	1·07
O_3	0·67
N_2O	0·51
CH_4	0·24
NH_3	0·11
HNO_3	0·07
NO_2	0·03
CF_2Cl_2	0·02
CH_3Cl	0·01
C_2H_4	0·01
SO_2	0·01

factors of the order of two and the validity of this assumption is discussed in the following section.

4. Scenario for future trends in concentration of atmospheric trace constituents

We are aware that a warming of the earth's surface by 1°K or more may significantly alter the global atmospheric circulation patterns which could result in a general poleward shift of agro-climatic zones (NAS 1977). Today, radiatively and chemically active trace gases are being injected into the atmosphere at an alarmingly increasing rate by human activities. This necessitates the quantitative estimation of the increase in earth's mean surface temperature (greenhouse effect) due to perturbations in atmospheric constituents. Our results (described in the previous section) indicate that the anthropogenic perturbations of the atmospheric gaseous composition are likely to eventually warm the earth–atmosphere system. However, these estimates may be subject to a large range of uncertainties arising due to possible errors in estimates for natural sources and sinks for the trace gases and, further, due to the errors in projected future increase in their emission rates. Thus, in our attempts to predict the greenhouse effect of trace constituents on climate, the factors influencing the abundance of these trace gases should be properly understood.

Water vapour plays a predominent role in modulating atmospheric and surface temperatures and our results indicate that a substantial greenhouse effect results from doubling of stratospheric water vapour content. There is no justification to support the assumption of a fixed relative humidity condition for the stratosphere. The stratospheric water vapour abundance is largely controlled by towering cumulus clouds, major volcanic eruptions, fleets of supersonic aircraft and many other factors which make it difficult to precisely project the long-term potential variation of water vapour abundance in the stratosphere.

The upward trend of global atmospheric CO_2 as a result of ever-increasing use of fossil fuels has been well-documented and projections of a global increase of the order of 100% by the year 2050 are probably reliable (WMO 1975). Beyond 2100, a peak atmospheric CO_2 concentrations might reach 4 to 8 times the preindustrial level (NAS 1977). Thus, the atmospheric CO_2 is likely to play a major role in future trends of the earth's radiation budget.

Recent studies (Fishman and Crutzen 1978) indicate that an appreciable fraction of tropospheric ozone is produced by photochemical oxidation of CO, CH_4 and other hydrocarbons in the presence of nitric oxide. These species have both biogenic and anthropogenic origin and, in addition, are synthesized within the troposphere by chemical processes. As pointed out by Ramanathan *et al* (1979), although the troposphere contains only 10% of the total atmospheric ozone, the IR opacity of tropospheric ozone is nearly the same as that of stratospheric ozone due to pressure broadening of the 9·6 μm band. Photochemical modelling studies of Logan *et al* (1978), Fishman *et al* (1979) and Hameed *et al* (1980) estimate that if the present growth rate of emission of various hydrocarbons is continued into the next century, the tropospheric ozone may double its present value.

The extensive use of nitrogen fertilizers provides the primary mechanism for the perturbation in atmospheric N_2O concentration. A large range of predictions of chemical modellers suggests that the atmospheric N_2O concentration may increase by as much as a factor of two by the year 2020. Probably the source of NH_3 would scale with that of N_2O and hence we would anticipate a potential increase in NH_3 of the same magnitude as that for N_2O.

The atmospheric concentrations of CH_4, C_2H_4 and CH_3Cl have increased in recent decades as a result of increased anaerobic decay processes and the decay of marine biological organisms. An increase in atmospheric HNO_3 is unavoidable due to the speedup of the nitrogen cycle. Combustion together with oxidation processes is responsible for the buildup of SO_2 in the atmosphere. The future projections of these gases in the atmosphere are difficult to assess and for our study here we have assumed that these gases are potentially variable by factors of the order of two.

The freons (CF_2Cl_2) seems to have a considerable influence on the infrared transparency of the atmosphere (Ramanathan 1975). The atmospheric concentrations of freons may increase by as much as 20 to 30 times if the present level of injection into the atmosphere is maintained (Molina and Rowland 1974). The primary reason for this expected buildup seems to be the lack of any significant tropospheric removal mechanism. The freons have a characteristic lifetime in the atmosphere of the order of 10 years. The changes in the greenhouse effect caused by freons may therefore influence the earth's climate more notably than those due to other trace constituents.

The above discussions highlight the need for accurate monitoring of the global trends in the concentration of atmospheric trace gases in any attempt to understand and predict man's impact on climate through the greenhouse effect. In this study, we have excluded the potential counter-role of aerosols which is important for a reliable climate prognostication.

5. Conclusions

This paper mainly presents the changes in the surface temperature of the earth for large assumed increases in the atmospheric trace gases. Though the surface warming due to abundance of a particular constituent may appear negligible, the combined greenhouse effect of minor atmospheric constituents is mostly additive and thus it may have a substantial effect on the earth's climate.

Since anthropogenic changes in the composition of the atmosphere are several, their influence on the greenhouse effect and climate must take into account all vital constituents and in this respect, our findings in table 2 may serve as a reference. The global trend of atmospheric trace constituents may undergo substantial non-linear changes in abundance. This necessitates a detailed study of the prediction of atmospheric chemical evolution. For more realistic appraisal of future climatic impact of atmospheric trace gases, account must be taken of the atmospheric dynamics and interaction of continuous changes in the composition of the atmosphere.

Acknowledgements

The authors are indebted to Dr V Ramanathan for providing his model and educating us on various aspects of this study. The computer facilities provided by the National Informatics Centre, New Delhi, are gratefully acknowledged.

References

Cess R D 1974 *J. Quant. Spectrosc. Radiat. Transfer* **14** 861

Fishman J and Crutzen P J 1978 *Nature* **274** 855

Fishman J, Ramanathan V, Crutzen P J and Liu S C 1979 *Nature* (*London*) **282** 818

Hameed S, Cess R D and Hogan J S 1980 *J. Geophys. Res.* **85** 7537

Lal M and Ramanathan V 1984 *J. Atmos. Sci.* **41** 2238

Logan J A, Prather M J, Wofsy S C and McElroy M B 1978 *Trans. R. Soc.* **290** 187

Manabe S and Strickler R F 1964 *J. Atmos. Sci.* **21** 361

Manabe S and Wetherald R T 1967 *J. Atmos. Sci.* **24** 241

Mastenbrook H J 1963 *Humidity and moisture* (New York: Reinhold) Vol. 2, p. 480

Molina M J and Rowland F S 1974 *Nature* (*London*) **249** 810

Murgatroyd R J 1960 *Proc. Symp. Atmos. Ozone, Oxford July* 1959 IUGG Monograph No. 3, (Paris: IUGG Publications Office) p. 30

NAS 1977 *Energy and climate*, (Washington, DC: National Academy of Sciences)

Ramanathan V 1975 *Science* **190** 50

Ramanathan V and Dickinson R E 1979 *J. Atmos. Sci.* **36** 1084

Ramanathan V 1981 *J. Atmos. Sci* **38** 918

Telegadas K and London J 1954 Sci. Rep. No. 1, Contract AF 19(122)-165, Res. Div., College of Engg., New York Univ., 52 pp.

WMO (World Meteorological Organisation) 1975 GARP Pub. 16, Geneva, Switzerland

Interaction of monsoon with northern hemisphere mid-latitude circulation

S T AWADE, M Y TOTAGI and S M BAWISKAR
Indian Institute of Tropical Meteorology, Pune 411 005, India

MS received 24 November 1983; revised 17 April 1985

Abstract. Fourier analysis has been used for the monthly mean northern hemispheric geopotential height for the levels 700 mb and 300 mb for the months April through August in bad monsoon years (1972, 74 and 79) and in years of good monsoon rainfall over India (1967, 73, 77). From the Fourier coefficients the transport of momentum and of sensible heat have been computed in wave number domain.

Waves 1 to 3 show contrasting features during years of good monsoon and bad monsoon. Northward transport of momentum across subtropical latitudes is larger in good monsoon years, while northward transport of sensible heat is larger in bad monsoon years. In good monsoon years there is a large divergence of momentum in the subtropics while there is a large convergence of momentum in the mid-latitudes. In bad monsoon years there is a large divergence of sensible heat in the sub-tropics, but a large convergence in the mid-latitudes.

These quantities show similar features in pre-monsoon (April to May) during good and bad monsoon years.

Keywords. Fourier analysis; mid-latitude circulation; sensible heat; momentum transport.

1. Introduction

Indian summer monsoon is a component of the planetary scale monsoon during the northern hemispheric summer season, and planetary scale monsoon is brought about and maintained by the redistribution of heat sources and sinks in which the differential heating between continents and oceans plays a dominant role. The purpose of this paper is to study the effect of mid-latitude and extra tropical circulation on the activity of the monsoon. This has been qualitatively studied earlier by a few workers (Ramaswamy 1958, 1962; Pisharoty and Desai 1956; Pisharoty and Asnani 1958; Ramamurthy 1969; Raman and Rao 1981).

Here we have computed the transport of momentum and of sensible heat in the years of good and bad summer monsoon in India in order to understand the anomalies in the monsoon activity in terms of global circulation of the atmosphere.

2. Data and method of analysis

Monthly mean northern hemispheric geopotential height data for the levels 700 mb and 300 mb at 5° lat/long intervals collected from hemispheric charts prepared by Free University of Berlin and Hydrometeorological service of USSR for the years 1967, 72, 73, 74, 77 and 79 for the months April through August have been subjected to Fourier analysis.

We have followed the standard definition of good and bad monsoon years as ractised by the India Meteorological Department. Of these 1967, 73 and 77 orrespond to good monsoon conditions over India. The years 1972, 74 and 79 orrespond to bad monsoon years. Monsoon performance in these years is given in able 1.

Using Fourier analysis, we have for height, z

$$z(\lambda) = \sum_{m=0}^{\infty} (a_m(\phi)\cos m\lambda + b_m(\phi)\sin m\lambda) \tag{1}$$

The amplitude R_m and phase ε_m of the mth wave are given by

$$R_m = (a_m^2 + b_m^2)^{1/2},\ \varepsilon_m = (1/m)\arctan(b_m/a_m) \tag{2}$$

Using geostrophic approximation for winds, we obtain the flux of angular momentum across a latitude circle by standing eddies (Lorenz 1966; Awade 1979; Awade *et al* 1981) which is given by

$$(2\pi a^2 \cos^2\phi/g)\int_{p_1}^{p_2} [\bar{U}^*\bar{V}^*]\mathrm{d}p \tag{3}$$

where,

$$[\bar{U}^*\bar{V}^*] = -(g^2/4\Omega^2 a^2 \sin^2\phi\cos\phi)\left[\frac{\partial\bar{z}^*}{\partial\lambda}\frac{\partial\bar{z}^*}{\partial\phi}\right] \tag{4}$$

$$\approx (g^2/4\Omega^2 a^2 \sin^2\phi\cos\phi)\sum_{m=1}^{16}\frac{1}{2}m^2 R_m^2\frac{\partial\varepsilon_m}{\partial\phi} \tag{5}$$

The flux of sensible heat across a latitude circle due to standing eddies is given by (Lorenz 1966),

$$(2\pi a\cos\phi/g)\int_{p_1}^{p_2} C_p[\bar{V}^*\bar{T}^*]\,\mathrm{d}p \tag{6}$$

where,

$$[\bar{V}^*\bar{T}^*] = -(g^2 p/2\Omega a R\sin\phi\cos\phi)\left[\frac{\partial\bar{z}^*}{\partial\lambda}\frac{\partial\bar{z}^*}{\partial p}\right] \tag{7}$$

$$\approx (g^2 p/2\Omega a R\sin\phi\cos\phi)\sum_{m=1}^{16}\frac{1}{2}m^2 R_m^2\frac{\partial\varepsilon_m}{\partial p}. \tag{8}$$

Here, the symbols [ ], * and – indicate the average over a latitude circle, deviation from

Table 1. Monsoon performance

Year	1967	1972	1973	1974	1977	1979
Percentage departure of rainfall from normal (June–September)	−0·3	−24·3	4·6	−12·2	4·9	−16·0

average over latitude circle and monthly time average respectively. Ω stands for the angular velocity of the earth and p_1 and p_2 are pressures at upper and lower levels respectively. Other symbols have their usual meaning.

3. Result and discussion

3.1 *Transport of momentum*

The transport of momentum was computed using (3) at 700 mb and 300 mb levels during pre-monsoon months (April and May) and monsoon months (June through August), hereafter, these will be referred to as A–M and J–A respectively.

In order to understand the broad features, we obtained the transport due to standing eddies contributed by long waves (waves 1 to 4), medium waves (waves 5 to 10) and short waves (waves 11 to 16) across the latitudes 20°N to 60°N. Table 2 gives the transport of momentum during A-M and J-A at 700 mb level. There is no contrast in both the periods at 700 mb level (table 2). Since the contrast is significant at 300 mb level during J-A, we consider this level in some detail. Table 3 gives the transport of momentum and of sensible heat during J-A contributed by long, medium and short waves and figure 1 shows the transport of momentum across 30°N at 300 mb level in wave number domain.

The contribution of momentum flux at 300 mb level during J-A by long waves between latitudes 20°N and 30°N is northward (table 3) and it is maximum across 30°N. It is larger in good monsoon years than in bad monsoon years at this latitude. At 60°N, the transport is southward. However, it is small. There is significant northward contribution by medium waves between latitudes 30°N and 50°N, but there is no contrast. The contribution by short waves is small. Long waves and indeed all waves show larger northward transport across 30°N in good monsoon years than in bad monsoon years.

Waves 1 and 3 are prominent across 30°N in all these years (figure 1). The transport by wave 3 across 30°N is larger and further northward in good monsoon years than in bad monsoon years. Wave 2 generally transports momentum southward. Waves 6 through 10 contribute to the northward transport in all these years.

3.2 *Meridional transport of sensible heat*

The transport of sensible heat computed across 20°N through 60°N using (6) at 500 mb level during monsoon months (June through August) for waves 1 to 16 for all these years are also given in table 3. Figure 2 depicts the vertical tilt for waves 1 and 2 during July and figure 3 gives the transport across 30°N at 500 mb level in the wave number domain. The transport of sensible heat during J-A by long waves across 20°N is southward in all these years (table 3). It is generally southward across 30°N in good monsoon and northward in bad monsoon. It is generally northward across 40°N (table 3) and variable across 50°N. At 60°N, the transport is northward. The transport due to medium waves is northward between latitudes 20°N and 60°N. The contribution by medium waves is significant in regions between latitudes 30°N and 40°N but there is no

Table 2. Meridional transport of momentum at 700 mb level during periods April to May and June through August by long, medium and short waves

Waves		Long (1 to 4)						Medium (5 to 10)						Short (11 to 16)					
Period	Lat.°N	Good monsoon years			Bad monsoon years			Good monsoon years			Bad monsoon years			Good monsoon years			Bad monsoon years		
		1967	1973	1977	1972	1974	1979	1967	1973	1977	1972	1974	1979	1967	1973	1977	1972	1974	1979
April to May	20	4	10	−11	13	−4	1	6	6	−2	11	8	−9	10	−3	8	1	−4	0
	30	10	53	31	31	33	48	−4	14	23	5	2	12	−2	6	9	3	6	−3
	40	31	51	36	45	63	49	10	10	15	3	12	4	−1	−1	−1	−1	2	−1
	50	9	−19	−15	1	17	25	18	3	8	12	4	−2	−8	1	−1	0	−1	3
	60	−5	−19	−25	−27	−25	−5	5	3	2	−2	−3	−1	0	−3	−2	0	0	1
June through August	20	−35	−29	−6	−48	3	−27	−2	1	16	7	10	−4	5	0	−11	1	−3	−12
	30	−16	4	19	4	9	11	19	12	9	4	14	6	16	−1	3	−7	0	−1
	40	34	26	31	23	35	33	7	12	12	12	2	−4	0	−6	2	2	1	0
	50	21	20	−2	12	10	16	−2	3	0	7	1	1	−1	1	3	0	−2	−1
	60	5	12	−8	−3	0	1	2	5	−1	−1	1	2	−2	0	0	1	1	1

Unit: 10^{17} gm m^2 sec^{-2} mb^{-1}

Table 3. Meridional transport of momentum and of sensible heat during the period June through August contributed by long, medium and short waves

aves	Long (1 to 4)						Medium (5 to 10)						Short (11 to 16)					
at.°N	Good monsoon years			Bad monsoon years			Good monsoon years			Bad monsoon years			Good monsoon years			Bad monsoon years		
	1967	1973	1977	1972	1974	1979	1967	1973	1977	1972	1974	1979	1967	1973	1977	1972	1974	1979
20	21	34	62	18	35	84	13	−10	−29	8	2	−22	3	3	16	4	−5	−5
30	59	101	67	34	52	38	62	30	38	39	22	35	6	12	12	−4	−4	2
40	60	−7	60	−15	−1	54	95	93	38	78	5	−9	1	3	−1	9	−3	1
50	28	5	9	−9	48	19	9	21	17	19	10	−32	9	−3	−4	1	−4	1
60	−3	31	−9	−5	6	−19	2	1	−17	3	2	−7	1	−2	−3	0	4	5
Unit: 10^{17} gm m^2 sec^{-2} mb^{-1}																		
20	−60	−40	−36	−31	−43	−23	−1	−2	14	0	8	7	0	4	−15	5	3	−1
30	−57	−21	2	−4	23	26	20	12	13	36	−4	13	−2	−2	3	−1	2	3
40	−2	43	33	37	0	−4	47	40	15	30	5	16	−1	1	−2	1	−2	2
50	1	−10	2	−4	−35	13	3	7	12	19	8	12	1	−1	−1	1	−2	0
60	9	−8	28	8	12	21	2	2	2	4	−2	−4	−12	0	0	0	−2	3
Unit: 10^{10} j sec^{-1} mb^{-1}																		

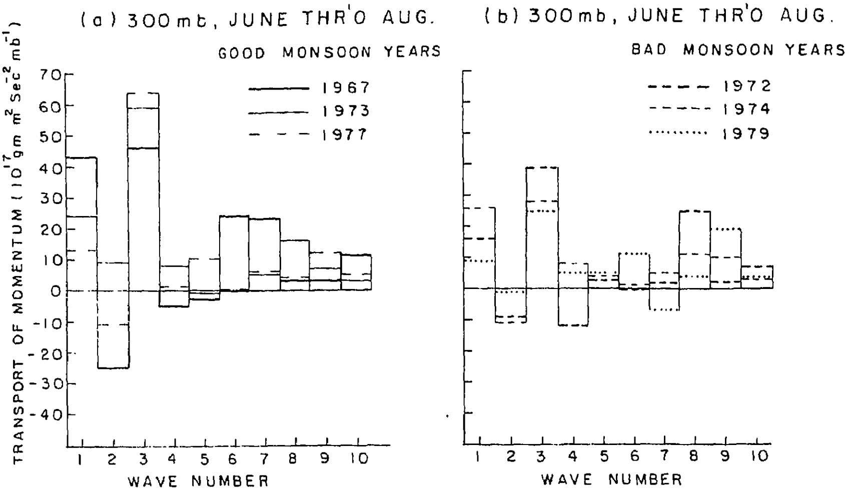

Figure 1. Meridional transport of momentum across 30°N at 300 mb level in wave number domain during the period June through August in (**a**) good monsoon years and (**b**) bad monsoon years.

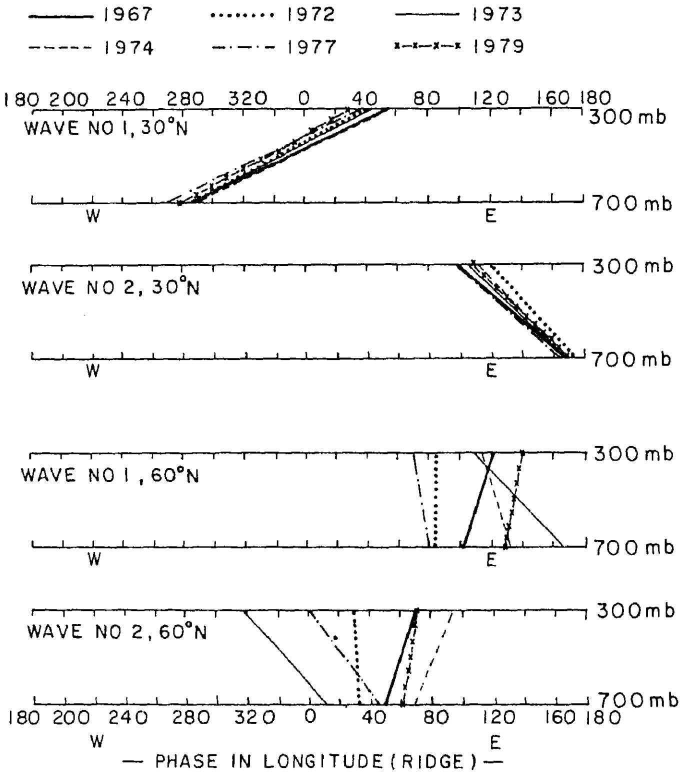

Figure 2. Vertical tilt for waves 1 and 2 at 30°N and 60°N during July month.

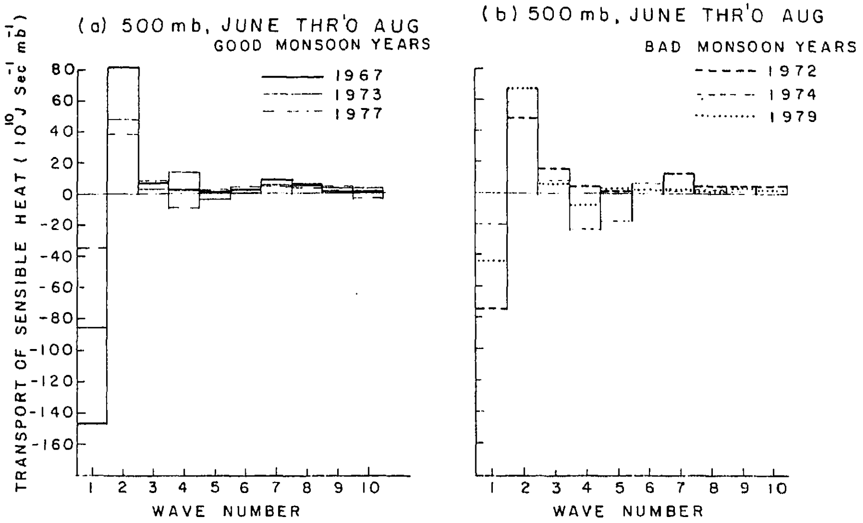

Figure 3. Meridional transport of sensible heat across 30°N at 500 mb level in wave number domain during the period June through August in (**a**) good monsoon years and (**b**) bad monsoon years.

contrast in these years. At high latitudes, the transport is small. The contribution to sensible heat by short waves is small.

It is noticed that the vertical tilt for wave 1 at 30°N is eastward in monsoon months and contributes to southward transport during the period J-A in all these years (figures 2 and 3). It is larger in good monsoon years than in bad monsoon years. Wave 2 tilts westward in vertical and transports sensible heat northward. Waves 1 and 2 contribute the most (figure 3). Waves 3 to 10 contribute to northward transport.

3.3 *Divergence of momentum and of sensible heat*

Table 4 gives the divergence of momentum and of sensible heat during the period J-A. In good monsoon years, there is larger divergence of momentum in subtropics and large convergence of momentum in mid-latitudes during J-A (table 4a). Our results are qualitatively in fair agreement with the results obtained for the year 1970 by Unni Nayar and Murakami (1978). Due to large convergence of momentum in mid-latitudes, the zonal westerlies in mid-latitudes will be stronger in good monsoon years and weaker in bad monsoon years. During weak monsoon activity, zonal westerly flow becomes of low zonal index and blocking high as per findings of many authors (Ramaswamy 1958, 1962; Ramamurthy 1969; Kanamitsu and Krishnamurti 1978). This can be understood through the following mechanism for wave zonal mean flow exchange described by the term

$$C(K_z, K_E) = [\bar{u}]\,(\partial/\partial y)\,[\bar{u}^*\bar{v}^*]$$

Further, this can be supported by the earlier results (table 2 of Awade *et al* 1982), where standing eddies supply more energy to zonal mean flow during good monsoon years.

Table 4a. Divergence of momentum at 300 mb level during the period June through August

Region	Latitudinal belt	Good monsoon years			Bad monsoon years		
		1967	1973	1977	1972	1974	1979
Subtropics	20–30°N	90	116	69	39	40	28
Mid-latitudes	30–50°N	−81	−120	−95	−58	−18	−87

Unit: 10^{17} gm m^2 sec^{-2} mb^{-1}

Table 4b. Divergence of sensible heat at 500 mb level during the period June through August

Region	Latitudinal belt	Good monsoon years			Bad monsoon years		
		1967	1973	1977	1972	1974	1979
Subtropics	20–30°N	22	27	55	57	53	59
Mid-latitudes	30–50°N	44	7	−5	−15	−50	−17

Unit: 10^{10} j sec^{-1} mb^{-1}

The mid-latitude westerlies therefore, will be stronger in good monsoon years when compared to bad monsoon years.

In bad monsoon years, there is large divergence of sensible heat in subtropics and large convergence in mid-latitudes during J-A (table 4b).

The bad monsoon activity is thus associated with greater divergence of sensible heat and consequently weakening of existing meridional temperature gradient in the tropics in summer. This causes abnormally low temperatures in the tropics in the bad monsoon years. Verma (1980) found that the upper troposphere over north India is cooler than normal during bad monsoon years. There prevailed abnormally low temperature over southern part of USSR, Iran, Afghanistan and north India in 1972 (Keshavamurthy and Awade 1974). The weakening of the temperature gradient in the tropics is manifested in less northward transport of momentum in bad monsoon.

3.4 *The contrast of transport of momentum and of sensible heat during pre-monsoon months* (*April and May*)

Table 5 gives the transport of momentum and of sensible heat across 30°N during April and May (premonsoon months) in these years to see whether there are any signatures in these quantities during April and May (before the commencement of the summer monsoon) which foretell the performance of monsoon rains.

It is observed that during April and May, the northward transport of momentum across 30°N at 300 mb level is larger in good monsoon than in bad monsoon years except in the year 1977. The year 1977 does not fit into the pattern. The northward transport of sensible heat at 500 mb level is larger in bad monsoon years than in good

	Level	Good monsoon years			Bad monsoon years		
		1967	1973	1977	1972	1974	1979
Momentum	300 mb	228	245	5	145	155	−84
Sensible heat	500 mb	27	10	18	79	57	22

Unit: Momentum: 10^{17} gm m^2 sec^{-2} mb^{-1}; Sensible heat: 10^{10} j sec^{-1} mb^{-1}.

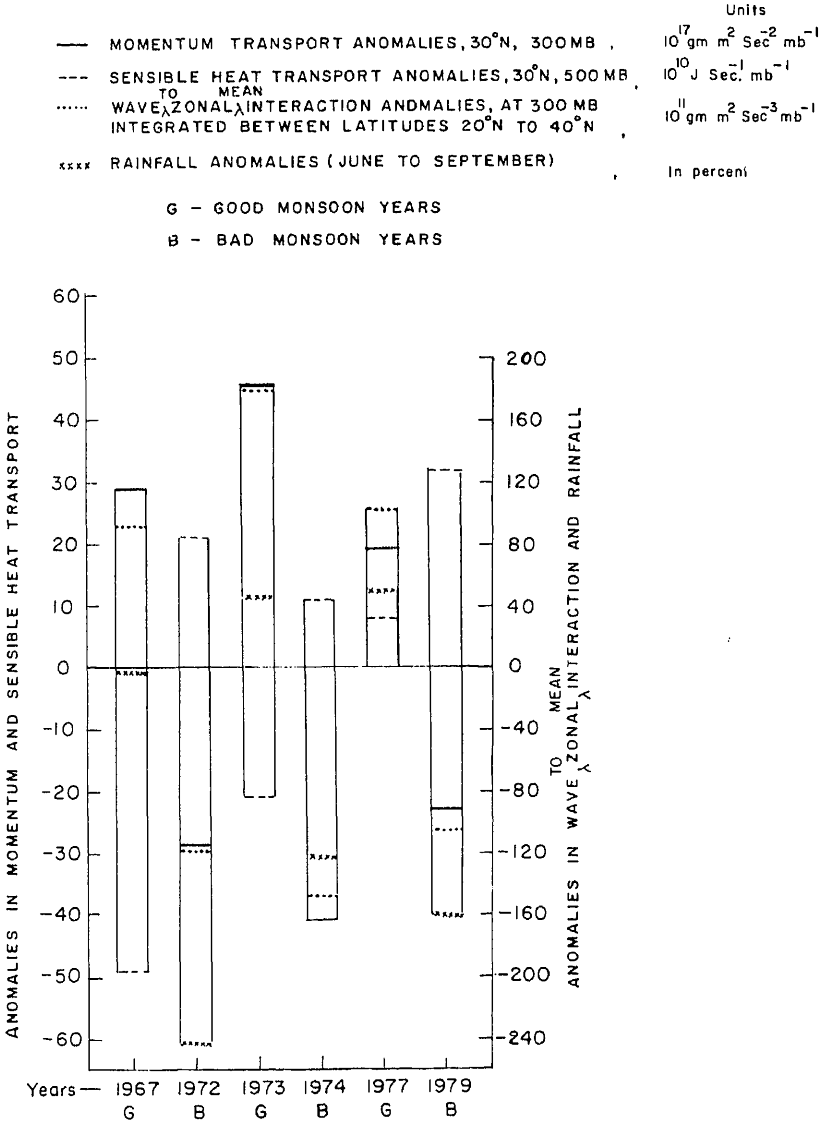

Figure 4. Comparison of anomalies during the period June through August in the transport of momentum, of sensible heat and wave to zonal mean interactions with anomalies in rainfall (%) in good and bad monsoon years.

monsoon years. Similar contrast is observed in the earlier section during June through August.

3.5 *Comparison of anomalies in the transport of momentum, of sensible heat and wave to zonal mean interactions with anomalies in rainfall.*

We have computed the average of six years and obtained the anomalies from these means for each quantity and for each year as shown in figure 4. The anomalies in rainfall are as given in table 1.

It is observed that the positive anomalies of rainfall (i.e. normal or good monsoon year) go with the positive anomalies of transport of momentum and wave to zonal mean flow interactions. However, it goes with the negative anomalies in case of sensible heat flux. In case of bad monsoon years, the anomalies in the rainfall, transports of momentum and wave to zonal mean flow interactions are negative while the anomalies in the sensible heat flux are positive. The authors are aware of the small sample of good and bad monsoon years. However, from the analysis we get a hint that contrast exists in years of good and bad monsoon activity. But we could arrive at convincing results if analysis is repeated for more cases.

5. Conclusions

Waves 1 through 3 show contrasting features during years of good and bad monsoon activity and the contrast is significant across 30°N at upper troposphere. The northward transport of momentum across 30°N is larger in good monsoon years than in bad monsoon years in both pre-monsoon and monsoon months.

In good monsoon years there is large divergence of momentum in sub-tropics while there is large convergence of momentum in mid-latitudes. In bad monsoon years, there is large divergence of sensible heat in subtropics and large convergence in mid-latitudes in mid-troposphere. This leads to a stronger than normal temperature gradient in good monsoon than in bad monsoon years and the westerlies become stronger in mid-latitudes and consequently the easterlies in the tropics.

Acknowledgement

The authors thank Dr Bh V Ramana Murthy, and Shri D R Sikka, for encouragement. They also thank Dr K S Raja Rao for helpful suggestions and Prof G C Asnani of the University of Nairobi for guidance.

References

Awade S T 1979 *Some features of the large-scale circulation during Indian southwest monsoon* Ph.D. Thesis, University of Poona

Awade S T, Totagi M Y and Sikka D R 1981 in *Proc. Int. Conf. on early results of* FGGE *and large scale aspects of its monsoon experiments, Geneva,* WMO 5–52 to 5–56

Awade S T, Totagi M Y and Bawiskar S M 1982 *Pure Appl. Geophys.* **120** 463

Kanamitsu M and Krishnamurti T N 1978 *Mon. Weather Rev.* **106** 331

Keshavamurty R N and Awade S T 1974 *Indian J. Meteorol. Geophys.* **25** 257

Lorenz E N 1966 Computations of the balance of angular momentum and poleward transport of heat: Observational studies of the atmospheric general circulation, Scientific Report No. 2, Planetary circulation project, Department of Meteorology, MIT, 32

Pisharoty P R and Desai B N 1956 *Indian J. Meteorol. Geophys.* **7** 333

Pisharoty P R and Asnani G C 1958 *Proc. monsoons of the world* (New Delhi: India Met. Dept.) 112

Ramamurthy K 1969 Some aspects of the 'BREAK' in the Indian southwest monsoon during July and August, India Meteorological Department, Forecasting Manual, Report No. IV—18.3

Raman C R V and Rao Y P 1981 *Proc. Int. Conf. early results of* FGGE *and large scale aspects of its monsoon experiments, Geneva* WMO 5–30 to 5–37

Ramaswamy C 1958 *Geophysics* **6** 455

Ramaswamy C 1962 *Tellus* **14** 337

Unni Nayar N S and Murakami T 1978 *Indian J. Meteorol. Hydrol. Geophys.* **29** 170

Verma R K 1980 *Mon. Weather Rev.* **108** 1072

Short range prediction with a multi-level primitive equation model

S S SINGH
Indian Institute of Tropical Meteorology, Pune 411 005, India

MS received 13 January 1984; revised 6 November 1984

Abstract. A five-level primitive equation model in a (x, y, p, t) coordinate system has been developed. A fairly sophisticated scheme of physical processes has been incorporated in the model. The model physics include air-sea interaction, cumulus parametrization, large scale condensation, dry convective adjustment, horizontal and vertical diffusion and simulated radiation. The initial balance between mass and motion fields has been obtained through a dynamic initialization scheme. The model has been integrated upto 48 hr using input data of a case of monsoon depression. The results of initialization and forecast have been presented and discussed. Wind, temperature and vertical velocity fields have been found to retain the observed map features; after the initialization, however, the surface pressure has been considerably modified. The model produced a reasonably good forecast up to 24 hr as far as the flow fields, rainfall region, structure of the depression and the movement of cyclonic circulation were concerned and beyond that damped rapidly. The rainfall rates were underestimated. Some of the shortcomings of the model are also discussed.

Keywords. Primitive equation model; numerical prediction; monsoon depression.

1. Introduction

A high resolution global model incorporating necessary physical processes is ideally suited for prediction over the monsoon belt. However, for the reason of economy and for the understanding and prediction of regional scale atmospheric systems, a regional model is highly desirable. A few tropical regional models have been developed for the research and experimental forecast and applied to case studies of the Indian summer monsoon (Krishnamurti *et al* 1976; Singh and Saha 1976; Das and Bedi 1978; Bedi *et al* 1976; Singh 1983). This study presents an application of a limited area five-level primitive equation model for prediction over the monsoon region.

2. Model equations

The model equation in a (x, y, p, t) coordinate system on Mercator projection in flux form may be written as

$$\frac{\partial u}{\partial t} + m^2\left[\frac{\partial}{\partial x}\left(u\frac{u}{m}\right) + \frac{\partial}{\partial y}\left(u\frac{v}{m}\right)\right] + \frac{\partial}{\partial p}(\omega u) - f^* v + mg\frac{\partial z}{\partial x} = -g\left(\frac{\partial \tau}{\partial p}\right)_x + F_u, \quad (1)$$

$$\frac{\partial v}{\partial t}+m^2\left[\frac{\partial}{\partial x}\left(v\frac{u}{m}\right)+\frac{\partial}{\partial y}\left(v\frac{v}{m}\right)\right]+\frac{\partial}{\partial p}(\omega v)+f^*u+mg\frac{\partial z}{\partial y}$$
$$=-g\left(\frac{\partial\tau}{\partial p}\right)_y+F_v, \quad (2)$$

$$\partial z/\partial p = -RT_v/pg, \quad (3)$$

$$m^2\left[\frac{\partial}{\partial x}\left(\frac{u}{m}\right)+\frac{\partial}{\partial y}\left(\frac{v}{m}\right)\right]+\frac{\partial\omega}{\partial p}=0, \quad (4)$$

$$\frac{\partial p_s}{\partial t}+mu_s\frac{\partial p_s}{\partial x}+mv_s\frac{\partial p_s}{\partial y}-\omega_s=0, \quad (5)$$

$$\frac{\partial}{\partial t}(C_pT)+m^2\left[\frac{\partial}{\partial x}\left(C_pT\frac{u}{m}\right)+\frac{\partial}{\partial y}\left(C_pT\frac{v}{m}\right)\right]+g\frac{\partial z}{\partial p}\omega$$
$$=\frac{\mathrm{d}Q}{\mathrm{d}t}-g\frac{\partial H}{\partial p}+C_pF_T, \quad (6)$$

$$\frac{\partial q}{\partial t}+m^2\left[\frac{\partial}{\partial x}\left(q\frac{u}{m}\right)+\frac{\partial}{\partial y}\left(q\frac{v}{m}\right)\right]+\frac{\partial}{\partial p}(q\omega)=M-g\frac{\partial W}{\partial p}+F_q, \quad (7)$$

$$T_v=T(1+0{\cdot}62q) \quad (8)$$

Equations (1) and (2) are the equations of motion in the east and north directions respectively. Equation (3) represents the hydrostatic law and (4) is the continuity equation. Equations (5) and (6) represent the surface pressure tendency and thermodynamic energy equation respectively. Equation (7) represents the moisture continuity equation and (8) is the virtual temperature correction equation.

3. Model structure and data

The domain of integration extends from 6°N to 36°N and 56°E to 106°E. The area is resolved by the uniform grid interval of 220 km on the Mercator projection. In the horizontal all the variables are defined at the same grid point (non-staggered grid). In the vertical, the model has four layers between 100 mb and 900 mb, with a spacing of 200 mb and a fifth layer of approximately 100 mb thickness between 900 mb and the ground surface (figure 1). The horizontal wind components and the geopotential height are specified at levels 200, 400, 600, 800 and 950 mb and the temperature, the specific humidity and the vertical velocity are set at 300, 500, 700 and 900 mb. Vertical velocity is assumed zero at 100 mb and computed at the lower boundary through continuity equation. The temperature field between 950 mb and the ground surface is extrapolated at each time-step from those of 700 and 900 mb. In the boundary layer between 950 mb and ground surface, no wind shear is assumed. The input data of 4 and 5 August 1968 have been chosen for the prediction experiment. Both days refer to the mature stage of a monsoon depression. Wind and temperature data are available at all standard pressure levels upto 100 mb, however there is no moisture observation beyond 500 mb level. Since the specific humidity (q) is required at 300 mb also, this is computed using the relative humidity value of 500 mb and the temperature of 300 mb.

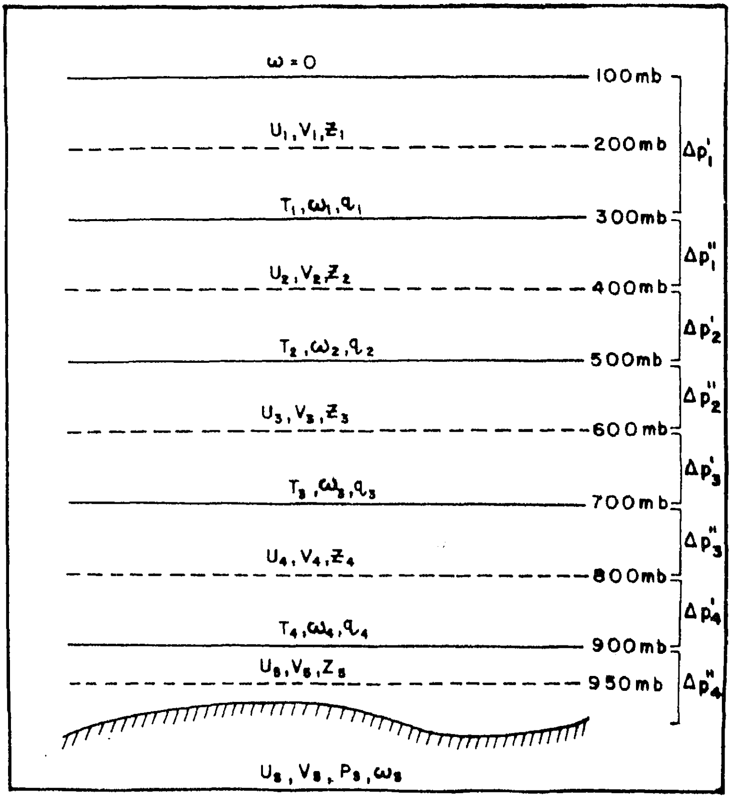

Figure 1. Vertical structure of five level primitive equation model.

In other words, no vertical variation in relative humidity beyond 500 mb level is assumed. A time step of 5 min for the grid length chosen was found suitable.

4. Boundary conditions

Rigid walls are specified between two outermost rows of gridpoints in the north and south directions where the normal component of motion vanishes, but tangential flow is permitted. In the east-west direction cyclic continuity is adopted by extending the domain by eight additional grid points on the eastern side and the variables are specified as

$$Q(L+8) = Q(2) \quad \text{and} \quad Q(1) = Q(L+7),$$

where L is the number of grid points in the east-west direction in the unextended outermost grid points using values of grid point inside. Following the above procedure the variables may be specified as follows at the north-south boundary,

$$\frac{\partial u}{\partial y} = \frac{\partial T}{\partial y} = \frac{\partial q}{\partial y} = \frac{\partial p_s}{\partial y} = 0; \quad \bar{v}^y = 0,$$

where $\bar{v}^y$ denotes the mean northward wind speed over the two outermost rows. For the evaluation of pressure tendency, u_s and v_s must be known. This is done by assuming zero wind shear between 950 mb and the ground surface. Using the above criterion, wind at the lower boundary may be specified,

$$u_s = u_{950}; \quad v_s = v_{950}.$$

5. Finite difference scheme

Following Okamura (1975), mass and energy conserving finite difference scheme for space derivatives has been adopted. We define the following two basic operators for finite differencing. The first operator is a finite difference form for the divergence of two physical quantities A and B,

$$D_x(A * B)_i \equiv \frac{1}{8d\Delta p_i}[\{A_{i+1}(\Delta p_{i+1} + \Delta p_i) + A_i(3\Delta p_i - \Delta p_{i-1})\}$$
$$(B_{i+1} + B_i) - \{A_{i-1}(\Delta p_{i-1} + \Delta p_i) + A_i(3\Delta p_i - \Delta p_{i-1})\}(B_i + B_{i-1})], \tag{9}$$

where i denotes the grid point in the x-direction, Δp_i the thickness of a layer in pressure difference, d the grid interval, D_x the finite difference with respect of x. It should be noted that the product $(A * B)$ is asymmetric on the right hand side of (9). A similar operator may be defined for D_y.

The second operator is expressed as

$$G_x(A, B) \equiv \frac{1}{4d}\{(A_{i+1} + A_i)(B_{i+1} - B_i) + (A_i + A_{i-1})(B_i - B_{i-1})\} \tag{10}$$

This is the finite difference scheme for the product of A and the derivative of B with respect to x. A similar operator may be defined for G_y. The centred difference scheme using three data levels has been adopted for vertical derivatives.

These operators ensure the energy conservation property of the governing equations in the finite difference form. Applying (9) and (10) to (1) through (8), the finite difference equations of the model equations are obtained. For marching in time, the Leapfrog scheme with an Asselin (1972) time filter is adopted.

6. Physical processes

6.1 *Sub-grid scale horizontal diffusion*

Horizontal diffusion is introduced in the momentum, thermodynamic and water vapour equations. A simple linear diffusion formula is used in the model as,

$$F_\alpha = \nu\nabla^2\alpha, \quad \alpha = u, v, T \text{ or } q.$$

e value of coefficient ν is determined following Leith (1969),

$$\nu = \gamma |\nabla\zeta| d^3$$

ere ζ is relative vorticity, d the grid distance, and γ is the empirically determined non-
iensional constant being set to 0·25.

Surface friction

e exchange of momentum between the air and the earth's surface in the surface layer
expressed by the stress vector

$$\boldsymbol{\tau} = \rho C'_D |\mathbf{V}_m| \mathbf{V}_m,$$

ere $C'_D = 0{\cdot}75\, C''_D$ and $\mathbf{V}_m$ is the wind vector at $Z = Z_m (= 10 \text{ m})$. The coef-
ent C''_D (relation for computing C''_D is given in §6.3) is calculated over the sea surface.
e coefficient over the land is set three times as large as the maximum value of C'_D over
sea surface. The following relation is used for stress at 900 mb and above,

$$\boldsymbol{\tau}_{900} = \rho Km \left(\frac{\partial \mathbf{V}}{\partial Z}\right)_{900} \qquad (p \geqslant 900 \text{ mb}),$$

$$\boldsymbol{\tau} = 0 \qquad (p < 900 \text{ mb})$$

ere $Km = l^2 \left| \left(\frac{\partial \mathbf{V}}{\partial Z}\right) \right|_{900}$ and $l = 30$ m.

Surface exchange of sensible heat and moisture

ie exchange of heat and moisture is evaluated by the bulk method and over land is set
zero.

In the bulk method, sensible heat flux from the sea surface, H_0 may be given as

$$H_0 = \rho C''_D C_p |\mathbf{V}_m| (T_0 - T_a).$$

r an unstable and neutral case:

$$(\Delta T = T_0 - T_a \geqslant 0)$$

$$C''_D = (1{\cdot}0 + 0{\cdot}066\,\Delta T) \times (0{\cdot}883 + 0{\cdot}084 |\mathbf{V}_m|) \times 10^{-3}.$$

r a stable case:

$$\Delta T = T_0 - T_a < 0$$

$$C''_D = (1{\cdot}0 + 0{\cdot}111\,\Delta T) \times (0{\cdot}889 + 0{\cdot}055 |\mathbf{V}_m|) \times 10^{-3},$$

iere T_0 is sea surface temperature and T_a the temperature of the air at the altitude of
(10 m).

Surface flux of water vapour (evaporation) is evaluated by the same formula as that
sensible heat

$$W_0 = \rho C''_D |\mathbf{V}_m| [q(T_0) - q(T_a)]$$

where $q(T_0)$ and $q(T_a)$ are specific humidity at sea surface temperature T_0, and at air temperature T_a.

Vertical eddy diffusion of sensible heat and moisture is evaluated in the following way:

$$H_0 = 0, \qquad p < 900\,\text{mb}$$

$$W = -\rho Km \frac{\partial q}{\partial z}, \quad Km = l^2 \left|\frac{\partial \mathbf{V}}{\partial z}\right|, \quad p \geqslant 700\,\text{mb},$$

$$W = 0. \qquad p < 700\,\text{mb}$$

H_0, C_D'' and W_0 are computed following Electronic Computation Centre (1980).

6.4 *Dry convective adjustment*

Dry convective adjustment is performed wherever superadiabatic lapse rates $(-\partial T/\partial p) > \gamma_d)$ were encountered. Following Kanamitsu (1975}, the adjustment modifies the vertical temperature distribution while preserving the dry static energy.

6.5 *Large scale condensation and stable heating*

If the relative humidity reaches 100 %, large scale condensation is assumed to take place. The relative humidity is not allowed to exceed 100 % as the excess water vapour is condensed instantaneously and humidity values are brought to their saturation values. Appropriate heating and humidity changes are introduced in the model equations following Manabe *et al* (1965). The scheme is briefly presented below.

The specific humidity (δq) and temperature (δT) are adjusted by solving the equation,

$$q + \delta q = q_s(T + \delta T, p),$$

$$C_p \delta T + L \delta q = 0.$$

Iterative procedures for solving the above equations are adopted following Manabe *et al* (1965). The condensed rain for the entire column is given by

$$P_r \text{ (large scale)} = -\frac{1}{g}\int_{100}^{p_s} \delta q \, \mathrm{d}p.$$

6.6 *Parametrization of cumulus convection*

The parametrization of cumulus convective scheme of Kuo (1965, 1974) modified by Kanamitsu (1975) and Krishnamurti *et al* (1976) has been invoked for computation of convective transport of heat and moisture. The large scale supply of moisture I is defined by the relation, troposphere.

I is partitioned into

$$I = I_\theta + I_q,$$

or $$I_q = bI,\ I_\theta = (1-b)I,$$

where I_θ is the part of the moisture supply which goes into enhancing the temperature field and I_q is a part that modifies the moisture field and b is the fraction of available moisture supply that modifies the moisture field. Two other quantities Q_θ and Q_q are determined by the relations

$$Q_\theta = -\frac{C_p}{Lg}\int_{P_B}^{P_T}\left[\left(\frac{T_s - T}{\Delta t}\right) + \frac{T}{\theta}\omega\frac{\partial\theta}{\partial p}\right]\mathrm{d}p,$$

$$Q_q = -\frac{1}{g}\int_{P_B}^{P_T}\left(\frac{q_s - q}{\Delta t}\right)\mathrm{d}p.$$

Here Δt denotes the cloud time scale. These two quantities Q_θ and Q_q are known and $Q = Q_\theta + Q_q$ is a measure of total moisture supply needed to cover a volume over a horizontal area with clouds. The two unknowns a_θ and a_q for (11) and (12) are defined by the relations,

$$a_\theta = I_\theta / Q_\theta,$$

$$a_q = I_q / Q_q.$$

Following Kuo (1965), the convective heating and moisture transport by convection at each level is expressed as follows:

$$\frac{\partial\theta}{\partial t} = -\omega\frac{\partial\theta}{\partial p} + a_\theta\left[\omega\frac{\partial\theta}{\partial p} + \frac{\theta}{T}\left(\frac{T_s - T}{\Delta t}\right)\right], \tag{11}$$

$$\frac{\partial q}{\partial t} = a_q\left(\frac{q_s - q}{\Delta t}\right), \tag{12}$$

and $$\int\frac{C_pT}{L\theta}\frac{\partial\theta}{\partial t}\mathrm{d}p = A + (1-b)I, \tag{13}$$

$$\int\frac{\partial q}{\partial t}\mathrm{d}p = bI, \tag{14}$$

where $$A = -\frac{1}{g}\int\frac{C_p}{L}\frac{T}{\theta}\omega\frac{\partial\theta}{\partial p}\mathrm{d}p.$$

In the prediction model, the cumulus scale heating and vertical flux of moisture are invoked only if the sounding is conditionally unstable and the net large scale convergence of flux of moisture in the vertical column is positive. In order to determine

b, (13) and (14) are equated to close the system. Thus,

$$b = (A+I)/2I,$$

$$a_q = (A+I)/2Q_q,$$

$$a_\theta = (I-A)/2Q_\theta.$$

The cloud time scale, Δt is set equal to 30 min in this experiment.

7. Initialization

The simplest initialization procedure for the primitive equation model is to balance mass and motion fields through a nonlinear balance equation. In this method geopotentials are obtained from nondivergent wind through a reverse balance equation and temperature is derived through hydrostatic relation. Vertical motion and horizontal divergence are set to zero initially. Singh and Saha (1976) and Singh (1977) applied this scheme of initialization to predict a case of monsoon depression and of tropical cyclone. Round-the-clock forecast movement of cyclonic circulation and flow patterns were reasonably good; but the temperature lapse rate in the initial and forecast fields were far from satisfactory mainly due to poor boundary conditions for the solution of the balance equation.

Kanamitsu (1975) and Kiangi (1977) showed that the dynamic initialization is superior to static initialization (balance equation solution) for the initial adjustment of mass and motion fields for the tropical atmosphere. The success of dynamic initialization experiment (Singh *et al* 1980) for the barotropic prediction of monsoon depression and the failure to obtain the realistic temperature and vertical velocity fields in an earlier version of the model (Singh and Saha 1976) motivated us to apply the dynamic initialization scheme for the present study. The formulation is essentially the same as that followed by Winninghoff (1973) and Kanamitsu (1975).

For the application of dynamic initialization the variables u, v, T, q, P_s are needed as inputs to the model. The observed wind field is initially modified so that the vertical motion at the lowest level of the model vanishes. This step is necessary to suppress the external gravity waves, at least initially and is called pre-initialization.

7.1 *Pre-initialization*

(i) From the observed wind, the stream function (ψ) and nondivergent part of wind u_ψ and v_ψ at each level are evaluated by the relation

$$\nabla^2\psi = m^2\left[\frac{\partial}{\partial x}\left(\frac{v_{\mathrm{ob}}}{m}\right) - \frac{\partial}{\partial y}\left(\frac{u_{\mathrm{ob}}}{m}\right)\right],$$

$$u_\psi = -m\frac{\partial\psi}{\partial y}, \quad v_\psi = m\frac{\partial\psi}{\partial x}.$$

(ii) The horizontal divergence from the observed wind at each level is computed. The divergence is adjusted such that the net divergence in a vertical column vanishes. Since the net divergence computed from the observed wind may not vanish, the correction in the divergence field is applied at levels where observations and analyses are not considered the best. The 200, 800 mb and surface levels are considered the best quality levels due to the large number of surface observations, pibal observations, commercial aircraft reports and satellite cloud motion vectors and as such the correction is applied only at 400 and 600 mb levels; at 200, 800 mb and surface levels the divergence is fixed. This is done through the following relation

$$(\nabla\cdot\mathbf{V})_k^{\text{corrected}} = (\nabla\cdot\mathbf{V})_k^{\text{observed}} - \beta_k \Bigg/ \left(\sum_{k=1}^{N} \beta_k \Delta p_k\right) \sum_{k=1}^{N} \Delta p_k (\nabla\cdot\mathbf{V})_k^{\text{observed}},$$

where Δp is the pressure difference between the two wind levels, k is the subscript for level and $\beta_k = 1$ for 400 and 600 mb and zero for 200, 800 mb and surface levels.

From the adjusted divergence the irrotational part of wind is evaluated as

$$\nabla^2\chi = \nabla\cdot\mathbf{V},$$

$$u_\chi = m\frac{\partial\chi}{\partial x}, \quad v_\chi = m\frac{\partial\chi}{\partial y}.$$

(iii) The adjusted wind is computed as

$$u_{\text{adj}} = u_\psi + u_\chi,$$

$$v_{\text{adj}} = v_\psi + v_\chi.$$

The geopotential height (z) is computed from the surface pressure and the observed temperature

$$\partial z/\partial p = -RT_v/pg.$$

Thus, all variables u, v, T, q, z and P_s are known initially.

7.2 *Dynamic initialization*

The common method for obtaining the balanced field through a dynamic initialization scheme is to insert the data for dominant variables into the prognostic equations and integrate back and forth around the initial time, applying a time differencing scheme which tends to suppress the gravity waves but does not affect meteorological component significantly. In the present study, a scheme suggested by Temperton (1976) has been applied. For a typical variable u, one iteration of the scheme is defined by

$$u^* = u^{(\nu)} + \Delta t\left(\frac{\partial u}{\partial t}\right)^{(\nu)},$$

$$u^{**} = u^* - \Delta t\left(\frac{\partial u}{\partial t}\right)^{*}, \qquad (15)$$

$$u^{\nu+1} = 3u^{(\nu)} - 2u^{**},$$

where ν is the iteration number. It can be shown that in one cycle of iteration a wave of frequency is damped by a factor $1-2\Delta t^2K^2\sigma^2$. The wave of frequency $K\sigma = \pm 1/(2)^{1/2}\Delta t$ will be completely removed after one cycle, while higher frequency waves will change sign at each iteration.

Although it is desirable to force the mass field to adjust towards wind field, in this experiment no consideration is given to the restoration of any variable and all fields are left free to adjust mutually. The iteration scheme (15) is applied for marching back and forth with Δt positive for odd cycles, which is replaced by $-\Delta t$ for even cycles. The diabatic heating is not incorporated during initialization, although the moisture continuity equation is included for temperature correction. There is very little chance for supersaturation to occur, however if such situation occurs, the excess moisture is removed without effecting any change in the temperature. During the present experiment such a situation did not occur at any grid point.

One step forward as given by (15) and one step backward with $\Delta t = -\Delta t$ constitutes one cycle of iteration. In this experiment ninety such cycles are performed to achieve the initial balance. The number of cycles is chosen arbitrarily as there is no theoretical criterion for achieving the convergence except that root mean square difference for basic fields (u, v, T and P_s) of two successive iterations with an interval of 10 cycles become exceedingly small.

8. Results of initialization experiment

Initialization and forecast results with the input of 4 and 5 August have been found to be similar; hence the results of only one input day i.e. 5 August will be presented and discussed. However, results of 4 August will also be discussed where it is relevant.

Table 1 which presents the root mean square difference for basic fields of two successive iterations, shows that at the end of the initialization experiment the rate of reduction is very slow.

Figures 2, 3, 4 and 5 present fields before and after the initialization of the surface pressure, wind at 800 and 200 mb, temperature at 700 and 300 mb, and vertical velocity at 700 and 300 mb respectively.

It may be seen from figures 2 through 5 that initialization smoothens the patterns of all variables. Maximum changes are noticed in the surface pressure; even the geometry of the circulation system is either lost or completely modified. Kanamitsu (1975) also

Table 1. Root mean square difference between successive iterations (interval of 10 cycles)

Cycle No.	P_s(mb)	u (ms^{-1})					v (ms^{-1})					T (°K)			
		950	800	600	400	200	950	800	600	400	200	900	700	500	300
10	1·44	0·12	0·12	0·12	0·15	0·29	0·16	0·16	0·15	0·18	0·49	0·06	0·08	0·08	0·12
20	0·57	0·08	0·08	0·06	0·06	0·18	0·12	0·11	0·09	0·07	0·31	0·03	0·04	0·05	0·09
30	0·33	0·07	0·07	0·05	0·05	0·14	0·10	0·10	0·08	0·06	0·26	0·02	0·03	0·04	0·08
40	0·23	0·07	0·06	0·05	0·04	0·12	0·10	0·09	0·07	0·05	0·22	0·01	0·03	0·04	0·07
50	0·18	0·06	0·05	0·04	0·04	0·10	0·09	0·08	0·06	0·04	0·19	0·01	0·03	0·03	0·06
60	0·14	0·06	0·05	0·04	0·04	0·09	0·08	0·07	0·06	0·04	0·17	0·01	0·02	0·03	0·05
70	0·12	0·05	0·05	0·03	0·04	0·08	0·07	0·06	0·05	0·04	0·16	0·01	0·02	0·03	0·05
80	0·10	0·05	0·04	0·03	0·03	0·07	0·07	0·06	0·05	0·03	0·14	0·01	0·02	0·03	0·05
90	0·09	0·05	0·04	0·03	0·03	0·06	0·06	0·05	0·04	0·03	0·13	0·01	0·02	0·02	0·04

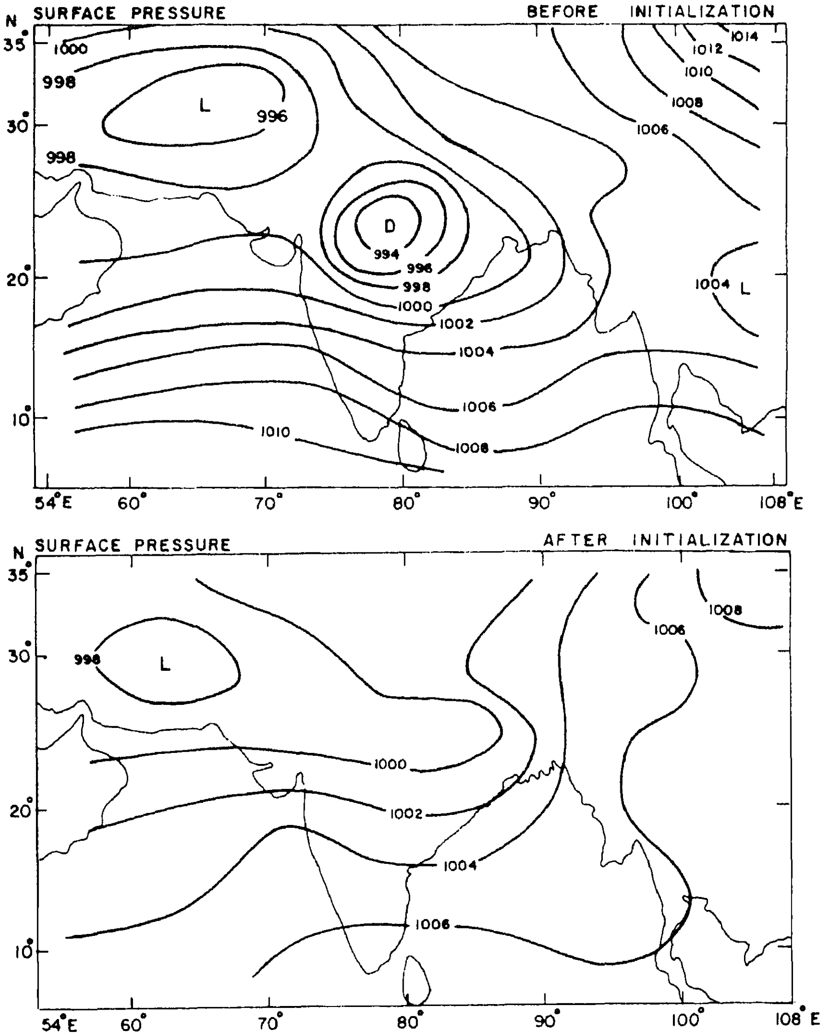

Figure 2. Change of surface pressure by initialization (unit: mb).

found similar results in his dynamic initialization experiment. Adjustment of surface pressure is not only affected by the surface wind but also by the vertically integrated divergence. The change in the surface pressure is obviously the reflection of adjustment of external gravity waves. Figures 3 and 4 and table 2 reveal that other variables like wind and temperature change very little after initialization. The insignificant change in temperature is the reflection of slight adjustment of internal gravity waves.

The vertical velocity patterns (figure 5) are considerably smoothed out without changing the basic patterns. Emergence of large vertical velocity values even after initialisation suggests the importance of the divergent part of the wind in the initial data of the monsoon region particularly for the input to the numerical model.

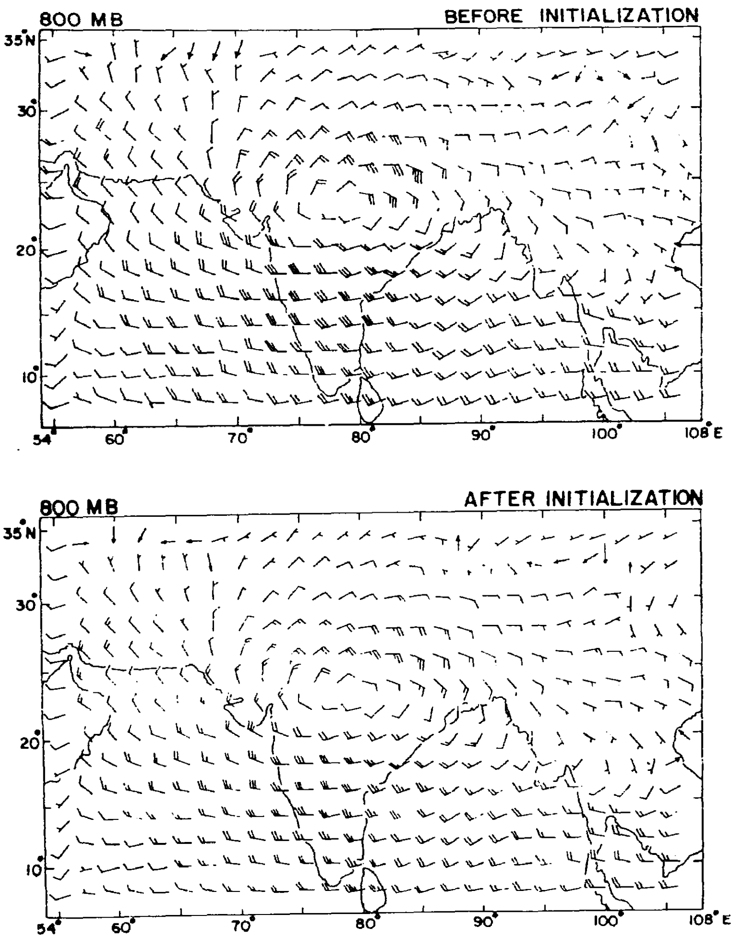

Figure 3a. Change of 800 mb wind by initialization (unit: knot).

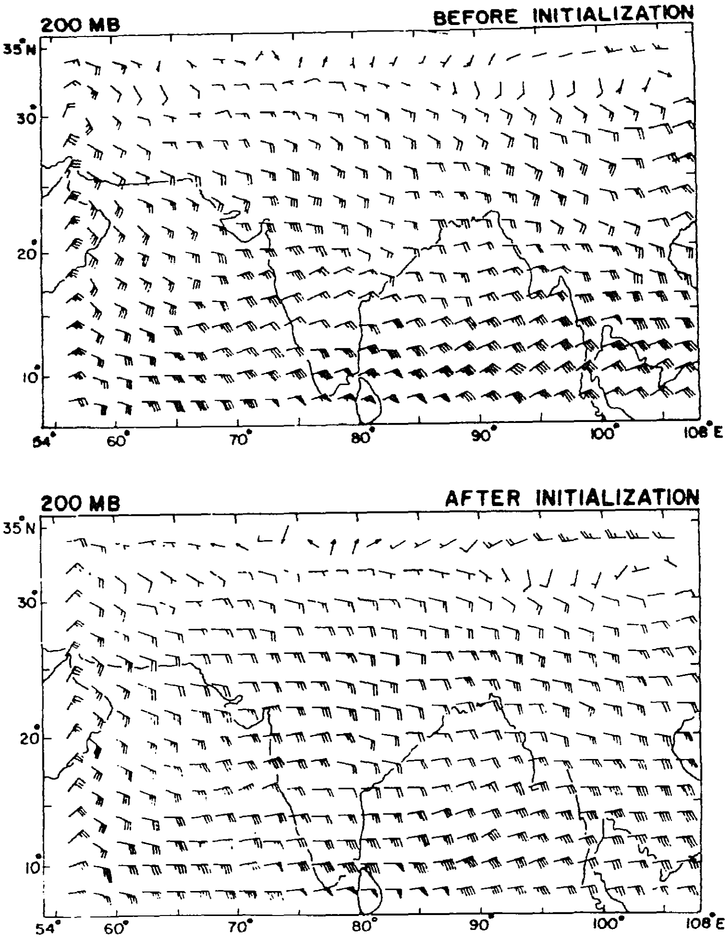

Figure 3b. Same as figure 3a except at 200 mb.

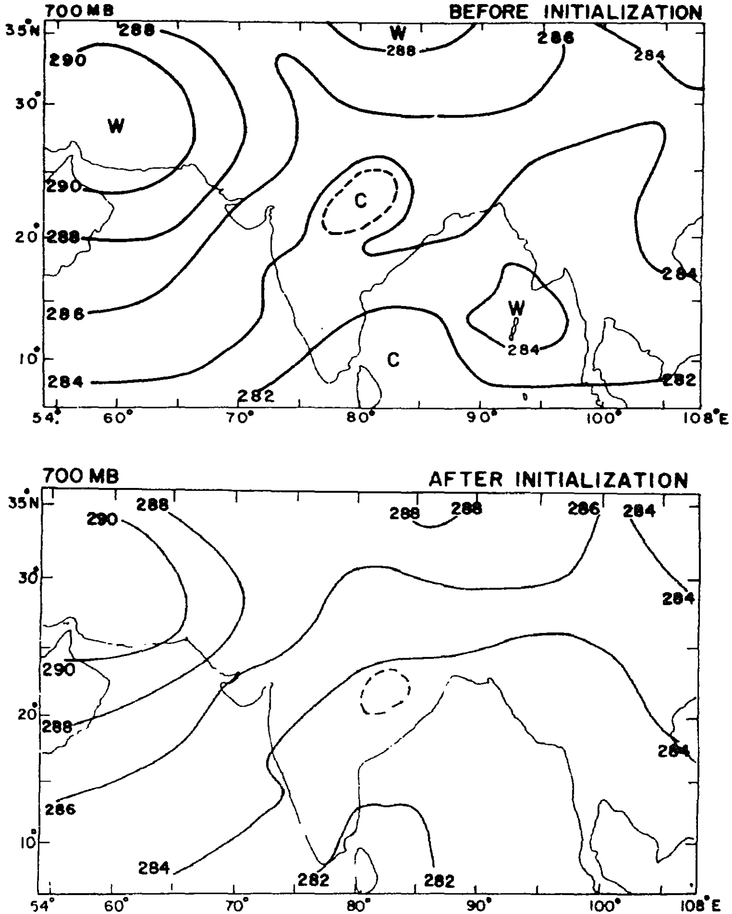

Figure 4a. Change of 700 mb temperature by initialization (unit: K).

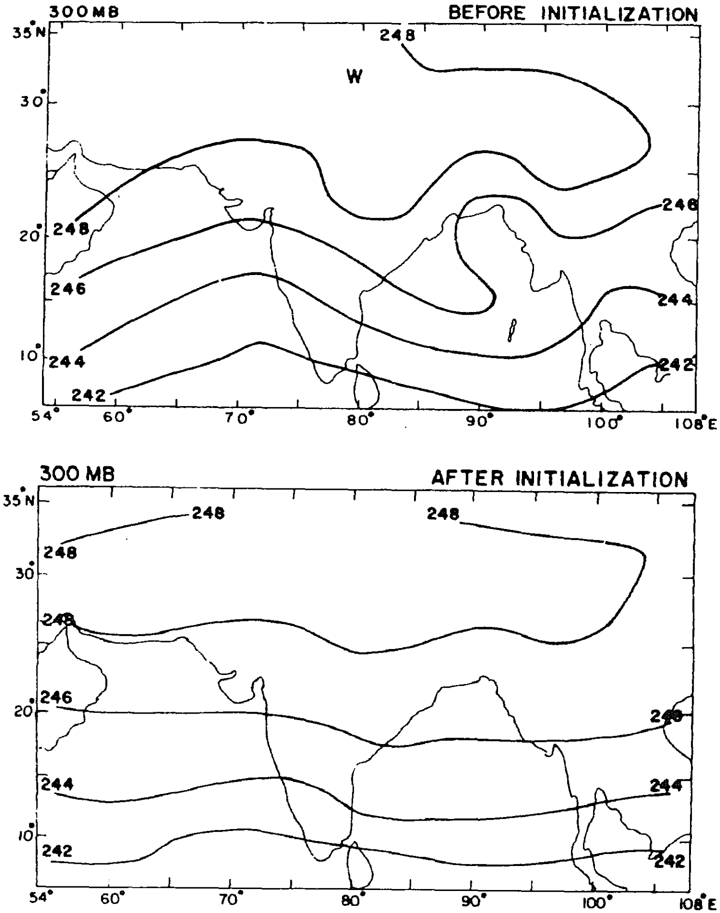

Figure 4b. Same as figure 4a except at 300 mb.

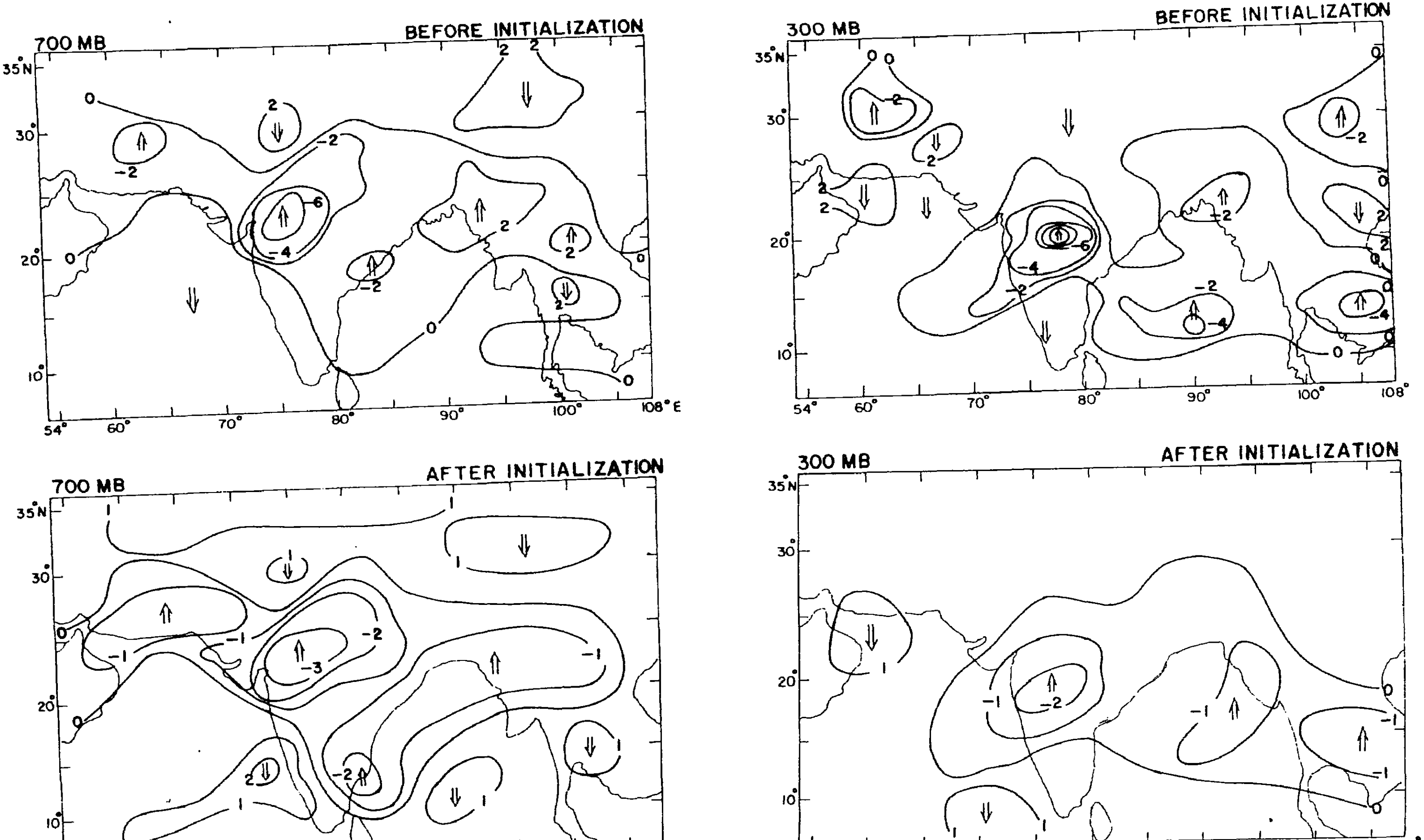
700 MB
BEFORE INITIALIZATION
300 MB
BEFORE INITIALIZATION
700 MB
AFTER INITIALIZATION
300 MB
AFTER INITIALIZATION
35°N
30°
20°
10°
54°
60°
70°
80°
90°
100°
108°E
108°
0
2
-2
-4
-6
-1
-3
1

Table 2. Root mean square difference (RMS) between the fields before and after the iterative initialization

Variables	Pressure levels	RMS difference	Variables	Pressure levels	RMS difference
P_s	Surface	2·97 mb	v	400	0·22 ms^{-1}
u	950	0·25 ms^{-1}	u	200	0·52 ms^{-1}
v	950	0·33 ms^{-1}	v	200	0·88 ms^{-1}
u	800	0·23 ms^{-1}	T	900	0·14°K
v	800	0·30 ms^{-1}	T	700	0·22°K
u	600	0·18 ms^{-1}	T	500	0·25°K
v	600	0·25 ms^{-1}	T	300	0·33°K
u	400	0·22 ms^{-1}			

9. Forecast results

The model has been integrated upto 48 hr with the input of 4 and 5 August 1968. As mentioned earlier the results of 5 August only will be presented. As considerable damping is noticed in the 48 hr forecast, the details of the 24 hr forecast are presented and discussed below; wherever necessary, the 48 hr results will also be discussed. Figures 6 and 7 depict the 24 hr forecast and corresponding verification charts in respect of wind at 800 and 200 mb and temperature at 700 and 300 mb respectively. Figure 8 gives the 24 hr forecast and corresponding verification charts in respect of the vertical velocity field at 700 mb. It may be seen from figure 6 that the forecast flow patterns and movement of the cyclonic system have been found reasonably good. The temperature field as seen from figure 7 is very well predicted at 300 mb; however prediction at 700 mb is not good. The upward vertical velocity maximum (figure 8) as expected is found in the western sector of the cyclonic system. The verification vertical velocity is computed from the observed divergence and as such it differs from the forecast vertical velocity. The difference is not merely due to inaccuracy in the forecast but also due to inherent errors in the computation of verification of vertical velocity from the observed divergence.

9.1 *The depression track*

Figure 9 depicts the tracks observed and predicted by one-level and five-level primitive equation models. The 24 hr forecast position of the centre of the depression is slightly better in the five-level primitive equation model; however the movement as seen in 48 hr is slower than the actual; it is also slower than that of barotropic prediction. Generally, the movement of the advecting system is very small as predicted by the barotropic model. Besides, the author has tested the movements of several depressions on the basis of the barotropic model and he finds the movement in the case of this series (4 to 6 August) is best predicted. Furthermore, the slower prediction movement after 24 hr (in the five-level model) may partly be attributed to the complete absence of orography from the model. It is well known that bottom topography can produce faster westward orography on the westward movement are being investigated and would be reported later.

9.2 *Vertical cross-sections of meridional wind, relative vorticity, temperature anomaly and vertical velocity along a zonal plane passing through 22° N*

9.2a *Meridional wind:* Figure 10 presents the observed and the predicted cross-sections of the meridional wind along a zonal plane passing through 22°N. The predicted northerly and southerly maxima coincide very well with the observed field. Furthermore, the eastward vertical tilt in the lower troposphere and the vertical extent of the cyclonic circulation are very well predicted. The separation distance between northerly and southerly maxima nearly coincide on 5 August; however, this distance is increased in the forecast field on 6 August suggesting broadening of the size of the depression.

9.2b *Relative vorticity:* The observed and the predicted relative vorticity cross-sections are illustrated in figure 11. The vorticity maximum is seen centred over the storm in the lower troposphere as expected. The vorticity maximum and its centre are very well predicted by the model, except that the predicted centre of the maximum lies slightly at a higher level than the observed. In general, the model has produced a good forecast of the vorticity field over the storm.

9.2c *Temperature anomaly:* The observed and the predicted vertical cross-sections of the temperature anomaly (difference from zonal mean) are presented in figure 12. The cold core in the lower troposphere is very well predicted although strong and slightly east of the actual location. The warm core above the storm in the upper troposphere is very well simulated by the model.

9.2d *Vertical velocity:* Figure 13 presents the predicted vertical cross-section of the vertical velocity. It may be seen that the maximum upward motion is centred over the storm in the middle troposphere as expected. Though the model has been successful in the prediction of vertical velocity, intensity has been found slightly weaker than usually expected (3–4 $\mathrm{mb\,S^{-1}}$) in the intense depression.

9.3 *Rainfall rates*

The 24 hr predicted versus observed rainfall is presented in figure 14. The total rainfall includes the convective and stable precipitation. It may be seen that the most intense rainfall occurs slightly west of the storm centre which has been predicted reasonably well by the model. Furthermore, the region of precipitation is also handled very well by the model. However, the amount in general is very much underestimated (one fifth of the actual). The reasonably good prediction of rainfall rates mainly depend on moisture analyses in the lower troposphere, distribution of vertical velocity, parametrization of cumulus convection and horizontal and vertical resolutions of the model. It is likely that most of the factors outlined above must have contributed to the poor prediction of

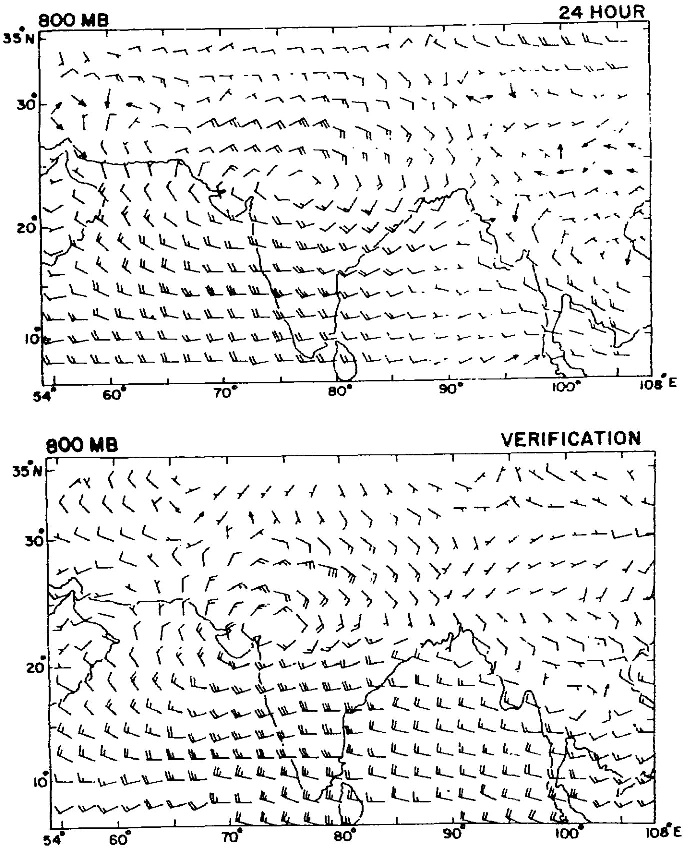

Figure 6a. 24 hr forecast and corresponding verification wind charts at 800 mb (unit: knot).

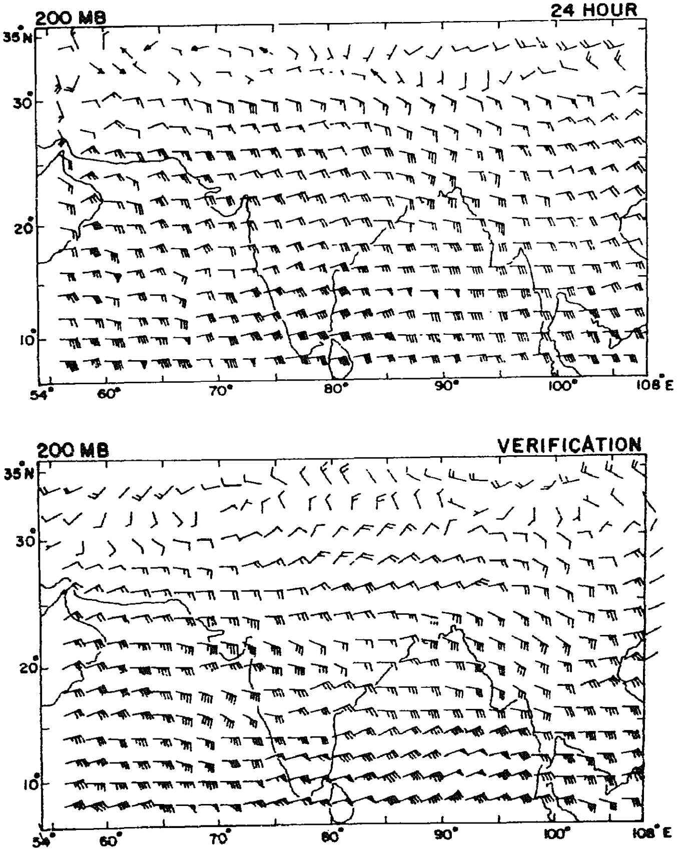

Figure 6b. 24 hr forecast and corresponding verification wind charts at 200 mb (unit: knot).

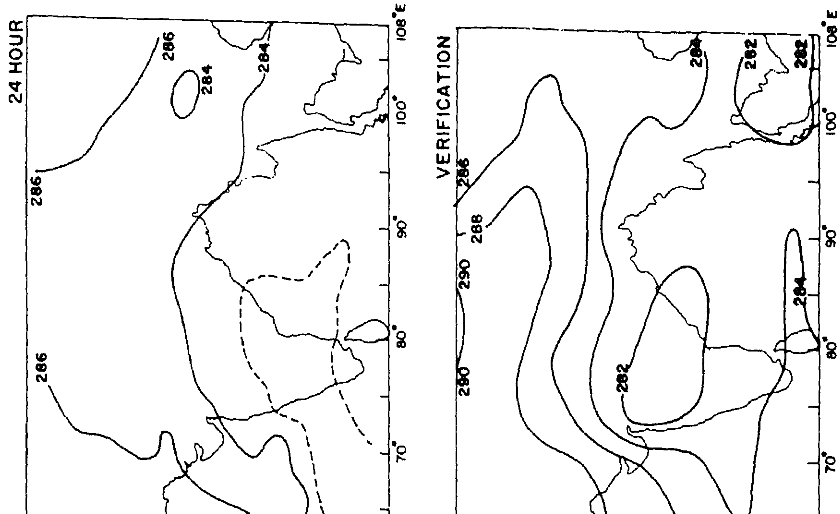

hr forecast and corresponding verification temperature
(unit: K).

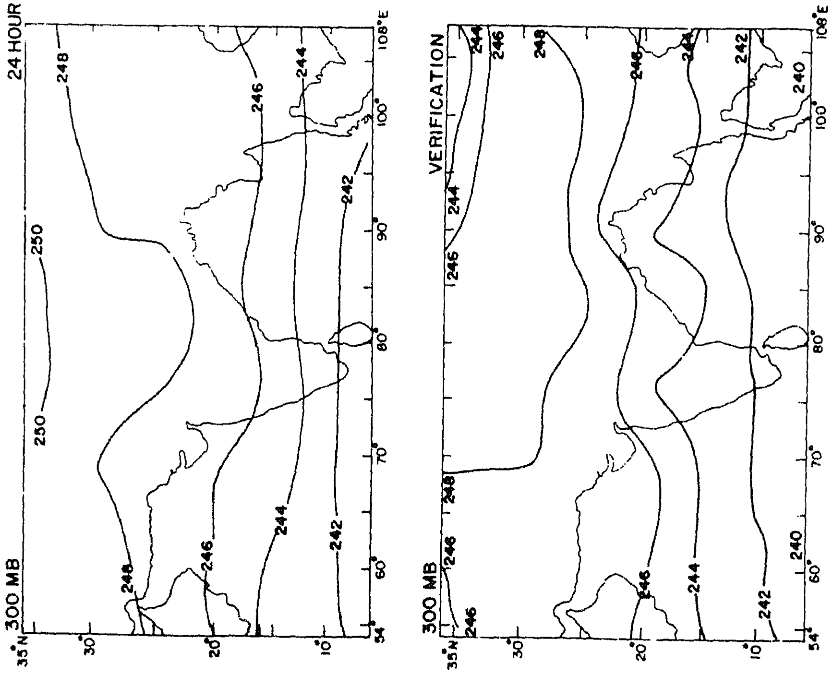

Figure 7b. 24 hr forecast and corresponding verification temperature charts at 300 mb (unit: K).

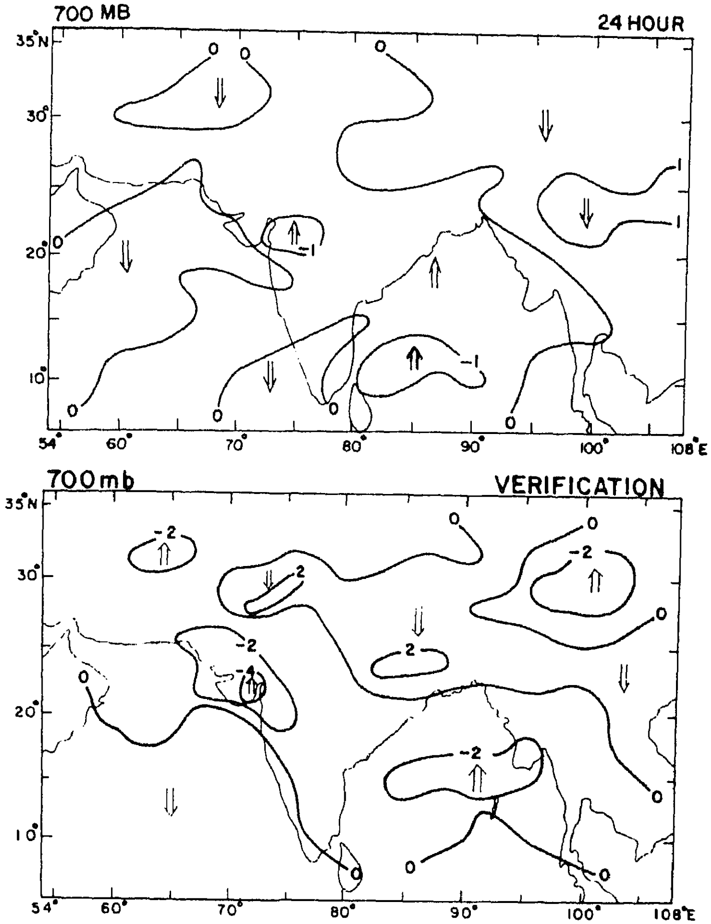

Figure 8. 24 hr forecast and corresponding verification vertical velocity chart at 700 mb (unit: 10^{-3} mb S^{-1}).

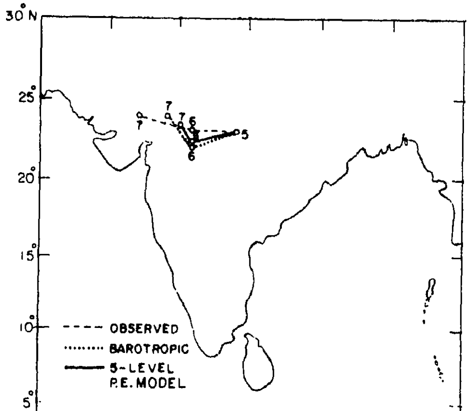

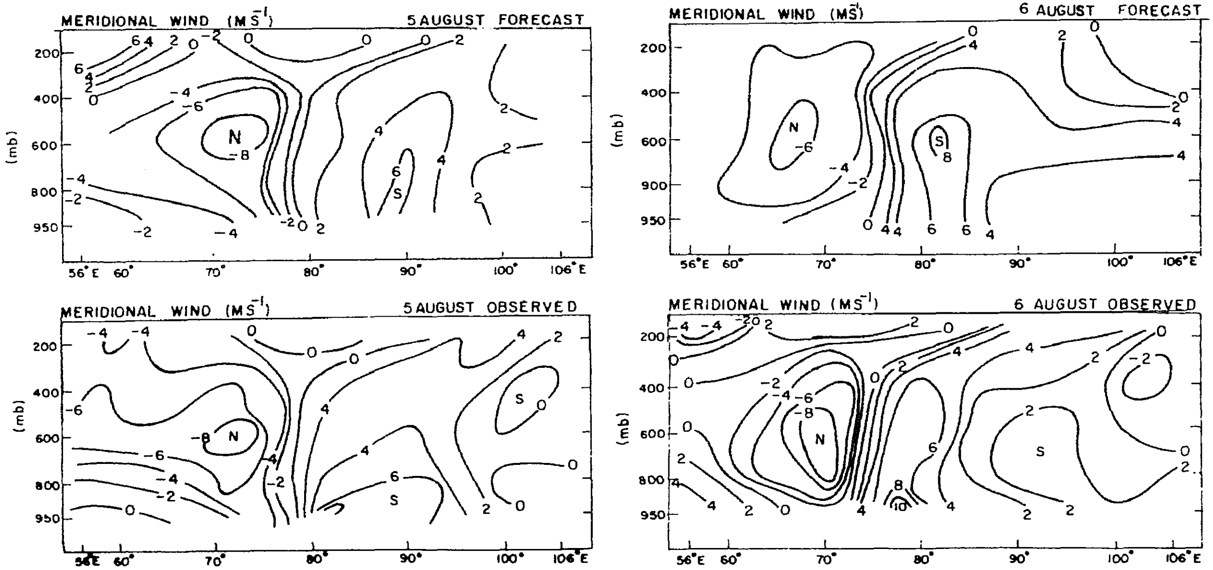

Figure 10. Observed versus predicted field of meridional wind v (m sec^{-1}) at 22°N for 0 and 24 hr. The cross-sections are on a zonal vertical plane.

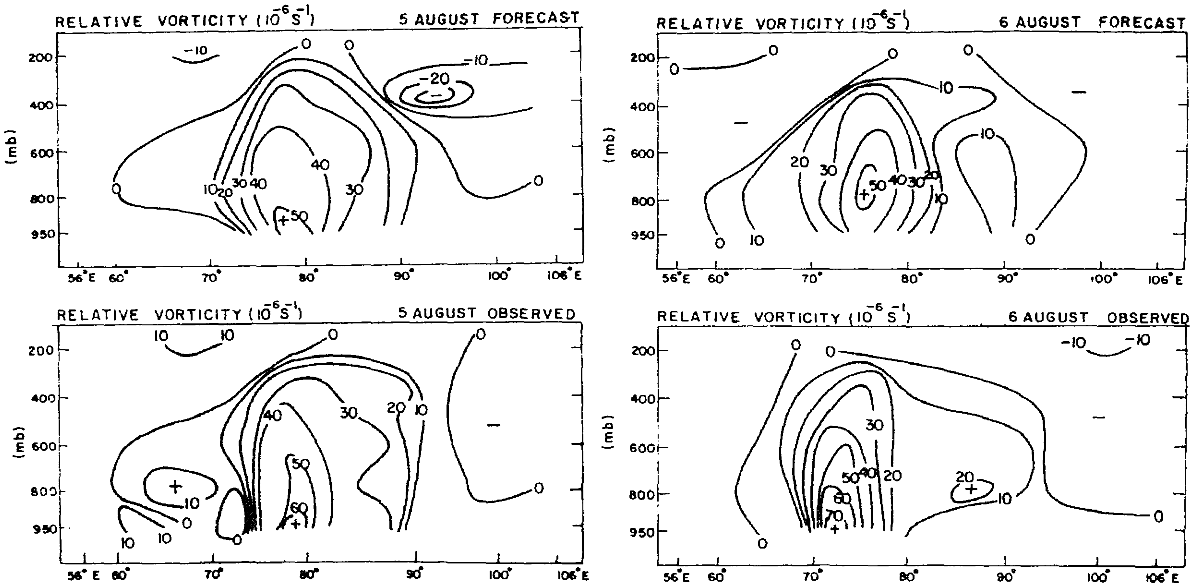

Figure 11. Observed versus predicted field of relative vorticity (sec^{-1}) at 22°N for 0 and 24 hr.

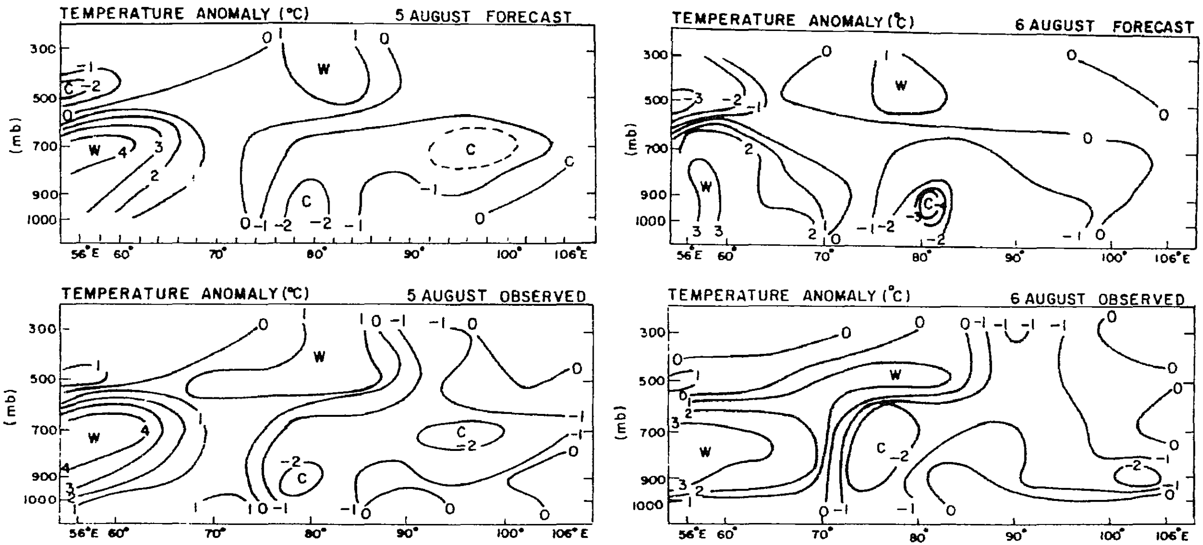

Figure 12. Observed versus predicted field of temperature anomaly (0_C) at 22°N for 0 and 24 hr.

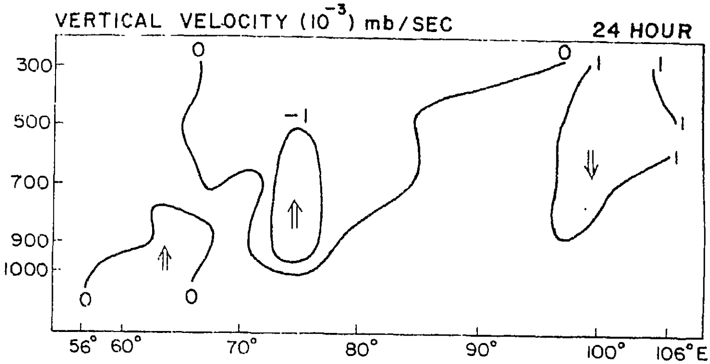

Figure 13. Predicted field of vertical velocity (10^{-3} mb sec^{-1}) at 22°N for 24 hr.

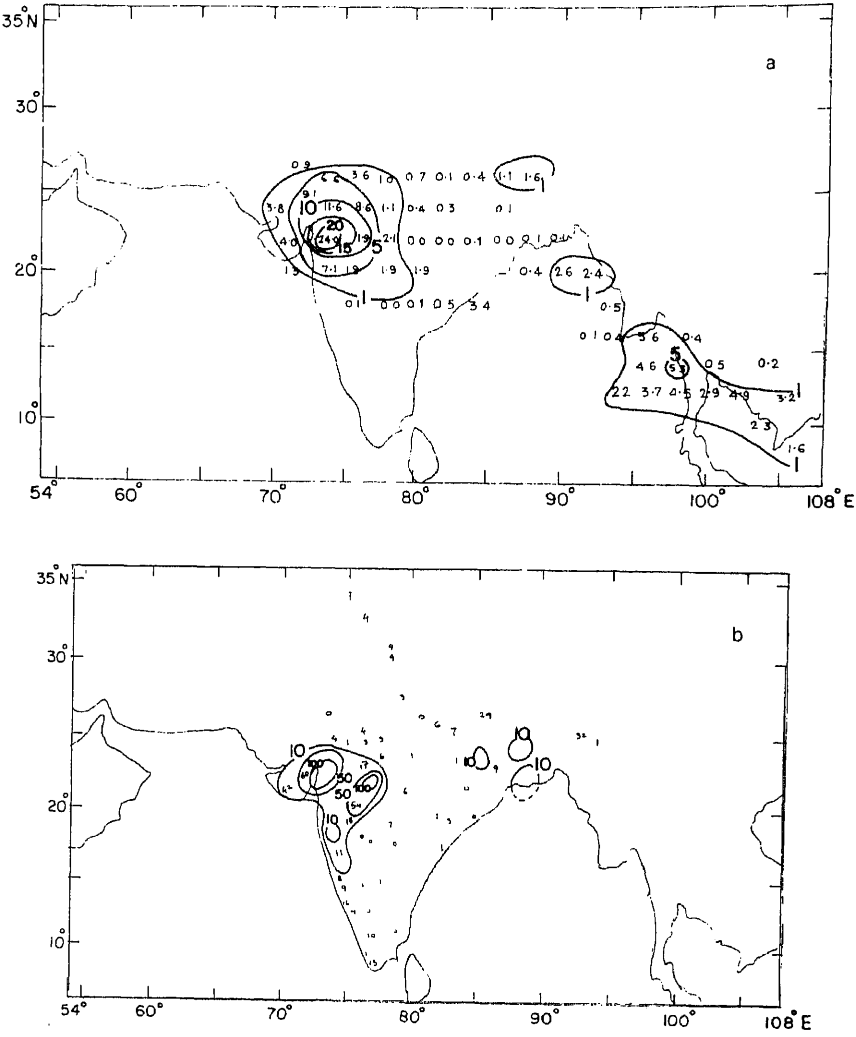

Figure 14. **a.** Predicted and **b.** observed, 24 hr total rainfall amounts (mm).

10. Concluding remarks

The model has produced reasonably good forecast upto 24 hours in respect of the circulation patterns, movement of the cyclonic system, cold core in the lower troposphere and warm core above the surface storm and the precipitation region, and beyond that damped significantly. The intensity of wind and vertical velocity are generally found weaker than the actual, particularly over the cyclonic circulation. The rainfall rates are very much underestimated by the model.

Although the model has produced a reasonably good forecast, it is necessary to point out its deficiency. The model suffers severely from the artificial specification of lateral boundary conditions. The tropical quasi-stationary long waves are a major source of energy for short-waves and the rate of energy transfer from longer waves to synoptic and subsynoptic scale waves is found to be quite large even in the time scale of a few days. For a realistic forecast of the synoptic scale of motion, the interaction of shorter waves with longer waves in model atmosphere should be taken into consideration. This could be accomplished by using a high resolution global model with sophisticated scheme of physical processes. Alternately, the boundary data of the regional model could be provided by the solution of a global model in which the regional model is nested. A third alternative could be to extend the domain of regional model in the east-west and north-south directions to ensure the interaction of different scales. In the present experiment, none of the above could be accomplished mainly due to limited computing facility. Another shortcoming of the model which is considered important is the oscillation of the divergence field during integration. After a few sensitivity experiments, it was noted that the present dynamic initialization which was carried out on limited domain is not capable of suppressing the inertial oscillation completely. This is a severe drawback of the model which is again closely linked with the lateral boundaries. As pointed out in §9.3 the rainfall rates are underestimated by the model. This could be due to unrealistic moisture analysis particularly in the lower troposphere, lack of proper resolution in the planetary boundary layer, weak vertical velocity and to some extent, underestimation of convective rainfall by the scheme of parametrization of cumulus convection in the region where convective rains are predominant. The weak vertical velocity and slow westward propagation of the cyclonic system are to a large extent due to complete absence of orography from the model. Furthermore, the regional model has coarse resolution in the horizontal and vertical directions and should have one more level in the planetary boundary layer and a horizontal grid size of 100 km. To handle the smooth orography effectively, the model should have the earth's surface with detailed orography as a coordinate surface (Phillips 1957). Some of these problems will be examined in future studies.

Acknowledgements

The author thanks Dr Bh V Ramana Murty and Shri D R Sikka for their keen interest. Part of the work was done by the author as WMO Fellow at Meteorological Research Institute, Tsukuba, Japan. He thanks Dr M Yamasaki and Mr H Ohnishi for their helpful discussions in programming the model physics. Thanks are due to Shri A Bandyopadhyay for assistance.

List of symbols

C_p	specific heat of air at constant pressure
F_q	sub grid scale diffusion of water vapour
F_T	sub grid scale diffusion of heat
F_u	horizontal diffusion of u-momentum
F_v	horizontai diffusion of v-momentum
f	Coriolis parameter
f^*	$f-m^2u\dfrac{\partial}{\partial y}\left(\dfrac{1}{m}\right)$
f_0	Coriolis parameter at 22°N
g	acceleration due to gravity
H	vertical eddy flux of sensible heat
M	sum of precipitation and evaporation
m	map factor
p	pressure
q	specific humidity
R	gas constant for dry air
T	temperature
T_s	convective cloud temperature
T_v	virtual temperature
t	time
u	zonal wind speed positive towards east
u_{ob}	observed zonal wind speed
v	meridional wind speed positive towards north
v_{ob}	observed meridional wind speed
W	vertical eddy flux of water vapour
x	coordinate axis towards east
y	coordinate axis towards north
z	geopotential height
β	Rossby parameter $\left(\equiv\dfrac{\mathrm{d}f}{\mathrm{d}y}\right)$
θ	potential temperature
τ	eddy stress vector
ϕ	geopotential
ψ	stream function
ω	vertical p-velocity
ω_s	vertical p-velocity at the surface
$\dfrac{\mathrm{d}Q}{\mathrm{d}t}$	diabatic heating

References

Asselin R 1972 *Mon. Weather Rev.* **100** 487

Bedi H S, Datta R K and Krichak R L 1976 *Meteorol. Gidrol.* **5** 39 (in Russian)

Das P K and Bedi H S 1978 *Indian J. Meteor. Hydrol. Geophys.* **29** 375

Electronic Computation Centre JMA 1980 Outline of the operational numerical weather prediction at JMA, Tokyo, 21 pp

Kanamitsu M 1975 On numerical prediction over global tropical belt Report 75-1, Department of Meteorology, Florida State University, 97 pp

Kiangi P M R 1977 *Arch. Meteorol. Geophys. Bioklimatol.* **A26** 349

Krishnamurti T N, Kanamitsu M, Godbole R, Chang C B, Carr F and Chow J H 1976 *J. Meteorol. Soc. Jpn* **54** 208

Krishnamurti T N, Molinari J, Pan H L and Wong V 1977 *Pure Appl. Geophys.* **115** 1357

Kuo H L 1965 *J. Atmos. Sci.* **22** 40

Kuo H L 1974 *J. Atmos. Sci.* **31** 1232

Leith C E 1969 *Proc. WMO/IUGG symposium on numerical weather prediction, Tokyo* 1968 (Tokyo: Japan Meteorological Agency) Vol. 1, p. 41

Manabe S, Smagorinsky J and Strickler R F 1965 *Mon. Weather Rev.* **93** 769

Okamura Y 1975 *J. Meteorol. Soc. Jpn* **53** 175

Phillips N A 1957 *J. Meteorol.* **14** 184

Singh S S 1977 *Some aspects of prognostic and diagnostic studies of Indian summer monsoon.* Ph.D. thesis, Banaras Hindu University, Varanasi, India, 32–74

Singh S S 1983 A limited area five level primitive equation model, Scientific Report R-038, Indian Institute of Tropical Meteorology, Pune

Singh S S and Saha K R 1976 *Proc. of IITM Symp. on Tropical Monsoons, Pune, India* 1976 p. 43

Singh S S, Kulkarni A A and Sikka D R 1980 *Mon. Weather Rev.* **108** 1315

Temperton C 1976 *Q. J. R. Meteorol. Soc.* **102** 297

Winninghoff F J 1973 *Mon. Weather Rev.* **101** 79

Proc. Indian Acad. Sci. (Earth Planet. Sci.), Vol. 94, No. 2, July 1985, pp. 185–186.
© Printed in India.

Correction of the paper "A study of meteorite falls"

FRANS E WICKMAN and CARL D PALMER[†]

Department of Geology, Stockholm University, S-10691 Stockholm, Sweden

[†] Department of Geological and Geophysical Sciences, University of Wisconsin, Milwaukee, Wisconsin 53201, USA

The corrections refer to the paper "A study of meteorite falls" published in this journal (Wickman and Palmer 1979). Figure 3 (p. 263) of that paper shows that an empirical linear relation exists between the logarithm of the number of observed and recovered falls and a power function of the distance between the impact point and the witness, r. It is also stated that the power function is r^2, however, the correct power function is $r^{1/2}$. The theory presented in the paper is therefore not valid.

One of us (FEW) has considered a number of other approaches based on various random walk models. They all seem to result in the incorrect r^2 - relationship. The reason for this is that important factors have probably been neglected.

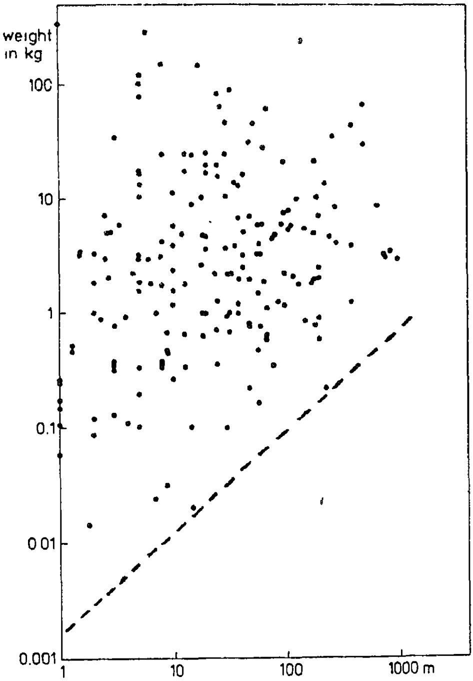

Figure 1. The weight of recovered meteorites from a fall as a function of the shortest distance between witnesses and impact points. The figure illustrates the fact that small falls are only recovered when they fall close to a witness. The line is only drawn to emphasize the two fields.

It would appear that the number of objects falling at the same time is such a factor. A shower will make it easier to find a piece in a given area. The first find also stimulates further search which possibly results in a smaller r - value. Yet elimination of the shower and semi-shower data from our statistics gives almost no change in the position or shape of the line in our figure 3.

Another factor is the size of the meteorite. Of those listed, the weight of the recovered objects varies between about 10 g and about 300000 g. Such reported values are in many cases minimum values. The visual and acoustic effects from the fall vary enormously for this mass range. It is likely that a greater effort to find the meteorite(s) is made when a spectacular fall occurs than when the effects are almost unnoticeable. In addition, the impact effects on the ground are much easier to observe for a large meteorite than for a small one. A study of the statistics of the falls used in the paper revealed noticeable effects (figure 1) in the range below 1000g. The dashed line is only drawn in order to emphasize the effect.

Other effects can certainly be of importance. At present it is impossible to decide whether the $r^{1/2}$ -relationship is fortuitous or can be derived from known principles. Nevertheless the empirical relationship is still valid. It is therefore of interest to have the functions and corrected parameters.

Survivor function: $\exp(-\beta r^{1/2})$;
Distribution function: $1-\exp(-\beta r^{1/2})$;
Density: $(\beta r^{-1/2}/2)\exp(-\beta r^{1/2})$;
where $\beta = 0.171\ \mathrm{m}^{-1/2}$;
Average distance: $2/\beta^2$ m or 69 m.

Reference

Wickman F E and Palmer C D 1979 *Proc. Indian Acad. Sci.* (*Earth Planet. Sci.*) **A88** 247

Interannual and long-term variability of the summer monsoon and its possible link with northern hemispheric surface air temperature

R K VERMA, K SUBRAMANIAM and S S DUGAM
Indian Institute of Tropical Meteorology, Pune 411 005, India

MS received 24 November 1983; revised 18 January 1985

Abstract. Some statistical properties of the summer monsoon seasonal rainfall for India during the last 100 years (1881–1980) are presented. The most recent decade of 1971–1980 shows the lowest value of standard-decadal average monsoon rainfall (86·40 cm) and is also characterised by the second highest value of coefficient of variation in monsoon rainfall (12·4 %). The combined last two standard-decadal period of 1961–1980 was the period of the largest coefficient of variation and the lowest average monsoon rainfall for India.

The possible influence of global climatic variability on the performance of the monsoon is also examined. Analyses of correlation coefficient show that a statistically significant positive relationship with a time-lag of about six months exists between monsoon rainfall and northern hemispheric surface air temperature. A cooler northern hemisphere during January/February leads to a poor monsoon.

All the major drought years during the last 3 decades had much cooler January/February periods over the northern hemisphere—1972 having the coldest January/February with a temperature departure of −0·94°C and the most disastrous monsoon failure.

Keywords. Variability of the summer monsoon; northern hemispheric surface air temperature; decadal averages; global climatic variability; monsoon failure; coefficients of variability; long range prediction.

1. Introduction

The Indian summer monsoon from June to September contributes about 75 % of the annual rainfall of the country and is, therefore, vital for the agricultural economy and prosperity of India. Although the definitive characteristic of the monsoon is a seasonal pattern, variations are observed on time-scales ranging from days to decades. Over larger time-scales, there are interannual variations in the seasonal precipitation leading to years of drought and flood. Variations on larger time-scales for periods upto or exceeding decades, have been revealed by more than hundred years of recorded data. The reasons for the variability on longer time-scales are not well understood and more study is required to gain insight into the physical factors responsible for such variations.

The period since 1960 has been characterised by large year-to-year variations in the summer monsoon activity over India. Increased variability has also been noticed in other climatic parameters all over the globe. Variability of monsoon on these longer time-scales has thus entered a new age of study in the context of the World Climatic Research Programme.

Monsoon is basically a thermally-driven large-scale circulation. It is, therefore, logical to expect that any global-scale thermal anomaly may have its influence on the monsoon. The present study deals with interannual and longer time-scale variability of the monsoon and its possible relationship with northern hemispheric (NH) surface temperature anomalies. For this purpose, summer monsoon seasonal rainfall for India has been taken as an index of the large-scale performance of the monsoon.

2. Data and analysis procedure

The data of summer monsoon seasonal rainfall for India were obtained from Parthasarathy and Mooley (1978) and updated to provide the recent 100-year series—from 1881 to 1980. The monsoon rainfall, in this series, has been computed by weighting the areas of the different meteorological sub-divisions. The time-series thus provides a long homogeneous series of monsoon rainfall.

The northern-hemispheric surface air temperature anomaly data for the same 100-year period of 1881 to 1980 have been obtained from the recent study of Jones *et al* (1982), which provides one of the most comprehensive, homogeneous and reliable temperature series of the northern-hemisphere. Using objective techniques, they have computed the monthly mean station data gridded on a 5° latitude by 10° longitude grid. The anomalies are computed with reference to optimum grid period of 1946–60 which has the best data coverage.

In the present study, we have analysed separately the two series to examine their year-to-year and long-term variability and have attempted to investigate a possible linkage between them.

3. Variability of the monsoon

Some aspects of long-term variability of monsoon rainfall were described earlier by Parthasarathy and Mooley (1976) and Banerjee and Raman (1976). Interannual variations in summer monsoon (June–September) rainfall of India for the period 1881–1980 are shown in figure 1. Monsoon performance is depicted in terms of percentage departure of rainfall from its long-term average. Taking the rainfall departure range of $\pm 10\%$ as the normal monsoon activity, extreme monsoon years are delineated by the values in excess of 10% and 20% departures. These departure values are almost equal to 1σ and 2σ respectively. There were fifteen major monsoon failures of which four (1899, 1918, 1972 and 1979) were the worst years when the rainfall departures were $\leqslant -20\%$ of the average, during the last 100 years. There were nine years of good monsoon in this period. Monsoon rainfall departures during the 1960s and 1970s showed a remarkable "Sawtooth" pattern (see figure 1) which is unique in the record and marks the last two decades as a period of unusual year-to-year variability.

Long-term variability of the summer monsoon during the past 100 years is analysed in terms of decadal statistics of rainfall and occurrence of extremes. Decadal variability is shown in table 1 (adapted from Parthasarathy and Mooley 1978, and updated). The following points are noteworthy: (a) The first two decades of the twentieth century were characterised by a low value of average rainfall ($\sim$ 87 cm). The decadal average thereafter increased progressively reaching a peak during 1941–1950 ($\sim$ 93 cm). It has, since then, been decreasing, reaching the lowest value ($\sim$ 86 cm) during 1971–1980 (b) Monsoon variability was high in the first two decades of the century, peaking at 13·6 % during 1911–1920. The variability was considerably low during the subsequent four-decades (1921–1960). The monsoon activity, since then, has shown increasingly large variability reaching a 12·4 % coefficient of variation in 1971–1980, the second highest value during the 100-year record. (c) Frequency of occurrence of extreme monsoons during different decades of the twentieth century is also shown in table 1 in the last two columns. In the first two decades of 1901–1920 there were as many as six major

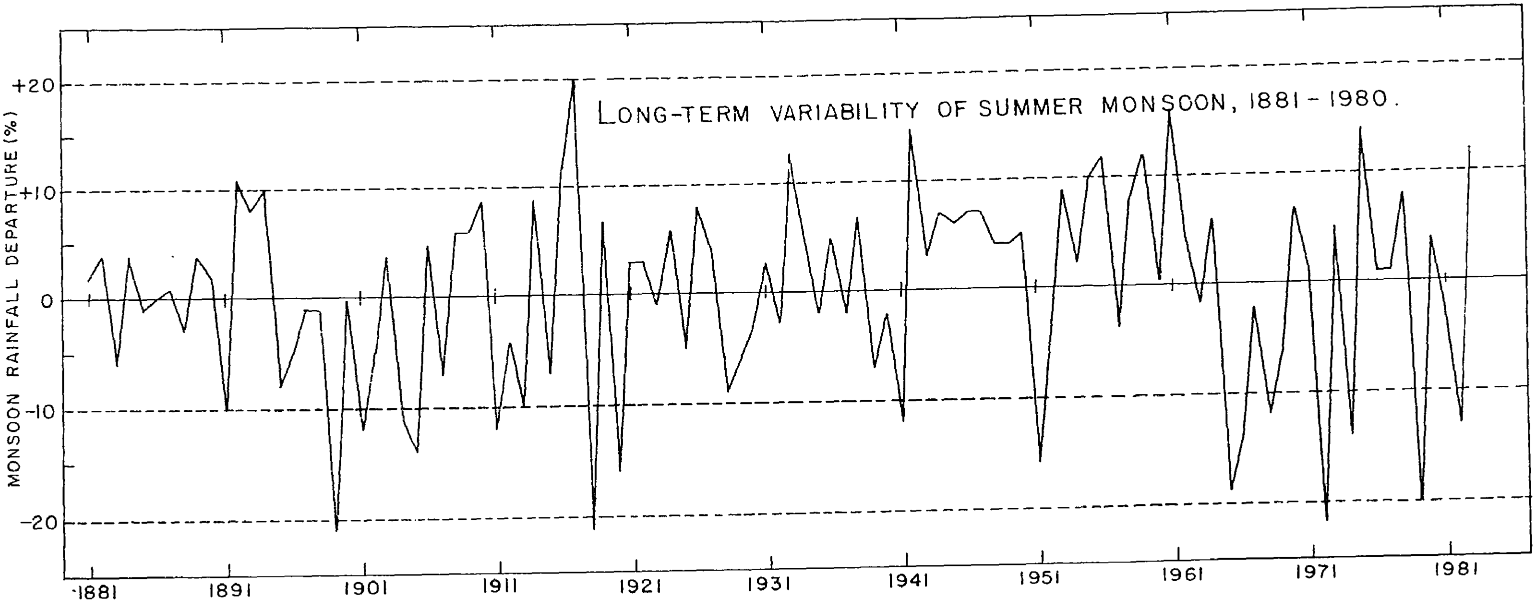

Figure 1. Summer monsoon (June–September) rainfall departure of India (%) for the 100 year period 1881–1980. Dotted lines of ±10% and ±20% are drawn to delineate years of extreme monsoon.

Table 1. Decadal variability of the summer monsoon: some statistics of the summer-monsoon rainfall of India (1881–1980) (after Parthasarathy and Mooley 1978, updated)

Decade	Average (cm)	Difference from long-term average of 88·75 (cm)	Standard deviation (cm)	Coefficient of variation (%)	Years of extreme monsoon	
					Bad (< −10% departure)	Good (> +10% departure)
1881–1890	89·61	+0·86	2·94	3·3	Nil	
1891–1900	87·01	−1·74	8·51	9·8	1899	1892
1901–1910	86·83	−1·92	7·95	9·2	1901, 1904, 1905	
1911–1920	86·89	−1·86	12·01	13·8	1911, 1918, 1920	1916, 1917
1921–1930	88·90	+0·15	4·76	5·4		
1931–1940	90·87	+2·12	5·23	5·8	Nil	1933
1941–1950	93·17	+4·42	5·90	6·3	1941	1942
1951–1960	91·40	+2·65	8·36	9·1	1951	1956, 1959
1961–1970	86·99	−1·76	−9·79	11·3	1965, 1966, 1968	1961
1971–1980	86·40	−2·35	10·74	12·4	1972, 1974, 1979	1975

monsoon failures. These decades were also characterised by low average rainfall and high coefficient of variation. This was followed by an epoch of a four-decadal period during which there were only two major monsoon failures (none during the decades of 1921–1930 and 1931–1940 and one each during the decades of 1941–1950 and 1951–1960). This epoch was also characterised by high average rainfall and low coefficient of variation. The two subsequent decades, 1961–1970 and 1971–1980, again witnessed a high frequency of monsoon failures numbering six, and was also characterised by low average rainfall and high coefficient of variation. Frequent occurrences of poor monsoons during epochs, broadly coinciding with the above mentioned epochs, were also reported by Joseph (1976) in his study of climate changes in monsoon and cyclones during 1891–1974.

4. Variability of northern-hemispheric surface air temperature

During the recent two decades there has been considerable interest in the long-term variability of global/hemispheric surface temperature because of its impact on climatic change. Some of the recent studies, which have estimated the interannual and long-term variability of surface temperature are by Lamb (1975), Mitchell (1975), Budyko (1977), Angell and Korshover (1978), Barnett (1978), and Yamamoto and Hoshiai (1979). Jones *et al* (1982) recently analysed the northern hemispheric surface temperature over the period 1881–1980. Within statistical uncertainties, their series appears to be homogeneous and representative of changes over the northern hemisphere.

In figure 2, we reproduce the figure of Jones *et al* depicting the time variation of northern hemispheric annual mean surface temperature anomalies from the 1946–60 mean. We have drawn two vertical dotted lines to delineate the three distinct epochs: (a) 1881–1920: A 40-year epoch of cooler northern hemisphere during late nineteenth and early twentieth century. (b) 1921–1960: A 40-year epoch of warmer northern hemisphere during mid-twentieth century (peaked in 1938). (c) 1961–1980: A current epoch of cooler northern hemisphere.

Table 2 shows decadal variability of annual and seasonal means of northern hemispheric surface air temperature anomaly in terms of mean and standard deviations. The annual mean shows an abrupt increase in the decadal mean from the

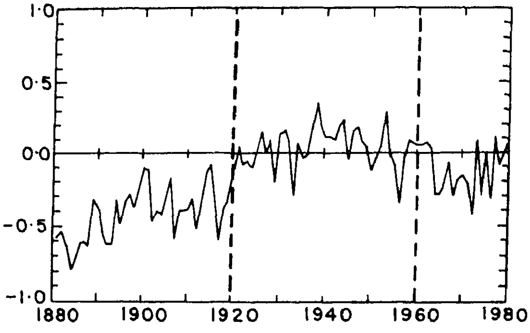

Figure 2. Northern hemisphere annual mean surface temperature anomalies from the 1946–1960 mean (°C) after Jones *et al* (1982). Vertical dotted lines are drawn to delineate three distinct climatic epochs.

Table 2. Decadal variability of annual and seasonal mean northern-hemispheric surface air temperature anomaly (1881–1980). Reference period 1946–60 (data source: Jones *et al* 1982)

Decade	Annual		Winter (Dec., Jan., Feb.)		Spring (Mar., Apr., May)		Summer (Jun., Jul., Aug.)		Autumn (Sep., Oct., Nov.)	
	Mean	σ	Mean	σ	Mean	σ	Mean	σ	Mean	σ
1881–1890	−0·57	0·15	−0·79	0·41	−0·46	0·29	−0·44	0·18	−0·61	0·17
1891–1900	−0·39	0·18	−0·76	0·54	−0·36	0·29	−0·21	0·13	−0·26	0·28
1901–1910	−0·36	0·14	−0·41	0·24	−0·30	0·26	−0·36	0·20	−0·35	0·22
1911–1920	−0·31	0·17	−0·44	0·43	−0·31	0·25	−0·23	0·18	−0·29	0·22
1921–1930	+0·00	0·12	−0·11	0·31	−0·03	0·18	+0·02	0·11	+0·09	0·15
1931–1940	+0·08	0·17	+0·03	0·28	+0·03	0·21	+0·12	0·12	+0·14	0·24
1941–1950	+0·09	0·12	+0·03	0·32	+0·14	0·10	+0·03	0·08	+0·16	0·15
1951–1960	+0·01	0·17	+0·11	0·28	−0·01	0·25	+0·03	0·15	−0·01	0·20
1961–1970	−0·13	0·15	−0·17	0·36	−0·08	0·21	−0·13	0·13	−0·10	0·20
1971–1980	−0·10	0·20	−0·18	0·31	+0·05	0·26	−0·10	0·19	−0·16	0·20
Total period 1881–1980	−0·17	0·26	−0·28	0·45	−0·13	0·30	−0·13	0·23	−0·13	0·32

first four decades of 1881–1920 compared to the subsequent decades 1921–1960. This is again followed by a relatively lesser but substantial decline during the decades 1961–1980. Decadal standard-deviations of annual mean anomaly remain of the same order throughout ten decades but is highest in the last decade 1971–1980.

Decadal variabilities of different seasons, more or less, follow the annual variability pattern. Winter, however, seems to be different, particularly during the cooler epochs. During these epochs the decadal mean anomaly and the decadal standard-deviation are maximum during winter.

5. Relationship between summer monsoon and NH surface air temperature

Figure 3 shows correlation coefficients between northern hemispheric monthly means of surface air temperature anomalies and summer monsoon rainfall departure of India

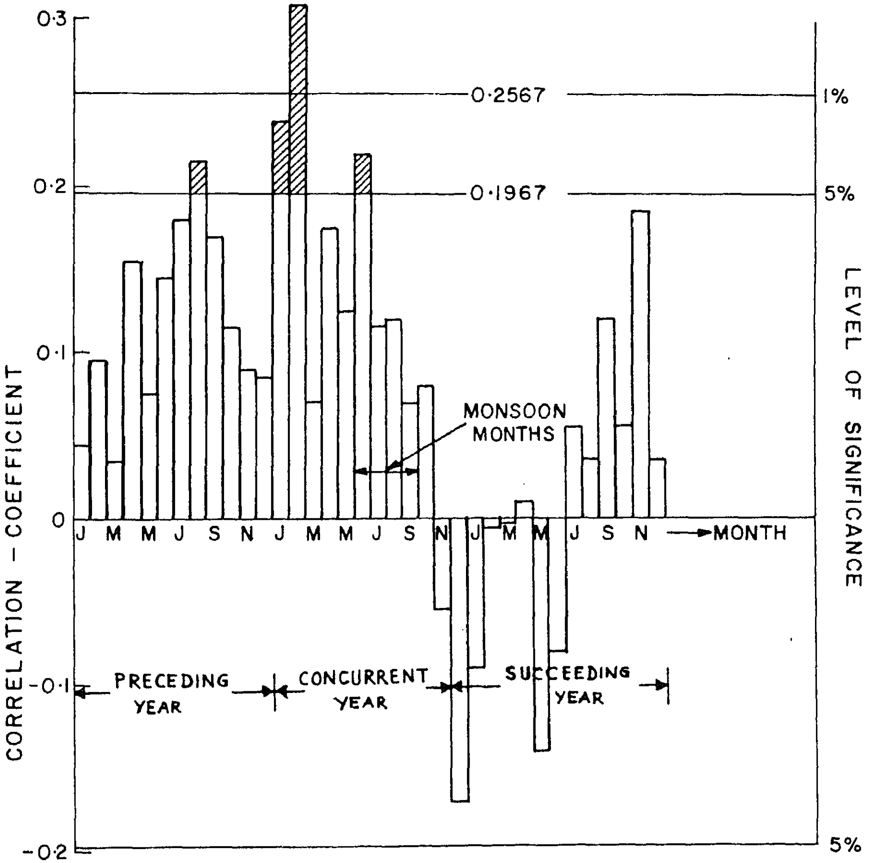

Figure 3. Correlation between summer monsoon rainfall departure of India and northern hemispheric monthly means of surface air temperature anomalies for 1881–1980. Monsoon rainfall is correlated successively with mean monthly temperature anomalies starting from January of the preceding year through December of the succeeding year.

for the 100-year data series of 1881–1980. For this purpose, monsoon rainfall departures of 100 years are correlated successively with (a) 100 values of monthly mean temperature anomalies of all the 12 months of the preceding year, (b) all the 12 months of the concurrent year and (c) all the 12 months of the succeeding year. Correlation coefficients are shown as ordinates along with lines of 5 % and 1 % levels of significance drawn to delineate significant correlations. There are only four months showing correlations higher than 5 % significant level. All these correlations are positive. These are: (a) August of the preceding year (5 % significant level) (b) January of the concurrent year (5 % significant level), (c) February of the concurrent year (1 % significant level) and (d) June of the concurrent year (5 % significant level). Correlation with combined January–February temperature anomaly is also very significant (at 1 % level).

To test the stability of the relationship, we have split the 100-year series into two equal series and computed the correlations similarly. Figure 4 depicts the correlations in the two split-up series. The second half period (1931–1980) more or less shows the same pattern of correlation as the 100-year series. The first half period (1881–1930), however, does not show any significant correlation. The time variation of relationship as shown in figure 5e seems to have some order and is not random. The physical mechanism responsible for this variation must be very complex and needs further investigation. It

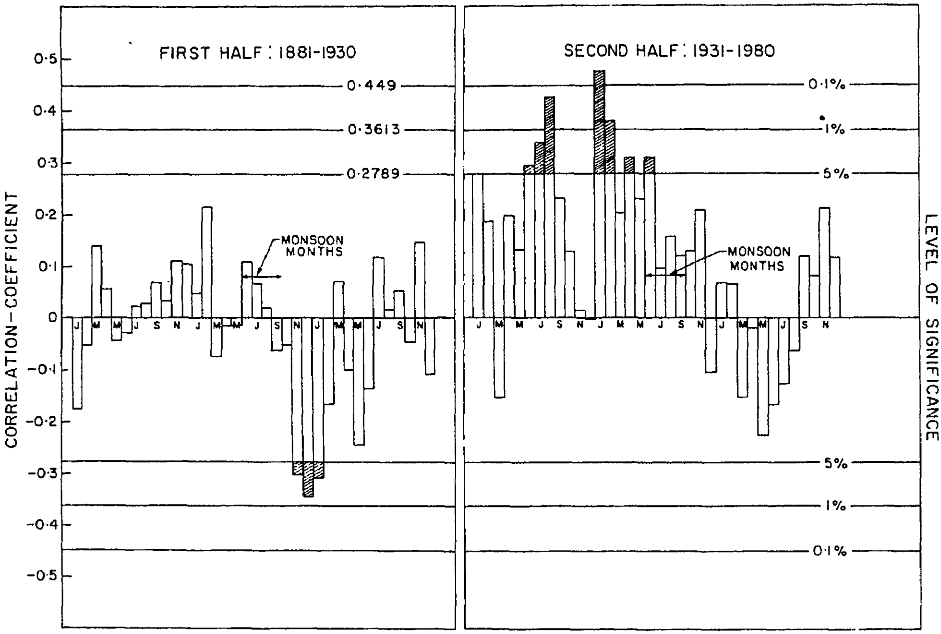

Figure 4. As in figure 3, except that the 100-year series is split into two equal series of 50 years.

Figure 5. Decadal variability of: (**a**) monsoon rainfall difference, (**b**) coefficient of variation of monsoon rainfall, (**c**) frequency of monsoon failures, (**d**) northern hemispheric surface air temperature anomaly (annual mean), and (**e**) correlation coefficient between monsoon rainfall and NH surface temperature during January–February: 1881–1980.

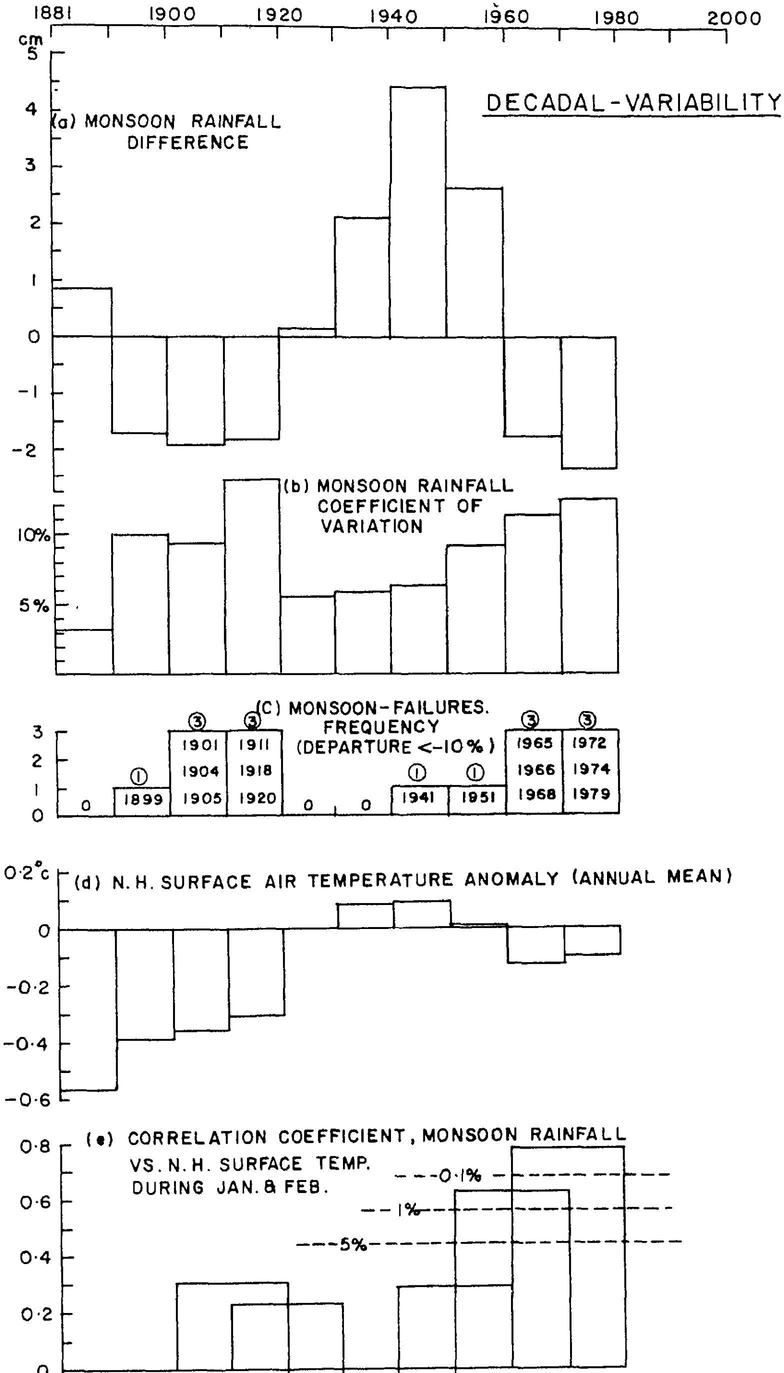
DECADAL-VARIABILITY
1881
1900
1920
1940
1960
1980
2000
cm
5
4
3
2
1
0
-1
-2
(a) MONSOON RAINFALL DIFFERENCE
(b) MONSOON RAINFALL COEFFICIENT OF VARIATION
10%
5%
(C) MONSOON-FAILURES. FREQUENCY (DEPARTURE <-10%)
3
2
1
0
0
①
1899
③
1901
1904
1905
③
1911
1918
1920
0
0
①
1941
①
1951
③
1965
1966
1968
③
1972
1974
1979
(d) N.H. SURFACE AIR TEMPERATURE ANOMALY (ANNUAL MEAN)
0·2°c
0
-0·2
-0·4
-0·6
(e) CORRELATION COEFFICIENT, MONSOON RAINFALL VS. N.H. SURFACE TEMP. DURING JAN. & FEB.
0·8
0·6
0·4
0·2
0
0·1%
1%
5%

may be noted here that many meteorological predictors have shown similar types of variation in their relationship with the monsoon rainfall. Consistent high correlation (CC varying from 0·5 to 0·8) for the past three decades, as shown in figure 5e, suggest that during the current epoch the relationship can be treated as sound.

6. Predictive potential of the relationship: long-range forecast of monsoon failure over India

The statistical relationship between monsoon and NH surface air temperature, as discussed in §5 indicates that an appreciably cooler northern-hemisphere during: (a) the preceding August (b) just past January and February and (c) concurrent June, may lead to deficient summer monsoon rainfall over India. Of these, the most important for prediction purposes are February and combined January–February, both showing positive correlation, significant at 1% level. It is relevant to refer here to the pioneering work of Blanford (1884) who found that the excessive winter and spring snowfall in the Himalayas was prejudicial to the subsequent monsoon rainfall of India. Blanford used this as one of the important factors for long-range forecasting of monsoon seasonal rainfall.

Considering the highly significant positive relationship between monsoon activity and the winter surface temperature anomaly over the northern-hemisphere, the most logical questions for long-range forecasting would obviously be what critical value of temperature anomaly should be considered as 'appreciably cooler' leading to possible failure of monsoon and also, how well the criterion performs when tested against an independent data-set. An attempt is made to answer these questions in the following paragraphs. The results are depicted in table 3.

Based on results discussed so far, the stable climate period of 1921–1950 is taken as the reference period. One standard deviation (σ) of winter time NH surface temperature anomaly for this reference period is taken as the critical value of anomaly. A period is defined as extreme warm or extreme cold if the temperature anomaly is $\geqslant +1\sigma$ or $\leqslant -1\sigma$ respectively. This criterion is applied to years of period independent of and after reference period (i.e. 1951–1980); and extreme years are delineated.

In table 3 standard-deviation values for January, February, January–February combined and winter (December, January, February), along with delineated extreme years are shown. Amongst these extreme thermally anomalous years, extreme monsoon years are also marked. Apparently there is no skill in forecasting good monsoon years as there is hardly any correspondence between a good monsoon year and an extreme warm year. But there is an extremely good correspondence between a bad monsoon year and a year of extreme cold winter during the past 3 decades.

All the bad monsoons of the last 3 decades (1951–1980) are accounted for when the criterion is applied with the January–February and winter temperature anomalies. The best result is obtained with the January–February temperature anomaly, i.e. when January–February surface temperature anomaly over the northern-hemisphere is that of "appreciably-cooler" category ($\leqslant -0{\cdot}4$°C); the ensuing monsoon is likely to be bad. However, there were also two such years, when the temperature anomalies were less than the critical values but the years were not bad monsoon years. Nevertheless, the relationship may be used for guidance in long-range forecasting of monsoon failure

Table 3. Standard deviation of winter NH surface air temperatures during the stable climate period of 1921–1950; and years of extreme temperature anomalies during the period independent of and after the sample period. Temperature anomaly in °C, shown in brackets.

		January	February	Jan. and Feb.	Winter (Dec., Jan., Feb.)
Standard Deviation σ(°C)		0·47	0·50	0·40	0·30
		1955 (+0·65)	1953 (+0·54),		
			1963 (+0·65)	1958 (+0·54)	●1956 (+0·39)
	Warm		1960 (+0·61),		1958 (+0·39)
	$\geqslant +1\sigma$	1958 (+0·74)	1973 (+0·59)		1980 (+0·37)
Extreme years		*1951 (−0·79)	*1951 (−0·79)	*1951 (−0·79)	*1951 (−0·51)
		1954 (−0·67)	*1965 (−0·54)	*1965 (−0·43)	*1965 (−0·46)
	Cool	*1966 (−0·72)	1967 (−0·55)	*1966 (−0·40)	*1966 (−0·31)
	$\leqslant -1\sigma$	1967 (−0·47)	1969 (−0·86)	1967 (−0·51)	1967 (−0·44)
		*1968 (−0·89)	*1972 (−0·71)	*1968 (−0·59)	*1968 (−0·32)
		1969 (−0·72)	*1979 (−0·88)	1969 (−0·79)	1969 (−0·81)
		*1972 (−1·16)		*1972 (−0·94)	1971 (−0·45)
		*1974 (−0·67)		*1974 (−0·57)	*1972 (−0·70)
				*1979 (−0·48)	*1974 (−0·44)
					*1979 (−0·39)

● Good monsoon (rainfall departures > 10%); *bad monsoon (rainfall departure < −10%).

7. Conclusions

The conclusions drawn in the present study are summarised in the following paragraphs as depicted through histograms (a)–(e) in figure 5 on the basis of the decadal variability in monsoon activity on one side and NH surface temperature on the other. Their relationship and variability in different epochs have special significance.

(a) The difference of the summer monsoon rainfall in India from its long-term average is an index of the large-scale performance of the monsoon. Its decadal variability is shown in figure 5a. Monsoon rainfall on a decadal average, was relatively less during the early part of this century (1891–1920), appreciably more during the mid-part (1931–1960) and decreased substantially during the last two decades (1961–1980).

(b) The coefficient of variation is an index of the variability of the monsoon rainfall. Its decadal variation is shown in figure 5b. Monsoon activity, on a decadal average, had large variability during the early part of this century, comparatively less variability in the middle and has been increasing since then. The combined last two decadal periods of 1961–1980 witnessed the largest variability during the last one hundred years.

(c) Decadal frequency of the large scale failure of monsoon rainfall leading to droughts over India is shown in figure 5c. There were frequent monsoon failures during the early part of the century (six years during 1901–1920), they were very much less frequent during the mid-century (only two years during 1921–1960) and have again become more frequent during the last two decades (six years during 1961–1980).

(d) Decadal variation of annual mean surface air temperature over the northern hemisphere is representative of global climatic changes and trends. This is shown in figure 5d. The northern hemisphere as a whole, had been relatively cooler during the early part of this century, became warmer during the mid-century (reaching a peak around 1940), and has been cooler again during the last two decades. Winter is characterised by the largest mean anomaly as well as the largest variability in temperature.

(e) A direct relationship seems to exist between monsoon and northern hemispheric winter surface temperature, the latter probably acting as one of the dominant forcings for the monsoon. The relationship is statistically very significant (at 5% level with January temperature anomaly and at 1% level with February and January–February combined temperature anomalies).

The relationship has been more significant during the last two decades of 1961–1980 (at 0·1% level with various combinations of winter months). The highest correlation coefficient of 0·77 is obtained with the temperature anomaly of the January–February period. In figure 5e, the two-decadal variation in correlation coefficient with the January–February temperature anomaly is shown. There appears to be some order in the variations of the relationship in different climatic epochs reaching a positive peak during the current cooler epoch.

The relationship assumes special significance because of the 6-months difference between the monsoon peak activity (July–August) and the NH surface temperature anomaly (January–February) that is significantly related with it in the present epoch. The relationship, thus, may provide guidance in long range forecasting of the monsoon, particularly of its failure about 3 to 4 months before its onset in June.

Acknowledgements

The authors are grateful to Dr R Ananthakrishnan for valuable suggestions and to Dr Bh V Ramana Murty and Mr D R Sikka for encouragement.

References

Angell J K and Korshover J 1978 *Mon. Weather Rev.* **106** 755
Banerjee A K and Raman C R V 1976 IMD Sc. Rep. No. 76/6
Barnett T P 1978 *Mon. Weather Rev.* **106** 1353
Blanford H F 1884 *Proc. R. Soc. (London)* **37** 3
Budyko M I 1977 *Tellus* **29** 193
Jones P D, Wigley T M L and Kelly P M 1982 *Mon. Weather Rev.* **110** 59
Joseph P V 1976 Proceedings of the IITM symposium on tropical monsoon, Pune, September 1976, pp. 378
Lamb H H 1975 WMO Report No. 421, pp. 473
Mitchell J M Jr 1975 *The changing global climate* (ed.) S P Singer (Dordrecht: D Reidel) 149
Parthasarathy B and Mooley D A 1978 *Mon. Weather Rev.* **106** 771
Yamamoto R and Hoshiai M 1979 *Mon. Weather Rev.* **107** 1239

Proc. Indian Acad. Sci. (Earth Planet. Sci.), Vol. 94, No. 3, November 1985, pp. 199–210.
© Printed in India.

Relationship between all-India summer monsoon rainfall and southern oscillation/eastern equatorial Pacific sea surface temperature

D A MOOLEY, B PARTHASARATHY and N A SONTAKKE
Indian Institute of Tropical Meteorology, Pune 411 005, India

MS received 24 November 1983; revised 15 March 1985

Abstract. The interannual variability of all-India summer monsoon (June to September) rainfall and its teleconnections with the southern oscillation index (SOI) and sea surface temperature (SST) anomaly of the eastern equatorial Pacific ocean have been examined for the period 1871–1978 for different seasons (i.e., winter, spring, summer and autumn). The relationship (correlation coefficient) between all-India summer monsoon rainfall and SOI for different seasons is positive and highly significant. Further examination of 10-, 20- and 30-year sliding window lengths' correlations, brings out the highly consistent and significant character of the relationships. The relationship between all-India monsoon rainfall and SST for different seasons is negative and is significant at 1 % level or above. Drought years are characterised by negative anomalies of SOI and positive anomalies of SST and vice versa with flood years. The relationship between SOI and SST is negative and significant at 0.1 % level.

The relationships between all-India summer monsoon rainfall, SOI and SST are expected to improve our understanding of the interannual variability of the summer monsoon.

Keywords. All-India rainfall; southern oscillation; Pacific sea surface temperature; sliding correlation.

1. Introduction

The agricultural economy of India with its large growing population is closely linked with the summer monsoon (June to September) which gives 75 to 90 % of the annual rainfall. The Indian summer monsoon is rightly described as the life and soul of the country because the livelihood of a large part of the country depends upon timely and adequate rains. Monsoon rainfall exhibits considerable year-to-year variations in its occurrence and sometimes produces calamities like droughts and floods. The large-scale behaviour of the monsoon over the Indian sub-continent can be regarded as an important manifestation of a planetary-scale phenomenon. The southern oscillation (SO) is one of the most important single mechanisms, especially in the tropical zone of the Pacific and Indian ocean sectors, responsible for fluctuations of the atmospheric circulation with climatic variations of irregular period about one to five years. Growing interest in understanding and in estimating the monsoon rainfall over India has recently resulted in many studies on the possible relationship between the amount and the distribution of the Indian monsoon rainfall with antecedent regional and global circulation features. A revival of interest in the SO and the related SST, El Nino phenomenon has occurred recently in connection with the identification of climatic regimes and atmospheric teleconnections. In view of this a detailed study has been made between the interannual variations of Indian summer monsoon rainfall and southern oscillation and east equatorial sea surface temperature during the period

2. Details of data

2.1 *Indian summer monsoon rainfall*

306 stations, one from each of the districts in the plain regions of India and distributed fairly uniformly over the country were selected to form the network of raingauge stations used in this study. The relevant rainfall data for the selected raingauge stations were collected from the records of the Additional Director General of Meteorology (Research), Poona (for details of data refer Mooley *et al* 1981, 1984). These stations have rainfall data from 1871 onwards. The hilly region of the country parallel to the Himalayan mountain range has not been considered in view of meagre raingauge network, and low areal representation of a raingauge in a hilly area. The area considered measures $2{\cdot}88 \times 10^6$ km^2 which is about 90% of the country. Summer monsoon season (June to September) area-weighted rainfall series was prepared for India as one unit (to be referred to as all-India series) by assigning district area as the weight for each raingauge station for the period 1871–1978. These summer monsoon rainfall data series for the period 1871 to 1978 have been utilized in the present study and is shown in figure 1. The mean all-India summer monsoon rainfall is 85·31 cm and it is 78% of the annual amount. The standard deviation of the series is 8·29 cm and coefficient of variation, 9·5%. Swed and Eisenhart's test of runs above and below the median shows that the series is homogeneous. The auto-correlation of the series is −0·116 which is too low to suggest any persistence in the series. Chi-square test indicates that the rainfall series, 1871–1978, is normally distributed (for further details refer Mooley and Parthasarathy 1984; Parthasarathy 1984).

2.2 *Southern oscillation index* (SOI)

The southern oscillation is an important mode (circulation) of the tropical atmosphere generally characterized by the exchange of air between the eastern (predominently land) and western (predominently ocean) hemispheres; the sea level pressure anomalies in the Indonesian–Australian region are negatively correlated with those in the southeast Pacific ocean high pressure belt. The term southern oscillation (SO) was first introduced by Walker and Bliss (1932, 1937). It is an important tropical circulation and is named by Bjerknes (1969) as east-west Walker circulation. A number of studies have been made to explore the relationship between the Indian summer monsoon rainfall and SO by many workers. Some of the noteworthy studies in this direction are Walker (1923, 1924), Troup (1965), Sikka (1980), Angell (1981), Pant and Parthasarathy (1981), Mooley and Parthasarathy (1983b) and Parthasarathy and Pant (1984, 1985).

Wright (1975) devised a pressure index, called the southern oscillation index (SOI), making use of sea level pressure data of eight stations (Capetown, Bombay, Djakarta, Darwin, Adelaide, Apia, Honolulu and Santiago) in the latitude zone of 30°S to 20°N. This index is considered to meet the requirement of an estimator of the tropical east-west circulation (Fleer 1981) and to interpret well the behaviour of the SO in every season for the period 1851 to 1974 and we have made use of this series in the present study.

The monthly SOI series for the period 1871–1974, have been combined into standard seasons relative to Indian summer monsoon, June, July, August and September (JJAS) as

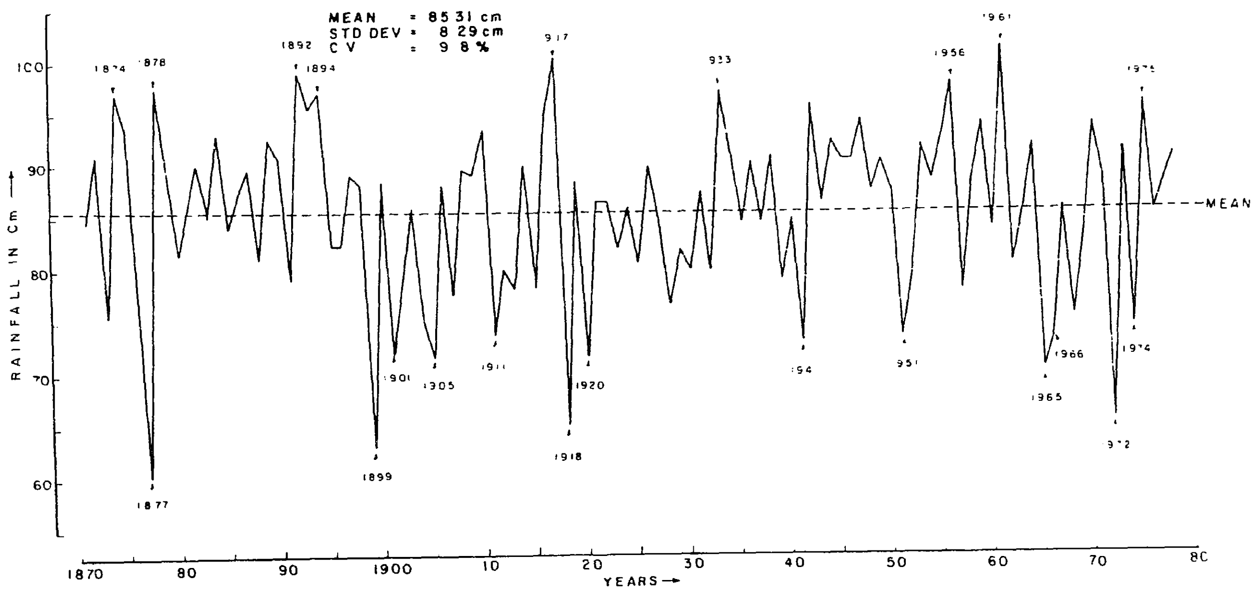

Figure 1. Summer monsoon (June to September) rainfall of India taken as one unit during 1871–1978

monsoon season, SOI-JJA, concurrent monsoon season (lag 0), (iv) the autumn SOI-SON, one season after monsoon (lag + 1) and (v) the succeeding winter seas DJF, two seasons after monsoon (lag + 2). The SOI series i.e. SOI-DJF, SOI-MAM, SOI- SOI-SON have been examined for homogeneity by Swed and Eisenhart's test a series are generally found to be homogeneous at 5% level. The auto-correlat these series do not indicate any persistence.

2.3 *Sea surface temperature* (*SST*) *anomalies in the equatorial eastern Pacific ocean*

The interaction between the atmosphere and the sea at the air-sea interface result coupling of the circulation systems of the atmosphere and the ocean. Since 70% earth's surface is covered with water and changes in SST are much slower comp the atmospheric fluctuations, it is obvious that the interannual variability of SST responsible for the variability of the atmospheric circulation and may reflect we rainfall regimes.

Studies by Khandekar (1979), Weare (1979), Joseph (1981), Pisharoty Anjaneyulu (1981), Ramesh Babu *et al* (1981), Webster (1981), Newell *et al* (19 Rasmusson and Carpenter (1982), have brought out the role of SST in tropi equatorial oceans in modifying the atmospheric circulation and in the distribu cloudiness and precipitation. Bjerknes (1969), Rowntree (1972), Shukla (1975) and Chervin (1978) and Keshavamurthy (1982), used general circulation mo study the response of the atmosphere to a fixed SST anomaly in the tropical Pac have shown that the atmosphere is much more closely coupled to the state underlying ocean in the tropics. Therefore, it is proposed to examine the relati between the all-India summer monsoon and SST anomaly of different seas eastern equatorial Pacific ocean.

Angell (1981) has prepared the seasonal SST anomaly values, which are averag the wide area of 0–10°S; 180–90°W of the equatorial Pacific ocean and wh available for the long-period from 1860 to 1979. We have utilized these data to e the relationship with Indian monsoon rainfall. The SST anomaly series for d seasons i.e. SST-DJF, SST-MAM, SST-JJA and SST-SON, for the period 1871–1978 ha examined for homogeneity. These have been found to be homogeneous at 5 There is no persistence noticed in the series.

3. Relationship with All-India summer monsoon rainfall

In order to understand the association between the Indian summer monsoon and the SOI/SST we adopted the following procedure (i) correlation analysis b the two series and (ii) examination of SOI/SST values for extreme, drought o rainfall years during the period.

Persistence or high auto-correlation in the individual series should be con while assessing the significance of cross-correlation between concurrent (Quenouille 1952; Scirremammano 1979). It is already seen from the earlier s that there is no persistence in any of the series considered and therefore there is no change in the degrees of freedom involved in assessing the significance of correlation coefficient (CC) between the two data series, that is $(N-2)$, where N is the number of years.

3.1 *Southern oscillation*

The CC between all-India rainfall series and SOI for the different seasons are given in table 1. The CC values for all seasons (except for SOI-DJF) are positive and significant at 0·1 % level showing an excellent relationship between the series for the whole period (104 years). This relationship continues to be excellent in the two halves of the series for SOI-JJA and SOI-SON seasons. However, for the SOI-MAM season in the first half of the series i.e. 1871–1922, the CC value is significant at 1 % level, whereas for the second half, 1923–1974 period, the significance is at 5 % level.

Consistency of the relationship for different periods of the series is examined by calculating the variations of the CC by the sliding window method (Bell 1977) using window widths of 10, 20 and 30 years. The highest and lowest CC noticed during different widths are shown in table 2. Sliding CC of 10-year width are highly fluctuating and the highest CC (more than 0·9 for JJA and SON seasons) is generally significant at 5 % or above. 20-year sliding window CC are less fluctuating compared to the 10-year width and highest CC are significant at 1 % level or above. 30-year sliding window length brings out the highly consistent and significant character of the relationships. These curves are shown in figure 2. The CC significant at 1 % level is indicated in the figure by a dashed line. It is seen from figure 2 that the CC for SOI-MAM season during the years 1881–95 period are high and significant at 1 % level. For SOI-JJA the CC are significant at 1 % level during the first half period of the series and oscillatory afterwards. For SOI-SON season the CC are significant at 1 % level or above throughout the period; this indicates the stability of the relationship.

Having seen the consistently significant relationship between SOI and all-India summer monsoon rainfall, it was decided to examine the values of Wright's SOI in extreme years i.e., in years of large-scale drought and flood. In order to identify the years of abnormal performance of the monsoon (i.e. droughts/floods), the criteria based on standard deviate, $t_i = (R_i - \bar{R})/\sigma$ has been adopted (for details of method refer to Mooley and Parthasarathy 1983a, 1984) and used here. It is already shown that all-

Table 1. Correlation coefficient between all-India summer monsoon rainfall and Wright's (1975) SOI for different seasons

SOI season	104 years (1871–1974)	52 years (1871–1922)	52 years (1923–1974)
DJF (lag − 2)	0·046	0·082	−0·293*
MAM (lag − 1)	0·357***	0·412***	0·288*
JJA (lag 0)	0·616***	0·671***	0·525***

ble 2. Highest and lowest CC between all-India summer monsoon rainfall and SOI for different seasons and with different sliding window widths

SOI for preceding MAM (lag − 1)		SOI for concurrent JJA (lag 0)		SOI for succeeding SON (lag + 1)		Significant table values at		
						*	**	***
Period	CC	Period	CC	Period	CC	5%	1%	0·1%
1940–49	+0·746*	1874–83	+0·927***	1874–83	+0·981***	0·63	0·76	0·87
1942–51	−0·529	1944–53	−0·164	1919–28	+0·188			
1905–24	−0·608**	1974–93	+0·862***	1974–93	0·885***	0·44	0·56	0·68
1919–38	−0·030	1919–38	−0·219	1919–38	+0·421			
1888–1917	+0·547**	1874–1903	+0·811***	1871–1900	+0·839***	0·36	0·46	0·57
1923–52	+0·054	1919–48	+0·317	1919–48	+0·496**			

t at 0·1% level; **significant at 1% level; *significant at 5% level

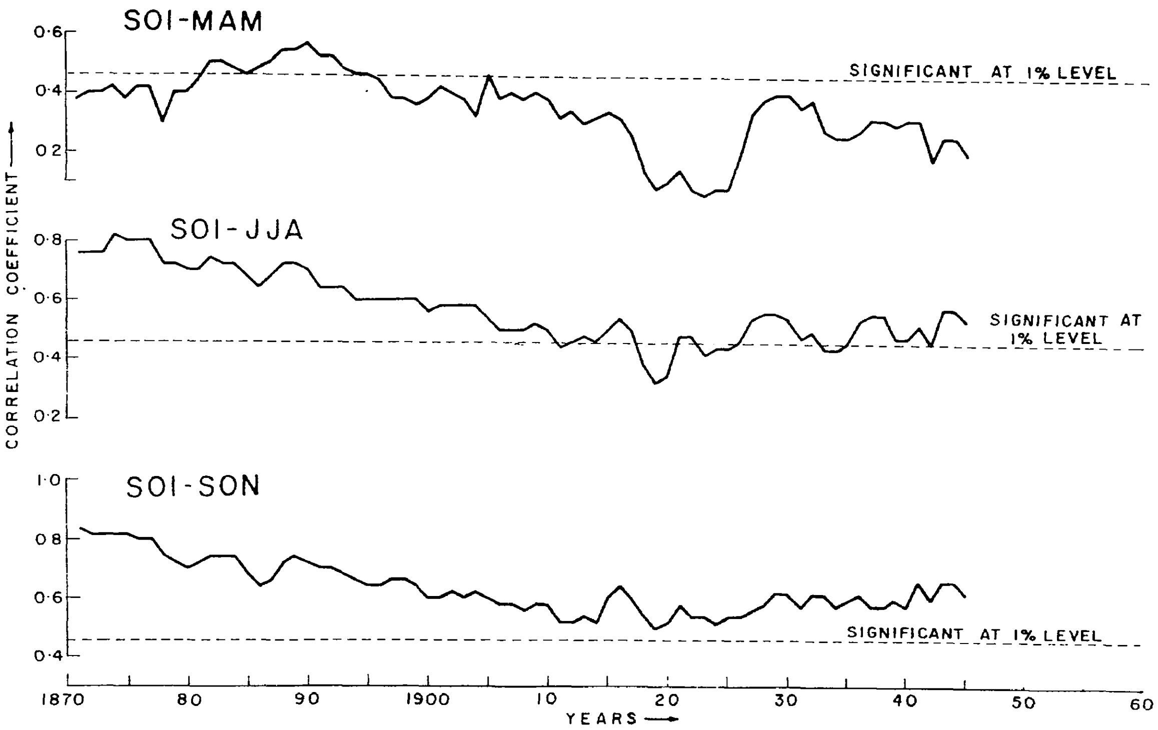

Figure 2. Variation of correlation coefficient between all-India summer monsoon rainfall and Wright's (1975) SOI of different seasons with 30-year sliding window width over the period 1871–1974.

India rainfall series is Gaussian distributed and the t_i values $-1\cdot28$ and $+1\cdot28$ indicate 10th and 90th percentile of the standard normal (Gaussian) distribution, and $R_i > 1\cdot28$ and $R_i < -1\cdot28$ have been taken as large-scale flood and drought years respectively. With these criteria 13 large-scale drought years and 9 large-scale flood years have been identified during the period 1871–1978. The drought years are 1877, 1899, 1901, 1905, 1911, 1918, 1920, 1941, 1951, 1965, 1966, 1972 and 1974; flood years are 1874, 1878, 1892, 1894, 1917, 1933, 1956, 1961 and 1975. These large-scale drought/flood years are marked suitably on the all-India summer monsoon rainfall curve in figure 1. On examination of SOI values for different seasons, it is seen that in the years of large-scale drought, SOI is invariably negative and in the years of large-scale flood it is positive. The composite means for the groups of large-scale drought (flood) years are given below.

Wright's SOI (composite mean) for different seasons

	SOI values for different seasons				
large-scale	lag −2 DJF	lag −1 MAM	lag 0 JJA	lag + 1 SON	lag + 2 DJF
drought years	−0·08	−0·45	−1·00	−0·73	−0·53
flood years	+0·27	+0·76	+1·23	+1·53	+0·78

The contrast for the concurrent and the succeeding seasons is much more than that for preceding seasons.

3.2 *Sea surface temperature* (SST) *anomalies in the equatorial eastern Pacific ocean*

The CC between all-India monsoon rainfall and SST anomaly series for the whole as well as two halves of the series for different seasons of SST have been calculated and it is found that there is strong negative correlation. These CC values along with significance levels are given in table 3, the main points are (a) the inverse relation between monsoon rainfall and SST anomaly is significant at 0·1 % level for concurrent JJA and succeeding SON seasons for the whole series as well as each of the two halves of the series and (b) the relationship for the preceding MAM season is significant at 5 % level only for the whole series and the first half of the series but not for the second half of the series.

Table 3. Correlation coefficient between all-India summer monsoon rainfall and equatorial Pacific sea surface temperature (SST of Angell 1981)

SST season	108 years (1871–1978)	54 years (1871–1924)	54 years (1925–1978)
DJF (lag − 2)	0·079	0·025	0·132
MAM (lag − 1)	−0·217*	−0·293*	−0·167
JJA (lag 0)	−0·475***	−0·467***	−0·521***
SON (lag + 1)	−0·600***	−0·656***	−0·555***
DJF (lag + 2)	−0·577***	−0·654***	−0·522***

***Significant at 0·1 % level; **significant at 1 % level; *significant at 5 % level

CC by sliding window method of widths 10, 20 and 30 years. The results for the highest/lowest CC are given in table 4. For 10- and 20-year sliding windows the fluctuations are greater compared to the 30-year window. The highest observed CCs are generally significant at 5 % or above. Consistent significant CCs are noticed for 30-year window widths series; these are shown in figure 3. For the SST-MAM series none of the CCs are significant at 1 % level. In the SST-JJA series the CC for the period 1895–1940 are low and not significant. For SST-SON highly significant CC are noticed up to the year 1910 and after 1940.

We have examined the SST anomaly values during large-scale drought/flood years. The mean values for the two groups of years are given in the following table.

Angell's SST (composite mean) for different seasons

	SST values for different seasons				
large-scale	lag − 2 DJF	lag − 1 MAM	lag 0 JJA	lag + 1 SON	lag + 2 DJF
drought years	+0·13	+0·33	+0·48	+0·88	+1·01
flood years	−0·03	−0·36	−0·26	−0·64	−0·61

Table 4. Highest and lowest CC between all-India summer monsoon rainfall and SST for different seasons and with different sliding window widths.

No. of years		SST for preceding MAM (lag − 1) Period	CC	SST for current JJA (lag 0) Period	CC	SST for succeeding SON (lag + 1) Period	CC
10	Highest	1922–31	+0·547	1878–87	0·384	1903–11 1904–12	+0·005
	Lowest	1901–10	−0·698*	1964–73	−0·909***	1936–45	−0·945***
20	Highest	1918–37	+0·009	1917–36	−0·249	1903–22	−0·229
	Lowest	1891–1910	−0·617**	1877–96	−0·698***	1926–45	−0·839***
30	Highest	1921–1950	+0·007	1919–48	−0·246	1889–1918	−0·250
	Lowest	1891–1920	−0·430*	1944–73	−0·654***	1919–48	−0·761***

***Significant at 0·1 % level; **significant at 1 % level; *significant at 5 % level

The anomaly is positive for drought years and the positive value is greater for succeeding seasons than for concurrent and preceding seasons. For the flood years the anomaly is negative, being smaller for the succeeding seasons than for the concurrent and preceding seasons.

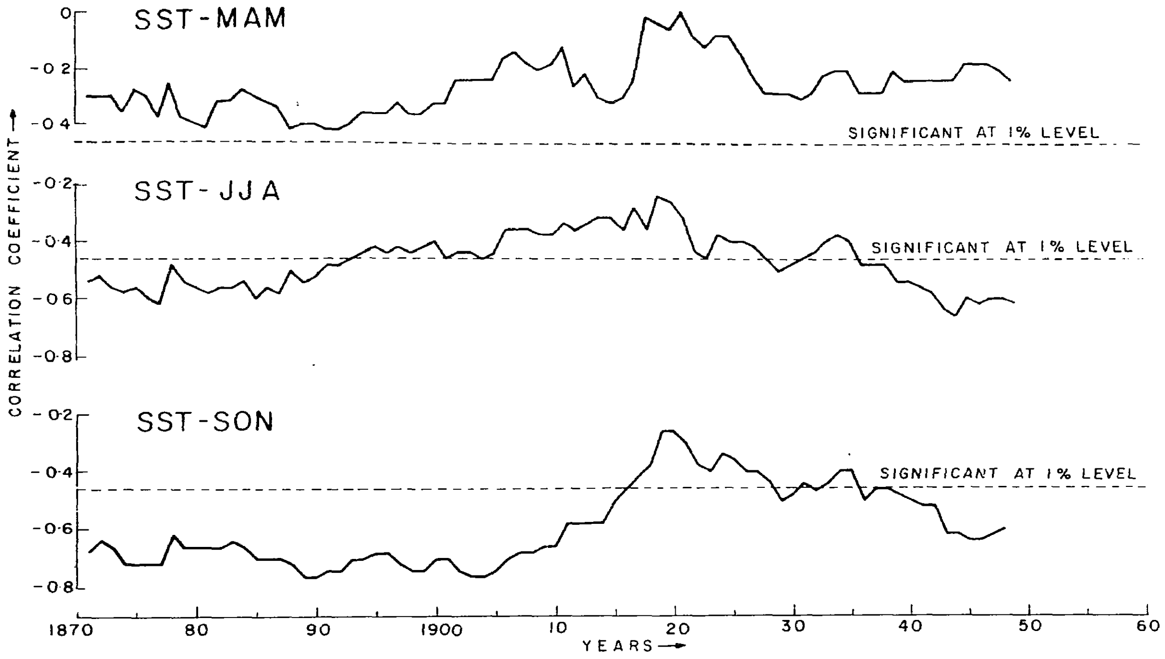

Figure 3. Variation of correlation coefficient between all-India summer monsoon rainfall and SST (Angell 1981) of different seasons with 30-year sliding window width over the period 1871–1978

Table 5. Correlation coefficient between Wright's (1975) SOI and Angelle's (1981) SST for concurrent periods with whole as well as two half periods

Season	104 years (1871–1974)	52 years (1871–1922)	52 years (1923–1974)
DJF (winter)	−0·646***	−0·720***	−0·617***
MAM (spring)	−0·587***	−0·673***	−0·576***
JJA (summer)	−0·617***	−0·653***	−0·587***
SON (autumn)	−0·758***	−0·767***	−0·784***

***Significant at 0·1 % level

Table 6. Correlation coefficient between Wright's (1975) SOI and Angell's (1981) SST for different lags and for the period 1871–1974

SST SOI	DJF	MAM	JJA	SON	DJF
DJF	−0·646***	−0·431***			
MAM	−0·566***	−0·587***	−0·501***		
JJA		−0·429***	−0·617***	−0·758***	
SON			−0·558***	−0·758***	−0·767***

***Significant at 0·1 % level

4. Relation between SOI and SST

The association between the different concurrent series of the SOI and SST has also been examined and table 5 gives the CC values. The CC are very high and negative for the whole period as well as the two halves of the series and significant at 0·1 % level. This indicates that SO and SST in the equatorial central Pacific ocean are highly interrelated and related also to the overall evolution of the circulation features of the tropical region. Strong coupling between these features is reflected in the behaviour of the Indian monsoon rainfall.

We have also examined the lag relationships between SOI and SST for the whole period and CC are given in table 6. The relationship is highly significant (0.1 % level) when SOI leads SST by one season.

5. Conclusions

Analysis of all-India summer monsoon rainfall and SOI, SST for the period 1871–1978 has brought out the following results;

(i) The relationship between all-India summer monsoon rainfall with SOI is positive, and that with SST is negative.
(ii) CC between all-India monsoon rainfall and SOI/SST anomaly for JJA and SON seasons for sliding 30-year period show consistency in high significance.
(iii) Drought years are characterised by negative anomalies of SOI and positive anomalies of SST and vice versa for flood years, the values being numerically higher for the concurrent and succeeding seasons.

(iv) SOI and SST are highly interrelated and are also related to the overall evolution of the circulation features of the tropical region.

Acknowledgements

The authors are grateful to Dr Bh V Ramana Murthy, for encouragement and to the Additional Director General of Meteorology (Research), Poona for the rainfall data. They are thankful to Dr J K Angell, NOAA, Air Resources Laboratories, USA for the sea surface temperature anomaly data over the eastern equatorial Pacific ocean. The authors are also thankful to Mr A A Munot and Mr D R Kothawale for help in computations.

References

Angell J K 1981 *Mon. Weather Rev.* **109** 230
Anjaneyulu T S S 1981 *Mausam* **31** 551
Bell G J 1977 *Weather* **32** 26
Bjerknes J 1969 *Mon. Weather Rev.* **97** 163
Fleer H 1981 *Bonn. Meteorol. Abh.* **26** 114
Joseph P V 1981 *Mausam* **32** 237
Julian P R and Chervin R M 1978 *Mon. Weather Rev.*, **106** 1433
Keshavamurthy R N 1982 *J. Atmos. Sci.* **39** 1241
Khandekar M L 1979 *Arch. Meteorol. Geophys. Bioklimatol.* **A28** 159
Mooley D A, Parthasarathy B, Sontakke N A and Munot A A 1981 *J. Climatol.* **1** 167
Mooley D A and Parthasarathy B 1983a *Variations of the global water budget.* (eds.) A S Perrot, M Baran and R Ratchiffe (Dordrecht: D Riedel) 239–252
Mooley D A and Parthasarathy B 1983b *Mon. Weather Rev.* **11** 967–978
Mooley D A and Parthasarathy B 1984 *Climatic Change* **6** 287
Newell R E, Selkirk R and Ebisuzaki W 1982 *J. Climatol.* **2** 357
Pant G B and Parthasarathy B 1981 *Arch. Meteorol. Geophys. Bioklimatol.* **B29** 245
Parthasarathy B 1984 *Proc. Indian Acad. Sci.* (*Earth Planet. Sci.*) **93** 371
Parthasarathy B and Pant G B 1984 *Tellus* **A36** 269
Parthasarathy B and Pant G B 1985 *J. Climatol.* **5** (in press)
Pisharoty P R 1981 *Monsoon dynamics* (eds.) J Lighthills and R P Pearce (London: Cambridge University Press) pp. 238–251
Quenouille M H 1952 *Associated measurements* (London: Butterworths) p. 242
Ramesh Babu V, Rao L V G and Varadachari V V R 1981 *Monsoon dynamics* (eds.) J Lighthills and R P Pearce (London: Cambridge University Press) p. 481
Rasmusson E M and Carpenter T H 1982 *Mon. Weather Rev.* **110** 354
Rowntree P R 1972 *Q. J. R. Meteorol. Soc.* **98** 290
Scirremammano F Jr 1979 *J. Phys. Oceanogr.* **9** 1273
Shukla J 1975 *J. Atmos. Sci.* **32** 503
Sikka D R 1980 *Proc. Indian Acad. Sci.* (*Earth Planet. Sci.*) **89** 639
Troup A J 1965 *Q. J. R. Meteorol. Soc.* **91** 490
Walker G T 1923 *Mem. India Meteorol. Dept.* **24** 75
Walker G T 1924 *Mem. India Meteorol. Dept.* **24** 275
Walker G T and Bliss E W 1932 *Mem. R. Meteorol. Soc.* **4** 53
Walker G T and Bliss E W 1937 *Mem. R. Meteorol. Soc.* **4** 119
Weare B C 1979 *J. Atmos. Sci.* **36** 2279
Webster P J 1981 *J. Atmos. Sci.* **38** 554
Wright P B 1975 An index of the Southern Oscillation, Climatic Research Unit, University of East Anglia, Norwich, England, Report No. CRU RP4, 20 pp.

ndian Acad. Sci. (Earth Planet. Sci.), Vol. 94, No. 3, November 1985, pp. 211–217.
ted in India.

al features of upper-tropospheric zonal wind and thermal fields g anomalous monsoon situations

L S HINGANE, S D PATIL and K RUPA KUMAR
Indian Institute of Tropical Meteorology, Pune 411 005, India

MS received 13 March 1985; revised 5 August 1985

Abstract. Global analyses of mean monthly zonal wind component and temperature at 200, 150 and 100 mb levels have been made for the region between 60°N and 60°S, for the months May through September during two poor monsoon years (1972 and 1979) and a good monsoon year (1975). Prominent and consistent contrasting features of the zonal wind and thermal fields have been identified, with reference to the monsoon performance over India. It has been noticed that the areal spreading of easterlies over the tropics and extratropics is significantly more during a good monsoon year. Shifting of the axis of the tropical easterly jet stream to a higher level and generally stronger easterlies also characterize good monsoon activity. The upper troposphere has been found to be considerably cooler during poor monsoon years.

Keywords. Southwest monsoon; drought; upper troposphere; zonal winds

ntroduction

g easterlies and the tropical easterly jet stream (TEJ) at the 100-150 mb level have
long been recognized to be among the main features of the Asian summer
oon. Some regional-scale studies were made to bring out the anomalies in the
wind and thermal fields associated with below normal monsoon activity leading
ge-scale droughts (Ananthakrishnan and Ramakrishnan 1963; Keshavamurty and
e 1974; Prakasa Rao 1975; Verma 1980). Continued presence of strong easterlies
g the breaks and significant cooling of the upper troposphere during poor
oon years are some of the important features noted in these studies. Kanamitsu
rishnamurti (1978) contrasted the 200 mb flow regimes during a drought year
) with those during a normal monsoon year (1967) over the global tropics for the
d 1 June to 31 August. Their study indicates that the spreading of the easterly wind
n the tropical belt is more pronounced in a normal monsoon year than in a poor
oon year. Hingane (1984) analysed the thermal and wind fields at 200, 150 and
b levels in the month of July for a good monsoon year (1975) and a poor
oon year (1979) and noted similar features. As a continuation of the above study in
e extensive manner, the present paper deals with the analysis of mean monthly
winds and thermal fields during the months May through September at 200, 150
0 mb levels, for the years 1975 (flood) and 1972 and 1979 (drought). The reason
ecifying these three levels for the study is that they represent certain characteristic
es of the upper troposphere, viz, the presence of an extratropical westerly jet

2. Data and analysis

Mean monthly data of wind and temperature at 200 mb, 150 mb and 100 mb levels for about 250 stations around the globe between 60°N and 60°S (see figure 1 of Hingane 1984) have been collected from the Monthly Climatic Data for the World (NOAA/WMO) for the months May through September of 1972, 1975 and 1979. Though the data concerned are only for three years, in view of the extreme anomalies in these years, it is expected that an idea of the characteristic features associated with them can be obtained. The zonal components of the wind at all the above levels have been calculated for each station. These data have been plotted and 90 maps giving the zonal wind field and the thermal field have been prepared. These maps have been examined in detail to identify the consistent contrasting features associated with good and poor monsoon years.

3. Results

The salient features observed in the analysis for contrasting summer monsoon situations are briefly noted below.

3.1 *Upper-air zonal wind field during May through September*

In the zonal wind field maps presented in this section, the areas covered by negative values of zonal component, which represent the easterly field, have been shaded by hatching to give a better contrast.

i) *May*:—During May 1975 the latitudinal as well as longitudinal extent of the easterly wind field at 100 mb in the tropical and extratropical regions is considerably more (figures 1 and 2). The easterlies at 150 mb (normal level of the axis of TEJ) were stronger during 1975 than during 1972 and 1979. Westerlies over Australia at all the three levels (viz, 100, 150 and 200 mb) were weaker in 1975 than in 1972 and 1979.

ii) *June*:—In 1975 at 100 mb level although the easterlies are found at more northern latitudes over the Pacific Ocean, they extend round the globe except between 50°W

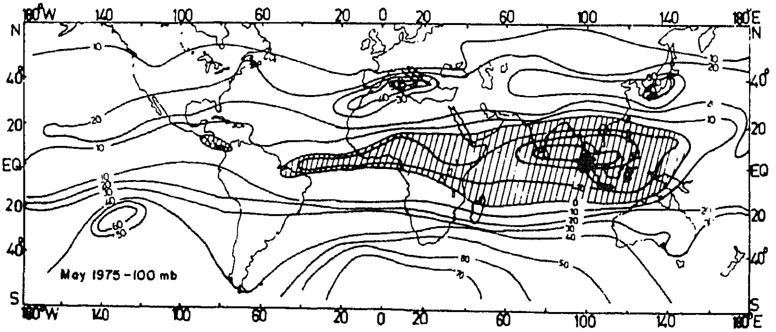

Figure 1. May 1975: zonal wind field at 100 mb (m sec^{-1}).

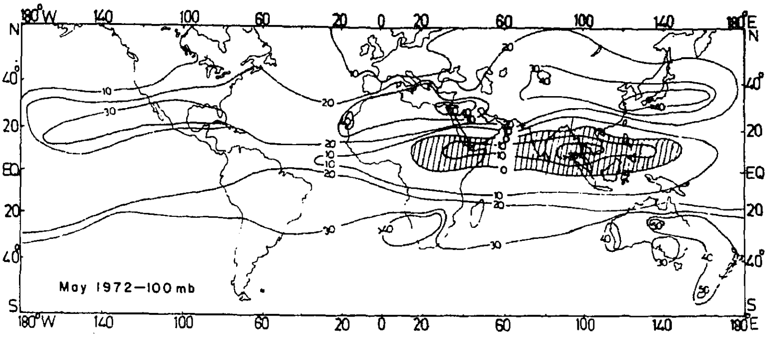

Figure 2. May 1972: zonal wind field at 100 mb (m sec^{-1}).

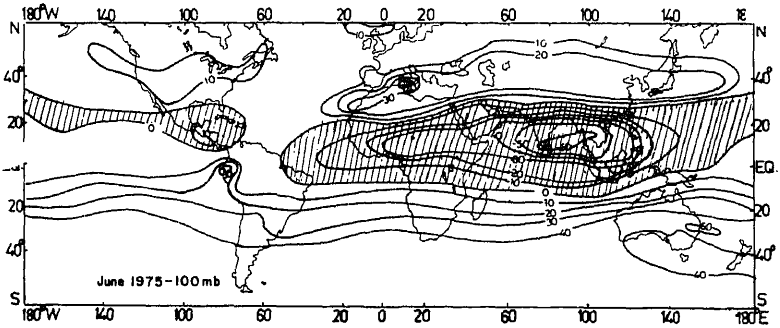

Figure 3. June 1975: zonal wind field at 100 mb (m sec^{-1}).

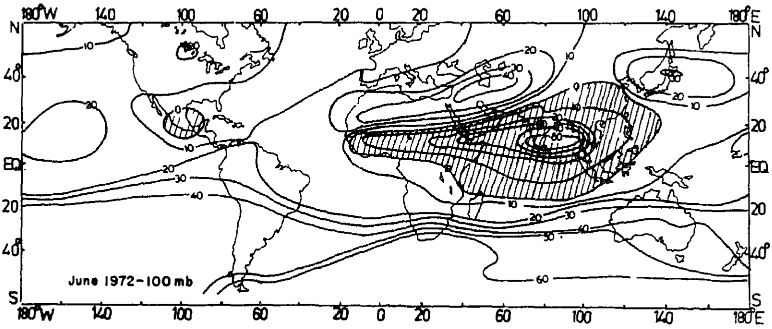

Figure 4. June 1972: zonal wind field at 100 mb (m sec^{-1}).

and 70°W, whereas in 1972 and 1979 they are mainly in the Eastern Hemisphere (figures 3 and 4). The easterlies over South Asia were significantly stronger in 1975 when compared to 1972 and 1979. Fairly strong westerlies are seen over north central Pacific in 1972 and 1979, whereas the same region has been covered by easterlies in 1975. No well-marked differences could be noticed at 150 mb and 200 mb levels.

iii) *July*:—In 1975 (figure 3 of Hingane 1984), the easterlies at 100 mb level extend o a broader belt of latitudes covering the whole of the tropics and parts of extratropical region and occur round the globe, compared to the narrow bands 1972 (figure 5) and 1979 (figure 2 of Hingane 1984). At the 150 mb level, longitudinal extent of the easterly wind field is more in 1975 than the others. interesting feature that can be seen in 1975 is that the easterlies are weaker 150 mb than those at 100 mb (see figure 6 of the present paper and figure 3 Hingane 1984). This feature suggests that the position of TEJ axis could have shif to the 100 mb level The wind shears also support this aspect. Westerlies w weaker at 150 mb over Australia in 1975 while they were stronger over the southe tip of South Africa at both 150 and 200 mb levels.

iv) *August*:—A majority of the Japanese stations show easterly wind components 1975, in contrast to the other years. Westerlies are weaker over Australia at 100 as well as 150 mb levels in 1975 than in 1972 and 1979. However, no significa differences could be observed at 200 mb zonal wind field.

v) *September*:—At the 100 mb level, the easterlies were extending into the equator Atlantic in 1975, whereas in 1972 and 1979 there was westerly wind field in tl area, separating the Afro-Asian and Mexican easterly fields. At 200 mb, the weste jet stream was well-established, fairly stronger and continuous over central A and Europe in 1975, when compared to the other years.

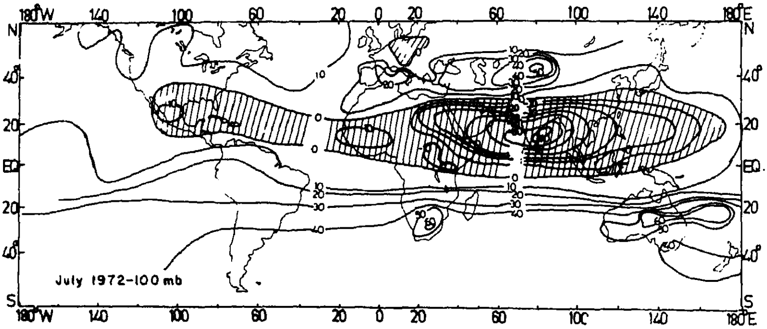

Figure 5. July 1972: zonal wind field at 100 mb ($m\ sec^{-1}$).

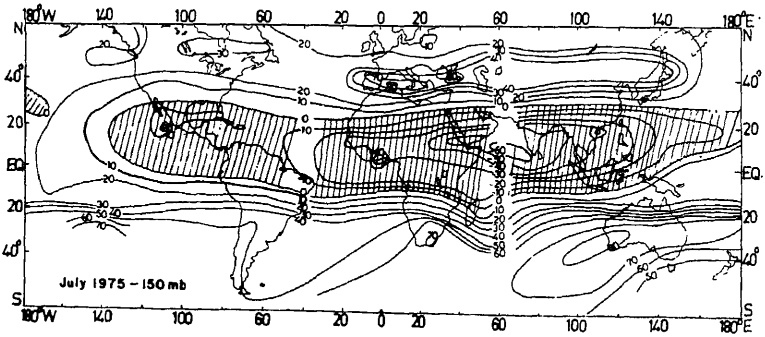

Figure 6. July 1975: zonal wind field at 150 mb ($m\ sec^{-1}$).

3.2 *Upper-air thermal features during May through September*

i) *May*:—Temperatures over India were markedly higher at all the three levels in 1975 when compared to 1972 and 1979 (see for example, figures 7 and 8).

ii) *June*:—Temperatures over India, particularly over the northern parts, continued to be higher at all the three levels in 1975, than in 1972 and 1979. At the 200 mb level, south Japan, southern Europe and adjoining USSR and North America were warmer in 1975 (figures 9 and 10) than in the other years.

iii) *July*:—The Indian region shows warmer conditions at both 100 mb and 150 mb levels in 1975, than in 1972 and 1979, the latter year showing the lowest temperatures. The Europian stations north of 40°N were having lower temperatures at 100 mb and 150 mb levels during 1975 than during 1972 and 1979. The equatorial eastern Pacific region was cooler at 150 mb and 200 mb levels in 1975 than in 1972 and 1979. At 200 mb, the whole of Australia and adjoining New Zealand and the poleward regions of North America were markedly cooler both in 1972 and 1979 than in 1975.

iv) *August*:—North India was slightly but definitely warmer at all the three levels in 1975, whereas Europe and South Africa were cooler during the same year at 100 and 150 mb levels.

v) *September*:—No significant contrast in the thermal field at any level could be noticed for this month.

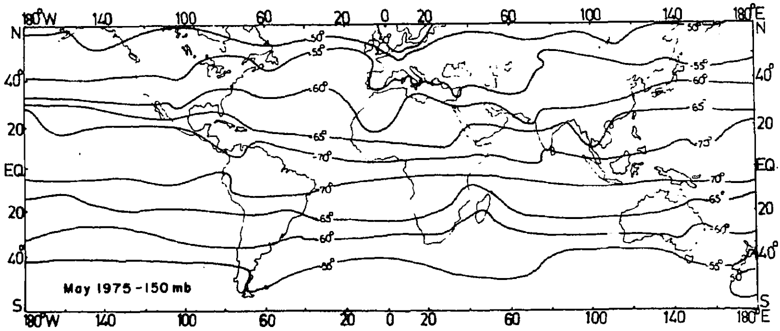

Figure 7. May 1975: temperature field at 150 mb (°C).

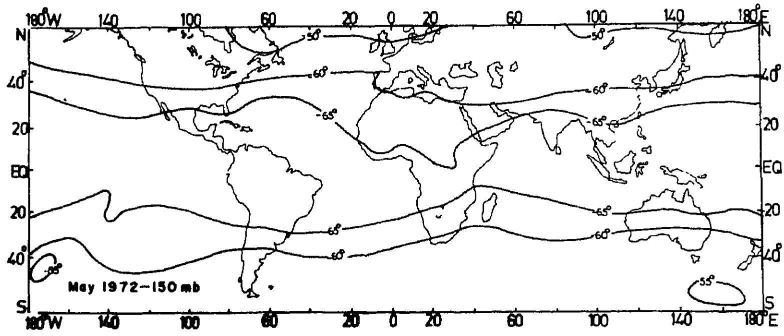

Figure 8. May 1972: temperature field at 150 mb (°C).

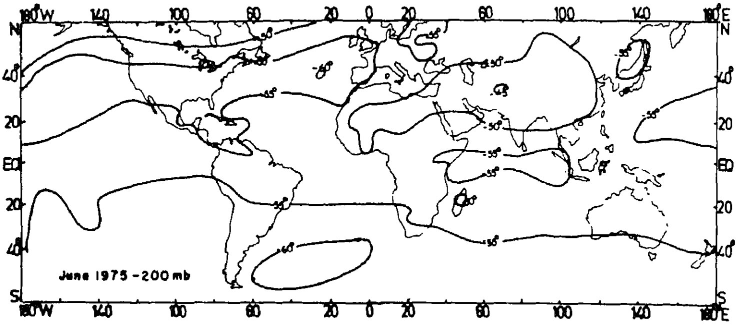

Figure 9. June 1975: temperature field at 200 mb (°C).

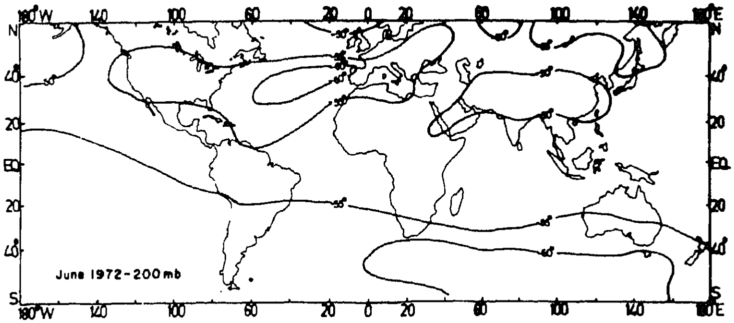

Figure 10. June 1972: temperature field at 200 mb (°C).

4. Discussion and conclusions

Results obtained from the analysis of several charts representing the monthly mean zonal wind and thermal fields during May through September indicate some definite contrasting upper-air features for poor and good monsoon years. The features noted for May, the month preceding the commencement of the southwest monsoon season over India, could be used to obtain an outlook of the monsoon performance.

The major contrasting features noticed in the case of the zonal wind field are with respect to the areal spreading and strength of the zonal component. During a good monsoon year, the longitudinal as well as latitudinal extents of the easterlies in the tropics and the adjoining extratropics were significantly more than that during a poor monsoon year. The normal position of the axis of TEJ (viz, 150 mb) is found to have shifted to a higher level (100 mb) during good monsoon activity. This fact is also reflected in the wind shear. The good monsoon is further characterized by stronger easterlies. At 150 mb level, westerlies over Australia and Europe were conspicuously weaker during most of the months in the good monsoon year.

Acknowledgements

The authors are thankful to Dr Bh V Ramana Murty, for encouragement, and to Dr G B Pant for showing keen interest.

References

Ananthakrishnan R and Ramakrishnan A R 1963 *Proc. of the symposium tropical meteorology, Rotarua, New Zealand*, (Wellington: New Zealand Meteorological Service) p. 144

Hingane L S 1984 *Proc. Indian Acad. Sci.* (*Earth Planet. Sci.*) **93** 105

Kanamitsu M and Krishnamurti T N 1978 *Mon. Weather Rev.* **106** 331

Keshavamurty R N and Awade S T 1974 *Indian J. Meteorol. Hydrol. Geophys.* **25** 257

Prakasa Rao G S 1975 *Indian J. Meteorol. Hydrol. Geophys.* **26** 535

Verma R K 1980 *Mon. Weather Rev.* **108** 1072

Proc. Indian Acad. Sci. (Earth Planet. Sci.), Vol. 94, No. 3, November 1985, pp. 219–235.
© Printed in India.

The sensitivity of the northern hemisphere summer mean meridional circulation to changes in the large scale eddy forcing

B N GOSWAMI
Centre for Atmospheric Sciences, Indian Institute of Science, Bangalore 560012, India

MS received 4 June 1984; revised 15 July 1985

Abstract. A zonally averaged version of the Goddard Laboratory for Atmospheric Sciences (GLAS) climate model is used to study the sensitivity of the northern hemisphere (NH) summer mean meridional circulation to changes in the large scale eddy forcing. A standard solution is obtained by prescribing the latent heating field and climatological horizontal transports of heat and momentum by the eddies. The radiative heating and surface fluxes are calculated by model parameterizations. This standard solution is compared with the results of several sensitivity studies. When the eddy forcing is reduced to 0·5 times or increased to 1·5 times the climatological values, the strength of the Ferrel cells decrease or increase proportionally. It is also seen that such changes in the eddy forcing can influence the strength of the NH Hadley cell significantly. Possible impact of such changes in the large scale eddy forcing on the monsoon circulation via changes in the Hadley circulation is discussed. Sensitivity experiments including only one component of eddy forcing at a time show that the eddy momentum fluxes seem to be more important in maintaining the Ferrel cells than the eddy heat fluxes. In the absence of the eddy heat fluxes, the observed eddy momentum fluxes alone produce subtropical westerly jets which are weaker than those in the standard solution. On the other hand, the observed eddy heat fluxes alone produce subtropical westerly jets which are stronger than those in the standard solution.

Keywords: Symmetric model; eddy transports; sensitivity experiments.

1. Introduction

The observed three cell structure of the zonally averaged time mean circulation (mean meridional circulation, MMC) depends on the distribution of the latent heating, radiative heating, sensible heat flux, transports of heat and momentum by large scale eddies and surface friction. The relative importance of these factors in maintaining the MMC has been studied by many authors (Starr 1948; Rossby and Starr 1949; Palmén 1949; Palmén *et al* 1958; Williams and Davies 1965; Kuo 1956; Saltzman and Vernekar 1971, 1972; Dickinson 1971a, b; Derome and Wiin-Nielsen 1972; Kurihara 1973; Wiin-Nielsen and Fuenzalida 1975; Schneider and Lindzen 1977; Schneider 1977; Taylor 1980; Held and Hou 1980). The aim of the present study is to examine the sensitivity of the MMC to changes in the fluxes of heat and momentum due to the large scale eddies. It is well known that large scale eddy transports of heat and momentum contribute significantly to the maintenance of the middle latitude Ferrel cells. However, the transports of heat and momentum by large scale eddies can also influence the strength of the Hadley circulation in the tropics. In a recent diagnostic study related to the NH winter MMC, Crowford and Sasamori (1981) showed that in the absence of the condensational heating in the tropics, the observed large scale eddy fluxes can maintain

Hadley cells in the tropics with about one-third the observed strength. In this study, we shall examine, in particular, the changes in the northern hemisphere (NH) Hadley circulation due to changes in the large scale eddy forcing. This study was motivated by the fact that, the fluctuations of the large scale eddies in the middle latitude do indeed seem to influence the subseasonal fluctuations of the south Asian summer monsoon. The southwest monsoon shows temporal fluctuations often resulting in long "breaks" in the rainfall. Such long and/or frequent breaks result in a drought situation. It was noted by synoptic meteorologists (e.g. Ramaswamy 1962) that a drastic change in the NH middle latitude circulation from the zonal to the Rossby regime is seen during the onset of a break. The large scale waves in the middle latitude can influence the Hadley circulation in two ways. Firstly, the eddies can influence the tropical circulation through lateral forcing on the northern boundary of the Hadley circulation. Mak (1969) examined this question by introducing stochastic lateral forcing at ±30° latitude in a tropical model. He prescribed the stochastic forcing in terms of second moment eddy statistics. Secondly, the eddies contribute to the heat and momentum budget requirements for maintaining the MMC and hence can influence the Hadley circulation through heat and momentum transports. It is this question that we want to examine in this study.

For the purpose of this study, a zonally symmetric version of the Goddard Laboratory of Atmospheric Sciences (GLAS) climate model was constructed. The zonally symmetric version of the GLAS climate model was obtained by putting all the longitudinal derivatives to zero in the GLAS climate model and contains the same physical parameterizations, resolution and numerical technique as the full climate model. The GLAS climate model has been described and its performance has been discussed by Shukla *et al* (1981). The symmetric version of the GLAS climate model has been discussed in some detail by Goswami *et al* (1984). Briefly, the symmetric model has a 4° latitude grid in the north south direction and nine σ levels in the vertical. For the experiments discussed in the paper, the radiative heating and surface fluxes are calculated using the model parameterizations. The latent heating distribution for these runs is prescribed. We also prescribe the horizontal fluxes of heat and momentum by the large scale eddies as input forcing from observations. The sources for these data are discussed in §2. As discussed in Goswami *et al* (1984), the cloud-radiative feed back has been omitted in these calculations. The lower boundary for all the experiments consists of an all ocean earth. A sea surface temperature distribution corresponding to the NH summer conditions is prescribed. By including the observed global eddy fluxes, a realistic distribution of the latent heating field and calculating the radiative and surface fluxes through model parameterizations, we obtain a control run corresponding to the NH summer condition. Then keeping boundary conditions and latent heating distribution the same, we carried out several sensitivity experiments by changing the observed eddy fluxes. For each run the model was integrated for about 150 days and it was found that the model reached a steady state for each run after about 60 days of integration. The fields presented in this paper were obtained by averaging over the last 60 days of integration in each case.

In §2, we discuss the data used in this study. In §3, the standard solution is presented and compared with observations. The deficiency of the standard solution is also discussed in this section. The results of the sensitivity experiments are presented in §4. The results are summarized and a few remarks are made in §5.

2. Model specifications and data used

The initial condition for all the experiments presented in this study correspond to a resting atmosphere ($u = v = 0$). Climatological distributions of the specific humidity and the temperature field are prescribed initially.

With only one exception (see §3.3), for all the experiments presented in this paper, the vertical eddy viscosity coefficient in the middle layer (ν_5) is taken to be approximately $11 \mathrm{~m}^2 \mathrm{~s}^{-1}$. The experiment described in §3.3 is designed to examine the sensitivity of the zonal winds to changes in the vertical eddy viscosity. For this experiment, ν_5 is taken to be $33 \mathrm{~m}^2 \mathrm{~s}^{-1}$. In our model the vertical eddy viscosity varies linearly with pressure.

The observed climatological mean global eddy fluxes for NH summer (June–July–August) used in this study were taken from Oort (1983). This mean was constructed from a 15 year (1958–1972) data set. The eddy fluxes used in this study are $[\overline{u'v'}]$, $[\bar{u}^*\bar{v}^*]$, $[\overline{v'T'}]$ and $[\bar{v}^*\bar{T}^*]$. These fluxes were obtained at intervals of 5° latitude between 80°S and 80°N and on 20 levels in the vertical between 1000 mb and 50 mb. We then interpolated the data to the 9 layers in the vertical and 4° latitude grid of our symmetric model. We employed a linear interpolation scheme using distance weighing (pressure weighing) for the horizontal (vertical) interpolation. These eddy fluxes are shown in figure 1. As there exist large uncertainties in obtaining the vertical fluxes of the large scale eddies from observations, we have not included the vertical transports of heat and momentum by the eddies in this study. We have also neglected variances, $[\overline{v'^2}]$ and $[\overline{u'^2}]$ in the momentum equation. Convergence and divergence of momentum and heat due to the eddies are calculated from the observed fluxes and used in the momentum and thermodynamic equations as time independent forcings. As with most of the other forcing functions, the eddy forcings are also applied to the momentum and the thermodynamic equations only every "physics time step" (i.e. 30 min).

The lower boundary for all the runs is all ocean with fixed sea surface temperature (SST). These runs correspond to the northern hemispheric (NH) summer condition. The SST used for these runs is the same as the one used for the summer runs described in Goswami *et al* (1984). The SST has a maximum at 18°N. The solar declimation is fixed at 15°N. The surface albedo is taken to be 7 % everywhere. The shortwave radiation, the longwave radiation and the boundary fluxes are calculated using the parameterization of the GLAS climate model. However, the latent heating field is not calculated in the model. Instead, we prescribe the latent heating field from the observed zonal mean precipitation distribution for June–July–August. The latent heating field used in this study and the equivalent precipitation distribution (dashed curve) are shown in figure 2a. This latent heating field is similar to the one calculated by Newell *et al* (1974) for the NH summer. As we are interested in only studying the role of the eddy forcing on the MMC, the finer details of the distribution of the latent heating field may not be important for our study.

The reason for prescribing the latent heating field from the observed zonally averaged precipitation distribution instead of calculating the same using the parameterization of the GLAS climate model is the following. The latent heating field calculated by the GLAS climate model depends crucially on the nature of the lower boundary (e.g. whether it is land or ocean). It is not possible to represent the earth's lower boundary in a realistic way in our symmetric model since each grid point

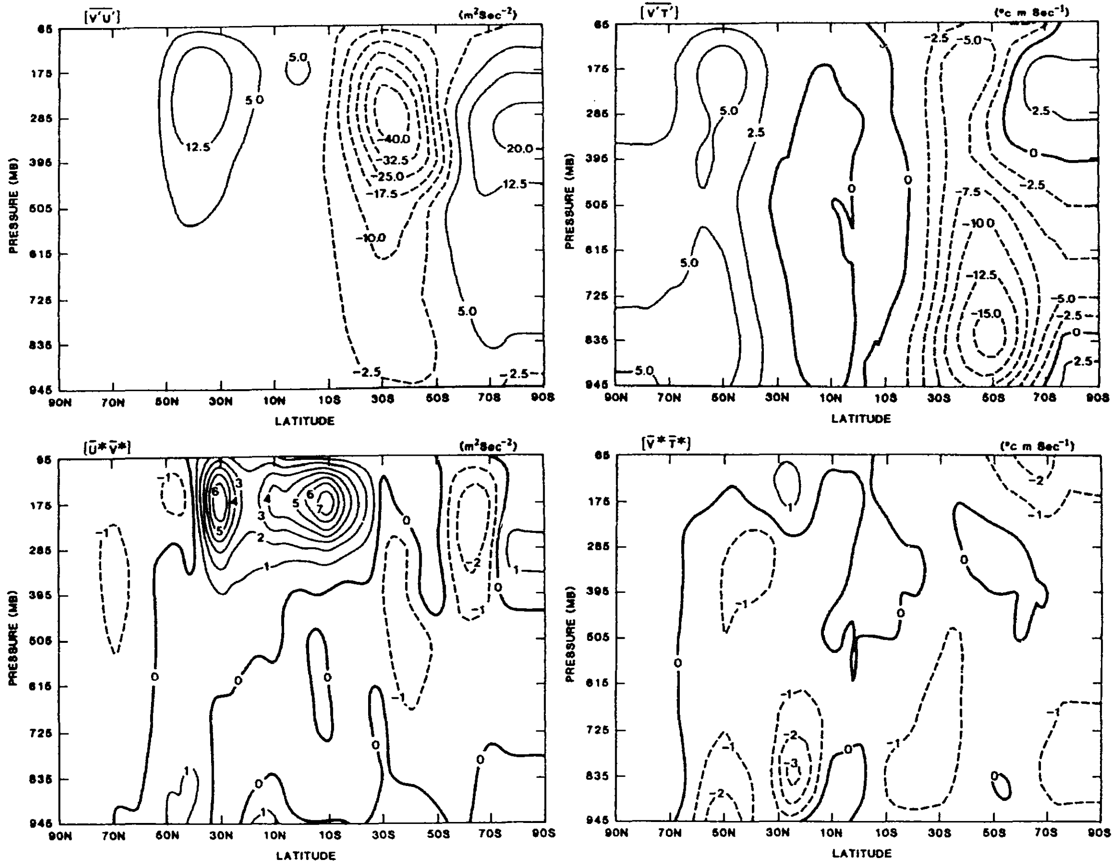

Figure 1. Climatological mean June–July–August transient and stationary eddy fluxes from observation. These eddy fluxes have been obtained from global statistics compiled by Oort (1983) and interpolated to the model grid.

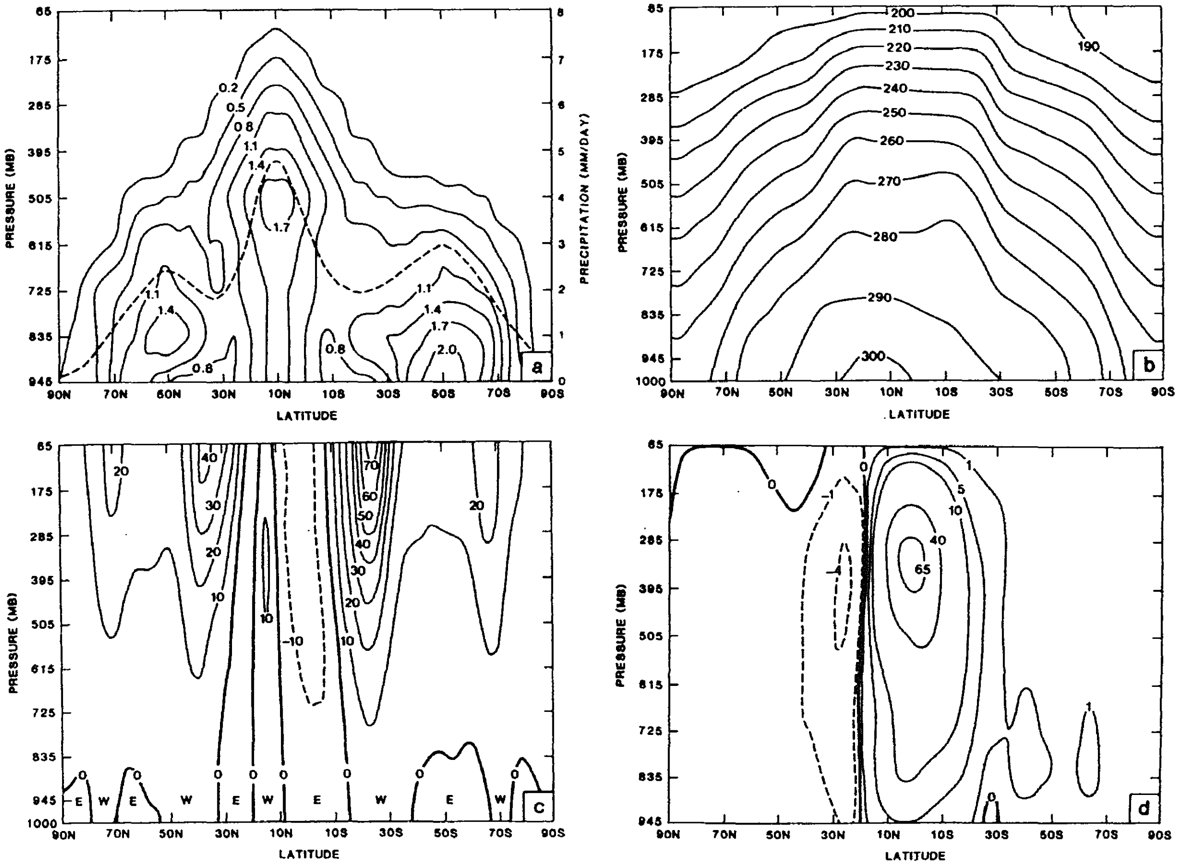

Figure 2. Northern hemisphere summer run without eddies, a) prescribed convective heating field, contour deg day^{-1}; b) temperature, contour interval 10°K; c) zonal wind, contour interval, 10 ms^{-1}; d) stream function, contour, 10^{10} kgs^{-1}.

simulate the observed zonally averaged latent heating field with our symmetric GLAS climate model. In order to study the role of the observed eddy forcing in maintaining the MMC, it is important that we have realistic representation of the other forcing functions. This is why we chose to use the observed latent heating field. As this field is derived from observed precipitation distribution, it implicitly contains the effect of the land-ocean inhomogeneities in the zonal direction in producing the latent heating field. But by prescribing an all ocean lower boundary with fixed SST we imposed a constraint on the sensible heat flux from the lower boundary. The implication of prescribing a fixed SST distribution on the strength of the Hadley cells will be discussed in §3.4.

3. The standard solution

3.1 *Northern hemisphere summer run without eddy fluxes*

We first carried out one integration in which the observed eddy fluxes were not included. The temperature, the zonal wind and the stream function for the steady state for this run are shown in figures 2b-d. The NH westerly jet occurs at about 40°N with maximum westerly winds of about 40 ms^{-1} at the center of the jet. The (southern hemisphere) SH westerly jet occurs at about 26°S with maximum westerly winds of about 70 ms^{-1} at the center of the jet. The surface easterlies appear in tropics between 14°S and 34°N with a westerly region between 6°N and 20°N. Surface easterlies again appear in the high latitudes. Although the westerlies in the subtropical jet stream are much stronger than those observed, the zonal wind distribution has the general characteristics of the observed NH summer mean zonal wind distribution. However, the stream function field shows that in the absence of the eddy fluxes the MMC is quite different from observed. In this case, the MMC has one direct cell in each hemisphere. Only a very weak and shallow Ferrel cell appears in the SH.

3.2 *Northern hemisphere summer run with observed eddy fluxes*

This run is similar to the one described in §3.1, but we now add the large scale eddy fluxes described in §2 as input forcing. The temperature, the zonal winds and the stream function for the steady state for this run are shown in figure 3. We notice that the eddies strengthen the westerlies in the subtropical jet in the NH. In the Southern Hemisphere, the westerly jet occurs at about 26°S with a maximum strength of about 70 ms^{-1}. In the Northern Hemisphere, the westerly jet occurs at about 35°N with a maximum strength of about 50 ms^{-1}. A secondary jet appears in high latitudes in the Southern Hemisphere. In the tropics, surface easterlies appear between 22°S and 34°N with a region of westerlies between 6°N and 18°N. The surface easterlies in the high latitudes also appear in the more or less correct positions.

The most dramatic change the eddies produce occurs in the stream function field. In

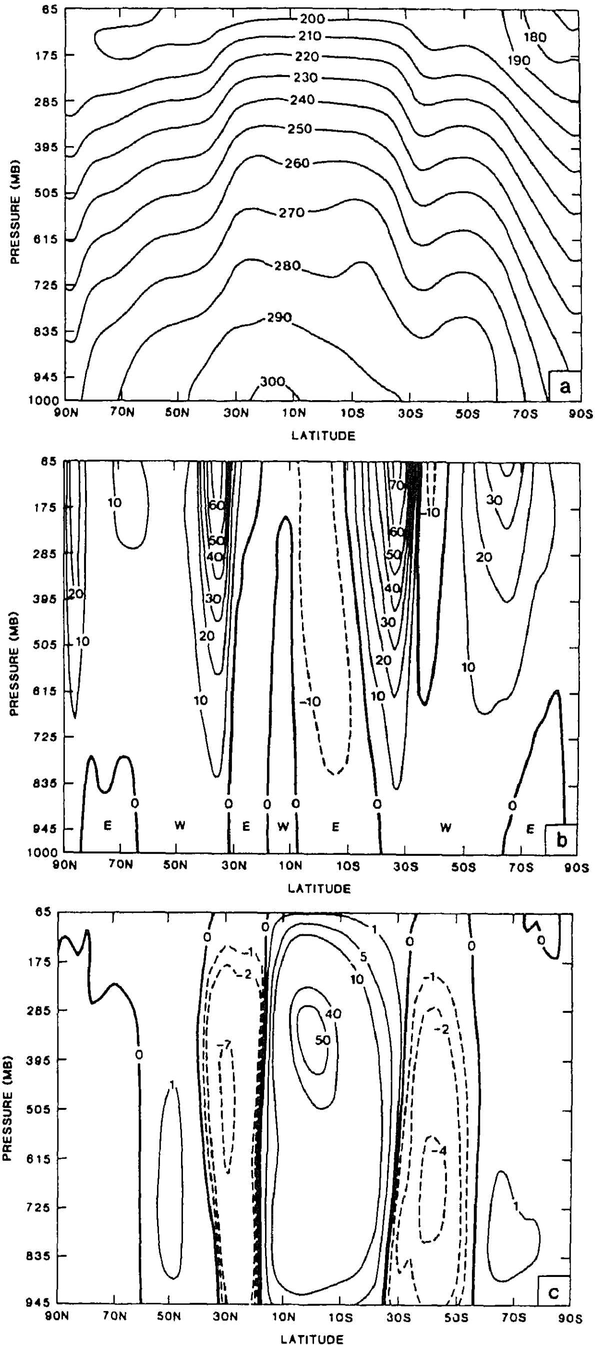

Figure 3. Northern hemisphere summer run with eddies, **a**) temperature, contour interval 10°K; **b**) zonal wind, contour interval 10 ms^{-1}; **c**) stream function, contour 10^{10} kgs^{-1}.

from observations by about a factor of 2 (Oort and Rasmusson 1971; Newell *et al* 1972). An explanation for obtaining such large mass fluxes in the Hadley cells is given in Goswami *et al* (1984). The gist of this explanation is reproduced in §3.4.

3.3 *NH summer run with observed eddy forcing and large vertical eddy viscosity*

In §3.2, we have shown that the observed eddy forcing together with a realistic distribution of the latent heating field produces a realistic MMC corresponding to the NH summer condition (see figure 3). However, we note from figure 3 that the westerlies in the subtropical jet stream are much larger than those observed. In this section we shall present results of an experiment showing that the strength of the subtropical westerly jet stream depends on the choice of the vertical eddy viscosity in our symmetric model.

We recall that the vertical eddy viscosity coefficient at the middle layer for the experiment described in §3.2 was 11 $m^2 s^{-1}$. We carried out an identical experiment (including the latent heating field and eddy forcing) except that we increased the vertical eddy viscosity coefficient such that ν in the middle layer is 33 $m^2 s^{-1}$. The model was again integrated until it reached a steady state. The temperatures, the zonal winds and the stream function for this steady state are shown in figure 4. We note from figure 4 that the strength of the westerlies in the NH jet is reduced to 30 ms^{-1} in this case as compared to 50 ms^{-1} in the low viscosity case (see figure 3). Similarly, the strength of the westerlies in the SH jet is reduced to 40 ms^{-1} as compared to 70 ms^{-1} in the low viscosity case. It is of interest to note that the zonal wind distribution for the high viscosity case (figure 4) is much closer to the observed zonal winds for the NH summer. The increase in the vertical eddy viscosity increases the strength of the NH Hadley cell by about 25% and decreases the SH Hadley cell by about 10%.

3.4 *Comments on the standard solution*

The behaviour of our model as the vertical eddy viscosity is increased is as predicted by simple model calculations. Held and Hou (1980) showed that if the heat source is fixed and internal viscosity is decreased, the jet stream zonal velocities are increased and sharper meridional jet stream structure is seen. This behaviour is seen in our model solutions also (figures 3 and 4).

There are several features of our standard solution that agree well with the observed mean meridional circulation. Examining the large vertical viscosity solution from our model (figure 4), we note that the position of the subtropical westerly jets correspond well with observations. The intensity ratio between the Hadley and Ferrel cells at the individual maxima is about 10:1 which compares well with the analysis of Newell *et al* (1972). The ratio between the strength of the Hadley cell in the summer hemisphere to the strength of the Hadley cell in the winter hemisphere is about 1:5 which also compare well with observations (Newell *et al* 1972).

However, there are a few features of our standard solution that do not agree well with the observed MMC. Firstly, the zonal winds simulated by the model do not have the closed maxima near 200 mb which is seen in the observations. As a result, the model simulated zonal winds near the upper boundary are stronger than those observed. This is related to the fact that the model simulates much colder temperatures in the upper

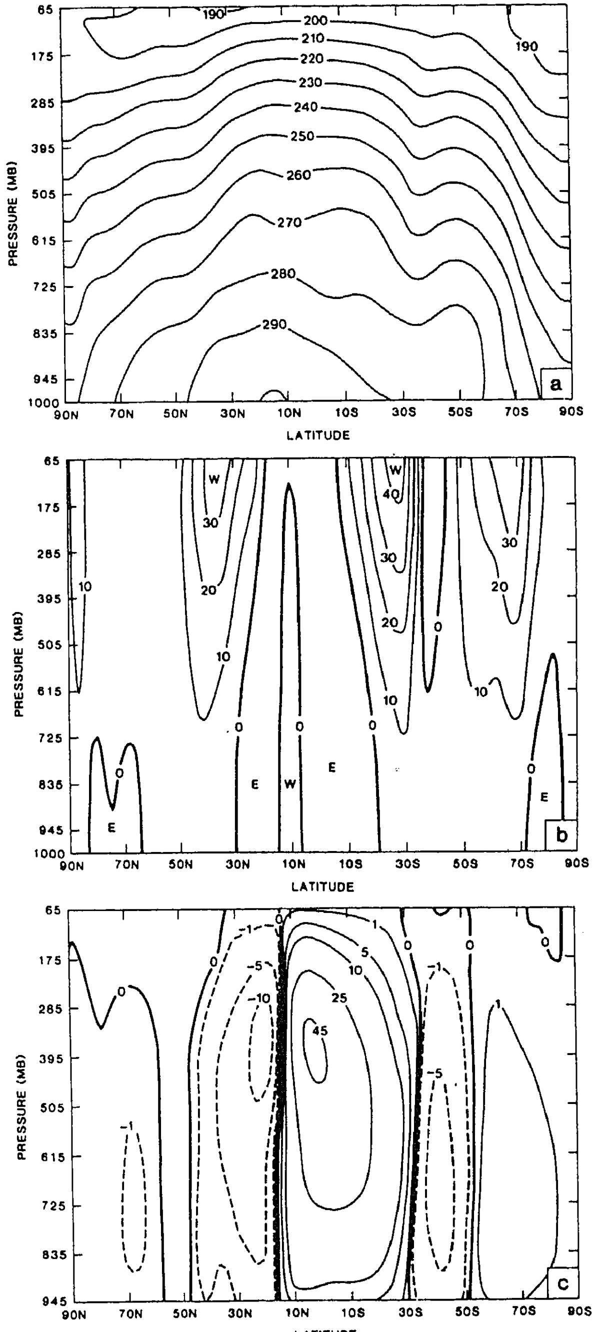
PRESSURE (MB)
65
175
285
395
505
615
725
835
945
1000
90N
70N
50N
30N
10N
10S
30S
50S
70S
90S
LATITUDE
190
200
210
220
230
240
250
260
270
280
290
a
W
E
40
30
20
10
0
b
-1
-5
-10
1
5
10
25
45
c

tropospheric polar regions (Shukla *et al* 1981). Another significant feature of our standard solutions is that the meridional mass flux in the Hadley cell is about twice the observed Hadley cell mass flux in summer (Oort and Rasmusson 1971; Newell *et al* 1972). An explanation regarding the large mass flux in our model simulated Hadley circulation is given in Goswami *et al* (1984). This feature apparently results from the neglect of cloud-radiation interaction in the radiative calculations. With the fixed SST distribution at the lower boundary, the removal of the cloud radiation feedback results in larger net outgoing long wave flux at the top of the atmosphere. In terms of Newtonian cooling approximation, it can be shown that, this leads to an effective radiative time constant for our model atmosphere which is about half the radiative time constant of the atmosphere. According to estimates using simple model calculations (Schneider 1977; Held and Hou 1980), the mass flux of the zonally symmetric Hadley cell should be inversely proportional to the radiative time constant. This seems to be the reason why our symmetric version of the GLAS climate model simulates Hadley cells with large mass fluxes.

Since the motivation of the present study is only to examine the sensitivity of the MMC to changes in the eddy forcing, the discrepancies between our standard solution and the observed MMC are not expected to influence our conclusions regarding the sensitivity experiments. We shall only derive qualitative conclusions regarding the role of various components of the eddy forcing on maintaining the MMC by comparing the sensitivity experiments with the standard solution. For this purpose the low internal viscosity run (figure 3) will be taken as the standard solution.

4. Sensitivity of the MMC to eddy forcing

In this section we present results of several sensitivity experiments. These experiments are designed to study the relative role of different eddy components. We shall also examine how the strength of the total eddy forcing affects the MMC. All other conditions for these runs including the prescribed convective heating, and vertical eddy viscosity are the same as described in §3.2.

4.1 *The role of the strength of the eddy forcing*

In order to study the response of the MMC to the strength of the eddy forcing, we carried out two experiments in one of which 0·5 times and in the other 1·5 times the observed eddy fluxes described in §2 are used. The model is integrated in both cases until it reaches a steady state. The stream function and the zonal wind for the steady state corresponding to the weak eddy forcing are shown in figures 5a, b, while those corresponding to the strong eddy forcing are shown in figures 5c, d.

Comparing the results of the weak eddy forcing case (figures 5a, b) with figure 3 we note that the reduced strength of the eddy forcing reduces the core strength of the NH subtropical westerly jet from $60\,\mathrm{ms^{-1}}$ to $50\,\mathrm{ms^{-1}}$. The tropical easterlies and SH subtropical westerly jet strength do not get affected appreciably by the reduction in the total eddy forcing. Moreover, we note that the easterly jet in the middle latitude seen in the standard solution (figure 3), is not seen in the reduced eddy forcing case. Thus the origin of the easterly jet may be traced to the heat and momentum transports by the

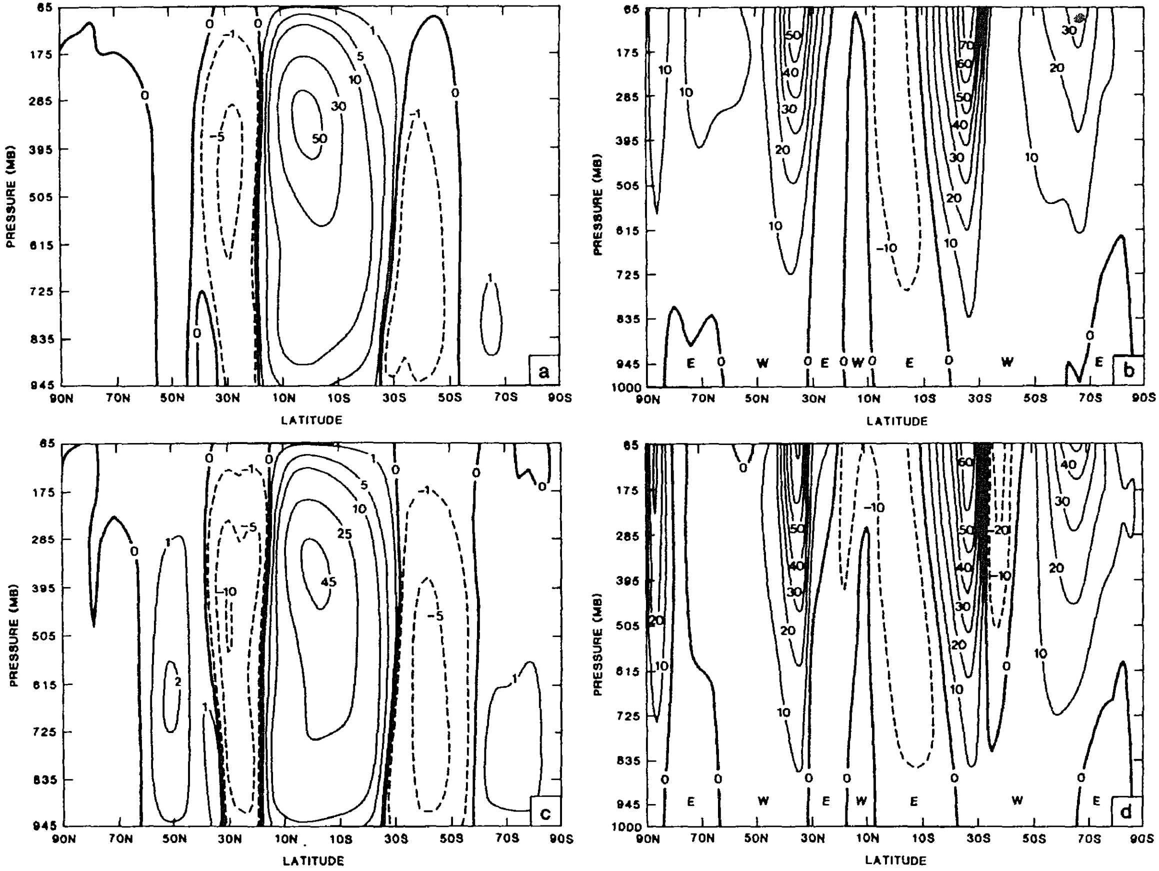

Figure 5. **a**) Stream function, contours $10^{10}\,\mathrm{kgs}^{-1}$, **b**) zonal wind, contours $10\,\mathrm{ms}^{-1}$ for a run with 0·5 times the observed eddy forcing. **c** and **d** represent stream function and zonal wind for a run with 1·5 times the observed eddy forcing.

large scale eddies. Comparing figures 5d and 5b, we note that the increase in the eddy forcing increases the strength of the NH westerly jet while it reduces the strength of the SH westerly jet.

Comparing the stream function fields for the reduced and increased eddy forcing cases (figures 5a, c) with the standard case (figure 3c) we note the following points. The decrease in the eddy forcing decreases the strength of the NH Ferrel cell by about a factor of 2 while that of the SH Ferrel cell is decreased by about a factor of 3. The decrease in the eddy forcing decreases the strength of the NH Hadley cell by about 30 % while it does not change the strength of the SH Hadley cell appreciably. Similarly, the increase in the eddy forcing increases the strength of the NH Ferrel cell by a factor of 2 but it increases the strength of the SH Ferrel cell only by about 25 %. The increase in the eddy forcing increases the strength of the NH Hadley cell by about 40 % while it reduces the strength of the SH Hadley cell by about 10 %.

4.2 *The role of eddy heat flux forcing only*

In this run we introduced only the observed eddy heat fluxes namely $[\overline{v'T'}]$ and $[\bar{v}^*\bar{T}^*]$ as input forcing and omitted the eddy momentum fluxes. The stream function and the zonal wind for the steady state for this run are shown in figure 6. The stream function field shows that the eddy heat flux alone cannot maintain the NH Ferrel cell. The strength of the SH Ferrel cell is also reduced by about a factor of 2 as compared to the standard solution (figure 3). The strength of the NH Hadley cell is reduced by about 30 %. Moreover, the westerly winds at the SH subtropical jet in this case are increased to $90\,\mathrm{ms}^{-1}$ as compared to $70\,\mathrm{ms}^{-1}$ in the case of the standard solution (figure 3).

4.3 *The role of eddy momentum flux forcing only*

This run is similar to the run described in §4.2. In this run we included only the observed eddy momentum fluxes, $[\overline{u'v'}]$ and $[\bar{u}^*\bar{v}^*]$ and neglected the eddy heat fluxes. The stream function and the zonal winds for the steady state obtained from this run are shown in figure 7. We note from the stream function field that the eddy momentum forcing alone can maintain the Ferrel cells in both hemispheres. The mass fluxes in the Ferrel cells in both hemispheres are smaller than those in the full eddy forcing case (figure 3). The strength of the NH Hadley cell is reduced by about 30 % in this case while the SH Hadley cell is maintained at the same strength as in the standard solution.

We also note that the eddy momentum forcing alone maintains much weaker westerly jets in both hemispheres. In this case the maximum westerly winds in the subtropical westerly jets are about $40\,\mathrm{ms}^{-1}$ in both hemispheres as compared to $60\,\mathrm{ms}^{-1}$ in the NH and $70\,\mathrm{ms}^{-1}$ in the SH in the full eddy forcing case.

It is interesting to note from figures 3, 6 and 7 that the eddy heat transports tend to strengthen the westerly jets but cannot maintain the observed Ferrel cells. On the other hand, the eddy momentum transports tend to reduce the strength of the westerly jets and can maintain fairly strong Ferrel cells.

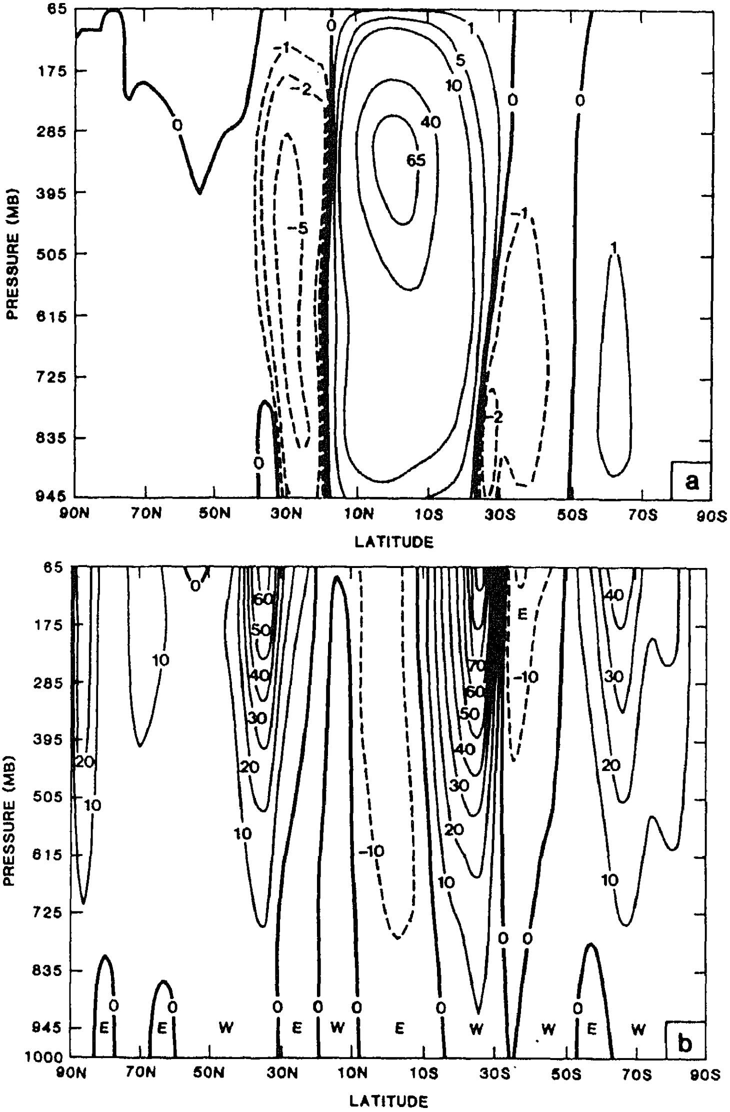

Figure 6. Summer run with eddy heat forcing only, **a**) stream function, **b**) zonal wind. Units are the same as in figure 3.

4.4 *The role of the stationary eddies*

In order to examine the role of the standing eddies in maintaining the MMC, we conducted one experiment in which we introduced only the transient eddy fluxes $[\overline{u'v'}]$ and $[\overline{v'T'}]$ and neglected the stationary eddy fluxes. The stream function and the zonal

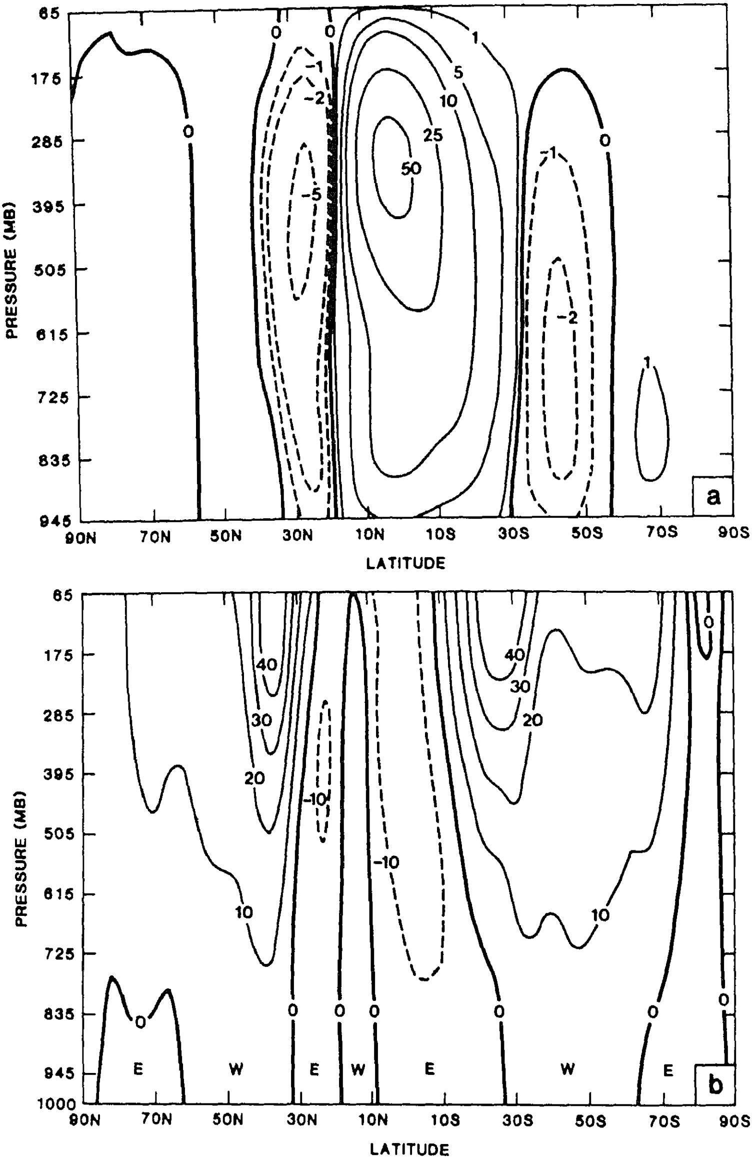

Figure 7. Summer run with eddy momentum forcing only, **a**) stream function, **b**) zonal wind. Units are the same as in figure 3.

absence of the stationary eddies, the NH westerly jet strength is reduced but the SH westerly jet is maintained at the same strength as in the case of the standard solution. In this case, Ferrel cells are maintained in both hemispheres but with reduced strength. The NH Hadley cell is also maintained with a reduced strength but the SH Hadley cell is maintained at the same strength as in the standard solution.

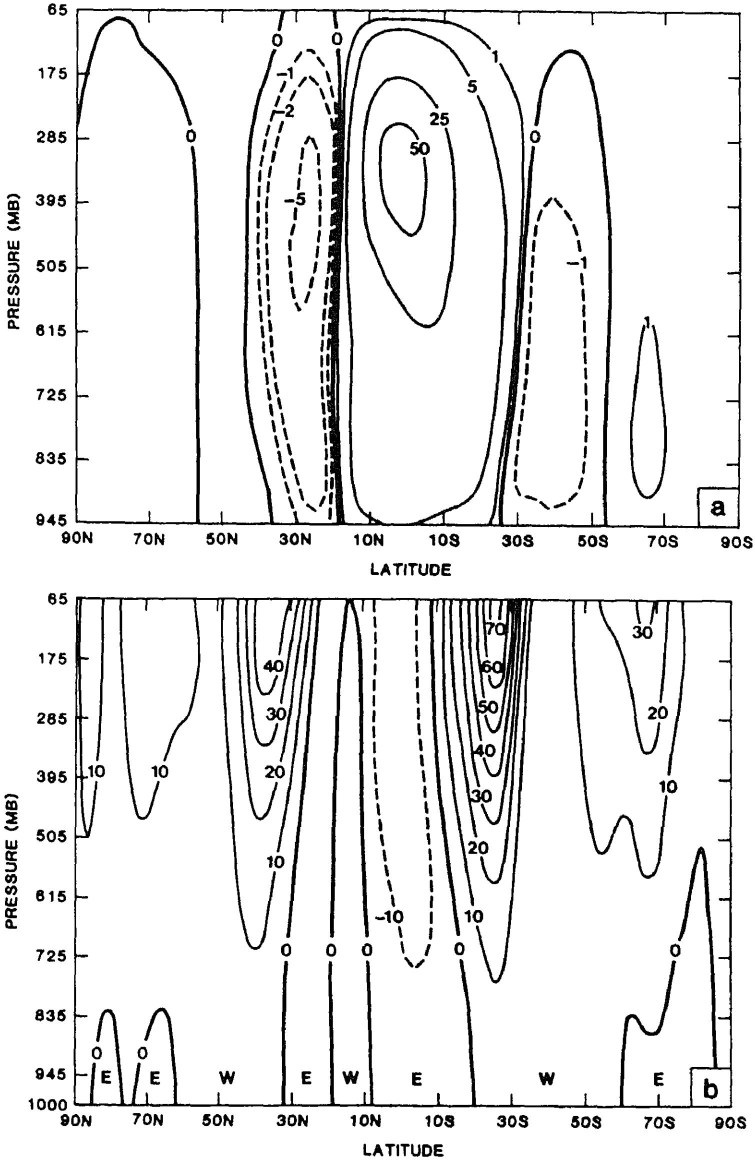

Figure 8. Summer run with transient eddy forcing only, **a**) stream function, **b**) zonal wind. Units are the same as in figure 3.

5. Conclusions and discussion

The role played by the large scale eddy activity in maintaining the mean meridional circulation in general and the Hadley circulation in particular is studied using a zonally averaged model.

When the eddy forcing consisting of climatological horizontal fluxes of heat and momentum by the transient and the stationary eddies is reduced to 0·5 times or increased to 1·5 times its climatological values, the strength of the Ferrel cells decrease or increase proportionally. This result is as expected since the Ferrel cells are essentially driven by the eddy forcing. However, we also note that the changes in the eddy forcing can influence the strength of the NH Hadley cell significantly. In the case when the eddy forcing is reduced to 0·5 times the climatological values, the strength of the NH Hadley cell reduces to about 30 % while it is increased by about 40 % when the eddy forcing is increased to 1·5 times. This result is in agreement with the results of Crawford and Sasamori (1981) in which they showed that even in the absence of the condensational heating, the eddy forcing could maintain Hadley cells in the tropics at about a third of its observed strength. Sensitivity experiments with respect to various components of the eddy forcing show that the eddy momentum fluxes seem to be more important in maintaining the Ferrel cells as compared to the eddy heat fluxes. Moreover, the eddy momentum fluxes tend to decrease the strength of the subtropical westerly jets while the eddy heat fluxes tend to increase them.

Thus, the results of this preliminary study indicate that the changes in the large scale eddies can indeed influence the monsoon circulation via changes in the strength of the NH Hadley cell. However, we must be cautious in drawing quantitative conclusions regarding the influence of the eddies on the monsoon circulation based on these results. This is because the monsoon circulation is actually a regional, reverse Hadley circulation anomaly, roughly between 40°E and 120°E embedded in the global Hadley circulation. Thus, diabatic heating field and eddy fluxes averaged over this region may be more important in maintaining the monsoon circulation. The latent heating field and the eddy fluxes used in this study were derived by zonally averaging the observed fields over an entire latitude circle. Thus, these forcing functions may not be representative forcing functions for the monsoon circulation. Therefore, it may be more meaningful to obtain latent heating field and eddy fluxes by averaging the observed fields between say, 40°E and 120°E and use these forcing functions in a zonally averaged model. We are currently engaged in deriving these regionally averaged forcing functions. In a later study, we shall examine the sensitivity of the monsoon circulation using such forcing functions.

Acknowledgements

I would like to thank Dr A Oort of GFDL, Princeton University for graciously providing me with the global eddy statistics even before it was published. I would also like to thank Dr J Shukla for many interesting discussions. Most of the computations related to this paper were carried out at NASA/Goddard Laboratory for Atmospheric Sciences Computer, Greenbelt, MD, USA.

References

Goswami B N, Shukla J, Schneider E K and Sud Y 1984 *J. Atmos. Sci.* **41** 5

Held I M and Hou A 1980 *J. Atmos. Sci.* **37** 515

Kuo H L 1956 *J. Meteorol.* **13** 561

Kurihara Y 1973 *J. Atmos. Sci.* **30** 25

Mak Man-Kin 1969 *J. Atmos. Sci.* **26** 41

Newell G R, Kidson J W, Vincent D G and Boer G J 1972 *The general circulation of the tropical atmosphere* (Cambridge, Mass: The MIT Press) Vol. 1

Newell G R, Kidson J W, Vincent D G and Boer G J 1974 *The general circulation of the tropical atmosphere* (Cambridge, Mass: The MIT Press) Vol. 2

Oort A H 1983 *Global atmospheric circulation statistics* 1958–1973 NOAA Professional Paper No. 14, US Government Printing Office, Washington DC

Oort A H and Rasmusson E M 1971 *Atmospheric circulation statistics* NOAA Professional paper No. 5, US Government Printing Office, Washington DC

Palmén E 1949 *J. Meteorol.* **6** 429

Palmén E, Riehl H and Vuorela L A 1958 *J. Meteorol.* **15** 271

Ramaswamy C 1962 *Tellus* **14** 337

Rossby C G and Starr V P 1949 *J. Meteorol.* **6** 288

Saltzman G and Vernekar A D 1971 *J. Geophys. Res.* **76** 1498

Saltzman G and Vernekar A D 1972 *J. Geophys. Res.* **77** 3936

Schneider E K 1977 *J. Atmos. Sci.* **34** 280

Schneider E K and Lindzen R S 1977 *J. Atmos. Sci.* **34** 263

Shukla J, Straus D, Randall D, Sud Y and Marx L 1981 *Winter and summer simulations with* GLAS *climate model* NASA Technical Memorandum 83868 (NTIS No. N 8218807) pp. 282

Starr V P 1948 *J. Meteorol.* **5** 39

Taylor K E 1980 *J. Atmos. Sci.* **37** 1

Wiin-Nielsen A and Fuenzalida H 1975 *Tellus* **27** 199

Williams G P and Davis D E 1965 *Quart. J. R. Meteorol. Soc.* **91** 471

© Printed in India.

Remote sensing of atmospheric water vapour from Bhaskara II SAMIR data and its comparison with NOAA-7 water vapour data

P N PATHAK, B S GOHIL and A SARKAR

Meteorology and Oceanography Division, Space Applications Centre, Ahmedabad 380053, India.

MS received 26 November 1984; revised 25 September 1985

Abstract. Applying the method of 'statistical linear regression', atomspheric water vapour over oceanic areas has been estimated from the 19 GHz and 22 GHz data of the satellite microwave radiometer (SAMIR) system onboard the Bhaskara II satellite. In the absence of any simultaneous *in situ* measurements on water vapour over ocean, the SAMIR-derived water vapour data have been compared with like data from the NOAA-7 satellite. It is suggested that a positive bias seen in the SAMIR data could be due to calibration errors in the basic data. In view of the observed bias, the original regression equation is modified and then used to obtain water vapour distributions over ocean for winter and south-west monsoon seasons using SAMIR data of several orbits.

Keywords. Remote sensing; water vapour; Bhaskara II SAMIR; NOAA satellite.

1. Introduction

Microwave radiometry from space has long been recognised as a powerful tool for meteorological and oceanographic applications. Several satellites carrying multichannel passive microwave radiometers have been launched over the last 15 years and their data have been successfully used for a variety of geo-physical applications as reviewed by several workers (e.g. Swift 1980; Staelin 1981; Njoku 1982 and Hariharan and Pandey 1983).

One of the unique capabilities of passive microwave sensors in space is their ability to measure atmospheric water vapour and liquid water over the ocean, even in the presence of most types of clouds. Measurements at the weak water vapour resonance absorption frequency 22·235 GHz and at nearby frequencies allow us to determine the total atmospheric water vapour over ocean. This has been very well demonstrated through experiments on board the Nimbus series of satellites as well as the Seasat satellite (e.g. see Staelin *et al* 1976; Njoku and Swanson 1983).

The Bhaskara II satellite, which was launched on 20 November 1981 in a near circular orbit at an altitude of about 525 km, carried on board a 3-frequency passive microwave radiometer system SAMIR*, operating at 19·35 GHz, 22·235 GHz and 31·4 GHz. Table 1 gives some essential characteristics of the SAMIR system.

It may be noted here that the three SAMIR radiometers have a *common* footprint of ~ 125 km diameter. The SAMIR system can be operated in two distinct modes called the *Normal* and *Alternate* modes. In the Normal mode the spin-axis of the spacecraft is maintained *perpendicular* to the orbital plane and consequently during each spin, observations by the three SAMIR radiometers are taken *along* the satellite ground trace at

---

*The acronym SAMIR is derived from *SA*tellite *MI*crowave *R*adiometer.

Table 1. Characteristics of the SAMIR system on board Bhaskara II.

System parameters	SAMIR radiometers R-1	 R-2	 R-3
Frequency (GHz)	31·4	19·35	22·235
RF bandwidth (MHz)	250	250	250
Integration time (ms)	300	300	300
RMS temperature sensitivity ΔT (K)	1	1	1
Spatial resolution (km)	125	125	125
View-angles with respect to nadir (normal mode)*	±2·8°, ±5·6°, 180° (zenith)		
View angles with respect to nadir (alternate mode)*	±2·8°, ±8·4°, ±14·0°, ±19·6°, ±25·2°, ±30·8°, ±36·4°, 180° (zenith)		

*Applicable to all the three radiometers.

four view angles with respect to the nadir direction. In the alternate mode, the spin-axis of the spacecraft is aligned *along a tangent* to the orbital plane at certain latitude and consequently the SAMIR radiometers scan *across* the satellite ground trace at a number of angular positions. In both these modes of operation the SAMIR system also measures the zenith cold sky temperature during each spin. The zenith measurement which corresponds to the lowest constant brightness temperature of ~ 3 K' is used in the calibration scheme together with the pre-launch calibration data taken at different temperatures in the thermo-vacuum chamber. Although the temperature sensitivity of the SAMIR system is not adequate enough for measuring the 3 K radiation, the use of this measurement in the calibration scheme allows us to approximately account for the small variations in the gain of the radiometers. It is possible that this calibration procedure may introduce some unknown bias in the data.

Reviews by Pathak *et al* (1983) and by Hariharan and Pandey (1983) give further details of the SAMIR system and also describe several studies related to the application of the SAMIR data to meteorology and oceanography.

The present paper deals with the estimation of total atmospheric water vapour (wv) content over ocean through the 'statistical regression method' using the normal mode SAMIR data at 19 GHz and 22 GHz. The SAMIR derived wv data are compared with the near-coincident wv data of the NOAA-7 satellite for a sizable data base. The comparison with NOAA wv data allows us to apply necessary bias correction to the SAMIR wv data. Finally, the SAMIR data over a few orbits have been used to determine latitudinal distribution of wv over the Arabian Sea during the northern hemisphere winter and the south-west monsoon. Preliminary results of this analysis are given by Pathak (1983a).

2. Estimation of atmospheric water vapour

In order to estimate atmospheric wv from the SAMIR data we have used the 'statistical' approach which was first suggested by Grody (1976) and later used by Pandey *et al* (1981) for estimating atmospheric water vapour from Bhaskara I SAMIR data. In this method the expected brightness temperature over ocean is simulated for a statistically representative set of atmospheres for the region of interest, and a regression is then performed between the geophysical parameter (in the present case, water vapour) and the simulated brightness temperatures. The resulting equation is then later used independently to derive atmospheric WV over the ocean by using the observed brightness temperatures.

The brightness temperature $T_B(\nu)$ at frequency ν, observed over the ocean by a satellite-borne microwave radiometer for a non-scattering atmosphere in local thermodynamic equilibrium is given by

$$T_B(\nu) = \tau_\nu(0, \infty)[T_s\varepsilon_s(\nu) + (1 - \varepsilon_s(\nu))T_{\text{sky}}(\nu)] + T_{\text{atm}}(\nu) \tag{1}$$

where

$\tau_\nu(0, \infty)$ = total transmittance = $\exp\left[-\int_0^\infty \alpha_\nu(z)\,\mathrm{d}z\right]$,

T_s = ocean surface temperature

$\varepsilon_s(\nu)$ = ocean surface emissivity at frequency ν,

$T_{\text{sky}}(\nu)$ = down-welling radiation

$= \int_0^\infty T(z)\alpha_\nu(z)\tau_\nu(0, z)\,\mathrm{d}z + T_{\cos}\tau_\nu(0, \infty)$,

$T_{\text{atm}}(\nu)$ = upwelling atmospheric radiation

$= \int_0^\infty T(z)\alpha_\nu(z)\tau_\nu(z, \infty)\,\mathrm{d}z$,

$\alpha_\nu(z)$ = total absorption due to atmospheric constituents at altitude z,

$T(z)$ = temperature of a thin atmospheric layer at altitude z,

$T_{\cos}$ = cosmic background temperature (~ 2·8 K)

The emissivity of the ocean surface depends on the ocean surface temperature, salinity and surface roughness, which, in turn is related to surface winds as shown by Hollinger (1971).

The brightness temperatures over ocean for 19 GHz and 22 GHz were simulated for various atmospheric and surface conditions as observed during the MONEX-79 observation period, May–July 1979. For the above simulation, the MONEX data from 690 shipborne upsonde flights giving profiles of atmospheric water vapour and temperature over the Arabian Sea and the Bay of Bengal regions have been used, along with the ship's surface observations. Also included in these profiles are 48 non-precipitating cloud models having different amounts of liquid water (LW) at different altitudes. Absorption models for WV and LW as described by Pandey *et al* (1980, 1981) have been used. The effect of ocean surface wind speed on the ocean surface emissivity, $\varepsilon_s(\nu)$, is taken into account following the work of Wisler and Hollinger (1977), which considers effects due to surface wind through roughness and foam. The statistics of relevant atmospheric and oceanic parameters used for the simulation is given in table 2.

After simulating the brightness temperatures for 19 GHz and 22 GHz for different atmospheric profiles, a multiple regression was performed between the input WV values and the simulated brightness temperature values. This gave the following regression

Table 2. Statistics of the various geophysical parameters used in the simulation analysis.

Parameter	Minimum value	Maximum value	Standard deviation
Total water vapour (mm)	30	77	6
Liquid water content (kg/m^2)	0·06	6·54	1·27
Surface wind speed (m/s)	0·0	16·0	2·85
Sea-surface-temperature (K)	298	304	1

equation:

$$\mathrm{WV} = 1{\cdot}26\,T_B(22) - 0{\cdot}75\,T_B(19) - 90{\cdot}65\ \mathrm{mm}, \tag{2}$$

with an RMS error of about 2 mm.

3. Comparison between SAMIR and NOAA water vapour data

In order to validate the SAMIR WV content obtained on the basis of the regression equation (2) derived above, we require a large data base of near-coincident *in situ* observations on WV over oceanic areas. For the present case, we do not have such *in situ* data and we have, therefore, chosen near-coincident WV data from NOAA-7 satellite for the purpose of comparison with the SAMIR WV data. This choice is based on an earlier study (Pathak 1983b), wherein it was demonstrated that the TIROS-N/NOAA WV data show excellent agreement with the *in situ* WV data from aircraft (dropsondes) and ships (upsondes) during MONEX-79 (May–July 1979) with RMS errors of 2–3 mm, even on a day-to-day basis. Cadet (1983) has also compared TIROS-N WV data with the corresponding MONEX-79 data from ships (upsondes) and found very good agreement between the two.

The TIROS-N/NOAA series of operational meteorological satellites carry a high resolution infrared sounder (HIRS) from which the amount of precipitable water (water vapour) in three broad layers (surface–700 mb, 700–500 mb and 500–300 mb) is available. The water vapour amounts for these three layers are combined to obtain the total WV in the atmosphere, which is then compared with the SAMIR WV data. Water vapour above 300 mb is implicitly neglected; this is generally $\leqslant 1$ mm.

The NOAA satellite provides WV data on a global scale with a spatial resolution of ~ 17 km for each observation. Being an infrared sensor, HIRS does not provide WV data for cloudy atmospheres. In contrast, however, SAMIR allows WV retrieval even for moderate cloud covers. For the present analysis, the NOAA-7 'finished product' data tapes for the period January–June 1982 have been obtained from the NOAA Environmental Data and Information Service, USA.

Total WV content from the SAMIR data has been calculated using (2) by considering observations only over open ocean. In order to avoid effects due to high emissivity of land, SAMIR data within ~ 200 km of the coast were not used in the analysis. No correction for the antenna pattern has been applied to the brightness temperature data. Njoku *et al* (1980) have shown that for reasonably homogeneous areas (such as over open ocean well away from major land areas), the errors introduced by neglecting sidelobes effect is not significant. Thus, for the present analysis where we have considered data only over open oceans, the antenna pattern correction may not be important. Internal consistency of the SAMIR data is checked by comparing brightness temperature (T_B) data at closely spaced beam centre positions. This is illustrated in figure 1 which shows T_B data corresponding to all four view angles for 19 GHz and 22 GHz, over the ocean, plotted as a function of latitude. It can be seen from this figure that a number of clusters, each having four data points, corresponding to four closely spaced beam centres, occur along the ground trace. From such a plot, mutual consistency of T_B values in each cluster helps in deciding the quality of the data. Secondly, wildly fluctuating T_B values can be easily identified and eliminated. For calculating WV from the SAMIR data, T_B values in each cluster were first averaged. This helped in reducing the error in the basic data.

For comparison with the NOAA WV data, spatial separation between SAMIR beam-centre position and NOAA observation position is restricted to 1° in latitude and 1° in longitude. This criterion is based on the fact that the spatial resolution of SAMIR is a circle of ~ 125 km diameter which is comparable to $1° \approx 110$ km. Time difference, Δt, between SAMIR and NOAA observations is limited to within 8 hr. For the complete data set, Δt has the following statistics:

$$\Delta t \leqslant 6\ \text{hr}—65\%;\ 6 \leqslant \Delta t \leqslant 7\ \text{hr}—23\%;\ 7 \leqslant \Delta t \leqslant 8\ \text{hr}—12\%.$$

The comparison is made for spot values of NOAA WV data without any spatial or temporal averaging. Figure 2 shows the extent of the geographical region over which

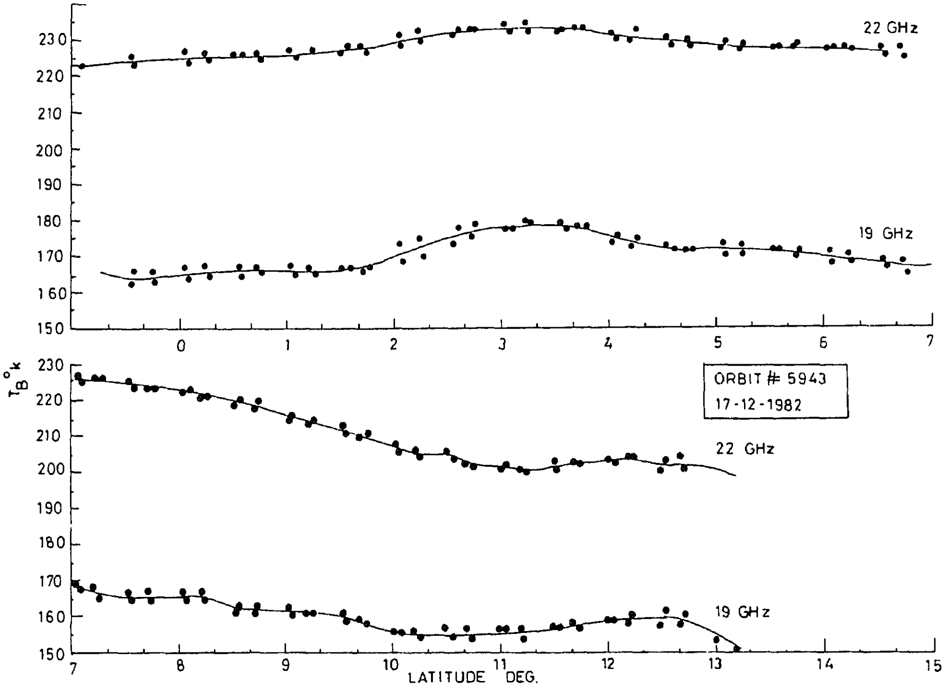

Figure 1. Brightness temperature (T_B) for 19 GHz and 22 GHz of SAMIR over ocean plotted as functions of latitude for orbit no. 5943.

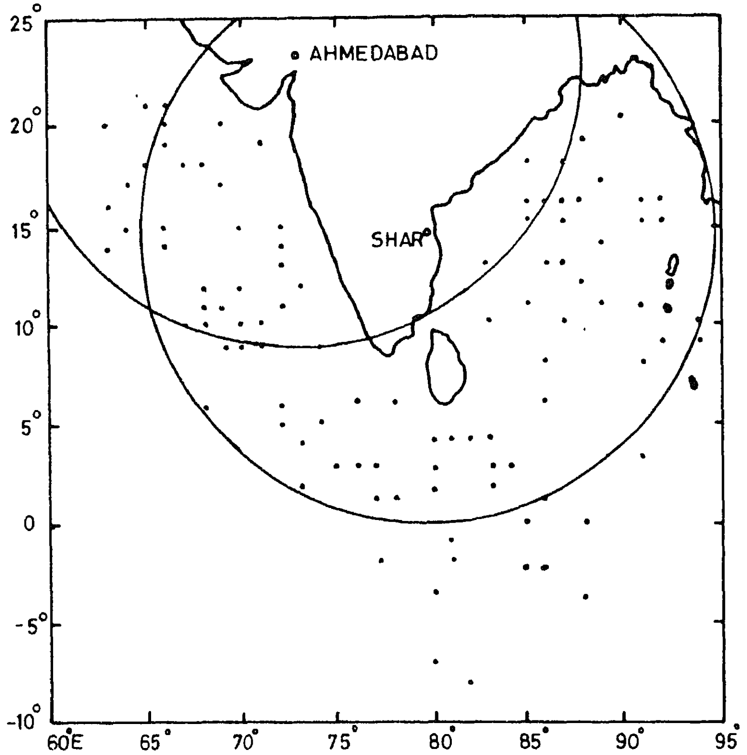

Figure 2. Geographical locations of the SAMIR derived water vapour data which are compared with the nearby NOAA water vapour data. The two circles represent the radio-visibility zones of the two ground stations (Ahmedabad and Shar) at 10° elevation.

he SAMIR and NOAA WV data have been compared. Although NOAA provides global data n wv, the coverage of Bhaskara II SAMIR data is restricted to the tropical Indian region orth of the equator (see figure 2) mainly by the radio-visibility zones of the SHAR and hmedabad ground stations which receive the SAMIR data in *real* time. However, on oard recording of SAMIR data has, at times, provided coverage over the southern atitudes also. Such on board recorded data have, in fact, been used in the present omparison to a limited extent.

Figure 3 shows a scatter diagram between the near-coincident SAMIR and NOAA WV ata. The SAMIR data used here correspond to about 100 orbits during the period anuary–June 1982. The range of NOAA WV values used here is 20–50 mm which is lightly different from that used for the simulation analysis in §2. The total number of ata points is 200 while the correlation coefficient is 0·98. The least squares fit line is iven by the following equation

$$\mathrm{WV}_{\mathrm{SAMIR}} = 1{\cdot}04\,\mathrm{WV}_{\mathrm{NOAA}} + 9{\cdot}85\ \mathrm{mm}. \tag{3}$$

he RMS error is ~ 5 mm, which is calculated on the basis of the scatter of the data. The mportant point to note is that there is a *positive bias* of about 10 mm on the SAMIR WV xis, while the slope is very close to 1. Figure 4 shows a histogram of the observed bias in he SAMIR WV values with respect to the NOAA WV data.

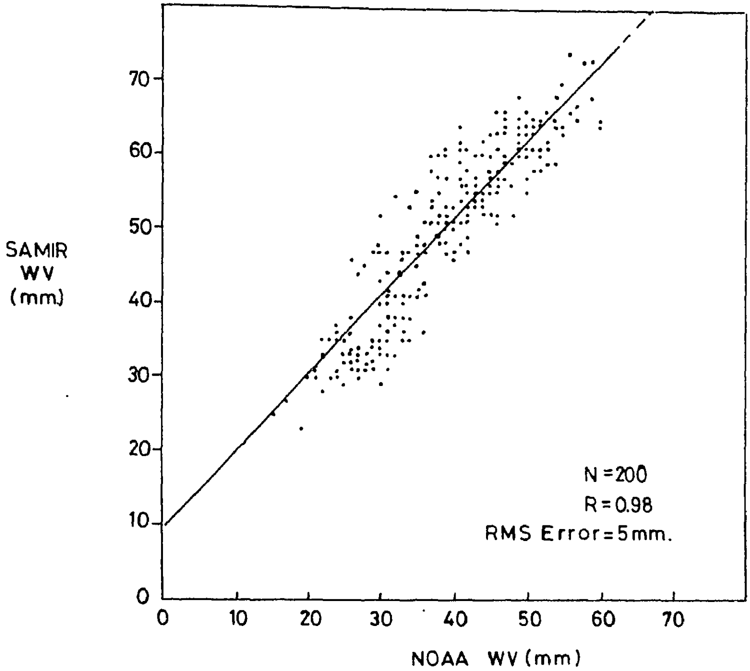

Figure 3. Scatter plot between SAMIR and NOAA water vapour data. N denotes the total number of data points while R is the correlation coefficient.

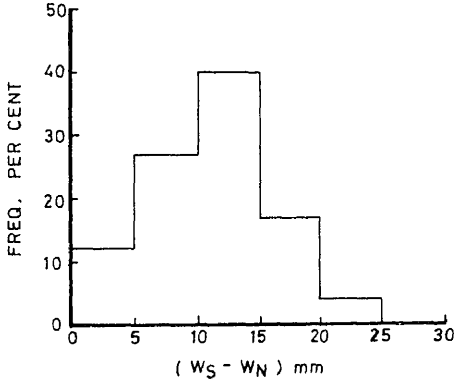

Figure 4. Histogram of the bias between the SAMIR and NOAA water vapour data (W_s = SAMIR WV, W_N = NOAA WV, in mm).

4. Discussion and conclusion

The above analysis clearly shows that based on the present regression equation (2) uncertainty in the values of atmospheric transmittances and inadequacy in the model connecting sea-surface wind speed and ocean surface emissivity, as used in the simulation analysis in §2. It should be noted here that uncertainties related to both the factors in (b) will be of a variable nature. It is, therefore, more likely that the constant bias observed in the SAMIR WV data could probably arise from the calibration procedure. It may be pointed out here that in many microwave remote sensing satellites such post-launch adjustments/corrections in the calibration constants or bias corrections in the geophysical parameters have to be effected based on the results of verification programmes (e.g. Staelin *et al* 1976; Lerner and Hollinger 1977; Pandey and Kakar 1983 etc.). In the present case, it is found that slight changes in the T_B values can bring down the WV values as calculated from (2). For example, a reduction of 5°K in the 22 GHz T_B values and an equal increase in 19 GHz T_B values would result in an overall reduction of $\sim$ 10 mm in the SAMIR derived WV values. Rather than effecting such arbitrary adjustments in the T_B data, we use (3) and introduce the bias correction,

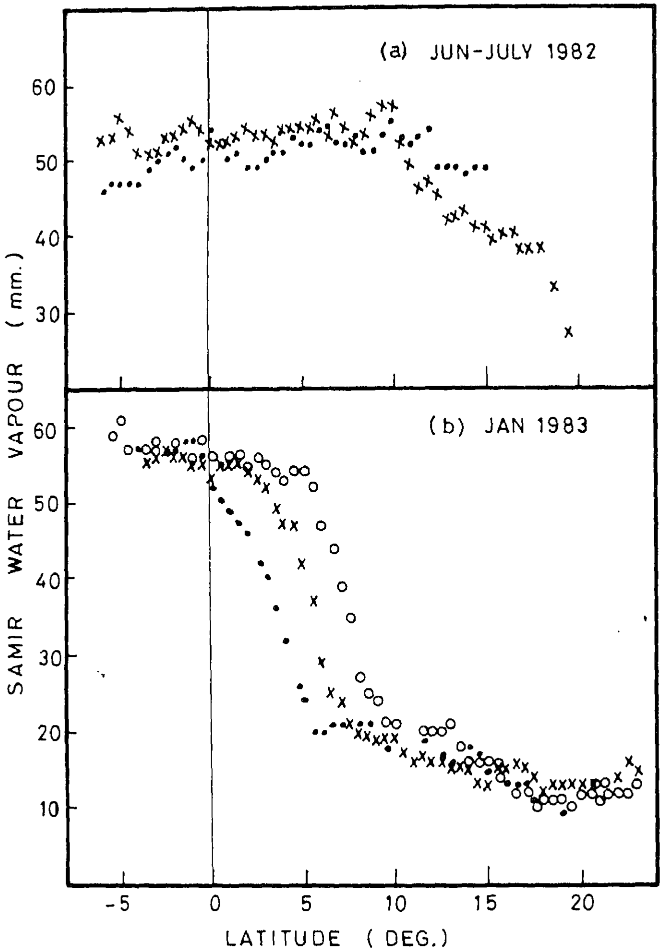

Figure 5. Latitudinal distributions of SAMIR WV over the Arabian sea for (**a**) two orbits during June–July 1982 and (**b**) three orbits during January 1983. Data for different orbits are shown by different symbols.

modifying the original regression equation (2) as follows:

$$\mathrm{WV} = 1{\cdot}21\, T_B(22) - 0{\cdot}72\, T_B(19) - 96{\cdot}63\,\mathrm{mm} \tag{4}$$

In the present work, we have used NOAA WV data in place of *in situ* data. It is therefore, important to consider the limitations of the NOAA data. The main limitation of the NOAA WV data is that the WV values are available only for clear (cloud-free) areas, whereas for cloudy areas no retrieval of WV is possible. Thus, the present comparison of SAMIR WV with the NOAA WV data can be considered essentially for a cloud-free atmosphere. The extension of the bias-corrected modified regression equation (4) to cloudy regions would perhaps require further validation through *in situ* measurements of WV by radiosondes. Another important limitation of the NOAA WV data, as noted by Gruber and Watkins (1979), is that there is an underestimation of WV for deep moist layers and an overestimation for a relatively dry layer. If this feature is indeed present in the present NOAA data, it might have affected the slope of the regression line in figure 3 to some extent. However, we do not have any means to check this effect in the present analysis.

The bias-corrected modified regression equation (4) has been used along with an expanded SAMIR data set (without reference to NOAA data) to determine latitudinal gradient of total WV over the ocean for two typical time periods. Figure 5 shows

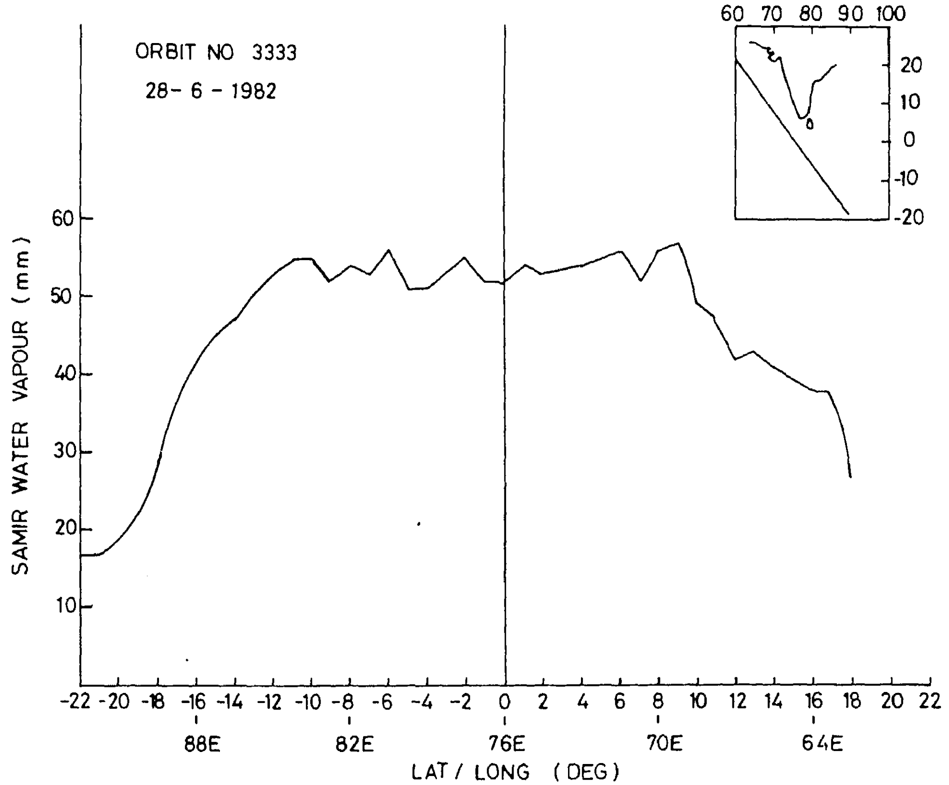

Figure 6. Latitudinal distribution of SAMIR WV over a large part of the Arabian Sea and southern Indian Ocean region obtained through onboard recording of the SAMIR data during a single orbit in June 1982. Approximate ground trace of the orbit is shown in the inset.

latitudinal gradients of total water vapour for two days in June–July 1982 during the south-west monsoon period and three days in January 1983 which is during the northern hemisphere winter. Both of these latitudinal distributions are mainly over the Arabian Sea region. It can be clearly seen that there is a marked difference between the two distributions. Whereas for the June–July period, the total wv is high (~ 50 mm) and practically constant from the equator to ~ 10°N, the January distribution shows a very sharp latitudinal gradient, with wv decreasing by almost a factor of four from the equator to 20°N. Both these distributions are consistent with the climatologically expected behaviour of wv during the south-west monsoon period and during the dry conditions of the northern winter (Peixoto and Oort 1983). Similar results were also reported on the basis of the Nimbus-5 data by Staelin *et al* (1976). Figure 6 shows the total wv distribution determined from the SAMIR data of orbit 3333 on 28 June 1982, wherein the data were recorded onboard the Bhaskara II satellite. This allowed mapping of wv over a large part of the Indian Ocean and Arabian Sea from 22°S to 18°N. This distribution shows high wv concentration (~ 50 mm) on either side of the equator from 10°S to 10°N and a sharp fall thereafter in both the hemispheres. In conclusion, it can be stated that the present comparison between SAMIR and NOAA WV data has been useful, in identifying a large positive bias in the SAMIR WV data, which could arise due to calibration errors.

After correcting for the observed bias, the wv values estimated from the SAMIR data are found to be consistent with the expected seasonal behaviour. It may be useful to further analyse the SAMIR data to decide whether there are any changes in the observed bias. Also, a few island and coastal stations radiosonde data, would be useful in deciding how the bias is spread between SAMIR and NOAA.

Acknowledgement

Thanks are due to Dr T A Hariharan for constant encouragement. We are also thankful to Shri S S Rana and Dr S M Bhandari for discussion and to Dr Pranav S Desai for useful suggestions and comments.

References

Cadet D L 1983 *Tellus* **B35** 329

Grody N C 1976 *IEEE Trans. Antennas Propag.* **AP-24** 153

Gruber A and Watkins C D 1979 *Satellite hydrology*, V Annual symposium of the American Water resources Association, (eds) M Deutich, D R Wiesnet and A Rango (Minnesota: American water resources Association) p. 115

Hariharan T A and Pandey P C 1983 *Proc. Indian Acad. Sci. (Eng. Sci)* **6** 233

Hollinger J P 1971 *IEEE Trans. Geosci. Electron* **GE-9** 165

Lerner R M and Hollinger J P 1977 *Remote Sensing of Environ.* **6** 251

Njoku E G 1982 *Proc. IEEE* **70** 728

Njoku E G, Christensen E J and Cofield R E 1980 *IEEE J. Oceanic Eng.* **OE-5** 125

Njoku E G and Swanson L 1983 *Mon. Weather Rev.* **111** 1977

Pandey P C, Gohil B S and Sharma A K 1980 *Mausam* **31** 539

Pandey P C, Gohil B S and Sharma A K 1981 *Mausam* **32** 17

Pandey P C and Kakar R K 1983 *IEEE Trans. Geosci. Electron.* **GE-21** 208

Pathak P N 1983a *Abstract book of national space science symposium*, Pune, Dec. 1983 p. 276

Pathak P N 1983b *Variations in the global water budget* (ed) A Street Perrott, M Beran and R Ratcliff, (Dordrecht: D Reidel) p. 89

Pathak P N, Desai P S and Hariharan T A 1983 *Indian J. Radio Space Phys.* **12** 141

Peixoto J P and Oort A H 1983 *Variations in the global water budget* (eds) A Street Perrott, M Beran and R Ratcliff (Dordrecht: D Reidel) p. 5

Staelin D H 1981 *IEEE Trans. Antennas Propag.* **AP-29** 683

Staelin D H, Kunzi K F, Pettyjohn R L, Poon R K L and Wilcox R W 1976 *J. Appl. Meteor.* **15** 1204

Swift C T 1980 *Boundary-Layer Meteorol.* **18** 25

Wisler M M and Hollinger J P 1977 NRL Memorandum Report 3661, Washington

Proc. Indian Acad. Sci. (Earth Planet. Sci.), Vol. 94, No. 3, November 1985, pp. 249–259.
© Printed in India.

A study on the sensitivity of the radar scattering coefficient to oceanic winds

ABHIJIT SARKAR and RAJ KUMAR

Meteorology and Oceanography Division, Space Applications Centre, Ahmedabad 380053, India

MS received 21 January 1985; revised 31 July 1985

Abstract. Sensitivity of the radar scattering coefficient to the oceanic wind vector in the mid-angular range for frequencies from L- to Ku- band is studied. This is based on computations of scattering coefficient via the two-scale scattering theory employing a semi-empirical model for the ocean spectrum suggested by Fung and Lee and the slope distribution by Cox and Munk. Higher frequency and incident angles of over 45 degrees seem to yield better wind sensitivity.

Keywords. Microwaves; radar scattering coefficient; ocean spectrum; sea surface wind speed.

1. Introduction

The scattering of microwaves from the sea surface has been explained reasonably well by the two-scale roughness model of the sea surface, where the small scale waves are assumed to satisfy the condition of the small perturbation method, while the large scale waves are assumed to satisfy the Kirchhoff approximation (Moore and Fung 1979). The two-scale roughness model used in conjunction with the wind sensitive sea spectrum has resulted in a relationship between the back scattering coefficient and the wind vector, which agrees with trends in the experimental scattering coefficient data (Fung and Lee 1982). The scattering coefficient data have been acquired by various airborne and spaceborne scatterometers, operating at different frequencies, polarization and observation configurations. The question as to what are the optimum system parameters so that the wind vector can be best inferred from the scattering coefficient measurements still remains to be satisfactorily answered. This paper makes a preliminary but systematic attempt towards that goal. The scattering coefficient (σ^0)-wind vector relationships for different frequencies are evaluated via computations of σ^0 based on the semi-empirical model of the ocean spectrum suggested by Fung and Lee (1982, 1983). To facilitate sensitivity study, this relationship has been first given a simple analytic form. The coefficients of this relationship have then been expressed in terms of polynomials of observation angles for different frequency bands and polarizations. This has enabled us to study the sensitivity of the scattering coefficient to wind speed and wind direction over the range of angles between 30 and 60 degrees for different frequency bands and polarizations. The sensitivity functions are expected to be useful in defining an optimum system for remote sensing of oceanic wind vector.

2. Scattering coefficient-wind relationship

$$\sigma^0 = A_0 + A_1 \cos\phi + A_2 \cos 2\phi \tag{1}$$

where

ϕ the angle between the incidence plane and the wind direction.

The coefficients A_0, A_1 and A_2 are generally related to surface wind speed. These coefficients can be expressed in terms of σ_u^0, σ_c^0 and σ_d^0, which represent scattering coefficients for the specific cases of upwind, crosswind and downwind directions respectively:

$$A_0 = \frac{\sigma_u^0 + 2\sigma_c^0 + \sigma_d^0}{4} \tag{2}$$

$$A_1 = \frac{\sigma_u^0 - \sigma_d^0}{2} \tag{3}$$

$$A_2 = \frac{\sigma_u^0 - 2\sigma_c^0 + \sigma_d^0}{4} \tag{4}$$

The specific values of σ_u^0, σ_c^0 and σ_d^0 can be expressed by relationships of the power law type:

$$\sigma^0 = aW^b, \tag{5}$$

where the coefficients a and b are functions of the incidence angle θ, polarization and frequency. The scattering coefficient σ^0 is computed by the two-scale roughness approach (Chan and Fung 1977) using the semi empirical two dimensional sea spectrum $S(K, \phi)$ suggested by Fung and Lee (1982, 1983) and the slope probability density function P_θ as given by Cox and Munk (1954). The geometry of scattering by a two-scale rough surface is illustrated in figure 1. The scattering coefficient σ_{pp}^0 by the above approach is given by

$$\sigma_{pp}^0 = \int_{-\infty}^{\infty} \int_{-\cot\theta}^{\infty} \sigma_{pp}^0(\theta', \phi)\, P_\theta(Zx', Zy')\, \mathrm{d}Z_x \mathrm{d}Z_y \tag{6}$$

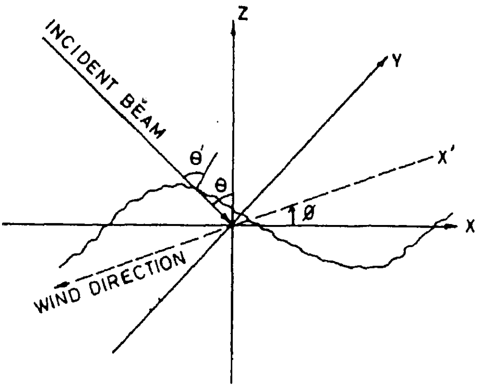

Figure 1. Geometry of two-scale rough surface scattering.

where

$$\sigma_{pp} = 8k^4 |\alpha_{pp}|^2 S(K, \phi)/K, \tag{7}$$

$pp = VV$ or HH polarization; θ' = local incidence angle; k = electromagnetic wavenumber; K = ocean wave number $= 2k \sin\theta$; θ = radar incidence angle; $Z'_x = Z_x \cos\phi + Z_y \sin\phi$, $Z'_y = Z_y \cos\phi - Z_x \sin\phi$, Z_x, Z_y = surface slopes along X and Y directions respectively.

$$\alpha_{hh} = R_h \cos^2\theta \tag{8}$$

$$\alpha_{vv} = R_v \cos^2\theta + (1 - 1/\varepsilon_y)\, T_v^2 \sin^2\theta/2 \tag{9}$$

R_h is the Fresnel reflection coefficient for horizontal polarization, R_v, T_v are the Fresnel reflection and transmission coefficients for vertical polarization, ε_y is the relative permittivity of the sea surface.

The spectrum used here (Fung and Lee 1983) has the following form:

$$S(K, \phi) = S(K)\left[(2\pi)^{-1} + C(1 - \exp(-3K^2))\cos 2\phi\right] \tag{10}$$

$$S(K) = \begin{cases} S_1(K), & K \leqslant 0{\cdot}04 \text{ rad/cm} \\ S_2(K), & K > 0{\cdot}04 \text{ rad/cm} \end{cases} \tag{11}$$

$$S_1(K) = (0{\cdot}0014/K^3) \exp\left[-0{\cdot}74 g^2/K^2 W^4\right] \tag{12}$$

$$S_2(K) = 0{\cdot}875(2\pi)^{p-1} g^{(1-p)/2} (1 + K^2/4{\cdot}3923)(K + K^3/13{\cdot}1769) \tag{13}$$

where g = gravitational acceleration; $p = 5 - \log U_*$; U_* = friction velocity (cm/sec), and C is a wind dependent coefficient. The term $S(K)$ significantly depends on the wind speed. The probability slope distribution function P_θ has been modelled as a two dimensional Gaussian distribution function (Cox and Munk 1954).

Four representative frequencies, viz, 1, 5, 9 and 13 GHz (belonging to L-, C-, X- and Ku- bands respectively) were selected for σ^0 calculations. Computed σ^0 data for different incidence angles at an interval of half a degree were used for power law fits with wind speed i.e. for the equation $\sigma^0 = a(\theta) W^{b(\theta)}$. The coefficients $a(\theta)$ and $b(\theta)$, thus generated, were given the form of functions of polynomials by the method of numerical curve fitting. The analytical expressions for $a(\theta)$ and $b(\theta)$ have the following form

$$a(\theta) = \exp\left(\frac{1}{10} \sum_{i=0}^{4} a_i \theta^i\right) \tag{14}$$

$$b(\theta) = \tan\left(\log e \sum_{i=0}^{3} b_i \theta^i\right) \tag{15}$$

The polynomials for both $a(\theta)$ and $b(\theta)$ were found to give excellent fits with RMS errors always less than 3 %. Tables 1 and 2 give the numerical values of $a(\theta)$ and $b(\theta)$ for all the cases. Similar analytical functions were earlier generated for the case of scattering in the quasi-specular range of incidence angles (Sarkar and Bhaduri 1984).

Table 1. Coefficients of polynomial for $a(\theta)$.

Frequency (GHz)	Polarization	ϕ (degree)	a_0	a_1	a_2	a_3	a_4
1	*HH*	0	123·2207	−13·9647	·3733	−4·7242E-03	2·15745E-05
		90	66·9564	−9·7345	·2502	−3·1697E-03	1·4345E-05
		180	30·0024	−6·0664	·1340	−·0159E-01	6·5992E-06
5	*HH*	0	−99·1490	7·1054	−·3281	·0524E-01	−2·9972E-05
		90	−3·4329	−1·8507	−·03206	·0106E-01	−8·5608E-06
		180	−2·5878	−2·1942	−·01208	6·8585E-04	−6·1646E-06
9	*HH*	0	−125·3527	9·2265	−·3866	·5876E-02	−3·2287E-05
		90	−37·9788	1·3275	−·1330	2·3937E-03	−1·4868E-05
		180	−25·8341	·0227	−·0857	·1694E-02	−1·1205E-05
13	*HH*	0	−188·9591	15·0596	−·5806	8·5886E-03	−4·6087E-04
		90	−93·7279	6·5711	−·3116	·4936E-02	−2·8001E-04
		180	−91·5667	6·1769	−·2947	·4680E-02	−·2672E-04
1	*VV*	0	126·1752	−14·3168	·4008	·5089E-02	·24079E-04
		90	72·9106	−10·0866	·2777	−·3534E-02	·16849E-04
		180	32·9566	−6·4185	·1615	−·1964E-02	·91034E-05
5	*VV*	0	−96·6940	6·8092	−·3033	·4923E-02	−·27787E-04
		90	−·9777	−2·1469	−·00733	·7483E-03	−·63759E-05
		180	−·13257	−2·4904	·01264	·3644E-03	−·39797E-05
9	*VV*	0	−122·9177	8·9326	−·3619	·5556E-02	−·30119E-04
		90	−35·5438	1·0337	−·1084	·2074E-02	−·12700E-04
		180	−23·3991	·2710	−·0611	·13749E-02	−·90374E-05
13	*VV*	0	−186·5084	14·7642	−·5560	·8268E-02	−·43917E-04
		90	−91·2772	6·2757	−·2869	·4616E-02	−·25831E-04
		180	−89·1160	5·8815	−·2701	·4360E-02	−·24551E-04

Since we are essentially concerned with two parameters namely wind speed W and wind direction ϕ, both $\partial\sigma^0/\partial w$ and $\partial\sigma^0/\partial\phi$ were computed. The sensitivities, as functions of incidence angle θ, for the L-, C-, X- and Ku-frequency bands and *HH* polarizations, are illustrated in figures 2–6. All of them confirm the expected behaviour of increase in sensitivity for higher frequencies. Fung and Lee (1982) have also shown qualitatively that the wind dependence of scattering coefficient increases with frequency and incidence angle. For wind speed higher than 15 m/sec, the increase in sensitivity is not significant. As far as sensitivity to wind speed alone is concerned, significant difference between X- and Ku- bands is not seen.

The curves for sensitivity to direction generally have double peaks, their levels depending upon the actual value of ϕ. In figure 2 are illustrated the curves for sensitivity of scattering coefficient to the wind direction for wind speeds of 10 and 15 m/sec. The behaviour of these curves for other wind speed values is found to be similar. The values of sensitivity to wind direction are generally found to be low.

Table 2. Coefficients of polynomials for $b(\theta)$.

Frequency	Polarization	ϕ (degree)	b_0	b_1	b_2	b_3
(GHz)	*HH*	0	−2·79753	15·76619	−19·08023	7·4977
1	and	90	−·567295	7·31430	−9·13235	3·65803
	VV	180	·88258	1·02593	−·82509	·30197
	HH	0	−·67386	7·7006	−7·14803	2·21335
5	and	90	−2·46066	13·75060	−15·03795	5·47711
	VV	180	−1·12791	10·54713	−11·6940	4·32868
	HH	0	·35279	4·63796	−3·54326	·85391
9	and	90	−1·84239	11·79946	−12·19866	4·25974
	VV	180	−·65313	9·39224	−10·19665	3·72259
	HH	0	·99687	2·67938	−1·14607	−0·083213
13	and	90	−1·10529	9·59061	−9·41842	3·14123
	VV	180	−·083323	7·62064	−7·9354	2·8039

Figure 6 shows the variation of directional sensitivity of the scattering coefficient over the range of ϕ between upwind and downwind for an incidence angle of 50 degrees. A periodic variation can be clearly discerned. In view of the original dependence of scattering coefficient on ϕ (1), the periodicity of the sensitivity curve can be easily understood. The pattern of the sensitivity curves for other incidence angles is similar. Keeping in mind sensitivities to speed and direction, it can be seen that incidence angles higher than 45 degree should be preferred from a sensitivity point of view.

4. Conclusions

1) It is seen that higher frequencies are more sensitive to wind speed as well as to wind direction. However for the X-band and the Ku-band curves are not significantly different. Hence attenuation and other considerations are important in opting for a particular frequency band among them.

2) The ϕ dependence of sensitivity curves rises steeply upto the incidence angle of about 45 degrees and thereafter the increment is not significant.

3) It can be also concluded that sensitivity is higher for lower wind speed. Hence there is a possibility of more accurate measurements in cases of low wind speeds in absolute terms.

4) The wind direction sensitivity of the scattering coefficient varies periodically with ϕ, with peaks around 60 degrees of ϕ.

5) There is no significant difference between the sensitivity curves for *HH* and *VV* polarization.

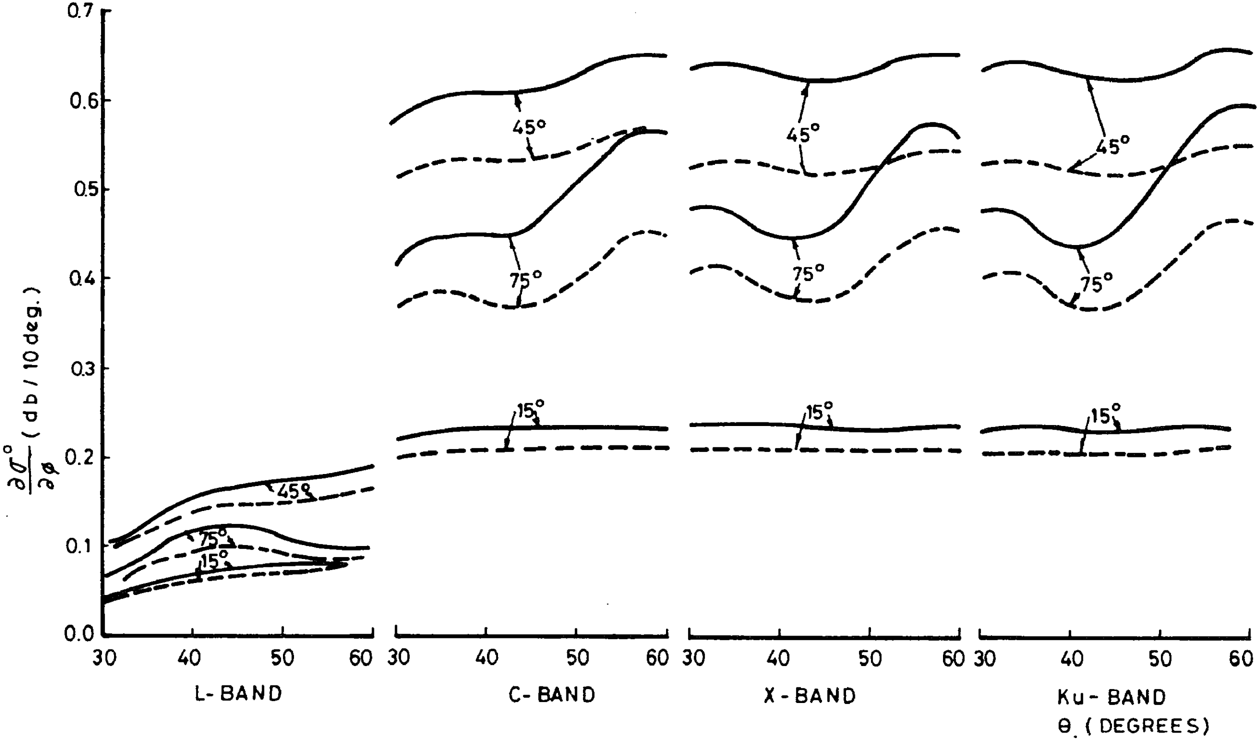

Figure 2. Sensitivity of scattering coefficient to wind direction versus incidence angle for L-, C-, X- and Ku-bands for different values of ϕ and wind speed values (———$W = 15$ m/s, ----$W = 10$ m/s).

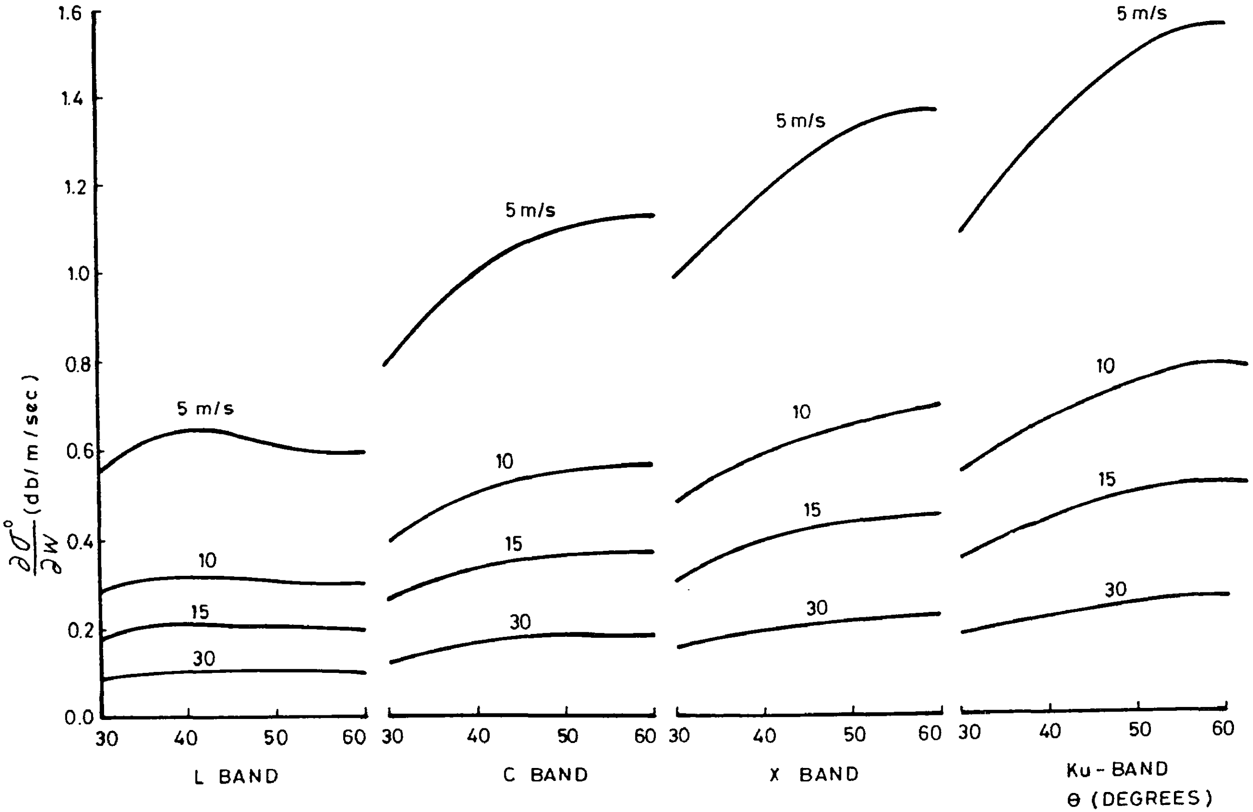

Figure 3. Sensitivity of scattering coefficient to wind speed versus incidence angle for L-, C-, X- and Ku- bands for upwind ($\phi = 0$ degree).

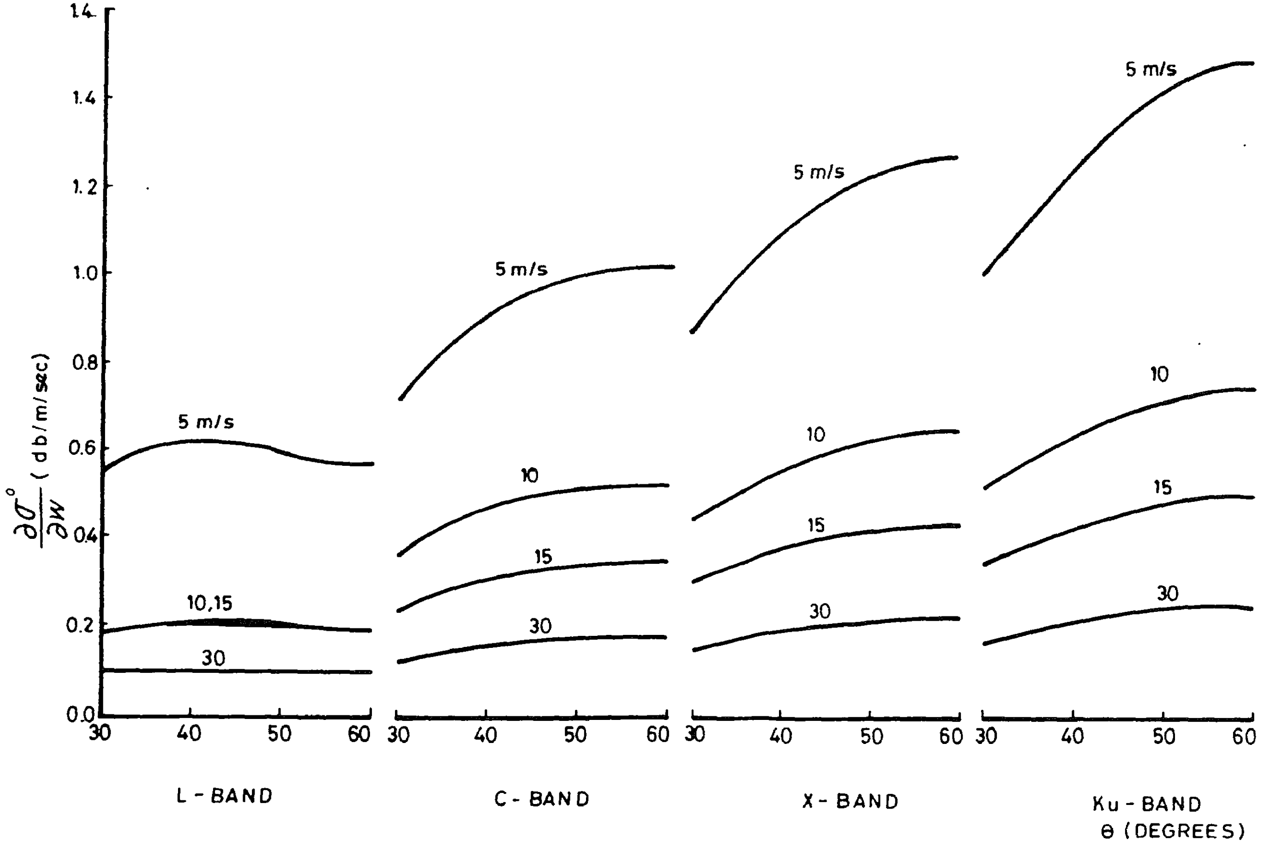

Figure 4. Sensitivity of scattering coefficient to wind speed versus incidence angle for L-, C-, X- and Ku- bands for ($\phi = 45$ degrees).

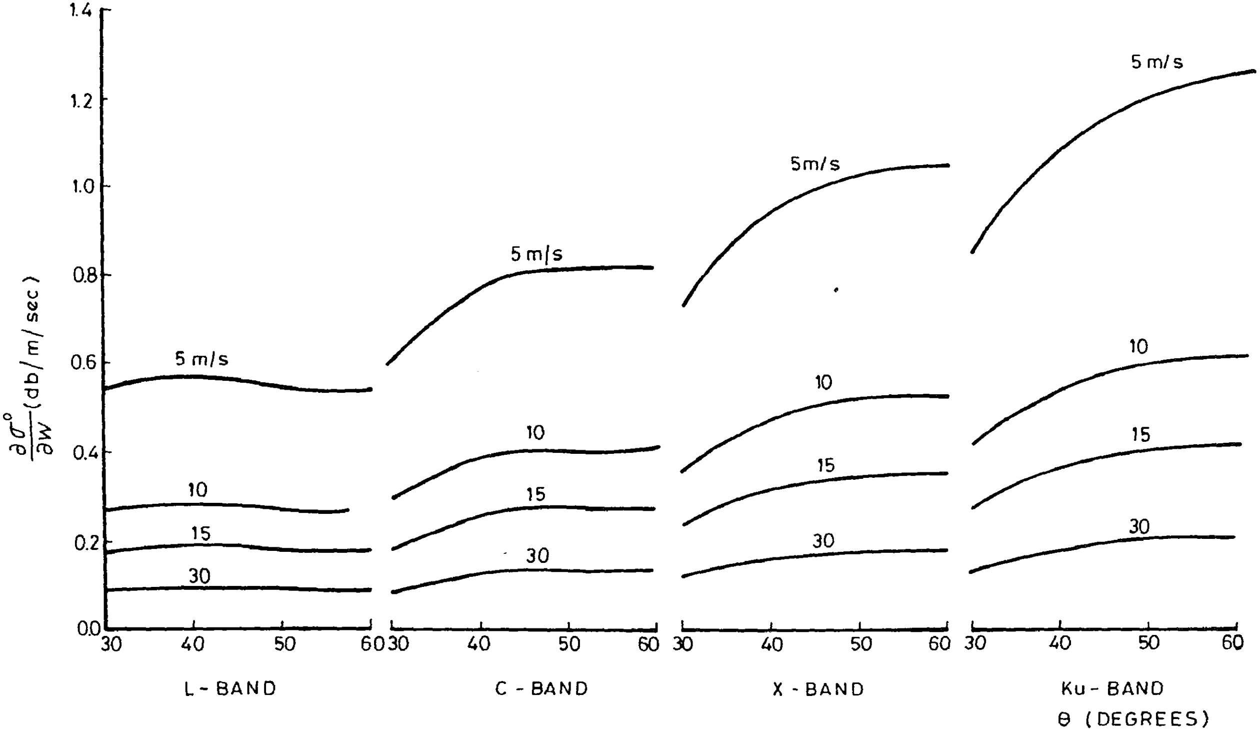

Figure 5. Sensitivity of scattering coefficient to wind speed versus incidence angle for L-, C-, X- and Ku-bands for crosswind ($\phi = 90$ degrees).

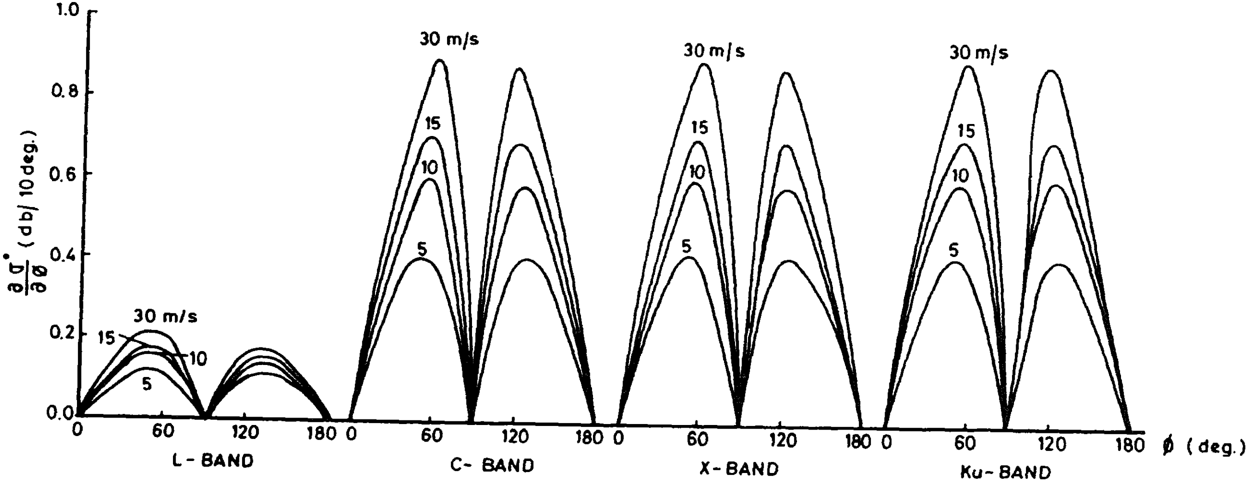

Figure 6. Sensitivity of scattering coefficient to wind direction versus ϕ for L-, C-, X- and Ku-bands for an incidence angle of 50 degrees.

Acknowledgements

The authors are grateful to Dr T A Hariharan for encouragement. Thanks are due to Dr P S Desai, Dr P C Pandey, Mr N S Pillai and other colleagues for useful discussion and critical evaluation of the work. The authors also wish to thank Dr W R Alpers, Max Planck Institute for encouraging comments.

References

Chan H L and Fung A K 1977 *J. Geophys. Res.* **82** 3439
Cox C and Munk W 1954 *J. Opt. Soc. Am.* **44** 838
Fung A K and Lee K K 1982 *IEEE J. Oceanic Eng.* **OE-7** 166
Fung A K and Lee K K 1983 *IGARSS* '83 *Digest* (San Francisco.) Vol. II
Moore R K and Fung A K 1979 *Proc. IEEE* **67** 1504
Sarkar A and Bhaduri L 1984 *Proc. Indian Acad. Sci.* (*Earth Planet. Sci.*) **93** 111
Ulaby F T, Bradley G A and Dobson M C 1979 *IEEE Trans. Geosci. Electron.* **GE-17** 33
Ulaby F T, Moore R K and Fung A K 1982 *Microwave remote sensing: active and passive* (Massachusetts: Addison-Wesley) Chap. 11.5

Proc. Indian Acad. Sci. (Earth Planet. Sci.), Vol. 94, No. 3, November 1985, pp. 261–267.
© Printed in India.

HF doppler observations on the occurrence of equatorial spread-F

B T VIKRAM KUMAR, P VELAYUDHAN NAIR and P B RAO
Department of Physics, University of Kerala, Kariavattom, Trivandrum 695 581, India

MS received 15 March 1985; revised 5 July 1985

Abstract. HF doppler observations of the vertical drift velocity and group height of the 5·5 MHz plasma frequency level of the post-sunset bottomside F-region obtained on a few ESF (equatorial spread-F) and non-ESF days at Trivandrum are presented. The results show that on the non-ESF days, the maximum group height attained is about 400 km and the maximum velocity is less than 30 m/sec. On the ESF days, however, the corresponding values are found to be in the range of 400–650 km and 30–50 m/sec. The ESF onset is found to be significantly delayed relative to the velocity peak indicating that it is more closely linked to the layer height than to the drift velocity.

Keywords. HF doppler observations; vertical shift velocity; group height; equatorial spread-F; drift velocity; layer height.

1. Introduction

The occurrence of equatorial spread-F (ESF) has been known for long, but significant advancement in the understanding of the phenomenon has been made only in recent years. The current understanding of ESF has come about through a variety of observational techniques as well as theoretical and computer simulation studies (for reviews, see: Basu and Kelley 1979; Fejer and Kelley 1980; Ossakow 1981). The basic process involving the operation of a hierarchy of instability mechanisms, which could account for most of the observed ESF characteristics, have been successfully identified. According to the current picture, ESF onset is believed to occur via the collisional Rayleigh-Taylor instability mechanism operating on the steep electron density gradient in the bottomside F-region when its altitude is high enough to overcome the recombination effects. Using VHF radar observations at Jicamarca, Farley *et al* (1970) have found that there is an altitude threshold of about 350 km for the bottom side (0·01 N_{max} level) for ESF onset to occur. The linear growth rate for the instability given by Ossakow *et al* (1979) indicates that an eastward electric field might also contribute in a significant way to the onset of ESF. Some indirect evidence that the growth rate of irregularities is governed initially by the background electric field is presented by Rastogi and Woodman (1978). Another important consequence of the background electric field is that it contributes significantly to the polarization of the plasma

2. Description of the experimental technique

The HF doppler radar consists of a pulse transmitter, a phase coherent receiver, the associated antennas and recording units. The block diagram of the system is given in figure 1. All the frequencies required for the system are generated by a master frequency synthesizer which has a long term frequency stability of better than one part in 10^7. A 5·5 MHz r.f. wave is modulated by a transmitter pulse having a pulse width of 100 μsec and a PRF of 50 Hz, in the modulator unit. The resulting modulated r.f. pulse is fed to the transmitter, in which the pulse undergoes various stages of amplification. The final output is a pulse of 3 kW peak power, which is fed to the 600 Ω folded dipole transmitting antenna through 600 Ω transmission lines.

The receiving system is shown in figure 2. The vertically transmitted signal gets reflected from the ionosphere and is received by a half-wave dipole, which is connected to the receiver through a coaxial cable. The received signal frequency is 5·5 MHz $\pm \Delta f$, where Δf is the doppler frequency. At the receiver input, it is mixed with a 5 MHz signal and the resulting 500 KHz $\pm \Delta f$ is amplified by the tuned IF amplifier. Now, for the second mixer, a 2 MHz signal from the frequency synthesizer is divided and phase-shifted so as to provide two phase quadrature local oscillator frequencies of 500 KHz. The amplified signal from the IF stage is mixed with each of these 500 kHz to obtain quadrature outputs at the doppler frequency of $\pm \Delta f$. Each of these quadrature outputs is passed through a balanced to unbalanced amplifier, a low-pass butterworth filter, and a sample and hold circuit. The sampling gate pulse is of 10 μsec duration and it occurs at the same rate as the transmitter PRF with a delay that can be varied over the inter-pulse period. The sampling circuit is followed by a FET-input operational amplifier operating as a voltage follower. These stages are identical for both the

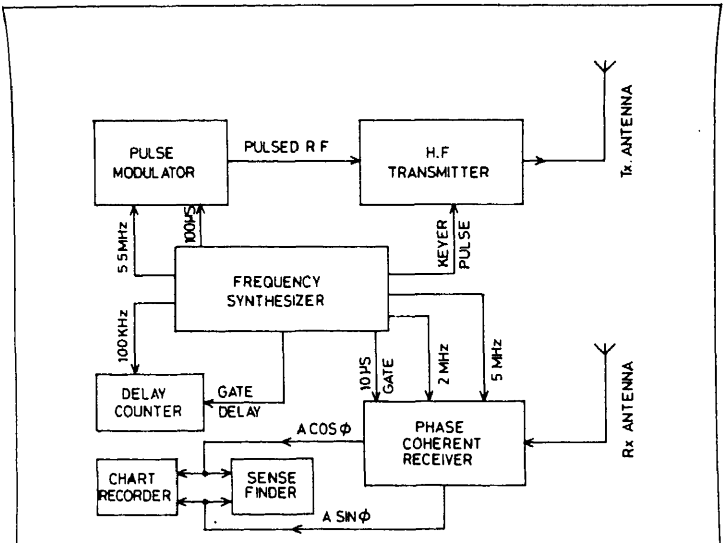

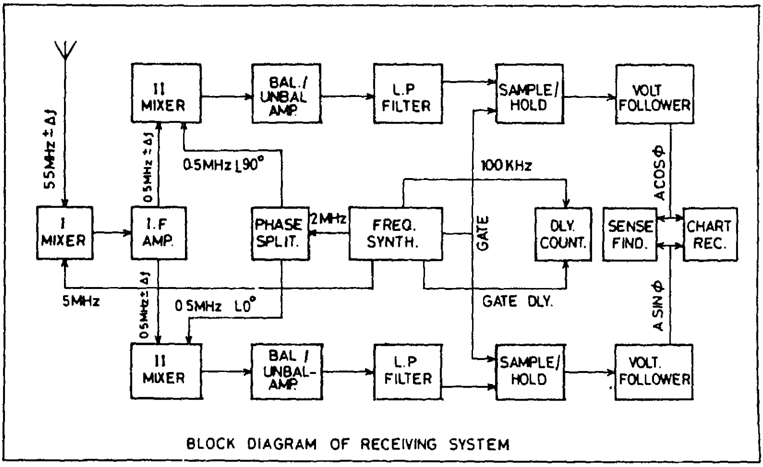

Figure 2. Block diagram of the phase coherent receiving system.

quadrature channels, termed as "cos" and "sin" channels. The final outputs from the receiver are slowly varying d.c., which are fed to a multi-channel stripchart recorder as well as to a sense detector, which resolves the sign of the doppler. The gate-delay pulse from the synthesizer is fed to a delay counter which counts and displays the delay with a resolution of 10 μsec. The chart recorder is normally run at a speed of 10 cm/min. Using this chart speed, it is possible to measure the doppler in the range 0 to ±2·5 Hz, which corresponds to a vertical velocity range of about 0 to ±70 m/sec. The uncertainties associated with the chart scaling are such that the doppler and hence the vertical drift velocity can be measured to an accuracy better than 2%.

Some sample records of the ionospheric signal on an ESF day are shown in figure 3. The sample records shown are for different time periods, before the onset of ESF, during ESF, and after ESF has disappeared. It can be seen that there is a rapid variation in doppler with time and the corresponding vertical drift velocities for the five sample times are: (a) 6 m/sec, (b) 16 m/sec, (c) 41 m/sec, (d) 15 m/sec and (e) 0·8 m/sec.

3. Observations and results

For the present observations, aimed at studying the conditions of occurrence of ESF, the system was operated in the evening from 1700 IST to the time when the critical frequency falls below the operating frequency, which occurs between midnight and 0300 IST. The doppler and group delay were recorded every five minutes. During ESF, range gating of the signal is very difficult due to the broadening of the returned pulse and the presence of multiple echoes. In such cases, the gate is kept at the strongest of the echoes, and from the records we judge that an uncertainty of about 30 km is possible in group height. Ten days of data are presented here, of which, five days are ESF days. The

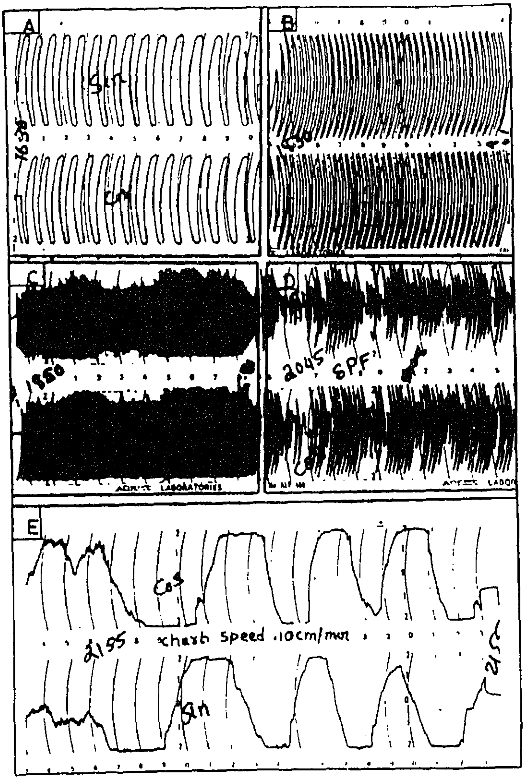

Figure 3. Sample doppler records of ionospheric signal on 15 March 1984, an ESF day. The first four panels represent data recorded for one minute with starting time: **A)** 1630 IST, **B)** 1830 IST, **C)** 1850 IST, **D)** 2045 IST, panel **(E)** represents data for two minutes starting at 2155 IST. Only panel **(D)** represents data during ESF. The chart speed is 10 cm/min for all records.

appropriate equatorial parameters, that the contribution due to decay doppler is in the range of about 5–20% during the period of interest to the current study. The higher values of decay doppler occur for short periods immediately following sunset and also later in the night when the operating frequency approaches the critical frequency. The decay doppler, however, is not expected to affect the results of the study seriously since its contribution is present on both ESF and non-ESF days to the same extent. The derived drift velocity may, therefore, be considered to represent essentially the true vertical drift of the 5·5 MHz plasma frequency level. A similar calculation on the group height shows that, in general, it is 50–100 km above the true height during the pre-midnight period of interest here. The time variations of both the drift velocity and the group height for all the ten days as well as their averages, obtained separately for the ESF and non-ESF days, are presented.

Figure 4 shows the time variations of the vertical drift and group height of the post-sunset F-region on different days. It can be seen that to start with, prior to sunset on all days, the velocity has a small positive value and the group height of the layer is in the range 300–350 km. The drift velocity starts to increase rapidly around 1800 hrs to reach

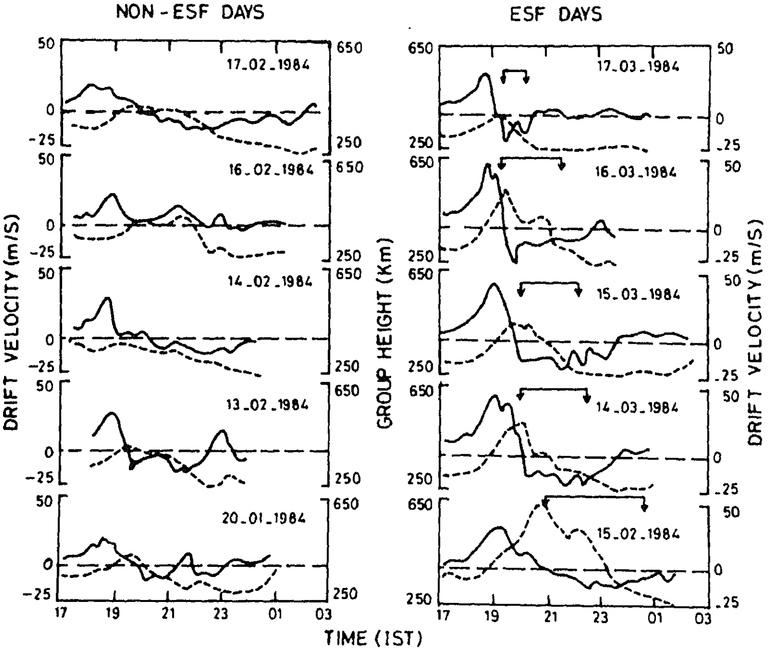

Figure 4. Time variations of drift velocity and group height on ESF and non-ESF days. (—— drift velocity; . . . . . . group height). The arrow marks indicate the period when ESF is present.

a maximum around 1900 hrs and then decreases to cross zero and becomes negative by 2100 hrs. The group height also increases following sunset and reaches a maximum at about the same time when the drift velocity goes through the transition from positive to negative. It is clear that the variations are more rapid and of greater magnitude on ESF days than on non-ESF days. On the non-ESF days, the maximum group height attained is around 400 km and the maximum velocity is less than 30 m/sec. On the ESF days, however, the maximum group height is in the range of 400–650 km and the maximum velocity is in the range of 30–50 m/sec. The example of March 17, 1984 seems to represent a border-line case with regard to the conditions conducive for the onset of ESF. On this day, the maximum group height was about 400 km and the maximum drift velocity was about 30 m/sec. There was an occurrence of weak spread-F for a duration of about an hour. Another feature which may be noted from figure 4 is that, once spread-F has occurred, it will disappear only after the group height has decreased below about 300 km. This is to be expected since, when the layer descends to lower heights crossing a threshold, the recombination effects begin to dominate over the conditions favourable for sustaining the spread-F. Figure 5 presents an average picture of the time

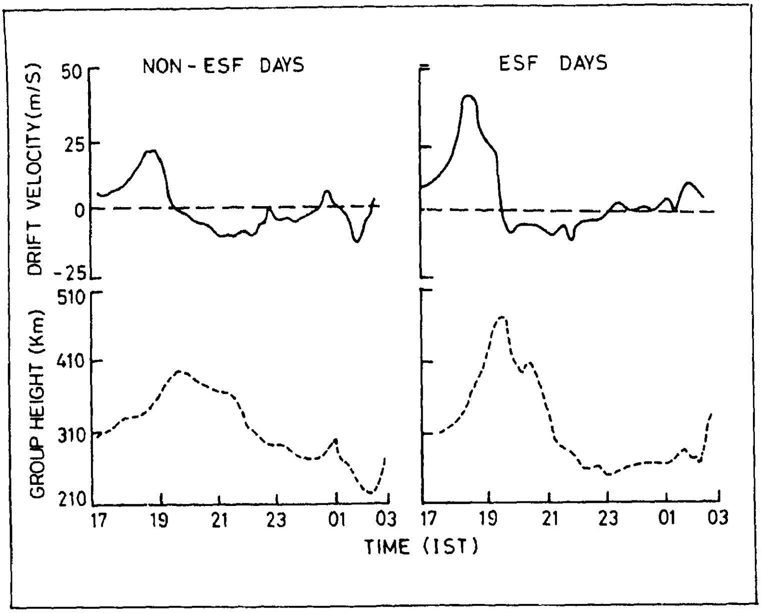

Figure 5. Average time variations of drift velocity and group height on ESF and non-ESF days (—— drift velocity; . . . . . . group height).

4. Discussion

The association of the occurrence of ESF with the post-sunset height rise of the F-layer has been known for long. Using radar backscatter measurements, Farley *et al* (1970) have found an altitude threshold for the bottomside of the F-layer for the onset of ESF. They observed that the bottomside, where the plasma density drops to 1 % of that at the F-layer peak, must be above about 350 km for ESF onset to occur. The above radar observations indicating an altitude threshold seem to be consistent with the conditions favourable for the collisional drift instability advanced by Hudson and Kennel (1975) to account for the short wavelengths of the irregularity spectrum. In recent years, a clear picture has emerged on the processes leading to the presence of a wide range of scale sizes of irregularities observed during ESF. It involves the operation of a hierarchy of instabilities first suggested by Haerendel (1974) and later developed by many workers as reviewed by Ossakow (1981). The growth rate of the collisional Rayleigh-Taylor instability, which seems to indicate ESF in the bottomside, is given by Ossakow *et al* (1979) as:

$$r = (1/L)(g/\nu_{in} + CE/B) - \nu_R$$

where L is the electron density scale height, E is the eastward component of the electric following sunset. Added to the steepening, if the altitude of the F-region is sufficiently high to overcome the recombination effects, plasma density fluctuations will begin to grow on the bottomside via the collisional Rayleigh-Taylor mechanism.

The post-sunset vertical drift velocity of the layer associated with the eastward electric field seldom exceeds 50 m/sec. That, this velocity alone is not enough to cause ESF onset is clear from figure 4 showing the onset to be significantly delayed relative to the velocity peak. The ESF onset, occurring around the same time as the peak of the group height, seems to depend more on the layer height than on the drift velocity, an observation consistent with that of Farley *et al* (1970). It has also been reported earlier by Chandra and Rastogi (1972a, b, 1978) that the maintenance of F-region at higher altitudes is an important condition for the occurrence of ESF. Their results have shown that on ESF days, drift reversals occur later than on non-ESF days suggesting that higher altitudes are attained for the F-region on ESF days. It may, however, be noted that high drift velocities cause the layer to rise to high altitudes and, therefore, a high drift velocity of the post sunset F-region may be taken as an indication that favourable conditions will be attained for the onset of ESF. It seems that if the drift velocity exceeds a value of about 30 m/sec, the layer will attain a high enough altitude to overcome the recombination effects for the density fluctuations to grow via the collisional Rayleigh-Taylor mechanism resulting in the onset of ESF. Another important consequence of the vertical drift velocity which is of interest to ESF is its possible contribution to the polarization of the plasma bubbles and hence to their vertical rise velocity (Anderson and Haerendel 1979). The results presented in figure 4, however, show that ESF onset as seen by the HF radar is well past the drift velocity peak indicating that the background electric field may not be contributing significantly to the plasma bubble polarization. In such a case, it is essentially the gravity-driven components which determine the polarization and the vertical rise velocity of the plasma bubbles.

Acknowledgements

The HF doppler system has been built under an ISRO sponsored RESPOND Project. We thank Dr N Balan and Mr N Sugunan for assistance.

References

Anderson D N and Haerendal G 1979 *J. Geophys. Res.* **84** 4251
Basu S and Kelley M C 1979 *Radio Sci.* **14** 471
Budden K G 1961 *Radio waves in the ionosphere* (London and New York: Cambridge Univ. Press) pp. 153
Chandra H and Rastogi R G 1972a *Ann. Geophys.* **28** 37
Chandra H and Rastogi R G 1972b *Ann. Geophys.* **28** 709
Chandra H and Rastogi R G 1978 *Indian J. Radio Space Phys.* **7** 265
Farley D T, Balsley B B, Woodman R F and Mc Clure J P 1970 *J. Geophys. Res.* **75** 7199
Fejer B G and Kelley M C 1980 *Rev. Geophys. Space Phys.* **18** 401
Haerendal G 1974 Report, Max-Planck Inst. fur Phys. und Astrophys., FRG
Hudson M K and Kennel C F 1975 *J. Geophys. Res.* **80** 4581
Ossakow S L, Zalesak S T, Mc Donald B E and Chaturvedi P K 1979 *J. Geophys. Res.* **84** 17
Ossakow S L 1981 *J. Atmos. Terr. Phys.* **43** 437
Rastogi R G and Woodman R F 1978 *J. Atmos. Terr. Phys.* **40** 485

Transient electromagnetic response due to a pair of horizontal conducting sheets in a loop field

R NAGENDRA, I B RAMAPRASADA RAO and SATYANARAYAN KABRA

Department of Geophysics and Centre of Exploration Geophysics, Osmania University, Hyderabad 500007, India

MS received 10 November 1983; revised 1 February 1985

Abstract. The transient electromagnetic response due to a pair of horizontal conducting sheets induced by a loop field is obtained. The response characteristics in the three different regions (above the upper sheet, between the two sheets and below the lower sheet) are briefly discussed.

In the first and second regions the composite response is characterised by an overburden response asymptote during early times and a target response asymptote during late times. The transition zones are characterised by shoulder-like bends. In the third region, the composite response increases in direct proportion to the induction number, eventually merging with the target response for large values of the induction number.

Keywords. Transient response; conducting sheets; transition zone; overburden.

1. Introduction

Quite often conductive economic mineral deposits occur as fissure veins, bedded type deposits, lenses, etc. in different kinds of relatively less conductive country rocks (Bateman 1958; Swayder 1967; Smironov 1967; Zakharov 1967). Among such country rocks, sedimentary and metamorphic rock types like dolomite, quartzite, phyllite, schist and gneiss are common. A distinctive feature of bedded and lens type mineral deposits is that they can be closely approximated by thin sheet-type conductors.

Usually the conductivities of such ore-bearing rocks vary between 10^{-2} to 10^{-5} seimens, while the conductivities of the ore bodies vary between 10^2–10^4 seimens (Parasnis 1968, 1971; Parkhomenko 1965). In certain frequently encountered geological settings, the ore reserves are covered by conductive soil layers. Usually the conductivities of overburden lie within the range 10^{-3} to 1 seimen (Vingoe 1972).

Thus a thin sheet representing a bedded-type deposit overlain by a less conductive sheet representing the overburden is an important physico-geological situation necessitating a detailed analytical study. Such conductive configurations in spherical and cylindrical geometries were studied by Nagendra *et al* (1980, 1981), for one loop transient measurements in the surface version.

Geophysical investigations in boreholes play a vital role in supplementing the information gathered from surface investigations. Quite often ore bodies missed during the drilling stage can be located in the vicinity by suitable geophysical investigations carried out in the borehole. Especially when the deposit is missed in the lithologs due to limited core recovery or when the bore cuts through a pinched-out region, borehole electromagnetic (EM) investigations offer valuable information in mapping the surrounding conductive inhomogeneities.

In the present paper, the transient electromagnetic response due to a pair of horizontal conducting sheets induced by a loop field (step excitation) is obtained. The response characteristics in the three different regions of the medium (I. above the upper sheet, II. between the two sheets and III. below the lower sheet) are briefly discussed in relation to the single shield (upper sheet), single target (lower sheet) responses. It is hoped that such a study would form the basis for analyzing surface and borehole transient EM data over sheet type bodies.

2. Derivation

Figure 1 illustrates the geometry of a pair of horizontal sheets referred to a cylindrical coordinate system (ρ, θ, z). The two sheets are assumed to be infinitely conducting ($\sigma_{1,2} \to \infty$) and infinitesimally thin ($T_{1,2} \to 0$), such that their conductances ($S_1 = \sigma_1 T_1$; $S_2 = \sigma_2 T_2$) are finite. The upper sheet is assumed to be located on the surface itself ($z = 0$), over which the transmitter loop of radius R is laid. The axis of the loop coincides with the z-axis (+ve downward) of the coordinate system. The primary vector potential due to the transmitter loop in the cylindrical co-ordinate system is given by (Makagonov 1969)

$$A_P = \frac{\mu_0 I R}{2} \int_0^\infty J_1(\lambda R) \cdot J_1(\lambda \rho) \cdot \exp(-\lambda z) \cdot d\lambda \tag{1}$$

In the cylindrical coordinate system (ρ, θ, z), the vector potential $\bar{A}$ satisfies the following wave equation

$$\frac{\partial^2 \bar{A}}{\partial \rho^2} + \frac{1}{\rho}\frac{\partial \bar{A}}{\partial \rho} + \frac{1}{\rho^2}\frac{\partial^2 \bar{A}}{\partial \theta^2} + \frac{\partial^2 \bar{A}}{\partial z^2} - k^2 \bar{A} = 0 \tag{2}$$

where $k = (i\omega\mu\sigma)^{1/2}$ is the wave number.

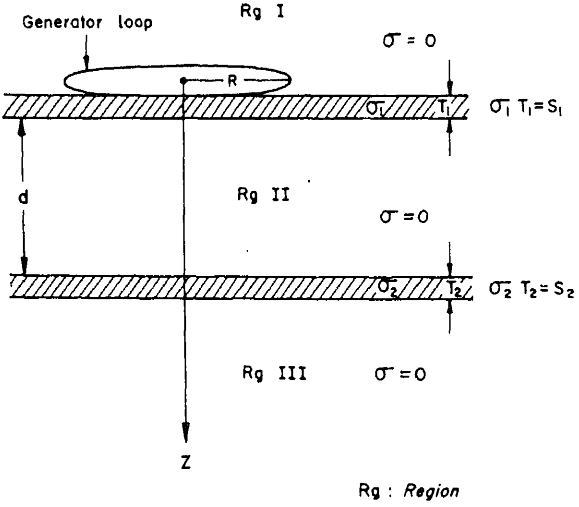

Figure 1. Geometry of a pair of horizontal sheets in a loop field.

In view of the axial symmetry of the chosen model $\bar{A}$ has only a θ component which is independent of θ and can be expressed as,

$$\bar{A} = \hat{a}_\theta \cdot A(r, z) \tag{3}$$

where $\hat{a}_\theta$ is the unit vector in the θ-direction, and $A(r, z)$ is a purely scalar function of r and z, which, for the sake of brevity will be referred to as A.

Converting $\hat{a}_\theta$ into the rectangular coordinate system, we have

$$\hat{a}_\theta = \hat{i}\cos\theta + \hat{j}\sin\theta \tag{4}$$

where $\hat{i}$ and $\hat{j}$ are unit vectors along x and y directions respectively.
Hence

$$\frac{\partial^2 \bar{A}}{\partial \theta^2} = -\hat{a}_\theta \cdot A \tag{5}$$

Making use of (5), (1) in regions not occupied by any conductors ($k = 0$) can be simplified as follows;

$$\frac{\partial^2 A}{\partial \rho^2} + \frac{1}{\rho} \cdot \frac{\partial A}{\partial \rho} - \frac{A}{\rho^2} + \frac{\partial^2 A}{\partial z^2} = 0. \tag{6}$$

Following the procedure of separable variables, solutions of (6) in the regions I, II and III (vide figure 1) can be written as follows, in accordance with the expression for A_p.

$$A_{\mathrm{I}} = M \cdot \{\exp(-\lambda z) + X_0 \cdot \exp(\lambda z)\} \tag{7}$$

$$A_{\mathrm{II}} = M \cdot \{X_1 \cdot \exp(-\lambda z) + X_2 \cdot \exp(\lambda z)\} \tag{8}$$

$$A_{\mathrm{III}} = M \cdot \{X_3 \cdot \exp(-\lambda z)\} \tag{9}$$

where $M\{\cdot\} = \frac{\mu_0 I R}{2} \int_0^\infty J_1(\lambda R) \cdot J_1(\lambda \rho) \cdot \{\cdot\} \cdot \mathrm{d}\lambda$ and X_m ($m = 0, 1, 2, 3$) are the arbitrary constants.

The term involving the positive exponent of λz is dropped out of (9) in view of the infinity constraints.

Following the boundary conditions (Wait 1969)

$$A_{\mathrm{I}} = A_{\mathrm{II}}; \quad \frac{\partial A_{\mathrm{I}}}{\partial z} = \frac{\partial A_{\mathrm{II}}}{\partial z} - i\omega\mu_0 S_1 \cdot A_{\mathrm{I,II}}\big|_{z=0} \tag{10}$$

$$A_{\mathrm{II}} = A_{\mathrm{III}}; \frac{\partial A_{\mathrm{II}}}{\partial z} = \frac{\partial A_{\mathrm{III}}}{\partial z} - i\omega\mu_0 S_2 A_{\mathrm{II,III}}\big|_{z=d} \tag{11}$$

the X-coefficients could be obtained as

$$X_0 = i\omega C[i\omega(1-p) + 2x(\alpha p + \beta)] \tag{12}$$

$$X_1 = -2x\alpha C[i\omega + 2\beta x] \tag{13}$$

$$X_2 = 2\alpha x p i\omega C \tag{14}$$

$$X_3 = -4C\alpha\beta x^2 \tag{15}$$

$$\alpha = (\mu_0 S_1 R)^{-1}, \beta = (\mu_0 S_2 R)^{-1}, x = \lambda R$$

where

$$\bar{d} = d/R,\ C = [(\omega - iK_1)(\omega - iK_2)(1-p)]^{-1}$$

$$p = \exp(-2x\bar{d}),\ K_{1,2} = \frac{x}{1-p}(\alpha + \beta \pm D),$$

$$D = [(\alpha - \beta)^2 + 4\alpha\beta p]^{1/2}$$

For evaluating the transient e.m.f. responses in the three different regions it is necessary to obtain inverse Fourier transforms of the X-functions given by

$$x_m(t) = \frac{1}{2\pi}\int_{-\infty}^{\infty} X_m(\omega)\cdot \underset{m=0,1,2,3}{\exp(i\omega t)}\cdot \mathrm{d}\omega \tag{16}$$

Accordingly we can write

$$x_0(t) = \frac{\alpha x}{D}\{(\beta - \alpha + D)\cdot \exp(-K_2 t) - (\beta - \alpha - D)\cdot \exp(-K_1 t)\} \tag{17}$$

$$x_1(t) = \frac{\alpha}{D}\{(2\beta x - K_2)\cdot \exp(-K_2 t) - (2\beta x - K_1)\cdot \exp(-K_1 t)\} \tag{18}$$

$$x_2(t) = \frac{\alpha p}{D}\{K_2 \cdot \exp(-K_2 t) - K_1 \cdot \exp(-K_1 t)\} \tag{19}$$

$$x_3(t) = \frac{2\alpha\beta x}{D}\{\exp(-K_2 t) - \exp(-K_1 t)\} \tag{20}$$

For measurements on the surface ($z = 0$) using the combined loop version, the transient e.m.f. is given by

$$\varepsilon_{\mathrm{I}}(t) = \mu_0 \pi I R \int_0^{\infty} \{J_1(x)\}^2 \cdot x_0(t)\cdot \mathrm{d}x \tag{21}$$

Two important limiting expressions of $\varepsilon_{\mathrm{I}}(t)$, viz, single upper sheet response $\varepsilon_{\mathrm{I}1}(t)$, single lower sheet response $\varepsilon_{\mathrm{I}2}(t)$, can be obtained by replacing $x_0(t)$ with $x_{01}(t)$ and $x_{02}(t)$ defined as follows:

$$x_{01}(t) = \underset{\beta \to \infty}{\mathrm{Lt}}\ x_0(t) = 2\alpha x \cdot \exp(-2\alpha x t) \tag{22}$$

$$x_{02}(t) = \underset{\alpha \to \infty}{\mathrm{Lt}}\ x_0(t) = 2\beta x \cdot \exp[-2x(\bar{d} + \beta t)] \tag{23}$$

For measurements along the borehole axis with a receiver loop of relatively small radius ($\rho \to 0$) applicable in regions II and III, e.m.f. ε is related to vector potential A as follows:

$$\varepsilon = \underset{\rho \to 0}{\mathrm{Lt}}\left\{\frac{\partial A}{\partial \rho} + \frac{A}{\rho}\right\} \tag{24}$$

Since $J_1(\lambda\rho)$ is the only term involving ρ in the expression for A, it is necessary to evaluate the following limit

$$\underset{\rho \to 0}{\mathrm{Lt}}\left\{\frac{\partial[J_1(\lambda\rho)]}{\partial \rho} + \frac{J_1(\lambda\rho)}{\rho}\right\} = \lambda \tag{25}$$

Accordingly expressions for the transient e.m.f. in regions II and III can be written as

$$\varepsilon_{\text{II}}(t) = \frac{\mu_0 I}{2R}\int_0^\infty x\cdot J_1(x)\big[x_1(t)\cdot \underset{0<\bar{z}<\bar{d}}{\exp}(-x\bar{z}) + x_2(t)\cdot\ \exp\ (x\bar{z})\big]\cdot \mathrm{d}x \tag{26}$$

$$\varepsilon_{\text{III}}(t) = \frac{\mu_0 I}{2R}\int_0^\infty x\cdot J_1(x)\cdot x_3(t)\cdot \underset{\bar{z}>\bar{d}}{\exp}(-x\bar{z})\cdot \mathrm{d}x \tag{27}$$

Where $\bar{z} = z/R$, z being the depth of measurement. The single upper sheet and single lower sheet limiting responses can be obtained for ε_{II} and ε_{III} making use of the following limiting expressions for $x_1(t)$, $x_2(t)$ and $x_3(t)$.

$$x_{11}(t) = \underset{\beta\to\infty}{\mathrm{Lt}}\ x_1(t) = 2\alpha x\cdot \exp(-2\alpha x t) \tag{28}$$

$$x_{12}(t) = \underset{\alpha\to\infty}{\mathrm{Lt}}\ x_1(t) = 0 \tag{29}$$

$$x_{21}(t) = \underset{\beta\to\infty}{\mathrm{Lt}}\ x_2(t) = 0 \tag{30}$$

$$x_{22}(t) = \underset{\alpha\to\infty}{\mathrm{Lt}}\ x_2(t) = 2\beta x\cdot \exp[-2x(\bar{d}+\beta t)] \tag{31}$$

$$x_{31}(t) = \underset{\beta\to\infty}{\mathrm{Lt}}\ x_3(t) = 2\alpha x\cdot \exp(-2\alpha x t) \tag{32}$$

$$x_{32}(t) = \underset{\alpha\to\infty}{\mathrm{Lt}}\ x_3(t) = 2\beta x\cdot \exp(-2\beta x t) \tag{33}$$

3. Numerical solution and results

For the purpose of numerical computation and graphical representation it would be more convenient to rewrite the expressions for ε_{I}, ε_{II} and ε_{III} [vide (21), (26) and (27)] along with their limiting responses in a non-dimensional parametric form as presented in table 1.

These expressions are utilised for computing the required transient responses. The numerical integration over the variable x is performed using Simpson's rule allowing for an error of ±5% in each case. The results are plotted in figures 2, 3 and 4 for certain values of the model parameters.

4. Discussion

Table 1. Normalized responses.

Region I: Combined loop measurements

$$\bar{\varepsilon}(\tau) = F_1 \varepsilon_{\mathrm{I}}(t)$$

$$= \int_0^\infty \frac{G(x)}{2D^1} \{(\xi - 1 + D^1)\cdot E_2 - (\xi - 1 - D^1)\cdot E_1\}\,\mathrm{d}x$$

$$\bar{\varepsilon}_1(\tau) = \int_0^\infty G(x)\cdot \exp(-2x\tau)\cdot \mathrm{d}x$$

$$\bar{\varepsilon}_2(\tau) = \xi \int_0^\infty \eta G(x)\cdot \exp(-2x\xi\tau)\cdot \mathrm{d}x$$

Region II: $(0 < \bar{z} < \bar{d})$—*Measurements with a receiver loop of negligible radius*

$$\bar{\varepsilon}(\tau) = F_2 \varepsilon_{\mathrm{II}}(t)$$

$$= \int_0^\infty \frac{L(x)}{2D^1}\Big[\{(2\xi x - K_2^1)E_2 - (2\xi x - K_1^1)E_1\}\delta$$

$$+ \{K_2^1 E_2 - K_1^1 E_1\}\frac{\eta}{\delta}\Big]\mathrm{d}x$$

$$\bar{\varepsilon}_1(\tau) = \int_0^\infty \delta x\, L(x)\cdot \exp(-2x\tau)\cdot \mathrm{d}x$$

$$\bar{\varepsilon}_2(\tau) = \int_0^\infty \xi\eta x \frac{L(x)}{\delta}\cdot \exp(-2x\xi\tau)\,\mathrm{d}x$$

Region III: $(\bar{z} > \bar{d})$—*Measurements with a receiver loop of negligible radius*

$$\bar{\varepsilon}(\xi\tau) = F_3 \cdot \varepsilon_{\mathrm{III}}(t)$$

$$= \int_0^\infty \frac{xL(x)}{D^1}[E_2 - E_1]\delta\,\mathrm{d}x$$

$$\bar{\varepsilon}_2(\xi\tau) = \int_0^\infty xL(x)\delta\cdot \exp(-2x\xi\tau)\,\mathrm{d}x$$

where,

$$F_1 = \frac{S_1}{2\pi I};\quad F_2 = \frac{S_1 R^2}{I}:\quad F_3 = \frac{S_2 R^2}{I}$$

$$G(x) = x\cdot[J_1(x)]^2;\quad L(x) = xJ_1(x)$$

$$E_1 = \exp(-K_1^1\tau);\quad E_2 = \exp(-K_2^1\tau)$$

$$\eta = \exp(-2x\bar{d});\ \delta = \exp(-x\bar{z})$$

$$\tau = \alpha t;\ \xi = S_1/S_2$$

$$K_{1,2}^1 = \frac{K_{1,2}}{\alpha};\quad D^1 = \frac{D}{\alpha}$$

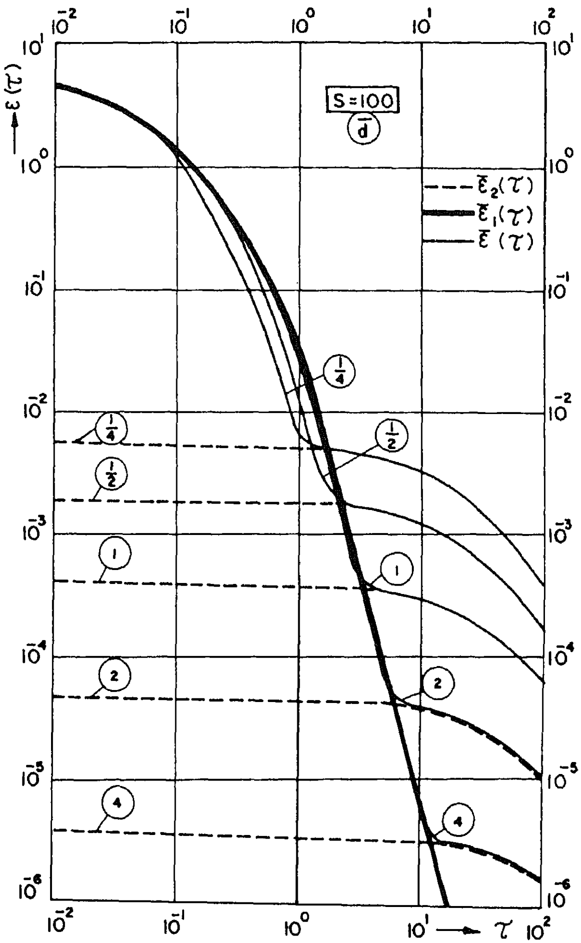

Figure 2. Transient e.m.f. response in region-I (combined loop version).

early times and the single lower sheet response $\bar{\varepsilon}_2(\tau)$ during the late times. Connecting these two time zones is a transition zone characterised by a shoulder-like bend in the composite response. Similar response characteristics were observed over a concentric spherical sheel-shell model by Nagendra *et al* (1980). In view of this, it can be concluded that the gross behaviour of the response is independent of the shield-target geometry.

The composite response function computed for point measurements are plotted in figure 3 for $S = 100$ and $\bar{d} = \frac{1}{4}, \frac{1}{2}, 1, 2, 4$; along with the single upper sheet and single lower sheet limiting functions. The receiver down the bore-hole is assumed to be kept at a depth of $0{\cdot}24\,R$. From this figure it can be observed that the composite response characteristics in region II are largely similar to those observed in region I, in relation to their corresponding asymptotic responses. However, an interesting aspect is that the composite response in region II displays an additional shoulder-like bend in the transition zone. This secondary bend decreases gradually in prominence with increasing $\bar{d}$. It appears that this characteristic is mainly related to the placement of the

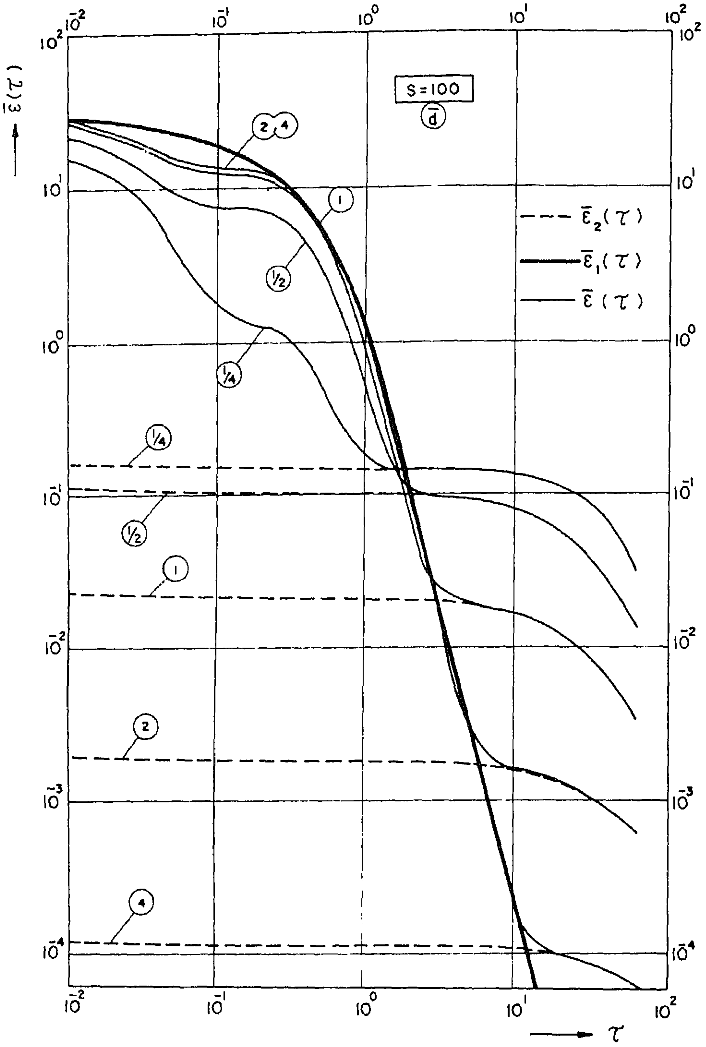

Figure 3. Transient e.m.f. response in region-II (receiver loop of negligible radius).

In figure 4 are plotted the composite response characteristics observed in region III as functions of $\xi\tau = \beta t$, for the following parameters

$$\bar{d} = 0{\cdot}5;\ \bar{z} = 4{\cdot}2;\ S = 1,\ 3{\cdot}16,\ 10,\ 31{\cdot}6,\ 100.$$

The abscissa is chosen as $\xi\tau$ in place of the usual τ for the sake of convenience, since the single upper sheet limiting response is never reached in the composite response characteristic. The curve labelled $S = \infty$, corresponds to the single lower sheet limiting response.

It can be observed from figure 4 that the composite response increases in magnitude in direct proportion to $\xi\tau$, during early times, eventually merging with the single lower sheet limiting response. The merger takes place at much earlier times for larger S values as expected.

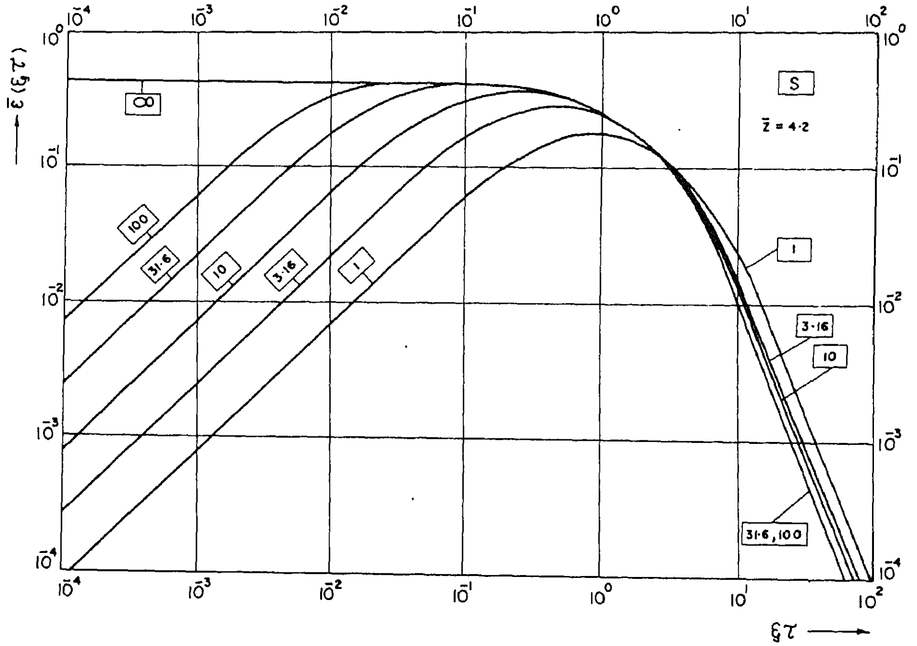

Figure 4. Transient e.m.f. response in region-III (receiver loop of negligible radius).

References

Bateman A M 1958 *Economic mineral deposits* (Bombay: Asia Publishing House) p. 111

Makagonov P P 1969 *IZV. Akad. Sci. USSR (in Russian)* **3** 57

Nagendra R, Ramaprasada Rao I B and Bhimasankaram V S 1980 *Geophys. Prospect.* **28** 269

Nagendra R, Ramaprasada Rao I B and Bhimasankaram V S 1981 *Bull.-Aust. Soc. Explor. Geophys.* **12** 29

Parasnis D S 1968 ABEM Geophysical memorandum 1/68

Parasnis D S 1971 ABEM Geophysical memorandum 4/71

Parkhomenko E I 1965 *Electrical properties of rocks* (in Russian) (Moscow: Nauka) p. 73

Smironov V I 1967 *Econ. Geol. Monogr.* **3** 219

Swayder F G 1967 *Econ. Geol. Monogr.* **3** 1

Vingoe P 1972 ABEM Geophysical memorandum 5/72

Wait J R 1969 *Geophysics* **34** 753

Zakharov E E 1967 *Econ. Geol. Monogr.* **3** 221

Proc. Indian Acad. Sci. (Earth Planet. Sci.), Vol. 94, No. 3, November 1985, pp. 279–282.
© Printed in India.

Emission spectrographic estimation of gold

K C JOSEPH
Department of Geology and Mining, Government of Madhya Pradesh, Raipur 492 001, India

MS received 23 May 1985

Abstract. A procedure for estimating minute quantities (parts per billion) of gold is described, based on dissolution of the sample in aqua regia, adsorption on activated charcoal, arcing of the charcoal ash, and measurement of the intensity of the emitted spectra.

Keywords. Emission spectrography; estimation of gold; gold adsorption; arcing of activated charcoal ash.

1. Introduction

The method is based on the dissolution of the sample containing gold in aqua regia. The dissolved gold is adsorbed from the solution by activated charcoal. After desorption of other elements, gold is estimated by its emission spectral intensity at 2675·95 and 2427·98 A on arcing of the activated coal ash.

2. Procedure

10 gms of the sample ground to -200 mesh is roasted at 550–600°C for one and a half hours in a muffle furnace, in a flat bottomed porcelain dish making sure that the thickness of the sample material does not exceed 5 mm.

The roasted sample is transferred to a 250 ml beaker and 20 ml of aqua regia are added. The sample is attacked for about 4 to 5 hours at a room temperature of 70–75°C with constant stirring on a hot plate, after which the beaker is removed from the hot plate, cooled and the syrupy material diluted to about 200 ml with water and stirred well. This sample solution is filtered through double ashless filter paper (No. 40 Whatman) using a buchner funnel. The filtrate is collected in a 250 ml conical flask and the residue rejected. 0.5 gms of AR quality activated charcoal, ground to -200 mesh is added to the filtrate in the conical flask (the ash content of the activated charcoal should not exceed 0·3–0·5 %). The conical flask with the solution is kept on a magnetic stirrer and stirred for 15 minutes at room temperature.

The solution is then filtered through a No. 40 Whatman filter paper using a buchner funnel and suction; the filtrate is rejected. The filter paper containing the sorbed charcoal is torn into small pieces (making sure that no charcoal is lost) and put into the same conical flask and 200 ml of 1 : 50 hydrochloric acid are added. The flask is then stirred for 25 minutes at room temperature. The contents of the conical flask are then filtered through a No. 40 filter paper, which is then transferred to a 30 ml flat-bottomed porcelain crucible and kept in a muffle furnace. The temperature of the furnace is slowly raised to 550°C and kept there for about one to one and a half hours, till the contents of rucible are completely converted to ash. During the ashing of the charcoal, access r should be allowed in the muffle furnace.

Arcing procedure

r conversion of the charcoal into ash, the crucible is taken out from the furnace and ed. Into the crucible 15 milligrams of flux* containing sp-2 graphite powder and AR ım carbonate in the proportion of 1 : 1 are added. The ash and the flux is then sferred completely to a 50 mm dia small agate mortar with the help of a brush and nd well. The whole of it is then transferred to the crater of a graphite electrode with ıelp of a funnel and weighing paper. The electrode used was of Union Carbide (USA) e, 0·180″ in diameter. The crater is of 8 mm depth and 3·2 mm dia. The crater aining the sample is then kept under an IR lamp for an hour and then arced using a ıter electrode of 0·120″ dia (Union Carbide, USA) and coned to 60°. The parameters ıe arcing are given in table 1.

old is estimated by its spectral intensity at 2627·96 Å. When the concentration is er, the second line is used. The result of analysis is taken as the mean value of two cent values of the standard.

Preparation of standards

ıilligrams of pure gold (Fisher Scientific Company, USA) metal was dissolved in ıl aqua regia at a temperature of 70–75°C on a hot plate with occasional stirring. dissolution is carried out in a partially covered 400 ml beaker in 1–2 hours. When dissolution of gold is complete, the contents of the beaker are completely sferred to a 200 ml volumetric flask by washing the beaker 8–10 times with 6 N HCl

Table 1. Arcing parameters

1. Spectrograph used	1·5 Meter Wadsworth (Jarrel-Ash)
2. Film	Kodak No. 1
3. Current	10 amps DC
4. Preburn	Nil
5. Exposure time	45 seconds
6. Slit width	8 μm
7. Slit height	1 mm
8. Arcing gap	3 mm adjusted throughout
9. Step filter	100/10
10. Developing	3 minutes at 72°F using Kodak 19 b developer with agitation.
11. Stop bath	30 seconds at 72°F with agitation.
12. Fixing	3 minutes using Kodak acid fixing salt with hardner and with agitation at 72°F.
13. Drying	5 minutes each of cold and hot blowing in automatic photoprocessor (Jarrel-Ash)

Margaret B Bergen—UN Expert in Spectrography, unpublished report 1981.

and made upto the mark with the same acid and shaken well. The resultant concentration of gold in the solution is 200 ppm or $2 \times 10^{-2}\%$ or 200 gms/tonne. Further dilutions are made as per table 2.

The amount of gold in the above standard is estimated by pipetting out 10 ml each of the above standards into a 250 ml conical flask and then adding 10 ml aqua regia to it. This solution of the standard is then diluted to 150 ml with water. 0·5 grams of activated charcoal is then added and the procedure applied for estimating the sample is repeated for the standard to obtain the spectral intensity of gold at 2675·95 and 2427·96 A. By a visual comparison of the spectrum of gold in the unknown sample with that of the known standard, the amount of gold in the unknown is easily obtained.

International standards have been analysed by this procedure and the results obtained were found very satisfactory. The results obtained are shown in table 3.

4. Conclusion

In the Department of Geology and Mining, Madhya Pradesh, 1225 samples which include soils, rocks and sediments have been analysed for gold by this procedure. The

Table 2. Dilutions made to prepare the standard solution

Au content in the initial gold solution (%)	Volume of initial gold solution taken (ml)	Volume of additional 6 N HCl added (ml)	Final volume of gold solution (ml)	Gold content in final solution	
				(%)	(gms/tonne)
2×10^{-2}	200	Nil	200	2×10^{-2}	200·0
2×10^{-2}	25	25	50	1×10^{-2}	100·0
1×10^{-2}	15	35	50	3×10^{-3}	30·0
1×10^{-2}	5	45	50	1×10^{-3}	10·0
3×10^{-3}	5	45	50	3×10^{-4}	3·0
1×10^{-3}	5	45	50	1×10^{-4}	1·0
3×10^{-4}	5	45	50	3×10^{-5}	0·30
1×10^{-4}	5	45	50	1×10^{-5}	0·10
3×10^{-5}	5	45	50	3×10^{-6}	0·03
1×10^{-5}	5	45	50	1×10^{-6}	0·01
3×10^{-6}	5	45	50	3×10^{-7}	0·003
1×10^{-6}	5	45	50	1×10^{-7}	0·001

Table 3. Results of estimation using international standards

Name of international standard used	Number of estimations done	Average value of gold obtained by this procedure (ppm)	Recommended gold value (ppm)
Gold ore MA-2†	6	Between 1 and 3	1·86*
Gold ore MA-1†	4	Between 10 and 30	17·8*

†Standards obtained from Canadian certified, Reference Materials project.

*Canada centre for Mineral and Energy Technology Report 80-6 E, and 81-13 E.

procedure has been found to be accurate for estimation of gold in parts per billion levels and the cost of analysis is relatively very low.

Acknowledgements

My sincere thanks to Mr G Taphyntsev, UN Economic Geologist for his guidance and to Dr S S Dave for his encouragement.

© Printed in India.

Oxygen and hydrogen isotopic ratios in groundwaters and river waters from India

S K BHATTACHARYA, S K GUPTA and R V KRISHNAMURTHY
Physical Research Laboratory, Navrangpura, Ahmedabad 380 009, India

MS received 19 June 1985; revised 21 September 1985

Abstract. A comprehensive set of measurements of oxygen and hydrogen isotopic ratios in groundwaters as well as waters from rivers, lakes, hot springs etc. taken from a variety of locations in India has been carried out for the first time. Isotopically the most depleted samples occur in the high altitude precipitations in the Himalayas e.g. in the lakes of Bhutan and the source water of the Ganga. The shallow groundwater data display a continental effect where the heavy isotope content decreases with distance from the coast (about 4 to 6 per mil decrease in $\delta\,^{18}O$ per 1000 km). The δ D and $\delta\,^{18}O$ of these fresh waters are linearly related and an analysis of this relation vis-a-vis the meteoric water line shows the unambiguous effect of enrichment due to evaporation from soils.

Keywords. Isotopic composition; groundwater; continental effect; monsoon vapour.

1. Introduction

Oxygen and hydrogen isotope ratios, $^{18}O/^{16}O$ and D/H, in groundwaters and precipitations hold important clues to a variety of problems related to regional hydrogeology. These ratios have been used to determine the origin and recharge area of local groundwaters (Burgman *et al* 1979; Weyer *et al* 1979), to infer palaeoclimatic conditions (Sonntag *et al* 1979), to study the mixing of large rivers and to determine the water balance of lakes (Fritz 1981; Gat 1981) etc. These studies are normally comprehended in the context of some prior knowledge about the characteristics of isotopic behaviour in any given region based on an initial data base. From this point of view there is very little available information pertaining to the Indian subcontinent except for the isotopic composition of precipitation which has been studied for about two decades at only one station, New Delhi and for a few intermittent years in Bombay and Shillong under a IAEA/WMO programme. The present study, originally aimed at filling this major gap, has revealed some interesting features in isotope hydrology of the North and Central Indian regions.

2. Sampling locations

In the initial phase of this study, attention was devoted to shallow groundwaters from North India. Eighty samples of shallow groundwaters were collected from an area located within the triangular sector, Ahmedabad–Calcutta–Delhi, in a field trip in March, 1983. The names of the places along the route are given in table 1 and sample numbers are marked in figure 1. The samples were collected mostly from open dug wells (DW) or hand pump wells (HP) whose depths were within 10 metres from the

Table 1. Oxygen and hydrogen isotope composition in water samples from North and Central India.

Sample no.	Place (source)*	δ^{18}O(‰)	δD(‰)
Groundwater			
1	Lasundra (HS)	−2·0	−12
2	Lasundra (DW)	−2·2	− 9
3	Tuva (HS)	−1·5	− 3
4	Tuva (DW)	+0·1	− 2
5	Bhatwada (DW)	−2·3	− 8
6	Dahod (DW)	−2·9	−13
7	Sardarpur (DW)	−1·9	−12
8	Mandu (DW)	−1·9	−12
9	Arjun Baroda (HP)	—	− 6
10	Bhorasa (DW)	−2·2	−14
11	Ashta (DW)	−2·0	−14
12	Bhopal (DW)	−2·4	−14
13	Bamori (HP)	−2·2	−10
14	Udaipura (DW)	−2·6	−10
15	NH 22/26 Crossing (HP)	−2·5	− 7
16	Mankadi (HP)	−2·8	—
17	Sihora (HP)	−3·3	−23
18	Murwara (HP)	−4·5	−30
19	Vikrampur (DW)	−5·5	−41
20	Nagod (DW)	−3·6	−24
21	Agdal (DW)	−4·4	−34
22	Dugdhua (DW)	−5·7	−38
23	Naidi (DW)	−5·5	−38
24	Kabsaur (HP)	−7·3	−50
25	Chandoli (HP)	−5·1	−36
26	Muthani (HP)	−5·9	−43
27	Sasaram (HP)	−5·2	−35
28	Kusanh (DW)	−5·1	−33
29	Jindapur (DW)	−5·8	−36
30	Barhi (HP)	−5·4	−32
31	Demonta (DW)	−7·5	−49
32	Kadal (DW)	−4·8	−34
33	Bagaldi (HP)	−4·9	−31
34	Khadia (HP)	−5·3	−37
35	Barsol (DW)	−3·8	−18
36	Kharagpur (HP)	−2·8	−12
37	Chinsura (HP)	−5·0	−30
38	Burdwan (HP)	−4·6	−31
39	Durgapur (HP)	−4·3	−28
40	Kanchandi (DW)	−3·3	−22
41	Tundi (HP)	−7·1	−46
42	Dwarpahari (HP)	−6·6	−41
43	Chakai (HP)	−6·8	−47
44	Mallipur (DW)	−5·6	−37
45	Avadhey (HP)	−5·6	−38
46	Rajgir (HS)	−8·1	−53
47	Nalanda (HP)	−5·5	−39
48	Bitha (HP)	−7·2	−49
49	Arrah (HP)	−5·9	−42

Table 1 (*Contd.*)

Sample no,	Place (source)*	$\delta^{18}O$(‰)	δD(‰)
50	Sinha Chawar (HP)	−6·6	−42
51	Mau (HP)	−4·1	−26
52	Mahamadpur (HP)	−7·5	−45
53	Surapur (HP)	−7·9	−50
54	Sultanpur (HP)	−7·5	−44
55	Asrapur (HP)	−7·6	—
56	Lucknow (HP)	−6·3	−41
57	Chakarpur (HP)	−6·6	−40
58	Bhognipur (HP)	−6·8	−46
59	Mehwa (HP)	−6·4	−43
60	Sirsaganj (HP)	−5·9	−42
61	Shahdra (DW)	−7·0	−44
62	Mathura (HP)	−6·3	−46
63	Gomat ka Pyau (HP)	−6·8	−42
64	Bulandsher (HP)	−7·7	−48
65	Shahdra Gandhi (HP)	−7·5	−47
66	Dunda Hera (HP)	−6·2	−47
67	Oddi (BW)	−6·3	−39
68	Sajapur (HP)	−5·3	−41
69	Sangteda (HP)	−6·3	−39
70	Shahpura (HP)	−5·7	−37
71	Kesupura (HP)	−5·3	−32
72	Ramnagar (DW)	−4·0	−27
73	Ajmer (HP)	−4·4	−27
74	Barr (HP)	−3·3	−21
75	Jadan (HP)	−4·9	−31
76	Sanderao (HP)	−1·3	− 8
77	Kojra-Pyau (DW)	−4·4	−26
78	Amirgarh (DW)	−3·6	−19
79	Sidhpur (DW)	−3·6	−19
80	Gota (HP)	−3·1	−15
Groundwater (*Contd.*)			
RJ-1	Churu (HP)	−4·0	—
G-1	Khedbrahma (DW)	−3·3	—
G-2	Parsa (DW)	−4·1	—
G-3	Ahmedabad (DW)	−3·0	—
G-4	Chotila (DW)	−2·5	—
G-5	Tulsi Shyam (HS)	−1·1	—
G-6	Samni, Veraval (HS)	−1·8	—
G-7	Chota Udaipur (HP)	−1·5	− 5
G-8a	Nawagam (OW)	−1·4	—
G-8b	Nawagam (BW)	−3·0	−15
G-9	Surat (HP)	−0·5	0.0
G-10	Saputara (lake)	−1·8	—
MP-1	Narsinghpur (HP)	−3·0	−22
MP-2	Dindori (DW)	−4·3	−27
MP-3	Amarkantak (DW)	−4·9	−40
M-1	Dhule (DW)	−0·8	− 6
M-2a	Ambolinaka, Bombay (HP)	−0·7	—
M-2b	Malad, Bombay (TW)	+0·2	—
M-3	Arabian Sea, Bombay (coast)	+0·5	—
M-3	Arabian Sea, Bombay (coast)	+0·8	—

Table 1 (Contd.)

Sample no.	Place (source)*	$\delta^{18}O(\permil)$	$\delta D(\permil)$
M-4	Pune (DW)	−2·0	—
AP-1	Hyderabad (BW)	−2·4	—
AP-2a	Waltair (HP)	−1·9	—
AP-2b	Waltair (HP)	−2·9	—
WB-1	Calcutta, Kashba (HP)	−4·4	−24
WB-2	Calcutta, Bandel (HP)	−4·1	−23
A-1	Jorhat (HP)	−5·1	−32
A-2	Bokakhat (HP)	−6·1	−32
A-3	Nowgaon (HP)	−6·0	—
A-4	Gauhati (HP)	−4·8	−31
UP-1	Nainital (lake)	−7·3	−49
UP-2	Bhimtal (lake)	—	−43
UP-3	Ranibag (lake)	—	−43
K-1	Srinagar (tap)	−6·5	−38
K-2	Dal (lake)	−7·5	−44
K-3	Wular (lake)	−7·5	−41
K-4	Manasbal (lake)	−5·8	−43
K-5	Telbal (lake)	−4·9	−39
BH-1	Phochu, Bhutan (lake)	−10.9	—
BH-2	Lunana (lake)	−12·4	—
BH-3	Thanza (lake)	−11·2	—
BH-4	Rimzichola (lake)	−9·9	—
River water			
R-1	Jhelum, Kashmir (June 82)	−7·0	−39
R-2	Koolnala, Kashmir (June 82)	−7·0	−37
R-3	Romu, Kashmir (June 82)	−7·4	−41
R-4	Sabarmati, Ahmedabad (October 81)	−1·9	−13
R-5	Bhagirathi, Devprayag (March 82)	−9·6	−61
R-6	Ganga, Rishikesh (March 82)	−9·2	−61
R-7	Yamuna, Mathura (March 82)	−7·8	−50
R-8	Chambal, Dholpur (March 82)	−2·4	−19
R-9	Betwa, Hamirpur (March 82)	−3·6	−29
R-10	Son, Ara (March 82)	−2·9	—
R-11	Gomti, Dobni (March 82)	−7·1	−48
R-12	Ghaghara, Elginbridge (March 82)	−8·4	−54
R-13	Gandak, Hajipur (March 82)	−8·9	−63
R-14	Damodar, Dhanbad (February 85)	−4·8	—
R-15	Brahmaputra, Goalpara (April 82)	—	−37
R-16	Manas, Goalpara (April 82)	−6·6	−41

*Dug well—DW; hand pump—HP; tube well—TW; bore well—BW; hot spring—HS; oil well—OW.

surface and are located, as far as possible, away from big rivers or canals of major irrigation systems. Subsequently, well samples were collected from cities like Surat, Bombay, Hyderabad (150 m bore well), Waltair, Calcutta, Gauhati, Srinagar etc. (see figure 1). In addition, several samples were taken from lakes and rivers from Kashmir,

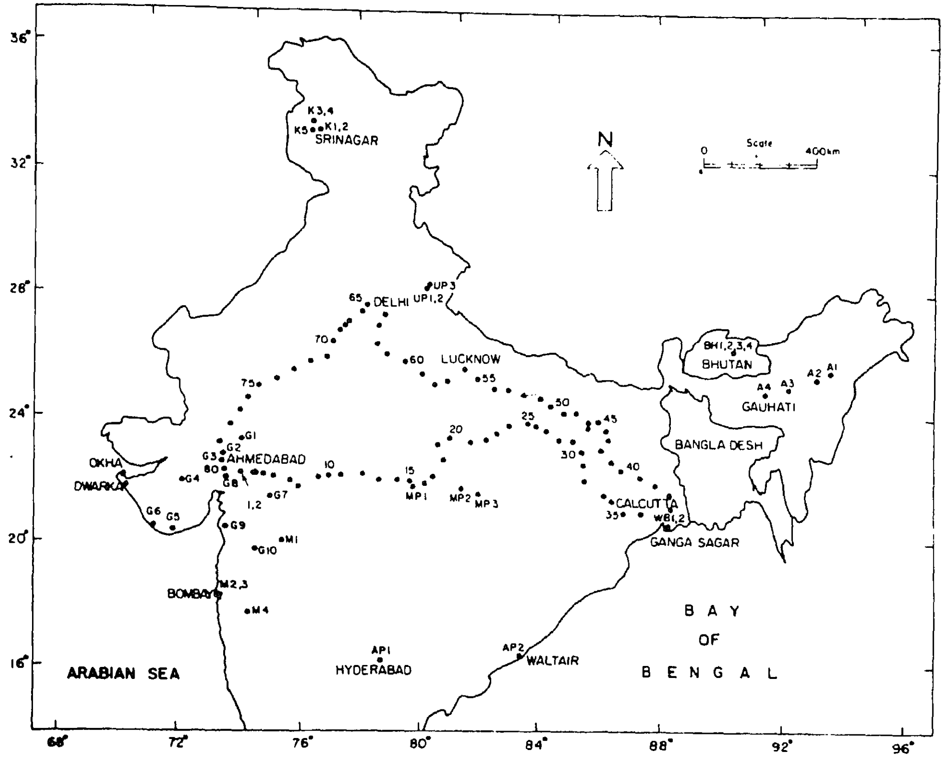

Figure 1. Locations from which groundwater (wells, lakes and hot springs) and river water samples were collected (see table 1 for names of the places).

UP, MP, Bhutan etc. including big rivers like the Ganga and the Brahmaputra at several places. These diverse water bodies were sampled to establish the isotopic characteristics of all available sources of surface waters.

During collection water was filled to the brim in pre-cleaned dry glass or plastic bottles and sealed tight to avoid evaporation. For dug wells, care was taken to sample the bottom part of the water column by sending an air-filled bottle upside down to the bottom and then tilting it. The samples were always analysed within about a month after they were brought to the laboratory to minimise evaporation during storage. Plastic bottles are especially susceptible to this effect (Prof. Munnich, private communication).

bottle (8 ml volume) at 25°C for 48 hours. After equilibration the CO_2 was purified of moisture and air in three stages and measured for oxygen isotope ratio in a VG Micromass 602 D mass spectrometer. One laboratory water standard (SAB) was measured for every set of 4 samples to (i) keep track of the reproducibility of the procedure and (ii) convert the measured ratios to final values relative to an international standard.

The D/H ratio was determined by following the procedure of Bigeleisen *et al* (1952) and Friedman and Hardcastle (1970). Briefly, about 10 mg of water, sealed in a capillary tube, was taken in a vacuum line and reduced to H_2 gas by reacting with uranium at 800°C. The completion of reduction was checked by measuring the yield of H_2 which was close to 100%. The gas was measured for its D/H ratio in a second VG Micromass 602 D machine within 12 hours of preparation. A constant check was maintained on the whole procedure by running the water standard (SAB) for every set of (5–10) samples.

The isotopic ratios are reported as deviations from the international standard Vienna-SMOW (standard mean ocean water) in parts per thousand (or per mil, ‰) as defined below:

$$\delta(^{18}\mathrm{O} \text{ or } \mathrm{D}) = \left[\frac{R_{\text{sample}}}{R_{\text{V-SMOW}}} - 1\right] \times 10^3 \ (‰)$$

where R refers to either $^{18}O/^{16}O$ atom ratio (for $\delta^{18}O$) or D/H atom ratio (for δD). The analytical reproducibility determined by repeated analysis of the laboratory standard is ± 0.1‰ for $\delta^{18}O$ and $\pm 1{\cdot}5$‰ for δD.

4. Results and discussion

The results of the measurements of $\delta^{18}O$ and δD in water samples are given in table 1. The data display a wide range in isotopic variation as expected from a large subcontinent. The $\delta^{18}O$ values range from $+0{\cdot}8$‰ (Arabian sea) to $-12{\cdot}4$‰ for a high altitude lake in Bhutan (Lunana). δD values of these two extreme cases were not measured. But for other samples δD values also show a large spread, ranging from 0‰ (for Surat with $\delta^{18}O$ of $-0{\cdot}5$‰) to -63‰ (Gandak at Hajipur in March, 1982 with $\delta^{18}O$ of $-8{\cdot}9$‰). Some of the notable features of the data are discussed below.

4.1 *Continental effect*

A survey of the δ-values in shallow groundwater (dug well and hand pump) samples with reference to figure 1 shows that as one moves away from coastal stations to interior stations the δ-values tend to decrease. To facilitate the visualisation of this effect the $\delta^{18}O$ values for the sample numbers (locations) 22 to 57 and A1 to A4 (eastern sector, figure 1) are plotted as a function of their distances from the nearest coast (close to the Hooghly estuary at Ganga Sagar) in figure 2. Similarly, the sample numbers (locations) 58 to 80 and a few other places in Gujarat and Rajasthan constitute the

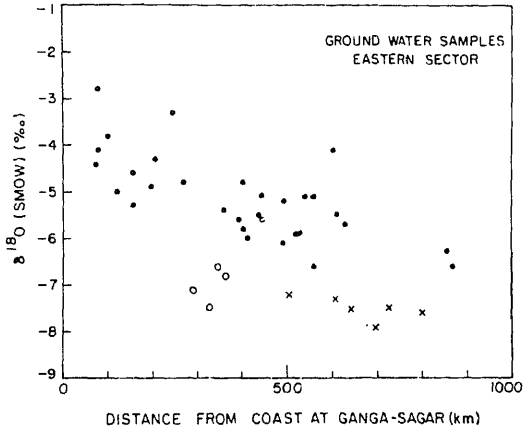

Figure 2. $\delta^{18}O$ values of the groundwater samples collected east of Lucknow (sample numbers 22 to 57 and A1 to A4 in table 1) as a function of the distance of the sampling locations from the nearest coastal point (taken as Ganga Sagar). × —samples taken from places close to big rivers and irrigation systems; O—samples taken from higher altitudes.

western sector and their $\delta^{18}O$ values are plotted as a function of their distances from the coast near Okha-Dwaraka in figure 3. Both these figures show that there is a gradual decrease in the heavy oxygen isotope concentration (i.e. in $\delta^{18}O$) with distance from the coast. Since it will be shown later that δD and $\delta^{18}O$ are linearly related, the same phenomenon is also seen in the case of heavy isotope of hydrogen.

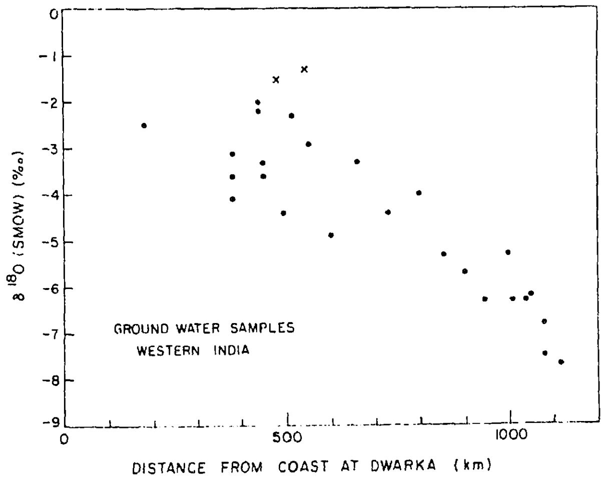

Figure 3. $\delta^{18}O$ values of the groundwater samples, collected west of Lucknow (sample numbers 58 to 80) and some locations from Gujarat, as a function of the distance of the

The above phenomenon is readily explained by considering the groundwater at any place as being essentially derived from the local precipitation. Zimmerman *et al* (1967) showed that year by year precipitations are deposited as different layers within the soil and are gradually mixed on their way down through the soil column. As a result the isotopic composition of shallow and locally derived groundwater generally matches the long term mean composition of precipitation over the recharge area (Gat 1981). Therefore, the observed variation in the isotopic composition of groundwaters with distance can be attributed to a similar variation found in the composition of precipitation on a continent.

The progressive ^{18}O depletion in rains falling over the continent can be explained by considering the formation of precipitation as a Rayleigh process, whereby a given airmass carrying a large amount of moisture evaporated from the ocean enters a continent through the coast and undergoes successive stages of rain-out as it moves farther and farther into the continent. The process of rain-out is accompanied by isotopic fractionation where the condensate is enriched relative to the vapour. Due to preferential removal of the heavy isotope in the liquid phase the remaining vapour becomes depleted in it and consequently each stage of precipitation is lower in $^{18}O/^{16}O$ or D/H than the preceding one. This phenomenon is known as the "continental effect" and has been described in detail by Rozanski *et al* (1982) in a model to explain the factors controlling the stable isotope composition of European precipitation.

In view of the above, the rationale for measuring distance from the nearest coast along the Calcutta-Lucknow direction for the eastern sector (figure 2) and along the Ahmedabad-Delhi direction for the western sector (figure 3) becomes clear. The first direction coincides with the general pattern of lower level wind movement in the Gangetic plains in North India during the south-west monsoon season (June to September) which accounts for more than eighty percent of the yearly precipitation (Rao 1976). These airmasses carry considerable amounts of moisture into the country through coastal West Bengal which is finally released as rains by convective cooling of the vapour masses at various regions as they gradually propagate along with the monsoon wind in the NWW direction.

For the Ahmedabad-Delhi sector the chief source of moisture is the Arabian sea since the low level wind in West India is nearly westerly or westsouthwesterly. The choice of an appropriate coastal point to measure the distance for the western sector cannot therefore be made unambiguously. We have taken the coast of Okha-Dwaraka as the representative point for the purpose of illustration.

The continental effect displayed in figures 2 and 3 is associated with relatively large scatter in $\delta^{18}O$ values. Part of this scatter in figure 2 is from 6 samples (denoted by crosses) which were taken from locations in close proximity to the Ganga (sample 24) and to the Gomti and the Ghaghara. The low lying areas in this region occasionally get flooded in the monsoon season by the Ganga and its tributaries. Additionally, extensive canal irrigation is prevalent in this area and therefore, in some cases the shallow groundwaters may have a substantial contribution from river waters with more negative $\delta^{18}O$ (e.g. Ghaghara water in March 1982, was found to have $\delta^{18}O$ of $-8{\cdot}4\,‰$) than that of the local precipitation.

A second set of 4 deviant points (denoted by open circles) from the systematic trend in figure 2 are from locations 31, 41, 42 and 43. These places are all on the Hazaribagh Plateau at elevations ranging from 300 m to 900 m. One possibility for the more negative $\delta^{18}O$ values of these samples is that they are derived from high altitude precipitations (Siegenthaler and Oeschger 1980). In figure 2 there are 3 samples which tend to show more positive values than the trend. These could be due to enrichment by intense evaporation in case of unused dugwells or recharge by locally evaporated water bodies in case of hand pumps.

The $\delta^{18}O$ values of near coastal stations in the eastern sector (e.g. Calcutta, Chinsura) are between $-4\,‰$ to $-5\,‰$ which are more negative than those for corresponding stations in the western sector (e.g. Ahmedabad, Chotila) lying between $-2\,‰$ to $-3\,‰$. Here again we suspect that a considerable contribution from rivers in the Gangetic West Bengal makes the resultant groundwater δ-values more negative than their local sources. This contamination would also render the apparent continental effect derived from groundwaters in the eastern sector less steep than it actually is. The western sector being free from the riverine contribution may therefore represent the real continental effect – which is about $6\,‰$ decrease per 1000 km distance from the coast (figure 3). This value is slightly higher than the value of about $4\,‰$ per 1000 km obtained by Sonntag *et al* (1979) based on their analysis of modern European groundwaters. This difference can be attributed to two factors: (a) in the present case the coastal distance is tentatively defined along a straight line from Dwaraka to Delhi which assumes that moisture is carried only from SW to NE thereby giving a smaller estimate of the distance involved and (b) the mechanism of rain production by convective lifting in western India is very different from the frontal lifting in western Europe which can result in a difference in fractionation mechanism operative in the Rayleigh process.

4.2 *$\delta D - \delta^{18}O$ relation*

A plot of δD versus $\delta^{18}O$ for all the stations where both the measurements are available is shown in figure 4. This shows that δD and $\delta^{18}O$ are linearly correlated (correlation coefficient, $r = 0{\cdot}94$) and the best fit line to the set of points is given by

$$\delta D = (6{\cdot}8 \pm 0{\cdot}1)\,\delta^{18}O + (2{\cdot}2 \pm 0{\cdot}4) \tag{1}$$

In contrast the weighted average δD and $\delta^{18}O$ values of precipitation for worldwide network stations of IAEA is given by (Yurtsever and Gat 1981).

$$\delta D = (8{\cdot}2 \pm 0{\cdot}1)\,\delta^{18}O + (10{\cdot}6 \pm 0{\cdot}6) \tag{2}$$

The slope *s* and intercept *d* of (1) are less than those of (2) which are based on much larger range of δD and $\delta^{18}O$ values ($\delta^{18}O$ range from $0\,‰$ $-26\,‰$) and hence more definitely determined. In regional analysis it is often seen that the $\delta D - \delta^{18}O$ relationship in precipitation differs from the global equation. For example, the slope and intercept for tropical island stations are 6·2 and 4·0 (Yurtsever and Gat 1981) respectively. The reasons for such deviations from the precipitation line (or the global meteoric water line, defined by Craig 1961) have been extensively discussed earlier by Dansgaard (1964) and later by Gat (1981, 1983) especially in relation to groundwater hydrology. It was shown that the intercept *d* (similar in concept to the deuterium excess parameter defined by $d = \delta D - 8\delta^{18}O$) tends to decrease as a result of evaporative processes at various stages from precipitation upto recharge of the groundwater aquifer.

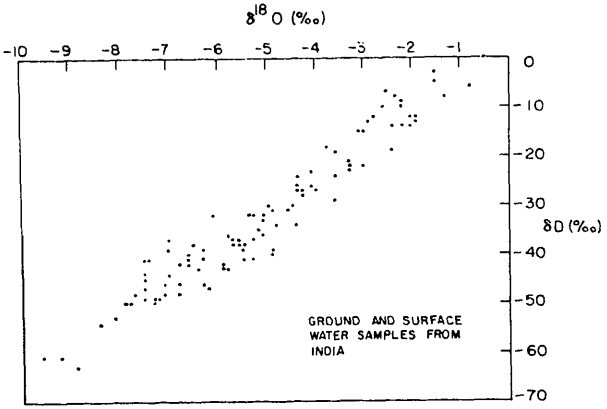

Figure 4. Plot of δ D versus δ^{18}O for water samples for which both the measurements were done. The data show that these two variables are linearly related (see text).

In order to assess the role of evaporation in the present case the limited amount of ecipitation data available for three Indian IAEA stations (New Delhi, Bombay and illong) are shown in figure 5 as a $\delta \mathrm{D} - \delta^{18}\mathrm{O}$ plot. It seems that the monsoonal rains e characterised by the following equation,

$$\delta \mathrm{D} = (7{\cdot}2 \pm 0{\cdot}1)\,\delta^{18}\mathrm{O} + (5{\cdot}1 \pm 0{\cdot}1). \tag{3}$$

As can be seen, the values of s and d are less than those of the global meteoric water ne (8·2 and 10·6 respectively). This suggests that the isotopic composition of

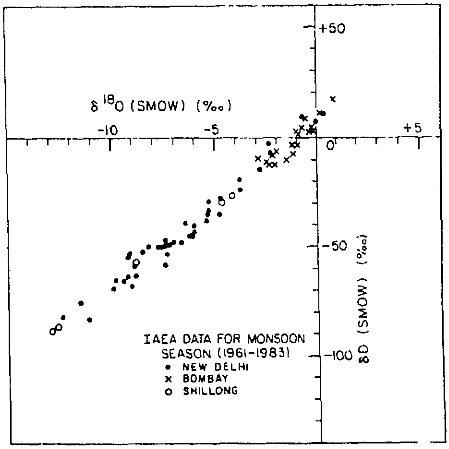

Figure 5. Plot of δ D versus δ^{18}O for rain-water samples collected during monsoon season (June to September) from three Indian stations showing a linear relation between these two variables. The data are taken from IAEA reports.

precipitation is modified by evaporation from falling raindrops. Similarly the still low values of *s* (6·8) and *d* (2·2) in groundwater [see (1)] are indicative of evaporation evapotranspiration from soils during the process of recharge. This will in turn mea that the groundwater isotopic composition is expected to be somewhat differe relative to local precipitation (see §4·3 below). This evaporative effect should depend local temperature, humidity, vegetation cover and a host of other regional paramete and thereby may introduce some part of the scatter superimposed on the continent effect as discussed earlier.

4.3 *Selection effect in Delhi*

In the context of groundwater investigations data of twenty four years of δ D and δ analyses (1961–1984) in total monthly precipitations in an IAEA operated station in N Delhi are available for comparison (see IAEA Technical Reports Series No. 96, 117, 1 147 and 165). From these data yearly weighted average values are first comput and then, based on 24 yearly averages, grand weighted averages of δ D and δ are computed to be −38 ‰ and −6·0 ‰ respectively. In contrast, the avera groundwater δ D and δ^{18}O values in the region around New Delhi (within 100 from Delhi corresponding to stations 63 to 68) are −44 ‰ and −6·6 ‰ respective Thus there seems to be a small depletion of 6 ‰ in δD and 0·6 ‰ in δ^{18}O groundwater relative to that in precipitation which presumably is feeding underground aquifers. This difference can be explained by proposing a selection eff operating in the recharge of the groundwater by precipitation, similar to one discuss by Vogel and Van Urk (1975) to explain parallel results obtained in South Africa. T IAEA data also show that the pre-monsoon rains (May and June) in Delhi are usua enriched as compared to monsoon showers (July and August). The late monso precipitations in September are further depleted and usually characterised by avera δ^{18}O values as low as −10 ‰. The difference in average monthly δ^{18}O precipitations during May to September in Delhi is intriguing since one would exp that the moisture required for the rains in these months is derived from the same t seas, namely, the Arabian Sea and the Bay of Bengal. The enrichment in pre and ea monsoon rains of May and June can be explained by an amount effect (Dansgaa 1964) whereby the heavier δ-values are due to the lower amount of precipitation those months. The amount effect is possibly related to evaporation from the falli raindrops (§4.2) whose influence is more pronounced in hot and relatively dry p monsoon months (less rainfall). The reason for the depletion of heavy isotopes in September rains is not very clear. One possible cause could be the change in the low level wind pattern in September whereby the supply of moisture from the Arabian se significantly reduced. The bulk of the September rains are thus derived from vapo supplied by the Bay of Bengal through easterlies and have depleted δ-values owing the continental effect discussed earlier. Notwithstanding the real mechanism of t effect it is likely that the early monsoon rains falling on parched grounds are more eas

Two samples of Arabian sea water near the Bombay coast were measured and found to have $\delta^{18}O$ values of 0·5 ‰ and 0·8 ‰ which lie within the range of values obtained by Duplessy *et al* (1981), namely, 0·5 ‰ to 0·8 ‰. Regarding the vapour composition, it was pointed out by Dansgaard (1964) that as a result of fast evaporation from the Arabian sea, monsoon vapour is not in thermodynamic equilibrium with sea water but more depleted in ^{18}O due to kinetic fractionation. Therefore, the first condensate from such vapour, being controlled essentially by equilibrium condensation, will be slightly lower in ^{18}O than the sea water. The groundwaters of Surat and Bombay (coastal stations) are expected to be derived from such condensation and will have consequently $\delta^{18}O$ value lower than the local sea water which is indeed the case.

5. Conclusions

This paper reports the first extensive set of oxygen and hydrogen isotope analyses in groundwaters, river and lake waters taken from a variety of locations in India. In addition to providing an overall view of the isotopic scenario the following interesting features are noted.

(i) The groundwaters show a large continental effect both in Ahmedabad-Delhi (western) sector and Calcutta-Delhi (eastern) sector. In the former, it is about 6 ‰ decrease per 1000 km distance from the coast, while in the latter case, only a lower limit (4 ‰ decrease per 1000 km) can be obtained due to possible river water contribution to aquifers.

(ii) The $\delta D - \delta^{18}O$ relationship is linear and has slope and intercept lower than those of the meteoric water line indicating evaporative enrichment. A comparison with similar relations found in IAEA data for precipitation at 3 Indian stations (New Delhi, Bombay and Shillong) shows that the evaporation takes place during (a) the fall of raindrops to the ground and (b) the recharge of groundwater through surface percolation.

(iii) The monsoon vapour over the Arabian sea and the west coast is derived from seawater by fast and non-equilibrium (kinetic controlled) evaporation.

(iv) The most depleted ^{18}O values in the subcontinent are found in the high altitude lakes of Bhutan followed by the upper reaches of the Ganga water near Devprayag and Rishikesh.

Acknowledgements

The authors are grateful to the DST, Government of India for a grant. They thank M/S M P K Kurup, K K Sivasankaran and R A Jani for help. We benefitted from discussions with Prof. P R Pisharoty, Prof. Rama, Prof. R Ananthakrishnan and Dr R Ramesh. Prof. B L K Somayajulu, Dr M M Sarin and Dr J N Goswami kindly helped in collection of some of the samples.

References

Bigeleisen J, Perlman M L and Prosser H C 1952 *Anal. Chem.* **24** 1356

Burgman J O S, Eriksson E, Kostov L and Moller A 1979 *Isotope hydrology* 1978 (*Proc. Int. Symp. Neuherberg*) (Vienna: IAEA) Vol. 1, p. 40

Craig H 1961 *Science* **133** 1702

Dansgaard W 1964 *Tellus* **16** 436

Duplessy J C, Be A W H and Blanc P L 1981 *Palaeogeogr. Palaeoclimatol, Palaeoecol.* **33** 9

Epstein S and Mayeda T 1953 *Geochim. Cosmochim. Acta* **4** 213

Friedman I and Hardcastle K 1970 *Geochim. Cosmochim. Acta* **34** 125

Fritz P 1981 *Stable isotope hydrology: deuterium and oxygen*-18 *in the water cycle* (eds) J R Gat and R Gonfiantini (Vienna: IAEA) p. 177

Gat J R 1981 *Stable isotope hydrology: deuterium and oxygen*-18 *in the water cycle* (eds) J R Gat and R Gonfiantini (Vienna: IAEA) p. 203

Gat J R 1983 *Palaeoclimates and palaeowaters: a collection of environmental isotope studies* (Vienna: IAEA) p. 3

Krishnamurthy R V 1984 *Stable isotope studies on sedimentary deposits and groundwaters and their climatic implications* Ph.D. thesis, Gujarat University p. 52

Rao Y P 1976 South-West Monsoon, *Meteorol. Monograph*, No. 1, India Meteorol. Dept., p. 1

Rozanski K, Sonntag C and Munnich K O 1982 *Tellus* **34** 142

Siegenthaler V and Oeschger H 1980 *Nature* **285** 314

Sonntag C, Klitzsch E, Lohnert E P, El-Shazley E M, Munnich K O, Junghans Ch, Thorweihe U, Weistroffer K and Swailem F M 1979 *Isotope hydrology* 1978 (*Proc. Int. Symp. Neuherberg*) (Vienna: IAEA) Vol. 2, p. 580

Vogel J and Van Urk H 1975 *J. Hydrol.* **25** 23

Weyer K U, Krouse H R and Horwood W C 1979 *Isotope hydrology* 1978 (*Proc. Int. Symp. Neuherberg*) (Vienna: IAEA) Vol. 1, p. 263

Yurtsever Y and Gat J R 1981 *Stable isotope hydrology: deuterium and oxygen*-18 *in the water cycle* (eds) J R Gat and R Gonfiantini (Vienna: IAEA) p. 103

Zimmerman U, Ehhalt D and Munnich K O 1967 *Isotopes in Hydrology* (Proc. Symp. Vienna) p. 567

Proc. Indian Acad. Sci. (Earth Planet. Sci.), Vol. 94, No. 3, November 1985, pp. 297–303.
© Printed in India.

Geochemistry of bauxites of Belgaum (Karnataka) and Yercaud (Tamil Nadu) areas

J N PATTAN* and S M APPANGOUDAR
Geology Department, Post-Graduate Centre, Sandur 583 119, India
*Present address: National Institute of Oceanography, Dona Paula, Goa 403 004, India

MS received 10 August 1984; revised 21 May 1985

Abstract. The major chemical components of bauxite deposits of Belgaum (76° 24′E : 15° 54′N) and Yercaud (78° 14′E : 11° 48′N) areas have been determined. A chemical continuity between parent rocks (zone I) to bauxites (zone IV) via clay (zone II) and laterites (zone III) clearly indicates that bauxites have been derived by *in situ* weathering of the respective parent rocks.

Keywords. Parent rocks; bauxites; *in situ* weathering.

1. Introduction

It is generally an accepted fact that the chemical composition of laterites, bauxites and associated clays is governed by various factors, viz, the amount of specific elements in the source rocks, the chemical association of specific elements with stable and unstable minerals during weathering, the intensity of drainage during weathering, and the relative enrichment of trace and minor elements in laterites and bauxites with respect to the crust (Valeton 1972).

The bauxites of Belgaum (76° 24′E : 15° 54′N), derived from basalts, and that of Yercaud (78° 14′E : 11° 48′N), derived from charnockites, were subjected to detailed geochemical analyses to determine the variations between them. Samples of bauxites, laterites, clays and source rocks have been collected in the vertical profiles of both the areas and analysed. The results are given in tables 1 and 2.

2. Geology of bauxite deposits

Sahasrabudhe (1978) gave an account of the geological distribution and reserves of bauxite deposits of the Belgaum region in detail. Later Balasubramaniam and Mora (1984) described the utilisation of bauxites from the Belgaum region. The bauxite deposits of Belgaum are located at comparatively low altitude, about 1025 mts from MSL, in the form of small discontinuous patches, irregular lenticular masses and covering the top of the small hillocks formed by basaltic rocks. Bauxite is massive, tough, compact and commonly exhibits oolitic to pisolitic texture. The presence of stalactitic structures of gibbsitic composition varying in length from 0·5 cms to 15 cms is noticed in some cavities near Hangarge about 8 kms due SW of Belgaum.

Table 1. Chemical analyses of bauxites, laterites, clays and basalts from DBS Hangarge bauxite mine, Belgaum area.

Sample no.	Depth (mts)	SiO_2	Al_2O_3	Fe_2O_3	TiO_2	Loss on ignition	FeO	CaO	MgO	NaO_2	K_2O	P_2O_5
B-1	0·3	3·88	51·08	12·00	3·36	27·40	0·37	0·50	—	0·10	0·08	0·109
B-2	2·0	2·12	56·48	8·57	6·25	24·92	0·50	0·23	—	0·30	0·05	0·119
B-3	3·3	2·29	48·34	20·00	4·17	23·36	0·12	0·43	0·2	0·10	0·31	0·015
B-4	5·0	2·16	52·83	10·75	3·08	29·56	0·37	0·62	0·81	0·08	Tra	0·064
B-5	6·6	1·50	56·10	8·00	3·34	29·24	0·50	0·41	—	0·18	0·20	0·013
B-6	10·0	2·82	45·70	25·71	4·79	18·56	0·37	0·51	—	0·24	0·31	0·080
B-8	12·0	3·12	44·71	21·14	6·25	21·78	0·24	0·50	0·21	0·10	0·42	0·061
B-9	13·3	2·20	57·50	3·71	3·47	31·72	0·24	0·30	0·20	0·10	0·05	0·001
B-10	16·6	4·68	52·86	4·71	4·18	30·12	0·24	1·24	0·51	0·18	0·11	0·039
B-11	18·3	3·24	54·73	4·71	4·47	30·86	0·24	0·51	—	0·10	0·25	0·001
B-12	20·0	1·21	60·10	2·85	5·12	29·72	0·12	0·23	—	0·20	0·10	0·027
B-13	22·0	3·20	56·32	6·48	3·79	28·52	0·37	0·31	—	0·21	0·18	0·033
B-14	23·0	2·52	55·00	5·20	5·56	27·64	0·24	1·34	0·58	0·10	0·21	0·052
B-27/1	23·6	37·00	39·26	8·57	2·78	12·76	0·12	—	—	0·02	Tra	0·040
B-27/2	25·0	42·42	32·96	5·71	2·05	15·60	0·12	—	—	0·03	0·05	0·046
B-27/3	26·3	42·40	27·55	9·37	2·05	15·48	0·12	0·62	—	0·03	0·21	0·047
B-52	27+	49·42	16·98	6·47	1·27	1·06	7·54	7·68	7·54	1·31	0·58	0·054

Sample nos. 1–14 laterites and bauxites; sample nos. 27/1, 27/2 and 27/3 clays; sample no. 52 average of six basalts.

Table 2. Chemical analyses of bauxites, laterites, clays and charnockites from hill no. 1 of Yercaud bauxite mine, Yercaud.

Sample no.	Depth (mts)	SiO_2	Al_2O_3	Fe_2O_3	TiO_2	Loss on ignition	FeO	CaO	MgO	Na_2O	K_2O	P_2O_5
S-1	0·3	3·00	50·58	18·85	1·39	23·72	0·37	0·13	0·01	0·04	0·02	0·05
S-2	2·0	4·98	50·43	12·57	1·39	27·38	0·25	0·14	0·01	0·09	0·04	0·033
S-3	3·3	5·02	55·72	2·58	1·21	32·88	0·12	0·11	0·20	0·02	0·02	0·027
S-4	5·0	2·54	47·29	20·57	1·15	25·72	0·75	0·15	—	0·30	Tra	0·270
S-5	6·0	3·66	51·18	11·42	1·25	28·68	1·00	0·14	0·02	0·10	0·02	0·047
S-6	8·3	3·40	52·09	8·57	1·21	31·12	0·37	0·40	0·02	0·20	0·05	0·001
S-8	10·0	3·30	40·45	25·71	1·20	25·76	0·50	0·20	0·01	0·50	0·04	0·051
S-10	12·0	6·10	49·97	12·00	1·15	26·68	1·00	0·15	0·02	0·10	Tra	0·705
S-12	12·6	4·12	42·43	26·28	1·10	22·44	0·50	0·42	0·03	0·50	Tra	0·132
S-14	13·3	6·94	49·43	10·57	1·29	26·84	2·00	0·12	—	0·20	Tra	0·132
S-14/1	15·0	42·98	33·11	2·28	1·01	18·00	0·12	—	—	0·05	0·04	0·038
S-14/2	18+	60·58	17·84	4·64	0·80	1·04	3·64	6·47	3·37	1·14	0·10	0·024

Sample nos. 1–14 laterites and bauxites; sample no. 14/1 average of two clays; sample no. 14/2 average of six charnockites.

of the Yercaud area are confined to the particular geomorphic horizons between 1679 mts and 1803 mts of the mighty hill ranges formed by the charnockite suite of rocks. They occupy the peaks of the hillocks which have characteristic flat topped surfaces. Generally, bauxite occurs as small lenses, lenticular masses and patches of bauxites and aluminous laterites occur in laterite with gradational borders. The colour of the bauxite varies from yellowish brown to reddish brown and it is of the lateritic type.

3. Analytical method

For chemical analyses samples have been crushed to −230 mesh. From these samples 0·2 gms of powder were taken and digested in teflon bombs. Alumina, titania, iron, calcium and magnesium were determined by using AAS (Verion 575 Techron Pvt, Australia). Sodium and potassium were determined by a flame photometer (Systronics) and phosphorus by a UV spectrophotometer (Verion 634 Techron Pvt, Australia). For digestion of rocks, 5 ml of 40 % HF, and for clays, laterites and bauxites 5 ml of HF and 1 ml of H_2SO_4 were used and heated at 150°C for one hour. After digesting, 50 ml of saturated boric acid were added and made up to 100 ml by adding distilled water. International rock standard and bauxite (BX-N) were used for reference. The analytical error was 1–8 %.

4. Results

Tables 1 and 2 clearly indicate that bauxites of the Belgaum area contain high proportions of alumina (44·71–60·10 %) and titania (3·36–6·25 %), low amounts of silica (1·21–4·68 %) and iron (2·85–25·71 %), and comparatively low phosphorus (0·001–0·119 %). Those of the Yercaud area contain comparatively low quantities of alumina (40·45–55·72 %) and titania (1·01–1·39 %), and high quantities of silica (2·54–6·94 %), iron (2·58–26·28 %) and phosphorus (0·001–0·705 %). There is not much variation in quantities of FeO, CaO, MgO, Na_2O and K_2O in both the areas. A positive correlation is noticed between Al_2O_3–TiO_2 and Al_2O_3–loss on ignition and negative correlation between Al_2O_3–SiO_2 and Al_2O_3–Fe_2O_3. Further Al_2O_3, TiO_2 and Fe_2O_3 decrease and SiO_2 increases with depth in both the areas.

4.1 *SiO_2–Al_2O_3–Fe_2O_3 system and the weathering line*

The average chemical composition of the parent rocks of the Belgaum (basalts) and the Yercaud (Charnockites) areas together with mean values in the weathering layers in laterite profiles are plotted in the triangular diagram of SiO_2–Al_2O_3–Fe_2O_3 (figure 1).

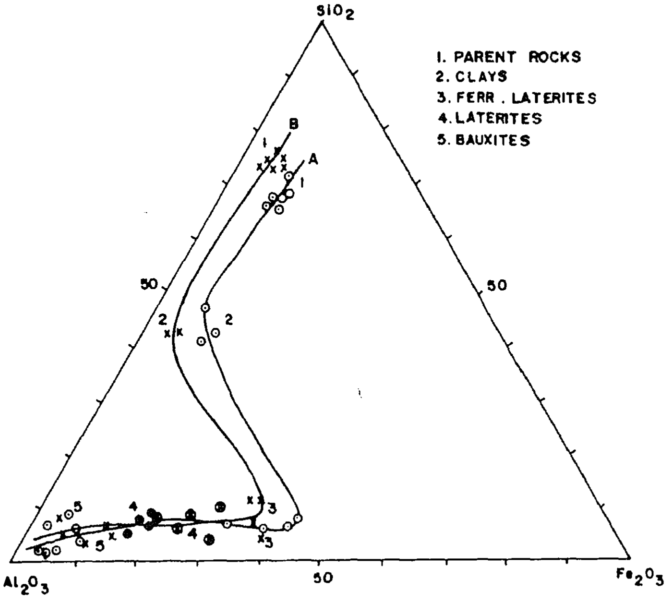

Figure 1. Triangular diagram between SiO_2, Al_2O_3 and Fe_2O_3 for bauxitic profiles of Belgaum (A) and Yercaud (B) areas.

Table 3. Ratio of major chemical constituents in parent rock and their lateritized products of Belgaum area

Substance	$\frac{Fe_2O_3}{Al_2O_3}$	$\frac{SiO_2}{Al_2O_3}$	$\frac{SiO_2}{Fe_2O_3}$	$\frac{TiO_2}{Al_2O_3}$	$\frac{TiO_2}{Fe_2O_3}$
Basalts	0·381	2·91	7·63	0·070	0·109
Clays	0·23	1·202	5·20	0·071	0·29
Laterites	0·19	0·055	0·25	0·084	0·42
Bauxites	0·057	0·038	0·66	0·108	1·90

4.2 *Major element ratio in profile section*

The bulk chemical ratios of major elements for different parts of the laterite profiles of Belgaum and Yercaud areas are given in tables 3 and 4 respectively. From these two tables the following observations are made.

Belgaum area. (i) The ratio of Fe_2O_3/Al_2O_3 decreases from basalts (0·381) to clays (0·238) to laterites (0·19) and to bauxites (0·057).

(ii) The ratio of SiO_2/Al_2O_3 decreases from basalts (2·91) to clays (1·201) to laterites (0·055) and to bauxites (0·038).

(iii) The ratio of SiO_2/Fe_2O_3 decreases from basalts (7·63) to clays (5·20) to laterites (0·25) and increases in bauxites (0·66).

(iv) The ratio of TiO_2/Al_2O_3 increases from basalts (0·070) to clays (0·0701) to laterites (0·084) and to bauxites (0·180).

Table 4. Ratio of major chemical constituents in parent rock and their lateritized products of Yercaud area

Substance	Fe_2O_3/Al_2O_3	SiO_2/Al_2O_3	SiO_2/Fe_2O_3	TiO_2/Al_2O_3	TiO_2/Fe_2O_3
Charnockites	0·26	3·46	13·06	0·05	0·17
Clays	0·07	1·28	18·63	0·44	0·031
Laterites	1·63	0·49	0·31	0·04	0·03
Bauxites	0·31	0·09	0·30	0·03	0·07

(v) The ratio of TiO_2/Fe_2O_3 increases from basalts (0·109) to clays (0·29) to laterites (0·42) and to bauxites (1·90).

Yercaud area: (i) The ratio of Fe_2O_3/Al_2O_3 does not show any linear variations.

(ii) The ratio of SiO_2/Al_2O_3 decreases from charnockites (3·46) to clays (1·28) to laterites (0·49) and to bauxites (0·09).

(iii) The ratio of SiO_2/Fe_2O_3 increases from charnockites (13·06) to clays (18·63) and decreases rapidly to laterites (0·31) and to bauxites (0·30).

(iv) The ratio of TiO_2/Al_2O_3 decreases from charnockites (0·05) to laterites (0·04) to bauxites (0·03) and increases in clays (0·44).

(v) The ratio of TiO_2/Fe_2O_3 decreases from charnockites (0·17) to clays (0·031) to laterites (0·030) and increases only in bauxites (0·07).

5. Conclusions

Bauxite deposits of the Belgaum area are characterised by high alumina, titania and low iron, silica and phosphorus contents whereas the Yercaud area bauxites contain comparatively low alumina, titania and high iron, silica and phosphorus. The triangular diagram of SiO_2–Al_2O_3–Fe_2O_3 indicates the process of desilicification, followed by deferrification, the alumina increasing gradually in both the areas, which resembles the laterite profile derived from the basaltic rocks of Mantenia, Madagascar (Schellmann 1977). The continuity between source rocks and bauxites via clays and laterites and the ratios of Fe_2O_3/Al_2O_3, SiO_2/Al_2O_3 and SiO_2/Fe_2O_3 decrease and those of TiO_2/Al_2O_3 and TiO_2/Fe_2O_3 increase from source rocks to clays to laterites to bauxites which clearly indicates that bauxites have been derived by *in situ* weathering of the respective parent rocks of both the areas.

Acknowledgements

One of the authors (JNP) is thankful to CSIR, New Delhi for financial assistance.

References

Balasubramaniam K S and Mora S 1984 *Proc. Indian Natl. Sci. Acad.* **A50** 397

Valeton I 1972 *Development in soil science. I. Bauxites*(Elsevier Publ. Co.) pp. 183–199

Schellmann W 1977 *Natural resources and development* (Tuibingin, W. Germany: Instt for Scientific Co-Operation) Vol. 5, pp. 119–134

Subramanian K S 1975 Proc. Third Regional Conf., Geology and Mineral resources of SE Asia, Bangalore, pp. 357–359

Sahasrabudhe Y S 1978 *Bull. Geol. Sur. India—Econ. Geol.* **A39** pp. 1–10

© Printed in India.

The Purimetla gabbros, Prakasam District, Andhra Pradesh, India

J RATNAKAR* and C LEELANANDAM

Geology Department, Osmania University, Hyderabad 500 007, India

*Present address: P.G. College of Science, Saifabad, Hyderabad 500 004, India

MS received 17 November 1984; revised 7 September 1985

Abstract. Gabbros at Purimetla occur in close association with the alkaline pluton. Petrography and petrochemistry of these gabbros indicate their tholeiitic nature. Chemical variation of these tholeiites suggests that an initial undersaturated tholeiitic magma yielded oversaturated fractions in the final stages of differentiation. Their regional distribution suggests that basic magmatism preceded the emplacement of the alkaline rocks in the Prakasam alkaline province.

Keywords. Gabbro; tholeiite; corona; diffusion; differentiation index; Andhra Pradesh (Purimetla/Prakasam District).

1. Introduction

The area around Purimetla in the Prakasam District of Andhra Pradesh experienced three Proterozoic magmatic emplacements. The first one produced gabbros, the second gave rise to a series of syenites constituting the Purimetla alkaline pluton and the third one produced ocellar lamprophyre dykes which traverse solely the alkaline pluton. Detailed petrographic accounts of the rocks of second and third magmatic emplacements have already been published (Leelanandam and Ratnakar 1980, 1983), and the present contribution incorporates only certain petrological aspects of the gabbros.

2. Field relationships

The gabbros occur at the northwestern and the southwestern boundaries of the alkaline pluton as triangular and roughly square-shaped masses respectively. The country rocks are granite gneisses and amphibolites; the contacts between these and the gabbros are fairly sharp (figure 1), without any chilled margins in the gabbros, suggesting that the country rocks were preheated at the time of intrusion. The gabbros are massive without perceptible layering which suggests that crystallization was not *in situ* and emplacement occurred as crystal mushes into the country rocks. The absence of xenoliths of country rocks (amphibolites and granite gneisses) in these rocks reflects their permissive emplacement and lower structural level (see Upton 1974, p. 230). The attitude of foliations of country rocks around the gabbro masses suggests their probable lopolithic form. However, gabbroic xenoliths are not uncommon in the alkaline pluton (figure 1). The xenolithic gabbros show occasional intermixing with the alkaline rocks with the resulting transitional contacts. Such a field relationship between the gabbros and alkaline rocks obviously indicates that the intrusion of the former preceded the latter.

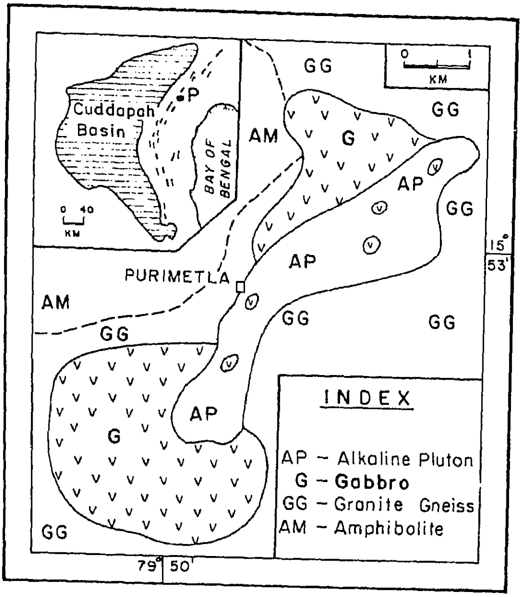

Figure 1. Lithological map of the Purimetla area. Inset map shows the location of P
(P) in the Archaean terrain (with trend lines) east of the Cuddapah Basin.

3. Methods of study

Modal analyses of the gabbros were done by the Swift automatic point counte
anorthite content of plagioclase feldspars was determined by measuring the exti
angles in sections perpendicular to X, showing two sets of cleavages parallel tc
and (010) planes (see Deer *et al* 1963). The unaltered and representative gabbros
area were analysed for SiO_2, Al_2O_3 and TiO_2 by spectrophotometry; CaO,
$Fe_2O_3^t$ and MnO by atomic absorption spectrophotometry (AAS-model-V
Techtron AA6); FeO by titrimetry; and K_2O and Na_2O by flame photometry,
Chemical Laboratories of the Atomic Minerals Division, Hyderabad. Precisio
accuracy were checked by analysing the samples in duplicate along with sta
samples.

4. Petrography

The gabbros are medium to coarse grained, heavy and dark coloured rocks. I
section they generally exhibit sub-ophitic texture; a few rocks exhibit meagre catac
deformative effects without erasing the original igneous textures.

The essential minerals are clinopyroxene, plagioclase, olivine, and orthopyr
while the accessories include biotite, opaques, sphene, apatite and calcite. The alter

Table 1. Modal compositions (vol %) of the Purimetla gabbros.

Sample	PU6	P39	Pt7A	Pt77	P30	P31
Plagioclase	38·9	37·4	45·5	49·0	59·4	76·6
Orthopyroxene	5·2	—	—	—	—	—
Clinopyroxene	30·0	40·5	24·3	25·2	14·3	—
Olivine	—	7·0	22·2	20·0	16·2	18·3
Biotite	1·0	—	—	0·4	1·0	0·4
Opaques	0·1	4·5	—	—	9·0	—
Sphene	0·1	—	—	0·4	0·1	—
Apatite	—	3·0	3·0	—	—	—
Calcite	0·1	3·6	—	2·0	—	0·1
Scapolite	0·1	4·0	5·0	3·0	—	4·6
IUGS nomenclature	Gabbro-norite		Olivine gabbros		Leuco-gabbros	

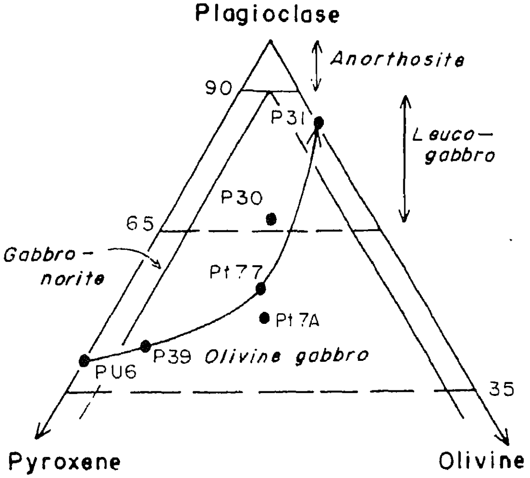

Figure 2. Triangular diagram (after IUGS 1973) showing linear modal variations of major minerals in the gabbros.

Occasionally absence of clinopyroxene leaves an anorthositic stamp on certain rocks (see for example P31 in figure 2). The crystallization sequence is chiefly controlled by fractionation of olivine, plagioclase and clinopyroxene and to some extent by orthopyroxene. Less commonly all these four mineral phases coexist in the same rock. Presence of biotite in traces may be interpreted to signify a tendency towards undersaturation in silica and involvement of little amounts of water in the closed petrogenetic system (see MacKenzie 1957; Morse 1969).

Subhedral *clinopyroxene* exhibits diallage (100) parting, zoning, exsolution lamellae of ilmeno-magnetite along *c* direction of the mineral, simple twinning, weak pleochroism in purple or pinkish colours (titan-augite), and contains partially included laths of plagioclase. Euhedral crystals of *plagioclase* (An_{46-68}) are characterised by the absence of zoning in rocks rich in this mineral and by normal zoning in those with less plagioclase; they further show interpenetration and polysynthetic twins in addition to Carlsbad twins. Euhedral to subhedral *orthopyroxene* rarely shows one set of cleavage but invariably exhibits strong pleochroism from brownish pink to violet colours.

Resorbed and sufficiently serpentinized grains of *olivine* are typified by coronation (Ratnakar 1981). The core of anhedral, corroded and fractured olivine is enveloped by a narrow shell of colourless clinopyroxene followed by a zone of pale-green amphibole with sharp contacts (figure 3). The other portion of the amphibole zone (i.e. portion very close to the adjacent plagioclase) is heavily intergrown with brownish vermicules of spinel to give a symplectitic appearance. Plagioclase, close to the coronas, characteristically exhibits clouding due to the disseminated spinel. This coronal sequence olivine-clinopyroxene-amphibole-plagioclase resembles the one reported from the Thessaloniki gabbros of North Greece (Sapountzis 1975). The shapes of the coronal minerals (clinopyroxene and amphibole) in the Purimetla gabbros are strictly controlled by the crystal outlines of olivine and plagioclase. Furthermore, the spinel-clouded plagioclase indirectly explains that these coronal minerals are formed by a simple process of two-way diffusion across the original olivine-plagioclase boundary in which iron and magnesium migrated into plagioclase, and aluminium and calcium into olivine (figure 4). Such reaction relations seem to be facilitated by hydrous environments which experienced a gradual fall of temperature (Griffin and Heier 1973).

Presence of resorbed olivine with coronas and orientation of opaque exsolution lamellae along the *c*-axis of clinopyroxene in gabbros indicate their tholeiitic nature (Sapountzis 1979).

5. Petrochemistry

The chemical analyses and CIPW norms of the Purimetla gabbros, along with the Nockolds' (1954) averages, are presented in table 2. The analyses are arranged in the increasing order of differentiation.

Table 2 reveals a close chemical proximity between gabbros of Purimetla (PU6 and Pt77) and the average olivine gabbro, 1, but not the average alkali gabbro, 2, of Nockolds. The chemical composition of the sample P31 is very close to that of the average anorthosite, 3, of Nockolds justifying its position near "anorthosite" field in figure 2.

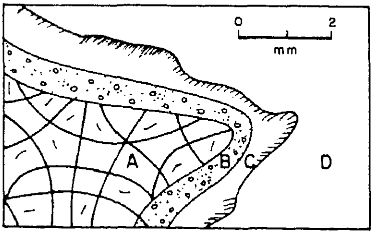

Figure 3. Corona structure with successive shells of clinopyroxene (B) and amphibole with vermicules of spinel (C) between olivine (A) and plagioclase (D)

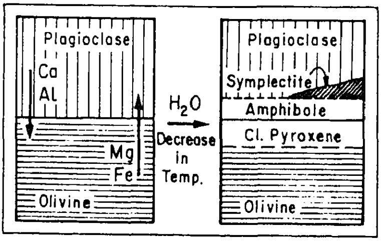

Figure 4. Visualised mode of origin of corona structure (for explanation see text)

Table 2a. Chemical analyses of the Purimetla gabbros with Nockolds' (1954) averages.

Oxide wt %	PU6	Pt77	P31	1	2	3
SiO_2	46·39	46·79	52·03	46·83	43·94	54·54
TiO_2	1·16	1·56	0·67	0·97	2·86	0·52
Al_2O_3	14·48	17·19	23·39	12·38	14·87	25·72
Fe_2O_3	3·19	3·38	1·83	1·91	4·85	0·83
FeO	8·40	7·10	2·70	8·20	7·80	1·46
MnO	0·17	0·13	0·07	0·14	0·16	0·02
MgO	12·97	9·12	3·32	10·03	9·31	0·83
CaO	10·49	10·49	11·89	11·36	12·37	9.62
Na_2O	2·00	2·56	2·63	2·03	2·32	4·66
K_2O	0·43	0·33	0·29	0·40	0·92	1·06
P_2O_5	0·11	0·07	0·07	0·12	0·44	0·11
$H_2O+/-$	0·06$^-$	0·06$^-$	0·06$^-$	0·63$^+$	0·66$^+$	0·63$^+$
LOI	0·22	0·18	0·61	—	—	—
Total	100·07	98·96	99·56			

Table 2b. CIPW norms.

	PU6		Pt77		P31	
Q	—		—		4·63	
or	2·56		1·95		1·71	
ab	16·77		21·48		22·22	
an	29·30		34·32		51·02	
wo	9·16	17·57	7·19	13·81	3·31	6·32
en	6·30		4·90		2·35	
fs	2·11		1·72		0·66	
en	3·23	4·34	4·63	6·22	6·06	7·71
fs	1·11		1·59		1·65	
fo	16·00	22·02	9·28	12·81	—	
fa	6·02		3·53		—	
mt	4·64		4·87		2·64	
il	2·20		2·98		1·27	
ap	0·26		0·17		0·01	
Total	99·66		98·61		97·53	
An/(An + Ab) × 100	63·3		61·2		69·6	
DI	19·33		23·43		28·56	

Samples PU6, Pt77 and P31 from Purimetla; 1, 2 and 3 are Nockolds' averages of olivine gabbro, alkali gabbro and anorthosite respectively; DI-differentiation index (normative Q + or + ab) of Thornton and Tuttle (1960).

The chemical variation of these rocks is demonstrated against MgO and differentiation index (DI) (Thornton and Tuttle 1960) (figure 5). SiO_2, Al_2O_3 and Na_2O show a regular increase, while CaO shows moderate to steep increase towards the culmination of differentiation. The anomalous increase of calcium is due to the highest amount of modal plagioclase in the sample (see P31 in table 1). The normative anorthite (An/

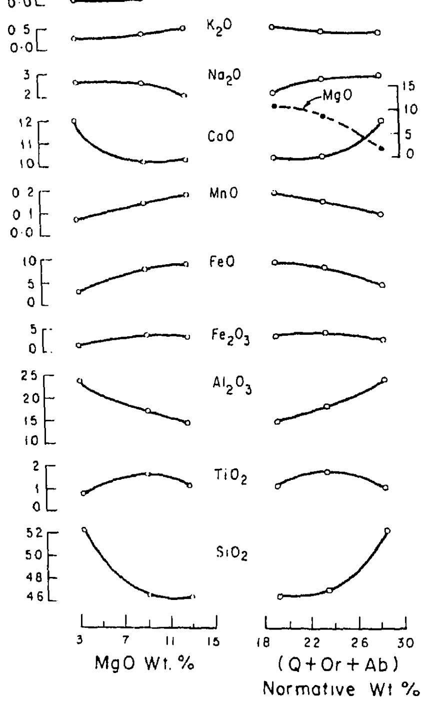

Figure 5. Major element oxide (wt %) variation against MgO and differentiation index (after Thornton and Tuttle 1960) in the Purimetla gabbros.

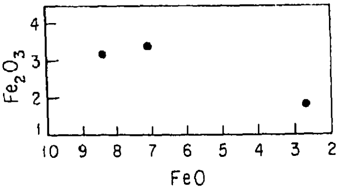

Figure 6. Variation of Fe_2O_3 and FeO in the Purimetla gabbros.

An + Ab) content also shows a perceptible increase towards the late stage of differentiation (table 2). Although a little range of variation is observed for sodium and potassium, the former shows positive correlation with DI because of increase in plagioclase while the latter shows a reciprocal relation owing to the depletion of modal biotite in these rocks. The progressive decrease of MgO against DI is mainly due to the diminution of the enstatite molecule of diopside and forsterite. Likewise the systematic and gentle fall of FeO can be correlated to the similar behaviour of "ferrosilite" of diopside and fayalite (table 2). Very minor enrichment of Fe_2O_3 in the middle stage member (compared to the early and late stage ones) is most likely due to the non-removal of sufficient iron from the magma in the form of magnetite under slightly reducing conditions. This is also revealed in the FeO-Fe_2O_3 plot (figure 6) in which a wide spread of the plots along the abscissa relative to the ordinate testifies the prevalence of reducing conditions at the time of intrusion of the magma (see Upton *et al* 1971).

The Purimetla gabbros are tholeiitic in character (figure 7a); they lack normative nepheline and have quartz and/or hypersthene. A very low content of alkalies ($Na_2O + K_2O$), less than 3% by weight (table 2), also suggests their non-alkaline nature (Yoder and Tilley 1962). Some gabbros of Purimetla appear to have high alumina basaltic affinity (for example Pt77 in figure 7b); such rocks contain considerable amounts of modal olivine typified by coronas, little normative quartz and/or hypersthene and higher amounts of Al_2O_3 (Kuno 1960; Morse 1969).

The presence of hypersthene and olivine in the norm of PU6 and Pt77 indicates their undersaturated tholeiitic character while that of quartz and hypersthene in P31 suggests its oversaturated tholeiitic nature (Yoder and Tilley 1962); the differentiation index increases from undersaturated to oversaturated tholeiites (see table 2).

In the AFM diagram these rocks define a clear but restricted compositional variation (figure 8). The closeness of the curve to the FM side of the triangle alludes that the parental magma was much more basic than the composition represented by the basic

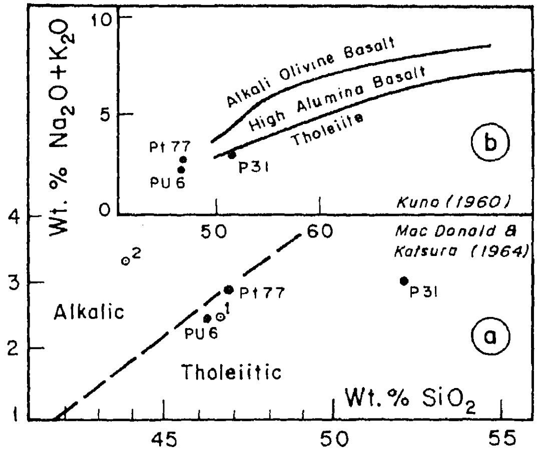

Figure 7. Alkali-silica diagrams (**a** and **b**) for the Purimetla gabbros (PU6, Pt77 & P31). For comparison Nockolds (1954) average olivine gabbro (1) and alkalic gabbro (2) are also plotted.

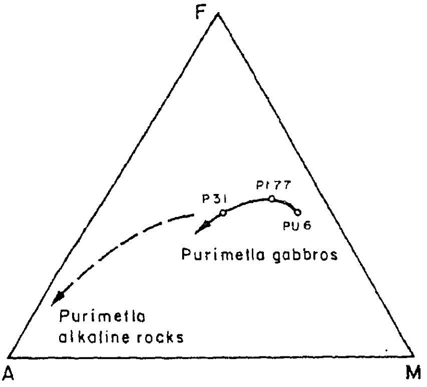

Figure 8. AFM diagram for the gabbros (solid curve) and alkaline rocks (discontinuous

end of the curve. Further it is seen in the AFM diagram that the early formed alkaline rocks of the pluton lie close to the late formed gabbroic rocks.

A very limited range of differentiation index from 19·33 to 28·56 is suggestive of curtailed temporal range of magmatic differentiation. It is during this period of reducing conditions, that the fractionation of iron took place which is reflected as perceptible convexity of the curve in the AFM diagram (figure 8).

6. Petrogenesis

The gabbros of Purimetla are formed from a tholeiitic basalt magma of possible mantle derivation. The crystallization sequence was dominated by olivine, plagioclase and clinopyroxene under low P_{H_2O} and reducing conditions. The magma underwent limited differentiation with a marked rise in the silica saturation from early undersaturated to late oversaturated member.

The rocks were emplaced as crystalline mushes and by preheating the country rocks during post-tectonic regime. The westward thrusting of the Eastern Ghat mobile belt resulted in crustal-thickening and -shortening, and mantle upwarp (Kaila and Bhatia 1981; Drury *et al* 1984) with subsequent emplacement of gabbros and alkaline rocks during different successive magmatic episodes in compressional margin setting.

7. Gabbro-alkaline rock association in the Prakasam alkaline province

7.1 *Sequence of emplacement*

Tholeiitic gabbros and alkaline rocks are the two important plutonic igneous rocks in the Prakasam alkaline province (Leelanandam 1981). There is a persistent tendency throughout this province for less differentiated magma to precede the more differentiated (cf., Upton 1974). Early tholeiitic magmas, intruded at different centres as at Chimakurti, Pasupugallu and Boggulakonda in this province, were chiefly committed to gabbro(norite)-anorthosite-troctolite range of differentiation at the time of intrusion. Alkaline rocks (with early intruded gabbros) at Settupalle (Srinivasan 1981), Purimetla (Leelanandam and Ratnakar 1980, 1983) and Uppalapadu (Leelanandam and Krishna Reddy 1981), in this province, post-date the tholeiitic magmatism. All these gabbroic and alkaline rock occurrences lie outside the eastern edge of the Cuddapah basin in an arbitrary zone 60 kms long and 20 km wide (see figure 1 in Leelanandam 1981). The early intrusion of the gabbroic rocks created focii of structural weakness which facilitated the intrusion of younger alkaline magma in this province, as in the case of the well known alkaline provinces of Greenland (Upton 1974) and the Kola Peninsula (Gerasimovskii *et al* 1974).

7.2 *Genetic relation*

The prevalence of alkaline ultramafic (melanocratic) cognate xenoliths in the alkaline plutons signifies that undersaturated basic magmas were precursors to the alkaline residues in evolution (Leelanandam and Ratnakar 1983). These parental magmas may be expected to have originated directly from the upper mantle (Gittins 1979) enriched in alkalies, or they may be derived from an early tholeiitic magma under variable degrees of clinopyroxene fractionation at depths 60-15 kms or by extended fractionation of basaltic magma under eclogite facies conditions (see Upton 1974). Periodic intrusion of this alkaline magma at different locales, subsequent to the early tholeiitic magmatism, in the Prakasam Province resulted in gabbro-alkaline rock association. The genetic meaning of this association, for instance at Purimetla, can be best understood from the field set-up (figure 1) and differentiation trends (figure 8) of these plutonic igneous rocks.

Acknowledgements

The authors are indebted to the Director, Atomic Minerals Division (AMD) for permission to analyse the Purimetla samples in the AMD Chemical Laboratories. One of the authors (JR) is thankful to the CSIR, New Delhi, for a fellowship.

References

Deer W A, Howie R A and Zussman J 1963 *Rock forming minerals* 4 *Framework silicates* (London: Longmans)
Drury S A, Harris N B W, Holt R W, Reeves-Smith G J and Wightman R T 1984 *J. Geol.* **92** 3
Gerasimovskii V I, Volkov V P, Kogarko L N and Polyakov A I 1974 in *The alkaline rocks* (ed.) H Sorensen (London: Wiley Interscience) p. 206
Gittins J 1979 in *The evolution of the igneous rocks* (ed.) H S Yoder (Princeton: Univ. Press) p. 351
Griffin W L and Heier K S 1973 *Lithos* **6** 315
IUGS 1973 *Geotimes* **18** 26
Kaila K L and Bhatia S C 1981 *Tectonophysics* **79** 129
Kuno H 1960 *J. Petrol.* **1** 121
Leelanandam C 1981 *Curr. Sci.* **50** 799
Leelanandam C and Krishna Reddy K 1981 *J. Geol. Soc. India* **22** 39
Leelanandam C and Ratnakar J 1980 *Q.J. Geol., Min. Metall. Soc. India* **52** 77
Leelanandam C and Ratnakar J 1983 *Q.J. Geol., Min. Metall. Soc. India* **55** 14
MacDonald D A and Katsura T 1964 *J. Petrol.* **5** 82
MacKenzie W S 1957 *Am. J. Sci.* **255** 481
Morse S A 1969 *Geol. Soc. Am., Mem.* **112** 140
Nockolds S R 1954 *Geol. Soc. Am. Bull.* **65** 1007
Ratnakar J 1981 *Geoviews* **9** 35
Sapountzis E S 1975 *Contrib. Mineral Petrol.* **51** 197
Sapountzis E S 1979 *J. Petrol.* **20** 37
Srinivasan T P 1981 *Geoviews* **9** 379
Thornton C P and Tuttle O F 1960 *Am. J. Sci.* **258** 342
Upton B G J 1974 in *The alkaline rocks* (ed.) H Sorensen (London: Wiley Interscience) 221
Upton B G J, Thomas J E and MacDonald R 1971 *Lithos* **4** 163
Yoder H S and Tilley C E 1962 *J. Petrol.* **3** 242

Proc. Indian Acad. Sci. (Earth Planet. Sci.), Vol. 94, No. 3, November 1985, pp. 315–321.
© Printed in India.

Framboidal pyrite from Mussoorie phosphorite and its geological implication

S C TRIPATHI

Department of Geology, Banaras Hindu University, Varanasi 221 005

MS received 19 July 1983; revised 15 October 1984

Abstract. The present paper records the occurrence of framboidal pyrite and algal pyrite in the Mussoorie phosphorite deposit. The significance of organic matter and sediment composition have also been discussed. The petrographic and analytical data indicate the dominant role of organic matter in the formation of pyrite. It is concluded from the textural study of pyrite that framboids have formed earlier in the sediment and subsequently the euhedral pyrite nucleated on them, gradually increasing in its abundance.

Keywords. Framboid; algal pyrite; phosphorite; organic matter; pyrite texture; Mussoorie.

1. Introduction

The marine, black Mussoorie phosphorite, intercalated with bedded black chert and carbonaceous shale, is the lower most unit of the Lower Tal Formation in the Dehradun district (Valdiya 1980). The samples for analysis were collected from the outcrops and underground mines of Maldeota phosphorite deposit (figure 1). The thin section study, reflected ore-microscopy and the x-ray powder diffraction results indicate that the chief phosphatic minerals are collophane, francolite and apatite in association with dolomite, calcite, quartz, pyrite, uraninite and organic matter. Chemical analysis of different varieties of phosphorite samples was carried out in order to understand the role of organic matter. Pyrite, phosphorite and organic matter are found closely associated with each other. The textural configurations of phosphorite represent a "primary fabric" (Patwardhan 1980).

2. Pyrite framboids in phosphorite

Occurrences of globular pyrite, previously understood as fossilized bacteria and named in American literature as 'framboid', have received considerable attention from earlier workers. Framboids are tiny aggregates of pyrite crystals generally between 1-100 μ in size and commonly arranged in a linear or concentric pattern.

Pyrite framboids are recognized in the Mussoorie phosphorite. They are generally spherical to sub-spherical in shape and vary in size from 1-150 μ. Framboids are found frequently arranged in linear fashion (figure 2), rarely concentric, but are also

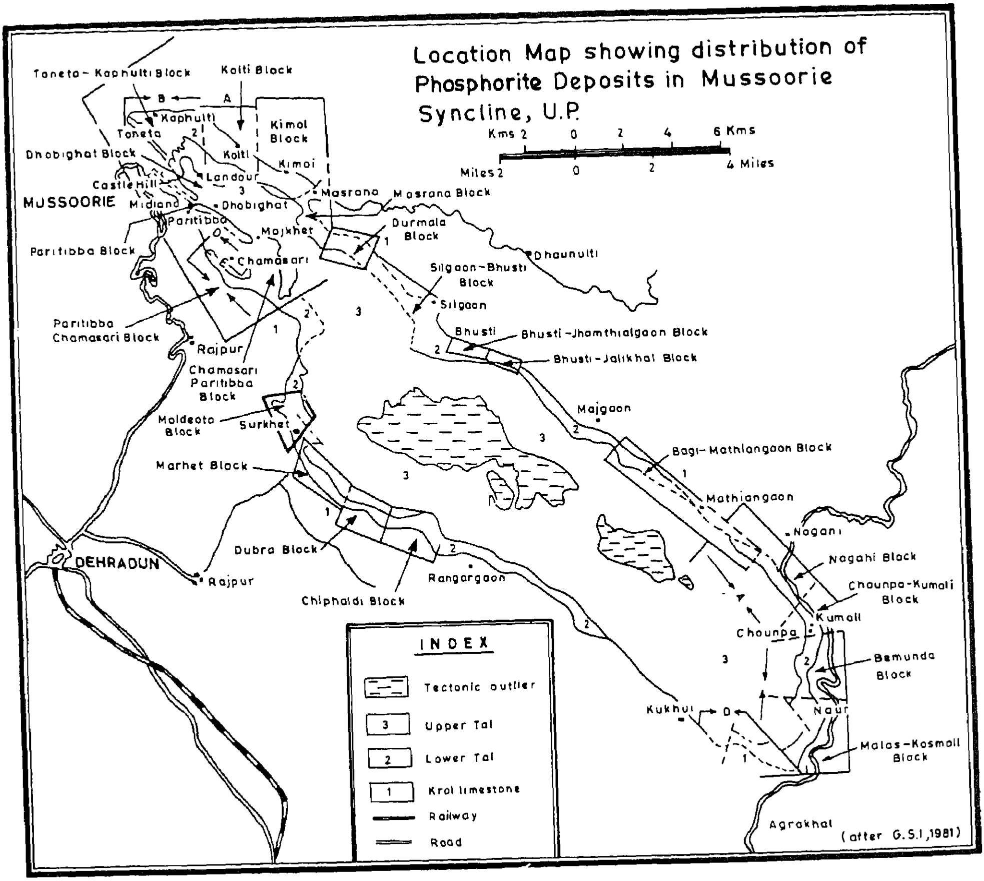

Figure 1. Location map showing the distribution of various phosphorite deposits in Mussoorie Syncline, in the Dehradun district (after Geological Survey of India 1981).

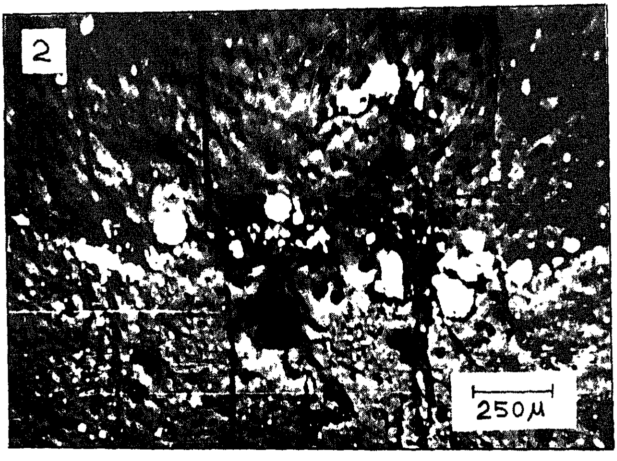

Figure 2. Pyrite framboids showing a linear arrangement (reflected light).

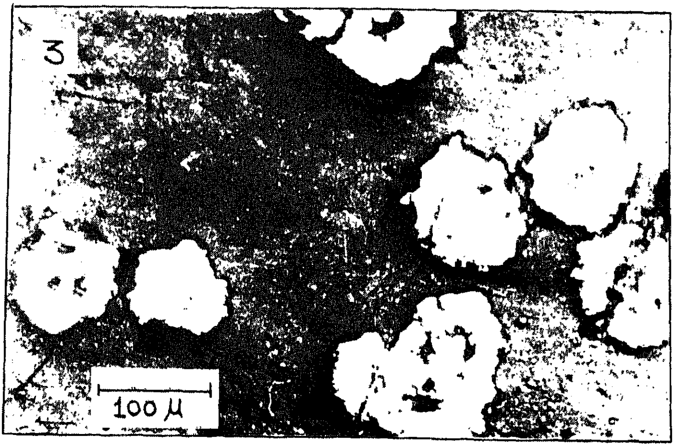

Figure 3. Pyrite framboids scattered in phosphate-organic matter (black). Note the development of crystal face (reflected light).

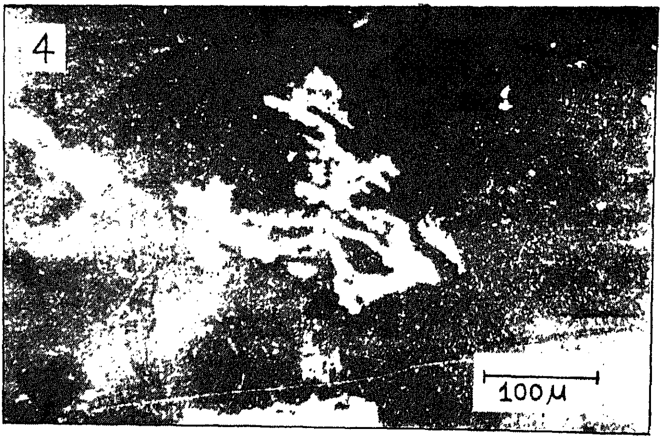

Figure 4. "Algal pyrite," note the structural peculiarities. (reflected light).

Other than framboids, pyrite also appears as well developed idioblastic crystals (figure 5), in thick and thin bands, interbedded with phosphate-organic matter which often show cross bedding. Pyrite has been commonly observed to grow symmetrically with textural configurations of phosphorite i.e. concordant layers of pyrite intergrown with stromatolites, oolites and pellets etc. Secondary veins of pyrite up to a maximum of one cm thickness are also fairly abundant in the deposit. The concentration of pyrite in phosphorite is generally very small rarely reaching up to 10%.

3. Origin of framboids

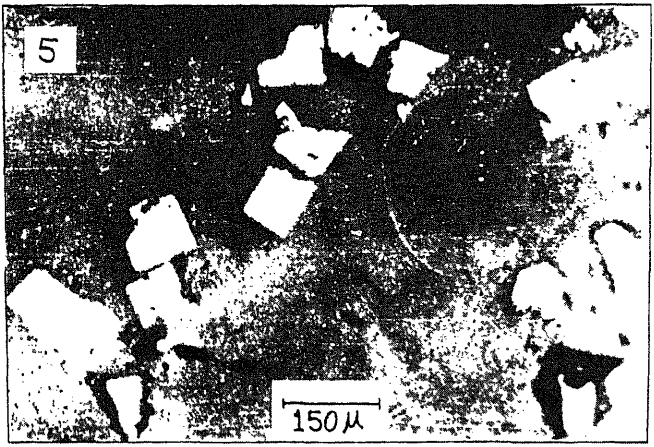

Figure 5. Idioblastic pyrite crystals scattered in phosphate-organic matter (reflected light).

origin. Some workers believe in the organic origin of framboids (Kalliokowski and Cathles 1969) while others support the inorganic hypothesis (Berner 1969; Farrand 1970; Riskard 1970; Kribek 1975; Sunagawa *et al* 1971).

Since framboids are reported both from sedimentary and volcanic rocks, it is possible that there may be more than one mode of their origin. The chemical synthesis of framboids and their discovery in hydrothermal deposits and igneous rocks (Steinike 1963, Love and Amstutz 1969), volcanogenic massive sulfide ores (Kuroko ores) of Japan (Matsukuma and Horikoshi 1970) and probably also in hydrothermal veins, certainly cast doubts on the role of organic matter in their formation. The author, however, tends to believe that organic matter plays a significant role in the formation of framboids (pyrite) particularly in the Mussoorie phosphorite, where it is primarily in association with organic matter.

4. Significance of organic matter

It is accepted nowadays that the chief source of H_2S for pyrite formation is sulphate reduction by bacteria (Berner 1978; Trudinger *et al* 1972). The sulphate reduction process consists of simultaneous oxidation of organic compound and reduction of interstitially present dissolved sulphate by heterotrophic micro-organisms living in sediments. Numerous laboratory studies indicate that sulphate reducing bacteria generally utilize simple organic molecules in the production of energy. Upon removal of dissolved oxygen from associated water by aerobic metabolism of organic matter, anaerobic sulphate reduction takes place within sediments, resulting in the production of H_2S.

Berner (1970) suggested that the available organic matter, defined as that which can be metabolized by sulphate reducing bacteria, is a primary factor limiting the amount of pyrite that can be formed in sediment. Without metabolizable organic matter, there can be no sulphate reduction and no pyrite formation. Therefore sediments high in available organic matter, should also be high in dissolved sulphide (H_2S) and ultimately ı pyrite content. It is also shown in the recent study by Berner and Raiswell (1983) ıere is a constant ratio between the rate of burial of organic carbon and pyrite ır in present day marine sediments.

mical data on different varieties of Mussoorie phosphorite (stromatolitic, oolitic, ıl, platy and fragmental phosphorites) also support Berner's (op. cit.) concept (see 1). It appears that these samples (commonly stromatolitic and oolitic phoses) showing high contents of organic carbon (C), also have higher percentages of sulphur (S) and therefore, also high iron content (Fe_2O_3). Analytical studies on ɔorie phosphorite by Mehrotra *et al* (1981) have also given similar results. Since c carbon is a crude measure of available organic matter, it is a primary limiting in the formation of pyrite in the Mussoorie phosphorite.

anic matter also plays an important role in the transformation of FeS to pyrite by ntal sulphur. In some situations the excess sulphur needed for complete ɔrmation may be lacking due to insufficient amount of sulphate reduction, ng from a low original concentration of organic matter. As a consequence of ate starvation', FeS may persist in sediments and crystallize as mackinawite, ɔtite and greigite (Berner 1970).

ɛase of Mussoorie phosphorite, however, no iron monosulphide mineral i.e. nawite, pyrrhotite or greigite, could be recognized. This clearly indicates ete transformation of FeS to pyrite by elemental sulphur. Since stromatolitic and phosphorite represent a shallow water depositional environment, elemental ır may be produced by oxidation of FeS and H_2S by dissolved oxygen mixed with ɛnts by current and wave agitation and its diffusion into the deep sediments.

Table 1. Chemical analysis of different types of Mussoorie phosphorite.

Chemical constituent	Type of phosphorite Strometolitic/ oolitic	Pelletal	Platy	Fragmental
P_2O_5	25·38	22·34	22·38	19·89
SiO_2	4·59	6·27	4·86	11·22
CaO	37·33	38·51	38·76	36·97
CO_2	15·80	14·93	15·40	15·33
Fe_2O_3	4·40	3·48	3·78	2·97
MgO	2·53	4·34	4·88	3·71
Al_2O_3	0·70	1·01	0·74	1·16
Na_2O	0·13	0·19	0·20	0·21
K_2O	0·27	0·35	0·29	0·53
F	2·20	2·02	1·86	1·48
Cl	0·03	0·21	0·09	0·25
H_2O^+	1·05	1·84	1·24	2·23
S (sulphide)	4·00	2·86	3·13	1·83
C (organic)	1·19	0·98	1·07	0·73
Total	99·60	99·34	99·79	98·51
F/P_2O_5	0·087	0·090	0·084	0·074
CO_2/P_2O_5	0·622	0·668	0·688	0·770
CaO/P_2O_5	1·470	1·723	1·775	1·864

Chemical data also suggest that the samples cannot be considered as typical fluorapatite due to the presence of higher contents of CO_2 and H_2O. The calculated ratios of CO_2/P_2O_5, F/P_2O_5 and CaO/P_2O_5 indicate a carbonate-hydroxyl-fluorapatite species (francolite) with its composition as $Ca_5(PO_4)_3$ (F, Cl, OH, CO_3). The CO_2/P_2O_5 ratio varies from 0·62 to 0·77 indicating a possible substitution of CO_3^{-2} for PO_4^{-3}. The ratio F/P_2O_5 ranges between 0·07 and 0·09 and the excess F is probably incorporated into the apatite lattice in order to balance the excess charge created by substitution of CO_3^{-2} for PO_4^{-3} (Gulbrandsen 1966). The CaO/P_2O_5 ratio varies between 1·47 and 1·86 suggesting a carbonate fluorapatite composition. The presence of higher contents of H_2O^+ also indicates the possible substitution of $(OH)_4$ for $(PO)_4$.

5. Pyrite texture and sediment composition

Sediment and pore water composition undoubtedly influence the nature and extent of intermediate iron sulphide, which may be formed and thereby determine the pyrite texture (Raiswell 1982). As discussed above, the rate of sulphate reduction is dependent on the abundance and quality of organic matter. Raiswell (op. cit.) also suggested that initially framboidal pyrite is formed by decomposition of freshly deposited, most radially metabolizable organic matter. Subsequently euhedral pyrite is formed by slow decomposition of local concentrations of organic matter. Goldhaber and Kaplan (1974) suggested separate pathways for the formation of framboidal and euhedral pyrite, depending upon metastable iron sulphide intermediates.

It has been observed in polished sections under reflected light that framboids appear to be somewhat larger in size and more massive than characteristic aggregates of tiny crystals. These seem to represent the stage between framboidal and euhedral pyrite, since no pyrite euhedra has been recognized within the framboid, and the secondary development of crystal faces in framboid (figure 2) also strengthens the view that framboidal pyrite is formed prior to the formation of euhedral pyrite. Framboids are formed earlier in the sediment by freshly deposited, fairly metabolizable organic matter and euhedral pyrite is developed later on the framboid and becomes progressively more abundant in the deposit.

With regard to the origin of 'algal pyrites', it is proposed that they might have originated by the precipitation of pyrite on some organic structure, giving them the algal appearance. Because of the syngenetic origin of pyrite with the phosphorite and organic matter, it is simultaneously grown with the textural development of phosphorite (oolites, stromatolites, pellets etc.). The development of different textures of pyrite in the Mussoorie phosphorite also indicate the heterogenous distribution, concentration and reactivity of organic matter and reactive iron content in the sediment.

6. Conclusion

Summarizing from the present study it can be concluded that organic matter, associated with phosphorite, is a controlling factor in the formation of spherical and sub-spherical pyrite framboids recognized in Mussoorie phosphorite. The chemical es of different varieties of phosphorite indicate that the samples are composed of iate-hydroxyl-fluorapatite (Francolite) with a composition $Ca_5(PO_4)_3$ (F, Cl, O_3). The textural study of pyrite has revealed that the framboids form earlier in liment and euhedral pyrite, nucleated on it, later becomes increasingly abundant deposit. 'Algal pyrite' is considered to have originated by the precipitation of on some organic structures.

wledgements

ithor is highly indebted to Prof. K K Singh, School of Studies in Geology, n University, Ujjain, for guidance. Thanks are also due to Prof. K V G K ile, IIT, Kanpur, for valuable suggestions. The author is also thankful to Prof. Iukerjee and Prof. M N Mehrotra, BHU, for valuable discussions and criticisms.

nces

K 1978 *Indian Mineral* **32** 63
R A 1969 *Econ. Geol. Bull. Soc. Econ. Geol.* **64** 383
R A 1970 *Am. J. Sci.* **268** 1
R A 1978 *Earth Planet. Sci. Lett.* **37** 492
R A and Raiswell R 1983 *Geochim. Cosmochim. Acta* **47** 855
M 1970 *Miner. Deposita* **5** 237
ber M B and Kaplan I R 1974 *The sea* (ed.) E D Goldberg Vol. 5, 569
ndsen R A 1966 *Geochim. Cosmochim. Acta* **30** 769
owski J and Cathles L 1969 *Bull. Geol. Soc. Finland* **41** 133
B 1975 *Miner. Deposita* **10** 389
G 1957 *Q.J. Geol. Soc. London* **113** 429
G and Amstutz G C 1966 *Fortschr. Miner.* **43** 273
G and Amstutz G C 1969 *Neues Jahrb. Miner. Monatsh.* **3** 97
uma T and Horikoshi E 1970 *Volcanism and ore genesis*, (ed.) T Tatsumi (Tokyo: Univ. Tokyo Press) 53
ra M N, Yadava R K and Mehrotra B N 1981 *Neues Jahrb. Miner., Abh.,* **142** 139
lhan A M 1980 Proc. 3rd Indian Geol. Congr., Poona, p. 347 Poona Univ. Press
R 1982 *Am. J. Sci.* **282** 1244
D T 1970 *Lithos* **3** 269
K 1963 *Econ. Geol. Bull. Soc. Econ. Geol.* **58** 998
wa I, Endo Y and Nakai N 1971 *Soc. Min. Geol. Jpn, Special issue,* **2** 10
ger P A, Lambert I B and Skyring G W 1972 *Econ. Geol. Bull. Soc. Econ. Geol.* **67** 1114
K S 1980 *Stratigraphy and correlations of lesser Himalayan formations* (eds.) K S Valdiya and S B tia p. 7 (N. Delhi: Hindustan Pub. Co.)

A study of the monsoonal beach processes around Alleppey, Kerala

N P KURIAN, T S SHAHUL HAMEED and M BABA
Centre for Earth Science Studies, Regional Centre, Cochin 682018, India

MS received 9 August 1984; revised 24 June 1985

Abstract. The responses of a sandy beach to the southwest monsoonal waves are studied based on biweekly observations. The onslaught of the first spell of monsoonal breakers causes maximum erosion in the sub-aerial section of the beach. However, further spells of high breakers do not affect this zone significantly. The erosion in the sub-aerial zone is followed by accretion in the nearshore zone and vice versa. Whereas the sub-aerial zone has a net erosion the total section of the beach including the nearshore zone shows near equilibrium condition. It is concluded that in spite of erosion or accretion of the sub-aerial zone, equilibrium conditions may be found in the total section of the beach.

Keywords. Beach processes; beach erosion: equilibrium beach.

1. Introduction

Studies on beach dynamics assume great importance for a coastline such as that of Kerala, which is of recent geological origin and is constantly threatened by severe erosion. Some literature on the beach processes for a few selected zones of this coastline are available (Moni 1973; Murthy 1977; Murthy and Varadachari 1980; Prasannakumar *et al* 1984, etc.) The present investigation aims at a detailed study of the beach processes in relation to the nearshore processes at Alleppey, which is a coastline about which little information is available in the literature. The study has been carried out during the most dynamic period of the year, viz, the southwest monsoon. Most of the studies on beaches are guided by the conventional definition of beach (CERC 1977) and considers only that portion of the profile which lies above the low water level. The present study has been extended to the nearshore zone, which, according to Komar (1976), is a part of the beach. The inclusion of the nearshore zone in the study is expected to give a more realistic picture of the beach processes and the sedimentation pattern.

2. Location

For the purpose of the study, a small stretch of coastline of 700 m length is selected at Alleppey (figure 1). The area of study is chosen so as to facilitate nearshore observations and measurements from the pier, which projects well into the sea. The coastline is straight, extending in a direction of 350–170° north. The beach upto a distance of about 80 m from the MLW line consists mostly of fine sand and the rest of the nearshore zone is composed of mud. The tide here is semidiurnal with a maximum range of 1 m.

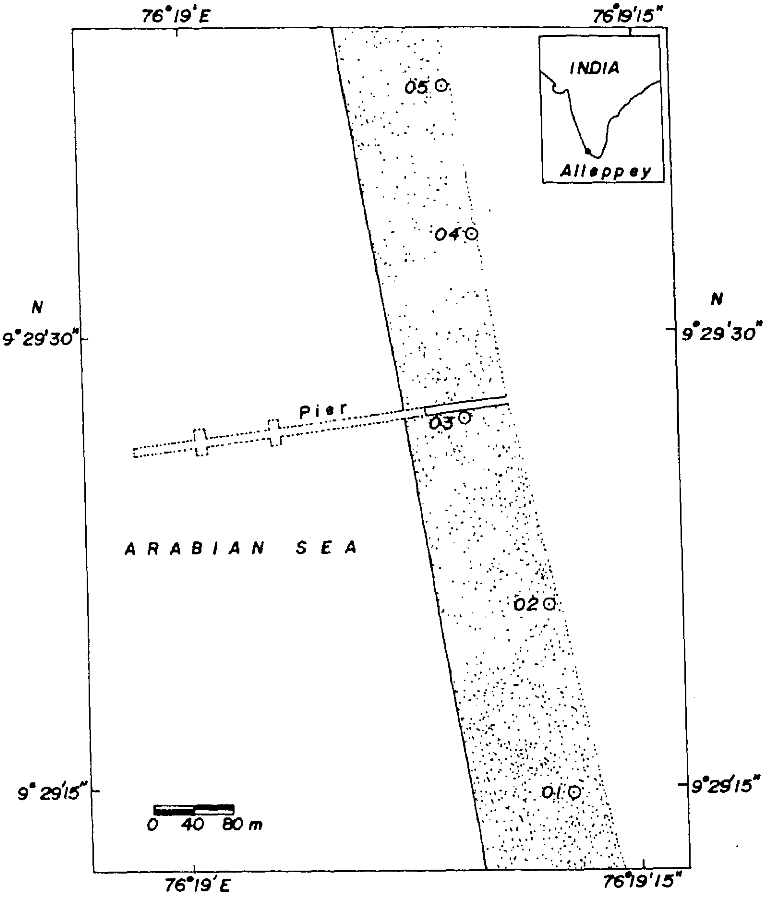

Figure 1. Location map and the area of study.

3. Methodology

The breaker parameters like period, direction and height were determined from the pier following the procedures adopted by Baba *et al* (1983) and Kurian *et al* (1984). Direction and speed of longshore currents were measured by following the trajectories of neutrally buoyant floats deployed in the surf zone. Beach profile measurements were carried out along five selected transects (figure 1) out of which the profile off Station 03 extends into the nearshore zone. The beach profile data have been used to quantify the erosion/accretion at each station and to study the onshore-offshore exchange of material.

4. Results

4.1 *Breaker characteristics*

The characteristics of the breaking waves vary considerably during this period (figure 2). From low initial values around 1·25 m the breaker heights reach high values like

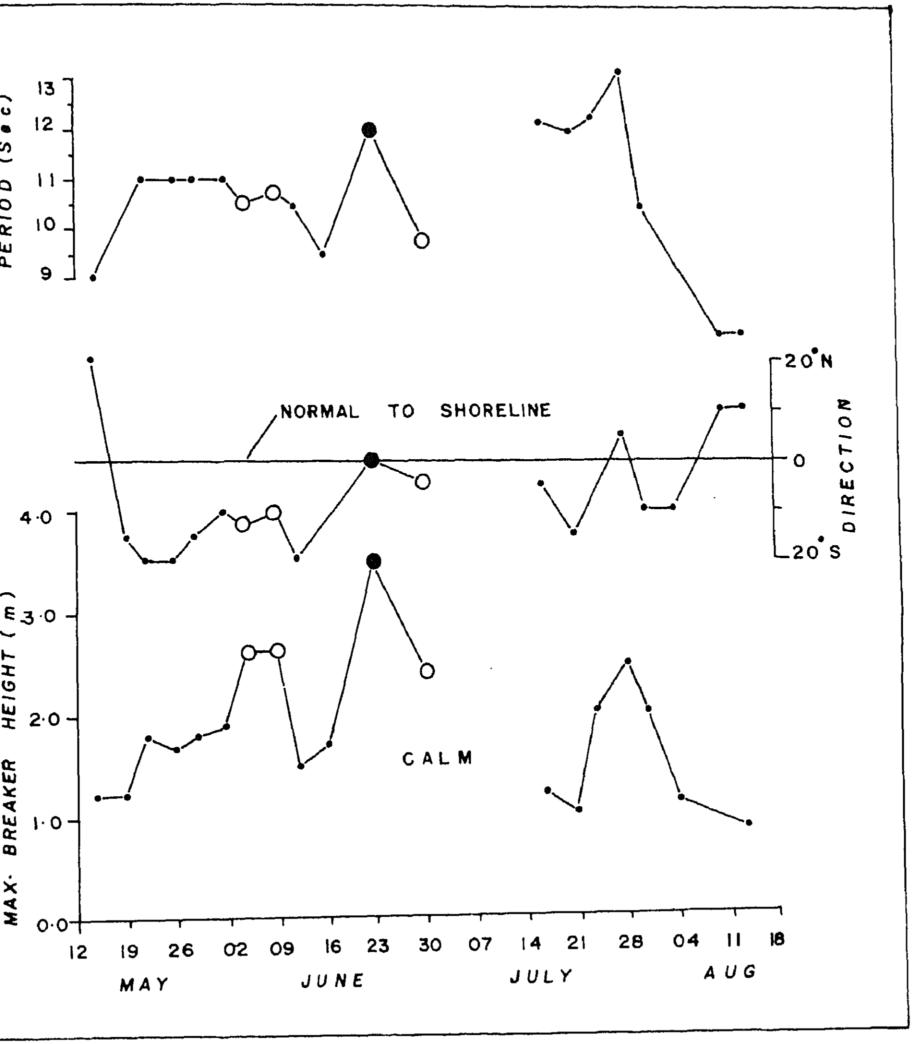

Figure 2. Variation of breaker parameters during the monsoon (•-plunging, ○-spilling and plunging, ●-spilling).

in the first half of June and after a spell of low values they reach a peak value of in the latter half of June. The distance of the breakers varies between 25 and 55 m the MLW line. Very calm sea conditions prevail in the first fortnight of July reas, from visual observations, it is seen that the adjacent nearshore zones have erate wave conditions. A moderate peak is observed by the end of July. The breaker

Due to different sets of wave trains from different directions non-persistent current directions are also observed occasionally. In May, the currents are generally sluggish and northerly in direction. However, by June the currents are mostly southerly and relatively strong. During July–August again sluggish currents are mostly observed. Southerly currents are dominant in the study area, both in magnitude and direction, especially on the southern side.

4.3 *Beach profile*

4.3a *Subaerial zone:* Since the pattern of variation in the profile is nearly the same for all stations, only the profile for station 03 (figure 4), which includes the nearshore also, is presented. However, the quantum of erosion/accretion at all stations have been computed and presented. Whereas the backshore of stations 1, 2, 4 and 5 are considerably wide extending upto 100 m, it is restricted to a maximum of 40 m for station 3 due to the base of the pier.

The beach at the start has a fair weather profile with two berms in the beginning of the season. With further advance of the season the recession of the second berm commences and scarps are formed in the foreshore. In the first quarter of June, drastic changes occur in the configuration. This zone undergoes extensive erosion resulting in considerable reduction in its width. However, by the middle of June the process is reversed and deposition is noticed. Again the process is reversed by the end of June and this zone undergoes some erosion till the beginning of July. Accretionary processes set in thereafter and by the third quarter of July this zone is considerably wide with the build-up of new berm. Erosional and accretional processes are alternatively observed in the succeeding weeks till the end of the study period.

From figure 5 it can be seen that all the stations follow more or less the same pattern of erosional or accretional tendency. However, the quantum of erosion/accretion varies from station to station. The two southernmost stations i.e., stations 01 and 02 suffer the maximum loss of about 50 m^3/m during this period. Station 04 is the least affected most of the time in this period and this station alone has a net accretion in the second fortnight of July, though for a brief period.

4.3b *Nearshore profile:* The nearshore profile is smooth in the beginning of the season (figure 4). However, as the season advances further, a break-point bar forms which extends offshore with the intensity of the breakers. With further increase in the intensity of breakers in the first quarter of June, multiple bars are observed extending upto a distance of about 70 m from MLW line and a net deposition as high as 90 m^3/m (figure 5) is found in the nearshore. Erosion of the nearshore zone takes place thereafter and the profile reaches almost the premonsoon position by the third quarter of July. However this process is interrupted by the end of July. In August erosion of the nearshore zone once again takes place, though this process is stopped by the middle of August. Thus this zone has a net accretion of 31 m^3/m during monsoon season.

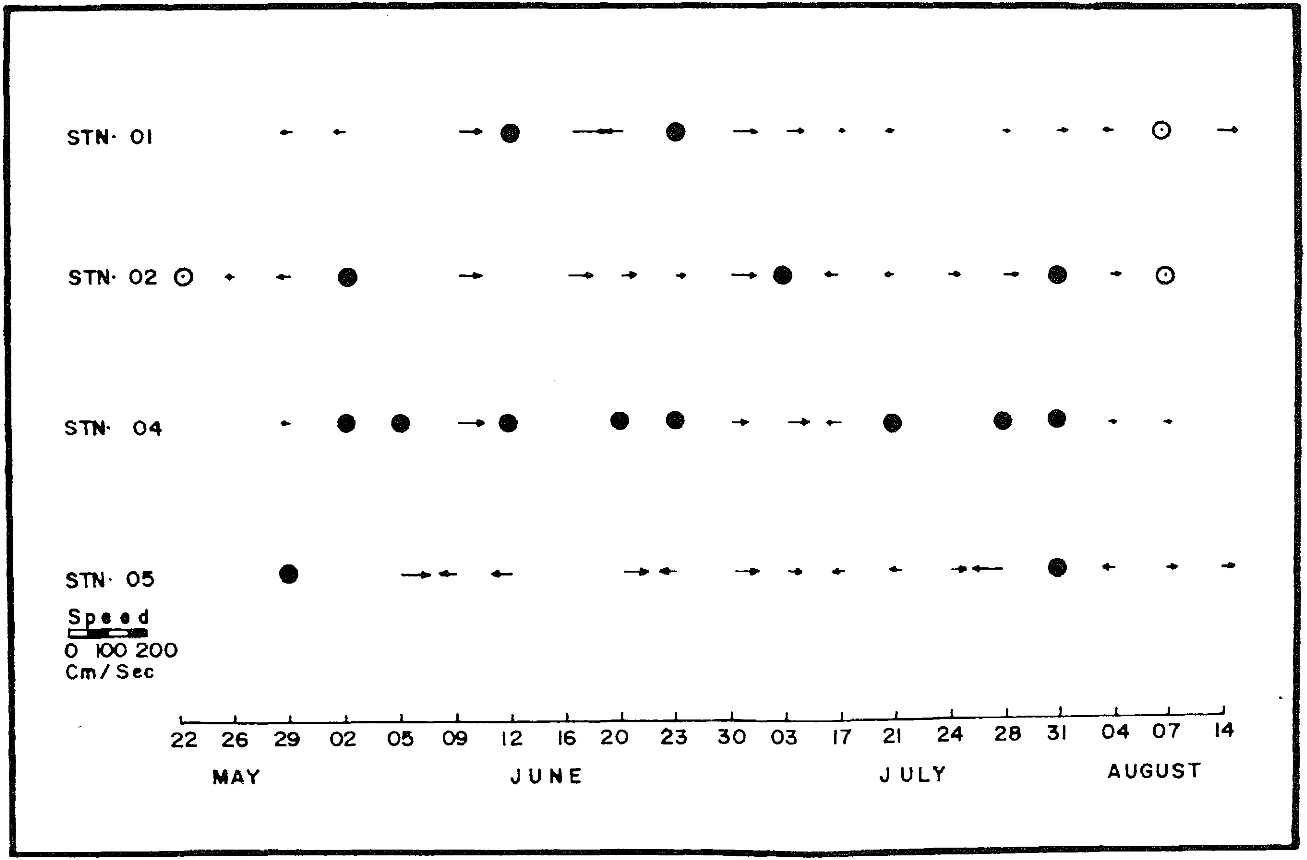

Figure 3. Longshore currents at the different stations (← upcoast (northerly); → downcoast (southerly); ● nonpersistent; ⊙ sluggish).

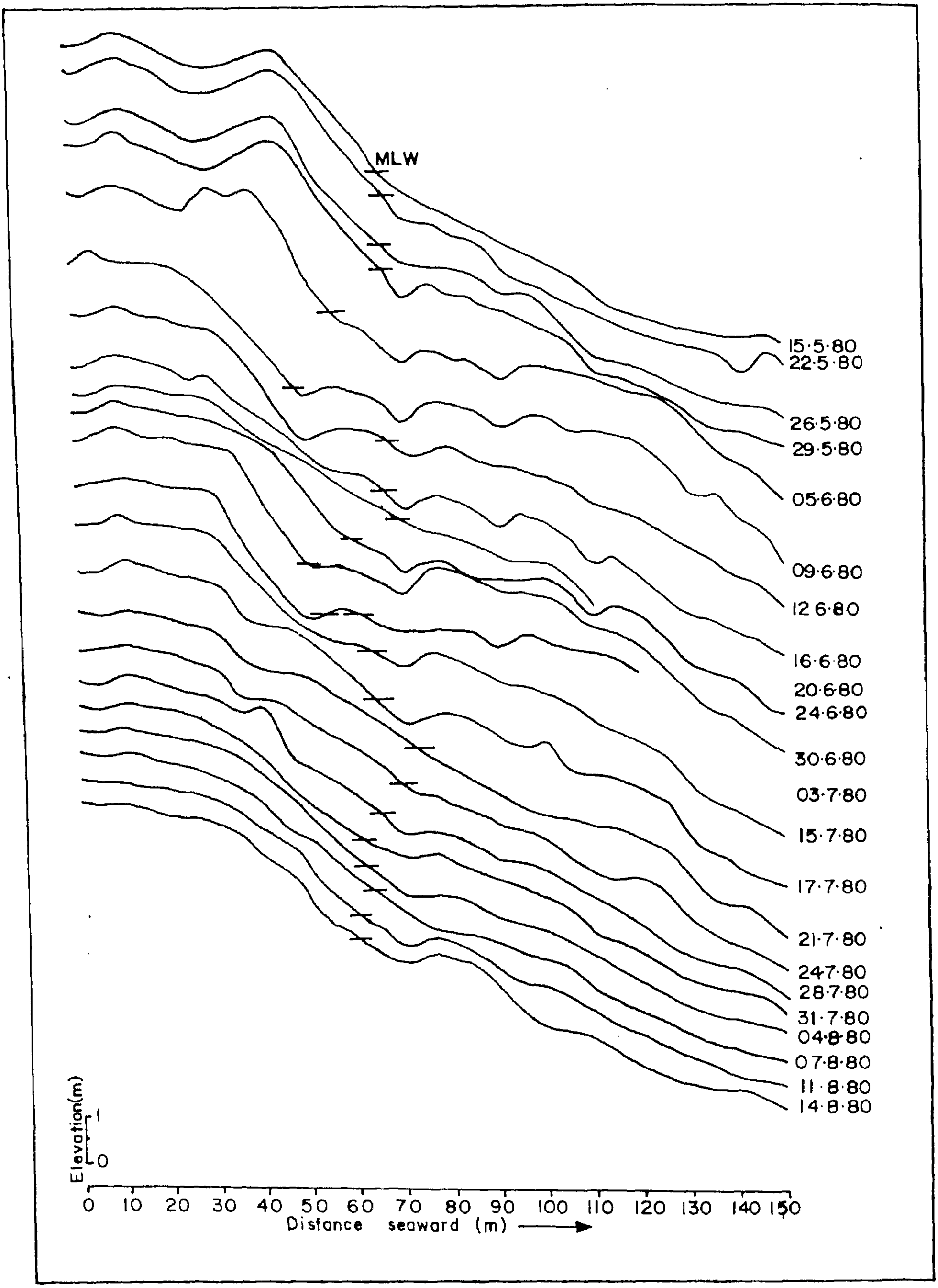

Figure 4. Beach profiles at station 20

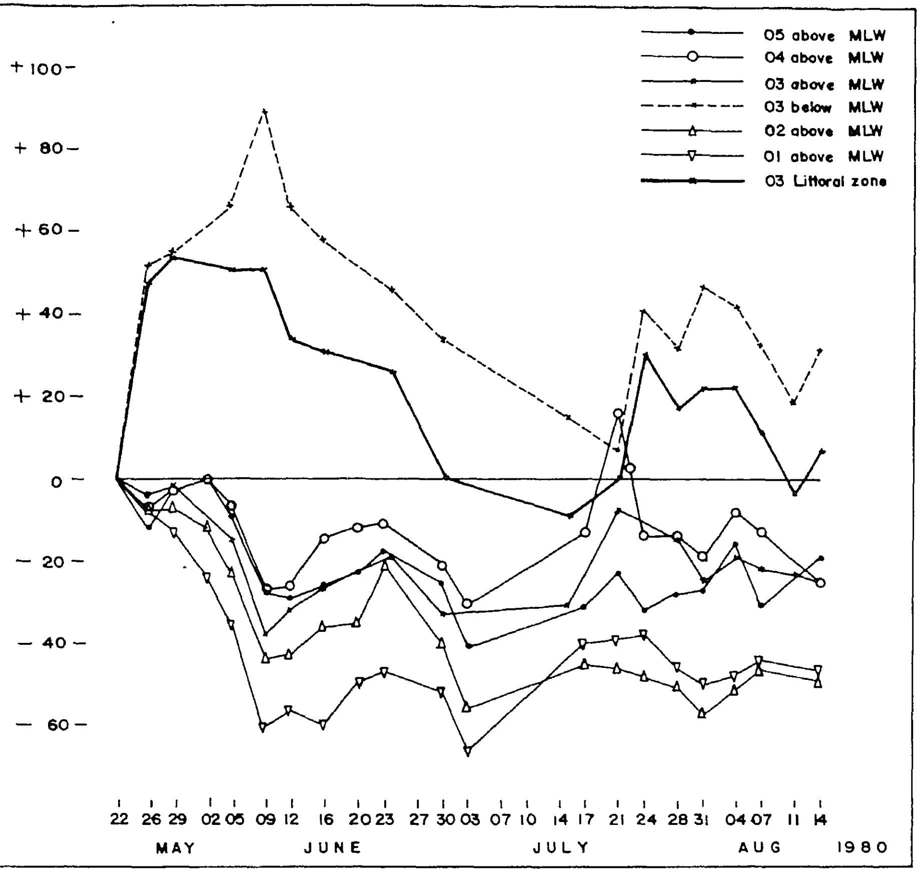

Figure 5. Cumulative erosion/accretion at the different stations.

Discussion

n the onset of monsoonal winds, the sea waves pick up and shortcrested steep waves lt from the interference of sea waves generated by the local wind and swells erated and transmitted by the general monsoonal winds. The high breakers lting from these have a disastrous effect on the beach face. The effect of the breakers be more pronounced owing to the increased wind and wave set-up during this od. The erosion from the beach face is followed by deposition in the inner nearshore hes and formation of longshore bars and troughs. The continuance of this process s to a shallow nearshore zone, as is observed by the first quarter of June. As a result, highest waves break further offshore, in the form of spilling breakers. The widening he surf zone leads to filtering of the high energy waves far away from the beach. ugh the steepest breakers of the season are observed in the last quarter of June, it period has a churning action (Komar 1976) on the substratum causing a high quantum of mud in suspension. It is possible that this mud suspension subsequently causes the occurrence of mud banks, which is a phenomena reported off this coast (Kurup 1977). The occurrence of mud banks in the inshore region of the study area is established from the calm conditions in the study area and the moderate wave conditions on either side and offshore of the study area. Erosion observed in the nearshore during this period may be due to the loss of material by way of mud suspension and alongshore transport. By the second week of July the mud bank starts disappearing and wave activity gets intensified. This leads to the onshore transport of material and subsequent accretion of the subaerial zone (figure 4). Once the nearshore profile is reshaped to the fair weather profile, any further intensification of sea conditions, as observed by the end of July, has more access to the subaerial zone resulting in onshore erosion and accretion in the nearshore zone.

A comparative study of the onshore-offshore and alongshore sediment transport could be made from figure 6. It is seen that erosion in the nearshore zone is followed by deposition in the subaerial zone and vice versa in most of the cases. Since the cases examined have more access to the straight line fit, which is indicative of complete onshore-offshore exchange, it could be concluded that the onshore-offshore transport dominates over alongshore transport during this season. That there are cases which depart widely from this straight line fit shows the occasional occurrence of alongshore transport of sediments. The periodic strengthening of the longshore current (figure 3) must be causing this alongshore transport.

The spatial and temporal variations in the quantum of erosion/accretion in the subaerial zone may be explained in relation to the longshore drift. Bowman and Dolan (1982) observed shadow zones due to the groin effect of a research pier. Even though the pier in the present study area is highly permeable as compared to the one examined by the above authors, the pier is found to be interrupting the sediment movement (Hameed *et al* 1984). Thus the higher quantum of erosion observed on the southern side could be due to the dominance of southerly longshore currents coupled with the groin effect of the pier. Due to the same reason, lesser loss of material could be expected on the northern side. But relatively more erosion has been observed at the northern most station (05) as compared to station 04. As no abnormal waves or currents are observed at this station, this erosion may be due to the end effect of the sea wall (CERC 1977), even though it is at a distance of 150 m north of station 05.

6. Conclusion

There is a net erosion in the beach (as per the conventional definition) during the monsoon season. If the nearshore portion alone is considered a net accretion is observed. But, if the beach on the whole is considered, there is more or less an equilibrium condition by the end of the monsoon period. Inspite of erosion or accretion of the subaerial zone, equilibrium conditions may be found in the total section of the beach (including the nearshore zone), as is indicated in the present study. Thus beach dynamics can be fully understood only from a study of the subaerial zone and the nearshore zone. The study underlines the necessity for a more inclusive definition of beach in the investigation of coastal processes as recommended by Komar (1976).

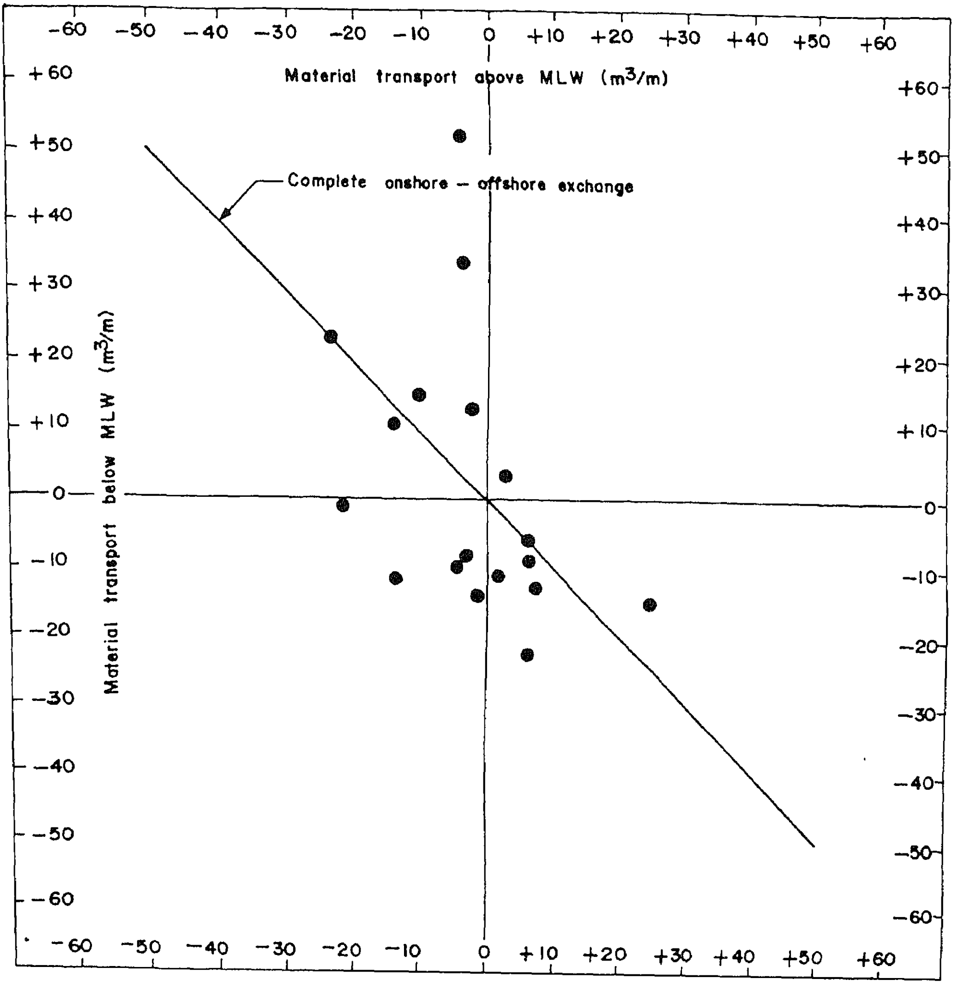

Figure 6. Scatter diagram of onshore-offshore changes.

Acknowledgements

The authors thank Dr H K Gupta for his keen interest and Dr T K Mallik, Marine Sciences Division for the encouragement and critical comments.

References

Baba M, Kurian N P, Thomas K V, Prasannakumar M, Shahul Hameed T S and Harish C M 1983 Study of the waves and refraction in relation to beach erosion along the Kerala Coast. Tech. Report No. 29 *Centre for Earth Science Studies*

Bowman M and Dolan R 1982 *Coast. Eng.* **6** 179

CERC 1977 US Army Corps of Engineers, Coastal Engineering Research Centre Shore Protection Manual Vol. I, II and III. US Government Printing Office, Washington, DC

Hameed T S S, Kurian N P and Baba M 1984 Impact of a permeable structure on shoreline development, Paper presented at the Seminar on environmental aspects of geology held at Trivandrum, Nov. 26–28.

Komar P D 1976 *Beach processes and sedimentation* (New Jersey: Prentice Hall) p. 429

Kurian N P, Shahul Hameed T S and Baba M 1984 Beach dynamics in relation to wave climate at Alleppey during monsoon season. Tech. Report No. 38 *Centre for Earth Science Studies*

Kurup P G 1977 *Bull. Dept. Mar. Sci. Univ. Cochin* **8** 72

Moni N S 1973 *J. Inst. Eng. (India)* **53** 346

Murthy C S 1977 *Studies on the physical aspects of shoreline dynamics at some selected places along the west coast of India* Ph.D. thesis, University of Kerala

Murthy C S and Varadachari V V R 1980 *Indian J. Mar. Sci.* **9** 31

Prasannakumar M, Kurian N P and Baba M 1984 A study of nearshore processes and beach profiles at Calicut. Technical Report No. 40, *Centre for Earth Science studies* pp. 12

Proceedings (Earth and Planetary Sciences)

Volume 94, 1985

SUBJECT INDEX

- Accelerator mass spectroscopy
  - Tracing quartz through the environment 1
- Algal pyrite
  - Framboidal pyrite from Mussoorie phosphorite and its geological implication 315
- All-India rainfall
  - Relationship between all-India summer monsoon rainfall and southern oscillation/eastern equatorial Pacific sea surface temperature 199
- Anomaly map
  - Anomaly map of Z component of the Indian subcontinent from magnetic satellite data 111
- Anorogenic magmatism
  - The Mannapra syenite, Central Kerala, India: Geochemistry, petrogenesis and bearing on anorogenic magmatism 43
- Annual erosion rates
  - Preliminary studies on the geochemistry of the Cauvery river basin 99
- Antarctica
  - Hydrography and circulation off the Antarctica in the Indian Ocean region 13
- Anthropogenic changes
  - Global temperature changes: relative importance of greenhouse constituents of the atmosphere as calculated with a 1-d radiative-convective model 139
- Arabian Sea
  - Summer cooling of the Arabian Sea—a review 117
- Arcing of activated charcoal ash
  - Emission spectrographic estimation of gold 279
- Atmospheric carbon dioxide
  - Global temperature changes: relative importance of greenhouse constituents of the atmosphere as calculated with a 1-d radiative-convective model 139

- Basal flow
  - Basal flow rate of Changme-Khangpu glacier, Sikkim Himalaya based on ^{32}Si and ^{210}Pb chronology 83
- Batholith
  - Petrology of thermally metamorphosed pelitic rocks in the Champawat Area, Kumaun Himalaya 57
- Bauxites
  - Geochemistry of bauxites of Belgaum (Karnataka) and Yeracaud (Tamil Nadu) areas 297
- Beach erosion
  - A study of the monsoonal beach processes around Alleppey, Kerala 323
- Beach processes
  - A study of the monsoonal beach processes around Alleppey, Kerala 323
- Bent
  - Comparison of electron density models with incoherent scatter radar observations at the equator 7
- Bhaskara II SAMIR
  - Remote sensing of atmospheric water vapour from Bhaskara II SAMIR data and its comparison with NOAA-7 water vapour data 237
- Bouguer reduced gravity
  - An analytical technique for rapid determination of surface rock density 91

- Cauvery river basin
  - Preliminary studies on the geochemistry of the Cauvery river basin 99
- Champawat
  - Petrology of thermally metamorphosed pelitic rocks in the Champawat Area, Kumaun Himalaya 57
- Circulation pattern
  - Hydrography and circulation off the Antarctica in the Indian Ocean region 13
- Climatological mean patterns
  - Summer cooling of the Arabian Sea—a review 117
- Coastal circulation
  - Monthly-mean wind stress along with coast of the north Indian Ocean 129
- Coefficients of variability
  - Interannual and long-term variability of the summer monsoon and its possible link with northern hemispheric surface air temperature 187
- Co-genetic behaviour
  - Preliminary studies on the geochemistry of the Cauvery river basin 99

Compact radio source
  Detection of large scale electron density irregularities during IPS observations at 103 MHz 77
Complex gradient
  Analysis of gravity gradients over a thin infinite sheet 71
Conducting sheets
  Transient electromagnetic response due to a pair of horizontal conducting sheets in a loop field 269
Continental effect
  Oxygen and hydrogen isotopic ratios in groundwaters and river waters from India 283
Corona
  The Purimetla gabbros, Prakasam District, Andhra Pradesh, India 305
Correlation coefficient
  An analytical technique for rapid determination of surface rock density 91
Correlation interferometer
  Detection of large scale electron density irregularities during IPS observations at 103 MHz 77
Correlation studies
  Vertical component MAGSAT anomalies and Indian tectonic boundaries 35
Cosmic ray produced isotopes
  Tracing quartz through the environment 1

Decadal averages
  Interannual and long-term variability of the summer monsoon and its possible link with northern hemispheric surface air temperature 187
Differentiation index
  The Purimetla gabbros, Prakasam District, Andhra Pradesh, India 305
Diffusion
  The Purimetla gabbros, Prakasam District, Andhra Pradesh, India 305
Digital filtering
  Quasi-biennial oscillation in geomagnetic disturbance field 29
Drift velocity
  HF doppler observations on the occurrence of equatorial spread-F 261
Drought
  Global features of upper-tropospheric zonal wind and thermal fields during anomalous monsoon situations 211

Eddy transports
  The sensitivity of the northern hemisphere summer mean meridional circulation to changes in the large scale eddy forcing 219
Ekman transport
  Monthly-mean wind stress along the coast of the north Indian Ocean 129
Electron density model
  Comparison of electron density models with incoherent scatter radar observations at the equator 7
Emission spectrography
  Emission spectrographic estimation of gold 279
Environmental radioisotopes
  Basal flow rate of Changme-Khangpu glacier, Sikkim Himalaya based on ^{32}Si and ^{210}Pb chronology 83
Equator
  Comparison of electron density models with incoherent scatter radar observations at the equator 7
Equatorial spread-F
  HF doppler observations on the occurrence of equatorial spread-F 261
Equilibrium beach
  A study of the monsoonal beach processes around Alleppey, Kerala 323
Erosion
  Tracing quartz through the environment 1
Estimation of gold
  Emission spectrographic estimation of gold 279

Fourier analysis
  Interaction of monsoon with northern hemisphere mid-latitude circulation 147
Framboid
  Framboidal pyrite from Mussoorie phosphorite and its geological implication 315

Gabbro
  The Purimetla gabbros, Prakasam District, Andhra Pradesh, India 305
Geochemistry
  The Mannapra syenite, Central Kerala, India: Geochemistry, petrogenesis and bearing on anorogenic magmatism 43
  Preliminary studies on the geochemistry of the Cauvery river basin 99
Geomagnetic field
  Quasi-biennial oscillation in geomagnetic disturbance field 29
Gold adsorption
  Emission spectrographic estimation of gold 279
Global climatic variability
  Interannual and long-term variability of the summer monsoon and its possible link with northern hemispheric surface air temperature 187

Global temperature changes
Global temperature changes: relative importance of greenhouse constituents of the atmosphere as calculated with a 1-d radiative-convective model 139
Grano-diorite
Petrology of thermally metamorphosed pelitic rocks in the Champawat Area, Kumaun Himalayas 57
Gravity interpretation
Analysis of gravity gradients over a thin infinite sheet 71
Gravity waves
Detection of large scale electron density irregularities during IPS observations at 103 MHz 77
Ground relief
An analytical technique for rapid determination of surface-rock density 91
Groundwater
Oxygen and hydrogen isotopic ratios in groundwaters and river waters from India 283
Group height
HF doppler observations on the occurrence of equatorial spread-F 261

HF doppler observations
HF doppler observations on the occurrence of equatorial spread-F 261
Himalaya
Basal flow rate of Changme-Khangpu glacier, Sikkim Himalaya based on ^{32}Si and ^{210}Pb chronology 83
Hornblende-hornfels facies
Petrology of thermally metamorphosed pelitic rocks in the Champawat Area, Kumaun Himalayas 57
Hornfels
Petrology of thermally metamorphosed pelitic rocks in the Champawat Area, Kumaun Himalayas 57
Hydrography
Hydrography and circulation off the Antarctica in the Indian Ocean region 13

Incoherent scatter radar
Comparison of electron density models with incoherent scatter radar observations at the equator 7
Indian Ocean
Hydrography and circulation off the Antarctica in the Indian Ocean region 13
in situ weathering
Geochemistry of bauxites of Belgaum (Karnataka) and Yeracaud (Tamil Nadu) areas 297
International reference ionosphere
Comparison of electron density models with incoherent scatter radar observations at the equator 7
Interplanetary scintillation
Detection of large scale electron density irregularities during IPS observations at 103 MHz 77
Ionospheric refraction
Detection of large scale electron density irregularities during IPS observations at 103 MHz 77
Isotopic composition
Oxygen and hydrogen isotopic ratios in groundwaters and river waters from India 283

Layer height
HF doppler observations on the occurrence of equatorial spread-F 261
Linear interpolation
An analytical technique for rapid determination of surface rock density 91
Long range prediction
Interannual and long-term variability of the summer monsoon and its possible link with northern hemispheric surface air temperature 187

Magnetic high
Anomaly map of Z component of the Indian subcontinent from magnetic satellite data 111
Magnetic low
Anomaly map of Z component of the Indian subcontinent from magnetic satellite data 111
MAGSAT anomalies
Vertical component MAGSAT anomalies and Indian tectonic boundaries 35
MAGSAT data
Anomaly map of Z component of the Indian subcontinent from magnetic satellite data 111
Meridional section
Hydrography and circulation off the Antarctica in the Indian Ocean region 13
Meteorite falls
Correction of the paper "A study of meteorite falls" 185
Microwaves
A study on the sensitivity of the radar scattering coefficient to oceanic winds 249
Mid-latitude circulation
Interaction of monsoon with northern hemisphere mid-latitude circulation 147
Mineralogy
The Mannapra syenite, Central Kerala, India: Geochemistry, petrogenesis and bearing on anorogenic magmatism 43
Momentum transport
Interaction of monsoon with northern hemisphere mid-latitude circulation 147

Monsoon depression
  Short range prediction with a multi-level primitive equation model 159
Monsoon failure
  Interannual and long-term variability of the summer monsoon and its possible link with northern hemispheric surface air temperature 187
Monsoon vapour
  Oxygen and hydrogen isotopic ratios in groundwaters and river waters from India 283
Mussoorie
  Framboidal pyrite from Mussoorie phosphorite and its geological implication 315

Narmada lineament
  Anomaly map of *Z* component of the Indian subcontinent from magnetic satellite data 111
NOAA satellite
  Remote sensing of atmospheric water vapour from Bhaskara II SAMIR data and its comparison with NOAA-7 water vapour data 237
Northern hemispheric surface air temperature
  Interannual and long-term variability of the summer monsoon and its possible link with northern hemispheric surface air temperature 187
North Indian Ocean
  Monthly-mean wind stress along the coast of the north Indian Ocean 129
Numerical prediction
  Short range prediction with a multi-level primitive equation model 159

Ocean spectrum
  A study on the sensitivity of the radar scattering coefficient to oceanic winds 249
Organic matter
  Framboidal pyrite from Mussoorie phosphorite and its geological implication 315
Overburden
  Transient electromagnetic response due to a pair of horizontal conducting sheets in a loop field 269

Pacific sea surface temperature
  Relationship between all-India summer monsoon rainfall and southern oscillation/eastern equatorial Pacific sea surface temperature 199
Parent rocks
  Geochemistry of bauxites of Belgaum (Karnataka) and Yeracaud (Tamil Nadu) areas 297
Pelitic
  Petrology of thermally metamorphosed pelitic rocks in the Champawat Area, Kumaun Himalaya 57
Petrogenesis
  The Mannapra syenite, Central Kerala, India: Geochemistry, petrogenesis and bearing on anorogenic magmatism 43
Phosphorite
  Framboidal pyrite from Mussoorie phosphorite and its geological implication 315
Power spectral analysis
  Quasi-biennial oscillation in geomagnetic disturbance field 29
Primitive equation model
  Short range prediction with a multi-level primitive equation model 159
Pyrite texture
  Framboidal pyrite from Mussoorie phosphorite and its geological implication 315

Quartz
  Tracing quartz through the environment 1
Quasi-biennial oscillation
  Quasi-biennial oscillation in geomagnetic disturbance field 29

Radar scattering coefficient
  A study on the sensitivity of the radar scattering coefficient to oceanic winds 249
1-d radiative-convective model
  Global temperature changes: relative importance of greenhouse constituents of the atmosphere as calculated with a 1-d radiative-convective model 139
Remote sensing
  Remote sensing of atmospheric water vapour from Bhaskara II SAMIR data and its comparison with NOAA-7 water vapour data 237

Sea surface wind speed
  A study on the sensitivity of the radar scattering coefficient to oceanic winds 249
Second derivatives
  Quasi-biennial oscillation in geomagnetic disturbance field 29
Sediment load
  Preliminary studies on the geochemistry of the Cauvery river basin 99
Sensible heat
  Interaction of monsoon with northern hemisphere mid-latitude circulation 147
Sensitivity experiments
  The sensitivity of the northern hemisphere summer mean meridional circulation to changes in the large scale eddy forcing 219
Slicing correlation
  Relationship between all-India summer monsoon rainfall and southern oscillation/eastern equatorial Pacific sea surface temperature 199

Southern oscillation
  Relationship between all-India summer monsoon rainfall and southern oscillation/eastern equatorial Pacific sea surface temperature 199
Southwest monsoon
  Global features of upper-tropospheric zonal wind and thermal fields during anomalous monsoon situations 211
Subsolidus reequilibration
  The Mannapra syenite, Central Kerala, India: Geochemistry, petrogenesis and bearing on anorogenic magmatism 43
Summer cooling
  Summer cooling of the Arabian Sea—a review 117
Surface heat losses
  Summer cooling of the Arabian Sea—a review 117
Surface rock density
  An analytical technique for rapid determination of surface rock density 91
Syenite
  The Mannapra syenite, Central Kerala, India: Geochemistry, petrogenesis and bearing on anorogenic magmatism 43
Symmetric model
  The sensitivity of the northern hemisphere summer mean meridional circulation to changes in the large scale eddy forcing 219

Tectonic boundaries
  Vertical component MAGSAT anomalies and Indian tectonic boundaries 35
Thin sheet
  Analysis of gravity gradients over a thin infinite sheet 71
Tholeiite
  The Purimetla gabbros, Prakasam District, Andhra Pradesh, India 305
Trace gases
  Global temperature changes: relative importance of greenhouse constituents of the atmosphere as calculated with a 1-d radiative-convective model 139
Transient response
  Transient electromagnetic response due to a pair of horizontal conducting sheets in a loop field 269
Transition zone
  Transient electromagnetic response due to a pair of horizontal conducting sheets in a loop field 269
Turbulent mixing
  Summer cooling of the Arabian Sea—a review 117

Upper troposphere
  Global features of upper-tropospheric zonal wind and thermal fields during anomalous monsoon situations 211
Upwelling
  Monthly-mean wind stress along the coast of the north Indian Ocean 129

Variability of the summer monsoon
  Interannual and long-term variability of the summer monsoon and its possible link with northern hemispheric surface air temperature 187
Vertical shift velocity
  HF doppler observations on the occurrence of equatorial spread-F 261

Water vapour
  Remote sensing of atmospheric water vapour from Bhaskara II SAMIR data and its comparison with NOAA-7 water vapour data 237
Wind stress
  Monthly-mean wind stress along the coast of the north Indian Ocean 129

X-ray fluorescence
  Preliminary studies on the geochemistry of the Cauvery river basin 99

Z component
  Anomaly map of *Z* component of the Indian subcontinent from magnetic satellite data 111
Zonal winds
  Global features of upper-tropospheric zonal wind and thermal fields during anomalous monsoon situations 211

AUTHOR INDEX

Agrawal P K
  see Negi J G 35
Alurkar S K
  Detection of large scale electron density irregularities during IPS observations at 103 MHz 77
Antony M K
  see Shetye Satish R 129
Appangoudar S M
  see Pattan J N 297
Arnold J R
  see Lal D 1
Arur M G
  Anomaly map of *Z* component of the Indian subcontinent from magnetic satellite data 111
Awade S T
  Interaction of monsoon with northern hemisphere mid-latitude circulation 147

Baba M
  see Kurian N P 323
Bains P S
  see Arur M G 111
Bawiskar S M
  see Awade S T 147
Bhattacharya S K
  Oxygen and hydrogen isotopic ratios in groundwaters and river waters from India 283
Bhonsle R V
  see Alurkar S K 77

Das K Brijraj
  Petrology of thermally metamorphosed pelitic rocks in the Champawat Area, Kumaun Himalaya 57
Dugam S S
  see Verma R K 187

Gohil B S
  see Pathak P N 237
Goswami B N
  The sensitivity of the northern hemisphere summer mean meridional circulation to changes in the large scale eddy forcing 219
Grieken R Van
  see Subramanian V 99
Gupta S K
  see Bhattacharya S K 283

Hameed T S Shahul
  see Kurian N P 323
Hingane L S
  Global features of upper-tropospheric zonal wind and thermal fields during anomalous monsoon situations 211

Joseph K C
  Emission spectrographic estimation of gold 279

Kabra Satyanarayan
  see Nagendra R 269
Krishna Kumar V
  see Shetye R Satish 129
Krishnamurthy R V
  see Bhattacharya S K 283
Kurian N P
  A study of the monsoonal beach processes around Alleppey, Kerala 323

Lal D
  Tracing quartz through the environment 1
Lal Jeevan
  see Arur M G 111
Lal M
  Global temperature changes: relative importance of greenhouse constituents of the atmosphere as calculated with a 1-d radiative convective model 139
Leelanandam C
  see Ratnakar J 305

Mathew Basil
  see Sharma G S 13
Mooley D A
  Relationship between all-India summer monsoon rainfall and southern oscillation/eastern equatorial Pacific sea surface temperature 199

Nagendra R
  Transient electromagnetic response due to a pair of horizontal conducting sheets in a loop field 269
Nair P Velayudhan
  see Vikram Kumar B T 261
Negi J G
  Vertical component MAGSAT anomalies and Indian tectonic boundaries 35
Nijampurkar V N
  Basal flow rate of Changme-Khangpu glacier, Sikkim Himalaya based on ^{32}Si and ^{210}Pb chronology 83

Palmer Carl D
  see Wickman Frans E 185
Parthasarathy B
  see Mooley D A 199
Pathak P N
  Remote sensing of atmospheric water vapour from Bhaskara II SAMIR data and its comparison with NOAA-7 water vapour data 237
Patil S D
  see Hingane L S 211
Pattan J N
  Geochemistry of bauxites of Belgaum (Karnataka) and Yeracaud (Tamil Nadu) areas 297

Raj Kumar
  see Sarkar Abhijit 249
Ram Babu H V
  see Sinha G D J Sivakumar 71
Ramdass G
  An analytical technique for rapid determination of surface rock density 91
Ramesh Babu V
  see Sastry J S 117
Rangarajan G K
  Quasi-biennial oscillation in geomagnetic disturbance field 29
Rao K C S
  see Lal M 139
Rao I B Ramaprasada
  see Nagendra R 269
Rao P B
  see Vikram Kumar B T 7
  see Vikram Kumar B T 261
Rao S M Varaprasada
  see Ramdass G 91
Ratnakar J
  The Purimetla gabbros, Prakasam District, Andhra Pradesh, India 305
Rupa Kumar K
  see Hingane L S 211

Santosh M
  The Mannapra syenite, Central Kerala, India: Geochemistry, petrogenesis and bearing on anorogenic magmatism 43
Sarkar A
  see Pathak P N 237
Sarkar Abhijit
  A study on the sensitivity of the radar scattering coefficient to oceanic winds 249
Sastry J S
  Summer cooling of the Arabian Sea—a review 117
Sharma A K
  see Alurkar S K 77
Sharma G S
  Hydrography and circulation off the Antarctica in the Indian Ocean region 13
Shenoi S Satheesh Chandra
  see Shetye R Satish 129
Shetye R Satish
  Monthly-mean wind stress along the coast of the north Indian Ocean 129
Singh S S
  Short range prediction with a multi-level primitive equation model 159
Sinha G D J Sivakumar
  Analysis of gravity gradients over a thin infinite sheet 71
Sontakke N A
  see Mooley D A 199
Subramaniam K
  see Verma R K 187
Subramanian V
  Preliminary studies on the geochemistry of the Cauvery river basin 99

t′ Dack L Van
  see Subramanian V 99
Thakur N K
  see Negi J G 35
Thara K G
  see Santosh M 43
Totagi M Y
  see Awade S T 147
Tripathi S C
  Framboidal pyrite from Mussoorie phosphorite and its geological implication 315

Vats H O
  see Alurkar S K 77
Verma R K
  Interannual and long-term variability of the summer monsoon and its possible link with northern hemispheric surface air temperature 187

Vijaya Raghava M S
see Ramadass G 91
Vikram Kumar B T
Comparison of electron density models with incoherent scatter radar observations at the equator 7
Vikram Kumar B T
HF doppler observations on the occurrence of equatorial spread-F 261
Wickman Frans E
Correction of the paper "A study of meteorite falls" 185